

Oscar Castro-Orgaz  
Willi H. Hager

# Shallow Water Hydraulics

EXTRAS ONLINE



Springer

# Shallow Water Hydraulics

Oscar Castro-Orgaz · Willi H. Hager

# Shallow Water Hydraulics



Springer

Oscar Castro-Orgaz  
University of Córdoba  
Córdoba, Spain

Willi H. Hager  
VAW, ETH Zürich  
Zürich, Switzerland

ISBN 978-3-030-13072-5      ISBN 978-3-030-13073-2 (eBook)  
<https://doi.org/10.1007/978-3-030-13073-2>

© Springer Nature Switzerland AG 2019

This work is subject to copyright. All rights are reserved by the Publisher, whether the whole or part of the material is concerned, specifically the rights of translation, reprinting, reuse of illustrations, recitation, broadcasting, reproduction on microfilms or in any other physical way, and transmission or information storage and retrieval, electronic adaptation, computer software, or by similar or dissimilar methodology now known or hereafter developed.

The use of general descriptive names, registered names, trademarks, service marks, etc. in this publication does not imply, even in the absence of a specific statement, that such names are exempt from the relevant protective laws and regulations and therefore free for general use.

The publisher, the authors and the editors are safe to assume that the advice and information in this book are believed to be true and accurate at the date of publication. Neither the publisher nor the authors or the editors give a warranty, expressed or implied, with respect to the material contained herein or for any errors or omissions that may have been made. The publisher remains neutral with regard to jurisdictional claims in published maps and institutional affiliations.

This Springer imprint is published by the registered company Springer Nature Switzerland AG  
The registered company address is: Gewerbestrasse 11, 6330 Cham, Switzerland

*To our Families*

# Preface

The purpose of *Shallow Water Hydraulics* is to present the theory and the computation of open channel flows using analytical, numerical, and experimental results. The book's target audience includes graduate and undergraduate students as well as practitioners of civil and environmental engineering. The book is conceptually divided into four parts: fundamental equations (Chap. 1), steady open channel flows (Chaps. 2–4), unsteady open channel flows (Chaps. 5–9), and special topics (Chaps. 10 and 11). As supporting learning material for students, a library of numerical codes is available in Chap. 12. The complexities of theory and numerical methods are progressively increased toward the end of the book, rendering pieces of the material useful for courses of different levels.

It appears impossible to start the presentation of a new open channel flow book without acknowledging the former works of Ven Te Chow (*Open Channel Hydraulics*, 1959) and Francis M. Henderson (*Open Channel Flow*, 1966). Despite Chow produced an encyclopedic treatise, it is Henderson's outstanding book that the authors followed. His presentation of concepts is simply unique, and although it was published more than 50 years ago, it is still a main reference. Credit deserves also the books of Subhash C. Jain (*Open Channel Flow*, 2001) and Hubert Chanson (*The Hydraulics of Open Channel Flow: An introduction*, 2004), similar to Henderson's, pursuing a clear and brilliant presentation of open channel flow concepts. These books offer a first open channel flow course, covering topics from steady flow to fundamental questions relating to unsteady flow. However, they are lacking a detailed exposition of numerical methods to solve the unsteady open channel flow equations. The books of Sergio Montes (*Hydraulics of Open Channel Flow*, 1998), M. Hanif Chaudhry (*Open Channel Flow*, 2008), and Eleuterio Toro (*Shock-Capturing Methods for Free Surface Shallow Flows*, 2001) cover these aspects in detail and can be used in an advanced open channel flow course. The above-quoted books were used by the first author to offer a course on *Operation of Rivers and Reservoirs* in the Environmental Hydraulics Master program held at the University of Córdoba, Spain. The purpose was to give students a complete overview on the computation of open channel flows, starting with the basic equations, continuing with the solution of steady open channel flows, penetrating

into the computation of unsteady open channel flows using modern numerical methods, and finally introducing advanced topics including flows on movable beds and sediment transport and non-hydrostatic flow modeling. The material of this book originated from the lecture notes prepared for this course, and deep recognition is therefore given to the books quoted above, which were used as a source of knowledge and inspiration for years.

The authors are of the opinion that it is better to start from generalized equations and then simplify the results using suitable approximations. From this perspective, the fundamental equations of open channel flow are settled producing a rigorous vertical integration of the 3D RANS equations (Chap. 1). The resulting mathematical statements are then simplified for selected flows; in particular, the implications of assuming the hydrostatic pressure distribution are discussed in detail. The emphasis of the book is directed to one-dimensional problems. The corresponding steady flows are therefore described using the energy and momentum principles, and a variety of numerical solutions to the algebraic and ordinary differential equations governing these flows are presented (Chaps. 2 and 3). The transitions across the critical depth, along with the formation of singular points in weir flow and the hydraulic jump beyond a sluice gate, are detailed (Chap. 4). The fundamental equations of unsteady open channel flows along with their continuous and discontinuous solutions are then presented, and modern shock-capturing finite-difference and finite volume methods to solve them are extensively described (Chaps. 5–9). A detailed description of dam break waves (Chap. 6) and sluice gate maneuvers in open channels treating them as the solution of a Riemann problem (Chap. 8) is provided. Special topics selected are the inclusion of sediment transport and movable beds in shallow water models, as used to predict geomorphic dam break waves (Chap. 10), and the computation of steady and unsteady non-hydrostatic free surface flows (Chap. 11).

A collection of hand-solved exercises along the book is not presented. Rather, the book offers to students and instructors a collection of source codes where each type of problem discussed in the book is implemented step by step. The collection of source codes is written in Visual Basic, and each code is inserted as a macro in Microsoft Excel®. Teaching experience indicated that this approach permits students an easy use of the material, and a productive interaction with the lecturer during the classes is generated.

The authors hope that after studying the book, the reader will have a solid background on the theory and computation of steady and unsteady open channel flows, permitting to advance to the study of more complex problems relating to two-dimensional numerical modeling of free surface flows.

Córdoba, Spain  
Zürich, Switzerland  
January 2019

Oscar Castro-Orgaz  
Willi H. Hager

## Acknowledgements

Oscar Castro-Orgaz would like to deeply thank Jerónimo Puertas Agudo, University of Coruña, Spain, for kindly providing him with his open channel flow lecture notes. This material was extensively used by the first author for teaching and to prepare the original part of this book relating to steady flows. In turn, it has had a profound influence on the first author's background on open channel hydraulics.

Deep thanks are also for Prof. M. J. Polo, University of Córdoba, for her suggestion to prepare this course.

# Contents

<b>1</b>	<b>Fundamental Equations of Free Surface Flows . . . . .</b>	1
1.1	Introduction . . . . .	1
1.1.1	Classification of Open Channel Flows . . . . .	1
1.1.2	Aims and Scope . . . . .	5
1.2	General Depth-Integrated Equations over a 3D Terrain . . . . .	5
1.2.1	Previous Open Channel Flow Developments . . . . .	5
1.2.2	3D Flow Equations . . . . .	8
1.2.3	General Kinematic Boundary Conditions . . . . .	10
1.2.4	Continuity Equation . . . . .	12
1.2.5	Momentum Equations . . . . .	13
1.3	Saint-Venant Theory . . . . .	19
1.3.1	2D Flows in the Horizontal Plane . . . . .	19
1.3.2	1D Cross-Sectional Averaged Equations . . . . .	24
1.4	Non-hydrostatic Theory . . . . .	33
1.4.1	1D Shallow Water Non-hydrostatic Equations . . . . .	33
1.4.2	Uniform and Gradually Varied Flow on Steep Slopes . . . . .	37
1.5	Sediment Transport and Movable Beds . . . . .	41
1.5.1	1D Cross-Sectional Averaged Continuity Equation . . . . .	41
1.5.2	1D Cross-Sectional Averaged $x$ -Momentum Equation . . . . .	43
	References . . . . .	47
<b>2</b>	<b>Energy and Momentum Principles . . . . .</b>	51
2.1	Introduction . . . . .	51
2.2	Energy Principle . . . . .	54
2.2.1	Specific Energy Head . . . . .	54
2.2.2	Location of Critical Flow . . . . .	59
2.2.3	Specific Energy Head for General Sections . . . . .	66
2.2.4	Critical Flow and Wave Motion . . . . .	67

2.2.5	Computation of Critical Flow in Arbitrary Sections . . . . .	73
2.2.6	Channel Transitions by Change of Bed Elevation . . . . .	78
2.2.7	Channel Transitions by Change of Channel Width . . . . .	89
2.3	Momentum Principle . . . . .	93
2.3.1	Specific Momentum . . . . .	93
2.3.2	Bélanger's Equation for the Hydraulic Jump . . . . .	98
2.3.3	Computation of Sequent Depths for General Cross Sections . . . . .	101
2.3.4	Transitions in Supercritical Flow . . . . .	106
2.4	Control Sections . . . . .	117
2.4.1	General . . . . .	117
2.4.2	Uniform Flow . . . . .	117
2.4.3	Critical Flow . . . . .	118
2.4.4	Weir Flows . . . . .	119
2.4.5	Gate Flows . . . . .	125
2.5	Application: Numerical Solution of Energy–Momentum Equations for Gate Flow . . . . .	132
	References . . . . .	134
<b>3</b>	<b>Computation of Steady Gradually-Varied Flows . . . . .</b>	<b>137</b>
3.1	Introduction . . . . .	137
3.2	Governing Equation of Non-uniform Flow . . . . .	137
3.3	Uniform Flow . . . . .	138
3.3.1	Definition . . . . .	138
3.3.2	Flow Resistance . . . . .	139
3.3.3	Uniform Flow Depth . . . . .	143
3.4	Flow Profiles in Prismatic Channels . . . . .	147
3.4.1	Qualitative Analysis . . . . .	147
3.4.2	Sketching of Flow Profiles . . . . .	156
3.4.3	Flow Profile for Unknown Discharge . . . . .	157
3.5	Computation of Steady Flow Profiles . . . . .	159
3.5.1	Governing Integral and Differential Equations . . . . .	159
3.5.2	Boundary Condition . . . . .	161
3.5.3	Analytical Solution . . . . .	163
3.5.4	Implicit Integral Method . . . . .	166
3.5.5	Explicit Integral Method . . . . .	169
3.5.6	Euler's Method . . . . .	169
3.5.7	Fourth-Order Runge–Kutta Method . . . . .	170
3.5.8	Predictor–Corrector Method . . . . .	172
3.6	Applications . . . . .	173
3.6.1	Test of High-Resolution Method . . . . .	173
3.6.2	Comparative of Numerical Methods . . . . .	173

3.6.3	Flow on Mild Slope . . . . .	175
3.6.4	Flow on Steep Slope . . . . .	175
3.7	Compound Channels . . . . .	178
	References . . . . .	180
<b>4</b>	<b>Computation of Steady Transcritical Open Channel Flows . . . . .</b>	<b>183</b>
4.1	Introduction . . . . .	183
4.2	Transition from Sub- to Supercritical Flow . . . . .	183
4.2.1	Formation of Singular Points in Free Surface Flows . . . . .	183
4.2.2	Determination of Water Surface Slope at Critical Point . . . . .	187
4.3	Transition from Super- to Subcritical Flows . . . . .	189
4.3.1	Control Volume Equation for Hydraulic Jump . . . . .	189
4.3.2	Determination of Hydraulic Jump Position . . . . .	193
4.4	Computational Examples . . . . .	196
4.4.1	Flow over Round-Crested Weirs . . . . .	196
4.4.2	Hydraulic Jump Beyond a Sluice Gate . . . . .	198
	References . . . . .	199
<b>5</b>	<b>Unsteady Open Channel Flows: Basic Solutions . . . . .</b>	<b>201</b>
5.1	Introduction . . . . .	201
5.2	Shallow Water Equations . . . . .	201
5.3	Discontinuous Solutions: Basic Equations of a Positive Surge . . . . .	203
5.3.1	Introduction . . . . .	203
5.3.2	Reynolds Transport Theorem . . . . .	205
5.3.3	Positive Surges Moving Upstream in Supercritical Flow . . . . .	210
5.3.4	Formulation Used in Finite Volume Methods . . . . .	213
5.4	Methods of Solution . . . . .	214
5.4.1	Shock-Capturing Methods . . . . .	214
5.4.2	Outline of Solution Methods . . . . .	216
5.5	Method of Characteristics . . . . .	217
5.5.1	SWE in Characteristic Form . . . . .	217
5.5.2	Initial and Boundary Conditions . . . . .	221
5.5.3	Wave Celerity . . . . .	228
5.6	Simple Wave Problem: Basic Equations of Rarefaction Waves . . . . .	230
5.6.1	The Simple Wave . . . . .	230
5.6.2	Rarefaction Wave: A Negative Surge . . . . .	232
5.7	Simplified Models: The Kinematic Wave . . . . .	234
5.8	Use of Non-conservative Form of SWE . . . . .	238
5.9	Limitations of SWE . . . . .	241

5.10	Hydrologic Routing . . . . .	242
5.10.1	Reservoir Routing . . . . .	242
5.10.2	Muskingum Channel Routing . . . . .	248
	References . . . . .	249
<b>6</b>	<b>Ideal Dam Break Waves . . . . .</b>	<b>253</b>
6.1	Introduction . . . . .	253
6.2	Dam Break Wave Under Dry Tailwater Conditions . . . . .	254
6.3	Dam Break Wave Under Wet Tailwater Conditions . . . . .	260
6.4	Computational Examples . . . . .	266
	References . . . . .	272
<b>7</b>	<b>Finite Difference Methods . . . . .</b>	<b>273</b>
7.1	Introduction . . . . .	273
7.2	Basic Numerical Aspects . . . . .	273
7.2.1	Remark on Basic Numerical Concepts . . . . .	273
7.2.2	Finite-Difference Approximations . . . . .	274
7.2.3	Shock-Capturing Schemes . . . . .	278
7.2.4	Explicit and Implicit Schemes: Stability . . . . .	280
7.3	Boundary and Initial Conditions . . . . .	285
7.3.1	Initial Conditions . . . . .	285
7.3.2	Boundary Conditions for Continuous Flows . . . . .	286
7.3.3	Boundary Conditions for Discontinuous Flows . . . . .	288
7.4	Explicit Schemes . . . . .	288
7.4.1	FTCS Scheme . . . . .	288
7.4.2	Lax' Diffusive Scheme . . . . .	290
7.4.3	MacCormack Predictor–Corrector Scheme . . . . .	291
7.4.4	MacCormack Scheme with Calibrated Artificial Viscosity . . . . .	292
7.4.5	TVD MacCormack Scheme . . . . .	293
7.4.6	Upwind Scheme . . . . .	295
7.5	Computational Examples . . . . .	300
7.5.1	Subcritical Dam Break Wave with Wet Tailwater . . . . .	300
7.5.2	Transcritical Dam Break Wave with Wet Tailwater . . . . .	303
7.5.3	Subcritical Surge . . . . .	303
7.5.4	Supercritical Surge . . . . .	307
7.5.5	Positive Surge with Friction . . . . .	308
	References . . . . .	309
<b>8</b>	<b>The Riemann Problem . . . . .</b>	<b>313</b>
8.1	Introduction . . . . .	313
8.2	Wet-Bed Exact Riemann Solver . . . . .	315
8.2.1	Wave Relations . . . . .	315
8.2.2	Solution of Star Region . . . . .	318

8.2.3	Complete Wave Profiles . . . . .	320
8.2.4	Possible Wave Patterns and Computation of Fluxes . . . . .	321
8.2.5	Computational Examples . . . . .	323
8.3	Dry-Bed Exact Riemann Solver . . . . .	327
8.3.1	Wet–Dry Interface . . . . .	327
8.3.2	Possible Wave Patterns . . . . .	327
8.4	Application: Gate Maneuvers in Open Channels . . . . .	332
8.4.1	Complete Gate Opening . . . . .	332
8.4.2	Partial Gate Opening . . . . .	333
8.4.3	Complete Gate Closure . . . . .	337
8.4.4	Partial Gate Closure . . . . .	338
8.4.5	Comparison with Experiments . . . . .	341
	References . . . . .	345
<b>9</b>	<b>Finite Volume Methods . . . . .</b>	<b>347</b>
9.1	Introduction . . . . .	347
9.2	Godunov-Type Schemes . . . . .	348
9.2.1	Conservative Formula . . . . .	348
9.2.2	Conservative Property: Definition of Numerical Discharge . . . . .	350
9.2.3	Godunov Upwind Numerical Flux . . . . .	351
9.2.4	Stability Condition . . . . .	355
9.2.5	Computational Sequence for Godunov First-Order Scheme . . . . .	358
9.3	Approximate Riemann Solvers . . . . .	361
9.3.1	HLL Riemann Solver . . . . .	361
9.3.2	Lax Numerical Flux . . . . .	365
9.3.3	Roe Riemann Solver . . . . .	368
9.4	Dry-Bed Treatment . . . . .	369
9.5	Source Terms . . . . .	370
9.5.1	Splitting Technique . . . . .	370
9.5.2	ODE Solvers . . . . .	372
9.5.3	Well-Balanced Schemes . . . . .	373
9.5.4	Treatment of Friction . . . . .	375
9.6	One-Sided First-Order Upwind Scheme . . . . .	376
9.7	MUSCL-Hancock Second-Order TVD Scheme . . . . .	378
9.7.1	MUSCL Reconstruction . . . . .	378
9.7.2	Slope Limiting . . . . .	380
9.7.3	Hancock Step . . . . .	383
9.7.4	Computational Sequence . . . . .	385
9.7.5	Surface Gradient Method . . . . .	386

<b>9.8</b>	<b>Boundary and Initial Conditions . . . . .</b>	388
9.8.1	Boundary Conditions . . . . .	388
9.8.2	Initial Conditions . . . . .	392
<b>9.9</b>	<b>Computational Examples . . . . .</b>	392
9.9.1	Ideal Dam Break Waves . . . . .	392
9.9.2	Dam Break Waves with Friction . . . . .	393
9.9.3	Positive Surge with Friction . . . . .	396
9.9.4	Hydraulic Jump Beyond a Sluice Gate . . . . .	399
9.9.5	Flow over Round-Crested Weirs . . . . .	401
9.9.6	Dam Break Wave Evolution over a Bottom Sill . . . . .	405
9.9.7	Solitary Wave Run-Up on a Plane Beach . . . . .	408
	<b>References . . . . .</b>	412
<b>10</b>	<b>Sediment Transport and Movable Beds . . . . .</b>	417
10.1	Introduction . . . . .	417
10.2	Flow Equations . . . . .	417
10.2.1	Shallow Water Equations . . . . .	417
10.2.2	Sediment Transport Layers and Bed Deformation . . . . .	419
10.2.3	Modified Flow Equations . . . . .	420
10.2.4	Total-Load Equation . . . . .	420
10.2.5	Sediment Transport Closure . . . . .	421
10.3	Numerical Scheme . . . . .	424
10.3.1	Conservation Laws . . . . .	424
10.3.2	First-Order Upwind Finite Volume Method . . . . .	424
10.3.3	Source Terms . . . . .	425
10.3.4	Stability Condition . . . . .	426
10.3.5	Computational Sequence . . . . .	426
10.4	Test Cases . . . . .	426
10.4.1	Dam Break Wave over Movable Bed . . . . .	426
10.4.2	Dike Erosion due to Overtopping . . . . .	430
	<b>References . . . . .</b>	433
<b>11</b>	<b>Numerical Modeling of Non-hydrostatic Free Surface Flows . . . . .</b>	435
11.1	Introduction . . . . .	435
11.2	Two-Dimensional Steady Potential Flow . . . . .	436
11.2.1	Basic Equations . . . . .	436
11.2.2	Picard Iteration . . . . .	438
11.2.3	Spillway Crest . . . . .	441
11.2.4	Steep Slope . . . . .	445
11.2.5	Flow over Round-Crested Weir: Numerical Method . . . . .	446
11.2.6	Transition from Mild to Steep Slope . . . . .	454
11.2.7	Flow over Trapezoidal Profiled Weir . . . . .	456

11.3	Unsteady Ideal Fluid Flow . . . . .	456
11.3.1	Two-Dimensional Serre Equations . . . . .	456
11.3.2	One-Dimensional Serre Equations . . . . .	461
11.3.3	Solitary Wave . . . . .	464
11.3.4	MUSCL-Hancock Scheme . . . . .	467
11.3.5	High-Order Scheme . . . . .	473
11.4	Unsteady Flow Test Cases . . . . .	475
11.4.1	Flow over Round-Crested Weir . . . . .	475
11.4.2	Solitary Wave Propagation . . . . .	480
11.4.3	Dam Break Wave . . . . .	484
	References . . . . .	489
<b>12</b>	<b>Numerical Library of Shallow Water Equations . . . . .</b>	<b>493</b>
12.1	The Library . . . . .	493
12.1.1	Introduction: Aims and Scope . . . . .	493
12.1.2	Summary of Available Codes . . . . .	494
12.2	Examples of Codes . . . . .	494
12.2.1	Gradually Varied Flow Computation Using Newton–Raphson Method . . . . .	494
12.2.2	Dam Break Wave Code . . . . .	501
12.2.3	Flooding over an obstacle code . . . . .	513
12.3	Using the Library . . . . .	532
12.3.1	Short Tutorial: Flooding of an Obstacle . . . . .	532
12.3.2	Example of Homework 1: Computation of Gradually- Varied Steady Flow Profiles . . . . .	538
12.3.3	Example of Homework 2: Wetting and Drying over Uneven Topography . . . . .	542
12.3.4	Example of Homework 3: Study of Different Discretizations of the Friction Source Term . . . . .	546
12.3.5	Example of Homework 4: Surge Reflection at a Wall . . . . .	549
12.3.6	Example of Homework 5: Analytical Solution for Transcritical Weir Flow . . . . .	552
	References . . . . .	555
	<b>Author Index . . . . .</b>	<b>557</b>
	<b>Subject Index . . . . .</b>	<b>561</b>

# Chapter 1

## Fundamental Equations of Free Surface Flows



### 1.1 Introduction

#### 1.1.1 Classification of Open Channel Flows

Open channel flow is the study of the movement of liquids with a free surface, which is by definition an interface in contact with the atmosphere. Beautiful examples of these flows are seen at dam spillways (Fig. 1.1a) or along rivers (Fig. 1.1b).

While these flows can be tackled with techniques of general fluid mechanics, this book is devoted to the use of approximate methods widely employed in civil and environmental engineering, namely the use of shallow water models. These refer to depth- or cross-sectional averaged models where the variation of the field variables in the vertical direction is only approximately accounted for, or even neglected (Vreugdenhil 1994; Toro 2001). Typical open channel flow problems are solved by assuming one-dimensional (1D) or two-dimensional (2D) flows in a horizontal plane. Common open channel flow sections in practice are irregular as in a river (Fig. 1.2a), trapezoidal for a hydropower canal (Fig. 1.2b), rectangular for a spillway chute (Fig. 1.2c) and circular for a sanitary sewer (Fig. 1.3d), among others.

To classify open channel flows, assume for the moment 1D flow. While the water moves in a channel, there are variations in depth and velocity both in space (coordinate  $x$ ) and time  $t$ . Let the water depth be  $h$  and the velocity  $U$  without rigorously defining these physical quantities at the current introductory stage. An open channel flow is classified based on the following features:

##### *Steady and unsteady flows*

A flow is steady if the flow variables do not change with time at a given position. If these change with time at a fixed position, the flow is referred to as unsteady. The flow is said also to be variable as it changes with time.



**Fig. 1.1** Examples of free surface flows **a** spillway of Aldeadávila Dam; photo taken from [https://es.wikipedia.org/wiki/Presa\\_de\\_Aldeadávila](https://es.wikipedia.org/wiki/Presa_de_Aldeadávila), **b** Amazon river flowing through the Amazon rainforest (photo of public domain by NASA)

#### *Uniform and non-uniform flows*

A flow is uniform if the flow variables are constant in space at a given instant of time. If the flow changes in space at an instant of time, the flow is non-uniform or varied.

#### *Gradually varied and rapidly varied flows*

Depending on the intensity of the change of flow variables with distance, the flow is gradually varied if this variation is small and rapidly varied if the variation is large.

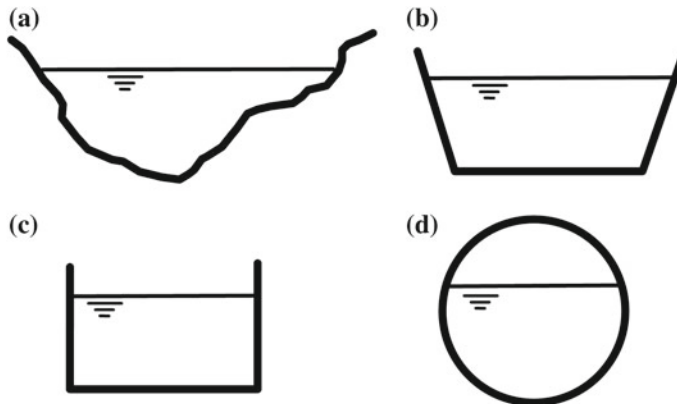


**Fig. 1.2** Typical channel flow sections **a** irregular, **b** trapezoidal, **c** rectangular, **d** circular

### *Hydrostatic and non-hydrostatic flows*

A useful approximation for fluid pressure in open channel flows is the hydrostatic law, implying that the pressure  $p_b$  at the bottom equals the weight of the water column above, that is,  $p_b = \rho gh$ , where  $h$  is the water depth,  $\rho$  the fluid density, and  $g$  the gravity acceleration. A non-hydrostatic channel flow does not obey this law, among other reasons, if streamline curvature or the channel bottom slope is large (Castro-Orgaz and Hager 2017).

Examples of open channel flows are presented in Fig. 1.3. In Fig. 1.3a, the flow is steady and uniform, whereas it is steady but non-uniform in Fig. 1.3b. A weak variation of the flow variables with distance is sketched in the latter gradually varied flow. Figure 1.3c represents unsteady uniform flow, a case rarely found in nature. The flow in Fig. 1.3d shows a smooth flood wave as an example of unsteady gradually varied flow. Figure 1.3e represents the propagation of a surge, which is basically a discontinuity in depth and velocity moving at a constant celerity. This flow is therefore unsteady and rapidly varied, given the abrupt variation in depth and velocity at the wavefront. In Chap. 5, this particular unsteady flow will be reduced to a steady flow problem in a reference system moving with the surge.

Figure 1.3f represents the steady flow over a spillway crest, down the chute up to a nearly horizontal tailwater channel ending on a free drop. At the spillway crest (Fig. 1.4a), the curvature of streamlines is large, inducing a non-hydrostatic pressure distribution (Castro-Orgaz and Hager 2017). This flow is therefore rapidly varied and non-hydrostatic.

Once the water reaches the chute, the variation of depth with distance remains small, and streamline curvature can be neglected, but the bed slope is so large that the resulting bottom pressure is less than the water weight  $\rho gh$ . This flow is therefore gradually varied and non-hydrostatic (Castro-Orgaz and Hager 2017). As the water reaches the tailwater channel, the flow depth abruptly increases on a very short distance (Fig. 1.4b), producing the so-called hydraulic jump. If air–water

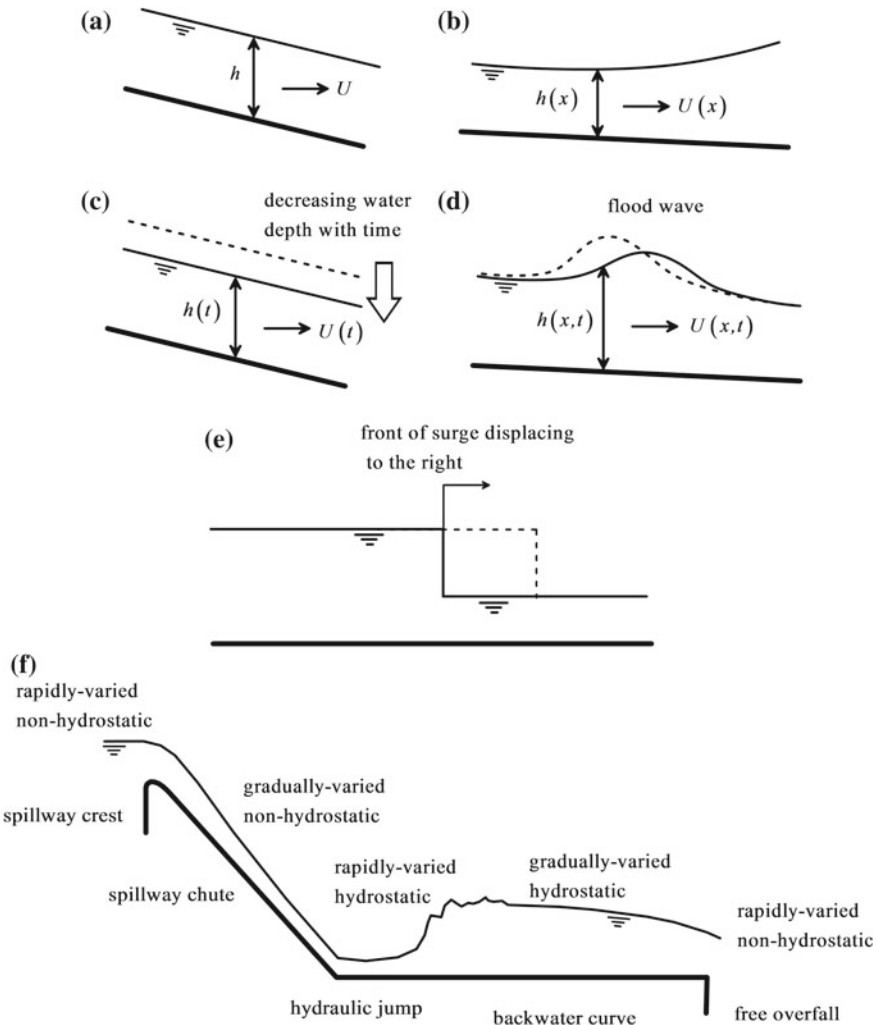


**Fig. 1.3** Open channel flow examples **a** steady uniform, **b** steady gradually varied, **c** unsteady uniform, **d** unsteady gradually varied, **e** unsteady rapidly varied, **f** varied flow over a dam and in tailwater channel

mixture effects are neglected, the pressure distribution within the hydraulic jump can be assumed to be hydrostatic (Khan and Steffler 1996a; Castro-Orgaz and Hager 2009). The flow is therefore rapidly varied and hydrostatic. Beyond the jump, the water surface profile in the nearly horizontal tailwater channel has a small variation of depth with distance, resulting in negligible streamline curvature. The flow is therefore gradually varied and hydrostatic. In the vicinity of the free drop,

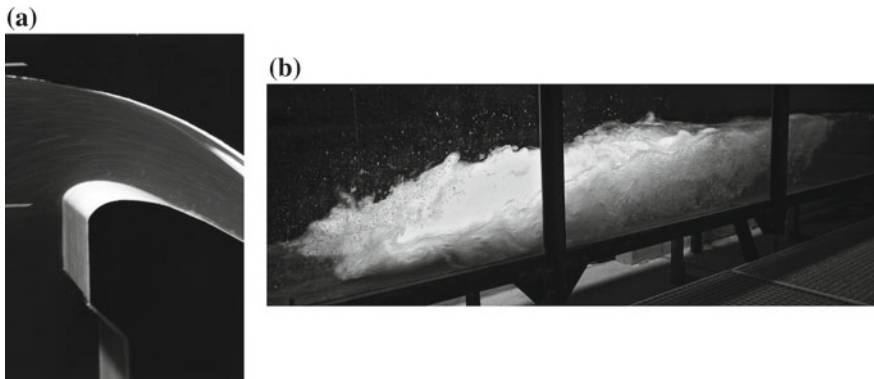


**Fig. 1.4** Rapidly varied flows at **a** spillway crest, **b** hydraulic jump

the variation of flow depth with distance is large, the streamline curvature is significant and the pressure distribution non-hydrostatic. The flow is therefore rapidly varied and non-hydrostatic.

### 1.1.2 *Aims and Scope*

The main purpose of this book is to present the theory and computation of open channel flows using the hydrostatic pressure approach. This type of model can be collectively named shallow water model. Both steady and unsteady flows will be tackled, as well as sediment transport problems. Unsteady flow computations will include both finite-difference and finite volume methods, focussing on 1D models. Extension to non-hydrostatic flows is considered in Chap. 11.

## 1.2 General Depth-Integrated Equations over a 3D Terrain

### 1.2.1 *Previous Open Channel Flow Developments*

In civil and environmental engineering applications, free surface flows are often treated using the one-dimensional (1D) continuity, momentum, and energy equations, in which information on the field variables across the flow section are averaged (Chow 1959; Henderson 1966; Liggett 1994; Montes 1998; Sturm 2001; Jain 2001; Chaudhry 2008). de Saint-Venant (1871) and Boussinesq (1877) are the fathers of depth-averaged open channel flow modeling, both proposing approximate models (Castro-Orgaz and Hager 2017). The rational development of 1D flow

models starts with the 3D equations of continuity, momentum and energy, which are integrated across a section normal to the channel bed (Keulegan 1942; Strelkoff 1969; Yen 1973). Prior to the averaging process, the full Navier–Stokes equations are time-averaged for a turbulent flow, resulting in the Reynolds equations. This development was first presented by Keulegan (1942) and Keulegan and Patterson (1943). Further studies were conducted by Jaeger (1956), Chen and Chow (1968), Yen (1975), Lai (1986), Liggett (1994), Montes (1998), Jain (2001) and Chaudhry (2008). The contributions of Strelkoff (1969) and Yen (1973, 1975) are notable, because they detail the fundamental differences between the 1D energy and momentum equations, retaining the flow equations as a function of averaging coefficients accounting for arbitrary distributions of velocity and pressure.



**Garbis Hovannes Keulegan** was born at Sebastia-Sivas, Armenia, in today's Turkey, on July 12, 1890, and passed away at age 99 on July 28, 1989, at Vicksburg MI. He left in 1912 his home country for the USA and started as an engineer at Ohio State University, graduating as a mathematician in 1915. He joined the American Forces in 1918 as a translator, starting in 1921 as a physicist at the National Bureau of Standards NBS. Until retirement in 1962, he was there primarily engaged as an expert in soil mechanics. He submitted a Ph.D. thesis in 1928 to the Johns Hopkins University, Baltimore MD.

Keulegan's interest in hydrodynamics was initiated with the inauguration of the National Hydraulic Laboratory established at NBS. He was one of the three staff members and greatly contributed with by now classic papers on turbulent flow in open channels, roll wave formation, water wave theory, and flow in curved pipes. During World War II, Keulegan was mainly active for the Beach Erosion Board in connection with the Allied Landing in France. He thus developed the theory of tides, the water wave theory furnishing information relating to the prediction of sea currents. His famous 1948 report on the experimental study of submarine sand bars was one of the few that remained unclassified. After the war, NBS was asked to furnish information

toward the basic laws of similitude involving density currents and the mixing of salt with freshwaters. Keulegan investigated both questions thoroughly and presented classic papers relating to the lock exchange experiments. His results on wave propagation and density currents were published in the 1950 book Engineering hydraulics of Rouse, and the 1966 book Estuary and coastline hydrodynamics of Ippen, respectively. Keulegan was awarded a number of prestigious decorations, including the National Medal of Science, Honorary Membership of ASCE, and in 1979 election to the National Academy of Engineering.

The coordinate system considered by Strelkoff (1969) and Yen (1973) to produce the cross-sectional averaged Reynolds equations was orthogonal and fitted to the terrain. This system is widely used in geophysical flow research (Savage and Hutter 1989, 1991; Pudasaini and Hutter 2007). Strelkoff (1969) and Yen (1973) transformed the Navier–Stokes equations in Cartesian coordinates to the terrain-fitted reference system stated by means of a rotation of axes to render two of the coordinates tangent to the terrain, and the third normal to it. While it is feasible to produce such a transformation from Cartesian to terrain-fitted coordinates, a simple axes rotation is not the exact mathematical operator, so that the channel flow equations developed by this procedure are not general. Dressler (1978) transformed the plane Euler equations in Cartesian coordinates to a boundary-fitted system of reference by using a Jacobian matrix. In his modified form of the Euler equations, the channel bed curvature appears. This feature is also observable in the granular mass flow equations by Savage and Hutter (1989, 1991). The discrepancy between Dressler (1978) and Savage and Hutter (1989, 1991), and the form of the Navier–Stokes equations to obtain 1D equations used by Strelkoff (1969) and Yen (1973), indicate that the equations developed by the latter apply strictly to flows over constant slope channels. The development by Strelkoff (1969) is also available from Jain (2001). The key message is that the Navier–Stokes equations in the developments of Strelkoff (1969) and Yen (1973) should be expressed in the terrain-fitted system of coordinates using a Jacobian matrix rather than a simple rotation of axes, because only then the averaging process is to be conducted. If the developments of Strelkoff (1969) and Yen (1973) are repeated with these considerations, additional terms including the terrain curvature appear, as those contained in the depth-averaged avalanche flow equations by Savage and Hutter (1989, 1991). The transformation of the Reynolds equations to any curvilinear system (orthogonal or not) is comprehensively reported by Rouse (1959) and Schlichting and Gersten (2000). A disadvantage of the 1D channel flow equations of Strelkoff (1969) or Yen (1973) is that undetermined averaging coefficients need to be mathematically closed for computations. These are difficult to evaluate, like those of the 1D energy equation for turbulent unsteady flow.

An alternative to terrain-fitted coordinates is the resort to Cartesian coordinates, despite this option was less used in open channel flows. Notable contributions to be

considered below are the works by Steffler and Jin (1993), Khan and Steffler (1996b, c), Denlinger and Iverson (2004), Iverson (2005), Denlinger and O'Connell (2008), and Iverson and Ouyang (2015). Note that the generalized free surface flow equations in Cartesian coordinates were given by Yen (1975), thereby removing the previous problem by the use of terrain-fitted coordinates.

Due to the increase of mathematical complexities while doing an averaging process in terrain-fitted coordinates, Cartesian coordinates will be generally used in this book. Further, given the difficulties in using the energy equation for depth-averaged turbulent unsteady flow computations over 3D terrain, the use of this (important) principle is limited to steady flow problems, and therefore presented in Chap. 2. The general 3D flow equations of mass and momentum will be depth-integrated to produce a general 2D averaged model in this chapter. This general formulation applies in practice to produce 2D computational models making suitable approximations to the field variables. For the case of 1D flow, the 2D-averaged flow equations will be laterally integrated, producing the corresponding cross-sectional averaged model. Sediment transport and movable beds are finally considered.

### 1.2.2 3D Flow Equations

Here the general depth-integrated equations for a mixture of fluid and sediments, bounded by arbitrary non-material interfaces, are developed. Consider a river flow represented by the movement of a continuum mixture of a fluid and solid with density  $\rho(x, y, z, t)$ , where  $(x, y, z)$  are the Cartesian coordinates and  $t$  is the time. The flow is therefore bounded by two general interface surfaces representing the free surface (subscript  $s$ ) and the terrain surface (subscript  $b$  for bed), given by the mathematical statements  $z = z_s(x, y, t)$  and  $z = z_b(x, y, t)$ , respectively (Fig. 1.5). The velocity components in the  $(x, y, z)$  directions are  $(u, v, w)$ .

With the mixture velocity  $\mathbf{V} = (u, w, v)$  as the barycentric velocity (Iverson 2005; Wu 2008), the mass conservation equation for the mixture is

$$\frac{\partial \rho}{\partial t} + \frac{\partial(\rho u)}{\partial x} + \frac{\partial(\rho v)}{\partial y} + \frac{\partial(\rho w)}{\partial z} = 0. \quad (1.1)$$

Likewise, in the horizontal–vertical Cartesian system of coordinates used, Newton's second law gives for the mixture the momentum equations (Iverson 2005; Wu 2008).

$$\frac{\partial}{\partial t}(\rho u) + \frac{\partial}{\partial x}(\rho u^2) + \frac{\partial}{\partial y}(\rho uv) + \frac{\partial}{\partial z}(\rho uw) = -\left(\frac{\partial \tau_{xx}}{\partial x} + \frac{\partial \tau_{xy}}{\partial y} + \frac{\partial \tau_{xz}}{\partial z}\right), \quad (1.2)$$

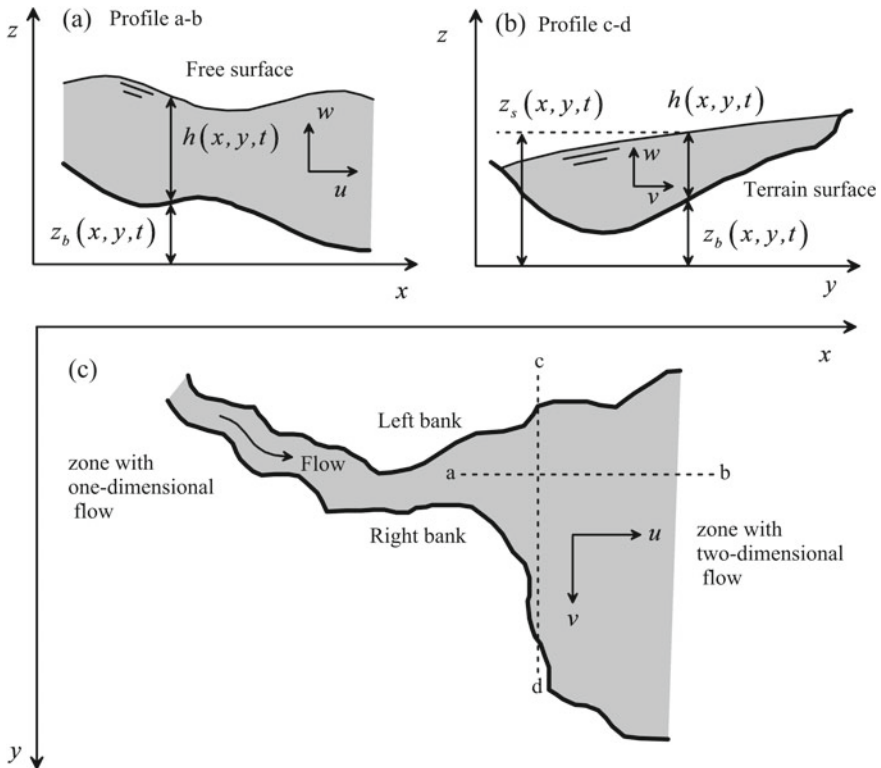


**Fig. 1.5** 3D open channel flow in a river **a** longitudinal section, **b** transverse section, **c** plan view

$$\frac{\partial}{\partial t}(\rho v) + \frac{\partial}{\partial x}(\rho uv) + \frac{\partial}{\partial y}(\rho v^2) + \frac{\partial}{\partial z}(\rho vw) = -\left(\frac{\partial \tau_{yx}}{\partial x} + \frac{\partial \tau_{yy}}{\partial y} + \frac{\partial \tau_{yz}}{\partial z}\right), \quad (1.3)$$

$$\frac{\partial}{\partial t}(\rho w) + \frac{\partial}{\partial x}(\rho uw) + \frac{\partial}{\partial y}(\rho vw) + \frac{\partial}{\partial z}(\rho w^2) = -\rho g - \left(\frac{\partial \tau_{zx}}{\partial x} + \frac{\partial \tau_{zy}}{\partial y} + \frac{\partial \tau_{zz}}{\partial z}\right). \quad (1.4)$$

Here  $g$  is the gravity acceleration and  $\tau_{ij}$  the stress tensor, with  $(i, j) = (x, y, z)$ , which is symmetric, i.e.  $\tau_{ij} = \tau_{ji}$ . Subscript  $i$  indicates the axis along which the stress acts, and  $j$  is the axis normal to the plane containing the stress. Moreover,  $\tau_{ij}$  is here introduced with the notation used in the environmental context, i.e., it is the negative value of the common stress tensor definition used in civil engineering (Iverson 2005). Equations (1.1)–(1.4) provide the starting point to generate a depth-integrated model.

### 1.2.3 General Kinematic Boundary Conditions

Prior to integrating Eqs. (1.1)–(1.4) in the  $z$ -direction, the general kinematic boundary condition at an interface will be presented (Iverson and Ouyang 2015; Castro-Orgaz and Hager 2017). Consider for illustrative purposes a river bed, whose general mathematical equation is written as

$$F(x, y, z, t) = z - z_b(x, y, t) = 0. \quad (1.5)$$

The material derivative of  $F$  following its motion is, therefore, given by

$$\frac{DF}{Dt} = \frac{\partial F}{\partial t} + \mathbf{U} \cdot \nabla F = 0, \quad (1.6)$$

where  $\mathbf{U}$  is the velocity vector representing the deformation of the river bed. Note that the velocity of displacement of an interface is not necessarily equal to that of the particles that are momentarily lying upon it. In general, the velocity of the displacement of a surface is given by the kinematic statement

$$\mathbf{U} = \mathbf{V}_b - M_b \mathbf{n}. \quad (1.7)$$

Here  $\mathbf{V}_b = (u_b, v_b, w_b)$  is the fluid mixture velocity on the surface,  $M_b$  is the net volume of fluid mixture crossing normal the interface “b” per unit area and time, and  $\mathbf{n}$  is the unit vector normal to the interface. Inserting Eq. (1.7) into Eq. (1.6) produces

$$\begin{aligned} \frac{DF}{Dt} &= \frac{\partial F}{\partial t} + (\mathbf{V}_b - M_b \mathbf{n}) \cdot \nabla F = \frac{\partial F}{\partial t} + \mathbf{V}_b \cdot \nabla F - M_b |\nabla F| \\ &= \frac{\partial F}{\partial t} + \frac{\partial F}{\partial x} u_b + \frac{\partial F}{\partial y} v_b + \frac{\partial F}{\partial z} w_b - M_b |\nabla F| = 0. \end{aligned} \quad (1.8)$$

The derivatives of  $F$  are

$$\frac{\partial F}{\partial t} = -\frac{\partial z_b}{\partial t}, \quad \frac{\partial F}{\partial x} = -\frac{\partial z_b}{\partial x}, \quad \frac{\partial F}{\partial y} = -\frac{\partial z_b}{\partial y}, \quad \frac{\partial F}{\partial z} = 1. \quad (1.9)$$

Inserting Eqs. (1.9) into Eq. (1.8), one finds

$$\frac{DF}{Dt} = -\frac{\partial z_b}{\partial t} - \frac{\partial z_b}{\partial x} u_b - \frac{\partial z_b}{\partial y} v_b + w_b - M_b |\nabla F| = 0. \quad (1.10)$$

Noting that the modulus of  $F$  is given by

$$|\nabla F| = \left[ \left( \frac{\partial F}{\partial x} \right)^2 + \left( \frac{\partial F}{\partial y} \right)^2 + \left( \frac{\partial F}{\partial z} \right)^2 \right]^{1/2} = \left[ \left( \frac{\partial z_b}{\partial x} \right)^2 + \left( \frac{\partial z_b}{\partial y} \right)^2 + 1 \right]^{1/2}, \quad (1.11)$$

Equation (1.10) gives after re-arrangement

$$\frac{\partial z_b}{\partial t} + \frac{\partial z_b}{\partial x} u_b + \frac{\partial z_b}{\partial y} v_b - w_b = -M_b \left[ \left( \frac{\partial z_b}{\partial x} \right)^2 + \left( \frac{\partial z_b}{\partial y} \right)^2 + 1 \right]^{1/2}, \quad (1.12)$$

or

$$\frac{\partial z_b}{\partial t} + \frac{\partial z_b}{\partial x} u_b + \frac{\partial z_b}{\partial y} v_b - w_b = -M_b \xi_b, \quad (1.13)$$

where

$$\xi_b = \left[ \left( \frac{\partial z_b}{\partial x} \right)^2 + \left( \frac{\partial z_b}{\partial y} \right)^2 + 1 \right]^{1/2}. \quad (1.14)$$

Equation (1.13) is the general kinematic boundary condition at the river bed. This equation must be preserved in depth-integrated models, regardless of using a non-slip or slip ( $u_b = v_b = w_b = 0$ ) assumption at the river bed. A similar equation applies for the free surface, resulting in

$$\frac{\partial z_s}{\partial t} + \frac{\partial z_s}{\partial x} u_s + \frac{\partial z_s}{\partial y} v_s - w_s = -M_s \xi_s, \quad (1.15)$$

where

$$\xi_s = \left[ \left( \frac{\partial z_s}{\partial x} \right)^2 + \left( \frac{\partial z_s}{\partial y} \right)^2 + 1 \right]^{1/2}. \quad (1.16)$$

### 1.2.4 Continuity Equation

Vertical integration of Eq. (1.1) yields

$$\int_{z_b}^{z_s} \left[ \frac{\partial \rho}{\partial t} + \frac{\partial(\rho u)}{\partial x} + \frac{\partial(\rho v)}{\partial y} + \frac{\partial(\rho w)}{\partial z} \right] dz = 0. \quad (1.17)$$

This integral relation is transformed by computing the following identities by application of Leibniz's rule:

$$\int_{z_b}^{z_s} \frac{\partial \rho}{\partial t} dz = \frac{\partial}{\partial t} \int_{z_b}^{z_s} \rho dz - \rho_s \frac{\partial z_s}{\partial t} + \rho_b \frac{\partial z_b}{\partial t}, \quad (1.18)$$

$$\int_{z_b}^{z_s} \frac{\partial(\rho u)}{\partial x} dz = \frac{\partial}{\partial x} \int_{z_b}^{z_s} \rho u dz - \rho_s u_s \frac{\partial z_s}{\partial x} + \rho_b u_b \frac{\partial z_b}{\partial x}, \quad (1.19)$$

$$\int_{z_b}^{z_s} \frac{\partial(\rho v)}{\partial y} dz = \frac{\partial}{\partial y} \int_{z_b}^{z_s} \rho v dz - \rho_s v_s \frac{\partial z_s}{\partial y} + \rho_b v_b \frac{\partial z_b}{\partial y}, \quad (1.20)$$

$$\int_{z_b}^{z_s} \frac{\partial(\rho w)}{\partial z} dz = \rho_s w_s - \rho_b w_b. \quad (1.21)$$

Summing Eqs. (1.18)–(1.21) produces

$$\begin{aligned} & \frac{\partial}{\partial t} \int_{z_b}^{z_s} \rho dz + \frac{\partial}{\partial x} \int_{z_b}^{z_s} \rho u dz + \frac{\partial}{\partial y} \int_{z_b}^{z_s} \rho v dz - \rho_s \frac{\partial z_s}{\partial t} + \rho_b \frac{\partial z_b}{\partial t} - \rho_s u_s \frac{\partial z_s}{\partial x} \\ & + \rho_b u_b \frac{\partial z_b}{\partial x} - \rho_s v_s \frac{\partial z_s}{\partial y} + \rho_b v_b \frac{\partial z_b}{\partial y} + \rho_s w_s - \rho_b w_b = 0, \end{aligned} \quad (1.22)$$

or,

$$\begin{aligned} & \frac{\partial}{\partial t} \int_{z_b}^{z_s} \rho dz + \frac{\partial}{\partial x} \int_{z_b}^{z_s} \rho u dz + \frac{\partial}{\partial y} \int_{z_b}^{z_s} \rho v dz \\ & - \rho_s \left( \frac{\partial z_s}{\partial t} + u_s \frac{\partial z_s}{\partial x} + v_s \frac{\partial z_s}{\partial y} - w_s \right) + \rho_b \left( \frac{\partial z_b}{\partial t} + u_b \frac{\partial z_b}{\partial x} + v_b \frac{\partial z_b}{\partial y} - w_b \right) = 0. \end{aligned} \quad (1.23)$$

Inserting the general kinematic boundary conditions Eqs. (1.13) and (1.15) into Eq. (1.23) yields

$$\frac{\partial}{\partial t} \int_{z_b}^{z_s} \rho dz + \frac{\partial}{\partial x} \int_{z_b}^{z_s} \rho u dz + \frac{\partial}{\partial y} \int_{z_b}^{z_s} \rho v dz + \rho_s M_s \xi_s - \rho_b M_b \xi_b = 0. \quad (1.24)$$

This is the general depth-integrated continuity equation.

### 1.2.5 Momentum Equations

Now, the  $x$ -momentum Eq. (1.2) is vertically integrated as

$$\begin{aligned} & \int_{z_b}^{z_s} \left[ \frac{\partial}{\partial t} (\rho u) + \frac{\partial}{\partial x} (\rho u^2) + \frac{\partial}{\partial y} (\rho uv) + \frac{\partial}{\partial z} (\rho uw) \right] dz \\ & = \int_{z_b}^{z_s} - \left( \frac{\partial \tau_{xx}}{\partial x} + \frac{\partial \tau_{xy}}{\partial y} + \frac{\partial \tau_{xz}}{\partial z} \right) dz. \end{aligned} \quad (1.25)$$

The following transformations are produced using again Leibniz's rule:

$$\int_{z_b}^{z_s} \frac{\partial}{\partial t} (\rho u) dz = \frac{\partial}{\partial t} \int_{z_b}^{z_s} \rho u dz - \rho_s u_s \frac{\partial z_s}{\partial t} + \rho_b u_b \frac{\partial z_b}{\partial t}, \quad (1.26)$$

$$\int_{z_b}^{z_s} \frac{\partial}{\partial x} (\rho u^2) dz = \frac{\partial}{\partial x} \int_{z_b}^{z_s} \rho u^2 dz - \rho_s u_s^2 \frac{\partial z_s}{\partial x} + \rho_b u_b^2 \frac{\partial z_b}{\partial x}, \quad (1.27)$$

$$\int_{z_b}^{z_s} \frac{\partial}{\partial y} (\rho u v) dz = \frac{\partial}{\partial y} \int_{z_b}^{z_s} \rho u v dz - \rho_s u_s v_s \frac{\partial z_s}{\partial y} + \rho_b u_b v_b \frac{\partial z_b}{\partial y}, \quad (1.28)$$

$$\int_{z_b}^{z_s} \frac{\partial}{\partial z} (\rho u w) dz = \rho_s u_s w_s - \rho_b u_b w_b, \quad (1.29)$$

$$\int_{z_b}^{z_s} \frac{\partial \tau_{xx}}{\partial x} dz = \frac{\partial}{\partial x} \int_{z_b}^{z_s} \tau_{xx} dz - (\tau_{xx})_s \frac{\partial z_s}{\partial x} + (\tau_{xx})_b \frac{\partial z_b}{\partial x}, \quad (1.30)$$

$$\int_{z_b}^{z_s} \frac{\partial \tau_{xy}}{\partial y} dz = \frac{\partial}{\partial y} \int_{z_b}^{z_s} \tau_{xy} dz - (\tau_{xy})_s \frac{\partial z_s}{\partial y} + (\tau_{xy})_b \frac{\partial z_b}{\partial y}, \quad (1.31)$$

$$\int_{z_b}^{z_s} \frac{\partial \tau_{xz}}{\partial z} dz = (\tau_{xz})_s - (\tau_{xz})_b. \quad (1.32)$$

Equations (1.26)–(1.32) form a set of identities that are substituted into Eq. (1.25), transforming it into

$$\begin{aligned} & \frac{\partial}{\partial t} \int_{z_b}^{z_s} \rho u dz - \rho_s u_s \frac{\partial z_s}{\partial t} + \rho_b u_b \frac{\partial z_b}{\partial t} + \frac{\partial}{\partial x} \int_{z_b}^{z_s} \rho u^2 dz - \rho_s u_s^2 \frac{\partial z_s}{\partial x} + \rho_b u_b^2 \frac{\partial z_b}{\partial x} + \frac{\partial}{\partial y} \int_{z_b}^{z_s} \rho u v dz \\ & - \rho_s u_s v_s \frac{\partial z_s}{\partial y} + \rho_b u_b v_b \frac{\partial z_b}{\partial y} + \rho_s u_s w_s - \rho_b u_b w_b = - \left[ \frac{\partial}{\partial x} \int_{z_b}^{z_s} \tau_{xx} dz - (\tau_{xx})_s \frac{\partial z_s}{\partial x} + (\tau_{xx})_b \frac{\partial z_b}{\partial x} \right. \\ & \left. + \frac{\partial}{\partial y} \int_{z_b}^{z_s} \tau_{xy} dz - (\tau_{xy})_s \frac{\partial z_s}{\partial y} + (\tau_{xy})_b \frac{\partial z_b}{\partial y} + (\tau_{xz})_s - (\tau_{xz})_b \right]. \end{aligned} \quad (1.33)$$

Collecting terms, one finds

$$\begin{aligned} & \frac{\partial}{\partial t} \int_{z_b}^{z_s} \rho u dz + \frac{\partial}{\partial x} \int_{z_b}^{z_s} \rho u^2 dz + \frac{\partial}{\partial y} \int_{z_b}^{z_s} \rho u v dz - \rho_s u_s \left( \frac{\partial z_s}{\partial t} + u_s \frac{\partial z_s}{\partial x} + v_s \frac{\partial z_s}{\partial y} - w_s \right) \\ & + \rho_b u_b \left( \frac{\partial z_b}{\partial t} + u_b \frac{\partial z_b}{\partial x} + v_b \frac{\partial z_b}{\partial y} - w_b \right) + \left\{ \frac{\partial}{\partial x} \int_{z_b}^{z_s} \tau_{xx} dz + \frac{\partial}{\partial y} \int_{z_b}^{z_s} \tau_{xy} dz \right. \\ & \left. - \left[ (\tau_{xx})_s \frac{\partial z_s}{\partial x} + (\tau_{xy})_s \frac{\partial z_s}{\partial y} - (\tau_{xz})_s \right] + \left[ (\tau_{xx})_b \frac{\partial z_b}{\partial x} + (\tau_{xy})_b \frac{\partial z_b}{\partial y} - (\tau_{xz})_b \right] \right\} = 0. \end{aligned} \quad (1.34)$$

Using Eqs. (1.13) and (1.15) produces

$$\begin{aligned} & \frac{\partial}{\partial t} \int_{z_b}^{z_s} \rho u dz + \frac{\partial}{\partial x} \int_{z_b}^{z_s} \rho u^2 dz + \frac{\partial}{\partial y} \int_{z_b}^{z_s} \rho u v dz + \rho_s u_s M_s \xi_s - \rho_b u_b M_b \xi_b + \frac{\partial}{\partial x} \int_{z_b}^{z_s} \tau_{xx} dz \\ & + \frac{\partial}{\partial y} \int_{z_b}^{z_s} \tau_{xy} dz - \left[ (\tau_{xx})_s \frac{\partial z_s}{\partial x} + (\tau_{xy})_s \frac{\partial z_s}{\partial y} - (\tau_{xz})_s \right] + \left[ (\tau_{xx})_b \frac{\partial z_b}{\partial x} + (\tau_{xy})_b \frac{\partial z_b}{\partial y} - (\tau_{xz})_b \right] = 0. \end{aligned} \quad (1.35)$$

Equation (1.35) represents the general  $x$ -momentum depth-integrated equation for non-hydrostatic mixture flows. Integrating Eq. (1.3) follows the same steps and no additional insights are regained. The result is

$$\begin{aligned} & \frac{\partial}{\partial t} \int_{z_b}^{z_s} \rho v dz + \frac{\partial}{\partial y} \int_{z_b}^{z_s} \rho v^2 dz + \frac{\partial}{\partial x} \int_{z_b}^{z_s} \rho u v dz + \rho_s v_s M_s \xi_s - \rho_b v_b M_b \xi_b + \frac{\partial}{\partial y} \int_{z_b}^{z_s} \tau_{yy} dz \\ & + \frac{\partial}{\partial x} \int_{z_b}^{z_s} \tau_{yx} dz - \left[ (\tau_{yy})_s \frac{\partial z_s}{\partial y} + (\tau_{yx})_s \frac{\partial z_s}{\partial x} - (\tau_{yz})_s \right] + \left[ (\tau_{yy})_b \frac{\partial z_b}{\partial y} + (\tau_{yx})_b \frac{\partial z_b}{\partial x} - (\tau_{yz})_b \right] = 0. \end{aligned} \quad (1.36)$$

Finally, the  $z$ -momentum Eq. (1.4) is vertically integrated, producing

$$\begin{aligned} & \int_{z_b}^{z_s} \left[ \frac{\partial}{\partial t} (\rho w) + \frac{\partial}{\partial x} (\rho uw) + \frac{\partial}{\partial y} (\rho vw) + \frac{\partial}{\partial z} (\rho w^2) \right] dz \\ & = -g \int_{z_b}^{z_s} \rho dz - \int_{z_b}^{z_s} \left( \frac{\partial \tau_{zx}}{\partial x} + \frac{\partial \tau_{zy}}{\partial y} + \frac{\partial \tau_{zz}}{\partial z} \right) dz \end{aligned} \quad (1.37)$$

Employing the transformations:

$$\int_{z_b}^{z_s} \frac{\partial}{\partial t} (\rho w) dz = \frac{\partial}{\partial t} \int_{z_b}^{z_s} \rho w dz - \rho_s w_s \frac{\partial z_s}{\partial t} + \rho_b w_b \frac{\partial z_b}{\partial t}, \quad (1.38)$$

$$\int_{z_b}^{z_s} \frac{\partial}{\partial x} (\rho uw) dz = \frac{\partial}{\partial x} \int_{z_b}^{z_s} \rho uw dz - \rho_s u_s w_s \frac{\partial z_s}{\partial x} + \rho_b u_b w_b \frac{\partial z_b}{\partial x}, \quad (1.39)$$

$$\int_{z_b}^{z_s} \frac{\partial}{\partial y} (\rho vw) dz = \frac{\partial}{\partial y} \int_{z_b}^{z_s} \rho vw dz - \rho_s v_s w_s \frac{\partial z_s}{\partial y} + \rho_b v_b w_b \frac{\partial z_b}{\partial y}, \quad (1.40)$$

$$\int_{z_b}^{z_s} \frac{\partial}{\partial z} (\rho w^2) dz = \rho_s w_s^2 - \rho_b w_b^2, \quad (1.41)$$

$$\int_{z_b}^{z_s} \frac{\partial \tau_{zx}}{\partial x} dz = \frac{\partial}{\partial x} \int_{z_b}^{z_s} \tau_{zx} dz - (\tau_{zx})_s \frac{\partial z_s}{\partial x} + (\tau_{zx})_b \frac{\partial z_b}{\partial x}, \quad (1.42)$$

$$\int_{z_b}^{z_s} \frac{\partial \tau_{zy}}{\partial y} dz = \frac{\partial}{\partial y} \int_{z_b}^{z_s} \tau_{zy} dz - (\tau_{zy})_s \frac{\partial z_s}{\partial y} + (\tau_{zy})_b \frac{\partial z_b}{\partial y}, \quad (1.43)$$

$$\int_{z_b}^{z_s} \frac{\partial \tau_{zz}}{\partial z} dz = (\tau_{zz})_s - (\tau_{zz})_b, \quad (1.44)$$

applied to Eq. (1.37), and subsequently grouping terms, leads to

$$\begin{aligned} & \frac{\partial}{\partial t} \int_{z_b}^{z_s} \rho w dz + \frac{\partial}{\partial x} \int_{z_b}^{z_s} \rho uw dz + \frac{\partial}{\partial y} \int_{z_b}^{z_s} \rho vw dz - \rho_s w_s \left( \frac{\partial z_s}{\partial t} + u_s \frac{\partial z_s}{\partial x} + v_s \frac{\partial z_s}{\partial y} - w_s \right) \\ & + \rho_b w_b \left( \frac{\partial z_b}{\partial t} + u_b \frac{\partial z_b}{\partial x} + v_b \frac{\partial z_b}{\partial y} - w_b \right) + g \int_{z_b}^{z_s} \rho dz + \left\{ \frac{\partial}{\partial x} \int_{z_b}^{z_s} \tau_{zx} dz + \frac{\partial}{\partial y} \int_{z_b}^{z_s} \tau_{zy} dz \right. \\ & \left. - \left[ (\tau_{zx})_s \frac{\partial z_s}{\partial x} + (\tau_{zy})_s \frac{\partial z_s}{\partial y} - (\tau_{zz})_s \right] + \left[ (\tau_{zx})_b \frac{\partial z_b}{\partial x} + (\tau_{zy})_b \frac{\partial z_b}{\partial y} - (\tau_{zz})_b \right] \right\} = 0. \end{aligned} \quad (1.45)$$

Using the kinematic boundary conditions results in

$$\begin{aligned} & \frac{\partial}{\partial t} \int_{z_b}^{z_s} \rho w dz + \frac{\partial}{\partial x} \int_{z_b}^{z_s} \rho u w dz + \frac{\partial}{\partial y} \int_{z_b}^{z_s} \rho v w dz + \rho_s w_s M_s \xi_s - \rho_b w_b M_b \xi_b + g \int_{z_b}^{z_s} \rho dz \\ & + \frac{\partial}{\partial x} \int_{z_b}^{z_s} \tau_{zx} dz + \frac{\partial}{\partial y} \int_{z_b}^{z_s} \tau_{zy} dz - \left[ (\tau_{zx})_s \frac{\partial z_s}{\partial x} + (\tau_{zy})_s \frac{\partial z_s}{\partial y} - (\tau_{zz})_s \right] \\ & + \left[ (\tau_{zx})_b \frac{\partial z_b}{\partial x} + (\tau_{zy})_b \frac{\partial z_b}{\partial y} - (\tau_{zz})_b \right] = 0. \end{aligned} \quad (1.46)$$

Equations (1.24), (1.35), (1.36), and (1.46) are the general non-hydrostatic depth-integrated mass and momentum conservation equations for mixture flows. This set of generalized equations accounts for density variations, movable beds, flows across the free surface and non-hydrostatic stresses over a 3D terrain. The flow can be turbulent or laminar, steady or unsteady, rotational or irrotational, uniform or non-uniform, and gradually varied or rapidly varied. The bed may be rigid or erodible, pervious or impervious, with steep or small slopes, and the free surface a material surface or receive flows. The fluid may be compressible or incompressible, with sediments in suspension or clear water (Yen 1973, 1975). With the general stress tensor considered, the model also applies to avalanche dynamics using the Mohr–Coulomb yield criterion (Iverson 2005). Open channel flows are turbulent; Reynolds decomposition is employed in these flows, splitting the flow variables into mean (denoted by bars) and fluctuating (denoted by primes) components, e.g.,  $u = \bar{u} + u'$ ,  $v = \bar{v} + v'$ ,  $w = \bar{w} + w'$ ,  $p = \bar{p} + p'$ ,  $\rho = \bar{\rho} + \rho'$ . By definition, the time-averaged value of a fluctuating component is zero. Employing these transformations, doing a time-averaging of the 3D equations, and neglecting viscous contributions, the symmetric stress tensor is (Rod 1980; White 1991, 2009)

$$\begin{aligned} \tau_{xx} &= p - \sigma_{xx}, & \tau_{yy} &= p - \sigma_{yy}, & \tau_{zz} &= p - \sigma_{zz}, \\ \tau_{xz} &= -\sigma_{xz}, & \tau_{xy} &= -\sigma_{xy}, & \tau_{yz} &= -\sigma_{yz}. \end{aligned} \quad (1.47)$$

Here  $\sigma$  denotes the turbulent Reynolds stress due to time averaging of the Navier–Stokes equations for fluid flow. The velocity field corresponding to this stress tensor is a time-averaged mathematical approach representing the mean turbulent motion. The Reynolds stresses are in reality terms originating from the acceleration, and, thus, are “apparent stresses.”

With this set of generalized equations, including variable density, turbulence, and non-hydrostatic pressures, simplified versions will be presented in the ensuing developments.



**Ben Chie Yen** was born on April 14, 1935, at Guangzhou, China, and passed away aged 66 years on December 23, 2001, at St. Louis IL, USA. He obtained his BS degree from the National Taiwan University in 1956, the civil engineer degree from University of Iowa in 1959, and earned his Ph.D. title there in 1965. After a short stay at Princeton University, he was from 1966 to 1976 Assistant and Associate Professor at the University of Illinois, Urbana, and from 1976 there Professor of civil engineering. Yen visited later a number of universities, including University of Karlsruhe in 1974, EPFL Lausanne in 1982, and National Taiwan University in 1983. He passed away following cardiovascular aneurysm.

Yen's Ph.D. thesis was in open channel flow, a topic that he pursued until the 1970s. He was able to distinguish between the energy and the momentum equations, resulting in two different formulations with the appropriate averaging coefficients and corresponding loss slopes. He then turned to the stormwater technology thereby investigating a number of its elements. He, for instance, pointed to the significant energy losses induced by junction manholes, a fact that was often neglected. Yen chaired the second Conference on Urban Drainage in 1982. He recognized the need to merge water quality and quantity experts by forming a new international group, the Joint Committee on Urban Storm Drainage JCUSD, which he chaired also from 1982. He further investigated unsteady sewer flows and eventually developed into an expert in this field. He was awarded the Hunter Rouse Hydraulic Engineering Lecture from the American Society of Civil Engineers ASCE in 1999 for "his fundamental work on open channel and flow resistance." He was further promoted during the 29th IAHR Congress held in Beijing to Honorary Member of IAHR.

### 1.3 Saint-Venant Theory

#### 1.3.1 2D Flows in the Horizontal Plane

In this section, the shallow water equations (SWE) for 2D flows of clear water ( $\rho = \text{const.}$ ) over a horizontal plane are derived. If the flow depth  $h(x, y, t)$  is smaller than the characteristic length in the  $(x, y)$ -plane, a scaling analysis reveals that, except for the near-bed boundary layer, the velocity components  $u$  and  $v$  can be assumed constant across  $h$  and equal to their depth-averaged values  $U$  and  $V$  (Liggett 1994). Therefore,

$$u(x, y, z, t) \approx U(x, y, t) = \frac{1}{h} \int_{z_b}^{z_s} u dz, \quad (1.48)$$

$$v(x, y, z, t) \approx V(x, y, t) = \frac{1}{h} \int_{z_b}^{z_s} v dz. \quad (1.49)$$

The depth-independent horizontal velocity components imply a slip velocity at the bed, thereby neglecting the high-velocity gradient confined to the thin bed boundary layer (Steffler and Jin 1993). Inserting this approximation into Eq. (1.23), noting that  $\rho = \text{const.}$ , assuming that there is no flow across the free surface and that the bottom is rigid and impervious, the depth-averaged continuity equation reduces to

$$\frac{\partial h}{\partial t} + \frac{\partial}{\partial x}(Uh) + \frac{\partial}{\partial y}(Vh) = 0. \quad (1.50)$$

Using the approximations stated above in Eq. (1.35), and neglecting stresses at the free surface, yields the depth-averaged  $x$ -momentum as

$$\begin{aligned} & \frac{\partial}{\partial t}(Uh) + \frac{\partial}{\partial x}(U^2 h) + \frac{\partial}{\partial y}(UVh) \\ &= -\frac{1}{\rho} \left[ \frac{\partial}{\partial x} \int_{z_b}^{z_s} \tau_{xx} dz + \frac{\partial}{\partial y} \int_{z_b}^{z_s} \tau_{xy} dz + (\tau_{xx})_b \frac{\partial z_b}{\partial x} + (\tau_{xy})_b \frac{\partial z_b}{\partial y} - (\tau_{xz})_b \right]. \end{aligned} \quad (1.51)$$

This needs further considerations about the stress tensor. Consider first the implications of using Eqs. (1.48)–(1.49) on the  $x$ -momentum balance. Basically, it amounts to assume that the Boussinesq velocity correction coefficients (Liggett 1994; Katopodes 2019), e.g.,

$$\beta_x = \frac{\int_0^h u^2 d\eta}{U^2 h}, \quad \beta_y = \frac{\int_0^h v^2 d\eta}{V^2 h}, \quad \beta_{xy} = \frac{\int_0^h u v d\eta}{U V h}, \quad (1.52)$$

are equal to unity, with  $\eta$  as the vertical distance above the channel bed. In uniform and one-dimensional gradually varied turbulent open channel flows, the velocity distribution is typically approximated by the logarithmic law of the wall (Fig. 1.6a), which for a rough bed is (White 1991, Montes 1998)

$$\frac{u}{u^*} = \frac{1}{\kappa} \ln \left( \frac{\eta}{k_s} \right) + B. \quad (1.53)$$

Here  $u^* = (\tau_b/\rho)^{1/2}$  is the shear velocity,  $\kappa (=0.41)$  the von Kármán constant,  $k_s$  the equivalent roughness height and  $B$  ( $\approx 8.5$ ) a constant of integration. Other velocity distributions as the power law and the wall-wake law are also used in open channel flow problems (Montes 1998; Chanson 2004).

The Boussinesq velocity correction coefficient is of the order of  $\beta_x \approx 1.05$  for these flows (Chow 1959; Henderson 1966; Chaudhry 2008). Thus, given the small contribution of the differential advection originating from the non-uniformity of  $u$  and  $v$  with depth, the Boussinesq velocity correction coefficients in the  $x$ - and  $y$ -directions are assumed to be unity. Likewise, Eq. (1.39) then reads for the depth-averaged  $y$ -momentum balance

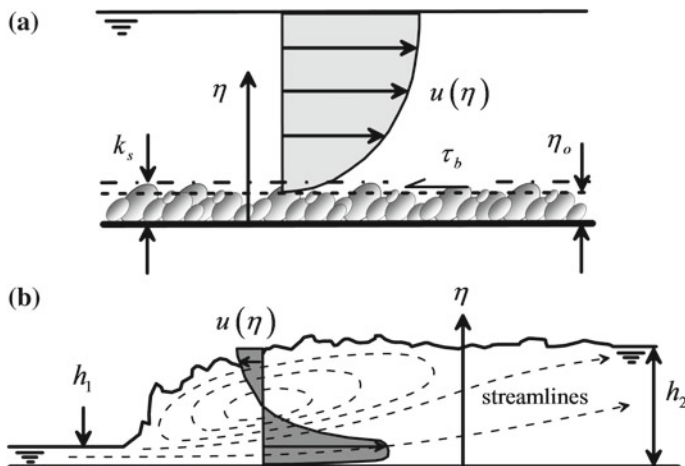


**Fig. 1.6** Examples of velocity distributions in open channel flows **a** log-law velocity distribution in rough-bed uniform open channel flow, **b** velocity distribution in hydraulic jumps, with a jet flow and a roller flow above

$$\begin{aligned} \frac{\partial}{\partial t}(Vh) + \frac{\partial}{\partial y}(V^2 h) + \frac{\partial}{\partial x}(VUh) \\ = -\frac{1}{\rho} \left[ \frac{\partial}{\partial y} \int_{z_b}^{z_s} \tau_{yy} dz + \frac{\partial}{\partial x} \int_{z_b}^{z_s} \tau_{xy} dz + (\tau_{yy})_b \frac{\partial z_b}{\partial y} + (\tau_{xy})_b \frac{\partial z_b}{\partial x} - (\tau_{yz})_b \right]. \end{aligned} \quad (1.54)$$

Caution is claimed here by pointing out that taking the velocity correction coefficients equal to unity is a legitimate approximation for gradually varied flows (setting aside compound channel flows), but not so in rapidly varied flows. A prominent example is the hydraulic jump (Fig. 1.4b). Within the region of high turbulence and shear, the  $u$ -velocity profiles are highly non-uniform in the vertical direction. The correction coefficients are easily of the order of  $\beta_x = 2.5$  (Fig. 1.6b), encompassing a jet-like flow which spreads below a recirculation vortex or roller (Khan and Steffler 1996a; Castro-Orgaz and Hager 2009). Obviously, these coefficients cannot be neglected. As will be shown in Chap. 5, the SWE permit to catch hydraulic jumps as local discontinuities, excluding the detailed variation of the field variables across it, including the free surface and the velocity profiles. This fact has double implications: (1) the SWE can detect a hydraulic jump, and identify it as a point-like discontinuity, but cannot resolve the flow within it; (2) there is no need to introduce any correction coefficient  $\beta$  given that the equations do not resolve the internal flow phenomena of a hydraulic jump. This feature must be fully accounted for only if a higher-order depth-averaged model is considered for resolving the detailed free surface profile of the hydraulic jump (Khan and Steffler 1996a; Castro-Orgaz and Hager 2009).

Using Eqs. (1.47) for the stress tensor  $\tau_{ij}$ , and neglecting stresses of depth-averaging in Eqs. (1.51) and (1.54), produces

$$\begin{aligned} \frac{\partial}{\partial t}(Uh) + \frac{\partial}{\partial x}(U^2 h) + \frac{\partial}{\partial y}(UVh) \\ = -\frac{1}{\rho} \left[ \frac{\partial}{\partial x} \int_{z_b}^{z_s} p dz + p_b \frac{\partial z_b}{\partial x} - (\sigma_{xy})_b \frac{\partial z_b}{\partial y} + (\sigma_{xz})_b \right], \end{aligned} \quad (1.55)$$

$$\begin{aligned} \frac{\partial}{\partial t}(Vh) + \frac{\partial}{\partial y}(V^2 h) + \frac{\partial}{\partial x}(VUh) \\ = -\frac{1}{\rho} \left[ \frac{\partial}{\partial y} \int_{z_b}^{z_s} p dz + p_b \frac{\partial z_b}{\partial y} - (\sigma_{xy})_b \frac{\partial z_b}{\partial x} + (\sigma_{yz})_b \right]. \end{aligned} \quad (1.56)$$

A typical assumption in the derivation of the gradually varied SWE is that the pressure distribution is hydrostatic. From Eq. (1.4), the vertical momentum balance is thus for a hydrostatic flow

$$\frac{dp}{dz} = -\rho g. \quad (1.57)$$

Integrating in the  $z$ -direction, taking zero pressure as reference at the free surface, yields

$$p = \rho gh \left(1 - \frac{\eta}{h}\right) = p_b \left(1 - \frac{\eta}{h}\right). \quad (1.58)$$

This is a linear distribution of fluid pressure (Fig. 1.7), with the bed pressure equal to the weight of the water column above, that is,

$$p_b = \rho gh. \quad (1.59)$$

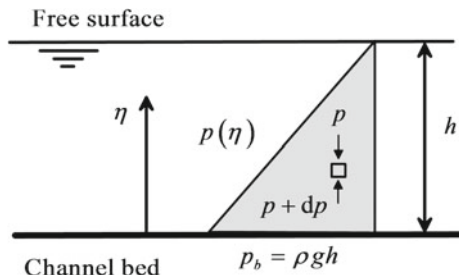
To highlight the conditions under which this approximation is valid, consider the general Eq. (1.46) for the  $z$ -momentum balance. This is an equation for the bottom pressure, which yields, by using Eq. (1.47) for the stress tensor, after assuming that  $(u, v, w)$  are approximated by the corresponding depth-averaged values  $(U, V, W)$ , material surfaces at the free surface and the bed ( $M_s = M_b = 0$ ), depth-averaged density, zero free surface stresses, and neglecting turbulent stresses due to depth-averaging,

$$p_b = \rho gh + \frac{\partial}{\partial t}(\rho Wh) + \frac{\partial}{\partial x}(\rho WUh) + \frac{\partial}{\partial y}(\rho WVh) + (\sigma_{zz})_b - (\sigma_{xz})_b \frac{\partial z_b}{\partial x} - (\sigma_{yz})_b \frac{\partial z_b}{\partial y}. \quad (1.60)$$

In addition to the simplifications introduced above ab initio, the following approximations are now required to reduce Eq. (1.60) to Eq. (1.59):

- Temporal rate of variation of  $W$  must be small. This is equivalent to neglect the local vertical acceleration.
- Velocity  $W$  must be negligible in comparison to  $U$  and  $V$ . The ratios  $W/U$  and  $W/V$  representing streamline inclinations are small, or, more precisely, their

**Fig. 1.7** Hydrostatic pressure distribution in open channel flow



variations in  $x$ - and  $y$ -directions, which represents the flow curvatures. This is equivalent to neglect the convective vertical acceleration.

- Turbulent normal stress  $\sigma_{zz}$  at the base must be negligible. This is only possible if the channel slope is small (see Sect. 1.4.1).
- Bed slopes in the  $x$ - and  $y$ -directions must be small.

Therefore, a hydrostatic flow resembles those occurring in a small slope channel with almost horizontal streamlines, a low turbulence level, and uniform velocities in the vertical direction. For non-hydrostatic problems, all or part of these effects must be accounted for in the momentum equations (Serre 1953; Stansby and Zhou 1998; Castro-Orgaz and Hager 2017). Introducing the hydrostatic pressure approximation in Eqs. (1.55)–(1.56) produces

$$\begin{aligned} \frac{\partial}{\partial t}(Uh) + \frac{\partial}{\partial x}(U^2 h) + \frac{\partial}{\partial y}(UVh) \\ = -gh \frac{\partial h}{\partial x} - gh \frac{\partial z_b}{\partial x} + \frac{1}{\rho} (\sigma_{xy})_b \frac{\partial z_b}{\partial y} - \frac{1}{\rho} (\sigma_{xz})_b, \end{aligned} \quad (1.61)$$

$$\begin{aligned} \frac{\partial}{\partial t}(Vh) + \frac{\partial}{\partial y}(V^2 h) + \frac{\partial}{\partial x}(VUh) \\ = -gh \frac{\partial h}{\partial y} - gh \frac{\partial z_b}{\partial y} + \frac{1}{\rho} (\sigma_{xy})_b \frac{\partial z_b}{\partial x} - \frac{1}{\rho} (\sigma_{yz})_b. \end{aligned} \quad (1.62)$$

To be coherent with Eq. (1.59), the bed slopes in the  $x$ - and  $y$ -directions are assumed to be small, eliminating the corresponding stress contributions due to slopes, resulting in the depth-averaged SWE or Saint-Venant equations (Vreugdenhil 1994; Toro 2001)

$$\frac{\partial}{\partial t}(Uh) + \frac{\partial}{\partial x}(U^2 h) + \frac{\partial}{\partial y}(UVh) = -gh \frac{\partial z_s}{\partial x} - \frac{1}{\rho} (\sigma_{xz})_b, \quad (1.63)$$

$$\frac{\partial}{\partial t}(Vh) + \frac{\partial}{\partial y}(V^2 h) + \frac{\partial}{\partial x}(VUh) = -gh \frac{\partial z_s}{\partial y} - \frac{1}{\rho} (\sigma_{yz})_b, \quad (1.64)$$

where the gradients of  $z_s = z_b + h$ , the free surface elevation, are used. Finally, with  $C_f$  as a bed friction coefficient, closure for the bed turbulent stresses is given by

$$(\sigma_{xz})_b = \rho C_f U (U^2 + V^2)^{1/2}, \quad (\sigma_{yz})_b = \rho C_f V (U^2 + V^2)^{1/2}. \quad (1.65)$$

### 1.3.2 1D Cross-Sectional Averaged Equations

Consider an open channel flow with a predominant movement in the  $x$ -direction, so that the flow geometry can be characterized taking vertical sections of area  $A$  (Fig. 1.8) and an axis connecting these sections. In general, the free surfaces within the cross sections will be inclined, but if these variations are gentle, a horizontal free surface on each flow area  $A$  can be assumed. Further, if the river is curved in plan, it is feasible to approximate  $x$  as the curvilinear distance following the axis if the channel curvatures are weak and can thus be neglected.

Consider a generic cross section with a horizontal free surface, as sketched in Fig. 1.9. The depth-averaged continuity Eq. (1.50) will be laterally integrated from the left to the right channel banks (points 1 and 2 in Fig. 1.9), resulting in

$$\int_{y_l}^{y_r} \left[ \frac{\partial h}{\partial t} + \frac{\partial}{\partial x} (Uh) + \frac{\partial}{\partial y} (Vh) \right] dy = 0. \quad (1.66)$$

**Fig. 1.8** Open channel flow with a predominant movement in the longitudinal direction

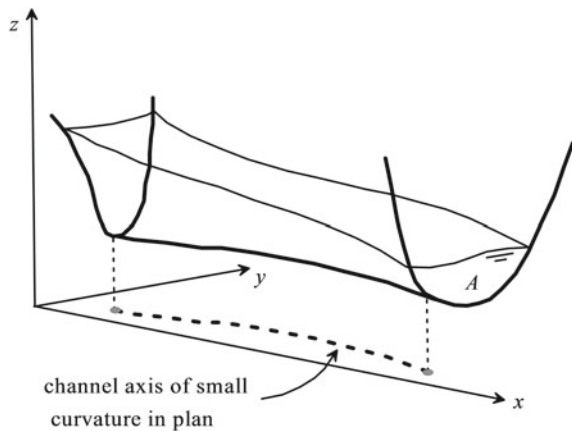
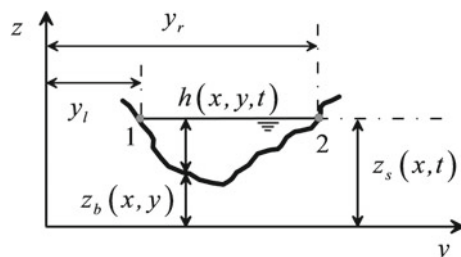


**Fig. 1.9** Generic cross section with horizontal free surface



Note that within the flow section both  $h$  and  $z_b$  are variable, but  $z_s$  is a constant. Now, the following identity is developed by application of Leibniz's rule:

$$\int_{y_l}^{y_r} \frac{\partial h}{\partial t} dy = \frac{\partial}{\partial t} \int_{y_l}^{y_r} h(x, y, t) dy - h_r \frac{\partial y_r}{\partial t} + h_l \frac{\partial y_l}{\partial t} = \frac{\partial A}{\partial t} - h_r \frac{\partial y_r}{\partial t} + h_l \frac{\partial y_l}{\partial t}, \quad (1.67)$$

where the flow area is defined by

$$A(x, t) = \int_{y_l}^{y_r} \int_{z_b}^{z_s} dy dz = \int_{y_l}^{y_r} h(x, y, t) dy. \quad (1.68)$$

The lateral integration of the second term in Eq. (1.66) yields

$$\int_{y_l}^{y_r} \frac{\partial(Uh)}{\partial x} dy = \frac{\partial}{\partial x} \int_{y_l}^{y_r} Uh dy - (Uh)_r \frac{\partial y_r}{\partial x} + (Uh)_l \frac{\partial y_l}{\partial x} = \frac{\partial Q}{\partial x} - (Uh)_r \frac{\partial y_r}{\partial x} + (Uh)_l \frac{\partial y_l}{\partial x}, \quad (1.69)$$

where the discharge  $Q$  is given by

$$Q(x, t) = \int_{y_l}^{y_r} \int_{z_b}^{z_s} u dy dz = \int_{y_l}^{y_r} Uh dy. \quad (1.70)$$

Integration of the remaining term related to  $V$  produces

$$\int_{y_l}^{y_r} \frac{\partial(Vh)}{\partial y} dy = (Vh)_r - (Vh)_l. \quad (1.71)$$

Summing Eqs. (1.67), (1.69) and (1.71) yields

$$\frac{\partial A}{\partial t} + \frac{\partial Q}{\partial x} + h_l \left( \frac{\partial y_l}{\partial t} + U_l \frac{\partial y_l}{\partial x} - V_l \right) - h_r \left( \frac{\partial y_r}{\partial t} + U_r \frac{\partial y_r}{\partial x} - V_r \right) = 0. \quad (1.72)$$

To further simplify Eq. (1.72), Chen and Chow (1968) assumed that the depth-averaged velocity field  $(U, V)$  must satisfy a kinematic boundary condition at the banks, whereas Jain (2001) considered the usual case of a cross section of zero water depth at the banks, e.g.,  $z_s = z_b$  (Fig. 1.9). One may state, therefore,

$$h_l \left( \frac{\partial y_l}{\partial t} + U_l \frac{\partial y_l}{\partial x} - V_l \right) = 0 \Rightarrow \begin{cases} \frac{\partial y_l}{\partial t} + U_l \frac{\partial y_l}{\partial x} - V_l = 0 & \Rightarrow \text{Option 1} \\ h_l = 0 & \Rightarrow \text{Option 2} \end{cases} \quad (1.73)$$

$$h_r \left( \frac{\partial y_r}{\partial t} + U_r \frac{\partial y_r}{\partial x} - V_r \right) = 0 \Rightarrow \begin{cases} \frac{\partial y_r}{\partial t} + U_r \frac{\partial y_r}{\partial x} - V_r = 0 & \Rightarrow \text{Option 1} \\ h_r = 0 & \Rightarrow \text{Option 2} \end{cases} \quad (1.74)$$

By using either of the two arguments, Eq. (1.72) simplifies to the section-averaged continuity equation

$$\frac{\partial A}{\partial t} + \frac{\partial Q}{\partial x} = 0. \quad (1.75)$$

Further, the  $x$ -momentum equation [Eq. (1.51)] will be laterally integrated. For convenience in ensuing developments, the identity

$$\int_{z_b}^{z_s} \left( \frac{\partial \tau_{xy}}{\partial y} + \frac{\partial \tau_{xz}}{\partial z} \right) dz = \frac{\partial}{\partial y} \int_{z_b}^{z_s} \tau_{xy} dz + (\tau_{xy})_b \frac{\partial z_b}{\partial y} - (\tau_{xz})_b, \quad (1.76)$$

is used to revert a step of the depth-integration process, resulting in

$$\frac{\partial}{\partial t} (Uh) + \frac{\partial}{\partial x} (U^2 h) + \frac{\partial}{\partial y} (UVh) = -\frac{1}{\rho} \left[ \frac{\partial}{\partial x} \int_{z_b}^{z_s} \tau_{xx} dz + (\tau_{xx})_b \frac{\partial z_b}{\partial x} + \int_{z_b}^{z_s} \left( \frac{\partial \tau_{xy}}{\partial y} + \frac{\partial \tau_{xz}}{\partial z} \right) dz \right]. \quad (1.77)$$

Considering the stress tensor given by Eqs. (1.47), (1.77) transforms to

$$\begin{aligned} \frac{\partial}{\partial t} (Uh) + \frac{\partial}{\partial x} (U^2 h) + \frac{\partial}{\partial y} (UVh) = & -\frac{1}{\rho} \left[ \frac{\partial}{\partial x} \int_{z_b}^{z_s} (p - \sigma_{xx}) dz + (p - \sigma_{xx})_b \frac{\partial z_b}{\partial x} \right. \\ & \left. - \int_{z_b}^{z_s} \left( \frac{\partial \sigma_{xy}}{\partial y} + \frac{\partial \sigma_{xz}}{\partial z} \right) dz \right]. \end{aligned} \quad (1.78)$$

Assuming hydrostatic pressure distribution and neglecting  $\sigma_{xx}$ , one may write Eq. (1.78) as

$$\frac{\partial}{\partial t} (Uh) + \frac{\partial}{\partial x} (U^2 h) + \frac{\partial}{\partial y} (UVh) = -\frac{1}{\rho} \left[ \frac{\partial}{\partial x} \left( \frac{1}{2} \rho g h^2 \right) + \rho g h \frac{\partial z_b}{\partial x} - \int_{z_b}^{z_s} \left( \frac{\partial \sigma_{xy}}{\partial y} + \frac{\partial \sigma_{xz}}{\partial z} \right) dz \right], \quad (1.79)$$

or,

$$\frac{\partial}{\partial t}(Uh) + \frac{\partial}{\partial x}(U^2h) + \frac{\partial}{\partial y}(UVh) = -gh \frac{\partial z_s}{\partial x} + \frac{1}{\rho} \left[ \int_{z_b}^{z_s} \left( \frac{\partial \sigma_{xy}}{\partial y} + \frac{\partial \sigma_{xz}}{\partial z} \right) dz \right]. \quad (1.80)$$

Equation (1.80) is now laterally integrated as

$$\int_{y_l}^{y_r} \left[ \frac{\partial}{\partial t}(Uh) + \frac{\partial}{\partial x}(Uh^2) + \frac{\partial}{\partial y}(UVh) \right] dy = \int_{y_l}^{y_r} \left[ -gh \frac{\partial z_s}{\partial x} + \frac{1}{\rho} \int_{z_b}^{z_s} \left( \frac{\partial \sigma_{xy}}{\partial y} + \frac{\partial \sigma_{xz}}{\partial z} \right) dz \right] dy. \quad (1.81)$$

The following identities are generated to integrate the acceleration terms [left-hand side of Eq. (1.81)]

$$\int_{y_l}^{y_r} \frac{\partial}{\partial t}(Uh) dy = \frac{\partial}{\partial t} \int_{y_l}^{y_r} Uh dy - (Uh)_r \frac{\partial y_r}{\partial t} + (Uh)_l \frac{\partial y_l}{\partial t}, \quad (1.82)$$

$$\int_{y_l}^{y_r} \frac{\partial(U^2h)}{\partial x} dy = \frac{\partial}{\partial x} \int_{y_l}^{y_r} U^2 h dy - (U^2h)_r \frac{\partial y_r}{\partial x} + (U^2h)_l \frac{\partial y_l}{\partial x}, \quad (1.83)$$

$$\int_{y_l}^{y_r} \frac{\partial(UVh)}{\partial y} dy = (UVh)_r - (UVh)_l. \quad (1.84)$$

Summing Eqs. (1.82)–(1.84) yields

$$\begin{aligned} \int_{y_l}^{y_r} \left[ \frac{\partial}{\partial t}(Uh) + \frac{\partial}{\partial x}(U^2h) + \frac{\partial}{\partial y}(UVh) \right] dy &= \frac{\partial Q}{\partial t} + \frac{\partial}{\partial x} \left( \frac{Q^2}{A} \right) \\ &+ (Uh)_l \left( \frac{\partial y_l}{\partial t} + U_l \frac{\partial y_l}{\partial x} - V_l \right) - (Uh)_r \left( \frac{\partial y_r}{\partial t} + U_r \frac{\partial y_r}{\partial x} - V_r \right), \end{aligned} \quad (1.85)$$

and, using Eqs. (1.73)–(1.74),

$$\int_{y_l}^{y_r} \left[ \frac{\partial}{\partial t}(Uh) + \frac{\partial}{\partial x}(U^2 h) + \frac{\partial}{\partial y}(UVh) \right] dy = \frac{\partial Q}{\partial t} + \frac{\partial}{\partial x} \left( \frac{Q^2}{A} \right). \quad (1.86)$$

In this process, the variation of  $U$  in the lateral direction was neglected. If the variation of the velocity component  $u$  within the cross section is accounted for, the momentum flux term  $Q^2/A$  should be multiplied by the Boussinesq correction coefficient for the section (Liggett 1994; Montes 1998), given by

$$\beta = \frac{\int_A u^2 dA}{(Q^2/A)}. \quad (1.87)$$

For a horizontal water surface within the cross section, the free surface slope term reads

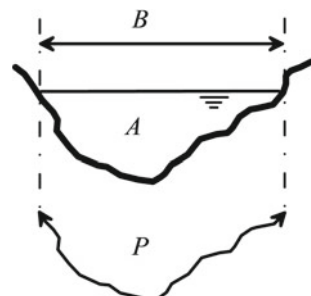
$$\int_{y_l}^{y_r} -g \frac{\partial z_s}{\partial x} h(x, y, t) dy = -g \frac{\partial z_s}{\partial x} \int_{y_l}^{y_r} h(x, y, t) dy = -g \frac{\partial z_s}{\partial x} A. \quad (1.88)$$

Using Green's theorem, the following identity is generated (Keulegan and Patterson 1943)

$$\int_{y_l}^{y_r} \int_{z_b}^{z_s} \left( \frac{\partial \sigma_{xy}}{\partial y} + \frac{\partial \sigma_{xz}}{\partial z} \right) dz dy = \int_A \left( \frac{\partial \sigma_{xy}}{\partial y} + \frac{\partial \sigma_{xz}}{\partial z} \right) dA = \oint_C (\sigma_{xy} dz - \sigma_{xz} dy), \quad (1.89)$$

where the line integral extends along a contour  $C$  as the sum of the wetted perimeter  $P$  (Fig. 1.10) and the free surface width  $B$ . The integrand of the line integral is the  $x$ -component of the fluid force exerted on the channel solid contour and free surface. This shear force is denoted by  $\tau_b$ , from which a mean shear stress  $\bar{\tau}_o$  is defined by

**Fig. 1.10** Definition of wetted perimeter



$$\oint_C (\sigma_{xy} dz - \sigma_{xz} dy) = \oint_C \tau_b dP = -\bar{\tau}_o P, \quad (1.90)$$

where stresses acting on the free surface are neglected.

Inserting Eqs. (1.86), (1.88), and (1.90) into Eq. (1.81) yields the cross-sectional averaged  $x$ -momentum balance as

$$\frac{\partial Q}{\partial t} + \frac{\partial}{\partial x} \left( \frac{Q^2}{A} \right) = -gA \frac{\partial z_s}{\partial x} - \frac{1}{\rho} \bar{\tau}_o P. \quad (1.91)$$

This equation is valid for non-prismatic channels and is a form widely used in river hydraulics computations (Cunge et al. 1980; Wu 2008). Defining the friction slope  $S_f$  as

$$S_f = \frac{\bar{\tau}_o P}{\rho g A} = \frac{\bar{\tau}_o}{\rho g R_h}, \quad (1.92)$$

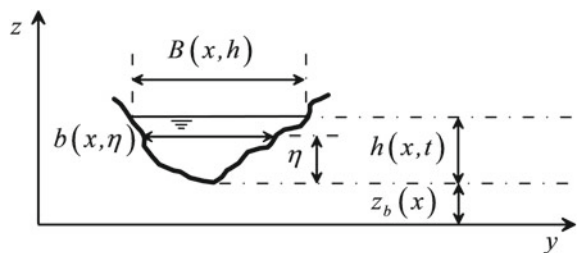
where  $R_h = A/P$  is the hydraulic radius, the following “slope form” results (Cunge et al. 1980; Chow et al. 1988)

$$\frac{\partial Q}{\partial t} + \frac{\partial}{\partial x} \left( \frac{Q^2}{A} \right) = gA \left( S_o - S_f - \frac{\partial h}{\partial x} \right), \quad (1.93)$$

where  $S_o = -\partial z_b / \partial x$  is the bottom slope. For practical computations, consider a flow depth and bed elevation taking as reference the thalweg; thus  $h = h(x, t)$  and  $z_b = z_b(x, t)$  (Fig. 1.11). Consider further a transformation of Eq. (1.93), which is widely used in practice. The hydrostatic pressure force on an arbitrary cross section is

$$F_p = \int_A p dA = \rho g \int_A (h - \eta) dA = \rho g \int_0^{h(x)} (h - \eta) b(x, \eta) d\eta, \quad (1.94)$$

**Fig. 1.11** Definition of flow depth and bed elevation in non-prismatic channel section



where the width  $b$  at elevation  $\eta$  is a function of  $x$  in non-prismatic channels (Fig. 1.11). The centroid of the flow section is defined by its depth below the free surface  $\bar{h}$ . Thus, from Eq. (1.94), one can write

$$\frac{F_p}{\rho g} = A\bar{h} = \int_A (h - \eta) dA = \int_0^{h(x)} (h - \eta) b(x, \eta) d\eta. \quad (1.95)$$

The product  $A\bar{h}$  is obviously the fundamental quantity determining the pressure forces. Now, its  $x$ -gradient is computed as follows (Cunge et al. 1980)

$$\begin{aligned} \frac{\partial}{\partial x} (A\bar{h}) &= \frac{\partial}{\partial x} \int_0^{h(x)} (h - \eta) b(x, \eta) d\eta = \int_0^{h(x)} \frac{\partial}{\partial x} [(h - \eta) b] d\eta = \int_0^{h(x)} \frac{\partial h}{\partial x} b d\eta + \int_0^{h(x)} (h - \eta) \frac{\partial b}{\partial x} d\eta \\ &= \frac{\partial h}{\partial x} \int_0^{h(x)} b d\eta + \int_0^{h(x)} (h - \eta) \frac{\partial b}{\partial x} d\eta = \frac{\partial h}{\partial x} A + \int_0^{h(x)} (h - \eta) \frac{\partial b}{\partial x} d\eta. \end{aligned} \quad (1.96)$$

This relation expresses the spatial variation of hydrostatic pressure forces per unit weight in a non-prismatic channel.

Inserting Eq. (1.96) into Eq. (1.93) produces the alternative form for non-prismatic channels

$$\frac{\partial Q}{\partial t} + \frac{\partial}{\partial x} \left( \frac{Q^2}{A} + gA\bar{h} \right) = gA(S_o - S_f) + g \int_0^{h(x)} (h - \eta) \frac{\partial b}{\partial x} d\eta. \quad (1.97)$$

In compound channels, the equivalent roughness height of the main channel is lower than in the flood plains, resulting in a significant lateral variation of the depth-averaged velocity  $U$  (Fig. 1.12). The result is that  $\beta$  becomes significant and must be accounted for in the momentum balance [Eq. (1.97)] as (Montes 1998; Sturm 2001; Jain 2001)

$$\frac{\partial Q}{\partial t} + \frac{\partial}{\partial x} \left( \beta \frac{Q^2}{A} + gA\bar{h} \right) = gA(S_o - S_f) + g \int_0^{h(x)} (h - \eta) \frac{\partial b}{\partial x} d\eta. \quad (1.98)$$

If the pressure is assumed to be hydrostatic and the velocity uniform, the specific momentum  $M$  in free surface flows is defined as (Jaeger 1956; Montes 1998)

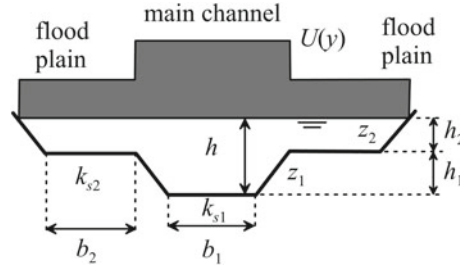


**Fig. 1.12** Lateral distribution of depth-averaged velocity component in  $x$ -direction for uniform flow in compound channel cross section, assuming that the velocity is constant in main channel and flood plains, each linked to a different value of the equivalent roughness  $k_s$

$$M = \int_A \left( \frac{u^2}{g} + \frac{p}{\rho g} \right) dA \approx \beta \frac{Q^2}{gA} + A\bar{h} \approx \frac{Q^2}{gA} + A\bar{h}. \quad (1.99)$$

The definition of  $M$  arises thus naturally from the application of the  $x$ -momentum balance, as evidenced on inspecting Eq. (1.97). For a prismatic channel, Eq. (1.98) reduces to

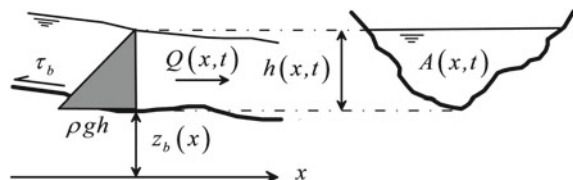
$$\frac{\partial Q}{\partial t} + \frac{\partial}{\partial x} \left( \frac{Q^2}{A} + gA\bar{h} \right) = gA(S_o - S_f). \quad (1.100)$$

This is a form widely employed to compute 1D unsteady free surface flows in prismatic channels (Chaudhry 2008) (Fig. 1.13).

A practical result is directly regained from Eq. (1.100). For steady flow in a hydraulic jump on a horizontal channel, neglecting friction forces, Eq. (1.100) may be integrated between the boundary sections upstream and downstream of the jump, where the flow is gradually varied, resulting in

$$\left( \frac{Q^2}{A} + gA\bar{h} \right)_{\text{upstream}} = \left( \frac{Q^2}{A} + gA\bar{h} \right)_{\text{downstream}}. \quad (1.101)$$

**Fig. 1.13** 1D unsteady free surface flow in prismatic channel



This states conservation of  $M$  between the boundaries of a control volume containing inside the rapidly varied flow produced within a hydraulic jump (Fig. 1.6b). This is the fundamental equation of hydraulic jumps, to be used in Chap. 4.

For steady flows, Eq. (1.93) yields

$$\frac{d}{dx} \left( \frac{Q^2}{A} \right) = -gA \frac{dh}{dx} - gA \frac{dz_b}{dx} - gAS_f, \quad (1.102)$$

or,

$$-\frac{Q^2}{A^2} \frac{dA}{dx} = -gA \frac{dh}{dx} - gA \frac{dz_b}{dx} - gAS_f. \quad (1.103)$$

For a non-prismatic channel, the  $x$ -derivative of the flow area  $A$  can be expressed as

$$\frac{dA}{dx} = \frac{\partial A}{\partial h} \frac{dh}{dx} + \left( \frac{\partial A}{\partial x} \right)_{h=\text{const.}}. \quad (1.104)$$

These partial derivatives are trivially simple to evaluate in man-made channels; for example, the result for a rectangular channel of variable width is

$$A(x, h) = b(x)h \Rightarrow \left( \frac{\partial A}{\partial x} \right)_{h=\text{const.}} = h \frac{db}{dx}, \quad \frac{\partial A}{\partial h} = b. \quad (1.105)$$

Inserting Eq. (1.104) into Eq. (1.103) yields

$$gA \left( 1 - \frac{Q^2}{gA^3} \frac{\partial A}{\partial h} \right) \frac{dh}{dx} = gA(S_o - S_f) + \frac{Q^2}{A^2} \left( \frac{\partial A}{\partial x} \right)_{h=\text{const.}}, \quad (1.106)$$

from which the ordinary differential equation describing the flow surface profile is (Le Méhauté 1976; Katopodes 2019)

$$\frac{dh}{dx} = \frac{S_o - S_f + \frac{Q^2}{gA^3} \left( \frac{\partial A}{\partial x} \right)_{h=\text{const.}}}{1 - \frac{Q^2}{gA^3} B} = \frac{S_o - S_f + \frac{F^2}{B} \left( \frac{\partial A}{\partial x} \right)_{h=\text{const.}}}{1 - F^2}. \quad (1.107)$$

Here the Froude number  $F$  is defined as

$$F = \frac{Q/A}{(gA/B)^{1/2}}, \quad (1.108)$$

and the free surface width  $B$  is determined from

$$\frac{\partial A}{\partial h} = \frac{\partial}{\partial h} \int_0^h b(x, \eta) d\eta = B. \quad (1.109)$$

The Froude number is a fundamental dimensionless number governing free surface flows. Its physical meaning will be explained in detail in Chap. 2. For a prismatic channel  $\partial A / \partial x = 0$ , and Eq. (1.107) simplifies to the steady gradually varied flow equation for prismatic channels

$$\frac{dh}{dx} = \frac{S_o - S_f}{1 - F^2}. \quad (1.110)$$

Equations (1.107) and (1.110) are widely used in open channel hydraulics, but it should be borne in mind that they are unreliable in highly curvilinear flows, as for flows over a dam spillway crest operating at a high head (Montes 1998).

## 1.4 Non-hydrostatic Theory

### 1.4.1 1D Shallow Water Non-hydrostatic Equations

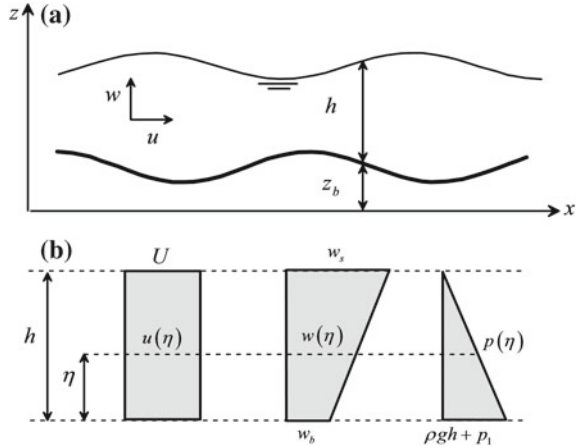
Steffler and Jin (1993) and Khan and Steffler (1996b, c) developed a depth-averaged non-hydrostatic 1D momentum model for flows in the vertical plane  $(x, z)$ , to be described here. Other approximations are presented in Chap. 11. Consider a 2D steady flow over a wavy bed (Fig. 1.14a). The velocity component  $u$  in the  $x$ -direction is approximated by its depth-averaged value  $U$ , like in the Saint-Venant theory, but the vertical velocity  $w$  and the non-hydrostatic fluid pressure  $p$  are assumed to vary linearly in the vertical direction (Fig. 1.14b). Assuming 1D flow in the  $x$ -direction, using Eq. (1.47) for the stress tensor and neglecting depth-averaged turbulent stresses, Eq. (1.51) takes the form

$$\frac{\partial}{\partial t}(Uh) + \frac{\partial}{\partial x} \left( U^2 h + \int_{z_b}^{z_s} \frac{p}{\rho} dz \right) = \frac{1}{\rho} \left[ -p_b \frac{\partial z_b}{\partial x} - (\sigma_{xz})_b + \sigma_{xx} \frac{\partial z_b}{\partial x} \right], \quad (1.111)$$

whereas Eq. (1.60) yields for 1D flow

$$p_b = \rho gh + \frac{\partial}{\partial t}(\rho Wh) + \frac{\partial}{\partial x}(\rho WUh) + (\sigma_{zz})_b - (\sigma_{xz})_b \frac{\partial z_b}{\partial x}. \quad (1.112)$$

**Fig. 1.14** 1D non-hydrostatic flow over uneven terrain **a** longitudinal profile, **b** assumed horizontal and vertical velocity, and pressure profiles



Simple shear along the bed slope with tangential stress  $\tau_b$  is considered. For this choice, the bed Reynolds stresses are given by (Steffler and Jin 1993; Castro-Orgaz and Hager 2017)

$$\begin{aligned} (\sigma_{zz})_b &= 2\tau_b \cos \theta \sin \theta, \\ (\sigma_{xx})_b &= -2\tau_b \cos \theta \sin \theta, \\ (\sigma_{xz})_b &= \tau_b (\cos^2 \theta - \sin^2 \theta), \end{aligned} \quad (1.113)$$

where  $\theta$  is the bed slope angle. It is therefore obvious that the bed Reynolds stresses are not negligible on steep slopes. For  $\theta \rightarrow 0$  the channel is of a small slope, resulting in

$$(\sigma_{zz})_b \approx 0, \quad (\sigma_{xx})_b \approx 0, \quad (\sigma_{xz})_b \approx \tau_b. \quad (1.114)$$

This is an approximation used in the Saint-Venant theory, but not here. The Reynolds stresses contribution in the  $x$ -momentum equation is thus

$$\begin{aligned} -(\sigma_{xx})_b \frac{\partial z_b}{\partial x} + (\sigma_{xz})_b &= 2\tau_b \cos \theta \sin \theta \left( \frac{\sin \theta}{\cos \theta} \right) + \tau_b (\cos^2 \theta - \sin^2 \theta) \\ &= \tau_b (\cos^2 \theta + \sin^2 \theta) = \tau_b. \end{aligned} \quad (1.115)$$

The Reynolds stresses contribution to the  $z$ -momentum balance is

$$\begin{aligned} (\sigma_{zz})_b - (\sigma_{zx})_b \frac{\partial z_b}{\partial x} &= 2\tau_b \cos \theta \sin \theta - \tau_b (\cos^2 \theta - \sin^2 \theta) \left( \frac{\sin \theta}{\cos \theta} \right) \\ &= \tau_b \sin \theta \left[ \frac{\sin^2 \theta + \cos^2 \theta}{\cos \theta} \right] = \tau_b \frac{\sin \theta}{\cos \theta} = \tau_b \frac{\partial z_b}{\partial x}. \end{aligned} \quad (1.116)$$

Inserting Eqs. (1.115)–(1.116) for a pure bed shear into Eqs. (1.111) and (1.112) gives

$$\frac{\partial}{\partial t}(Uh) + \frac{\partial}{\partial x} \left( U^2 h + \int_{z_b}^{z_s} \frac{p}{\rho} dz \right) = -\frac{p_b}{\rho} \frac{\partial z_b}{\partial x} - \frac{\tau_b}{\rho}, \quad (1.117)$$

$$p_b = \underbrace{\rho g h}_{\text{hydrostatic term}} + \underbrace{\rho \frac{\partial}{\partial t}(Wh)}_{\text{local acceleration}} + \underbrace{\rho \frac{\partial}{\partial x}(WUh)}_{\text{convective acceleration}} + \underbrace{\tau_b \frac{\partial z_b}{\partial x}}_{\text{Reynolds stresses}}. \quad (1.118)$$

The vertical velocity  $w$  is assumed to vary linearly with depth (Fig. 1.14b). Its depth-averaged value  $W$  is thus given by

$$W = \frac{w_s + w_b}{2}, \quad (1.119)$$

where the free surface and bed kinematic boundary conditions are, respectively,

$$w_s = \frac{\partial}{\partial t}(h + z_b) + U \frac{\partial}{\partial x}(h + z_b), \quad (1.120)$$

$$w_b = \frac{\partial z_b}{\partial t} + U \frac{\partial z_b}{\partial x}. \quad (1.121)$$

A distribution  $p = p(z)$  must be introduced into Eq. (1.117) for model closure. A linear distribution is assumed following Khan and Steffler (1996b) and Denlinger and Iverson (2004)

$$p = p_b \left( 1 - \frac{\eta}{h} \right) = (p_1 + \rho g h) \left( 1 - \frac{\eta}{h} \right), \quad (1.122)$$

where  $p_1$  is the difference between the actual  $p_b$  and the hydrostatic bottom pressure ( $\rho g h$ ). The non-hydrostatic pressure force is thus

$$\int_{z_b}^{z_s} p dz = \int_0^h p d\eta = \rho g \frac{h^2}{2} + \frac{hp_1}{2}. \quad (1.123)$$

Inserted into Eq. (1.117) yields

$$\frac{\partial}{\partial t}(Uh) + \frac{\partial}{\partial x} \left( U^2 h + g \frac{h^2}{2} + \frac{hp_1}{2\rho} \right) = -\frac{p_b}{\rho} \frac{\partial z_b}{\partial x} - \frac{\tau_b}{\rho}, \quad (1.124)$$

or

$$\frac{\partial}{\partial t}(Uh) + \frac{\partial}{\partial x} \left( U^2 h + \frac{hp_b}{2\rho} \right) = -\frac{p_b}{\rho} \frac{\partial z_b}{\partial x} - \frac{\tau_b}{\rho}. \quad (1.125)$$

This equation is the non-hydrostatic Boussinesq-type  $x$ -momentum equation developed by Khan and Steffler (1996b, c), with closure for  $p_b$  given by Eq. (1.118). For steady flow, the system of equations to solve is

$$\frac{dM}{dx} = -\frac{p_b}{\rho} \frac{dz_b}{dx} - \frac{\tau_b}{\rho}, \quad (1.126)$$

$$M = U^2 h + \frac{hp_b}{2\rho}, \quad (1.127)$$

$$p_b = \rho gh + \rho \frac{d}{dx}(WUh) + \tau_b \frac{dz_b}{dx}. \quad (1.128)$$

$$W = \frac{w_s + w_b}{2}. \quad (1.129)$$

$$w_s = U \frac{d}{dx}(h + z_b), \quad (1.130)$$

$$w_b = U \frac{dz_b}{dx}. \quad (1.131)$$

Inserting Eqs. (1.129)–(1.131) in Eq. (1.128) produces after some manipulations

$$p_b = \rho gh + \rho \frac{U^2}{2} \left[ h \frac{d^2 h}{dx^2} - \left( \frac{dh}{dx} \right)^2 - 2 \frac{dh}{dx} \frac{dz_b}{dx} + 2h \frac{d^2 z_b}{dx^2} \right] + \tau_b \frac{dz_b}{dx}. \quad (1.132)$$

Using the result for  $p_b$ , the specific momentum  $M$  is thus

$$M = g \frac{h^2}{2} + h U^2 \left[ 1 + \frac{1}{4} h \frac{d^2 h}{dx^2} - \frac{1}{4} \left( \frac{dh}{dx} \right)^2 + \frac{1}{2} h \frac{d^2 z_b}{dx^2} - \frac{1}{2} \frac{dh}{dx} \frac{dz_b}{dx} \right] + \frac{h}{2} \frac{dz_b}{dx} \frac{\tau_b}{\rho}. \quad (1.133)$$

Inserting Eqs. (1.132)–(1.133) into Eq. (1.126), a third-order ODE describing  $h = h(x)$  results. This is a Boussinesq-type equation; the solution of this type of equation is presented in Chap. 11. This equation can be used to describe the rapidly varied non-hydrostatic flow over a spillway crest (Figs. 1.3f and 1.4a). For details see Castro-Orgaz and Hager (2017). Note that important non-hydrostatic effects accounted for in Eqs. (1.132)–(1.133) originate from the curvature terms  $\partial^2 h / \partial x^2$  and  $\partial^2 z_b / \partial x^2$ , but non-negligible contributions are also introduced by the slope terms  $\partial h / \partial x$  and  $\partial z_b / \partial x$ . An alternative but similar equation suitable for potential flows is used in Chap. 11.

#### 1.4.2 Uniform and Gradually Varied Flow on Steep Slopes

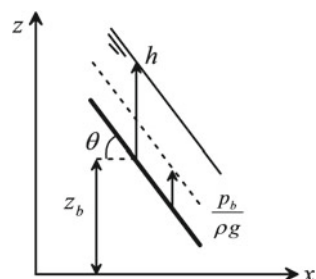
Consider uniform flow on a steep slope (Fig. 1.15), for which the flow depth is a constant and there are not spatial variations of any flow variable. Equations (1.126) and (1.128) simplify then to

$$\tau_b = -p_b \tan \theta, \quad (1.134)$$

$$p_b = \rho gh + \tau_b \tan \theta. \quad (1.135)$$

Combining Eqs. (1.134) and (1.135) results in the non-hydrostatic bottom pressure on a steep slope as (Chaudhry 2008; Castro-Orgaz et al. 2015; Castro-Orgaz and Hager 2017)

**Fig. 1.15** 1D  
non-hydrostatic uniform flow  
on a steep slope



$$\frac{p_b}{\rho g} = \frac{h}{1 + \tan^2 \theta} = h \cos^2 \theta. \quad (1.136)$$

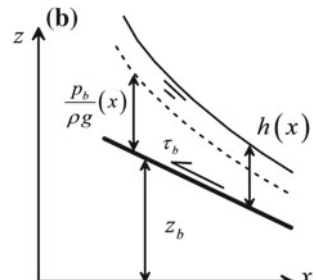
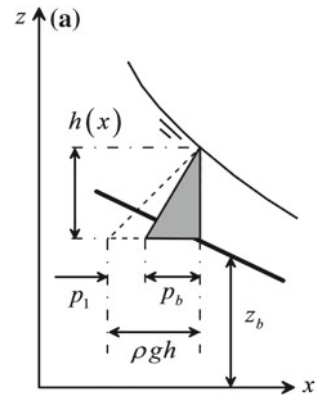
Equation (1.136) indicates that the bottom pressure on a steep slope is non-hydrostatic. This is a classic result (e.g. Chow 1959; Henderson 1966) already highlighted by Lauffer (1935). Consider gradually varied flows on a steep slope (Fig. 1.16), for which the variation of  $h$  with  $x$  is small. Castro-Orgaz and Hager (2017) demonstrate that Eq. (1.136) can be used in gradually varied non-hydrostatic flows on steep slopes. Splitting the bottom pressure in hydrostatic and non-hydrostatic ( $p_1$ ) components reads

$$\frac{p_b}{\rho g} = \frac{h}{1 + \tan^2 \theta} = \frac{p_1}{\rho g} + h, \quad (1.137)$$

which yields for  $p_1$

$$\frac{p_1}{\rho g} = - \frac{\left( \frac{dz_b}{dx} \right)^2}{1 + \left( \frac{dz_b}{dx} \right)^2} h. \quad (1.138)$$

**Fig. 1.16** 1D  
non-hydrostatic gradually  
varied flow on a steep slope  
**a** vertical pressure profile,  
**b** free surface and bottom  
pressure head line



The vertical pressure distribution is therefore linear with this value of  $p_1$  for the non-hydrostatic correction (Fig. 1.16a). The specific momentum  $M$  is thus

$$M = U^2 h + g \frac{h^2}{2} + \frac{hp_1}{2\rho} = U^2 h + g \frac{h^2}{2} - g \frac{\left(\frac{dz_b}{dx}\right)^2 h^2}{1 + \left(\frac{dz_b}{dx}\right)^2} \frac{h^2}{2} = U^2 h + g' \frac{h^2}{2}, \quad (1.139)$$

where  $g'$  is the enhanced gravity to account for slope effects (Denlinger and Iverson 2004; Denlinger and O'Connell 2008), given by

$$g' = g \frac{1}{1 + \left(\frac{dz_b}{dx}\right)^2}. \quad (1.140)$$

The bottom pressure head is thus rewritten as

$$p_b = \rho gh + p_1 = \rho gh \left[ 1 - \frac{\left(\frac{dz_b}{dx}\right)^2}{1 + \left(\frac{dz_b}{dx}\right)^2} \right] = \rho g' h. \quad (1.141)$$

Inserting Eqs. (1.139) and (1.141) into Eq. (1.126) produces the gradually varied flow equation on a steep slope as

$$\frac{d}{dx} \left( U^2 h + g' \frac{h^2}{2} \right) = -g' h \frac{dz_b}{dx} - \frac{\tau_b}{\rho}. \quad (1.142)$$

With  $U = q/h$  as the depth-averaged horizontal velocity, Eq. (1.142) transforms into

$$\frac{dh}{dx} \left[ 1 - \frac{q^2}{g' h^3} \right] = - \frac{dz_b}{dx} - \frac{\tau_b}{\rho g' h}. \quad (1.143)$$

The stress  $\tau_b$  acts tangentially to the sloping plane (Steffler and Jin 1993) (Fig. 1.16b). Therefore, it is parametrized as (Khan and Steffler 1996b)

$$\tau_b = \rho C_f U_o^2, \quad (1.144)$$

with  $C_f$  as the bed friction coefficient and  $U_o$  as the velocity component parallel to the sloping plane. The velocity components of the Boussinesq-type model [given by Eqs. (1.126–1.131)] in the  $(x, z)$  directions are  $(U, W)$ . The following approximation is now used (Khan and Steffler (1996b)

$$U_o \approx (U^2 + W^2)^{1/2}. \quad (1.145)$$

For uniform flow on a steep slope,

$$W = U \left( \frac{dz_b}{dx} \right). \quad (1.146)$$

Using this relation for gradually varied flows, the coupling of Eqs. (1.145)–(1.146) generates

$$U_o = U \left[ 1 + \left( \frac{dz_b}{dx} \right)^2 \right]^{1/2}. \quad (1.147)$$

Thus, combining Eqs. (1.144) and (1.147) yields the bottom shear stress as

$$\tau_b = \rho C_f U^2 \left[ 1 + \left( \frac{dz_b}{dx} \right)^2 \right], \quad (1.148)$$

from which the friction slope on a steep bottom slope is

$$S_f = \frac{\tau_b}{\rho g h} = C_f F^2 \left[ 1 + \left( \frac{dz_b}{dx} \right)^2 \right]. \quad (1.149)$$

Equation (1.143) can be rewritten with  $F = q/(gh^3)^{1/2}$  as

$$\frac{dh}{dx} = \frac{-\frac{dz_b}{dx} - S_f \left[ 1 + \left( \frac{dz_b}{dx} \right)^2 \right]}{1 - F^2 \left[ 1 + \left( \frac{dz_b}{dx} \right)^2 \right]}. \quad (1.150)$$

Inserting Eq. (1.149) then yields

$$\frac{dh}{dx} = \frac{-\frac{dz_b}{dx} - C_f F^2 \left[ 1 + \left( \frac{dz_b}{dx} \right)^2 \right]^2}{1 - F^2 \left[ 1 + \left( \frac{dz_b}{dx} \right)^2 \right]}. \quad (1.151)$$

This is the gradually varied flow equation for non-hydrostatic flow on steep rectangular channels. It will be considered in Chap. 3.

## 1.5 Sediment Transport and Movable Beds

### 1.5.1 1D Cross-Sectional Averaged Continuity Equation

Consider in this section the development of the cross-sectional averaged continuity equation for flows of variable density  $\rho(x, t)$  flowing over a movable bed (Fig. 1.17). Important flows of this kind are dam break waves over erodible beds (Wu 2008; Cantero-Chinchilla et al. 2016). We start with the general depth-integrated continuity equation [Eq. (1.23)]

$$\begin{aligned} \frac{\partial}{\partial t} \int_{z_b}^{z_s} \rho dz + \frac{\partial}{\partial x} \int_{z_b}^{z_s} \rho u dz + \frac{\partial}{\partial y} \int_{z_b}^{z_s} \rho v dz \\ - \rho_s \left( \frac{\partial z_s}{\partial t} + u_s \frac{\partial z_s}{\partial x} + v_s \frac{\partial z_s}{\partial y} - w_s \right) + \rho_b \left( \frac{\partial z_b}{\partial t} + u_b \frac{\partial z_b}{\partial x} + v_b \frac{\partial z_b}{\partial y} - w_b \right) = 0. \end{aligned} \quad (1.152)$$

The free surface is taken as a material surface, and the bed is considered erodible, but a non-slip kinematic boundary conditions is implemented, that is,  $u = v = w = 0$  at the bed (Wu 2008). Equation (1.152) reduces then to

$$\frac{\partial}{\partial t} \int_{z_b}^{z_s} \rho dz + \frac{\partial}{\partial x} \int_{z_b}^{z_s} \rho u dz + \frac{\partial}{\partial y} \int_{z_b}^{z_s} \rho v dz + \rho_b \frac{\partial z_b}{\partial t} = 0. \quad (1.153)$$

Taking average values of  $u$ ,  $v$ , namely  $(U, V)$ , and  $\rho$ , denoted by the same symbol to simplify notation, Eq. (1.153) simplifies to

$$\frac{\partial}{\partial t} (\rho h) + \frac{\partial}{\partial x} (\rho Uh) + \frac{\partial}{\partial y} (\rho Vh) + \rho_b \frac{\partial z_b}{\partial t} = 0. \quad (1.154)$$

Note that the movable bed due to sediment transport is accounted for by inclusion of the time derivative  $\partial z_b / \partial t$  in the continuity equation. An average value of density is used, but a Reynolds decomposition of this variable into mean and

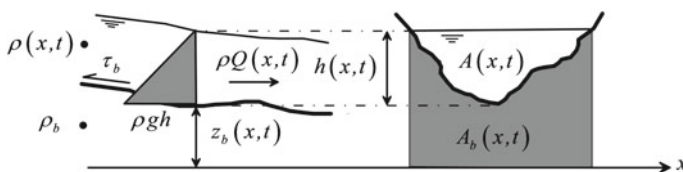


**Fig. 1.17** One-dimensional flow with movable bed and sediment transport

fluctuating parts is not done here for the sake of simplicity. Lateral integration of Eq. (1.154) from the left to the right channel bank yields

$$\int_{y_l}^{y_r} \left[ \frac{\partial}{\partial t} (\rho h) + \frac{\partial}{\partial x} (\rho Uh) + \frac{\partial}{\partial y} (\rho Vh) + \rho_b \frac{\partial z_b}{\partial t} \right] dy = 0. \quad (1.155)$$

The following identities are generated by application of Leibniz's rule:

$$\begin{aligned} \int_{y_l}^{y_r} \frac{\partial}{\partial t} (\rho h) dy &= \frac{\partial}{\partial t} \int_{y_l}^{y_r} \rho h dy - (\rho h)_r \frac{\partial y_r}{\partial t} + (\rho h)_l \frac{\partial y_l}{\partial t} \\ &= \frac{\partial}{\partial t} (\rho A) - (\rho h)_r \frac{\partial y_r}{\partial t} + (\rho h)_l \frac{\partial y_l}{\partial t}, \end{aligned} \quad (1.156)$$

$$\begin{aligned} \int_{y_l}^{y_r} \frac{\partial(\rho Uh)}{\partial x} dy &= \frac{\partial}{\partial x} \int_{y_l}^{y_r} \rho Uh dy - (\rho Uh)_r \frac{\partial y_r}{\partial x} + (\rho Uh)_l \frac{\partial y_l}{\partial x} \\ &= \frac{\partial}{\partial x} (\rho Q) - (\rho Uh)_r \frac{\partial y_r}{\partial x} + (\rho Uh)_l \frac{\partial y_l}{\partial x}, \end{aligned} \quad (1.157)$$

$$\int_{y_l}^{y_r} \frac{\partial(\rho Vh)}{\partial y} dy = (\rho Vh)_r - (\rho Vh)_l, \quad (1.158)$$

$$\begin{aligned} \rho_b \int_{y_l}^{y_r} \frac{\partial z_b}{\partial t} dy &= \rho_b \frac{\partial}{\partial t} \int_{y_l}^{y_r} z_b dy - \rho_b (z_b)_r \frac{\partial y_r}{\partial t} + \rho_b (z_b)_l \frac{\partial y_l}{\partial t} \\ &= \rho_b \frac{\partial A_b}{\partial t} - \rho_b z_s \left( \frac{\partial y_r}{\partial t} - \frac{\partial y_l}{\partial t} \right) = \rho_b \frac{\partial A_b}{\partial t} - \rho_b z_s \frac{\partial B}{\partial t}, \end{aligned} \quad (1.159)$$

where  $A_b$  is the bed area above the reference datum (Fig. 1.17). Summing Eqs. (1.156)–(1.159) generates

$$\begin{aligned} \frac{\partial}{\partial t} (\rho A) + \frac{\partial}{\partial x} (\rho Q) + h_l \left( \frac{\partial y_l}{\partial t} + U_l \frac{\partial y_l}{\partial x} - V_l \right) - \rho h_r \left( \frac{\partial y_r}{\partial t} + U_r \frac{\partial y_r}{\partial x} - V_r \right) \\ + \rho_b \frac{\partial A_b}{\partial t} - \rho_b z_s \frac{\partial B}{\partial t} = 0. \end{aligned} \quad (1.160)$$

Using Eqs. (1.73)–(1.74), and dropping the term related to  $\partial B/\partial t$ , which is not considered in river flow models for fast geomorphic flows (Wu 2008), Eq. (1.160) yields finally

$$\frac{\partial}{\partial t}(\rho A) + \frac{\partial}{\partial x}(\rho Q) + \rho_b \frac{\partial A_b}{\partial t} = 0. \quad (1.161)$$

### 1.5.2 1D Cross-Sectional Averaged $x$ -Momentum Equation

We start with the general depth-integrated  $x$ -momentum equation [Eq. (1.34)]

$$\begin{aligned} & \frac{\partial}{\partial t} \int_{z_b}^{z_s} \rho u dz + \frac{\partial}{\partial x} \int_{z_b}^{z_s} \rho u^2 dz + \frac{\partial}{\partial y} \int_{z_b}^{z_s} \rho u v dz - \rho_s u_s \left( \frac{\partial z_s}{\partial t} + u_s \frac{\partial z_s}{\partial x} + v_s \frac{\partial z_s}{\partial y} - w_s \right) \\ & + \rho_b u_b \left( \frac{\partial z_b}{\partial t} + u_b \frac{\partial z_b}{\partial x} + v_b \frac{\partial z_b}{\partial y} - w_b \right) + \left\{ \frac{\partial}{\partial x} \int_{z_b}^{z_s} \tau_{xx} dz + \frac{\partial}{\partial y} \int_{z_b}^{z_s} \tau_{xy} dz \right. \\ & \left. - \left[ (\tau_{xx})_s \frac{\partial z_s}{\partial x} + (\tau_{xy})_s \frac{\partial z_s}{\partial y} - (\tau_{xz})_s \right] + \left[ (\tau_{xx})_b \frac{\partial z_b}{\partial x} + (\tau_{xy})_b \frac{\partial z_b}{\partial y} - (\tau_{xz})_b \right] \right\} = 0. \end{aligned} \quad (1.162)$$

This simplifies upon assuming that the free surface is a material surface and using a non-slip velocity at the bed, to

$$\begin{aligned} & \frac{\partial}{\partial t} \int_{z_b}^{z_s} \rho u dz + \frac{\partial}{\partial x} \int_{z_b}^{z_s} \rho u^2 dz + \frac{\partial}{\partial y} \int_{z_b}^{z_s} \rho u v dz + \left\{ \frac{\partial}{\partial x} \int_{z_b}^{z_s} \tau_{xx} dz + \frac{\partial}{\partial y} \int_{z_b}^{z_s} \tau_{xy} dz \right. \\ & \left. - \left[ (\tau_{xx})_s \frac{\partial z_s}{\partial x} + (\tau_{xy})_s \frac{\partial z_s}{\partial y} - (\tau_{xz})_s \right] + \left[ (\tau_{xx})_b \frac{\partial z_b}{\partial x} + (\tau_{xy})_b \frac{\partial z_b}{\partial y} - (\tau_{xz})_b \right] \right\} = 0. \end{aligned} \quad (1.163)$$

Neglecting stresses at the free surface, it further simplifies to

$$\begin{aligned} & \frac{\partial}{\partial t} \int_{z_b}^{z_s} \rho u dz + \frac{\partial}{\partial x} \int_{z_b}^{z_s} \rho u^2 dz + \frac{\partial}{\partial y} \int_{z_b}^{z_s} \rho u v dz + \frac{\partial}{\partial x} \int_{z_b}^{z_s} \tau_{xx} dz \\ & + \frac{\partial}{\partial y} \int_{z_b}^{z_s} \tau_{xy} dz + (\tau_{xx})_b \frac{\partial z_b}{\partial x} + (\tau_{xy})_b \frac{\partial z_b}{\partial y} - (\tau_{xz})_b = 0. \end{aligned} \quad (1.164)$$

Now, depth-averaged values of  $u$ ,  $v$ , and  $\rho$  are taken, resulting in

$$\begin{aligned} \frac{\partial}{\partial t}(\rho Uh) + \frac{\partial}{\partial x}(\rho U^2 h) + \frac{\partial}{\partial y}(\rho UVh) \\ = - \left[ \frac{\partial}{\partial x} \int_{z_b}^{z_s} \tau_{xx} dz + \frac{\partial}{\partial y} \int_{z_b}^{z_s} \tau_{xy} dz + (\tau_{xx})_b \frac{\partial z_b}{\partial x} + (\tau_{xy})_b \frac{\partial z_b}{\partial y} - (\tau_{xz})_b \right]. \end{aligned} \quad (1.165)$$

Using the identity [Eq. (1.76)]

$$\int_{z_b}^{z_s} \left( \frac{\partial \tau_{xy}}{\partial y} + \frac{\partial \tau_{xz}}{\partial z} \right) dz = \frac{\partial}{\partial y} \int_{z_b}^{z_s} \tau_{xy} dz + (\tau_{xy})_b \frac{\partial z_b}{\partial y} - (\tau_{xz})_b, \quad (1.166)$$

the following alternative form of Eq. (1.165) is obtained

$$\frac{\partial}{\partial t}(\rho Uh) + \frac{\partial}{\partial x}(\rho U^2 h) + \frac{\partial}{\partial y}(\rho UVh) = - \left[ \frac{\partial}{\partial x} \int_{z_b}^{z_s} \tau_{xx} dz + (\tau_{xx})_b \frac{\partial z_b}{\partial x} + \int_{z_b}^{z_s} \left( \frac{\partial \tau_{xy}}{\partial y} + \frac{\partial \tau_{xz}}{\partial z} \right) dz \right]. \quad (1.167)$$

The stress tensor given by Eqs. (1.47) is used, and again noted that even though the velocity field  $(u, v, w)$  represents the time-averaged velocity field when this stress tensor is used, we do not conduct here a Reynolds decomposition of density for simplicity's sake. Once the stress tensor is introduced into Eq. (1.167), neglecting normal turbulent stresses and assuming a hydrostatic pressure distribution, the resulting equations is

$$\begin{aligned} \frac{\partial}{\partial t}(\rho Uh) + \frac{\partial}{\partial x}(\rho U^2 h) + \frac{\partial}{\partial y}(\rho UVh) = - \frac{\partial}{\partial x} \int_{z_b}^{z_s} \rho g(z_s - z) dz \\ - \rho gh \frac{\partial z_b}{\partial x} + \int_{z_b}^{z_s} \left( \frac{\partial \sigma_{xy}}{\partial y} + \frac{\partial \sigma_{xz}}{\partial z} \right) dz, \end{aligned} \quad (1.168)$$

or,

$$\begin{aligned} \frac{\partial}{\partial t}(\rho Uh) + \frac{\partial}{\partial x}(\rho U^2 h) + \frac{\partial}{\partial y}(\rho UVh) &= -\frac{\partial}{\partial x}\left(\frac{1}{2}\rho gh^2\right) \\ &\quad - \rho gh\frac{\partial z_b}{\partial x} + \int_{z_b}^{z_s} \left(\frac{\partial \sigma_{xy}}{\partial y} + \frac{\partial \sigma_{xz}}{\partial z}\right) dz. \end{aligned} \quad (1.169)$$

Expanding the pressure gradient terms yields

$$\begin{aligned} \frac{\partial}{\partial t}(\rho Uh) + \frac{\partial}{\partial x}(\rho U^2 h) + \frac{\partial}{\partial y}(\rho UVh) &= -\rho gh\frac{\partial h}{\partial x} - \frac{1}{2}gh^2\frac{\partial \rho}{\partial x} \\ &\quad - \rho gh\frac{\partial z_b}{\partial x} + \int_{z_b}^{z_s} \left(\frac{\partial \sigma_{xy}}{\partial y} + \frac{\partial \sigma_{xz}}{\partial z}\right) dz, \end{aligned} \quad (1.170)$$

and using the gradient of the free surface, Eq. (1.170) transforms into

$$\begin{aligned} \frac{\partial}{\partial t}(\rho Uh) + \frac{\partial}{\partial x}(\rho U^2 h) + \frac{\partial}{\partial y}(\rho UVh) &= -\rho gh\frac{\partial z_s}{\partial x} \\ &\quad - \frac{1}{2}gh^2\frac{\partial \rho}{\partial x} + \int_{z_b}^{z_s} \left(\frac{\partial \sigma_{xy}}{\partial y} + \frac{\partial \sigma_{xz}}{\partial z}\right) dz. \end{aligned} \quad (1.171)$$

This is a suitable form of the depth-integrated  $x$ -momentum equation for flows with sediment transport over movable beds. Lateral integration of Eq. (1.171) from the left to the right channel bank yields

$$\begin{aligned} &\int_{y_l}^{y_r} \left[ \frac{\partial}{\partial t}(\rho Uh) + \frac{\partial}{\partial x}(\rho U^2 h) + \frac{\partial}{\partial y}(\rho UVh) \right] dy \\ &= \int_{y_l}^{y_r} \left[ -\rho gh\frac{\partial z_s}{\partial x} - \frac{1}{2}gh^2\frac{\partial \rho}{\partial x} + \int_{z_b}^{z_s} \left(\frac{\partial \sigma_{xy}}{\partial y} + \frac{\partial \sigma_{xz}}{\partial z}\right) dz \right] dy. \end{aligned} \quad (1.172)$$

The following identities are generated by application of Leibniz's rule:

$$\int_{y_l}^{y_r} \frac{\partial}{\partial t} (\rho Uh) dy = \frac{\partial}{\partial t} \int_{y_l}^{y_r} \rho Uh dy - (\rho Uh)_r \frac{\partial y_r}{\partial t} + (\rho Uh)_l \frac{\partial y_l}{\partial t}, \quad (1.173)$$

$$\int_{y_l}^{y_r} \frac{\partial}{\partial x} (\rho U^2 h) dy = \frac{\partial}{\partial x} \int_{y_l}^{y_r} \rho U^2 h dy - (\rho U^2 h)_r \frac{\partial y_r}{\partial x} + (\rho U^2 h)_l \frac{\partial y_l}{\partial x}, \quad (1.174)$$

$$\int_{y_l}^{y_r} \frac{\partial}{\partial y} (\rho UVh) dy = (\rho UVh)_r - (\rho UVh)_l. \quad (1.175)$$

Summing Eq. (1.173)–(1.175) yields, using Eqs. (1.73–1.74),

$$\int_{y_l}^{y_r} \left[ \frac{\partial}{\partial t} (\rho Uh) + \frac{\partial}{\partial x} (\rho U^2 h) + \frac{\partial}{\partial y} (\rho UVh) \right] dy = \frac{\partial}{\partial t} (\rho Q) + \frac{\partial}{\partial x} \left( \rho \frac{Q^2}{A} \right). \quad (1.176)$$

For a horizontal water surface across the cross section

$$\int_{y_l}^{y_r} -g \frac{\partial z_s}{\partial x} h dy = -g \frac{\partial z_s}{\partial x} \int_{y_l}^{y_r} h dy = -g \frac{\partial z_s}{\partial x} A. \quad (1.177)$$

Using Green's theorem, the average shear stress is given by

$$\int_{y_l}^{y_r} \int_{z_b}^{z_s} \left( \frac{\partial \sigma_{xy}}{\partial y} + \frac{\partial \sigma_{xz}}{\partial z} \right) dz dy = -\bar{\tau}_o P. \quad (1.178)$$

Lateral integration of the term containing the density gradient yields

$$\int_{y_l}^{y_r} \frac{1}{2} g h^2 \frac{\partial \rho}{\partial x} dy = \frac{1}{2} g \frac{\partial \rho}{\partial x} \int_{y_l}^{y_r} h^2 dy = \frac{1}{2} g \frac{\partial \rho}{\partial x} \int_{y_l}^{y_r} h (h dy) = \frac{1}{2} g \frac{\partial \rho}{\partial x} \int_A h dA = \frac{1}{2} g \frac{\partial \rho}{\partial x} h_p A. \quad (1.179)$$

Using Eqs. (1.176)–(1.179), the cross-sectional averaged  $x$ -momentum equation is (Wu 2008)

$$\frac{\partial}{\partial t}(\rho Q) + \frac{\partial}{\partial x}\left(\rho \frac{Q^2}{A}\right) = -\rho g A \frac{\partial z_s}{\partial x} - \bar{\tau}_o P - \frac{1}{2} g \frac{\partial \rho}{\partial x} h_p A, \quad (1.180)$$

or

$$\frac{\partial}{\partial t}(\rho Q) + \frac{\partial}{\partial x}\left(\rho \frac{Q^2}{A}\right) = -\rho g A \frac{\partial z_s}{\partial x} - \rho g A S_f - \frac{1}{2} g \frac{\partial \rho}{\partial x} h_p A. \quad (1.181)$$

This is a widely used momentum model for 1D river flows with sediment transport (Wu 2008). In this equation, the variable fluid density in space and time due to sediment transport is fully accounted for.

## References

- Boussinesq, J. (1877). Essai sur la théorie des eaux courantes [Essay on the theory of water flow]. *Mémoires présentés par divers savants à l'Académie des Sciences*, Paris 23, pp. 1–680 (in French).
- Cantero-Chinchilla, F., Castro-Orgaz, O., Dey, S., & Ayuso, J. L. (2016). Nonhydrostatic dam break flows II: One-dimensional depth-averaged modelling for movable bed flows. *Journal of Hydraulic Engineering*, 142(12), 04016069.
- Castro-Orgaz, O., & Hager, W. H. (2009). Classical hydraulic jump: Basic flow features. *Journal of Hydraulic Research*, 47(6), 744–754.
- Castro-Orgaz, O., & Hager, W.H. (2017). Non-hydrostatic free surface flows. In *Advances in geophysical and environmental mechanics and mathematics* (696 pages), Berlin: Springer, <https://doi.org/10.1007/978-3-319-47971-2>.
- Castro-Orgaz, O., Hutter, K., Giráldez, J. V., & Hager, W. H. (2015). Non-hydrostatic granular flow over 3D terrain: New Boussinesq-type gravity waves? *Journal of Geophysical Research: Earth Surface*, 120(1), 1–28.
- Chanson, H. (2004). *The hydraulics of open channel flows: An introduction*. Oxford, UK: Butterworth-Heinemann.
- Chaudhry, M. H. (2008). *Open-channel flow* (2nd ed.). Berlin: Springer.
- Chen, C. L., & Chow, V. T. (1968). Hydrodynamics of mathematically simulated surface runoff. *Hydraulic Engineering Series No. 18, Civil Engineering Studies*. Urbana-Champaign: University of Illinois.
- Chow, V. T. (1959). *Open channel hydraulics*. New York: McGraw-Hill.
- Chow, V. T., Maidment, D. R., & Mays, L. W. (1988). *Applied hydrology*. New York: McGraw-Hill.
- Cunge, J. A., Holly, F. M., & Verwey, A. (1980). *Practical aspects of computational river hydraulics*. London: Pitman.
- de Saint-Venant, A.B. (1871). Théorie du mouvement non permanent des eaux, avec application aux crues des rivières et à l'introduction des marées dans leur lit [Theory of unsteady water movement, applied to floods in rivers and the effect of tidal flows]. *Comptes Rendus de l'Académie des Sciences*, 73, 147–154; 73, 237–240 (in French).
- Denlinger, R. P., & Iverson, R. M. (2004). Granular avalanches across irregular three-dimensional terrain: 1. Theory and computation. *Journal of Geophysical Research: Earth Surface*, 109(F1), F01014. <https://doi.org/10.1029/2003JF000085>.

- Denlinger, R. P., & O'Connell, D. R. H. (2008). Computing nonhydrostatic shallow-water flow over steep terrain. *Journal of Hydraulic Engineering*, 134(11), 1590–1602.
- Dressler, R. F. (1978). New nonlinear shallow flow equations with curvature. *Journal of Hydraulic Research*, 16(3), 205–222.
- Henderson, F. M. (1966). *Open channel flow*. New York: MacMillan.
- Iverson, R. M. (2005). Debris-flow mechanics. In M. Jakob & O. Hungr (Eds.), *Debris flow hazards and related phenomena* (pp. 105–134). Heidelberg: Springer-Praxis.
- Iverson, R. M., & Ouyang, C. (2015). Entrainment of bed material by Earth-surface mass flows: Review and reformulation of depth-integrated theory. *Reviews of Geophysics*, 53(1), 27–58. <https://doi.org/10.1002/2013rg000447>.
- Jaeger, C. (1956). *Engineering fluid mechanics*. Edinburgh: Blackie and Son.
- Jain, S. C. (2001). *Open channel flow*. New York: Wiley & Sons.
- Katopodes, N. D. (2019). *Free surface flow: Shallow-water dynamics*. Oxford, UK: Butterworth-Heinemann.
- Keulegan, G. H. (1942). Equation of motion for the steady mean flow of water in open channels. *Journal of Research*, US National Bureau of Standards, 29, 97–111.
- Keulegan, G. H., & Patterson, G. W. (1943). Effect of turbulence and channel slope in translation waves. *Journal of Research*, US National Bureau of Standards, 30, 461–512.
- Khan, A. A., & Steffler, P. M. (1996a). Physically-based hydraulic jump model for depth-averaged computations. *Journal of Hydraulic Engineering*, 122(10), 540–548.
- Khan, A. A., & Steffler, P. M. (1996b). Modelling overfalls using vertically averaged and moment equations. *Journal of Hydraulic Engineering*, 122(7), 397–402.
- Khan, A. A., & Steffler, P. M. (1996c). Vertically averaged and moment equations model for flow over curved beds. *Journal of Hydraulic Engineering*, 122(1), 3–9.
- Lai, C. (1986). Numerical modelling of unsteady open-channel flow. In *Advances in hydroscience*, 14, 161–333.
- Lauffer, H. (1935). Druck, Energie und Fliesszustand in Gerinnen mit grossem Gefälle [Pressure, energy and condition of flow in channels of high bottom slope]. *Wasserwirtschaft*, 30(7), 78–82 (in German).
- Le Méauté, B. (1976). *An introduction to hydrodynamics and water waves*. New York: Springer.
- Liggett, J. A. (1994). *Fluid mechanics*. New York: McGraw-Hill.
- Montes, J. S. (1998). *Hydraulics of open channel flow*. Reston VA: ASCE Press.
- Pudasaini, S. P., & Hutter, K. (2007). *Avalanche dynamics*. Berlin: Springer.
- Rodi, W. (1980). *Turbulence models and their application in hydraulics: A state-of-the-art review*. Dordrecht: IAHR.
- Rouse, H. (1959). *Advanced mechanics of fluids*. New York: Wiley and Sons.
- Savage, S. B., & Hutter, K. (1989). The motion of a finite mass of granular material down a rough incline. *Journal of Fluid Mechanics*, 199, 177–215.
- Savage, S. B., & Hutter, K. (1991). The dynamics of avalanches of granular materials from initiation to runout, I. Analysis. *Acta Mechanica*, 86(1–4), 201–223.
- Schlichting, H., & Gersten, K. (2000). *Boundary layer theory*. Berlin, Germany: Springer.
- Serre, F. (1953). Contribution à l'étude des écoulements permanents et variables dans les canaux [Contribution to the study of steady and unsteady channel flows]. *La Houille Blanche*, 8(6–7), 374–388; 8(12), 830–887 (in French).
- Stansby, P. K., & Zhou, J. G. (1998). Shallow-water flow solver with non-hydrostatic pressure: 2D vertical plane problems. *International Journal for Numerical Methods in Fluids*, 28(3), 541–563.
- Steffler, P. M., & Jin, Y. C. (1993). Depth-averaged and moment equations for moderately shallow free surface flow. *Journal of Hydraulic Research*, 31(1), 5–17.
- Strelkoff, T. (1969). One dimensional equations of open channel flow. *Journal of the Hydraulics Division*, ASCE, 95(3), 861–876.
- Sturm, T. W. (2001). *Open channel hydraulics*. New York: McGraw-Hill.
- Toro, E. F. (2001). *Shock-capturing methods for free-surface shallow flows*. New York: Wiley.
- Vreugdenhil, C. B. (1994). *Numerical methods for shallow water flow*. Dordrecht NL: Kluwer.

- White, F. M. (1991). *Viscous fluid flow*. New York: McGraw-Hill.
- White, F. M. (2009). *Fluid mechanics*. New York: McGraw-Hill.
- Wu, W. (2008). *Computational river dynamics*. London, U.K.: Taylor and Francis.
- Yen, B. C. (1973). Open-channel flow equations revisited. *Journal of the Engineering Mechanics Division*, ASCE, 99(EM5), 979–1009.
- Yen, B. C. (1975). Further study on open-channel flow equations. Sonder-Forschungsbereich, 80/T/49, Universität Karlsruhe, Germany.

# Chapter 2

## Energy and Momentum Principles



### 2.1 Introduction

From Chap. 1, the cross-sectional averaged equations based on the three-dimensional (3D) conservation laws of mass and momentum are (Montes 1998; Jain 2001)

$$\frac{\partial A}{\partial t} + \frac{\partial Q}{\partial x} = 0, \quad (2.1)$$

$$\frac{1}{g} \frac{\partial Q}{\partial t} + \frac{\partial M}{\partial x} = A(S_o - S_f). \quad (2.2)$$

Here,  $Q$  is the discharge,  $A$  cross-sectional area,  $g$  the gravity acceleration,  $S_o$  the bottom slope,  $S_f$  the friction slope,  $x$  the streamwise horizontal coordinate,  $t$  the time, and  $M$  the momentum function. For a flow of uniform velocity and hydrostatic pressure distributions,  $M$  reduces to (Jaeger 1956; Montes 1998)

$$M = \int_A \left( \frac{u^2}{g} + \frac{p}{\rho g} \right) dA \approx \frac{Q^2}{gA} + A\bar{h}. \quad (2.3)$$

Here,  $u$  is the velocity component in the  $x$ -direction,  $p$  fluid pressure, and  $\bar{h}$  the depth below the free surface of the centroid of area  $A$ . Equation (2.2) is only valid for prismatic channels. Equations (2.1)–(2.2) are differential equations even for the simple case of steady gradually varied flow. The conservation laws can be expressed in integral form if an integration in the flow direction  $x$  is accomplished by considering a control volume of finite length. However, not all hydraulic problems are solved by the isolated consideration of mass and momentum conservations. Energy conservation in integral form needs to be added. Its use is

alternative, or complementary, to the application of the momentum principle. In this chapter, the one-dimensional (1D) integral forms of the mass, momentum and energy conservation principles are presented and used to solve fundamental steady open channel flow problems.

For steady flow, Eqs. (2.1)–(2.2) transform to

$$\frac{dQ}{dx} = 0, \quad (2.4)$$

$$\frac{dM}{dx} = A(S_o - S_f). \quad (2.5)$$

The differential form of the energy equation must be considered now. The total energy head  $H$  is defined based on the total energy flow across section  $A$  as (Jaeger 1956)

$$H = \frac{1}{UA} \int_A \left( \frac{u^2 + v^2 + w^2}{2g} + \frac{p}{\rho g} + z \right) udA. \quad (2.6)$$

Herein, the kinetic energy due to the velocity components ( $u, v, w$ ), the potential energy due to elevation  $z$ , and the work done by fluid pressure  $p$  are accounted for (Liggett 1994; Montes 1998). Consider gradually varied flow in a channel of small bottom slope, and assume that the velocity components  $v = w = 0$ . Further, assume that  $u$  is uniform across cross section  $A$  and equal to the mean value  $U = Q/A$ , and that the vertical pressure distribution follows the hydrostatic law. Under these simplifications, Eq. (2.6) yields with  $z_b = z_b(x)$  as the bottom elevation relative to an arbitrary datum (Jaeger 1956; Montes 1998)

$$H = \frac{1}{UA} \int_A \left( \frac{u^2 + v^2 + w^2}{2g} + \frac{p}{\rho g} + z \right) udA \approx z_b + h + \frac{U^2}{2g} = z_b + h + \frac{Q^2}{2gA^2}. \quad (2.7)$$

This relation is a true energy equation and shall not be mistakenly linked to Bernoulli's equation resulting from the integration of the momentum equation along the streamlines in inviscid and incompressible steady fluid flow (Rouse 1938; Liggett 1994; Montes 1998). For steady flow with constant discharge  $Q$ , the differential energy equation obtained from the first law of thermodynamics states that the variation of  $H$  equals the rate of conversion of energy into heat (Liggett 1994; Montes 1998) (Fig. 2.1)

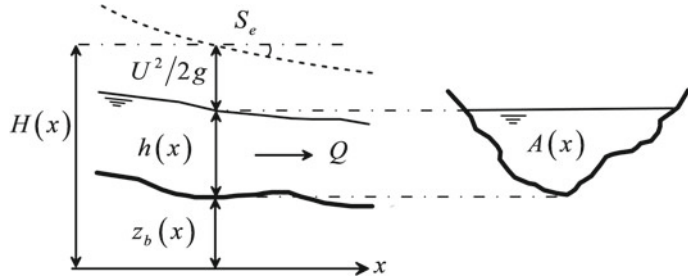


**Fig. 2.1** Definition sketch for differential form of energy principle under steady flow

$$\frac{dH}{dx} = -S_e, \quad (2.8)$$

where  $S_e$  is the gradient of dissipated energy or the energy head slope. Note that conceptually  $S_e$  is different from  $S_f$ ; the former is a measure of the internal energy dissipation within a volume of fluid, whereas  $S_f$  represents the external shear forces acting on the boundaries of the control volume.

Equations (2.4), (2.5), and (2.8) are the differential forms of the mass, momentum, and energy balances for hydrostatic pressure and uniform velocity distributions (Yen 1973); their integration along a control volume of length ( $x_1-x_2$ ) (Fig. 2.2) yields (Jain 2001)

$$Q_1 - Q_2 = 0, \quad (2.9)$$

$$M_1 - M_2 = \int_{x_2}^{x_1} A(S_o - S_f) dx, \quad (2.10)$$

$$H_1 - H_2 = - \int_{x_2}^{x_1} S_e dx. \quad (2.11)$$

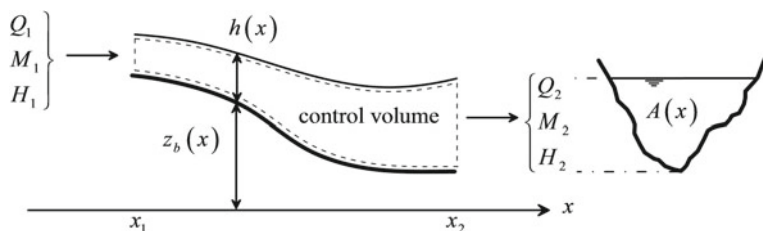


**Fig. 2.2** Control volume for steady flow in a prismatic channel of arbitrary cross section

These equations are statements to be satisfied for any flow within a control volume. Non-hydrostatic pressure and non-uniform velocity distributions could be accounted for in  $H$  and  $M$  (Jaeger 1956; Montes 1998; Jain 2001). The boundary sections are usually positioned in a gradually varied flow zone, allowing for a simple evaluation of  $H$  and  $M$  as functions of the local flow depth. Given the absence of mass sources/sinks (e.g., rain/infiltration), Eq. (2.9) states constant discharge across the control volume. However, neither  $M$  nor  $H$  is conserved within the control volume given the terms related to  $S_f$  and  $S_e$ , acting as sinks of momentum and energy. Even though this is the general situation, there are many cases where these terms can be neglected. For example, in a hydraulic jump on a horizontal bottom, the shear forces are smaller than the pressure forces plus momentum flux, resulting in  $M = \text{const.}$  from Eq. (2.10). The energy dissipation is significant and cannot be overlooked, however. This is an example on how energy and momentum laws are used as complementary principles: The momentum equation is used to compute the flow depth  $h_2$  at the downstream section of the jump for known values of  $Q$  and  $h_1$ , whereas Eq. (2.11) is applied to evaluate the energy dissipation produced by the hydraulic jump.

## 2.2 Energy Principle

### 2.2.1 Specific Energy Head

The concept of specific energy was introduced by Bakhmeteff (1912, 1932); it is one of the most powerful steady open channel flow tools. Consider a fluid flow without energy dissipation ( $S_e = 0$ ). Thus, Eq. (2.11) yields

$$H_1 = H_2 = H = z_b + h + \frac{Q^2}{2gA^2} = \text{const.} \quad (2.12)$$

The specific energy head  $E$  is defined taking the channel bottom as reference. Thus,

$$E = h + \frac{Q^2}{2gA^2}. \quad (2.13)$$

It represents therefore the total energy head above the channel bottom at any section. Inserting Eq. (2.13) into Eq. (2.12) produces

$$z_b(x) + E(x) = \text{const.} \quad (2.14)$$

This is the equation governing ideal fluid flow across channel transitions, to be used below. It is a suitable approximation in gradual transitions involving a smooth

variation of bottom elevation and channel shape, without zones of flow separation where energy losses have to be accounted for (Rouse 1938; Montes 1998). What are the properties of Eq. (2.13)? Consider a rectangular channel of width  $b$ , with  $A = bh$ , and unit discharge  $q = Q/b$ . Equation (2.13) is rewritten as

$$E = h + \frac{U^2}{2g} = h + \frac{q^2}{2gh^2}. \quad (2.15)$$

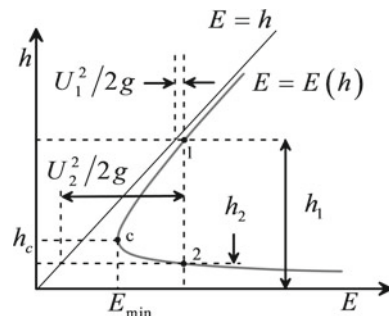
Consider the variation of  $E$  with  $h$  for  $q = \text{const}$ . Equation (2.15) is re-arranged as

$$(E - h)h^2 = \frac{q^2}{2g} = \text{const}. \quad (2.16)$$

This is a cubic in  $h$ , plotted in Fig. 2.3. Of the three roots, one is negative, lacking of physical meaning and therefore discarded. The curve has the asymptotes  $(E-h) = 0$  and  $h = 0$ . The first asymptote is a straight line inclined  $45^\circ$  with respect to the  $E$ -axis. The second asymptote is the  $E$ -axis. The three roots of Eq. (2.16) are determined analytically for a given value of  $E$  (Chanson 2004; Jeppson 2011).

Consider a given value of  $E$ . If a vertical line is plotted in Fig. 2.3, the intersection with the curve  $E = E(h)$  yields two points 1 and 2. For a given discharge, a certain specific energy head is possible for two different values of the flow depth, namely  $h_1$  and  $h_2$ . These are called *alternate depths* (Henderson 1966; Jain 2001). Note from Fig. 2.3 that at point 1, flow depth  $h$  corresponds to the dominant part of  $E$ , whereas the velocity head  $U^2/(2g)$  is small. At point 2, where the value of  $E$  is identical, the trend is reversed:  $U^2/(2g)$  is the dominant term, whereas  $h$  is small. This observation suggests that each of the alternate depths represents a different regime, one of small velocity and large flow depths (hydrostatic forces) and the other representing a flow of small depth at high velocity. The slow velocity regime is referred to as “subcritical flow,” whereas the high-speed flow regime involves “supercritical flow.” The limit between these two states is marked by point c in Fig. 2.3, referred to as the “critical flow condition,” representing the point for which the value of  $E$  is the minimum possible for a given value  $q$ . It is impossible to

**Fig. 2.3** Specific energy head curve for constant unit discharge



transport the flow rate  $q$  with a value of  $E$  below  $E_{\min}$ , therefore. The flow depth at critical condition is called critical (subscript  $c$ ) flow depth  $h_c$ . Critical flow is an important tool in open channel hydraulics and includes important properties, the first introduced in Fig. 2.3, namely minimum specific energy. From Eq. (2.15), a quadratic relation between the alternate depths exists.



**Boris Aleksandrovich Bakhmeteff** (written Bakhmetev in Russian) was born on May 14, 1880, at Tbilisi, and passed away aged 71 years on July 21, 1951, at Brookfield, CT, USA. He graduated in 1903 as a civil engineer from the Institute of Engineers, St. Petersburg, receiving the Ph.D. degree in 1911. He then was appointed as Professor of hydraulics and mechanics at the Polytechnic Institute and in parallel focused on water power as Consulting Engineer. Successes in his career led in 1917 to his appointment as the first Russian Ambassador to the USA following the czarist regime, a position held until 1922. He never returned to his native country but established a practice as a hydraulic consultant in New York, NY. He became US citizen in 1935. He was Professor of civil engineering since 1931 at Columbia University, New York.

Bakhmeteff was an innovator of advanced theories of fluid mechanics and an authority on open channel hydraulics. His textbooks *Hydraulics of Open Channels*, and *Mechanics of Turbulent Flow* were outstanding and marked the dawn of hydraulic research in the USA. He specifically was able to introduce the specific energy and momentum functions and the distinction between sub- and supercritical flows in open channels based on these concepts. His research on hydraulic jumps was notable. He was awarded the 1937 James Laurie ASCE Prize, the 1944 J. C. Stevens Award, and the 1947 Norman Medal. He was a quiet but generous philanthropist and helped displaced persons to establish themselves in the USA. He was elected Honorary Member of ASCE in 1945.

Let us quantify critical flow. Differentiation of Eq. (2.15) with respect to  $h$  produces

$$\frac{dE}{dh} = 1 - \frac{q^2}{gh^3}. \quad (2.17)$$

Setting this expression equal to zero, the extreme of the  $E-h$  curve yields the critical flow condition, namely

$$1 - \frac{q^2}{gh_c^3} = 0. \quad (2.18)$$

The value of the critical depth in the rectangular channel is thus

$$h_c = \left( \frac{q^2}{g} \right)^{1/3}. \quad (2.19)$$

Inserting Eq. (2.18) into Eq. (2.15), the minimum specific energy head is

$$E_{\min} = h_c + \frac{q^2}{2gh_c^2} = h_c \left( 1 + \frac{1}{2} \frac{q^2}{gh_c^3} \right) = \frac{3}{2} h_c. \quad (2.20)$$

The critical depth equals two-thirds of the minimum specific energy, therefore,

$$h_c = \frac{2}{3} E_{\min}. \quad (2.21)$$

The velocity head at the critical flow condition is thus

$$E_{\min} = h_c + \frac{U_c^2}{2g} = \frac{2}{3} E_{\min} + \frac{U_c^2}{2g} \Rightarrow \frac{U_c^2}{2g} = \frac{1}{3} E_{\min} = \frac{1}{2} h_c. \quad (2.22)$$

In addition, Eq. (2.18) can be rewritten as

$$\frac{q^2}{gh_c^3} = \frac{U_c^2}{gh_c} = 1, \quad (2.23)$$

or

$$F = \frac{U_c}{(gh_c)^{1/2}} = 1. \quad (2.24)$$

The Froude number  $F$  is unity at the critical flow condition, therefore. From Fig. 2.3, subcritical flow (e.g., point 1) is characterized by  $U < U_c$  and thus  $F < 1$ . Likewise, for supercritical flow (e.g., point 2)  $U > U_c$  and  $F > 1$ . Using the critical depth  $h_c$  as scaling length, Eq. (2.15) is rewritten as

$$\frac{E}{h_c} = \frac{h}{h_c} + \frac{1}{2} \left( \frac{h}{h_c} \right)^{-2}. \quad (2.25)$$

This is the dimensionless specific energy head curve, plotted in Fig. 2.4. It is a universal curve for rectangular channel flow, involving the critical flow condition  $E/h_c = 3/2$ .

There is another interesting feature of Eq. (2.15). Let us rewrite it as

$$q^2 = 2gh^2(E - h). \quad (2.26)$$

Consider the variation of  $q$  with  $h$  under constant specific energy head  $E$  (Fig. 2.5). Note that  $q = 0$  either if the flow depth is zero or if  $E = h$ . The maximum of the curve follows from differentiation of Eq. (2.26) with respect to  $h$  for  $E = \text{const.}$ , yielding

$$2q \frac{dq}{dh} = 4gh(E - h) - 2gh^2 = 4ghE - 6gh^2. \quad (2.27)$$

For  $dq/dh = 0$  in Eq. (2.27) results critical flow, expressed as

$$h_c = \frac{2}{3}E. \quad (2.28)$$

Inserting Eq. (2.28) into Eq. (2.26) produces

$$q_{\max}^2 = 2g \left( \frac{2}{3}E \right)^2 \left( E - \frac{2}{3}E \right) = 2 \left( \frac{2}{3} \right)^2 gE^2 \frac{1}{3}E = \left( \frac{2}{3} \right)^3 gE^3. \quad (2.29)$$

**Fig. 2.4** Dimensionless specific energy head curve for rectangular channel

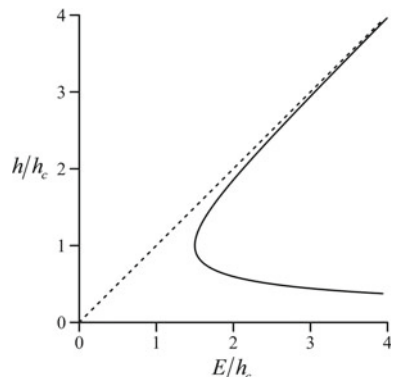
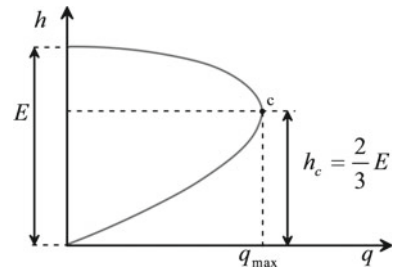


**Fig. 2.5** Discharge curve for constant specific energy



The maximum discharge is thus

$$q_{\max} = \left(\frac{2}{3}\right)^{3/2} (gE^3)^{1/2}. \quad (2.30)$$

Under the critical flow condition, the discharge is a maximum for the available value of the specific energy head. This is an important result of great relevance to establish the head–discharge curve of control structures based on the critical flow theory (Jaeger 1956; Bos 1976; Ackers et al. 1978; Montes 1998), as shown below.

Another way of expressing Eq. (2.30) is

$$q_{\max} = C_d (gE^3)^{1/2}, \quad (2.31)$$

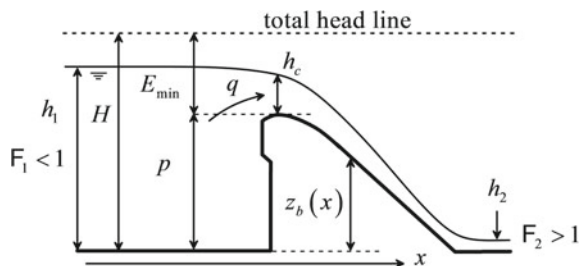
where  $C_d$  is the so-called discharge coefficient

$$C_d = \left(\frac{2}{3}\right)^{3/2}. \quad (2.32)$$

## 2.2.2 Location of Critical Flow

Consider the position where critical flow is established. Figure 2.6 shows a sketch for shallow ideal fluid flow over a dam crest. This flow is discussed in Chap. 4, but here introduced to illustrate an important case of critical flow, following Henderson (1966).

**Fig. 2.6** Critical flow over a dam spillway



Given that the total energy head  $H$  is a constant, Eq. (2.14) is applied. The flow over the spillway crest changes from upstream subcritical to downstream supercritical. The detailed computation of the free surface profile is described in Chap. 4. Differentiation of Eq. (2.14) with respect to  $x$  produces

$$\frac{dE}{dx} + \frac{dz_b}{dx} = \frac{dE}{dh} \frac{dh}{dx} + \frac{dz_b}{dx} = 0, \quad (2.33)$$

or, using Eq. (2.17),

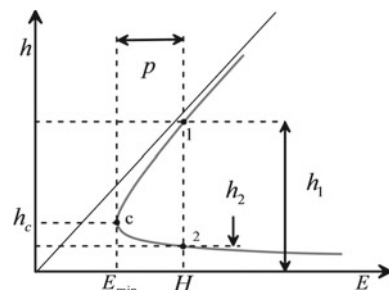
$$\left(1 - \frac{q^2}{gh^3}\right) \frac{dh}{dx} + \frac{dz_b}{dx} = (1 - F^2) \frac{dh}{dx} + \frac{dz_b}{dx} = 0. \quad (2.34)$$

This represents a mathematical identity to be satisfied at any point of the flow profile. Just upstream of the weir crest  $dz_b/dx > 0$ , the flow is subcritical ( $F < 1$ ), so that  $dh/dx < 0$ . Downstream of the crest  $dz_b/dx < 0$ , the flow is supercritical ( $F > 1$ ), and  $dh/dx$  is again negative, based on Eq. (2.34). At the weir crest, there is continuity in the free surface slope, which must be therefore negative. Note that at the weir crest  $dz_b/dx = 0$ . Thus, Eq. (2.34) is satisfied for the case  $dh/dx = 0$ , which implies a nonzero value of  $dE/dh$ , but also for the case  $F = 1$  with  $dh/dx \neq 0$  (Henderson 1966). This last option corresponds to the minimum value of the specific energy head at the weir crest, so that the critical depth is established there. The flow over the spillway is represented in the  $E-h$  plane in Fig. 2.7.

The discharge over the spillway crest is then the maximum possible for the available energy head, with  $C_d = (2/3)^{3/2}$ . In this analysis, it is assumed that energy dissipation and non-hydrostatic effects due to curvilinear streamlines can be neglected. Consideration of these flow phenomena would modify the value of  $C_d$  from its ideal value in practice. Energy dissipation would tend to decrease  $C_d$ , whereas the effects of curvilinear motion are to increase it (Castro-Orgaz and Hager 2017).

Critical flow can be demonstrated to occur at the maximum of the bottom profile, but not at a minimum. Differentiation of Eq. (2.34) with respect to  $x$  produces

**Fig. 2.7** Critical flow over a dam spillway represented in the  $E-h$  plane



$$\left(1 - \frac{q^2}{gh^3}\right) \frac{d^2h}{dx^2} + \frac{3q^2}{gh^4} \left(\frac{dh}{dx}\right)^2 + \frac{d^2z_b}{dx^2} = 0. \quad (2.35)$$

Inserting  $F = q/(gh^3)^{1/2}$  gives

$$(1 - F^2) \frac{d^2h}{dx^2} + \frac{3}{h} F^2 \left(\frac{dh}{dx}\right)^2 + \frac{d^2z_b}{dx^2} = 0. \quad (2.36)$$

Let  $F = 1$  for critical flow, the free surface slope at the critical section is (Hager 2010)

$$\left(\frac{dh}{dx}\right)_c = \pm \left(-\frac{h_c}{3} \frac{d^2z_b}{dx^2}\right)_c^{1/2}. \quad (2.37)$$

Real solutions to Eq. (2.37) result for a bed curvature at the critical section  $d^2z_b/dx^2 < 0$ ; e.g., the bed profile must be convex, as is characteristic for a spillway. For a concave bottom profile imaginary numbers result, excluding a real solution at a minimum elevation of the bottom profile.

Consider a rectangular horizontal channel with a gradual variation of channel width. Examples of this structure are flumes used for discharge measurement (Montes 1998) (Fig. 2.8).

To apply the 1D approach pursued here, the contraction-expansion of the sections must be gradual, to avoid flow separation and 3D effects. For an ideal fluid flow, the energy head remains constant, given by

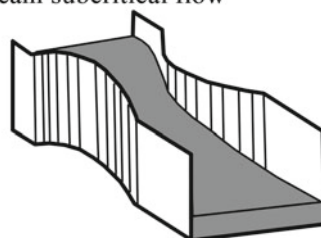
$$E = h + \frac{Q^2}{2gb^2h^2} = \text{const.} \quad (2.38)$$

Differentiation of Eq. (2.38) with respect to  $x$  yields

$$\frac{dE}{dx} = \frac{dh}{dx} - \frac{Q^2}{gb^2h^3} \frac{dh}{dx} - \frac{Q^2}{gb^3h^2} \frac{db}{dx} = 0, \quad (2.39)$$

**Fig. 2.8** Critical flow in a flume with gradual channel contraction-expansion

upstream subcritical flow



downstream supercritical flow

or

$$\frac{dh}{dx} (1 - F^2) - F^2 \frac{h db}{b dx} = 0. \quad (2.40)$$

Critical flow  $F = 1$  is therefore formed where  $db/dx = 0$  from Eq. (2.40). An important complementary property is that critical flow is established at the section of minimum width in a channel contraction, but not at a maximum width section in an expansion. To demonstrate this feature, let us differentiate Eq. (2.39) with respect to  $x$ , producing

$$\begin{aligned} & \frac{d^2h}{dx^2} \left( 1 - \frac{Q^2}{gb^2h^3} \right) \frac{dh}{dx} - \frac{Q^2}{gb^3h^2} \frac{d^2b}{dx^2} + \frac{3Q^2}{gb^4h^2} \left( \frac{db}{dx} \right)^2 \\ & + \frac{4Q^2}{gb^3h^3} \frac{dh}{dx} \frac{db}{dx} + \frac{3Q^2}{gb^2h^4} \left( \frac{dh}{dx} \right)^2 = 0, \end{aligned} \quad (2.41)$$

or, written as function of  $F$ ,

$$\frac{d^2h}{dx^2} (1 - F^2) \frac{dh}{dx} - \frac{h}{b} F^2 \frac{d^2b}{dx^2} + \frac{3h}{b^2} F^2 \left( \frac{db}{dx} \right)^2 + \frac{4}{b} F^2 \frac{dh}{dx} \frac{db}{dx} + \frac{3}{h} F^2 \left( \frac{dh}{dx} \right)^2 = 0. \quad (2.42)$$

Noting that  $F = 1$  is formed where  $db/dx = 0$ , Eq. (2.42) simplifies to

$$-\frac{h_c}{b} \frac{d^2b}{dx^2} + \frac{3}{h} \left( \frac{dh}{dx} \right)^2 = 0, \quad (2.43)$$

from which the water surface slope at the critical section is (Hager 2010)

$$\left( \frac{dh}{dx} \right)_c = \pm \left( \frac{h_c^2}{3b} \frac{d^2b}{dx^2} \right)_c^{1/2}. \quad (2.44)$$

To obtain a physically relevant solution, the channel sidewall curvature at the critical section,  $d^2b/dx^2$ , must be positive. Critical flow is thus only established at the flume throat. The typical transcritical flow profile in the Venturi flume is shown in Fig. 2.9.

The specific energy head curve along the Venturi flume is not unique, as for spillway flow, due to the streamwise variation of  $b = b(x)$ . The function is in this case (Fig. 2.10)

**Fig. 2.9** Transcritical flow in Venturi flume: **a** free surface profile  $h(x)$  along channel axis and **b** plan view with  $b = b(x)$

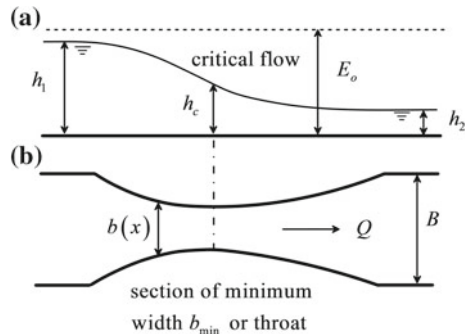
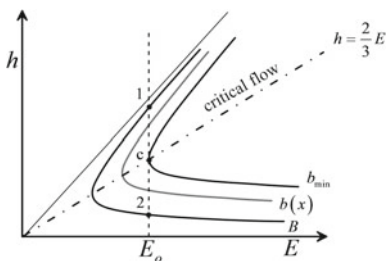


**Fig. 2.10** Critical flow in a Venturi flume represented in the  $E$ - $h$  plane

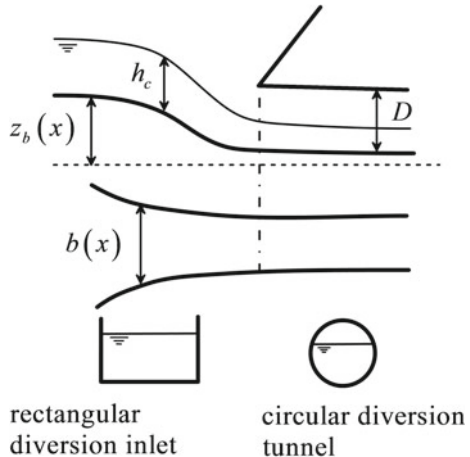


$$E(x, h) = h + \frac{Q^2}{2gh^2b(x)^2} = h + \frac{q(x)^2}{2gh^2}. \quad (2.45)$$

The effect induced by the variation of  $b$  with  $x$  is better revealed by considering the unit discharge  $q = q(x) = Q/b(x)$ . An increase of  $q$  produces an increase of the critical depth and thus a displacement of the  $E$ - $h$  function (Fig. 2.10). For a constant value of the specific energy head  $E_o$  across the Venturi flume, critical flow takes place at the section of minimum width, whereas points 1 and 2 in the curve corresponding to width  $B$  are the up- and downstream sub- and supercritical flow depths, respectively (Fig. 2.10).

The two basic mechanisms to produce critical flow, namely the (1) contraction of the channel section and (2) elevation of the bottom profile, can be combined simultaneously in a transition structure. An example is the inlet to a tunnel diversion (Fig. 2.11). The inlet structure is used to convey the flow of a river across the diversion tunnel, while a dam is under construction (Vischer and Hager 1998). The transition between the river and the circular tunnel can be designed using a rectangular channel of gradual decrease in the width and increase in the bottom slope, to accelerate the river flow from sub- to supercritical tunnel flow, thereby avoiding backwater effects. Another example is the non-prismatic spillway channel used in small earth dams (Chow 1959; Castro-Orgaz et al. 2008). The variation of bottom slope combined with channel width moves the critical flow section away from the

**Fig. 2.11** Channel transition involving variations of width and elevation: sketch of inlet to diversion tunnel (Vischer and Hager 1998)



spillway crest to an undetermined position within the channel structure. To determine the position of critical flow in these transition structures, the total energy head, e.g.,

$$H = z_b(x) + h + \frac{Q^2}{2gb(x)^2h^2} = \text{const.} \quad (2.46)$$

is differentiated with respect to \$x\$, resulting in

$$\frac{dH}{dx} = \frac{dz_b}{dx} + \frac{dh}{dx} - \frac{Q^2}{gb^2h^3} \frac{dh}{dx} - \frac{Q^2}{gb^3h^2} \frac{db}{dx} = 0. \quad (2.47)$$

Rewriting it as function of the Froude number  $F = Q/(gb^2h^3)^{1/2}$  produces

$$\frac{dz_b}{dx} + \frac{dh}{dx} \left(1 - F^2\right) - F^2 \frac{h}{b} \frac{db}{dx} = 0. \quad (2.48)$$

For critical flow  $F = 1$ , the location of the critical section must satisfy the relation

$$\frac{dz_b}{dx} - \frac{h_c}{b} \frac{db}{dx} = 0. \quad (2.49)$$

The definition of critical depth is from Eq. (2.24)

$$h_c = \left(\frac{Q^2}{gb^2}\right)^{1/3}. \quad (2.50)$$

Inserting into Eq. (2.49) yields

$$\frac{dz_b}{dx} - \frac{Q^{2/3}}{g^{1/3} b^{5/3}} \frac{db}{dx} = 0. \quad (2.51)$$

Accounting for the functions  $z_b = z_b(x)$  and  $b = b(x)$  in Eq. (2.51) gives a mathematical identity that allows for computing the position of the critical section  $x_c$  in a rectangular transition structure under ideal fluid flow.

To illustrate the application of Eq. (2.51), consider an example of Jain (2001) (Fig. 2.12). A rectangular transition structure ends at a free overfall, involving a linear width reduction and a parabolic weir profile, given by the equations (dimensions in m)

$$z_b = \frac{x}{15} \left( 2 - \frac{x}{15} \right), \quad b = 6 - \frac{x}{10}. \quad (2.52)$$

The discharge is  $Q = 30 \text{ m}^3/\text{s}$  and the length of the structure 30 m.

Computing the derivatives

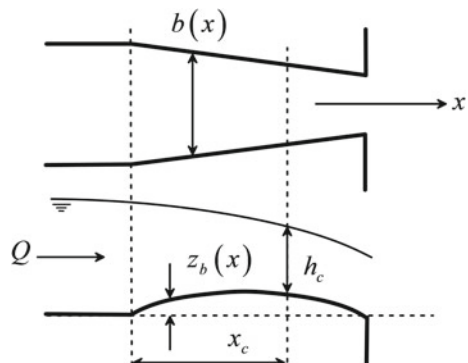
$$\frac{dz_b}{dx} = \frac{2}{15} \left( 1 - \frac{x}{15} \right), \quad \frac{db}{dx} = -\frac{1}{10}, \quad (2.53)$$

and inserting into Eq. (2.51) yield the implicit equation

$$f(x_c) = \frac{2}{15} \left( 1 - \frac{x_c}{15} \right) + \frac{1}{10} \frac{Q^{2/3}}{g^{1/3}} \left( 6 - \frac{x_c}{10} \right)^{-5/3} = 0. \quad (2.54)$$

Solving it by trial-and-error yields  $x_c \approx 20 \text{ m}$ , whereas the position of maximum elevation is  $x = 15 \text{ m}$ . Therefore, the channel contraction effect shifts the critical flow section downstream of the weir crest. A transition structure would keep the

**Fig. 2.12** Transition structure with linear reduction of channel width and parabolic bottom profile (adapted from Jain 2001)



critical flow section located at the weir crest ( $dz_b/dx = 0$ ) only if the throat ( $db/dx = 0$ ) is located there too. This is a practical design approach used for weirs and flumes for discharge measurement (Montes 1998). In practice, energy dissipation needs to be accounted for (Castro-Orgaz et al. 2008), as well as the inclusion of arbitrary cross sections.

### 2.2.3 Specific Energy Head for General Sections

For any cross section, the specific energy head is

$$E = h + \frac{Q^2}{2gA^2}. \quad (2.55)$$

Its representation in the  $E$ - $h$  plane yields a curve similar to that of Fig. 2.3. The critical flow condition is in this case

$$\frac{dE}{dh} = 1 - \frac{Q^2}{gA^3} \frac{dA}{dh} = 0, \quad (2.56)$$

or, with  $dA/dh = B$  as the free surface width,

$$\frac{Q^2}{gA^3} B = 1. \quad (2.57)$$

In general, Eq. (2.57) must be solved numerically to compute the critical depth  $h_c$  for a given discharge  $Q$  and cross-sectional geometry. Inserting Eq. (2.57) into Eq. (2.55), the minimum (subscript min) specific energy head is

$$E_{\min} = h_c + \frac{1}{2} \frac{A_c}{B_c}. \quad (2.58)$$

Equations (2.55)–(2.58) are applied to non-rectangular cross sections with gradually varied flow. However, there is a particular case where these are inaccurate, due to the assumption of uniform velocity across the cross section, namely for compound channel flow. The specific energy head then is (Sturm 2001)

$$E = h + \alpha \frac{Q^2}{2gA^2}, \quad (2.59)$$

where  $\alpha$  is the Coriolis velocity correction coefficient, given for 1D gradually varied flow by the expression (Jaeger 1956)

$$\alpha = \frac{\int_A (u^2 + v^2 + w^2) u dA}{U^3 A} \approx \frac{\int_A u^3 dA}{U^3 A}. \quad (2.60)$$

For gradually varied flows,  $\alpha$  is of the order of 1.1–1.15 (Chow 1959; Chaudhry 2008), and its consideration is seldom a critical issue (Liggett 1994). However, in compound channel flows, it can be large, and more importantly, it forces a notable modification of the behavior of the  $E = E(h)$  curve, with two points of minimum specific energy head (Sturm 2001).

### 2.2.4 Critical Flow and Wave Motion

Consider a static mass of water of depth  $h$  on which a perturbation is produced, say, by the impact of a rigid body, i.e., a stone (Fig. 2.13a). It produces a series of circular waves that propagate in the radial direction with celerity  $c$  (Fig. 2.13b, c). Assume that the stone acts as a continuous source of perturbations, not decaying in time.

The circular wave pattern generated at point “O” after time  $t$  has advanced a distance  $ct$  in the radial direction (Fig. 2.13c). If the wave amplitude is small, the celerity  $c$  is deduced by applying the energy conservation principle, because the energy loss linked to the traveling wave front can be neglected for a small amplitude wave. For finite amplitude waves, the momentum balance shall be used, given that the energy loss may be significant, as detailed in Chap. 5. Consider a small amplitude 1D wave traveling over still water (Fig. 2.14a). This unsteady motion is reduced to a steady flow by considering an observer traveling with wave speed (Chow 1959). The steady flow observed in this moving frame is depicted in Fig. 2.14b. It is obtained by superimposing the wave celerity ( $-c$ ) to the unsteady flow. The continuity equation then simply yields

$$q = -ch. \quad (2.61)$$

Energy conservation for the equivalent steady flow produces (Chow 1959; Henderson 1966)

$$H = h + \Delta h + \frac{c^2 h^2}{2g(h + \Delta h)^2} = h + \frac{c^2}{2g}. \quad (2.62)$$

Solving Eq. (2.62) for  $c$  and assuming that  $\Delta h \ll h$ , given the small wave height, yields

**Fig. 2.13** Perturbations generated on still water: **a** stone falling, **b** wave generation, **c** circular wave pattern

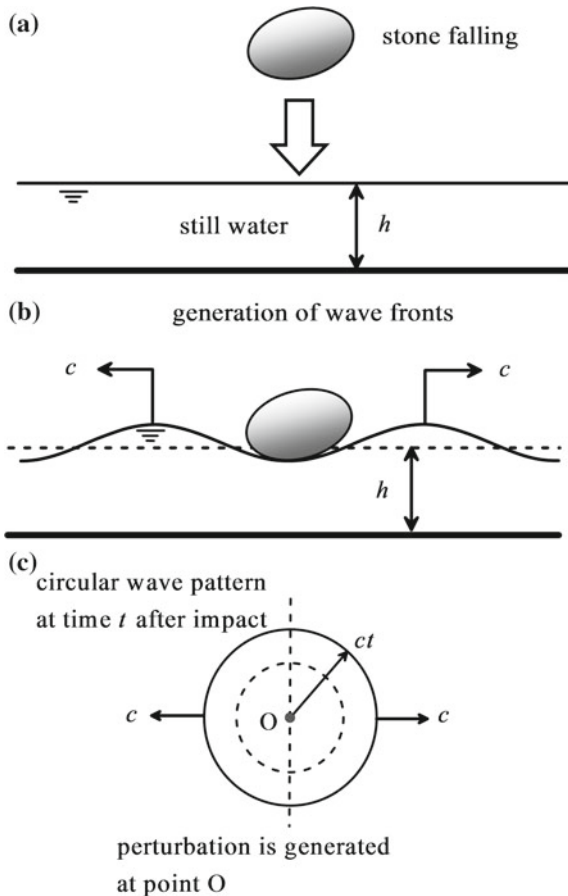
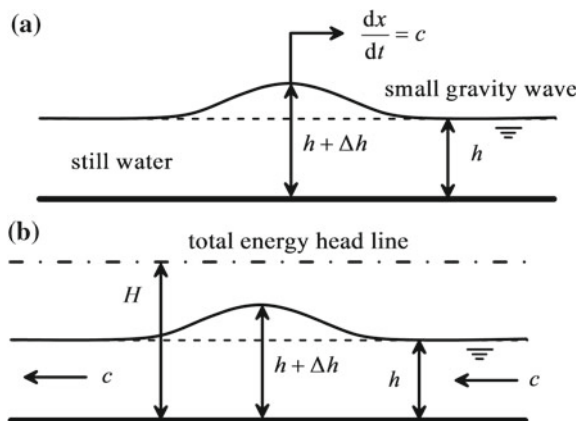


**Fig. 2.14** Small gravity perturbation traveling on still water: **a** unsteady flow motion and **b** equivalent steady flow seen by observer traveling with the wave



$$c = \left[ \frac{2g(h + \Delta h)^2}{2h + \Delta h} \right]^{1/2} \approx (gh)^{1/2}. \quad (2.63)$$

The quantity  $c = (gh)^{1/2}$  is the propagation celerity of small gravity waves over still water. Consider now that the fluid is moving at a constant velocity  $U$  (Fig. 2.15a). This fluid flow produces a displacement of the circular wave pattern generated on still water. In this case,  $c$  is still the wave celerity, i.e., its velocity of displacement relative to fluid flow. Consider first the case  $U < c$ . The absolute displacement velocity of each wave front is

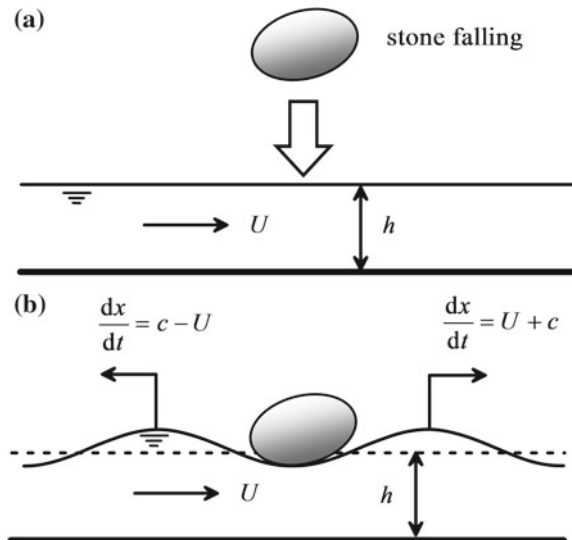
$$\frac{dx}{dt} = U \pm c. \quad (2.64)$$

Given that the wave spreads to both the left and the right, and that  $c > U$ , there is one wave front traveling to the left at speed  $c-U$  and another to the right at  $U+c$  (Fig. 2.15b). In still water, the wave patterns are concentric circular fronts (Fig. 2.16a), but for  $U < c$ , there is a displacement of circular waves to the right, with a wave front propagating to the left (Fig. 2.16b).

Manipulation of Eq. (2.64) yields

$$\frac{dx}{dt} = U \pm c = c \left( \frac{U}{c} \pm 1 \right) = c(F \pm 1), \quad (2.65)$$

**Fig. 2.15** Perturbations generated on a water flow slower than celerity  $c$  of the gravity waves: **a** stone falling and **b** wave generation



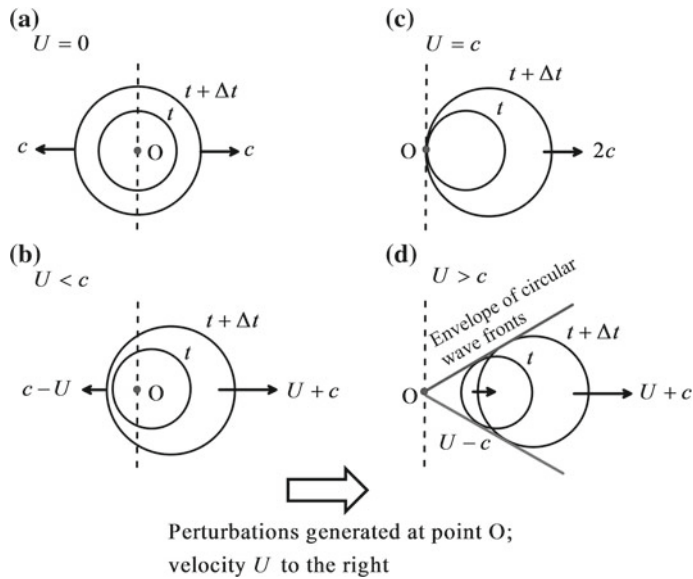
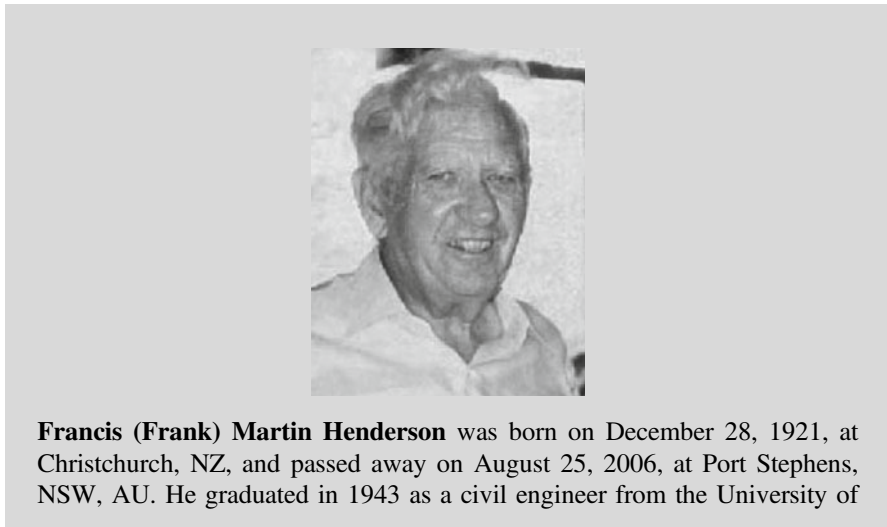


**Fig. 2.16** Wave patterns in **a** still water, **b** subcritical flow, **c** critical flow, **d** supercritical flow; adapted from Chow (1959)

where  $F$  is the Froude number, defined as

$$F = \frac{U}{c} = \frac{U}{(gh)^{1/2}} = \frac{\text{Fluid velocity}}{\text{Celerity of small gravity wave}}. \quad (2.66)$$



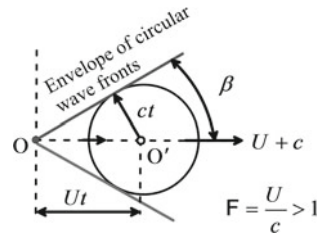
Canterbury, NZ. After war service, he gained the M.Sc. degree from Victoria University, Wellington, NZ. He then joined in 1952 its staff at the School of Engineering, where he was particularly involved in the development of the first axial flow jet boat. After two sabbaticals at the University of Michigan in 1956, and University of Cambridge in 1964, he was appointed as Professor of hydraulics and Deputy Head of his alma mater. In 1968, he took over the position of Head of the Civil Engineering Department, University of Newcastle, NSW. During the following 15 years until retirement, he served as Dean of Engineering and spent sabbaticals at the University of London in 1974 and at the University of Alberta, Edmonton, CA, in 1977. From 1983, he was a consultant, with engineering projects in Australia, Southeast Asia, and New Zealand.

The National Water Committee of the Institution of Engineers, Australia, decided in 1998 to mark the lifelong achievements of Emeritus Professor Henderson: During the Henderson Oration, his educational, professional, and scientific achievements were awarded. The highlights of his professional career are therein described, including model tests resulting in a shock wave reduction, vortex generation at intakes, and computer works to investigate fluid transients. Victor Streeter (1909–2015) has had a great influence on Henderson's professional knowledge during his visit to University of Canterbury in 1952 and during Henderson's stay at the University of Michigan. The latter stay marked the initiation of two papers on flow over ski jumps published in the French journal *La Houille Blanche* in the early 1960s. Later, Henderson was involved in the preparation of his famous book Open Channel Flow, which made him known among hydraulicians and may be considered his legacy in hydraulics.

Physically,  $c$  is the velocity of information transmission relating to the variation of the equilibrium conditions. The transmission of information by small gravity waves is the mechanism used by free surface flow to adjust from non-equilibrium to a new equilibrium state (steady flow) (Puertas and Sánchez 2001).

$U < c$  implies that  $F < 1$ . This flow is called subcritical, and physically, small gravity perturbations travel both in the up- and in the downstream directions. The case  $U = c$  results in  $F = 1$ , that is, the flow is critical, and the wave pattern as plotted in Fig. 2.16c. An additional feature of critical flow regained here is that the wave celerity traveling against the fluid flow is zero. At the point of perturbation origin (point "O" in Fig. 2.16c), the waves moving upstream are blocked and cannot propagate to the left. Waves can only propagate in the downstream direction with the absolute velocity  $dx/dt = 2c$ .

**Fig. 2.17** Angle of shock front in supercritical flow



$U > c$  implies  $F > 1$ . This flow is called supercritical; small gravity perturbations travel only in the downstream direction. Remember that  $c$  is the celerity of shallow water waves only if the wave amplitude is small as compared with the water depth. Therefore, a small gravity wave cannot propagate against flow direction in supercritical flow. However, as will be shown in Chap. 5, a finite amplitude gravity wave can propagate in the upstream direction of supercritical flow if it is large enough. The circular wave patterns are displaced along the longitudinal axis a quantity  $Ut$ , and there is an envelope of all circular fronts, which is itself a wave front or a supercritical shock (Fig. 2.16d). Its angle with the fluid flow direction is from simple geometry (Fig. 2.17)

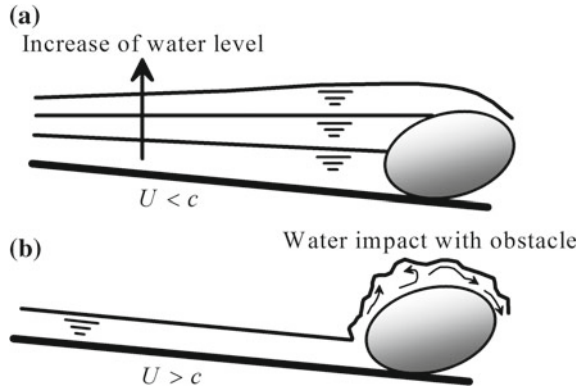
$$\sin \beta = \frac{ct}{Ut} = \frac{1}{F}. \quad (2.67)$$

The physical difference between sub- and supercritical flows is illustrated using an example of Puertas and Sánchez (2001). Consider an obstacle (stone) placed in a steady and uniform stream. If it is inserted into an initially uniform subcritical stream ( $U < c$ ), a gradual water-level variation is produced (Fig. 2.18a) (unsteady and rapidly varied flow effects are overlooked for the sake of simplicity). The gradual elevation of the water level is transmitted in the upstream direction as a smooth wave front. The water level will increase in response to the upstream discharge received, until the flow starts to spill over the stone, evolving in the long term to a new steady state (equilibrium condition). Note from this example that the obstacle influences the conditions of the upstream flow. The obstacle presence is “informed to the approach flow by small gravity waves.” This information transmission by gravity waves “informs” the upstream flow that there is an obstacle downstream, so that the flow is able to adapt its condition to that situation.

If the stone is placed into an initially uniform supercritical stream ( $U > c$ ) (Fig. 2.18b), there is no possibility of transmitting the information in the upstream direction, so that the approach flow is not informed about the obstacle presence. The water then impacts the obstacle and spills over it.<sup>1</sup> The present analysis is qualitative, given that it is in reality an unsteady flow, but highlights the

<sup>1</sup>In this introductory example, the possibility of having a hydraulic jump is overlooked. The hydraulic jump is the way water changes from super- to subcritical flow, to be detailed in the next section. It is basically a finite amplitude perturbation in steady flow.

**Fig. 2.18** Transmission of information by small gravity waves in **a** subcritical flow and **b** supercritical flow; adapted from Puertas and Sánchez (2001)



basic difference between sub- and supercritical flows: Subcritical flows are affected by perturbations produced downstream of a section, whereas supercritical flows are not affected. Any variation of flow depth or discharge in a channel produces small gravity wave fronts transmitting information by these perturbations, producing a transition to a new equilibrium condition.

### 2.2.5 Computation of Critical Flow in Arbitrary Sections

General

The critical depth for an arbitrary cross-sectional shape follows by solving the equation

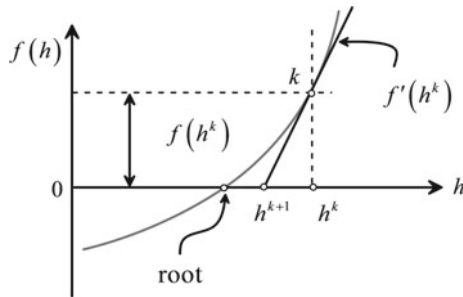
$$\frac{Q^2}{gA(h)^3}B(h) = 1, \quad (2.68)$$

or

$$f(h) = Q^2 - g\frac{A(h)^3}{B(h)} \equiv 0. \quad (2.69)$$

The problem is, for a given channel shape and discharge  $Q$ , to find the value of the flow depth by which  $f(h) = 0$  in Eq. (2.69). This computation must be generally conducted using numerical methods. Of the various root-finding methods available in the literature, the Newton–Raphson method is applied (Hoffman 2001; Jeppson 2011). Consider a generic function  $f = f(h)$  sketched in Fig. 2.19. To conduct iterations of Eq. (2.69), a previous trial value of  $h$  is required. Consider the known value of  $h$  at iteration “ $k$ ”, for which  $f(h^k)$  is nonzero. The tangent to  $f(h)$  at  $k$  is

**Fig. 2.19** Illustration of Newton–Raphson method



$$f'(h^k) = \left( \frac{df}{dh} \right)^k = \frac{f^k}{h^k - h^{k+1}}. \quad (2.70)$$

A better approximation to the root of Eq. (2.69) is therefore given by the intersection of the tangent line with the  $h$ -axis, e.g.,

$$h^{k+1} = h^k - \frac{f^k}{(df/dh)^k}. \quad (2.71)$$

Equation (2.71) is known as Newton–Raphson iterative formula, allowing for an ordered convergence to the root. Limitations are that the function  $f$  must admit to form the derivative  $df/dh$  and that the initial value of  $h$  to start iterations must be a suitable estimate of the root, to ensure convergence (see Hoffman 2001 for details).

The derivative needed in Eq. (2.71) is

$$\frac{df}{dh} = -g \left( 3A^2 - \frac{A^3}{B^2} \frac{dB}{dh} \right). \quad (2.72)$$

A convergence criterion to the iteration algorithm based on Eq. (2.71) is

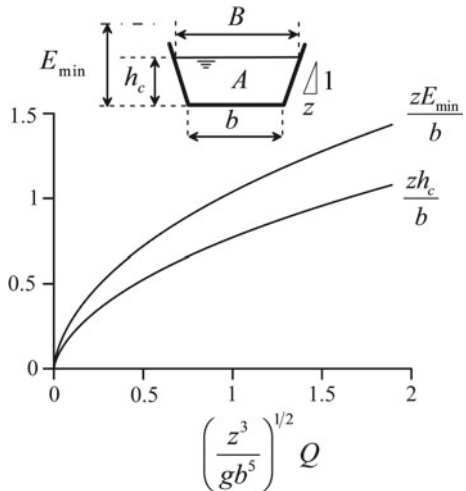
$$\left| \frac{f^{k+1} - f^k}{f^k} \right| \leq \varepsilon, \quad (2.73)$$

that is, if the new iteration value yields an error below a specific tolerance  $\varepsilon$ , usually taken as  $10^{-6}$ , the actual numerical value is of acceptable quality and therefore taken as the numerical solution for the critical depth.

Trapezoidal cross section

For a trapezoidal section (Fig. 2.20), the flow area  $A$  and free surface width  $B$  are

**Fig. 2.20** Relative critical depth  $zh_c/b$  and minimum specific energy head  $zE_{\min}/b$  versus relative discharge  $\left(\frac{z^3}{gb^5}\right)^{1/2}Q$  in trapezoidal channel



$$\begin{aligned} A &= bh + zh^2, \\ B &= b + 2zh. \end{aligned} \quad (2.74)$$

A suitable initial value to start iterations is the critical depth of the rectangular section of the trapezoidal bottom width  $b$

$$h_c = \left( \frac{Q^2}{gb^2} \right)^{1/3}. \quad (2.75)$$

A code with this scheme implemented is on the side file “*criticaldepth\_NR.xls*”, in Chap. 12. For a channel of base width  $b = 1$  m, side slope  $z = 2$  and  $Q = 5$  m<sup>3</sup>/s, the program yields  $h_c = 0.8346$  m after six iterations. The critical depth and minimum specific energy of the trapezoidal channel are shown in dimensionless form in Fig. 2.20 (Henderson 1966). These functions are obtained as follows. Inserting Eq. (2.74) into Eq. (2.69) yields

$$\frac{Q^2}{g(bh_c + zh_c^2)^3} (b + 2zh_c) = 1, \quad (2.76)$$

or, as plotted in Fig. 2.20

$$\frac{z^3 Q^2}{gb^5} = \frac{\left[ \left(1 + \frac{zh_c}{b}\right) \left(\frac{zh_c}{b}\right) \right]^3}{\left(1 + 2\frac{zh_c}{b}\right)}. \quad (2.77)$$

The minimum specific energy head is thus

$$E_{\min} = h_c + \frac{Q^2}{2g(bh_c + zh_c^2)^2}, \quad (2.78)$$

or

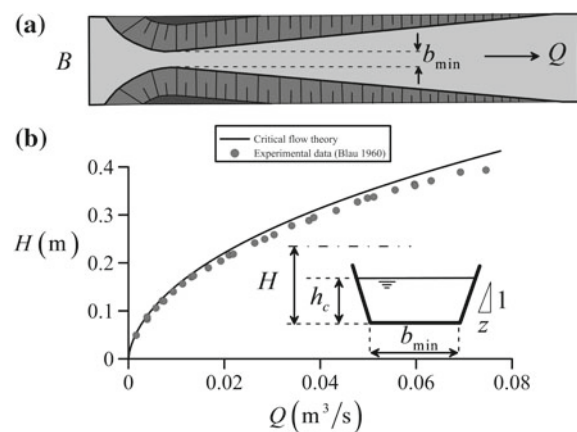
$$\frac{zE_{\min}}{b} = \frac{zh_c}{b} + \frac{\frac{z^3 Q^2}{gb^5}}{2[(1 + \frac{zh_c}{b})(\frac{zh_c}{b})]^2}. \quad (2.79)$$

To determine the head–discharge curve  $Q = Q(E_{\min})$ , computations are explicit: A value of  $h_c$  is selected, from which the discharge  $Q$  is obtained from Eq. (2.76) and the specific energy head from Eq. (2.78). An important application of the critical flow theory is to determine the head–discharge relation of control structures generating critical flow, as the Venturi flume. Assuming that energy losses are negligible, the total head  $H$  at the inlet is equal to  $E_{\min}$ , with the critical depth established at the throat, where  $b = b_{\min}$ . The theory is compared with the data of Blau (1960) in Fig. 2.21, for a Venturi flume of base width  $b = 0.0665$  m and  $z = 0.299$ , indicating a fair agreement. Deviations between the theory and experiments with increasing discharge are due to non-hydrostatic effects at the critical flow section (Montes 1998; Hager 2010).

### Circular cross section

The basic flow variable needed to compute critical flow in a circular cross section of diameter  $D$  is the central angle  $\theta$

**Fig. 2.21** Head–discharge relation of Venturi flume:  
a plan view and b relation  $Q(H)$



$$\theta = 2\cos^{-1}\left(1 - 2\frac{h_c}{D}\right). \quad (2.80)$$

The free surface width  $B$  and the flow area  $A$  are then given by (Jain 2001; Sturm 2001)

$$\begin{aligned} B &= D \sin\left(\frac{\theta}{2}\right), \\ A &= \frac{D^2}{8}(\theta - \sin \theta). \end{aligned} \quad (2.81)$$

Inserting Eq. (2.81) into Eq. (2.68) yields

$$\frac{Q^2}{gD^5} = \frac{1}{512} \frac{(\theta - \sin \theta)^3}{\sin(\theta/2)}. \quad (2.82)$$

The minimum specific energy head follows by substituting Eq. (2.81) into Eq. (2.58), resulting in

$$\frac{E_{\min}}{D} = \frac{h_c}{D} + \frac{1}{16} \frac{(\theta - \sin \theta)}{\sin(\theta/2)}. \quad (2.83)$$

The computation of the head–discharge relation is simple. First, a value of  $h_c$  is selected, from which  $\theta$  is computed from Eq. (2.80). The value of  $Q^2/(gD^5)$  is then given by Eq. (2.82) and the value of  $E_{\min}/D$  by Eq. (2.83). These relations are plotted in Fig. 2.22.

The theory is applied to compute the head–discharge relation of a circular culvert with critical depth at its inlet (Henderson 1966). Without energy losses at the pipe inlet, the specific energy head  $E_{\min}$  equals the upstream water depth  $H$ , as long as the approach flow velocity head is small. Computing the  $[Q^2/(gD^5); H/D]$  data pairs along the interval of the dimensionless discharge investigated by Toman et al. (2014) results in a fair agreement between the critical flow theory and the experimental data (Fig. 2.23).

To compute the critical depth of a circular section of diameter  $D$  for a discharge  $Q$ , however, numerical computations are required to solve Eq. (2.68) iteratively. A code based on the Newton–Raphson scheme is implemented in Chap. 12 in the file “*criticaldepth\_NR\_pipe.xls*”. For a channel of  $D = 1$  m and  $Q = 1$  m<sup>3</sup>/s, the program yields  $h_c = 0.573$  m after three iterations.

**Fig. 2.22** Critical depth  $h_c/D$  and minimum specific energy head  $E_{\min}/D$  versus  $Q/(gD^5)^{1/2}$  in circular pipe

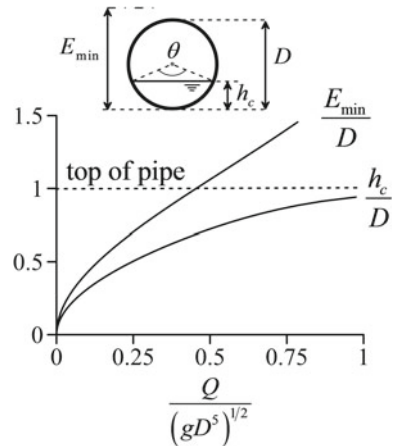
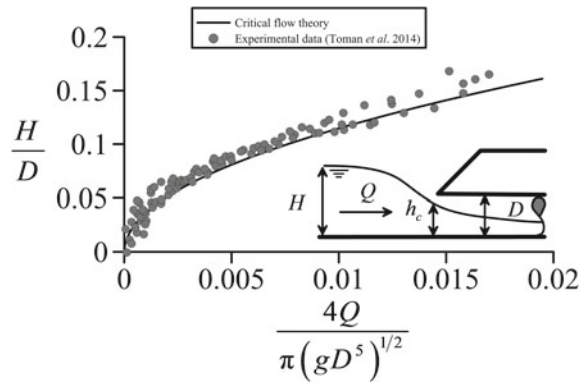


**Fig. 2.23** Head–discharge relation in a circular culvert with critical flow at the inlet



## 2.2.6 Channel Transitions by Change of Bed Elevation

### Sub-subcritical flow

Consider the free surface profile in a channel transition consisting of a smooth hump, to avoid separation losses, located in a prismatic rectangular channel in which an ideal uniform fluid flow of flow depths up- and downstream of the hump is established. First, the profiles will be discussed qualitatively using the specific energy head diagram, and then computations are detailed. Consider ideal fluid flow toward the hump under subcritical flow with  $q$  as the unit discharge,  $H$  the total energy head, and  $Z$  the maximum hump elevation (Fig. 2.24). From Eq. (2.14) for ideal and steady flow,

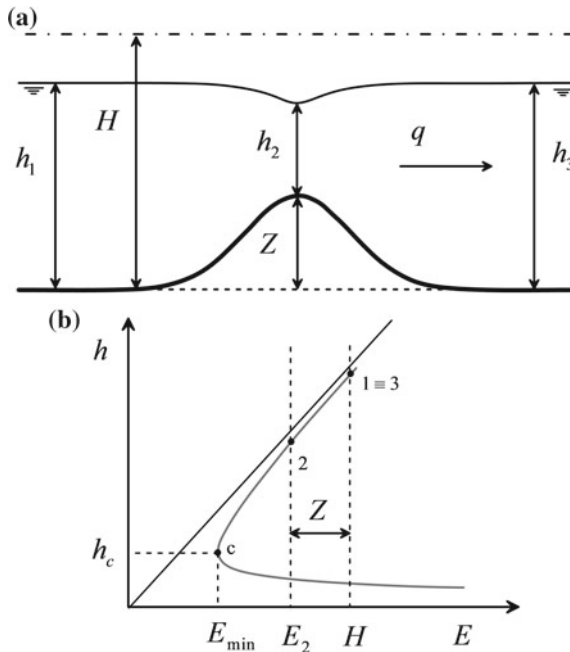


**Fig. 2.24** Subcritical flow over a hump: **a** geometry and **b** specific energy head diagram

$$H = E_1 = E_2 + Z = E_3. \quad (2.84)$$

Therefore, the specific energy head at the hump crest (point 2) is

$$E_2 = H - Z. \quad (2.85)$$

In this example, it was assumed, as observed on the specific energy head diagram, that  $E_2 > E_{\min}$ . The flow depth at point 2 is therefore above  $h_c$ , and the water surface forms a depression as it crosses the hump (Figs. 2.24 and 2.25).



**Fig. 2.25** Experiment with subcritical flow over a hump [taken from movie Fluid Motion in a Gravitational Field, by Rouse (1961), IIHR-Hydroscience & Engineering, the University of Iowa]

### Super-supercritical flow

If supercritical flow approaches the obstacle with identical values of  $H$  and  $q$  as for  $F < 1$ , a representation of the flow conditions in the specific energy head diagram shows that the flow depth over the obstacle increases (Figs. 2.26 and 2.27), again for  $E_2 > E_{\min}$ .

The value of  $Z$  resulting from equaling  $E_2$  and  $E_{\min}$  is the maximum possible to pass the flow rate  $q$  with the specific energy head  $H$  at the inlet of the hump. It is, therefore,

$$Z_{\max} = H - E_{\min}. \quad (2.86)$$

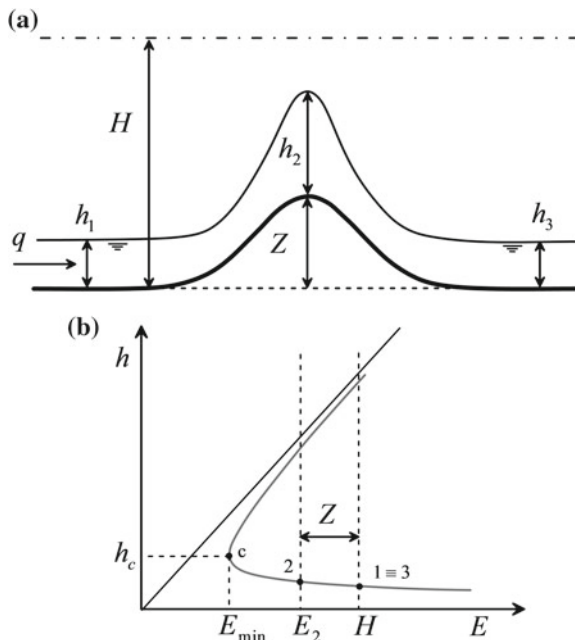
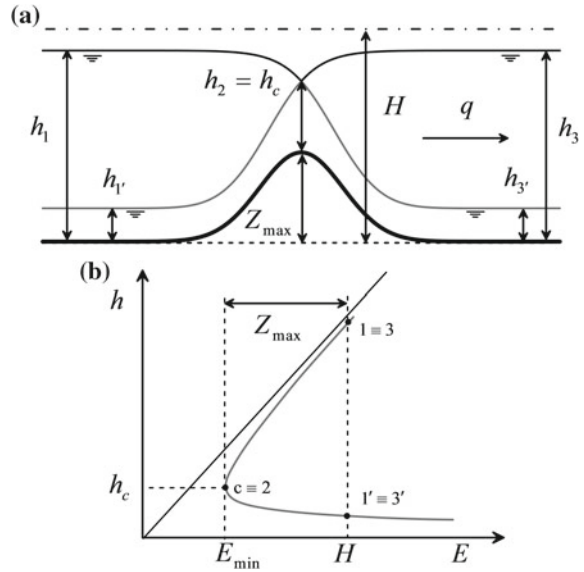


**Fig. 2.26** Supercritical free surface profile over a hump: **a** geometry and **b** representation on the specific energy head diagram



**Fig. 2.27** Experiment with supercritical flow over a hump [taken from movie Fluid Motion in a Gravitational Field, by Rouse (1961), IIHR-Hydroscience & Engineering, the University of Iowa]

**Fig. 2.28** Sub- and supercritical free surface profiles over a hump with critical flow at the crest:  
**a** geometry and **b** specific energy head diagram



For this value of  $Z$ , the crest flow depth equals the critical depth both for the sub- and for the supercritical profiles (Fig. 2.28). The computation of the flow profiles is now detailed.

As the water flows over the obstacle, each section is subject to a different value of specific energy head imposed by the upstream condition, namely  $E(x) = H - z_b(x)$ . The problem is to compute the alternate depth corresponding to the flow regime selected (sub- or supercritical) for the value of  $E$  at section  $x$ . Equation (2.15) is written as

$$\left(\frac{h}{h_c}\right)^3 - \frac{E}{h_c} \left(\frac{h}{h_c}\right)^2 + \frac{1}{2} = 0. \quad (2.87)$$

Equation (2.87) can be rewritten as (Selby 1973)

$$\chi^3 + a\chi + b = 0, \quad (2.88)$$

where

$$\chi = \frac{h}{h_c} - \frac{1}{3} \frac{E}{h_c}, \quad a = -\frac{1}{3} \left(\frac{E}{h_c}\right)^2, \quad b = \frac{1}{27} \left[ -2 \left(\frac{E}{h_c}\right)^3 + \frac{27}{2} \right]. \quad (2.89)$$

The two positive solutions to Eq. (2.88) are (Selby 1973; Chanson 2004; Jeppson 2011)

$$\frac{h}{h_c} = \frac{E}{h_c} \left[ \frac{1}{3} + \frac{2}{3} \cos\left(\frac{\Gamma}{3}\right) \right], \quad (2.90)$$

for subcritical flow, and

$$\frac{h}{h_c} = \frac{E}{h_c} \left[ \frac{1}{3} + \frac{2}{3} \cos\left(\frac{\Gamma}{3} + \frac{4\pi}{3}\right) \right], \quad (2.91)$$

for supercritical flow, where

$$\cos \Gamma = 1 - \frac{27}{4} \left( \frac{E}{h_c} \right)^{-3}. \quad (2.92)$$

The free surface profile can thus be analytically computed for given  $z_b = z_b(x)$ ,  $q$ , and  $H$ .

For non-rectangular sections, the alternate depths must be determined numerically. A numerical computation method is presented that is applied to these cases. The algorithm for the rectangular section is presented, and the numerical solution is compared with the analytical result. Let the specific energy head at section  $x$  be

$$E(x) = H - z_b(x). \quad (2.93)$$

To determine the flow depth, a root search procedure is applied to the function

$$f(x) = h + \frac{q^2}{2gh^2} - E(x). \quad (2.94)$$

The Newton–Raphson iterative formula reads

$$h(x)^{k+1} = h(x)^k - \frac{f(x)^k}{[df(x)/dh]^k}, \quad (2.95)$$

where the derivative of  $f$  is

$$\frac{df(x)}{dh} = 1 - \frac{q^2}{gh^3}. \quad (2.96)$$

To start iterations, a suitable initial value of  $h(x)$  is needed, corresponding to the same regime of the root. For subcritical flow, the starting value is obtained by assuming that the kinetic energy head can be neglected in the specific energy

equation, whereas the specific energy head equals the kinetic energy head for supercritical flow, e.g.,

$$h(x)^{k=0} = \begin{cases} E(x), & \text{if } 1 - \frac{q^2}{gh^3} < 1 \\ \left[ \frac{q^2}{2gE(x)} \right]^{1/2}, & \text{if } 1 - \frac{q^2}{gh^3} > 1. \end{cases} \quad (2.97)$$

Consider as test case a Gaussian hump of profile  $z_b$  (m) =  $0.2\exp[-0.5\{x\text{ (m)}/0.24\}^2]$ . A subcritical flow profile for  $q = 0.2$  m<sup>2</sup>/s and  $H = 0.45$  m was computed analytically and numerically, with the results compared in Fig. 2.29. The codes used for the simulations are available in the files “Analytical\_hump\_subsuper.xls” and “Hump\_NR.xls” in Chap. 12, respectively. Note that the accuracy of the numerical method is excellent, supporting its extension to other cross-sectional channel shapes.

A supercritical flow profile was generated using the same data as for  $F < 1$ , and the analytical results are compared with the numerical solution in Fig. 2.30. As previously, the agreement between both solutions is excellent.

**Fig. 2.29** Computation of subcritical flow profile over a Gaussian hump

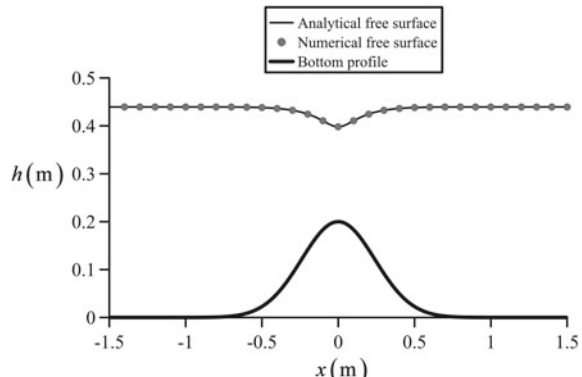
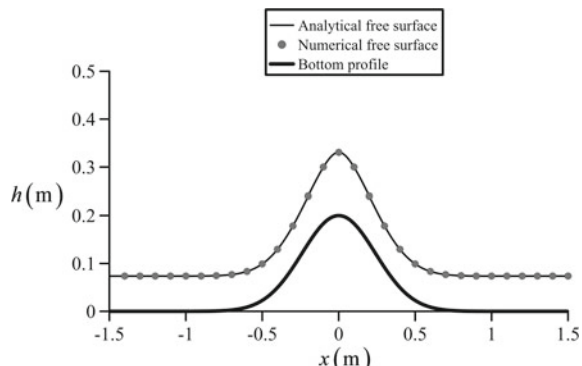


**Fig. 2.30** Computation of supercritical flow profile over a Gaussian hump



### Sub-supercritical flow

An additional possible flow profile involves a change from upstream subcritical flow to downstream supercritical flow (Fig. 2.31). This profile is obtained by setting critical flow at the crest and joining the upstream subcritical profile obtained with Eq. (2.90) with a downstream supercritical profile determined from Eq. (2.91). Obviously, for this situation to occur, the flow depths up- and downstream from the obstacle might not be equal. Rather, the two flow depths correspond to the alternate depths for the specific energy head  $H = Z_{\max} + E_{\min}$  (Fig. 2.31).

It is pertinent to mention that for a given upstream subcritical alternate depth  $h_1$ , the value of  $h_3$  is determined analytically by the alternate depth equation (Fig. 2.31)

$$H = h_1 + \frac{q^2}{2gh_1^2} = h_3 + \frac{q^2}{2gh_3^2}, \quad (2.98)$$

so that

$$h_1 - h_3 = \frac{q^2}{2g} \left( \frac{1}{h_1^2} - \frac{1}{h_3^2} \right), \quad (2.99)$$

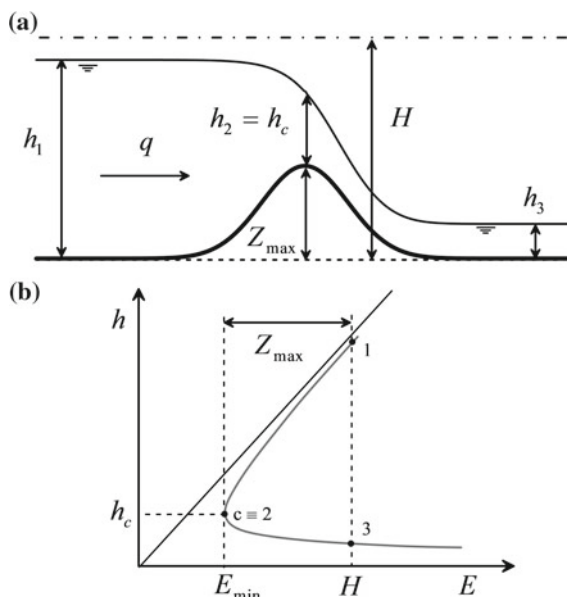


**Fig. 2.31** Transcritical flow profile over a hump: **a** geometry and **b** specific energy head diagram

or

$$h_1 - h_3 = \frac{q^2}{2g} \left( \frac{h_1^2 - h_3^2}{h_3^2 h_1^2} \right) = \frac{q^2}{2g} \frac{(h_1 - h_3)(h_1 + h_3)}{h_3^2 h_1^2}. \quad (2.100)$$

After simplification, the result is (Subramanya 1986)

$$h_3^2 h_1^2 - \frac{q^2}{2g} (h_1 + h_3) = 0. \quad (2.101)$$

For given  $q$  and  $h_1$ , Eq. (2.101) is a quadratic equation in  $h_3$ , which is easily solved.

Consider now how a transcritical flow profile as that of Fig. 2.31 is established in a channel for given water depths up- and downstream of the obstacle. Consider upstream subcritical flow ( $q, H$ ) and a maximum hump elevation  $Z$  satisfying

$$E_2 = H - Z < E_{\min}. \quad (2.102)$$

As plotted in the specific energy head diagram (Fig. 2.32), the vertical line labeled  $X-X'$  does not cut the specific energy head diagram for discharge  $q$ . The line  $E_2 = \text{const.}$  is outside the range of possible physical solutions (Rouse 1938, 1950), so that the flow rate  $q$  cannot be transported over the obstacle with the available specific energy  $H \equiv E_1$ . The upstream specific energy head must be raised until the specific energy head on the crest corresponds to the minimum possible  $E_{\min}$  for the flow to pass the obstacle. This is in fact what the water flow does: As the water flow  $q$  approaches the obstacle with the upstream head  $H$ , an unsteady flow motion is induced, given the impossibility to pass the obstacle. The obstacle acts as a perturbation, and this situation is gradually transmitted to the approach flow by small gravity waves propagating into the upstream direction at celerity  $(gh)^{1/2}$  relative to the flow. In response to this feedback, the upstream flow receives the message and begins to increase its upstream specific energy, establishing a new equilibrium condition. Once the water flows over the crest at critical flow condition, the upstream energy head is fixed by the new point  $1'$  as  $E_{1'} = Z + E_{\min} > E_1$ . The new head over the obstacle is then  $E_{1'}$ . The upstream specific energy increase from  $E_1$  to  $E_{1'}$  is accomplished by a backwater curve of necessary length to produce an adaptation of flow depths from  $h_1$  to  $h_{1'}$  producing the exact increase needed in the specific energy. This type of curve<sup>2</sup> will be described in Chap. 3, given that frictional effects are relevant.

---

<sup>2</sup>This type of gradually varied flow profile is called M1-type curve. The role of friction is important, as well as that of the upstream bottom slope  $S_o$ . As will be demonstrated in Chap. 3, a form equivalent to Eq. (2.8) is  $dE/dx = S_o - S_e$ , with  $S_o > S_e$  for the M1 curve, so that  $E$  is increased in the flow direction. A certain length is necessary to increase the specific energy by the quantity  $\Delta E$  needed to pass the obstacle. This specific energy gain is locally lost beyond the obstacle in a hydraulic jump. The relation describing the energy loss in a hydraulic jump will be presented in the next section.

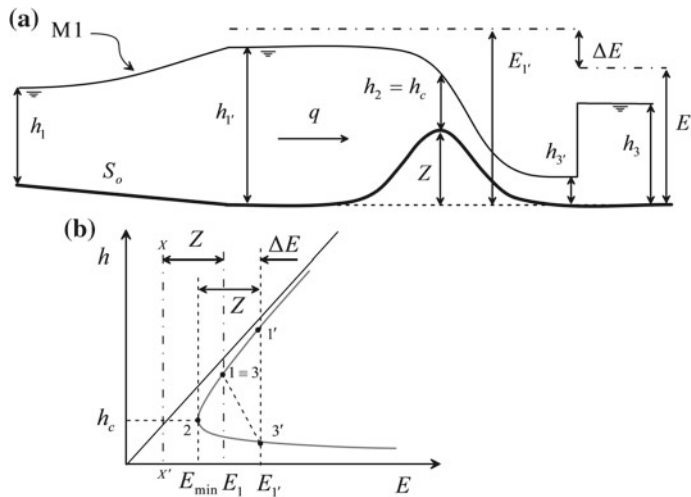


**Fig. 2.32** Transcritical ideal flow profile over a hump as result of choked upstream subcritical flow: **a** geometry and **b** specific energy head diagram

### Super-subcritical flow

From the crest, the water flows down the tailwater face of the hump under the supercritical regime without any energy losses, reaching point 3' downstream of the hump. The specific energy head at this point is  $E_{1'}$ , which is larger than the value of the specific energy head  $E_1$  far downstream of the obstacle. To return to this flow condition, the water must lose the specific energy head gained by approaching the hump, namely  $E_1 - E_{1'}$ , and change from the super- to the subcritical regime. This is accomplished by a hydraulic jump, the physical phenomenon producing such flow transition, accompanied by significant energy losses equal to  $\Delta E = E_{1'} - E_1$ . The flow profile over the obstacle is 1-1'-c-3'-3, therefore.

After having described the entire free surface profile, it is observed that the obstacle “forces” the upstream flow to increase its water depths from  $h_1$  to  $h_{1'}$ . As this occurs, namely that the upstream flow conditions are affected, the flow is said to be “choked.”

Consider an upstream supercritical flow obeying Eq. (2.102). Again, the upstream flow must increase its specific energy to pass the obstacle. However, from gradually varied flow computations to be described in Chap. 3, it is not possible to gain this specific energy in supercritical flow. To increase the specific energy head and passing the obstacle, the upstream flow must change from super- to subcritical flow. Obviously, this transition is accompanied by an energy loss to be supplied by a backwater curve under subcritical flow. The flow over the obstacle is depicted in Fig. 2.33. The upstream supercritical flow at section 1 changes to subcritical flow at section 1', with the energy loss  $\Delta E_j$  across the hydraulic jump. The energy head at the crest must be the minimum possible to pass the flow,  $E_{\min}$ . Thus, the required

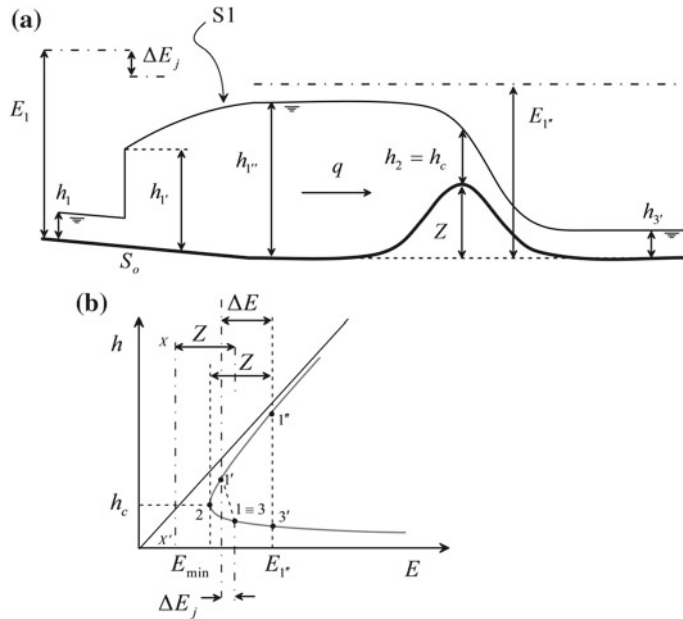


**Fig. 2.33** Transcritical flow profile over a hump resulting in choked upstream supercritical flow: **a** geometry and **b** specific energy head diagram

energy just upstream of the obstacle is  $E_{1''} = Z + E_{\min}$ . Therefore, the flow conditions must change from section 1' to section 1'' by a gradually varied flow profile (curve type S1, Chap. 3) of the length necessary to supply the increase in the specific energy head needed,  $\Delta E$ , namely (Fig. 2.32)

$$\Delta E = E_{\min} + Z + \Delta E_j - E_1. \quad (2.103)$$

The upstream supercritical flow is therefore choked. Beyond the crest, the flow reaches the toe of the hump under supercritical condition up to section 3', without any loss of energy. A gradually varied flow profile in the tailwater portion permits the adaptation from 3' to 3. The flow profile over the obstacle is therefore 1-1'-1''-c-3'.

This type of flow profile is produced if a supercritical flow over an obstacle, shown in Fig. 2.26, suffers a reduction of discharge; the effect is highlighted in Fig. 2.34 using the specific energy head diagram, with  $q_2 < q_1$ . The upstream flow depth  $h_1$  is kept constant with a gate. Then, the discharge is reduced, say, by maneuvers with a pump. The conditions at the upstream section change from point 1 to 1', which obviously has less specific energy head than the original upstream flow. This specific energy head is insufficient to pass the obstacle, so it shall be increased. The only way to increase the specific energy head of a supercritical flow approaching an obstacle is by jumping to subcritical flow and producing a back-water effect (Fig. 2.33). Rouse (1961) studied this phenomenon by starting with the

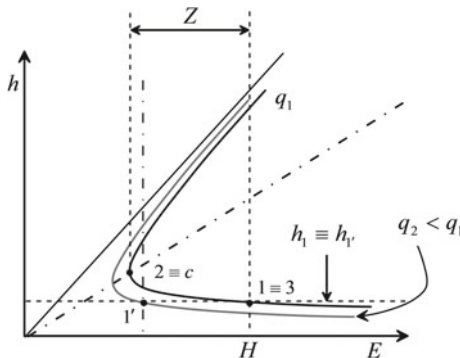


**Fig. 2.34** Discharge reduction in supercritical flow over a hump under constant upstream flow depth



**Fig. 2.35** Experiment with supercritical flow over a hump choked by discharge reduction [taken from movie Fluid Motion in a Gravitational Field, by Rouse (1961), IIHR-Hydroscience & Engineering, the University of Iowa]



**Fig. 2.36** Experiment with transcritical flow over a hump [taken from movie Fluid Motion in a Gravitational Field, by Rouse (1961), IIHR-Hydroscience & Engineering, the University of Iowa]

supercritical profile of Fig. 2.27, then reducing the discharge, and inducing the propagation of a surge in the upstream direction (Fig. 2.35), which, once reaching steady state, transforms into a hydraulic jump located in the upstream channel, leading to a transcritical flow profile over the hump (Fig. 2.36).

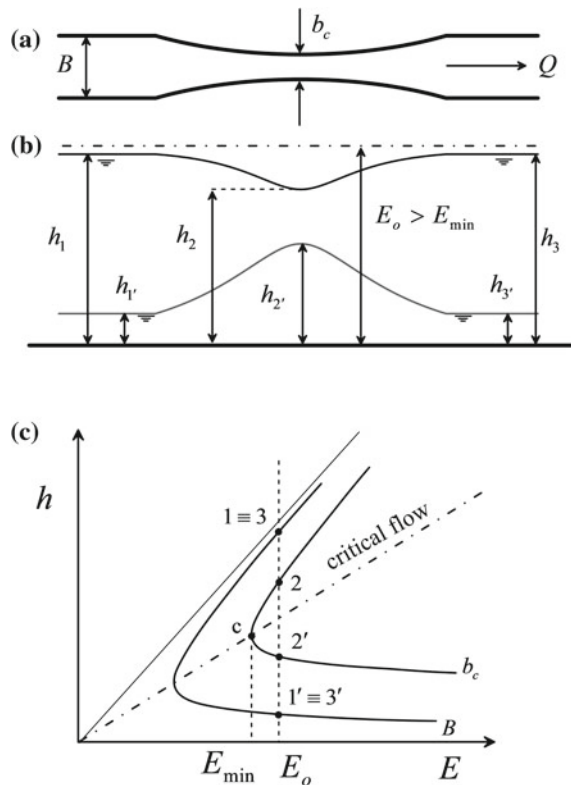
### 2.2.7 Channel Transitions by Change of Channel Width

Consider now the transition along a gradual contraction-expansion in a rectangular and horizontal channel (Fig. 2.37). The upstream channel width is  $B$ , its minimum width at the throat  $b_c$ , and the upstream specific energy head  $E_o$ . The analytical solution given by Eqs. (2.90)–(2.92) permits the computation of the flow profiles. If the up- and downstream flow conditions are subcritical, the flow passage across the contraction-expansion produces a depression-elevation of the water surface. If  $E_o > E_{\min}$ , the critical depth is not reached at any point along the structure (Fig. 2.37). Note that the critical depth in a channel of variable width is different at each section, given by

$$h_c(x) = \left[ \frac{Q^2}{gb(x)^2} \right]^{1/3}. \quad (2.104)$$

However, as previously demonstrated, critical flow can only be established at the throat. The value of  $E_{\min}$  is therefore the minimum specific energy at the throat. Its

**Fig. 2.37** Sub- and supercritical profiles across a contraction-expansion:  
a plan, b geometry, c specific energy head diagram



value is reached at the throat for the available value of  $E_o$  if the throat width is  $b_{\min}$  as

$$E_o \equiv E_{\min} = \frac{3}{2} \left[ \frac{Q^2}{gb_{\min}^2} \right]^{1/3}, \quad (2.105)$$

or

$$b_{\min} = Q \left( \frac{2}{3} \right)^{-3/2} (g E_o^3)^{-1/2}. \quad (2.106)$$

For the two cases plotted in Fig. 2.37,  $b_c > b_{\min}$ . If the up- and downstream flow conditions are supercritical, the flow passage across the contraction-expansion produces an elevation-depression of the water surface (Fig. 2.37). If the value of  $E_o$  is kept constant and the value of  $b_c$  is reduced to  $b_{\min}$ , the sub- and supercritical profiles reach critical flow at the throat (Fig. 2.38).

**Fig. 2.38** Sub- and supercritical profiles across a contraction-expansion of minimum throat width:  
a plan, b geometry, c specific energy head diagram

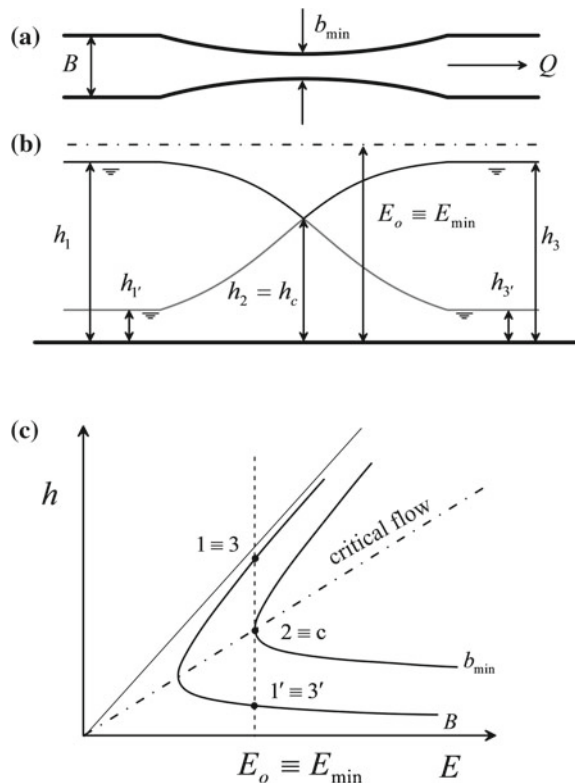
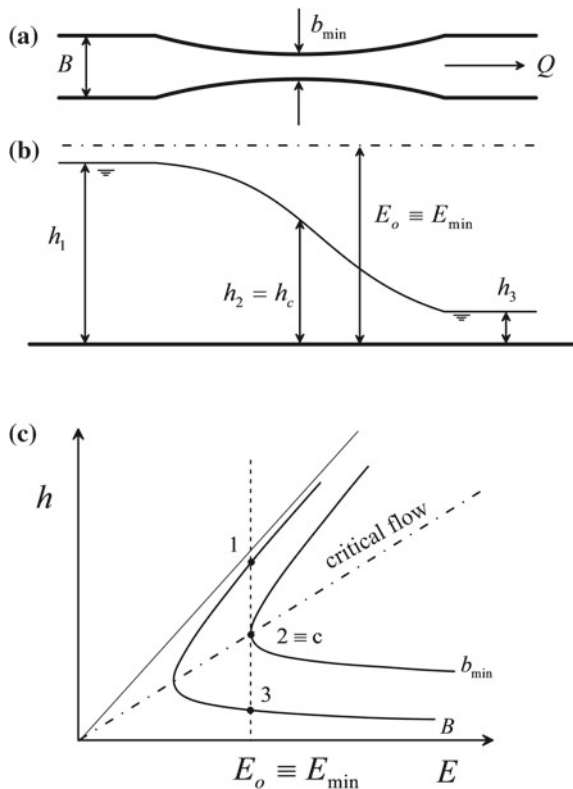


**Fig. 2.39** Transcritical profile across a contraction-expansion of minimum throat width: **a** plan, **b** geometry, **c** specific energy head diagram



An additional possible profile involves the transition from upstream subcritical to downstream supercritical flow (Fig. 2.39). A further reduction of  $b_c$  below  $b_{\min}$  produces a transcritical flow profile and chocking of the upstream flow, with a hydraulic jump at the flume exit, for upstream subcritical flow, and an upstream hydraulic jump if it were supercritical.

Transcritical flow in a Venturi flume tested by Khafagi (1942) is considered in Fig. 2.40. The inlet is a converging circular arc transition of radius  $R = 0.545$  m,

$$b(x) = b_c + 2 \left[ R - \left( R^2 - (x - 0.3)^2 \right)^{1/2} \right]. \quad (2.107)$$

The origin of the  $x$ -coordinate is at contraction start. The contraction is followed by a constant width throat 0.05 m long and a 1:8 linear expansion to recover the original flume width, given with  $b_c = 0.12$  m by

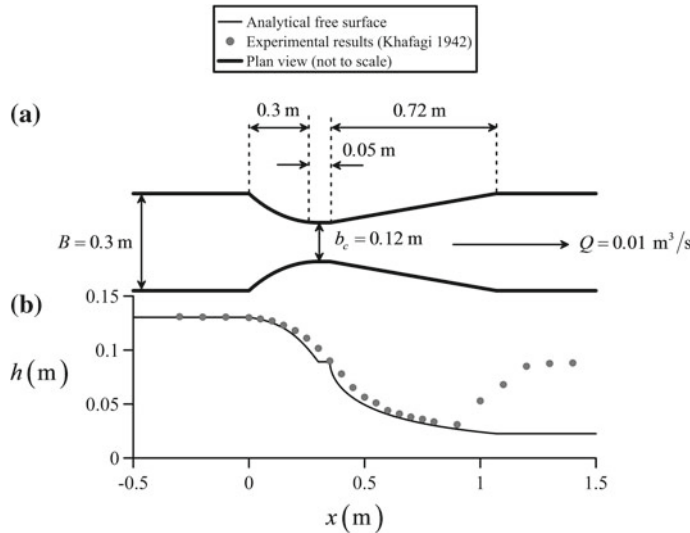


**Fig. 2.40** Transcritical profile in a Venturi flume: **a** plan and **b** comparison of test data with theory

$$b(x) = b_c + 2 \left[ \frac{1}{8} (x - 0.35) \right]. \quad (2.108)$$

Consider the measured free surface profile for  $Q = 0.01 \text{ m}^3/\text{s}$ . The analytical solution of Eqs. (2.90)–(2.92) was used to generate a theoretical profile, noting that  $E = E_o = E_{\min}$  at all sections, e.g.,

$$E = E_o \equiv E_{\min} = \frac{3}{2} \left[ \frac{Q^2}{gb_c^2} \right]^{1/3}. \quad (2.109)$$

The value of the critical depth at each section is different, however [see Eq. (2.104)]. That is, upstream from the flume throat, the subcritical flow profile at section  $x$  of the circular arc transition is

$$\frac{h(x)}{h_c(x)} = \frac{E_o}{h_c(x)} \left[ \frac{1}{3} + \frac{2}{3} \cos \left( \frac{\Gamma}{3} \right) \right], \quad (2.110)$$

where

$$\cos \Gamma = 1 - \frac{27}{4} \left[ \frac{E_o}{h_c(x)} \right]^{-3}. \quad (2.111)$$

Along the 0.05-m-long throat, the water depth is constant and equal to the critical depth for width  $b_c = 0.12$  m. Along the linear expansion, the supercritical flow profile is

$$\frac{h(x)}{h_c(x)} = \frac{E_o}{h_c(x)} \left[ \frac{1}{3} + \frac{2}{3} \cos \left( \frac{\Gamma}{3} + \frac{4\pi}{3} \right) \right]. \quad (2.112)$$

A comparison of the analytical solution and the experimental data reveals fair agreement, although the water depth along the throat is clearly not a constant. Deviations of experiments and predictions are mainly due to non-hydrostatic effects (Hager 2010). Note further the presence of a hydraulic jump in the tailwater, which is not predicted by the present computations based on constant energy head.

The analytical solution of Eqs. (2.90)–(2.92) was used to compute the free surface profile of the transition structure shown in Fig. 2.12. A subcritical flow profile was computed upstream of the critical section using Eq. (2.90), whereas the supercritical profile downstream from the critical section was determined using Eq. (2.91). It is thereby necessary to evaluate the specific energy head  $E(x)$  and the critical depth  $h_c(x)$  at each section. The specific energy head along this transition is different at each section and given by  $E(x) = H - z_b(x)$ . The total energy head is a constant to be evaluated using the critical flow section. From Eq. (2.54), it is located at  $x_c \approx 20.026$  m using the Newton–Raphson method. Channel width and bottom elevation at the critical section are thus  $b_c = 3.997$  m and  $z_b = 0.887$  m from Eq. (2.52). The total energy head is then

$$\begin{aligned} H &= z_b(x_c) + E_{\min} = z_b(x_c) + \frac{3}{2} \left[ \frac{Q^2}{gb_c^2} \right]^{1/3} \\ &= 0.887 + \frac{3}{2} \left[ \frac{30^2}{9.81 \cdot 3.997^2} \right]^{1/3} \approx 3.573 \text{ m}. \end{aligned} \quad (2.113)$$

With the known value of the total head, the application of Eqs. (2.90)–(2.91) is immediate, using Eq. (2.52) to evaluate  $b(x)$  and  $z_b(x)$  (Fig. 2.41).

## 2.3 Momentum Principle

### 2.3.1 Specific Momentum

The use of the specific energy concept is useful for flows where the energy losses can be neglected. This amounts to ensure that there are no flow separation zones. If however, the energy loss is unknown in advance, an alternative method of analysis must be devised. This method is based on the use of the momentum principle (Liggett 1994; Montes 1998). Consider for illustrative purposes the hydraulic jump

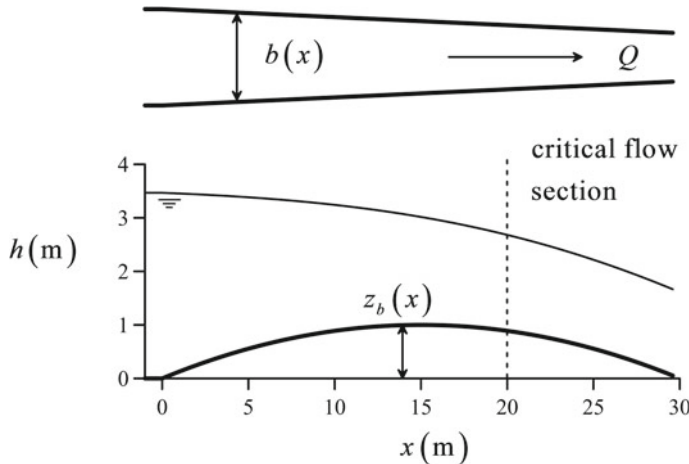


**Fig. 2.41** Transcritical profile in a flume of parabolic bottom profile with a linear width contraction (see Fig. 2.12)

(Fig. 2.42a, b). Its internal flow is highly turbulent, with a markedly non-uniform turbulent velocity profile. The energy loss is unknown, so the energy principle is unsuited here. Consider steady flow in a horizontal channel where the discharge is  $Q$  and the upstream water depth  $h_1$ ; the problem is to find the tailwater depth  $h_2$  of the hydraulic jump. A control volume to apply the momentum principle is shown in Fig. 2.42c. Its boundary sections are located outside the zone of rapidly varied flow, where the pressure is hydrostatic and the velocity distribution close to uniform. Neglecting the shear forces due to turbulent flow acting on the boundaries of the control volume, Eq. (2.10) yields

$$M_1 = M_2, \quad (2.114)$$

that is, the momentum function  $M$  is conserved in the hydraulic jump, with

$$M = A\bar{h} + \frac{Q^2}{gA} = \text{const.} \quad (2.115)$$

For a rectangular channel of width  $b$ , Eq. (2.115) simplifies to

$$M = (bh)\frac{h}{2} + \frac{Q^2}{gbh} = b\frac{h^2}{2} + b\frac{q^2}{gh}, \quad (2.116)$$

from which arises the definition of specific momentum  $S$  (Jaeger 1956; Henderson 1966; Montes 1998)

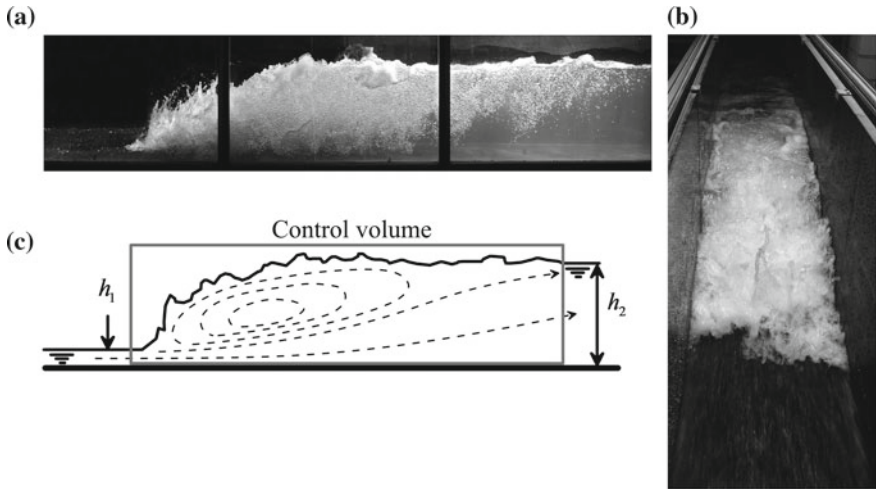


**Fig. 2.42** Hydraulic jump: **a** side view of laboratory test, **b** top view showing details of turbulence within the roller, **c** definition sketch to apply the control volume approach

$$S = \frac{M}{b} = \frac{h^2}{2} + \frac{q^2}{gh}. \quad (2.117)$$

The specific momentum  $S$  is only a function of flow depth  $h$  and unit discharge  $q$ , as the specific energy [see Eq. (2.15)]; it is a quantity conserved in hydraulic jumps.

Equation (2.117) is rewritten as

$$h\left(S - \frac{h^2}{2}\right) = \frac{q^2}{g} = \text{const.} \quad (2.118)$$

This is a cubic in  $h$ , plotted in Fig. 2.43. The curve has one asymptote for  $h = 0$ , e.g., the  $S$ -axis, and tends to the hydrostatic thrust  $(1/2)h^2$  for  $h \rightarrow \infty$ . As observed, there is a point of minimum  $S$  in Fig. 2.43. This point is determined from the derivative

$$\frac{dS}{dh} = \frac{d}{dh} \left( \frac{h^2}{2} + \frac{q^2}{gh} \right) = h - \frac{q^2}{gh^2} = h \left( 1 - \frac{q^2}{gh^3} \right), \quad (2.119)$$

rewritten as

$$\frac{dS}{dh} = h \frac{dE}{dh} = h(1 - F^2). \quad (2.120)$$

Using Eq. (2.120), the minimum of the  $S = S(h)$  curve is therefore

$$\frac{dS}{dh} = 0 \Rightarrow F = 1, \quad h_c = \left(\frac{q^2}{g}\right)^{1/3}. \quad (2.121)$$

This result indicates another property of critical flow ( $F = 1$ ), namely minimum specific momentum. The minimum value of  $S$  is thus

$$S_{\min} = \frac{h_c^2}{2} + \frac{q^2}{gh_c} = \frac{3}{2}h_c^2. \quad (2.122)$$

Consider a vertical line plotted in Fig. 2.43, for which the intersection with the  $S = S(h)$  curve yields points 1 and 2. The flow depth  $h_1 < h_c$  and, therefore, the regime for this point involves supercritical flow. Likewise, for point 2 results  $h_2 > h_c$ , implying subcritical flow. Points 1 and 2 are determined based on  $S = \text{const.}$  and, thus, represent the boundary flow depths of a hydraulic jump. In general, the two depths of the specific momentum curve obtained by setting  $S = \text{const.}$  are called *sequent depths* or *conjugate depths*, and shall not be confused with the alternate depths originating from the specific energy principle. Equation (2.117) is written in dimensionless form as

$$\frac{S}{h_c^2} = \frac{1}{2} \left(\frac{h}{h_c}\right)^2 + \left(\frac{h}{h_c}\right)^{-1}. \quad (2.123)$$

This universal function is plotted in Fig. 2.44 with Eq. (2.25) for the dimensionless specific energy head curve. The two curves together reveal that for a hydraulic jump, which implies  $S = \text{const.}$ , the value of  $E$  is not conserved, resulting in an energy loss. This issue is of relevance to be explored below. For rectangular channel flow, similar to what was done for the alternate depths as function of  $E$ , the analytical solution for the sequent depths as function of  $S$  is from Eq. (2.118), the solution of the cubic in  $h/h_c$

**Fig. 2.43** Specific momentum curve for constant unit discharge

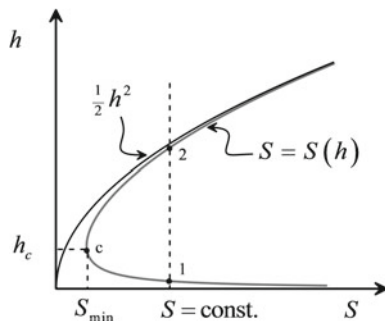
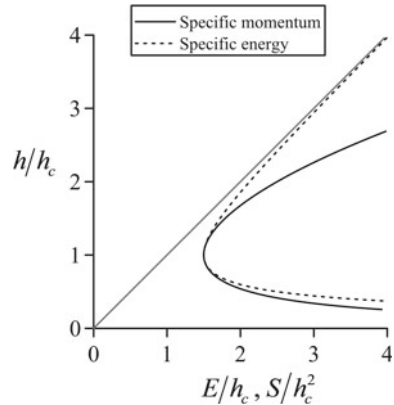


**Fig. 2.44** Dimensionless specific momentum and energy head curves in rectangular channel flow



$$\left(\frac{h}{h_c}\right)^3 - 2\frac{S}{h_c^2} \left(\frac{h}{h_c}\right) + 2 = 0. \quad (2.124)$$

By using a trigonometric transformation, the two positive solutions of Eq. (2.124) are (Selby 1973; Jeppson 2011)

$$\frac{h}{h_c} = 2 \left( \frac{2}{3} \frac{S}{h_c^2} \right)^{1/2} \cos \left( \frac{\Lambda}{3} \right), \quad (2.125)$$

for subcritical flow, and

$$\frac{h}{h_c} = 2 \left( \frac{2}{3} \frac{S}{h_c^2} \right)^{1/2} \cos \left( \frac{\Lambda}{3} + \frac{4\pi}{3} \right), \quad (2.126)$$

for supercritical flow, where

$$\cos \Lambda = - \left( \frac{2}{3} \frac{S}{h_c^2} \right)^{-3/2}. \quad (2.127)$$

The solution for the sequent depths is thus trivially simple for rectangular channel flow.

The specific energy and momentum concepts are two of the most notable tools for steady open channel flow analyses. It is widely recognized in the literature that the specific energy head curve was first developed by Bakhmeteff (1912). The first diagram is reprinted in Fig. 2.45, corresponding to  $q = 1 \text{ m}^2/\text{s}$ . Inspecting Fig. 2.45, it appears evident that the function  $S = S(h)$  is plotted superimposed with the  $E = E(h)$  curve. Bakhmeteff denoted  $S$  by the letter “ $\theta$ ” in his 1912 book.

**Fig. 2.45** Original figure of Bakhmeteff (1912) who published the first  $E$ - $h$  diagram (pp. 39 and 40). Note that the momentum function  $\theta(h)$  is presented simultaneously

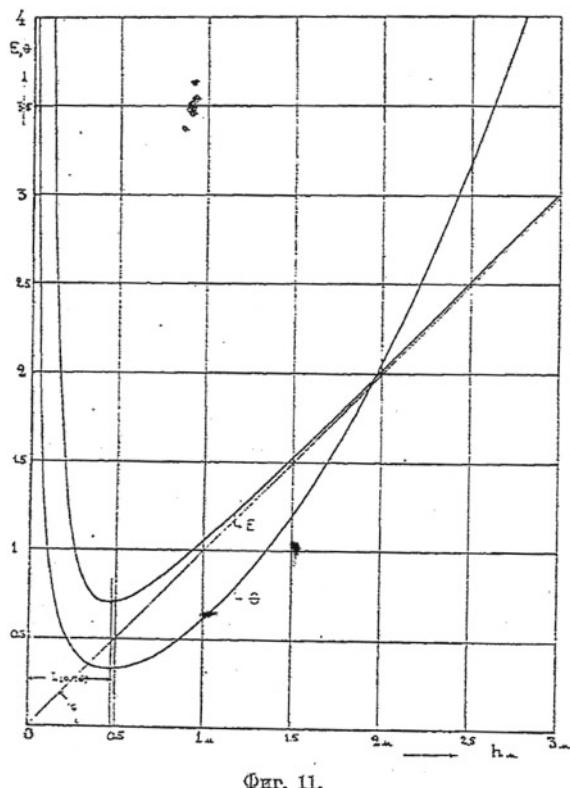


Fig. 11.

Although it appears trivial, it is not, because the two curves of Fig. 2.45 are the  $E(h)$  and  $S(h)$  functions, both having been first developed by Bakhmeteff (1912). This confirms that the origin of the specific momentum concept is simultaneous to that of the specific energy. *Both should be credited to Bakhmeteff* (Castro-Orgaz and Sturm 2018).

### 2.3.2 Belanger's Equation for the Hydraulic Jump

Consider now Eq. (2.117) applied between the boundary sections of a hydraulic jump (Fig. 2.42c)

$$S = \frac{h_1^2}{2} + \frac{q^2}{gh_1} = \frac{h_2^2}{2} + \frac{q^2}{gh_2}. \quad (2.128)$$

This equation allows for a relation linking  $h_1$  with the unknown value of  $h_2$ . Equation (2.128) is rewritten as

$$\frac{1}{2}(h_1^2 - h_2^2) + \frac{q^2}{g} \left( \frac{1}{h_1} - \frac{1}{h_2} \right) = 0, \quad (2.129)$$

or

$$\frac{1}{2}(h_2 - h_1)(h_2 + h_1) - \frac{q^2}{g} \left( \frac{h_2 - h_1}{h_1 h_2} \right) = 0. \quad (2.130)$$

Simplification yields

$$\frac{1}{2}h_1 h_2 (h_2 + h_1) - \frac{q^2}{g} = 0, \quad (2.131)$$

which is a quadratic equation in  $h_2$ , e.g.,

$$\frac{1}{2}h_1 h_2^2 + \frac{1}{2}h_1^2 h_2 - \frac{q^2}{g} = 0. \quad (2.132)$$

Its solution reads

$$\frac{h_2}{h_1} = \frac{1}{2} \left[ -1 + \left( 1 + 8\mathcal{F}_1^2 \right)^{1/2} \right], \quad \mathcal{F}_1^2 = \frac{q^2}{g h_1^3}. \quad (2.133)$$

This relation is Bélanger's equation for the sequent depth ratio of a hydraulic jump in a horizontal, rectangular, and frictionless channel (Bélanger 1849; Montes 1998).

The important point on how momentum and energy principles act complementary is: The momentum balance applied to a hydraulic jump is a valuable tool that permits, as shown, to compute the tailwater depth  $h_2$  of the hydraulic jump regardless of the internal flow complexities. Once the momentum principle is applied, the energy principle can be used to complete the analysis and determine the hydraulic energy loss, unknown in advance. It is given by

$$\begin{aligned} \Delta E &= \left( h_1 + \frac{q^2}{2gh_1^2} \right) - \left( h_2 + \frac{q^2}{2gh_2^2} \right) = (h_1 - h_2) + \frac{q^2}{2g} \left( \frac{1}{h_1^2} - \frac{1}{h_2^2} \right) \\ &= (h_1 - h_2) + \frac{q^2}{2g} \left( \frac{h_2^2 - h_1^2}{h_1^2 h_2^2} \right). \end{aligned} \quad (2.134)$$

From Eq. (2.131), one gets

$$\frac{q^2}{g} = \frac{1}{2} h_1 h_2 (h_2 + h_1), \quad (2.135)$$

which, inserted into Eq. (2.134), yields

$$\Delta E = \frac{(h_2 - h_1)^3}{4h_2 h_1}. \quad (2.136)$$

Using the specific energy  $E_1$  of the upstream supercritical flow, it is written in dimensionless form as

$$\frac{\Delta E}{E_1} = \frac{\left(\frac{h_2}{h_1} - 1\right)^3}{4(h_2/h_1)\left(1 + \frac{1}{2}F_1^2\right)}. \quad (2.137)$$

The computational process is illustrated graphically with the aid of Fig. 2.46, where the  $E(h)$  and  $S(h)$  curves are plotted for the known unit discharge  $q$ . With the known value of  $h_1$ , the corresponding  $S$  value is determined, giving point “a” in Fig. 2.46b. The vertical line plotted with this value of  $S$  yields a cut with  $S(h)$  at point “b”, which is the subcritical tailwater depth  $h_2$  of the hydraulic jump. Horizontal lines plotted from “a” and “b” cut with the  $E(h)$  curve, yielding the corresponding specific energies at both points (points “c” and “d”, respectively). Their difference is the energy head dissipated by the hydraulic jump. This sequence is conducted analytically using Eqs. (2.133) and (2.137). Their accuracy is verified in Fig. 2.47, where the experimental data of Bretz (1988) were used for validation. Note the small deviation of the latter with predictions due to the neglected boundary shear effect.

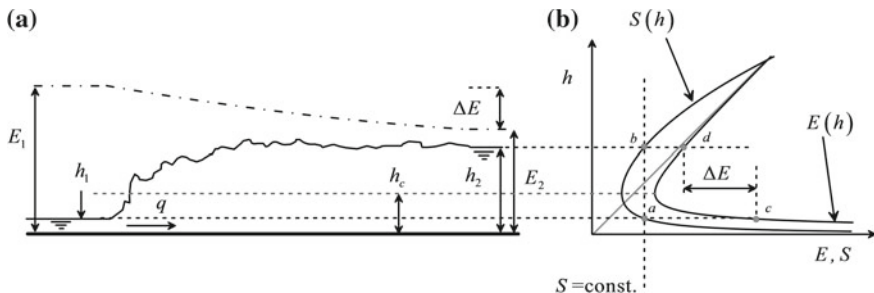
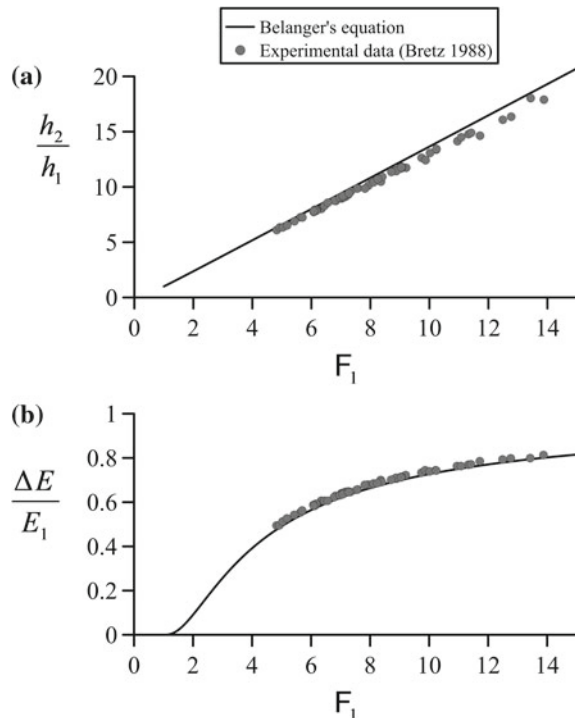


**Fig. 2.46** Sequent depth  $h_2$  and energy loss  $\Delta E$  of a hydraulic jump in a rectangular, horizontal, and frictionless channel: **a** hydraulic jump profile and **b** specific energy and momentum diagrams

**Fig. 2.47** Experimental verification of the sequent depth ratio  $h_2/h_1(F_1)$  and energy head loss  $\Delta E/E_1(F_1)$  for the hydraulic jump in a rectangular, horizontal, and frictionless channel



### 2.3.3 Computation of Sequent Depths for General Cross Sections

General

For an arbitrary cross section, the momentum function depends on the discharge  $Q$  and the flow depth  $h$  as

$$M = A\bar{h} + \frac{Q^2}{gA}. \quad (2.138)$$

The functional relation with  $h$  is determined by the particular cross-sectional geometry. For an arbitrary cross section, a plot  $M = M(h)$  has a similar shape to the  $S = S(h)$  curve plotted in Fig. 2.43, with a point of minimum  $M$ , determined from

$$\frac{dM}{dh} = \frac{d}{dh} \left( A\bar{h} + \frac{Q^2}{gA} \right) = \frac{d}{dh}(A\bar{h}) - \frac{Q^2}{gA^2} \frac{dA}{dh} = A - \frac{Q^2}{gA^2} B = A \left( 1 - \frac{Q^2}{gA^3} B \right), \quad (2.139)$$

rewritten as

$$\frac{dM}{dh} = A \frac{dE}{dh} = A(1 - F^2). \quad (2.140)$$

Thus, the minimum value of  $M$  is reached for critical flow ( $F = 1$ ) regardless of channel shape.

### Symmetrical trapezoid

For a trapezoidal section of base width  $b$  and side slope  $1:z$ , the flow area  $A$  is

$$A = bh + zh^2, \quad (2.141)$$

and the  $A\bar{h}$  term is, upon decomposing the trapezoid into a rectangle and two triangles,

$$A\bar{h} = bh \frac{h}{2} + zh^2 \frac{h}{3} = b \frac{h^2}{2} + z \frac{h^3}{3}. \quad (2.142)$$

The momentum function is thus

$$M = \frac{h^2}{6}(2zh + 3b) + \frac{Q^2}{g(bh + \frac{1}{2}zh^2)}. \quad (2.143)$$

To compute the sequent depths for a prescribed value of the momentum function  $M_o$ , a numerical solution is necessary (Jeppson 2011). The Newton–Raphson formula

$$h^{k+1} = h^k - \frac{f^k}{(df/dh)^k}, \quad (2.144)$$

with

$$f = M - M_o, \quad \frac{df}{dh} = \frac{dM}{dh}, \quad (2.145)$$

yields

$$h^{k+1} = h^k - \frac{(M - M_o)^k}{[A(1 - F^2)]^k}. \quad (2.146)$$

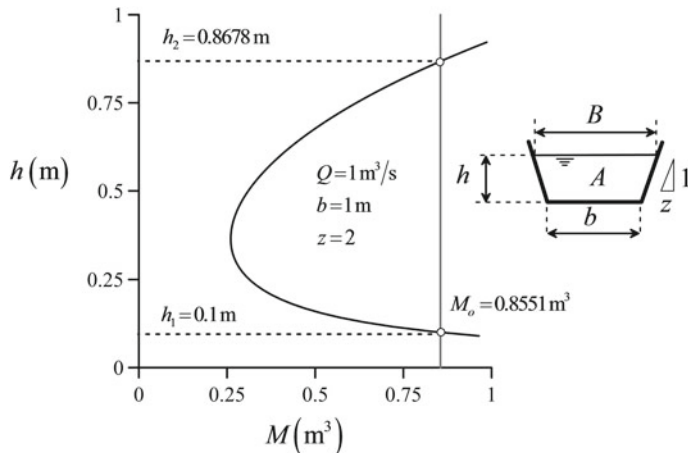


**Fig. 2.48** Example of sequent depth computation in a trapezoidal section

A code of this scheme is available on the file “*conjugatedepth\_trapezoidal.xls*”, Chap. 12. Figure 2.48 illustrates the computational process. For a supercritical flow with  $Q = 1 \text{ m}^3/\text{s}$  and  $h_1 = 0.1 \text{ m}$  in a trapezoidal channel of  $b = 1 \text{ m}$  and  $z = 2$ , the problem is to determine the sequent depth of a hydraulic jump. Figure 2.48 shows the  $M$ - $h$  curve and a vertical line corresponding to the value of the momentum function of the supercritical flow,  $M_o = 0.8551 \text{ m}^3$ . The program yields the conjugate depth  $h_2 = 0.8678 \text{ m}$ . Both sequent depths are plotted on the  $M$ - $h$  diagram.

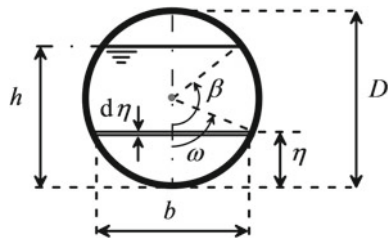
### Circular

For a circular section of diameter  $D$  (Fig. 2.49), the  $A\bar{h}$  term of the momentum function is determined by integrating the corresponding elementary relations, developed as follows.

Consider the flow geometry as sketched in Fig. 2.49; the following identities apply

$$\begin{aligned}
 b &= 2(\sin \omega) \frac{1}{2} D, \\
 \eta &= \frac{1}{2} D - (\cos \omega) \frac{1}{2} D, \\
 d\eta &= (\sin \omega) \frac{1}{2} D d\omega, \\
 h - \eta &= \frac{1}{2} D \cos \omega + \frac{1}{2} D \cos(\pi - \beta) \\
 &= \frac{1}{2} D(\cos \omega - \cos \beta).
 \end{aligned} \tag{2.147}$$

**Fig. 2.49** Determination of the flow area and profundity of the centroid in a circular section



A first immediate result is the computation of the flow area as

$$A = \int_0^h bd\eta = \int_0^\beta \frac{D^3}{2} \sin^2 \omega d\omega = \frac{D^2}{4} (\beta - \sin \beta \cos \beta), \quad (2.148)$$

by using the primitive function

$$\int_0^\beta \sin^2 \omega d\omega = \frac{1}{2}\beta - \frac{1}{2}\sin \beta \cos \beta. \quad (2.149)$$

Now, the  $A\bar{h}$  term is defined by

$$A\bar{h} = \int_0^h (h - \eta) dA, \quad (2.150)$$

which, by use of Eq. (2.147), transforms to

$$A\bar{h} = \int_0^\beta \frac{D^3}{4} (\cos \omega - \cos \beta) \sin^2 \omega d\omega. \quad (2.151)$$

With the aid of Eq. (2.149) and the auxiliary primitive function

$$\int_0^\beta \cos \omega \sin^2 \omega d\omega = \frac{1}{3} \sin^3 \beta, \quad (2.152)$$

integration of Eq. (2.151) produces

$$\begin{aligned} A\bar{h} &= \frac{D^3}{4} \left( \frac{1}{3} \sin^3 \beta - \frac{1}{2} \beta \cos \beta + \frac{1}{2} \sin \beta \cos^2 \beta \right) \\ &= \frac{D^3}{24} (3 \sin \beta - \sin^3 \beta - 3\beta \cos \beta). \end{aligned} \quad (2.153)$$

Using Eqs. (2.149) and (2.153), the momentum function of the circular section is finally (Henderson 1966)

$$\begin{aligned} M &= A\bar{h} + \frac{Q^2}{gA} = \frac{D^3}{24} (3 \sin \beta - \sin^3 \beta - 3\beta \cos \beta) \\ &\quad + \frac{4Q^2}{gD^2(\beta - \sin \beta \cos \beta)}. \end{aligned} \quad (2.154)$$

This function is used to compute the sequent depths of hydraulic jumps as previously explained for the trapezoidal section if the pipe flow is not pressurized; i.e., the subcritical sequent depth does not touch the pipe top.

If the upstream supercritical flow changes to pressurized flow, the hydraulic jump is said to be “incomplete” (Montes 1998; Jeppson 2011) (Fig. 2.50). For a transition from upstream supercritical to downstream pressurized flow, the momentum balance applied to the hydraulic jump control volume produces (Montes 1998; Jeppson 2011)

$$A\bar{h}_1 + \frac{Q^2}{gA_1} = A_t \frac{D}{2} + A_t \frac{p_t}{\rho g} + \frac{Q^2}{gA_t}. \quad (2.155)$$

Here,  $A_t = \pi D^2/4$  is the area of the pipe flowing full and  $p_t$  the pressure at the pipe top. Denoting by  $M_t$  the momentum function for a gravity pipe flow flowing full

$$M_t = A_t \frac{D}{2} + \frac{Q^2}{gA_t}, \quad (2.156)$$

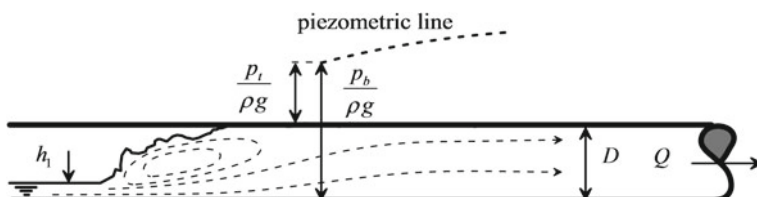


**Fig. 2.50** Incomplete hydraulic jump in a circular pipe

the pressure head on the pipe top is

$$\frac{p_t}{\rho g} = \frac{M_1 - M_t}{A_t}, \quad (2.157)$$

where  $M_1$  is the momentum function of the supercritical flow, to be evaluated using Eq. (2.154). A simple method to check if an incomplete hydraulic jump appears is to compare  $M_1$  with  $M_t$ . If  $M_1 > M_t$ , the downstream flow is pressurized, whereas for  $M_1 < M_t$  the hydraulic jump is computed on the basis of Eq. (2.154).

### 2.3.4 Transitions in Supercritical Flow

#### General

Non-uniform sub- and supercritical flows in channel transitions are computed by using the 1D approach and the specific energy diagram. This method is generally valid for subcritical flows, but may not be accurate for supercritical flows, because it is applied only to supercritical flows in a prismatic, rectangular channel. If changes in boundary shape occur, 2D oblique standing waves are generated, and an alternative method of attack is required. Consider the flow in a straight rectilinear channel with parallel walls (Fig. 2.51). Two steady sources of perturbations are therefore generated at the inlet. Given that  $U > (gh)^{1/2}$ , circular waves originating at the sides do not include the source point itself, and the tangents to the circular waves form two wave fronts intersecting and being reflected to the opposite wall and further transmitted downstream. The phenomenon produces a diamond-type wave pattern (Fig. 2.51). For supercritical flow, these standing wave patterns appear due to flow perturbations, as a wall deflection. Their computation is detailed below.

#### Abrupt wall deflection

Given that the flow is 2D in the horizontal plane, the 1D control volume theory previously development must be generalized. Reynolds' transport theorem states the conservation of mass and momentum for a control volume CV surrounded by a control surface CS as (Liggett 1994; White 2009)

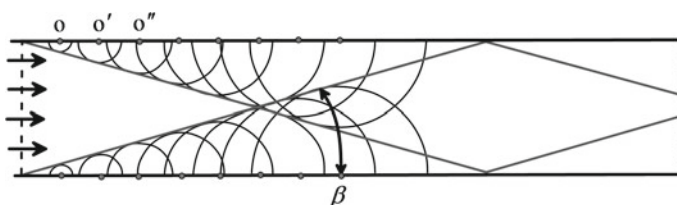


**Fig. 2.51** Supercritical flow in rectilinear channel with parallel walls involving two steady sources of perturbations at the inlet

$$\frac{d}{dt} \iiint_{CV} \rho dv + \iint_{CS} \rho (\mathbf{V} \cdot \mathbf{n}) dA = 0, \quad (2.158)$$

$$\mathbf{f} = \frac{d}{dt} \iiint_{CV} \rho \mathbf{V} dv + \iint_{CS} \rho \mathbf{V} (\mathbf{V} \cdot \mathbf{n}) dA. \quad (2.159)$$

Here,  $\mathbf{f}$  is the force vector (resultant of body plus surface forces),  $\mathbf{V}$  the velocity vector,  $\mathbf{n}$  the unit normal to the control surface,  $\rho$  water density,  $v$  the volume, and  $A$  the area. Consider in this section steady supercritical flow in a horizontal and frictionless channel. Further, the parallel-streamlined approach flow has depth  $h_1$  and velocity  $U_1$  deflected by a wall of angle  $\theta$  (Fig. 2.52a).

Shear forces are neglected, and pressures are assumed to be hydrostatic (Fig. 2.52b). Due to the wall deflection, the streamlines downstream of the local perturbation will adjust and become parallel to the tailwater wall direction. However, this directional change is accompanied by an oblique shock front crossing the supercritical stream at angle  $\beta$  (Fig. 2.52c).

Consider the control volume sketched in Fig. 2.53 to apply Eqs. (2.158)–(2.159). Its extreme boundaries are parallel to the shock direction, and a unit width is considered. The side faces of the control volume are by definition streamlines, so there is no flow across them. Thus, Eq. (2.158) reduces to

$$Q_1 = Q_2 = Q. \quad (2.160)$$

Consider the velocity  $U$  decomposed in the normal (subscript  $n$ ) and tangential (subscript  $t$ ) directions to the shock front. Equation (2.160) is therefore rewritten as

$$Q = U_{1n} h_1 = U_{2n} h_2 = h_1 U_1 \sin \beta = h_2 U_2 \sin(\beta - \theta). \quad (2.161)$$

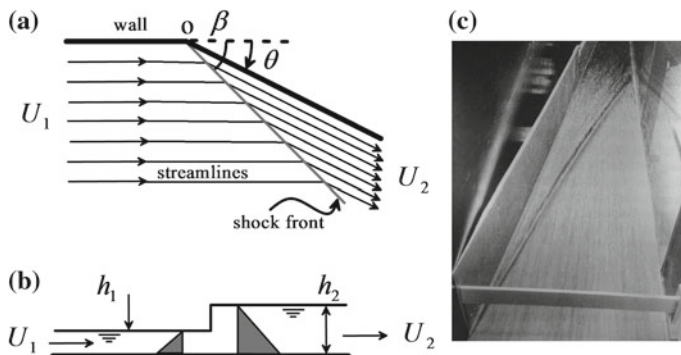


**Fig. 2.52** Oblique shock wave due to abrupt wall deflection: **a** plan view, **b** section along streamline, **c** photograph of model test

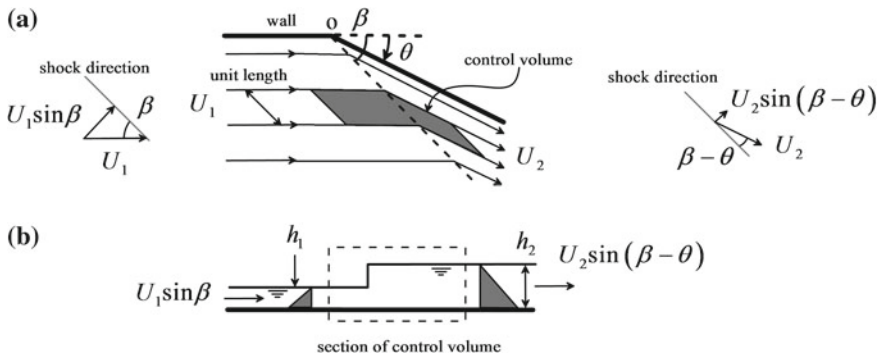


**Fig. 2.53** Application of (- -) control volume approach to oblique shock wave: **a** plan and **b** section

Equation (2.159) simplifies with  $\mathbf{f}_p$  as the resultant of the pressure forces acting on the control surface to

$$\mathbf{f}_p = \rho \mathbf{V}_2 Q - \rho \mathbf{V}_1 Q. \quad (2.162)$$

Equation (2.162) is now projected in the normal direction, producing

$$\frac{1}{2} \rho g h_1^2 - \frac{1}{2} \rho g h_2^2 = \rho U_{2n} Q - \rho U_{1n} Q. \quad (2.163)$$

Inserting Eq. (2.161) and re-arranging yields (Jain 2001)

$$\frac{1}{2} g h_1^2 + h_1 U_1^2 \sin^2 \beta = \frac{1}{2} g h_2^2 + h_2 U_2^2 \sin^2(\beta - \theta). \quad (2.164)$$

Now, Eq. (2.162) is projected in the tangential direction. Note for the control volume selected that pressure forces acting on each streamline in the tangential direction are in equilibrium side by side, so there is no net pressure force acting in this direction. The momentum balance reduces then to

$$0 = \rho U_{2t} Q - \rho U_{1t} Q, \quad (2.165)$$

or

$$U_1 \cos \beta = U_2 \cos(\beta - \theta). \quad (2.166)$$

From Eqs. (2.161) and (2.164) follows (Ippen 1951)

$$\frac{h_2}{h_1} = \frac{1}{2} \left[ \left( 1 + 8F_1^2 \sin^2 \beta \right)^{1/2} - 1 \right], \quad F_1 = \frac{U_1}{(gh_1)^{1/2}}. \quad (2.167)$$

Equation (2.167) can be recast in the alternative form

$$\sin \beta = \frac{1}{F_1} \left[ \frac{1}{2} \frac{h_2}{h_1} \left( 1 + \frac{h_2}{h_1} \right) \right]^{1/2}. \quad (2.168)$$

Note that for a finite shock  $h_2/h_1 > 1$ . Only for shocks of infinitesimal height, namely for  $h_2 \approx h_1$  results  $\sin \beta = 1/F_1$  from Eq. (2.168) as the shallow water wave solution [see Eq. (2.67)]. These disturbance lines or oblique wave fronts (or shocks) are sometimes called oblique hydraulic jumps, which is not adequate. The flow in the downstream portion of these waves is supercritical, so the oblique standing waves represent transitions from super- to supercritical flow with different directions of the streamlines. Given that a hydraulic jump is a transition from super- to subcritical flows, the term “oblique hydraulic jump” should be avoided. Under chocking conditions, it is possible to have an oblique hydraulic jump, but this is a particular case. We will therefore denominate these waves as oblique standing or shock waves. The term “shock wave in supercritical flow” is also a typical nomenclature in dam hydraulics (Vischer and Hager 1998). The celerity  $c$  of the oblique shock wave is (Ippen 1951)

$$c = (gh_1)^{1/2} \left[ \frac{1}{2} \frac{h_2}{h_1} \left( 1 + \frac{h_2}{h_1} \right) \right]^{1/2} \equiv U_1 \sin \beta. \quad (2.169)$$

Given that  $c$  equals the velocity component normal to the shock front, the wave is steady. From Eqs. (2.161) and (2.166), another identity to be satisfied by  $h_2/h_1$  is

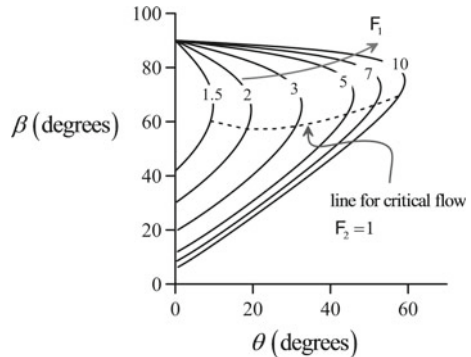
$$\frac{h_2}{h_1} = \frac{\tan \beta}{\tan(\beta - \theta)}. \quad (2.170)$$

Equating Eqs. (2.167) and (2.170) results in

$$\frac{\tan \beta}{\tan(\beta - \theta)} = \frac{1}{2} \left[ \left( 1 + 8F_1^2 \sin^2 \beta \right)^{1/2} - 1 \right]. \quad (2.171)$$

The angle  $\beta$  is a function of  $F_1$  and  $\theta$ , as indicated by Eq. (2.171). Its solution is obtained numerically by any standard technique, as the Newton–Raphson method. However, it is illustrative to represent graphically  $\beta = \beta(\theta)$  with  $F_1$  as a parameter, as did Ippen (1951) (Fig. 2.54).

**Fig. 2.54** Oblique shock wave diagram of Ippen (1951)



The ratio of Froude numbers up- and downstream of the shock origin is from Eq. (2.166) (Jain 2001)

$$\frac{F_2}{F_1} = \left( \frac{h_1}{h_2} \right)^{1/2} \frac{\cos \beta}{\cos(\beta - \theta)}. \quad (2.172)$$

It is of interest to plot in Fig. 2.54 the line defining critical flow in the tailwater shock portion, e.g.,

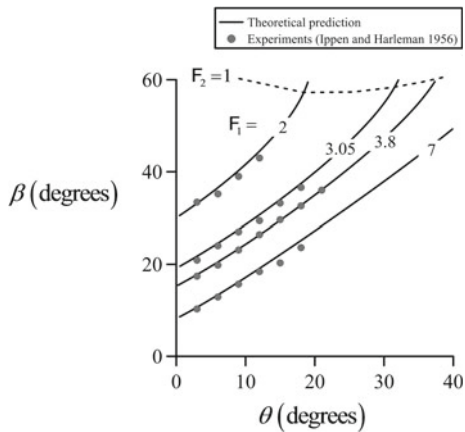
$$1 = F_1 \left( \frac{h_1}{h_2} \right)^{1/2} \cos \beta [1 + \tan^2(\beta - \theta)]^{1/2}, \quad (2.173)$$

or, with the aid of Eq. (2.170),

$$\left( \frac{h_2}{h_1} \right)^{1/2} - F_1 \cos \beta \left[ 1 + \frac{\tan^2 \beta}{(h_2/h_1)^2} \right]^{1/2} = 0. \quad (2.174)$$

Using Eq. (2.167) for  $h_2/h_1$ , Eq. (2.174) was numerically solved and the result is plotted in Fig. 2.54. For a constant value of  $F_1$ ,  $\beta$  increases with  $\theta$  up to a maximum value and then decreases. For  $\beta = 90^\circ$  and  $\theta = 0$ , there is no oblique standing wave but rather a hydraulic jump, given the change from super- to subcritical flow. This steady wave is not related to the wall deflection, but rather the result of a tailwater effect. Note from the diagram that for a given value of  $\theta$  two values of  $\beta$  are possible, one for downstream supercritical flow ( $F_2 > 1$ ) and the other for subcritical flow ( $F_2 < 1$ ). The first case is relevant to the practical design of channels with supercritical flows, given that the wave pattern is only determined by the upstream flow condition, namely  $F_1$ . The angle of the cross-wave and its propagation in the downstream direction by successive reflections at the channel walls only depends on the upstream conditions. However, for  $F_2 < 1$ , there is a tailwater effect, propagating a surge against the supercritical flow until a steady wave pattern

**Fig. 2.55** Verification of oblique shock wave diagram



is formed in conformity with Eq. (2.171). Therefore, this oblique shock with a transition from super- to subcritical flow depends on a particular combination of upstream and downstream flow conditions. The oblique shock diagram is verified in Fig. 2.55 for supercritical tailwater conditions using the experiments by Ippen and Harleman (1956).

Consider now supercritical flow in a channel where a wall is deflected by the angle  $\theta$ , whereas the other wall remains fixed. As previously explained, an oblique wave front starting at point A crosses the flow at angle  $\beta_1$  reaching the opposite wall. The flow is subjected thus by a new perturbation at point B, so that the incident shock is reflected, crossing the flow at a new angle  $\beta_2$ . The flow beyond shock AB becomes parallel to the deflected wall, with a value of  $F_2 < F_1$ , along with  $\beta_2 > \beta_1$ . This new shock reaches the opposite channel wall at point C and is reflected with angle  $\beta_3$ , with streamlines beyond the shock BC parallel to the rectilinear wall, and  $F_3 < F_2$ . The perturbation is further propagated downstream, tending toward critical flow with each new reflection (Fig. 2.56).

#### Continuous curved wall with positive deflection

If the wall angle varies continuously as  $\theta(x)$ , the continuous curve is divided into portions of rectilinear walls of discrete deflections  $\Delta\theta$  to compute the corresponding  $\Delta h$  across each oblique shock wave (Fig. 2.57). For an upstream value  $F_1 > 1$ , any change  $\Delta h$  due to a flow disturbance occurs along wave fronts, crossing the stream at angle  $\beta$ . This wave angle is linked to a finite change  $\Delta\theta$  in the direction of the

**Fig. 2.56** Reflection of oblique shock waves at channel walls (adapted from Ippen 1951)

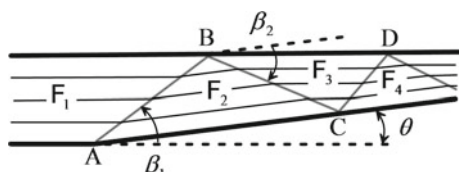
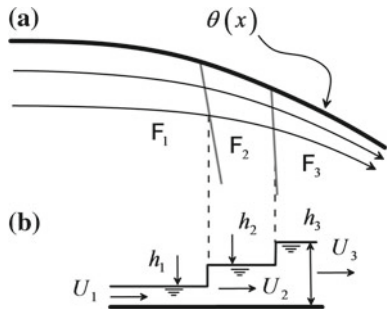


**Fig. 2.57** Supercritical flow with continuous concave wall deflection: **a** plan and **b** longitudinal section along a streamline. The wall deflection is continuous but might not be small, given that the formation of shocks is considered



boundary shape. Any continuous boundary of arbitrary shape is a streamline, and the change of depth and velocity along it can therefore be computed. In a curved channel, the lateral boundary streamline is the origin of all disturbance lines or wave fronts. The complete characteristics of the supercritical flow are therefore determined by the boundary shape (Fig. 2.57). For the concave wall shown, the shock lines converge and the water depth increases along the streamlines.

Consider the trigonometric identity

$$\tan(\beta - \theta) = \frac{\tan \beta - \tan \theta}{1 + \tan \beta \tan \theta}. \quad (2.175)$$

Equation (2.170) is thus rewritten as

$$\frac{h_2}{h_1} = \frac{\tan^2 \beta \tan \theta + \tan \beta}{\tan \beta - \tan \theta}. \quad (2.176)$$

Defining  $h_2 = \Delta h + h_1$ , one obtains from Eq. (2.176)

$$\frac{\Delta h}{h} = \frac{\tan \theta (1 + \tan^2 \beta)}{\tan \beta - \tan \theta} = \frac{\sec^2 \beta \tan \theta}{\tan \beta - \tan \theta}. \quad (2.177)$$

### Continuous solutions for gradual wall deflections

It was already demonstrated that for a positive wall deflection (Fig. 2.53) the streamlines converge and a discontinuous solution, namely the oblique shock wave, is formed. In a negative wall deflection, however, streamlines diverge and discontinuous solutions are not formed, invalidating the former solutions. Rather, a continuous depression wave is the correct flow solution (Liggett 1994; Montes 1998). An approximate method applicable to the analysis of negative wall deflections is now presented. The method is also applicable to positive wall deflections if

these are small and shocks are not formed. Consider infinitesimal wave jumps, namely  $\Delta h \rightarrow dh$ , associated with small wall deflections, for which  $\tan \beta \gg \tan \theta$ ,  $\tan \theta \rightarrow \theta$ , and  $\theta \rightarrow d\theta$ . Using these simplifications in Eq. (2.177) yields

$$\frac{dh}{d\theta} = \frac{h}{\sin \beta \cos \beta}. \quad (2.178)$$

For an infinitesimal oblique wave, Eq. (2.168) simplifies to

$$\sin \beta = \frac{1}{F_1} \left[ \frac{1}{2} \frac{h_2}{h_1} \left( 1 + \frac{h_2}{h_1} \right) \right]^{1/2} \approx \frac{1}{F} = \frac{(gh)^{1/2}}{U}. \quad (2.179)$$

Substitution into Eq. (2.178) yields (Ippen 1951)

$$\frac{dh}{d\theta} = \frac{U^2}{g} \tan \beta. \quad (2.180)$$

For infinitesimal perturbations, the energy loss is negligible and the specific energy head remains constant. The velocity head is thus

$$\frac{U^2}{2g} = E - h. \quad (2.181)$$

Noting from Eq. (2.179) that

$$\tan \beta = (F^2 - 1)^{-1/2}, \quad (2.182)$$

and inserting Eqs. (2.181)–(2.182) into Eq. (2.180) yield the ODE

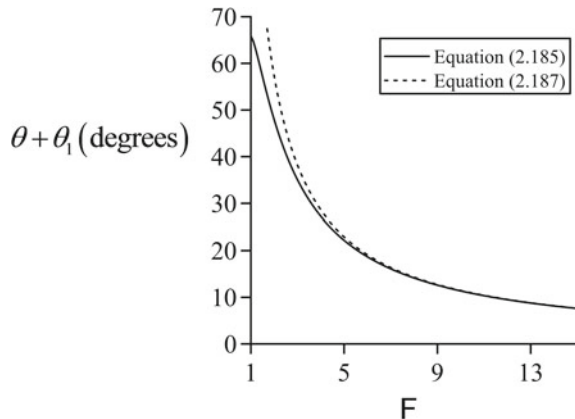
$$\frac{dh}{d\theta} = \frac{2(E - h)h^{1/2}}{(2E - 3h)^{1/2}}. \quad (2.183)$$

It describes the propagation of infinitesimal perturbations due to a continuous wall curvature. The integral of Eq. (2.183) is (Ippen 1951)

$$\theta = 3^{1/2} \tan^{-1} \left[ \left( \frac{\frac{h}{2E/3}}{1 - \frac{h}{2E/3}} \right)^{1/2} \right] - \tan^{-1} \left[ 3^{-1/2} \left( \frac{\frac{h}{2E/3}}{1 - \frac{h}{2E/3}} \right)^{1/2} \right] - \theta_1, \quad (2.184)$$

or, with  $\theta_1$  as constant of integration determined by the condition that  $\theta = 0$  for  $F = F_1$ ,

**Fig. 2.58** Gradual wall deflection  $\theta = \theta(F)$  in supercritical flow with constant specific energy head  $E$



$$\theta = 3^{1/2} \tan^{-1} \left[ \frac{3^{1/2}}{(F^2 - 1)^{1/2}} \right] - \tan^{-1} \left[ \frac{1}{(F^2 - 1)^{1/2}} \right] - \theta_1. \quad (2.185)$$

Equation (2.185) directly links  $\theta$  to  $F$ . For the solution produced here, the perturbation lines are no more defining a discontinuous solution. Rather, these are lines of constant flow depth determined by the boundary angle  $\theta(x)$  at the origin of them on the wall. An additional relation based on constant specific energy head  $E = h[1 + (1/2)F^2] = \text{const.}$  is

$$\frac{h}{h_1} = \frac{F_1^2 + 2}{F^2 + 2}. \quad (2.186)$$

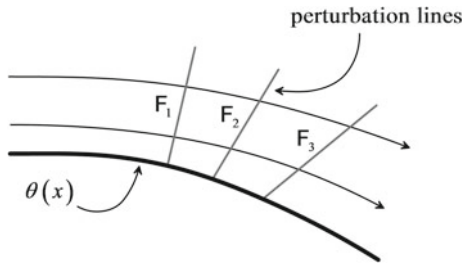
Equation (2.185) (Fig. 2.58) is of paramount interest in the design of channel structures. For example, if the streamlines are given, the changes in  $h/E$  or  $F$  along the streamlines are immediately determined by Eqs. (2.185)–(2.186). In the inverse case, it is possible to determine the boundary shape  $\theta(x)$  needed to produce prescribed changes in  $h/E$  and  $F$ . For large values of  $F$ , this relation is approximated by (Ippen 1951)

$$\theta = \frac{2}{F} - \theta_1. \quad (2.187)$$

A comparison of Eqs. (2.185) and (2.187) in Fig. 2.58 indicates that the latter is an accurate approximation of the former if  $F > 5$ .

For a continuous convex wall (Fig. 2.59), the streamlines are deflected away from the original boundary alignment. Due to the negative wall deflection angle ( $\theta < 0$ ), the water depth decreases along the streamlines (Liggett 1994; Montes

**Fig. 2.59** Supercritical negative waves in continuous convex wall along with perturbation lines or constant flow depth lines



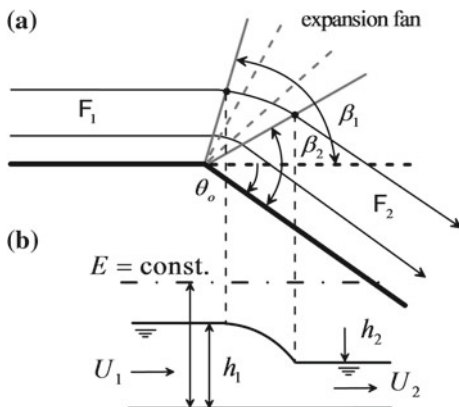
1998). This case can be analyzed assuming  $E = \text{const.}$  and thus resorting to Eq. (2.185). To apply Eq. (2.185) to a positive wall deflection (Fig. 2.57a), the angle variation must be weak, such that the disturbance lines do not intersect thereby producing a shock (Liggett 1994). The flow at an abrupt negative wall deflection (Fig. 2.60a) can be considered as the limit of a convex wall deflection if the length of the transition curve tends to zero. In this case, the origin of all the disturbance lines is unique and located at the wall break. The continuous solution is an expansion fan defined by the lines of constant water depth (Fig. 2.60b) (Liggett 1994). The up- and downstream perturbation angles are

$$\beta_1 = \sin^{-1} \left( \frac{1}{F_1} \right), \quad \beta_2 = \sin^{-1} \left( \frac{1}{F_2} \right). \quad (2.188)$$

For the known values of  $h_1$  and  $U_1$ , the value of  $F_1 = U_1/(gh_1)^{1/2}$  is fixed, and the constant  $\theta_1$  is determined from Eq. (2.185) as

$$\theta_1 = 3^{1/2} \tan^{-1} \left[ \frac{3^{1/2}}{(F_1^2 - 1)^{1/2}} \right] - \tan^{-1} \left[ \frac{1}{(F_1^2 - 1)^{1/2}} \right]. \quad (2.189)$$

**Fig. 2.60** Supercritical abrupt wall deflection: **a** plan view of expansion fan and **b** water surface profile along a streamline

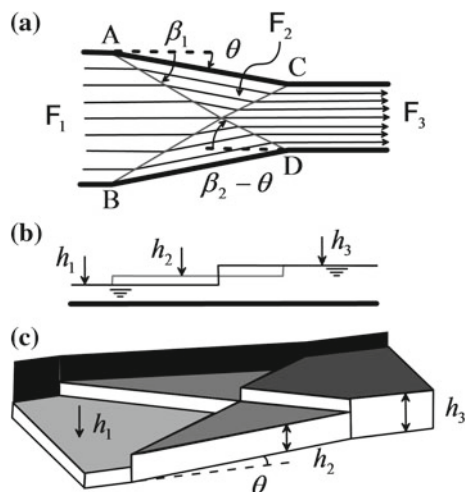


Equation (2.185) is then used to compute  $F_2$  for the value of the wall deflection  $\theta_o$ , either numerically or with the aid of Fig. 2.58. Once  $F_2$  is known, the flow depth  $h_2$  is determined by resorting to Eq. (2.186) and the value of  $\beta_2$  computed by Eq. (2.188)<sub>2</sub>. If  $F_1 > 5$ , it is feasible to use the simpler Eq. (2.187).

### Channel contraction

A positive wall deflection produces an oblique shock increasing the water depth, whereas a negative wall deflection produces a centered depression wave with the opposite effect. This fact is applied to the design of channel transition structures, wherein positive and negative waves are superposed to minimize the transmission of standing waves in the tailwater. The channel contraction (Fig. 2.61) in supercritical flow is a special case where the wall deflections produce two positive oblique wave fronts originating at points A and B that intersect and then are propagated into the tailwater. The length of the channel contraction is selected so that the wave fronts arrive just at its ends (points C and D). These positive waves thus interact with the negative waves originating at the same corners, with a theoretical cancelation of the wave effects (Ippen and Dawson 1951). This design approach would work only for the design discharge and is based on assuming that the interaction of positive and negative waves exactly cancels each other (Vischer and Hager 1998).

**Fig. 2.61** Design of channel contraction with minimum of wave transmission: **a** plan view, **b** free surface profiles along centerline and channel wall, **c** 3D view



## 2.4 Control Sections

### 2.4.1 General

A hydraulic control section involves a unique relation between the flow depth  $h$  and the discharge  $Q$  and vice versa, e.g.,  $Q = Q(h)$  or  $h = h(Q)$  (Henderson 1966). A control section is used as boundary condition in water surface profile computations; thus, their discharge characteristics need to be known in advance (Jain 2001). Further, they are used at selected locations for water discharge measurement purposes (Bos 1976). Here, the usual control sections in open channel flows are described, namely *uniform flow*, *critical flow*, and the *artificial channel control* (Rouse 1950; Jain 2001). The latter is a device inserted into a flow which generates a head–discharge rating curve. It produces a large perturbation choking the flow, resulting in a subcritical approach flow that changes to a supercritical flow downstream of the structure. Examples are weirs and gates. Most artificial channel controls involve complex flow phenomena as non-hydrostatic pressure, fluid recirculation, and boundary layers. Here, only an introduction to typical channel controls is given. Montes (1998) provides an extensive discussion on the fluid flow fundamentals of head–discharge rating curves of hydraulic structures.

### 2.4.2 Uniform Flow

The steady gradually varied flow equation for prismatic channels is [see Eq. (1.110)]

$$\frac{dh}{dx} = \frac{S_o - S_f}{1 - F^2}, \quad (2.190)$$

where  $S_o$  is the channel bottom slope and  $S_f$  the friction slope. Uniform flow is regained by setting  $dh/dx = 0$  into Eq. (2.190), resulting in

$$S_f = S_o. \quad (2.191)$$

If a parametrization of the type  $S_f = C_f F^2$  (valid for a wide rectangular channel) is used in Eq. (2.191), with  $C_f$  as a boundary shear resistance coefficient, it is easy to infer that a rating curve  $Q = Q(h_N)$ , or  $h_N = h_N(Q)$ , emerges, where  $h_N$  is the uniform flow depth. Particular parametrizations for general cross sections are discussed in Chap. 3. Here, it is noted that uniform flow is a particular control section where the discharge is related to the flow depth through a resistance coefficient and the bottom slope.

### 2.4.3 Critical Flow

Critical flow is determined from Eq. (2.57), which generates a rating curve  $Q = Q(h_c)$ , or  $h_c = h_c(Q)$ . The frequent location of critical flow sections to start water surface profile computations is at the maximum elevation of a round-crested weir (Fig. 2.6) or at the maximum contraction in a non-prismatic channel section (Fig. 2.9). For a channel with both variable elevation and cross section, the position of the critical flow section is unknown in advance and must be determined by a singular point analysis (Figs. 2.11 and 2.12) (Chow 1959; Montes 1998; Hager 2010). Once the critical depth and its location are determined, the result is used as boundary condition to compute sub- and supercritical free surface profiles. Note that for supercritical flow computations in a non-prismatic channel the free surface is bi-dimensional due to standing waves, so that the one-dimensional gradually varied flow equation breaks down. Another case where the use of the critical flow theory needs careful attention relates to the flow in zones of non-hydrostatic flow conditions, as in the vicinity of a free overfall in a rectangular and horizontal channel, or at the transition from a mild to a steep bottom slope (Castro-Orgaz and Hager 2017). In the former case, the critical flow section is located  $(3\text{--}4)h_c$  from the brink section (Fig. 2.62a), and the brink flow depth is  $h_b = 0.715h_c$  (Rouse 1938). The approach flow to the free fall is non-hydrostatic and supercritical. To conduct gradually varied water surface profile computations, it is assumed that the critical flow section is located at the brink section, given the small reach with non-hydrostatic flow (Henderson 1966). Likewise, the flow near a slope break is non-hydrostatic (Rouse 1938), with the critical flow section shifted upstream to the small slope reach (Fig. 2.62b). For gradually varied flow computations, the critical depth is taken at the slope break (Henderson 1966).

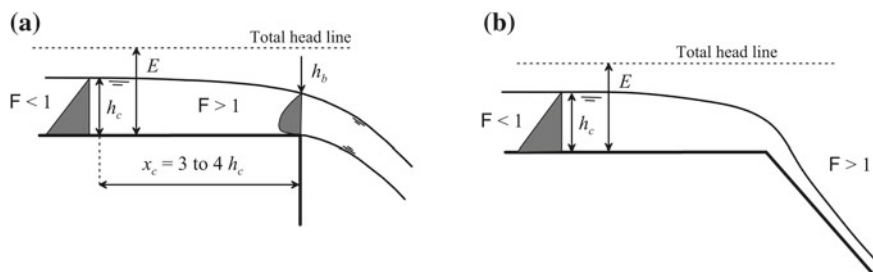


**Fig. 2.62** Critical flow at **a** free overfall and **b** transition from mild to steep slope

### 2.4.4 Weir Flows

Broad-crested weir

A rectangular broad-crested weir is a hump that produces choking of the upstream flow and thus critical flow conditions along the weir crest. Under ideal hydrostatic fluid flow, the streamlines are parallel along the crest, and the crest flow depth equals the critical depth  $h_c$  (Chanson 2004) (Fig. 2.63). The discharge equation is then [see Eq. (2.31)]

$$q = C_d (g E_{\min}^3)^{1/2}, \quad C_d = \left(\frac{2}{3}\right)^{3/2}. \quad (2.192)$$

Under real fluid flow conditions, there is flow separation around the upstream corner of the weir (Fig. 2.64a), with the corresponding recirculation of fluid. This recirculation produces an energy loss and thus a reduction of  $C_d$  below its ideal fluid flow value  $(2/3)^{3/2}$  (Castro-Orgaz and Hager 2017). Other weir types used in practice are the round-nosed broad-crested weir, the embankment weir, and the round-crested weir (Fig. 2.64).

Round-nosed broad-crested weir

If the upstream corner of the broad-crested weir is rounded (Fig. 2.64b), flow separation is suppressed. The flow will pass above the weir smoothly, with parallel streamlines, behaving like an inviscid fluid. The exception is the flow close to the wall, which is influenced by fluid viscosity given the significant reduction in velocity to comply with the nonslip wall condition. A boundary layer<sup>3</sup> starts its development close to the inlet section, but remains usually thin and rarely reaches the free surface.

A generalization of Eq. (2.192) is (Montes 1998; Castro-Orgaz and Hager 2017)

$$q = C_d (g H_o^3)^{1/2}, \quad (2.193)$$

where  $H_o$  is the upstream head over the weir. The discharge coefficient of the round-nosed broad-crested weir is theoretically determined for hydrostatic flow ( $H_o/L < 0.33$ ) correcting the critical flow theory by viscous effects resorting to the boundary layer theory, resulting in  $\delta_L^*$  as the boundary layer displacement thickness at the weir end section in (Ackers et al. 1978)

---

<sup>3</sup>The boundary layer displacement thickness  $\delta^*$  is the virtual shift of the potential flow from a solid wall due to viscous effects (Montes 1998; White 2009).

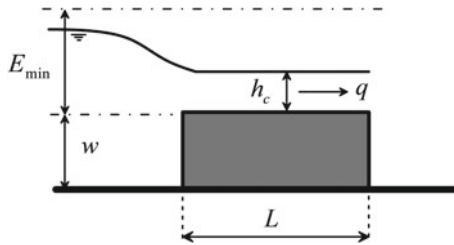


**Fig. 2.63** Ideal fluid flow over rectangular broad-crested weir

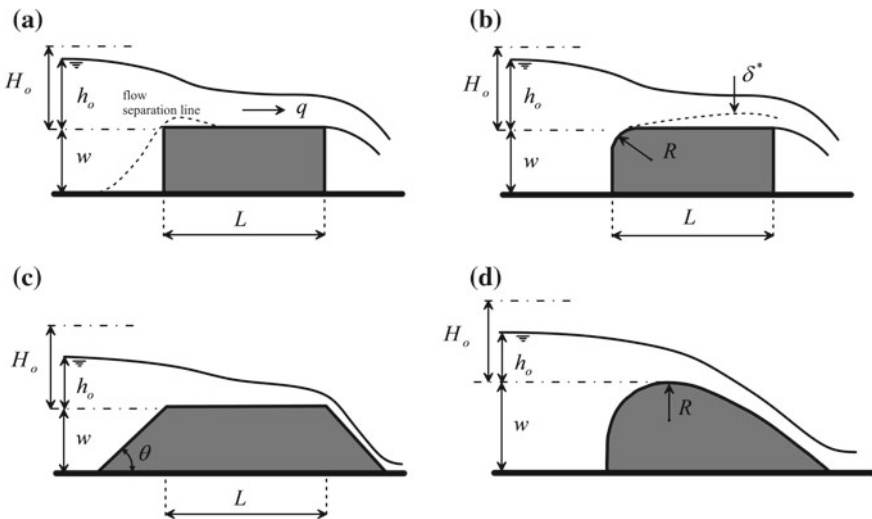


**Fig. 2.64** Flow over weirs: **a** rectangular broad-crested, **b** round-nosed broad-crested ( $H_o/L < 0.33$ ), **c** embankment, **d** round-crested

$$C_d = \left(\frac{2}{3}\right)^{3/2} \left(1 - \frac{\delta_L^*}{H_o}\right)^{3/2}, \quad (2.194)$$

where

$$H_o = h_o + w + \frac{q^2}{2g(h+w)^2}. \quad (2.195)$$

The boundary layer displacement thickness can be estimated with  $\varepsilon$  as the roughness height from (White 2009)

$$\frac{\delta_L^*}{L} = 0.001 + 0.2 \left( \frac{e}{L} \right)^{-1/2}. \quad (2.196)$$

In reality, the flow over a broad-crested weir is surprisingly complex and depends on the value of  $H_o/L$ . For  $0.1 < H_o/L < 0.33$ , the streamlines are parallel over the weir crest and the pressure distribution is hydrostatic, but viscous effects have to be accounted for, e.g., by using Eq. (2.195) (Ackers et al. 1978). For  $0.33 < H_o/L < 1.5$ , the streamlines over the weir are curvilinear and the discharge characteristics are governed by the non-hydrostatic pressure field. For  $H_o/L > 1.5$ , the flow separates from the crest and the weir behaves like a sharp-crested weir (Montes 1998). For  $H_o/L < 0.1$ , the pressure is non-hydrostatic and viscous effects are relevant, resulting in an undular weir flow pattern attenuated by friction (Castro-Orgaz and Hager 2017).

### Embankment weir

The embankment weir is a broad-crested weir with added slopes up- and downstream of the crest (Fig. 2.64c), forming a trapezoid (Hager 2010). The related flow phenomena are complex, as already discussed, involving action of non-hydrostatic pressure and bed friction depending on the dimensionless parameter  $H_o/L$  (Montes 1998, Hager 2010). From a practical viewpoint, the free flow discharge characteristics are estimated from the empirical equation (Sargison and Percy 2009)

$$C_d = 2^{1/2} (0.43 + 0.06 \sin[\pi(\xi - 0.55)] - 0.0396 \cdot \theta(\text{rad}) + 0.0029), \\ \xi = \frac{H_o}{H_o + L}, \quad (2.197)$$

where the effect of the upstream slope angle  $\theta$  is accounted for. The predicted discharge using Eqs. (2.193)–(2.197) is compared in Fig. 2.65 with data by Sargison and Percy (2009) relating to trapezoidal weirs with  $w = 0.25$  m and  $L = 0.5$  m.

The discharge characteristics for free flow are obtained by resorting to the energy principle and assuming that critical flow takes place on the weir crest [see Eq. (2.192)], tuning the equations with corrections due to fluid flow phenomena like non-hydrostaticity or boundary friction. To apply these equations, it is a requirement that the tailwater flow depth must not affect the control section (Ackers et al. 1978). An illustrative example on how increased tailwater flow depth affects weir flow is shown in Fig. 2.66. For a low tailwater depth (Fig. 2.66a), the flow is critical somewhere on the crest and the discharge characteristics are as for free flow. A hydraulic jump is formed at the toe of the weir. If the tailwater level is raised, the hydraulic jump starts moving upstream along the downstream weir face (Fig. 2.66b), stopping once a steady-state equilibrium in a control volume containing the surge is reached. If the level is further increased (Fig. 2.66c), the

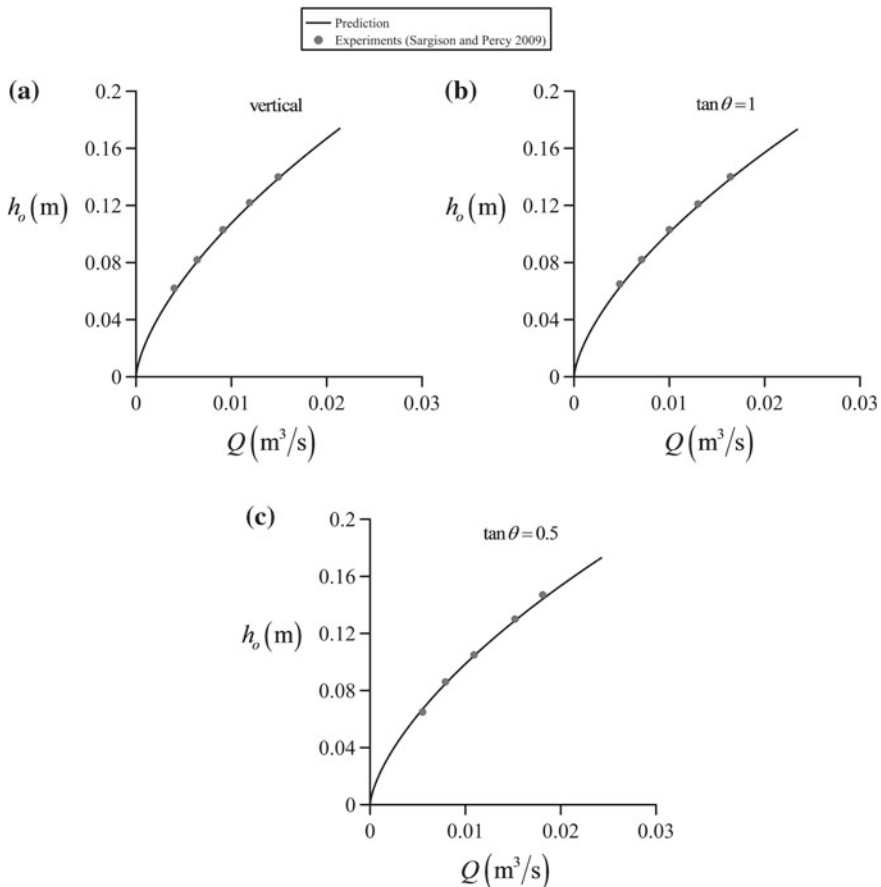


**Fig. 2.65** Computation of rating curves of embankment weir for different upstream slopes

hydraulic jump disappears, and the flow in the vicinity of the slope break will be non-hydrostatic and near-critical, producing a steady wave train in the tailwater portion of the structure. For an even larger tailwater flow depth, the structure is submerged and the flow is subcritical along the entire weir (Fig. 2.66d). The weir acts as a “control section” for free flow conditions. In the other cases, it behaves like a transition in bed elevation.

#### Round-crested weir

The round-crested weir (Fig. 2.64d) is another important type of weir used both as dam overflow and as a water discharge measurement structure (Montes 1998; Castro-Orgaz and Hager 2017). Its discharge characteristics are governed by the non-hydrostatic flow field over the weir (Rouse 1938), with  $C_d$  given by

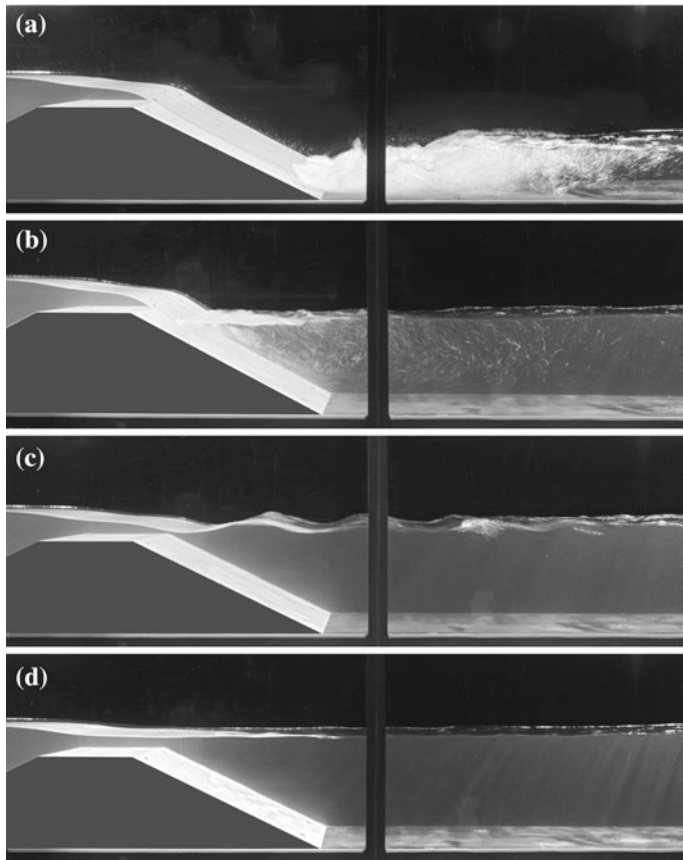


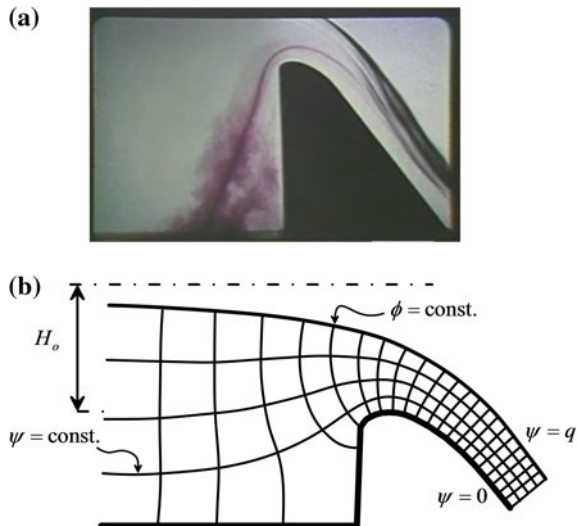
**Fig. 2.66** Effect of increasing tailwater depth: **a** free flow over the crest with hydraulic jump at weir toe, **b** hydraulic jump on downstream slope near slope break, **c** hydraulic jump disappears but a train of standing waves typical of non-hydrostatic flow is formed, **d** submerged weir and subcritical flow

$$C_d = \left(\frac{2}{3}\right)^{3/2} C_o, \quad (2.198)$$

where  $C_o$  is a non-hydrostatic correction coefficient. It is determined with good accuracy using potential flow methods (Liggett 1994; Montes 1998). An irrotational and inviscid (potential) flow obeys the Laplace equation for the potential function  $\phi$  as

$$\frac{\partial^2 \phi}{\partial x^2} + \frac{\partial^2 \phi}{\partial z^2} = 0, \quad (2.199)$$

**Fig. 2.67** Potential flow over round-crested weir:  
**a** photograph of model test showing a streamline with added colorant (Rouse 1961; IIHR-Hydroscience & Engineering, the University of Iowa) and **b** potential flow net



with  $z$  as the vertical coordinate. For an incompressible fluid, the stream function  $\psi$  satisfies also the Laplace equation,

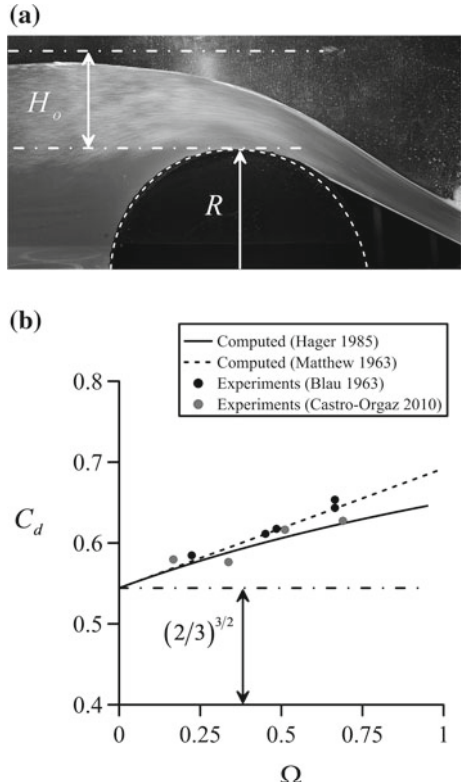
$$\frac{\partial^2 \psi}{\partial x^2} + \frac{\partial^2 \psi}{\partial z^2} = 0. \quad (2.200)$$

The lines  $\psi = \text{const.}$  are streamlines, and the velocity vector is tangent to them. The equipotential lines  $\phi = \text{const.}$  are normal to the streamlines at intersection points, forming the flow net of a potential flow (Fig. 2.67) (Rouse 1938; White 2009). While solving the elliptic problem posed by Eqs. (2.199)–(2.200) subject to appropriate boundary conditions for a given value of  $H_o$ , the discharge  $q$  emerges as part of the solution and thus  $C_o$ . The disadvantage is that complex numerical methods are required for this task (Montes 1998). Approximate methods to solve Eqs. (2.199)–(2.200) are available based on the so-called Boussinesq approximation (Castro-Orgaz and Hager 2017) (see Chap. 11). If the ratio  $\Omega = H_o/R$  is small, a correction to the discharge coefficient of critical (non-hydrostatic) potential flow over a round-crested weir is with  $R$  as the bottom curvature at the weir crest (Matthew 1963; Castro-Orgaz and Hager 2017)

$$C_o = 1 + \frac{22 H_o}{81 R} = 1 + \frac{22}{81} \Omega. \quad (2.201)$$

This equation is valid for  $H_o/R < 0.5$  provided that the weir is of a minimum size as to avoid scale effects originating from viscosity and surface tension (Castro-Orgaz and Hager 2017). For higher heads, an empirical version of Eq. (2.201) is (Hager 1985)

**Fig. 2.68** Flow over round-crested weir:  
**a** photograph of circular weir model and **b** discharge characteristics



$$C_o = 1 + \frac{3\Omega}{11 + 4.5\Omega}. \quad (2.202)$$

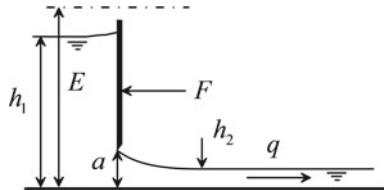
Equations (2.201)–(2.202) are favorably compared in Fig. 2.68 with experimental data on parabolic (Blau 1963) and circular (Castro-Orgaz 2010) weirs.

#### 2.4.5 Gate Flows

Free gate flow

Consider a vertical sluice gate inserted into a channel where the discharge is  $q$ . The gate opening is  $a$ , and the upstream energy head and flow depth are  $E$  and  $h_1$ , respectively. The approach flow is uniform and subcritical, whereas the flow issued below the gate is supercritical with uniform flow depth  $h_2$ . Note the flow contraction from the gate of opening  $a$  to the uniform flow depth  $h_2$  due to the curvilinear flow (Rouse 1938; Montes 1998) (Fig. 2.69).

**Fig. 2.69** Free flow from a vertical sluice gate



If energy losses are neglected, conservation of energy head reads

$$E = h_1 + \frac{q^2}{2gh_1^2} = h_2 + \frac{q^2}{2gh_2^2}. \quad (2.203)$$

Note that Eq. (2.203) can be written as

$$h_1 - h_2 = \frac{q^2}{2g} \left( \frac{1}{h_2^2} - \frac{1}{h_1^2} \right) = \frac{q^2}{2g} \frac{(h_1 - h_2)(h_1 + h_2)}{h_2^2 h_1^2}, \quad (2.204)$$

resulting in

$$\frac{q^2}{2g} = \frac{h_2^2 h_1^2}{(h_1 + h_2)}. \quad (2.205)$$

The contraction coefficient of sluice gate flow is  $C_c = h_2/a$ ; defining the discharge coefficient  $C_d$  as

$$C_d = \frac{q}{a(2gh_1)^{1/2}}, \quad (2.206)$$

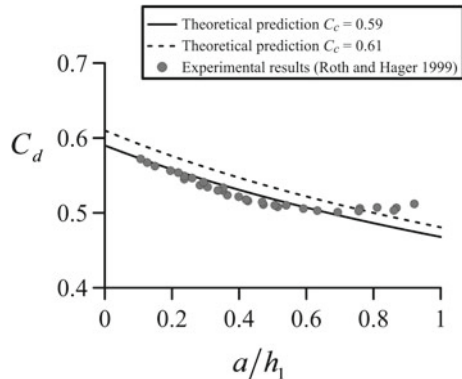
the dimensionless form of Eq. (2.205) is (Rouse 1950)

$$C_d = C_c \left( 1 + \frac{C_c a}{h_1} \right)^{-1/2}. \quad (2.207)$$

The contraction coefficient  $C_c$  is a function of  $h_1/a$  (Montes 1998), as observed also from experiments by Roth and Hager (1999).

The theoretical value resulting from potential flow methods is  $C_c = 0.61$  (Montes 1998). Equation (2.207) is compared in Fig. 2.70 with the experiments of Roth and Hager (1999) using  $C_c = 0.61$  and  $0.59$ , resulting in a better match for the latter value. Note that the sluice gate acts as a control section if the gate opening is small enough to produce supercritical flow in the tailwater. It is immediate to obtain the relations  $F_1^2 = 2C_d^2(a/h_1)^2$  and  $h_c/a = F_1^{2/3}h_1/a$ . From these identities, the gate opening equals the critical depth roughly for  $a/h_1 = 0.55$ . Once the gate

**Fig. 2.70** Discharge characteristics of free sluice gate flow  $C_d = C_d(a/h_1)$



opening equals the critical depth, the downstream flow turns unstable due to the presence of standing non-hydrostatic waves typical of near-critical flows (Montes 1998). In this case, there is no uniform flow downstream of the gate, and the relevance of  $C_c$  is obsolete. For larger gate openings, the waves progressively disappear, leading to a hydrostatic subcritical flow downstream of the gate. For practical purposes, the gate can be considered to act as a control section for  $a/h_1 < 0.6$ , with  $C_c = 0.6$ . For larger gate openings, the gate acts as a local obstruction to the flow.

The force  $F$  on the gate is now evaluated by application of the momentum balance, producing after insertion of Eq. (2.205),

$$F = \rho g \left[ \left( \frac{h_1^2}{2} + \frac{q^2}{gh_1} \right) - \left( \frac{h_2^2}{2} + \frac{q^2}{gh_2} \right) \right] = \frac{1}{2} \rho g \frac{(h_1 - h_2)^3}{h_1 + h_2} = \frac{1}{2} \rho g \frac{(h_1 - C_c a)^3}{h_1 + C_c a}. \quad (2.208)$$

This is another example on the complementary usage of the energy and momentum principles; once the discharge  $q$  is determined from the energy principle, the momentum principle is used to evaluate the force acting on the gate. In dimensionless form, it is

$$\frac{F}{\rho g \frac{1}{2} h_1^2} = \frac{(1 - C_c a/h_1)^3}{1 + C_c a/h_1}. \quad (2.209)$$

### Gate flow with rejected hydraulic jump

Consider free flow past a vertical sluice gate in a rectangular channel of equal width as the gate, with a tailwater flow depth that exactly equals the sequent depth of the contracted flow depth  $h_2$  (Fig. 2.71). A hydraulic jump is therefore formed beyond the sluice gate. If  $h_3$  is lower than the sequent depth  $h_2$ , a hydraulic jump would still be formed but further shifted into the tailwater. A water surface profile of super-critical flow starting at the contracted section should be formed to increase the flow depth and then equal the actual tailwater level through a hydraulic jump. These cases are detailed in Chap. 4, given that the surface profile from the vena contracta section is governed by friction.

It is common in the field monitoring of canal networks to install up- and downstream of sluice gates ultrasonic sensors to measure  $h_1$  and  $h_3$ . We will form the resulting system of equations needed to compute the unknowns  $q$  and  $h_2$  for the case depicted in Fig. 2.71a. The energy equation applied between the upstream section and the contracted section is

$$E = h_1 + \frac{q^2}{2gh_1^2} = h_2 + \frac{q^2}{2gh_2^2}, \quad (2.210)$$

with the discharge given by Eq. (2.205). The momentum equation applied between the contracted and the tailwater sections reads

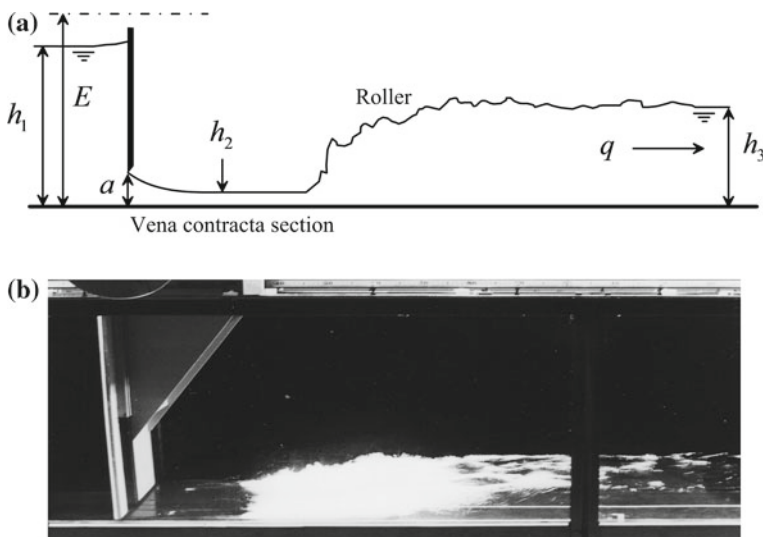


**Fig. 2.71** Free flow across sluice gate with rejected hydraulic jump: **a** definition sketch and **b** photograph of model test

$$S = \frac{h_2^2}{2} + \frac{q^2}{gh_2} = \frac{h_3^2}{2} + \frac{q^2}{gh_3}. \quad (2.211)$$

It can be rewritten as

$$\frac{1}{2}(h_2 - h_3)(h_2 + h_3) = \frac{q^2}{g} \left( \frac{h_2 - h_3}{h_3 h_2} \right), \quad (2.212)$$

from which the discharge is given by

$$\frac{q^2}{g} = \frac{1}{2}(h_2 + h_3)h_3 h_2. \quad (2.213)$$

Equating  $q$  from Eqs. (2.205) and (2.213) results in the quadratic equation for  $h_2$

$$\left( -\frac{1}{2}h_3 \right)h_2^2 + \left( -\frac{1}{2}h_3^2 + 2h_1^2 - \frac{h_1 h_3}{2} \right)h_2 + \left( -\frac{1}{2}h_1 h_3^2 \right) = 0. \quad (2.214)$$

Thus, once  $h_2$  is computed the discharge  $q$  follows using either Eq. (2.205) or (2.213). This is an illustrative example highlighting how conservation of energy in the sluice gate problem, and momentum in the hydraulic jump, is used simultaneously. In a final step, if needed, the force  $F$  on the gate and the energy loss  $\Delta E$  of the hydraulic jump are determined by application of the momentum and the energy balances to the gate and the hydraulic jump, respectively. The use of the energy-momentum equations in sluice gate problems is known as the EM method.

#### Gate flow with submerged hydraulic jump

Consider again the case depicted in Fig. 2.71a. The conjugate depth of the supercritical contracted flow depth  $h_2' = C_c a$  is

$$h_2' = \frac{1}{2}C_c a \left[ \left( 1 + 8F_1^2 \right)^{1/2} - 1 \right]. \quad (2.215)$$

If  $h_2' = h_3$ , the case of Fig. 2.71a occurs. If  $h_2' > h_3$ , the jump is further rejected into the tailwater and the gate operates under free flow conditions, with a backwater curve starting from the vena contracta section. However, if the gate is operating under free flow conditions and a tailwater depth is imposed such that  $h_2' < h_3$ , a moving hydraulic jump (surge) is shifted upstream, becoming drowned once reaching the gate section; an alternative flow model is required in this particular case. The basic assumption, in addition to the hydrostatic pressure distribution, is that the flow velocity in the roller of the hydraulic jump is small and can be

neglected (Henderson 1966; Castro-Orgaz et al. 2013). Conservation of energy between the approach flow section to the gate and the vena contracta section yields

$$E = h_1 + \frac{q^2}{2gh_1^2} = h + \frac{q^2}{2gh_2^2}. \quad (2.216)$$

Observe that the kinetic flow energy is given by the velocity in the vena contracta. Conservation of momentum between the vena contracta and the tailwater section gives

$$S = \frac{h^2}{2} + \frac{q^2}{gh_2} = \frac{h_3^2}{2} + \frac{q^2}{gh_3}. \quad (2.217)$$

Equations (2.216)–(2.217) are the EM equations for submerged flow below a sluice gate (Henderson 1966). In field conditions, ultrasonic sensors are used to measure  $h_1$  and  $h_3$ . The unknowns are therefore  $q$  and  $h$  (Fig. 2.72).

Equation (2.216) is rewritten as

$$h_1 - h = \frac{q^2}{2g} \left( \frac{1}{h_2^2} - \frac{1}{h_1^2} \right), \quad (2.218)$$

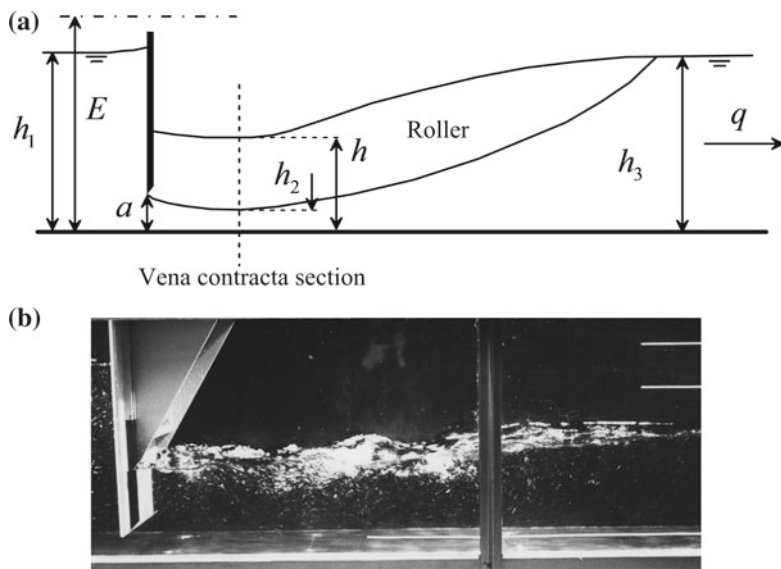


**Fig. 2.72** Submerged flow below sluice gate: **a** definition sketch and **b** photograph of model test

and Eq. (2.217) as

$$\frac{1}{2}(h^2 - h_3^2) = \frac{q^2}{g} \left( \frac{1}{h_3} - \frac{1}{h_2} \right) = 0. \quad (2.219)$$

Equating  $q$  from Eqs. (2.218)–(2.219) produces

$$\frac{1}{2}(h^2 - h_3^2) = \frac{2(h_1 - h)h_2^2h_1^2}{(h_1 + h_2)(h_1 - h_2)} \left( \frac{h_2 - h_3}{h_3h_2} \right), \quad (2.220)$$

which is a quadratic equation in  $h$ , e.g.,

$$\begin{aligned} \frac{1}{2}h^2 + \left[ 2h_2 \left( \frac{h_2}{h_3} - 1 \right) \left( 1 - \frac{h_2^2}{h_1^2} \right)^{-1} \right] h - \left[ \frac{1}{2}h_3^2 + 2h_2h_1 \left( \frac{h_2}{h_3} - 1 \right) \left( 1 - \frac{h_2^2}{h_1^2} \right)^{-1} \right] \\ = 0. \end{aligned} \quad (2.221)$$

Using the definitions  $h_2 = C_c a$ ,  $Y = h/h_3$ , Eq. (2.221) is written in dimensionless form as

$$\begin{aligned} \frac{1}{2}Y^2 + \left[ 2\frac{C_c}{r_3} \left( \frac{C_c}{r_3} - 1 \right) \left( 1 - \frac{C_c^2}{r_1^2} \right)^{-1} \right] Y - \left[ \frac{1}{2} + 2\frac{C_c r_1}{r_3^2} \left( \frac{C_c}{r_3} - 1 \right) \left( 1 - \frac{C_c^2}{r_1^2} \right)^{-1} \right] \\ = 0, \end{aligned} \quad (2.222)$$

where  $r_1 = h_1/a$  and  $r_3 = h_3/a$ . This is written in compact form as

$$aY^2 + bY + c = 0, \quad (2.223)$$

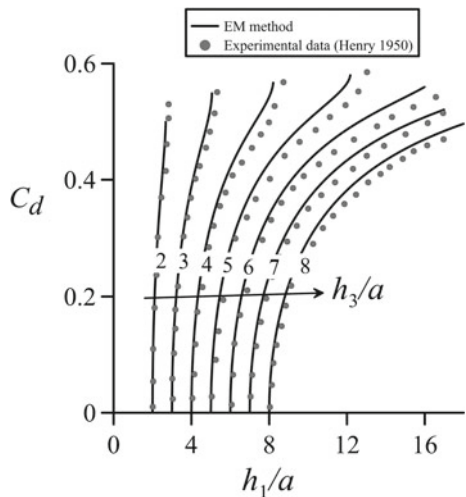
with the physically relevant solution

$$Y = \frac{-b + (b^2 - 4ac)^{1/2}}{2a}. \quad (2.224)$$

From Eq. (2.218), one can write using the definition of  $C_d$  given by Eq. (2.206)

$$\left( 1 - \frac{h}{h_1} \right) = C_d^2 a^2 \left( \frac{h_1^2 - h_2^2}{h_2^2 h_1^2} \right) = C_d^2 a^2 \frac{(h_1 + h_2)(h_1 - h_2)}{h_2^2 h_1^2}, \quad (2.225)$$

**Fig. 2.73** Discharge characteristics  $C_d = C_d(h_1/a, h_3/a)$  for a submerged vertical sluice gate flow



from which  $C_d$  is given by

$$C_d = C_c \left[ \left( 1 - \frac{r_3}{r_1} Y \right) \left( 1 - \frac{C_c^2}{r_1^2} \right)^{-1} \right]^{1/2}. \quad (2.226)$$

For given values of  $h_1/a$  and  $h_3/a$ , Eq. (2.222) is solved for  $Y$  and then Eq. (2.226) for  $C_d$ . This task was accomplished and is presented in Fig. 2.73 in the so-called Henry (1950) diagram. As observed, the theoretical prediction is in fair agreement with experiments. If a precise water discharge estimation is required, however, a more advanced model is needed by relaxing some of the starting assumptions (Castro-Orgaz et al. 2013), as that of zero roller flow velocities or negligible energy losses across the gate. Note that these computations are to be conducted only if the tailwater flow depth  $h_3$  is larger than the conjugate depth of  $h_2$ , given by Eq. (2.215). Computations in Fig. 2.73 were conducted until Eq. (2.224) produced real solutions. In general, the result to identify a free flow using Eq. (2.215) is not identical to that derived from Eq. (2.224), due to the special form of the equations adopted (Jeppson 2011).

## 2.5 Application: Numerical Solution of Energy–Momentum Equations for Gate Flow

Open channel flow applications frequently involve the simultaneous solution of nonlinear systems of equations (Jeppson 2011). In this section, the Newton–Raphson method is generalized for these cases using as practical example the EM

gate problem shown in Fig. 2.71. The numerical solution of this problem is formulated defining two functions  $F_1$  and  $F_2$ , for which the roots have to be determined, namely

$$F_1 = \left( h_1 + \frac{q^2}{2gh_1^2} \right) - \left( h_2 + \frac{q^2}{2gh_2^2} \right) \equiv 0, \quad (2.227)$$

$$F_2 = \left( \frac{h_2^2}{2} + \frac{q^2}{gh_2} \right) - \left( \frac{h_3^2}{2} + \frac{q^2}{gh_3} \right) \equiv 0. \quad (2.228)$$

As in the Newton–Raphson method for a single equation, iterations start with a guessed solution for  $q$  and  $h_2$ , generally not being correct. Using a Taylor series development truncated to the first term, the new solution at iteration  $k + 1$  is forced to produce zero residuals, e.g.,

$$\begin{aligned} F_1^{k+1} &= F_1^k + \left( \frac{\partial F_1}{\partial q} \right)^k (q^{k+1} - q^k) + \left( \frac{\partial F_1}{\partial h_2} \right)^k (h_2^{k+1} - h_2^k) \equiv 0, \\ F_2^{k+1} &= F_2^k + \left( \frac{\partial F_2}{\partial q} \right)^k (q^{k+1} - q^k) + \left( \frac{\partial F_2}{\partial h_2} \right)^k (h_2^{k+1} - h_2^k) \equiv 0. \end{aligned} \quad (2.229)$$

These equations are rewritten as

$$\begin{aligned} -F_1^k &= \left( \frac{\partial F_1}{\partial q} \right)^k \Delta q + \left( \frac{\partial F_1}{\partial h_2} \right)^k \Delta h_2, \\ -F_2^k &= \left( \frac{\partial F_2}{\partial q} \right)^k \Delta q + \left( \frac{\partial F_2}{\partial h_2} \right)^k \Delta h_2, \end{aligned} \quad (2.230)$$

or in matrix form

$$\begin{pmatrix} -F_1 \\ -F_2 \end{pmatrix}^k = \begin{pmatrix} \frac{\partial F_1}{\partial q} & \frac{\partial F_1}{\partial h_2} \\ \frac{\partial F_2}{\partial q} & \frac{\partial F_2}{\partial h_2} \end{pmatrix}^k \begin{pmatrix} \Delta q \\ \Delta h_2 \end{pmatrix}. \quad (2.231)$$

With  $\mathbf{F}$  as the vector of residuals,  $\mathbf{J}$  the Jacobian matrix, and  $\mathbf{X}$  the vector of unknowns,

$$\mathbf{F} = \begin{pmatrix} F_1 \\ F_2 \end{pmatrix}, \quad \mathbf{J} = \begin{pmatrix} \frac{\partial F_1}{\partial q} & \frac{\partial F_1}{\partial h_2} \\ \frac{\partial F_2}{\partial q} & \frac{\partial F_2}{\partial h_2} \end{pmatrix}, \quad \mathbf{X} = \begin{pmatrix} q \\ h_2 \end{pmatrix}, \quad (2.232)$$

Equation (2.231) is written as

$$-\mathbf{F} = \mathbf{J} \cdot \Delta \mathbf{X}. \quad (2.233)$$

The solution of the linear system of equations yields

$$\Delta \mathbf{X} = -\mathbf{J}^{-1} \cdot \mathbf{F}, \quad (2.234)$$

which can be accomplished using an LU decomposition (Hoffman 2001; Press et al. 2007). The Newton–Raphson vector formula for updating the solution is then

$$\mathbf{X}^{k+1} = \mathbf{X}^k - (\mathbf{J}^{-1} \cdot \mathbf{F})^k. \quad (2.235)$$

Equation (2.235) must be iteratively applied until the residuals of  $\mathbf{X}$  are below a prescribed tolerance. For the present example, the elements of the Jacobian matrix are

$$\begin{aligned} \frac{\partial F_1}{\partial q} &= \frac{q}{gh_1^2} - \frac{q}{gh_2^2}, \\ \frac{\partial F_1}{\partial h_2} &= -(1 - F_2^2), \\ \frac{\partial F_2}{\partial q} &= \frac{2q}{gh_2} - \frac{2q}{gh_3}, \\ \frac{\partial F_2}{\partial h_2} &= h_2(1 - F_2^2). \end{aligned} \quad (2.236)$$

A code to solve the problem is implemented in the file “*EM\_sluicegate.xls*”, available in Chap. 12. An LU decomposition is applied using a program adapted from Press et al. (2007). For the test case  $h_1 = 1$  m and  $h_3 = 0.5$  m, the program yields after five iterations  $h_2 = 0.0778$  m and  $q = 0.3322$  m<sup>2</sup>/s, which is in full agreement with the analytical solution [Eqs. (2.213)–(2.214)]. This numerical code can be easily adapted to other channel cross sections for which no analytical solutions exist, as well as for submerged flow conditions.

## References

- Ackers, P., White, W. R., Perkins, J. A., & Harrison, A. J. M. (1978). *Weirs and flumes for flow measurement*. New York: Wiley.  
 Bakhmeteff, B. A. (1912). *О неравномерном движении жидкости в открытом русле* [Varied flow of liquids in open channels]. Russia: St Petersburg (in Russian).  
 Bakhmeteff, B. A. (1932). *Hydraulics of open channels*. New York: McGraw-Hill.

- Bélanger, J. B. (1849). *Notes sur le Cours d'Hydraulique*. [Notes on the Course in Hydraulics]. Mém. Ecole Nat. Ponts et Chaussées, Paris, France, session 1849–1850, 222 p (in French).
- Blau, E. (1960). *Die modellmässige Untersuchung von Venturikanälen verschiedener Größen und Form* [Model examination of Venturi channels of different sizes and shapes]. Mitteilung 8 der Forschungsanstalt für Schifffahrt, Wasser-und Grundbau. Berlin: Akademie-Verlag (in German).
- Blau, E. (1963). *Der Abfluss und die hydraulische Energieverteilung über einer parabelförmigen Wehrschwelle* [Flow and the hydraulic energy distribution over a parabolic weir]. Mitteilung 7, 5–72. Forschungsanstalt für Schifffahrt, Wasser und Grundbau, Berlin (in German).
- Bos, M. G. (1976). *Discharge measurement structures*. Publication 20. Wageningen, Netherlands: International Institute for Land Reclamation (ILRI).
- Bretz, N. V. (1988). *Ressaut hydraulique forcé par seuil* [Hydraulic jump forced by a sill]. Communication 2, Laboratoire de Constructions Hydrauliques, EPFL Lausanne, Switzerland (in French).
- Castro-Orgaz, O. (2010). Approximate modeling of 2D curvilinear open channel flows. *Journal of Hydraulic Research*, 48(2), 213–224.
- Castro-Orgaz, O., Giraldez, J. V., & Ayuso, J. L. (2008). Transcritical flow due to channel contraction. *Journal of Hydraulic Engineering*, 134(4), 492–496.
- Castro-Orgaz, O., & Hager, W. H. (2017). *Non-hydrostatic free surface flows*. Advances in geophysical and environmental mechanics and mathematics (696p). Berlin: Springer. <https://doi.org/10.1007/978-3-319-47971-2>.
- Castro-Orgaz, O., Mateos, L., & Dey, S. (2013). Revisiting the Energy-Momentum method for rating vertical sluice gates under submerged flow conditions. *Journal of Irrigation and Drainage Engineering*, 139(4), 325–335.
- Castro-Orgaz, O., & Sturm, T. W. (2018). Boris A. Bakhmeteff and the development of the specific energy and momentum concepts. *Journal of Hydraulic Engineering*, 144(12), 02518004.
- Chanson, H. (2004). *The hydraulics of open channel flows: An introduction*. Oxford, UK: Butterworth-Heinemann.
- Chaudhry, M. H. (2008). *Open-channel flow* (2nd ed.). Berlin: Springer.
- Chow, V. T. (1959). *Open channel hydraulics*. New York: McGraw-Hill.
- Hager, W. H. (1985). Critical flow condition in open channel hydraulics. *Acta Mechanica*, 54(3–4), 157–179.
- Hager, W. H. (2010). *Wastewater hydraulics: Theory and practice*. Berlin: Springer.
- Henderson, F. M. (1966). *Open channel flow*. New York: MacMillan.
- Henry, H. R. (1950). *A study of flow from a submerged sluice gate* (M.S. thesis). Department of Mechanics and Hydraulics, State University of Iowa, Iowa City IA.
- Hoffman, J. D. (2001). *Numerical methods for engineers and scientists* (2nd ed.). New York: Marcel Dekker.
- Ippen, A. T. (1951). Mechanics of supercritical flow. *Transactions of ASCE*, 116, 268–295.
- Ippen, A. T., & Dawson, J. H. (1951). Design of channel contractions. *Transactions of ASCE*, 116, 326–346.
- Ippen, A. T., & Harleman, D. R. F. (1956). Verification of theory for oblique standing waves. *Transactions of ASCE*, 121, 678–694.
- Jaeger, C. (1956). *Engineering fluid mechanics*. Edinburgh: Blackie and Son.
- Jain, S. C. (2001). *Open channel flow*. New York: Wiley.
- Jeppson, R. (2011). *Open channel flow: Numerical methods and computer applications*. Boca Raton: CRC Press.
- Khafagi, A. (1942). *Der Venturikanal: Theorie und Anwendung* [Venturi flume: Theory and application]. Versuchsanstalt für Wasserbau, Eidgenössische Technische Hochschule Zürich, Mitteilung 1. Leemann, Zürich, Switzerland (in German).
- Liggett, J. A. (1994). *Fluid mechanics*. New York: McGraw-Hill.
- Matthew, G. D. (1963). On the influence of curvature, surface tension and viscosity on flow over round-crested weirs. *Proceedings of ICE*, 25, 511–524; 28, 557–569.

- Montes, J. S. (1998). *Hydraulics of open channel flow*. Reston VA: ASCE Press.
- Press, W. H., Teukolsky, S. A., Vetterling, W. T., & Flannery, B. P. (2007). *Numerical recipes: The art of scientific computing* (3rd ed.). Cambridge: Cambridge University Press.
- Puertas, J., & Sánchez, M. (2001). *Apuntes de Hidráulica de canales* [Open channel hydraulics lecture notes]. Civil Engineering School, University da Coruña, Spain (in Spanish).
- Roth, A., & Hager, W. H. (1999). Underflow of standard sluice gate. *Experiments in Fluids*, 27(4), 339–350.
- Rouse, H. (1938). *Fluid mechanics for hydraulic engineers*. New York: McGraw-Hill.
- Rouse, H. (1950). *Engineering hydraulics*. New York: Wiley.
- Rouse, H. (1961). *Fluid motion in a gravitational field*: IIHR Movies, University of Iowa.
- Sargison, J. E., & Percy, A. (2009). Hydraulics of broad-crested weirs with varying side slopes. *Journal of Irrigation and Drainage Engineering*, 135(1), 115–118.
- Selby, S. M. (1973). *Standard mathematical tables*. Cleveland: CRC.
- Sturm, T. W. (2001). *Open channel hydraulics*. New York: McGraw-Hill.
- Subramanya, K. (1986). *Flow in open channels*. New Delhi: Tata McGraw-Hill.
- Toman, E. M., Skaugset, A. E., & Simmons, A. N. (2014). Calculating discharge from culverts under inlet control using stage at the inlet. *Journal of Irrigation and Drainage Engineering*, 140(2), 06013003.
- Vischer, D. L., & Hager, W. H. (1998). *Dam hydraulics*. New York: Wiley.
- White, F. M. (2009). *Fluid mechanics*. New York: McGraw-Hill.
- Yen, B. C. (1973). Open-channel flow equations revisited. *Journal of the Engineering Mechanics Division*, ASCE, 99(EM5), 979–1009.

# Chapter 3

## Computation of Steady Gradually-Varied Flows



### 3.1 Introduction

Steady open channel flow is generally non-uniform. In gradually-varied flows, the changes of depth and velocity in space are small, so that streamline curvature effects can be neglected. If the channel bottom slope is small, then the hydrostatic vertical pressure distribution prevails. This chapter presents water surface profile computations of steady gradually-varied flows in prismatic channels, including qualitative sketches of the flow profiles by analyzing the nature of the governing equation and numerical methods to produce accurate solutions. The chapter focuses on flows with constant discharge, thereby overlooking the analysis of spatially varied flows with either increasing or decreasing discharge (Montes 1998; Hager 2010).

### 3.2 Governing Equation of Non-uniform Flow

The momentum principle yields for a prismatic channel the system [Eq. (1.100)],

$$\frac{dM}{dx} = gA(S_o - S_f), \quad (3.1)$$

$$M = \frac{Q^2}{gA} + A\bar{h}. \quad (3.2)$$

Here,  $M$  is the momentum function,  $S_f$  the friction slope,  $Q$  the discharge,  $A$  the flow area,  $x$  the streamwise coordinate,  $g$  the gravity acceleration,  $\bar{h}$  the depth of the

section centroid below the free surface, and  $S_o$  the bottom slope. The gradually-varied flow equation resulting from Eqs. (3.1)–(3.2) is [Eq. (1.110)],

$$\frac{dh}{dx} = \frac{S_o - \frac{\tau_o}{\rho g R_h}}{1 - B \frac{Q^2}{g A^3}} = \frac{S_o - S_f}{1 - F^2}, \quad (3.3)$$

where  $\tau_o$  is the boundary shear stress,  $R_h = A/p$  the hydraulic radius,  $p$  the wetted perimeter,  $B$  the free surface width,  $h$  the flow depth,  $\rho$  the water density, and  $F$  the Froude number. Equation (3.3) was first presented by Bélanger (1828).

The energy principle yields, with  $E$  as the specific energy and  $S_e$  the gradient of dissipated energy (Montes 1998; Chanson 2004) the system

$$\frac{dE}{dx} = S_o - S_e, \quad (3.4)$$

$$E = h + \frac{Q^2}{2gA^2}. \quad (3.5)$$

Equation (3.3) is obtained from Eqs. (3.4)–(3.5) if the gradient of dissipated energy  $S_e$  equals the friction slope  $S_f$  (Yen 1973, 1991, 2002; Montes 1998). Note that the velocity distribution coefficients are neglected in the systems (3.1)–(3.2) and (3.4)–(3.5). Given that the energy (Coriolis) and momentum (Boussinesq) velocity correction coefficients are different theoretically, gradually-varied flows are defined by a unique ODE [Eq. (3.3)] *if and only if* the velocity correction coefficients are assumed to be unity and the friction slope equals the gradient of dissipated energy. Both slopes are different from a theoretical point of view (Yen 1973, 2002): the friction slope is a measure of the shear forces acting on the channel boundaries, whereas the gradient of dissipated energy is a measure of all the losses accumulated by the entire mass of fluid. For gradually-varied flows in a prismatic channel, both are equal once the velocity distribution is assumed to be uniform. At abrupt variations of the channel cross-section, e.g., expansions or contractions, local energy losses due to eddies become significant. These additional losses have to be introduced empirically into gradually-varied flow computations by using local energy-loss coefficients (Montes 1998). In this chapter, we limit the analysis to flow profiles along prismatic reaches.

### 3.3 Uniform Flow

#### 3.3.1 Definition

Uniform flow is the simplest case of non-uniform flow, obtained by setting the variation of depth with distance equal to zero in Eq. (3.3), that is,

$$\frac{dh}{dx} = 0 \Rightarrow S_o - S_f = 0 \Rightarrow \tau_o = \rho g R_h S_o. \quad (3.6)$$

The constant flow depth satisfying Eq. (3.6) is defined as the *normal* or *uniform* flow depth  $h_N$ . In uniform flow, the friction slope is identical to the channel bottom slope. To compute the uniform flow depth for a given  $S_o$  resorting to Eq. (3.6), a parametrization of the bed-shear stress  $\tau_o$  as function of the flow variables is required. This task is accomplished below.

### 3.3.2 Flow Resistance

Rouse (1965) parametrized the boundary shear stress in open channel flows by defining the general relation

$$\frac{\tau_o}{\rho U^2} = \Theta(R, F, \varepsilon, C, N, U). \quad (3.7)$$

Here,  $R = UD/v$  is the Reynolds number,  $U$  the mean velocity,  $D$  the hydraulic diameter,  $v$  the kinematic viscosity,  $F$  the Froude number,  $\varepsilon = k_s/D$  the relative roughness,  $k_s$  the equivalent wall roughness height,  $C$  the effect of the cross-sectional shape,  $N$  the effect of non-uniform flow, and  $U$  the unsteadiness effect. While Eq. (3.7) is a general statement from dimensional analysis, it is difficult to find particular expressions in practice, given the nonlinear interactions of the various hydraulic numbers (Yen 2002). For the specific case of steady uniform flow, Eq. (3.7) reduces to (Yen 2002)

$$\frac{\tau_o}{\rho U^2} = \Theta(R, \varepsilon) = \frac{f}{8}, \quad (3.8)$$

where  $f$  is the Darcy–Weisbach friction factor. The resistance factor  $C = (8g/f)^{1/2}$  is called Chezy coefficient. Thus, the so-called Moody diagram is a particular case of Eq. (3.7) (Rouse 1965; Yen 2002). Inserting Eq. (3.8) into Eq. (3.6) produces

$$\frac{f}{8} \rho U^2 = \rho g R_h S_f, \quad (3.9)$$

which is the Darcy–Weisbach equation (Chanson 2004),

$$S_f = f \frac{1}{4R_h} \frac{U^2}{2g} = f \frac{1}{D} \frac{U^2}{2g}. \quad (3.10)$$

Note that in open channel flows  $D = 4R_h$ . The problem is thus reduced to find a suitable predictor for  $\Theta(R, \varepsilon)$  in Eq. (3.8). Open channel flow is generally turbulent ( $R > 2000$ ) (White 1991, 2003), and attention is therefore limited to this regime. A Colebrook-White type formula suitable for open channel flows is (Yen 2002)

$$f^{-1/2} = -a \log_{10} \left[ \frac{4\varepsilon}{b} + \frac{c}{4Rf^{1/2}} \right], \quad (3.11)$$

where the empirical coefficients ( $a, b, c$ ) adopt different values, depending on the literature source [see Yen (2002) for a detailed discussion]. Here, the values proposed by Henderson (1966) ( $a = 2, b = 12, c = 2.5$ ) are used. Equation (3.11) is plotted in Fig. 3.1 using these coefficients, by numerically solving it for given values of  $R$  and  $\varepsilon$ .

The limiting form of Eq. (3.11) for turbulent smooth flows ( $\varepsilon = 0$ ) is

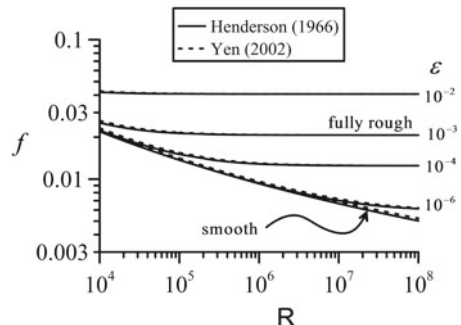
$$f^{-1/2} = -2 \log_{10} \left( \frac{2.5}{4Rf^{1/2}} \right), \quad (3.12)$$

whereas for turbulent rough flows ( $R \rightarrow \infty$ ) one gets the explicit equation

$$f = \frac{1}{4} \left[ -\log_{10} \left( \frac{1}{3}\varepsilon \right) \right]^{-2}. \quad (3.13)$$

In hydraulic smooth flows, the wall roughness elements are submerged into the laminar viscous sub-layer, and the flow resistance is fully determined by  $R$  (White 1991, 2003). In hydraulic rough flows, the roughness elements emerge above the thin viscous sub-layer, and the flow resistance is a form drag, fully determined by  $\varepsilon$  (White 1991, 2003). Between these two limits, the flow is transitional, and the flow resistance is a function of both  $R$  and  $\varepsilon$ . Many practical open channel flow problems are likely to be fully rough, resorting to Eq. (3.13) and greatly simplifying computations, therefore. However, smooth flows are also usual in open channel laboratory facilities. Thus, it is equally important to have a simple predictor for  $f$  in these flows.

**Fig. 3.1** Moody-type diagram for turbulent open channel flows



As noted from Fig. 3.1, a good explicit approximation to Eq. (3.12) is (Yen 2002; Fenton 2010)

$$f = \frac{1}{4} \left[ -\log_{10} \left( \frac{1.95}{R^{0.9}} \right) \right]^{-2}. \quad (3.14)$$

By simply combining the limiting forms for rough and smooth flows, given by Eqs. (3.13) and (3.14), the following explicit formula is obtained (Yen 2002, Fenton 2010)

$$f = \frac{1}{4} \left[ -\log_{10} \left( \frac{\varepsilon}{3} + \frac{1.95}{R^{0.9}} \right) \right]^{-2}. \quad (3.15)$$

This equation is plotted in Fig. 3.1 and compared to Eq. (3.11), resulting in an excellent match. Applying Eq. (3.15) in combination with Eq. (3.10) provides a simple and physically sound method to compute flow resistance in open channels. Usual values of the roughness height are given in Table 3.1.

Another widely used flow resistance relation for turbulent rough open channel flows is the Gauckler–Manning–Strickler (GMS) equation (Sturm 2001; Yen 2002)

$$S_f = \frac{n^2 U^2}{R_h^{4/3}}, \quad (\text{SI}) \quad (3.16)$$

where  $n$  is Manning's dimensional resistance coefficient (units are  $L^{-1/3}T$  in SI). The value of  $n$  depends on the boundary roughness, but it lacks a direct physical meaning (Yen 1991). Traditional methods for determining  $n$  include the use of tables (see Table 3.2) or estimations based on photographs (Chow 1959; Chaudhry 2008). In practice, however, a method for computing  $n$  is based on fitting water surface computations to observations, if available (Puertas and Sánchez 2001). The compatibility of Eqs. (3.10) and (3.16) implies (Yen 2002)

$$\frac{f}{8} = \frac{gn^2}{R_h^{1/3}}, \quad (3.17)$$

which permits to express  $n$  as function of  $f$ . This relation indicates that  $n$  is a function of  $R$ ,  $\varepsilon$  and the water depth  $h$ .

**Table 3.1** Values for roughness height (Jain 2001)

Material	$k_s$ (mm)
Steel	0.05–0.2
Cast iron	0.25–1
Cement	0.3–1.2
Concrete	0.5–3

**Table 3.2** Typical values for Manning's  $n$  (Chaudhry 2008)

Material	$n$ ( $\text{sm}^{-1/3}$ )
Steel	0.012
Cast iron	0.013
Corrugated metal	0.025
Lucite	0.009
Glass	0.01
Cement	0.011
Concrete	0.013
Wood	0.012
Clay	0.013
Masonry	0.025
Rock cuts	0.035
Clean natural stream	0.03
Natural stream with gravel	0.04

It is of interest to assess if Eq. (3.17) permits a reasonable estimate for  $n$  with  $f$  given by Eq. (3.15). An empirical equation used to estimate  $n$  as function of  $k_s$  is (Jaeger 1956; Chaudhry 2008)

$$n = \frac{k_s^{1/6}}{21.1}. \quad (\text{SI}) \quad (3.18)$$

Fenton (2010) took Eq. (3.18) as reference and conducted the corresponding comparison, concluding that agreement between Eqs. (3.15)–(3.17) and Eq. (3.18) results if the coefficient 21.1 in Eq. (3.18) is reduced by 10–20%. Chaudhry (2008) quoted for computing  $n$  as function of  $k_s$  the formula

$$n = \frac{k_s^{1/6}}{8.25g^{1/2}}, \quad (\text{SI}) \quad (3.19)$$

which is considered here. Inserting Eqs. (3.19) into (3.17) yields

$$\frac{gn^2}{R_h^{1/3}} = \frac{f}{8} = \frac{g^{4/3}\varepsilon^{1/3}}{8.25^2 g} \approx 0.0233\varepsilon^{1/3}. \quad (3.20)$$

This is compared in Fig. 3.2 with Eq. (3.13) for the fully rough flow, rewritten as

$$\frac{gn^2}{R_h^{1/3}} = \frac{1}{8}f = \frac{1}{32} \left[ -\log_{10} \left( \frac{1}{3}\varepsilon \right) \right]^{-2}. \quad (3.21)$$

Both equations reasonably agree, as observed in Fig. 3.2. From a theoretical viewpoint, a drawback of using Manning's  $n$  is its non-homogeneous form. Units are  $L^{-1/3}T$  in SI, with the temporal dimension due to the absence of  $g$  in Eq. (3.16). A time dimension in a resistance coefficient lacks a physical meaning, because the measure of surface roughness must be the same irrespective of the gravity field, e.g., a surface has the same roughness on the Earth and on the Moon (Yen 1991). Yen (1991, 2002) offered a smart remedy defining a Manning's coefficient  $n'$  given by

$$n' = ng^{1/2}. \quad (3.22)$$

Manning's equation is thus simply rewritten as

$$S_f = \frac{n'^2 U^2}{g R_h^{4/3}}. \quad (3.23)$$

The unit of  $n'$  is  $L^{1/6}$  in SI, which is reasonable for the measure of a roughness; it is only related in this way to the dimension length. Note that Eq. (3.22) is implicit in the empirical Eq. (3.19), which relates  $n'$  to  $k_s^{1/6}$ , with  $k_s$  as a physical-based quantity. It permits to write Eq. (3.23) as (Chaudhry 2008)

$$U = 8.25 \frac{g^{1/2}}{k_s^{1/6}} S_f^{1/2} R_h^{4/3}. \quad (3.24)$$

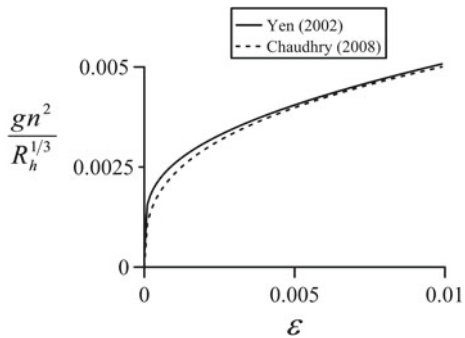
Equation (3.24) is a modified Manning equation suitable for river flows simply replacing  $k_s$  by a mean particle diameter of the bed surface layer.

### 3.3.3 Uniform Flow Depth

In this section, the computation of the normal depth will be presented using Manning's equation with a constant value of  $n$ . Similar computations are accomplished by adopting the Darcy–Weisbach equation or a variable  $n$  with flow depth resorting to Eq. (3.17). Inserting the continuity equation  $Q = UA$  into Eq. (3.16) produces, with  $S_f = S_o$ ,

$$Q = \frac{S_o^{1/2}}{n} A R_h^{2/3}. \quad (3.25)$$

**Fig. 3.2** Dimensionless Manning coefficient as a function of relative roughness



Rewriting Eq. (3.25) as

$$\frac{nQ}{S_o^{1/2}} = AR_h^{2/3}, \quad (3.26)$$

one can define the root-finding problem as

$$f(h) = A(h)[R_h(h)]^{2/3} - \frac{nQ}{S_o^{1/2}} \equiv 0. \quad (3.27)$$

Therefore, for a given channel shape and values of  $Q$ ,  $n$  and  $S_o$ , the flow depth by which  $f(h) = 0$  in Eq. (3.27) is the uniform flow depth  $h_N$ . The computation must be conducted using numerical methods. Given a known value of  $h$  at iteration “ $k$ ” for which  $f(h^k) \neq 0$ , a better approximation to the root of Eq. (3.27) is given by the Newton–Raphson iterative formula (Hoffman 2001; Jeppson 2011)

$$h^{k+1} = h^k - \frac{f^k}{(df/dh)^k}. \quad (3.28)$$

The derivative needed in Eq. (3.28) is

$$\frac{df}{dh} = \frac{d}{dh} \left( AR_h^{2/3} \right) = R_h^{2/3} \frac{dA}{dh} + \frac{2}{3} AR_h^{-1/3} \frac{dR}{dh}, \quad (3.29)$$

or, after some manipulation, noting that  $B = dA/dh$  and  $R = A/p$ ,

$$\frac{df}{dh} = AR_h^{2/3} \left( \frac{5B}{3A} - \frac{2}{3p} \frac{dp}{dh} \right). \quad (3.30)$$

Equation (3.28) is applied recursively until the difference between two successive approximations is down to a prescribed tolerance  $\epsilon \approx 10^{-6}$ , e.g.,

$$\left| \frac{h^{k+1} - h^k}{h^k} \right| \leq 10^{-6}. \quad (3.31)$$

As a practical example, consider uniform flow in a prismatic channel of symmetrical trapezoidal cross-section (Fig. 3.3). The flow area  $A$ , free surface width  $B$ , wetted perimeter  $p$ , side slope  $1:z$ , and hydraulic radius  $R_h$  are

$$\begin{aligned} A &= bh + zh^2, \\ B &= b + 2zh, \\ p &= b + 2h(1 + z^2)^{1/2}, \\ R_h &= \frac{A}{p}. \end{aligned} \quad (3.32)$$



**Ven Te Chow** was born on 14 August, 1919, at Hangchow, China, passing away aged 62 years on 30 July, 1981, at Urbana IL, USA. He was educated at the National Chiao Tung University, Hsingchu, Taiwan, from where he received in 1946 his B.S. degree. In 1948, he graduated from Penn State University with an M.S., and in 1950 obtained his Ph.D. degree from the University of Illinois. He was there until 1955 assistant professor, until 1958 associate professor when being appointed professor of hydraulic engineering. Chow was closely related to international congresses of the International Association of Hydraulic Research IAHR, of Hydrological Sciences IAHS, and the Intl. Union of Geodesy and Geophysics IUGG. He was the editor of the series *Advances in Hydroscience* of which a total of 14 books were published until 1986. He was also the founder and first editor of *Water International*. He was elected in 1975 to Academia Sinica, the highest honor offered to a scholar in China. He was a founder and the first president of the International Water Resources Association (IWRA).

Chow was internationally known for his contributions to the sciences of hydrology and water resources development. In the 1950s, Chow's main activity was a thorough development of hydraulics, mainly by his 1955 paper on backwater curves, but particularly by his outstanding 1959 hydraulics book. This work summarizes all aspects of hydraulics just when the computer age began. It reads superbly because of conciseness, excellence, and up-to-date information in all aspects of open channel flow. It may be considered one of the masterpieces in hydraulics through the ages. Chow added in 1964 with the Handbook of applied hydrology substantially to the science of hydrology and was editor of the Journal of Hydrology since 1969.

To apply Eq. (3.28), a plausible initial value of  $h_N$  is required. Assuming a wide rectangular channel ( $z = 0$ ) of width  $b$  ( $R_h \approx h$ ), Eq. (3.26) yields the following initial guess for the normal depth

$$h^{k=0} = \left( \frac{Qn}{bS_o^{1/2}} \right)^{3/5}. \quad (3.33)$$

The wetted perimeter derivative needed to apply Eq. (3.30) for the trapezoidal section is

$$\frac{dp}{dh} = 2(1+z^2)^{1/2}. \quad (3.34)$$

A code with this scheme implemented is on the file “*normaldepth\_NR\_Manning.xls*”, in Chap. 12. For a channel of base width  $b = 2$  m, slope  $z = 5$ ,  $n = 0.015$   $\text{sm}^{-1/3}$ ,  $S_o = 0.001$  and  $Q = 15 \text{ m}^3/\text{s}$ , the program yields  $h_N = 1.181 \text{ m}$  after four iterations.

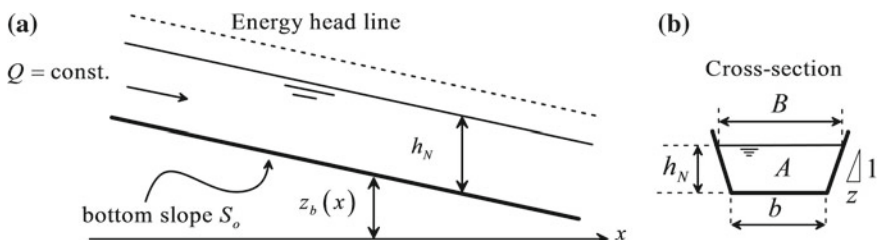


**Fig. 3.3** Uniform flow in trapezoidal channel **a** streamwise profile, **b** transverse section

## 3.4 Flow Profiles in Prismatic Channels

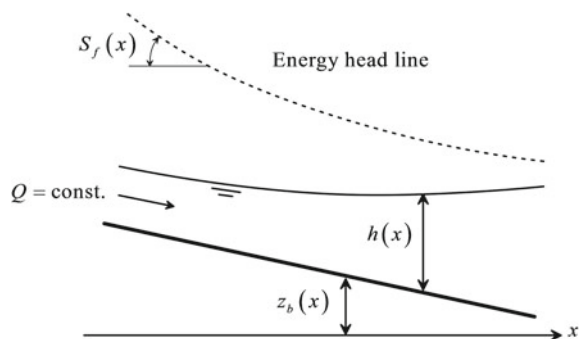
### 3.4.1 Qualitative Analysis

In gradually-varied flows (GVF), the water surface profiles are determined by solving the first-order ODE Eq. (3.3) (Bakhmeteff 1912, 1932; Woodward and Posey 1941; Chow 1959; Henderson 1966). The typical solution is  $h = h(x)$ , i.e., a weak evolution of the flow depth along the  $x$ -spatial coordinate (Fig. 3.4). Given that the flow is steady and discharge is constant, the velocity is computed using the flow area  $A$  as  $U = Q/A$  once the water surface position is determined. This information is of paramount relevance to understand the operation of rivers and canals. Note that the velocity is assumed constant within the cross-section, equal to its average value  $U$ . Further, streamline curvature is weak and the bottom slope small, so that the vertical water depth equals the bottom pressure head. Due to the variation of both  $h$  and  $U$  with  $x$ , all other relevant hydraulic quantities experience a space variation, as for example, the friction slope  $S_f$ , which is no more equal to the bottom slope  $S_o$  as for uniform flow.

While it should be possible to directly numerically solve Eq. (3.3), it is advisable to first analyze the nature of the solutions. This is known as *qualitative analysis*, while the numerical computation corresponds to a *quantitative analysis* (Subramanya 1986; Jain 2001; Sturm 2001). In the qualitative analysis, we intend to depict all possible variations of the flow profile for the case of constant discharge in prismatic channels. One of the strongest reasons to conduct a qualitative analysis is that the fundamental concepts of GVF emerge from it, and these could pass unnoticed to the student by conducting a direct numerical integration. In fact, the qualitative analysis provides the necessary tools to critically assess the results of a numerical integration method, to be presented.

Before entering deeper into the problem, the fundamental concepts are rescued. The normal depth  $h_N$  is defined by the following implicit equation, assuming Manning's equation to quantify flow resistance effects,

**Fig. 3.4** Gradually-varied flow in open channels



$$Q - \frac{S_o^{1/2}}{n} A R_h^{2/3} = 0 \Rightarrow h(x) \equiv h_N \Rightarrow S_o = S_f. \quad (3.35)$$

Given that the channel is prismatic, the normal depth is represented by a straight line parallel to the bed along the channel, called normal depth line (NDL).

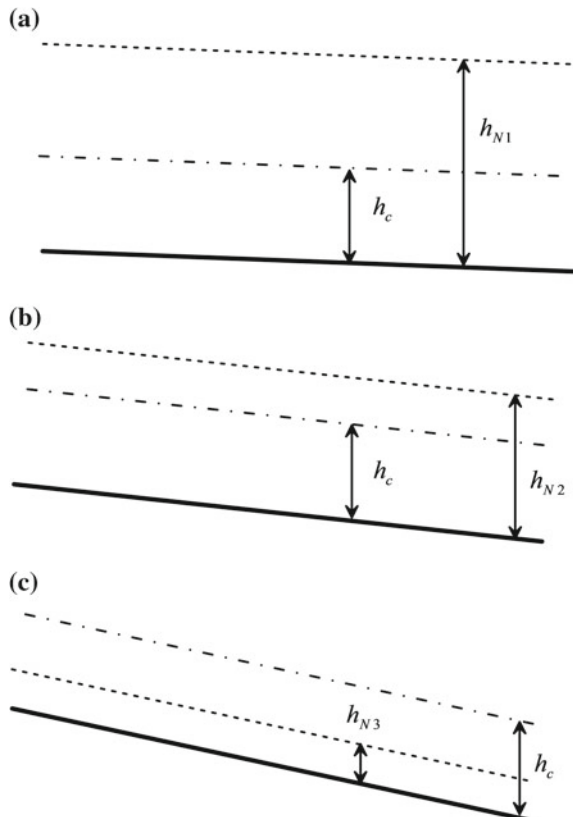
Further, the critical depth  $h_c$  is determined by the implicit equation (Chap. 2)

$$Q^2 - g \frac{A^3}{B} = 0 \Rightarrow h(x) \equiv h_c \Rightarrow F = 1. \quad (3.36)$$

Similar arguments reveal that the critical depth is also a constant along a prismatic channel. If we plot the critical depth in the channel, it is represented by a straight line parallel to the bed, referred to as the critical depth line (CDL).

As an example, the NDL and CDL are plotted in Fig. 3.5 for a channel with constant  $Q$  for different values of the bottom slope. As the critical depth is independent of the bottom slope, in the absence of cross-section variations, it remains

**Fig. 3.5** Normal and critical depth lines in a channel of constant discharge  $Q$  for three different values of the bottom slope  $S_{o1} < S_{o2} < S_{o3}$  [adapted from Puertas and Sánchez (2001)]



unchanged. Note that for the cases (a) and (b), the normal depth is above the critical depth, but for case (c), the bottom slope is large, so that the normal depth is below the critical depth. This suggests that there is a particular value of the bottom slope for which the normal depth exactly equals the critical depth. This value is called critical slope  $S_c$ ; it is determined as follows. The normal depth equation is

$$S_o = \frac{n^2 Q^2}{A^2 R_h^{4/3}}. \quad (3.37)$$

Inserting the critical flow condition  $F = 1$  produces

$$S_c = \frac{n^2 \left( g \frac{A^3}{B} \right)}{A^2 R_h^{4/3}} = \frac{n^2 g \frac{A}{B}}{R_h^{4/3}}. \quad (3.38)$$

Note that the critical slope is determined by  $n$ , the cross-sectional geometry, and the flow depth  $h_N = h_c$ . As  $h_c$  is a function of  $Q$ ,  $S_c$  is also variable with it. However, the critical slope  $S_c$  is independent of the actual bottom slope. The following classification is therefore feasible:

Mild slope (M):  $S_o < S_c$ ;  $h_N > h_c$

Steep slope (S)<sup>1</sup>:  $S_o > S_c$ ;  $h_N < h_c$

Critical slope (C):  $S_o = S_c$ ;  $h_N = h_c$

Horizontal slope (H):  $S_o = 0$ ;  $h_N \rightarrow \infty$

Adverse slope (A):  $S_o < 0$ ;  $h_N$  without physical meaning.

For classification purposes, the flow region is divided into three zones determined by the CDL and NDL (Fig. 3.6). The letters of each slope will be combined with the numbers of the three zones to classify the possible flow profiles.

The first step in the qualitative analysis is to determine if the flow profile increases ( $dh/dx > 0$ ) or decreases ( $dh/dx < 0$ ) in the flow direction. This task is accomplished by studying the signs of the numerator ( $S_o - S_f$ ) and denominator ( $1 - F^2$ ) of Eq. (3.3), which vary depending on the flow zone (1, 2, 3). If  $h > h_N$ , then  $U < U_N$  and thus friction losses are less than for uniform flow, e.g.,  $S_f < S_o$ . Likewise, if  $h < h_N$ , then  $S_f > S_o$ . As to the flow regime, if  $h > h_c$ , then  $F < 1$  and the flow is subcritical. For  $h < h_c$ , the flow is supercritical with  $F > 1$ .

As an example, consider the flow profile in zone 1 ( $h > h_N > h_c$ ) for a mild sloping channel ( $h_N > h_c$ ) (Fig. 3.7). Given that  $h > h_N$ , one gets  $S_f < S_o$ . Further, the flow is subcritical  $F < 1$ . The sign of the GVF equation is thus

---

<sup>1</sup>In the present context, a steep slope implies that the normal depth is below the critical depth. However, a steep slope as used here shall be “mild” physically, that is,  $1 + S_o^2 \approx 1$ . Otherwise slope corrections are necessary in the GVF Eq. (3.3) [see Chap. 1, Eq. (1.151)]. A steep slope in hydraulic structures implies that  $1 + S_o^2 > 1$ , to be discussed at the end of this chapter.

**Fig. 3.6** Flow zones to analyze gradually-varied flow profiles

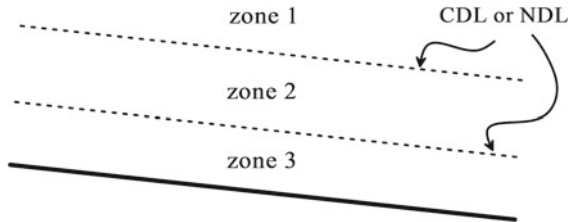
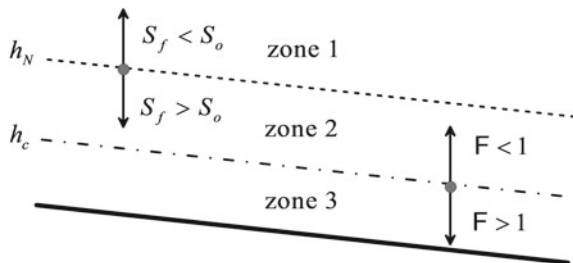


**Fig. 3.7** Flow zones in mild sloping channels [adapted from Puertas and Sánchez (2001)]



$$\frac{dh}{dx} = \frac{S_o - S_f}{1 - F^2} = \frac{+}{+} = +. \quad (3.39)$$

The M1 type flow curve thus increases in the flow direction. Following the same methodology, all the possible M-type flow profiles are summarized in Table 3.3. The column  $dE/dx = S_o - S_f$  indicates the profiles with either an increase or decrease of the specific energy.

**Table 3.3** Classification of GVF profiles

Slope	Zone	Profile	Depths	$S_o - S_f$	$1 - F^2$	$dh/dx$
Mild	1	M1	$h > h_N > h_c$	+	+	+
	2	M2	$h_N > h > h_c$	-	+	-
	3	M3	$h_N > h_c > h$	-	-	+
Steep	1	S1	$h > h_c > h_N$	+	+	+
	2	S2	$h_c > h > h_N$	+	-	-
	3	S3	$h_c > h_N > h$	-	-	+
Critical	1	C1	$h > h_N = h_c$	+	+	+
	3	C3	$h_N = h_c > h$	-	-	+
Horizontal	2	H2	$h > h_c$	-	+	-
	3	H3	$h_c > h$	-	-	+
Adverse	2	A2	$h > h_c$	-	+	-
	3	A3	$h_c > h$	-	-	+

Adapted from Montes (1998)

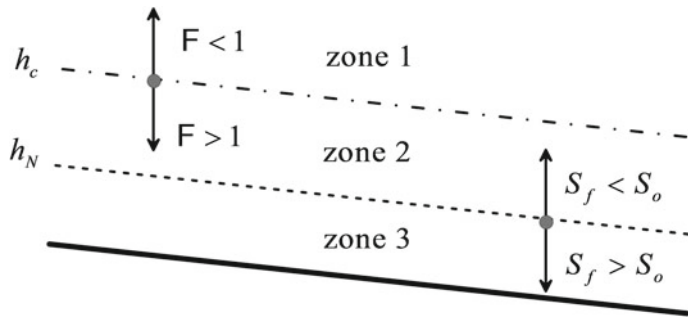


**Fig. 3.8** Flow zones in steep sloping channels [adapted from Puertas and Sánchez (2001)]

For the steep slope channels, the flow zones are presented in Fig. 3.8 following the same methodology. As example, the supercritical ( $F > 1$ ) flow in zone 2 ( $h_c > h > h_N$ ) has  $S_f < S_o$ , resulting in  $dh/dx < 0$ , that is, the S2 curve is decreasing in the flow direction. Following the same procedure, a classification of the remaining S-type flow profiles entails no difficulty; all the possible profiles are summarized in Table 3.3, including the critical, horizontal, and adverse flow profiles.

To plot the water surface profile, it is necessary not only to know the sign of  $dh/dx$  in the flow zone, but also the tendency of the water surface profile toward the reach boundaries (Jain 2001; Chaudhry 2008). The following trends prevail as the flow depth approaches the critical depth, normal depth, or becomes very large:

$$\begin{aligned} h \rightarrow h_c &\Rightarrow \frac{dh}{dx} \rightarrow \infty \quad \text{if } S_o \neq S_f, \\ h \rightarrow h_N &\Rightarrow \frac{dh}{dx} \rightarrow 0 \quad \text{if } F \neq 1, \\ h \rightarrow \infty &\Rightarrow \frac{dh}{dx} \rightarrow S_o. \end{aligned} \tag{3.40}$$

As the flow approaches the critical depth, the water surface slope becomes vertical. It simply implies that the critical depth is not a mathematical solution of GVF in prismatic channels, whereas it is for non-prismatic channels of variable slope, to be discussed in Chap. 4. As the flow approaches the normal depth, the profile tends to the NDL, e.g., the normal depth is an asymptotic value only. As the flow depth becomes very large, the velocity tends to zero, as do both  $S_f$  and  $F$ . It implies that the flow depth gradient equals  $S_o$ , i.e., the flow surface is horizontal,  $d(h + z_b)/dx = 0$  (remember that  $S_o = -dz_b/dx$ ).

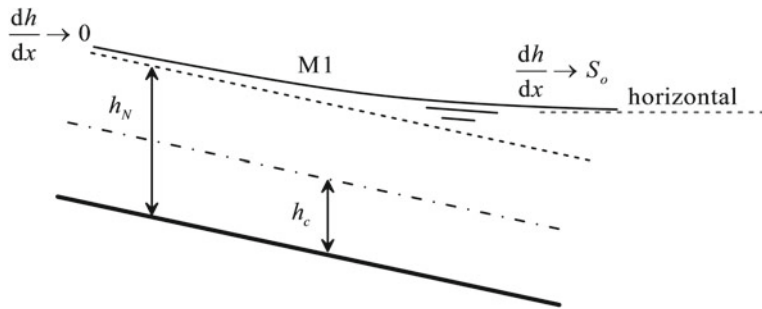
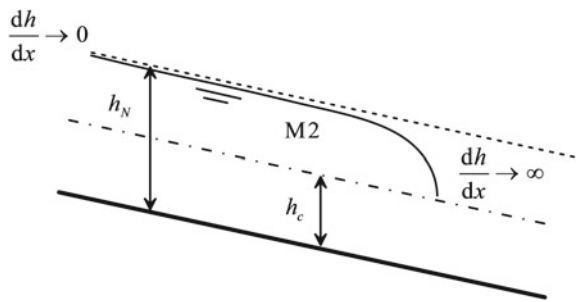


**Fig. 3.9** M1 water surface profile

**Fig. 3.10** M2 water surface profile



Consider now the M1 type water surface profile. An ascending free surface profile in zone 1 must approach to the left the uniform flow depth, and to the right produce large water depths. From Eq. (3.40), the flow profile approaches in the upstream direction asymptotically the uniform flow depth, and to the right it has a horizontal asymptote (Fig. 3.9). For the M2 water surface profile, there is a trend to uniform flow to the left, and to critical depth to the right, given that  $dh/dx < 0$ . The corresponding flow profile is sketched in Fig. 3.10.

For the S2 curve in a steep slope, the flow starts close to the critical depth and gradually approaches the uniform flow (Fig. 3.11).

Following the same methodology and combining the cases of Table 3.3 with Eqs. (3.40), all possible free surface profiles are presented in Fig. 3.12. Several real-life cases are presented in Fig. 3.13 following Chow (1959).

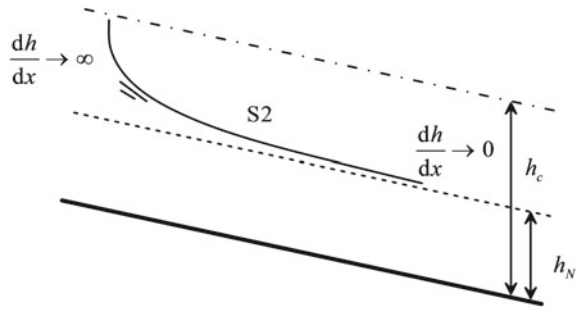


**Fig. 3.11** S2 water surface profile

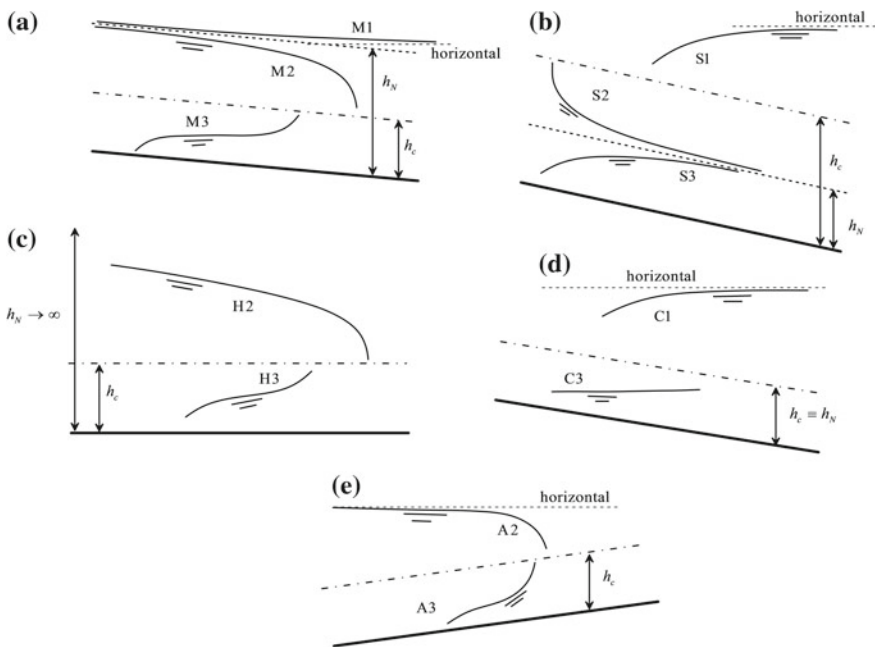


**Fig. 3.12** Flow profiles in **a** mild, **b** steep, **c** horizontal, **d** critical, and **e** adverse slopes

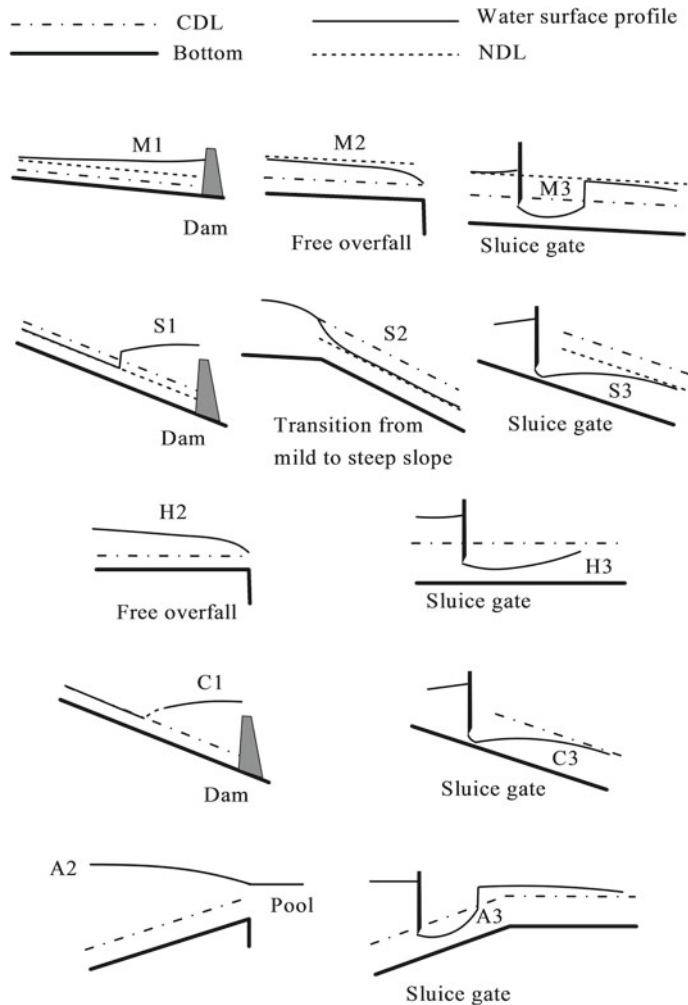


**Fig. 3.13** Real-life cases of water surface profiles [adapted from Chow (1959)]



**Danny Lee Fread** was born on 17 July, 1938, at Tuscola IL, passing away aged 70 years on 5 February, 2009, at Huntington PA, USA. He worked a plethora of jobs to pay his way through his Liberal Arts and Engineering degrees from Carthage College, Kenosha WI, and the University of Missouri-Rolla, Rolla MO. After working for Texaco, he returned to his Alma Mater to continue his education, receiving the Ph.D. degree in civil engineering in 1971. He joined the Office of Hydrology at the National Weather Service then in Silver Spring MD as a research hydrologist. Inspired by the tragedy of the failure of Grand Teton Dam in 1972, his research focused on developing computer models to forecast the flow of flooding rivers and dam failures. His computer models were used around the globe. Fread received national awards for his work, including the Department of Commerce Gold Medal, the Huber Research Prize from the American Society of Civil Engineers ASCE, its 1976 J. C. Stevens Award, and the Association of State Dam Safety Officials National Award of Merit. He also was a Fellow of the American Meteorological Society. He ended his career as Director of the Office of Hydrology. Following his retirement, he moved with his wife to Pennsylvania to be near their daughter and family.

The 1973 ASCE paper presents a conceptual model to alleviate flood damages due to overtopping failures of future small earthfill dams including the erosion pattern. The potential reduction in the reservoir release due to the proposed erosion-retarding layer is also investigated. A method to determine the optimum layer location is provided to minimize the maximum possible reservoir release due to a gradually-breached earth dam. The transient reservoir flow is simulated by a numerical model based on the solution of the one-dimensional Saint-Venant equations, solved by the method of characteristics subjected to appropriate boundary conditions. The numerical simulation provides the reduction in release discharge in terms of various parameters.

### 3.4.2 Sketching of Flow Profiles

In general, a real channel presents reaches of different lengths, slopes, sections, and roughness. The actual free surface profile will be a composite surface assembling some of the elementary profiles depicted in Fig. 3.12. Before computing profiles numerically, the sketching process is as follows (Chow 1959; Jain 2001; Chaudhry 2008):

1. Plot the bottom profile (use distorted scale in the vertical) and assign roughness values to each reach.
2. Compute  $h_N$  for each channel reach using Eq. (3.35) and plot the NDL.
3. Compute  $h_c$  for each channel reach using Eq. (3.36) and plot the CDL.
4. Locate all possible control sections, namely a critical depth control (CDC), normal depth control (NDC), and artificial channel control (ACC) (e.g., a weir or a gate). In a CDC, the flow is subcritical upstream and supercritical downstream. The probable position of a NDC is upstream of the reach in subcritical flow and downstream of the reach in supercritical flow. A NDC is an asymptotic state. In an ACC, the flow is subcritical upstream of it and supercritical downstream.
5. Starting at each control section, draw sub- and supercritical profiles in the up- and downstream directions, respectively. Check possible interactions of control sections.
6. If the flow is supercritical upstream of the reach and subcritical downstream, a hydraulic jump may form within the reach. The jump may also not be formed, resulting in fully sub- or supercritical flow along the reach. The position of the jump can be plotted tentatively, though its formation will be discussed in depth in Chap. 4.

As an example, two illustrative cases presented by Subramanya (1986) are plotted in Fig. 3.14. In case (a), the three slopes of the channel are mild. Note that the values of the NDL for each reach are above the CDL. The gate on the reach c–e is an ACC that produces subcritical flow upstream and supercritical flow downstream. At the free overfall (section e), the critical depth is attained at a distance of three to four times  $h_c$  from the brink section (Rouse 1938). Given that this distance is small, the critical depth control section is assumed to be established just at the brink in GVF computations. Thus, the brink section is a control section interacting with the vena contracta section (point d), which is the control section induced by the gate. From the vena contracta, a supercritical M3 profile develops, whereas the brink section will force a subcritical M2 profile. To have compatibility of both profiles, a hydraulic jump is formed within the reach. Cases where the gate is drowned or the jump rejected out of the reach will be discussed in Chap. 4. At point c, the flow is subcritical as forced by the gate. Starting at this point, a M1 subcritical profile is formed in the reach b–c. If this reach is long, as assumed here, the normal depth will be asymptotically approached and established at point b. From point b, an M2 profile is formed up to the upstream section a.

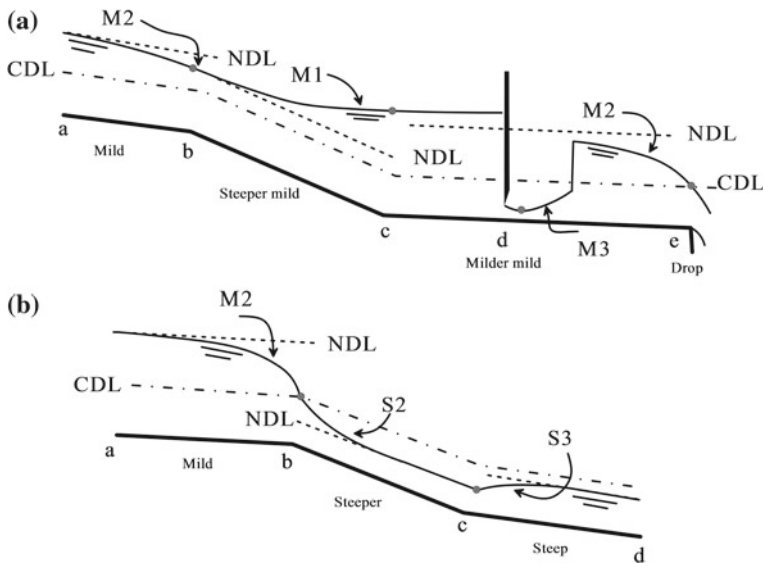


**Fig. 3.14** Examples of GVF profiles with various controls [adapted from Subramanya (1986)]

In case (b), a mild slope is followed by two steep slopes. Note again the values of the NDL as compared with the CDL. In the absence of any other control, it is assumed that the normal depth (NDC) is established upstream in reach a–b, and downstream in reach b–c. As the flow in the mild slope reach is subcritical, and supercritical on the steep slope, a CDC is established, in this case just at the slope break (point b). The flow profile upstream of b is therefore an M2 profile, whereas downstream of it, an S2 profile develops. At point c, a NDC was assumed, so that an S3 profile is formed within reach c–d.

### 3.4.3 Flow Profile for Unknown Discharge

The sketching methodology for the free surface profile previously explained is based on the assumption of known discharge. However, sometimes, the discharge is unknown and must be determined as part of the solution itself. The case of a channel releasing water from a reservoir is an example (Fig. 3.15). Consider a constant slope channel of rectangular cross-section of width  $b$ . The basic known magnitude is the water surface elevation at the reservoir. If the elevation of the channel invert intake is known, then the water depth at the channel inlet  $H$  is available. In the forthcoming analysis, the velocity head in the reservoir and the intake entrance losses are neglected.

The problem is thus to determine the discharge  $Q$  released from the reservoir by the channel. As the discharge is unknown, it is not possible to compute  $h_N$  and  $h_c$ ,

which are needed to determine the type of control section of the flow profile. Thus, the solution must be conducted by iteration. Assume first that the channel is steep (Fig. 3.15a). In this case, the critical depth is given by

$$h_c = \frac{2}{3}H, \quad (3.41)$$

which is established at the channel inlet, with the released discharge given by

$$Q = b \left( \frac{2}{3} \right)^{3/2} (gH^3)^{1/2}. \quad (3.42)$$

Now, the steep slope assumption shall be checked. Therefore, the critical slope  $S_c$  is computed by resorting to Eq. (3.38), and compared to the channel slope  $S_o$ . If  $S_o > S_c$ , then the initial assumption is correct, the channel is thus steep and computations are finished. The normal depth is not needed to compute  $Q$ , but it can be determined from Manning's equation to have the complete solution to the flow conditions. If  $S_o < S_c$ , the channel is not steep, and computations need to be reconsidered. For a mild slope channel (Fig. 3.15b), uniform flow is established assuming that the channel is long. In this case, a normal depth control governs the channel intake, resulting in the energy equation

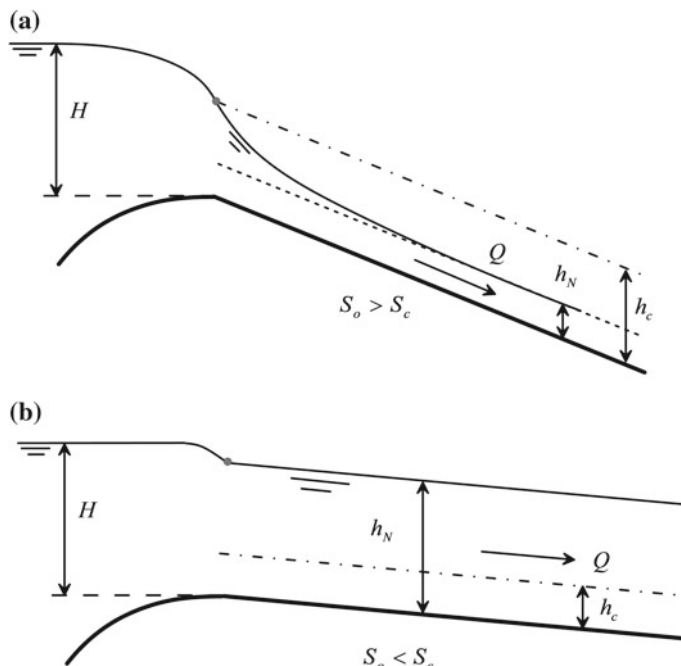


**Fig. 3.15** Discharge released from a reservoir for **a** mild and **b** steep slope channels

$$H = h_N + \frac{Q^2}{2gb^2h_N^2}. \quad (3.43)$$

Using Manning's equation to evaluate  $Q$ , Eq. (3.43) is rewritten as

$$H = h_N + \frac{S_o}{2gn^2}R_h^{4/3} = h_N + \frac{S_o}{2gn^2} \left( \frac{bh_N}{b+2h_N} \right)^{4/3}. \quad (3.44)$$

This is a nonlinear implicit equation to be solved iteratively to determine  $h_N$ , for example, by using the Newton–Raphson method. Once this task is accomplished, the discharge is

$$Q = \frac{S_o^{1/2}}{n} AR_h^{2/3} = \frac{S_o^{1/2}}{n} (bh_N) \left( \frac{bh_N}{b+2h_N} \right)^{2/3}, \quad (3.45)$$

and the critical depth

$$h_c = \left( \frac{Q^2}{gb^2} \right)^{1/3}. \quad (3.46)$$

Resorting to Eq. (3.38), the critical slope  $S_c$  can be updated for the correct discharge  $Q$ . This solution process was implemented in the file *Lake\_discharge.xls* available from Chap. 12. As application example, consider a rectangular channel of  $b = 4$  m,  $n = 0.013$   $\text{sm}^{-1/3}$  releasing water from a reservoir with  $H = 1$  m. For a slope  $S_o = 0.01$ , the program yields  $h_c = (2/3)$  m,  $Q = 6.82 \text{ m}^3/\text{s}$ ,  $h_N = 0.438$  m and  $S_c = 0.00278$ . The channel is therefore steep and the control section is a CDC at the channel inlet (Fig. 3.15a). If the slope is  $S_o = 0.0001$ , a comparison with  $S_c$  shows that the steep slope assumption is incorrect, and computations are conducted again assuming mild slope with a NDC at the inlet. The program then yields the output  $h_c = 0.322$  m,  $Q = 2.289 \text{ m}^3/\text{s}$ ,  $h_N = 0.983$  m and  $S_c = 0.00295$ . Given that  $0.0001 < 0.00295$ , the mild slope assumption is correct.

## 3.5 Computation of Steady Flow Profiles

### 3.5.1 Governing Integral and Differential Equations

The GVF equation is a first-order ODE describing the variation of  $h(x)$ , written as

$$\frac{dh}{dx} = \frac{S_o - S_f}{1 - F^2} = f(h). \quad (3.47)$$

For a prismatic channel  $S_o$  is a constant, whereas both  $S_f$  and  $F$  are functions of  $h$  alone. For GVF computations, the friction slope  $S_f$  is determined from the previously explained formulae for uniform flow. In general, the  $f$  function depends on the cross-sectional shape and the resistance law adopted. The values of  $S_o$ ,  $n$  and  $Q$  are assumed to be known for the solution. Unfortunately, there is not an exact analytical solution of Eq. (3.47), given that  $f$  is a complex nonlinear function, so that numerical methods are necessary.

The GVF equation for non-prismatic channels involving variations in bottom slope and cross-sectional shape is [Eq. (1.107)]

$$\frac{dh}{dx} = \frac{S_o - S_f + \frac{Q^2}{gA^3} \left( \frac{\partial A}{\partial x} \right)_{h=\text{const.}}}{1 - \frac{Q^2}{gA^3} B} = \frac{S_o - S_f + \frac{F^2}{B} \left( \frac{\partial A}{\partial x} \right)_{h=\text{const.}}}{1 - F^2}, \quad (3.48)$$

which is rewritten as

$$\frac{dh}{dx} = f(x, h). \quad (3.49)$$

For the sake of generality in the presentation of numerical methods, consider Eq. (3.49) despite our function will be  $f = f(h)$  for prismatic channels. As Eq. (3.49) is a first-order ODE, any numerical method to solve this kind of equation can be adopted in principle. A variety of such techniques will be presented in this chapter.

There is an alternative method, however. Equation (3.49) is the differential form of the energy (or momentum) equation in GVF. It is thus possible to use an integral rather than a differential equation. The energy equation in integral form reads [Eq. (2.11)]

$$E_2 - E_1 = \int_{x_1}^{x_2} (S_o - S_e) dx, \quad (3.50)$$

where the specific energy is  $E = h + Q^2/(2gA^2)$ . Equation (3.50) is applicable to prismatic and non-prismatic channels. For a constant slope reach, Eq. (3.50) produces

$$E_2 = E_1 + S_o(x_2 - x_1) - \int_{x_1}^{x_2} S_e dx. \quad (3.51)$$

To apply Eq. (3.51), the integral of the gradient of dissipated energy (or energy slope) is numerically approximated. Techniques to solve Eq. (3.49) or its integral form, Eq. (3.50), will be presented in the next sections.

### 3.5.2 Boundary Condition

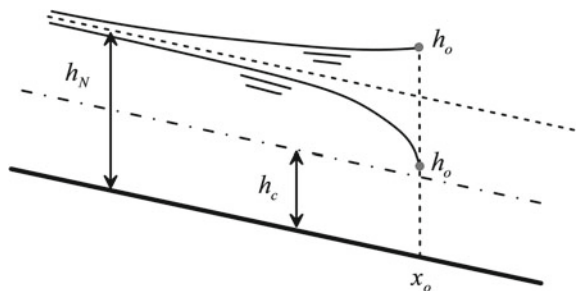
The GVF equation is a first-order ODE subject to a boundary condition  $h(x = x_o) = h_o$ , e.g., a position where the flow depth is known for a given discharge  $Q$ , i.e., (Fig. 3.16)

$$\frac{dh}{dx} = f(x, h), \quad (3.52)$$

$$h(x = x_o) = h_o.$$

The boundary condition is usually a control section, corresponding to a section where the function  $h = h(Q)$  is available. Typical control sections in open channel flow are a critical flow section, a uniform flow section, or an artificial channel control, as a weir or a gate. Once the control section is identified, and  $h_o$  determined for  $Q$ , the nature of the control section determines the direction of integration of Eq. (3.49), as briefly outlined while explaining the sketching process. The usual case is to integrate a subcritical flow profile in the upstream direction, and a supercritical flow profile in the downstream direction, as will be discussed. It should be remarked that Eq. (3.49) is simply an ODE which can be integrated into both the up- and downstream directions regardless of the value of  $F$  (Apelt 1971). However, numerical errors are sensitive to the integration direction and care should be taken (Fread and Harbaugh 1971; Jain 2001). The direction of integration is simply marked by the position of the control section that is usually known in practice. We illustrate this point by taking the critical flow section as an example. Consider the transition from a mild to a steep slope (Fig. 3.17). The critical depth is a constant, but there are two different normal depths, one for each value of the slope such that  $h_{N2} > h_c > h_{N1}$ . The flow tends asymptotically to uniform flow far upstream and downstream from the slope transition, namely for  $x \rightarrow \pm \infty$ . To pass from the upstream uniform subcritical flow to the downstream uniform supercritical flow, a varied flow profile is formed crossing eventually the critical depth. While in the vicinity of the slope break the flow is curvilinear and the critical depth is formed upstream of the break at a distance close to  $3h_c$  (Rouse 1938), this non-hydrostatic transition is short and the critical section is taken at the slope break for GVF

**Fig. 3.16** Boundary condition to solve the GVF equation



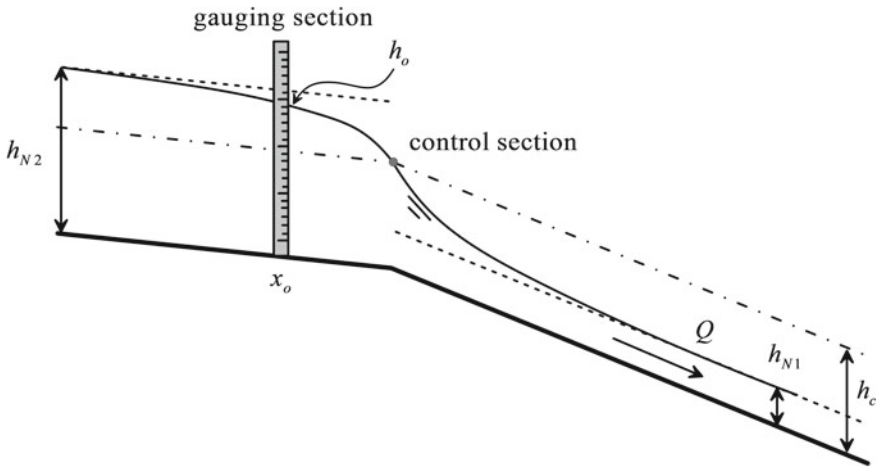


**Fig. 3.17** Control and gauging sections in transition from mild to steep slope

computations. The critical flow section is thus a channel control producing upstream subcritical flow and downstream supercritical flow. Therefore, the directions of integration are in the up- and downstream directions for the sub- and supercritical profiles, respectively, starting at a CDC. Note that at the critical depth  $dh/dx \rightarrow \infty$ . Therefore, the CDC is taken in practice as

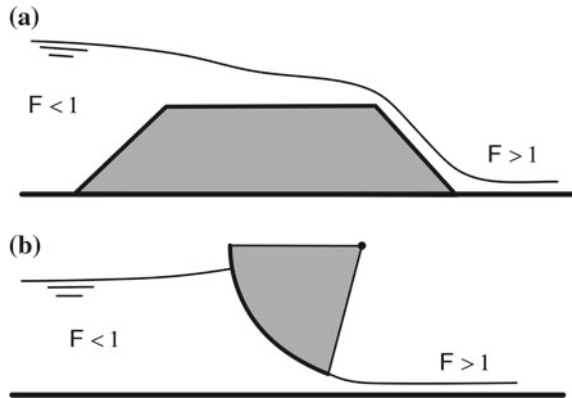
$$h(x = x_o) = h_c \pm \varepsilon, \quad (3.53)$$

where  $\varepsilon$  is a small number. The inverse transition from super- to subcritical flow occurs in the form of a hydraulic jump, and thus is not a control section.

From this discussion follows that the “usual” position of the control section is at the downstream end in a subcritical reach. Likewise, the usual position of a control section in a supercritical flow reach is at its upstream end. Accordingly, the GVF computational rule of determining the profiles is in the upstream direction for subcritical flow and in the downstream direction for supercritical flows. This is in agreement with the physical fact that perturbations travel both up- and downstream for subcritical flow, thus being influenced by what occurs at the end of the reach, whereas supercritical flows are only influenced by perturbations induced upstream of the reach. Subcritical flows are thus subject to a downstream control, whereas supercritical flows to an upstream control. This will be further discussed once unsteady flow is introduced in Chap. 5.

Consider now the setup of Fig. 3.17 in a laboratory facility. An experimentalist may take a measurement at the gauging section  $x_o$  and then get a known  $h_o$  for  $Q$ , which is different from the standard control section at the slope break. This section could be used to integrate Eq. (3.49) in the up- and downstream directions, by which a portion of the subcritical profile would be computed in the downstream

**Fig. 3.18** Flow conditions induced by artificial channel controls (ACC) **a** weir, **b** gate



direction. This process is mathematically correct; it can be used instead of the classical rule, if data are available.

A weir or a gate (Fig. 3.18) is an artificial channel control (ACC) producing upstream subcritical flow ( $F < 1$ ) and downstream supercritical flow ( $F > 1$ ). The normal depth is reached asymptotically at the upstream end in a subcritical reach and at the downstream end in a supercritical reach. At the uniform depth  $dh/dx \rightarrow 0$ , so that the NDC is taken in practice with  $\varepsilon$  as a small number as

$$h(x = x_o) = h_N \pm \varepsilon. \quad (3.54)$$

### 3.5.3 Analytical Solution

Analytical solutions to gradually-varied flow problems are rare. A notable exception is the solution due to Bresse (1860) for the wide rectangular channel. In addition to its historical interest, the main purpose of presenting such a solution is that it is exact; therefore, it can be used to examine the accuracy of numerical schemes. Using Chezy's resistance coefficient  $C$ , Eq. (3.3) can be written for the rectangular channel as

$$\frac{dh}{dx} = \frac{S_o - \frac{Q^2}{C^2 A^2 R_h}}{1 - \frac{Q^2}{gA^3} B} = \frac{S_o - \frac{Q^2}{C^2 b^2 h^2 R_h}}{1 - \frac{Q^2}{gb^2 h^3}}. \quad (3.55)$$

Assuming that the channel is very wide, the hydraulic radius is approximated by the flow depth, resulting in the GVF equation

$$\frac{dh}{dx} = \frac{S_o - \frac{Q^2}{C^2 b^2 h^3}}{1 - \frac{Q^2}{g b^2 h^3}} = S_o \frac{1 - \frac{Q^2}{S_o C^2 b^2 h^3}}{1 - \frac{Q^2}{g b^2 h^3}} = S_o \frac{1 - \frac{h_N^3}{h^3}}{1 - \frac{h_c^3}{h^3}}. \quad (3.56)$$

In Eq. (3.56),  $h_N$  and  $h_c$  are the normal and critical depths, given, respectively, by

$$h_N = \left( \frac{Q^2}{S_o C^2 b^2} \right)^{1/3}, \quad (3.57)$$

$$h_c = \left( \frac{Q^2}{g b^2} \right)^{1/3}.$$

Equation (3.56) can be integrated numerically using various methods. However, it has an exact analytical solution, to be used to check the accuracy of any scheme, as already stated. A dimensionless flow depth  $u = h/h_N$  is defined. Inserting it into Eq. (3.56) gives

$$\frac{du}{dx} = \frac{S_o}{h_N} \frac{1 - u^{-3}}{1 - \xi u^{-3}}, \quad (3.58)$$

where  $\xi = (h_c/h_N)^3$ . Separating the variables permits to write

$$\begin{aligned} \frac{S_o}{h_N} dx &= \frac{1 - \xi u^{-3}}{1 - u^{-3}} du = \left( \frac{1}{1 - u^{-3}} - \xi \frac{u^{-3}}{1 - u^{-3}} \right) du \\ &= \left( \frac{u^3}{u^3 - 1} - \xi u^{-3} \frac{u^3}{u^3 - 1} \right) du = \left( \frac{u^3}{u^3 - 1} - \xi \frac{1}{u^3 - 1} \right) du \\ &= \left( 1 + \frac{1}{u^3 - 1} - \xi \frac{1}{u^3 - 1} \right) du = \left( 1 + \frac{1 - \xi}{u^3 - 1} \right) du. \end{aligned} \quad (3.59)$$

Integrating the result produces

$$\int_0^x \frac{S_o}{h_N} dx = \int_0^u \left( 1 + \frac{1 - \xi}{u^3 - 1} \right) du, \quad (3.60)$$

that is,

$$\frac{S_o}{h_N} x = u - (1 - \xi) \int_0^u \frac{1}{1 - u^3} du = u - (1 - \xi) \Phi(u), \quad (3.61)$$

where  $\Phi(u)$  is the integral

$$\Phi(u) = \int_0^u \frac{1}{1-u^3} du. \quad (3.62)$$

Equation (3.61) can be recast in the more usual form

$$x = \frac{h_N}{S_o} \left[ u - \left( 1 - \frac{h_c^3}{h_N^3} \right) \Phi(u) \right], \quad u = \frac{h(x)}{h_N}, \quad (3.63)$$

where  $\Phi(u)$  was first obtained by Bresse (1860, p. 248) as<sup>2</sup>

$$\Phi(u) = \frac{1}{6} \ln \left[ \frac{u^2 + u + 1}{(u - 1)^2} \right] + \frac{1}{3^{1/2}} \tan^{-1} \left( \frac{2u + 1}{3^{1/2}} \right) + C_1, \quad (3.64)$$

or in the alternative form (Bresse 1860, p. 249) quoted by Chow (1959, p. 258) and Jaeger (1956, p. 72)

$$\Phi(u) = \frac{1}{6} \ln \left[ \frac{u^2 + u + 1}{(u - 1)^2} \right] - \frac{1}{3^{1/2}} \cot^{-1} \left( \frac{2u + 1}{3^{1/2}} \right) + C_1. \quad (3.65)$$

The term  $C_1$  in Eq. (3.64) is an arbitrary constant. Equation (3.64) is plotted in Fig. 3.19 for  $C_1 = 0$ . Note the singularity at  $u = 1$ , implying that the uniform flow is not a possible value. The specific value of  $C_1 = 0$  is of no concern, since Eq. (3.63) is applied in practice between two successive sections  $x_{i+1}$  and  $x_i$ , where the flow depths are  $h_{i+1}$  and  $h_i$ , respectively, such that the constant is eliminated, e.g.,

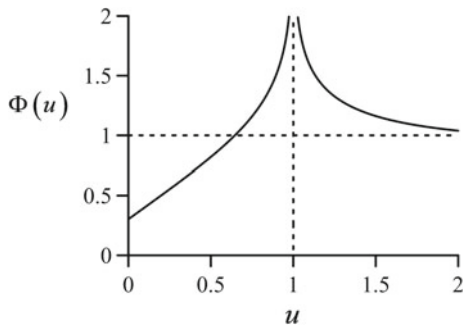
$$x_{i+1} = x_i + \frac{h_N}{S_o} \left[ (u_{i+1} - u_i) - \left( 1 - \frac{h_c^3}{h_N^3} \right) (\Phi_{i+1} - \Phi_i) \right]. \quad (3.66)$$

Applying Eq. (3.66) involves an inverse computation: starting with the known point  $(x_i, h_i)$  an increment in the water depth is defined such that  $h_{i+1} = h_i \pm \Delta h$ . With the known values of normalized water depths  $u_i$  and  $u_{i+1}$ ,  $\Phi(u)$  is evaluated at both points, thereby applying Eq. (3.66) to obtain the coordinate  $x_{i+1}$  where the depth is  $h_{i+1}$ . This process is conducted as many times as

---

<sup>2</sup>The reader is warned that Bresse's solution appeared mistyped in many publications in the form  $\Phi(u) = \frac{1}{6} \ln \left[ \frac{u^2 + u + 1}{(u - 1)^2} \right] - \frac{1}{3^{1/2}} \tan^{-1} \left( \frac{3^{1/2}}{2u + 1} \right) + C_1$ , which is obviously not the solution. Jan (2014, p. 24) detailed the integration process step-by-step. The typo appears to originate from C. J. Posey in Rouse (1950, p. 613).

**Fig. 3.19** Bresse's (1860) function for GVF profiles



desired to get the free surface profile. Note that although the computational sequence looks like a numerical scheme, it is not. The solution is analytical and therefore the value of  $\Delta h$  arbitrary, since Eq. (3.66) is only a relation between two analytical points of the flow profile.

### 3.5.4 Implicit Integral Method

In this section, a numerical method based on the integral form of the energy balance, namely Eq. (3.51), is presented. The technique is called *standard step method* (Chow 1959) and consists in dividing the channel reach into a number of segments with their boundaries located at selected positions, and then solve the algebraic equation for the unknown flow depth at one of the extremes. This technique is widely used in river hydraulics, and it is implemented in program HEC-RAS (Brunner 2016). Here, we follow the presentation by Fread and Harbaugh (1971). Consider a channel reach divided for simplicity's sake into segments of equal length  $\Delta x$  (Fig. 3.20).

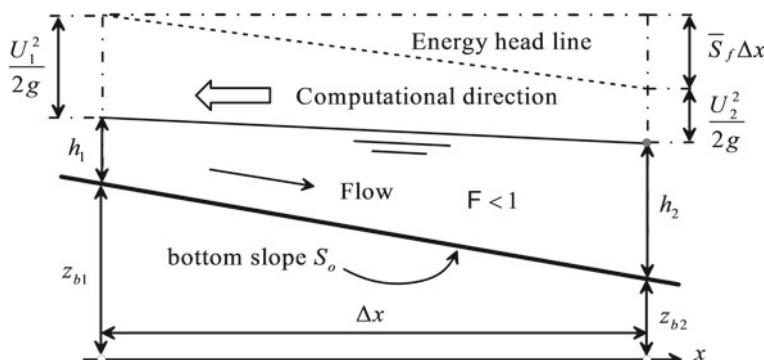


**Fig. 3.20** Energy balance in gradually-varied flow (subcritical flow case)

Using the trapezoidal rule to evaluate the integral of the friction slope, one gets

$$\int_x^{x+\Delta x} S_f dx = \frac{1}{2} (S_{f1} + S_{f2}) \Delta x, \quad (3.67)$$

which permits to write Eq. (3.51) as

$$E_1 = E_2 - S_o \Delta x + \frac{1}{2} (S_{f1} + S_{f2}) \Delta x, \quad (3.68)$$

or, in the alternative form

$$z_{b1} + h_1 + \frac{Q^2}{2gA_1^2} = z_{b2} + h_2 + \frac{Q^2}{2gA_2^2} + \frac{1}{2} (S_{f1} + S_{f2}) \Delta x, \quad (3.69)$$

demonstrating the energy balance between Sections 1 and 2. Other approximations to the average friction slope are discussed by Montes (1998). Consider the case of computing a subcritical flow profile ( $F < 1$ ). The probable location of the control section is downstream of the reach, so flow conditions at point 2 are fully determined by a former computation. Therefore, flow conditions at point 1 are to be determined. The problem consists of solving the nonlinear implicit equation (Fread and Harbaugh 1971)

$$f(h_1) \equiv h_1 + \frac{Q^2}{2gA_1^2} - \frac{\Delta x}{2} \frac{n^2 Q^2}{A_1^2 R_{h1}^{4/3}} + F = 0, \quad (3.70)$$

where Manning's equation was used and  $F$  is the known function

$$F = S_o \Delta x - h_2 - \frac{Q^2}{2gA_2^2} - \frac{\Delta x}{2} \frac{n^2 Q^2}{A_2^2 R_{h2}^{4/3}}. \quad (3.71)$$

The solution of Eq. (3.70) is conducted here using the Newton–Raphson method as

$$h_1^{k+1} = h_1^k - \frac{f^k}{(df/dh_1)^k}, \quad (3.72)$$

with  $k$  as the iteration index. Since  $\Delta x$  is usually small, the initial value of  $h_1$  is taken as  $h_2$ . For the computation of a supercritical flow profile ( $F > 1$ ), the upstream water depth is  $h_2$  and the unknown water depth  $h_1$  is located at the downstream

boundary. The equations presented are thus applied just taking a negative value of  $\Delta x$  to conduct computations in the flow direction.

The derivative needed in Eq. (3.72) is

$$\frac{df}{dh_1} = \frac{d}{dh_1} \left( h_1 + \frac{Q^2}{2gA_1^2} - \frac{\Delta x}{2} \frac{n^2 Q^2}{A_1^2 R_{h1}^{4/3}} + F \right) = \frac{d}{dh_1} \left( E_1 - \frac{1}{2} \Delta x S_{f1} \right). \quad (3.73)$$

The derivative of  $E$  is

$$\frac{dE_1}{dh_1} = 1 - F_1^2 = 1 - B_1 \frac{Q^2}{gA_1^3}, \quad (3.74)$$

and one gets from  $S_{f1}$

$$\begin{aligned} \frac{dS_{f1}}{dh_1} &= \frac{d}{dh_1} \left( \frac{n^2 Q^2}{A_1^2 R_{h1}^{4/3}} \right) = n^2 Q^2 \left( -\frac{2}{A_1^3 R_{h1}^{4/3}} \frac{dA_1}{dh_1} - \frac{4}{3A_1^2 R_{h1}^{1+4/3}} \frac{dR_1}{dh_1} \right) \\ &= \frac{n^2 Q^2}{A_1^2 R_{h1}^{4/3}} \left( -\frac{2B_1}{A_1} - \frac{4}{3R_{h1}} \frac{dR_1}{dh_1} \right) \\ &= S_{f1} \left[ -\frac{2B_1}{A_1} - \frac{4}{3R_{h1}} \left( \frac{1}{p_1} \frac{dA_1}{dh_1} - \frac{A_1}{p_1^2} \frac{dp_1}{dh_1} \right) \right] \\ &= S_{f1} \left[ -\frac{2B_1}{A_1} - \frac{4}{3} \left( \frac{1}{A_1} \frac{dA_1}{dh_1} - \frac{1}{p_1} \frac{dp_1}{dh_1} \right) \right] \\ &= S_{f1} \left( -\frac{10B_1}{3A_1} + \frac{4}{3} \frac{1}{p_1} \frac{dp_1}{dh_1} \right). \end{aligned} \quad (3.75)$$

Inserting Eqs. (3.74) and (3.75) into Eq. (3.73), the final result is

$$\frac{df}{dh_1} = 1 - B_1 \frac{Q^2}{gA_1^3} - \frac{1}{2} \Delta x S_{f1} \left( -\frac{10B_1}{3A_1} + \frac{4}{3} \frac{1}{p_1} \frac{dp_1}{dh_1} \right). \quad (3.76)$$

The method can be used directly in non-prismatic channels with variations of bottom slope and cross-sectional shape. If adequate flow resistance predictors and energy velocity correction coefficients are introduced, it applies even to compound channels (Brunner 2016). It permits also an easy incorporation of form losses.

### 3.5.5 Explicit Integral Method

For convenience, consider again Eq. (3.68), rewritten as

$$E_2 - E_1 = S_o \Delta x - \frac{1}{2} (S_{f1} + S_{f2}) \Delta x. \quad (3.77)$$

Starting with the known point  $(x_i, h_i)$ , an increment in the water depth is defined such that  $h_{i+1} = h_i \pm \Delta h$ . Assume that  $E = E(h)$  and  $S_f = S_f(h)$  only, i.e., the channel is prismatic. Thus, one can write

$$\Delta x = x_2 - x_1 = \frac{E_2 - E_1}{S_o - \frac{1}{2} (S_{f1} + S_{f2})}. \quad (3.78)$$

From this equation, we can compute the position  $x_2$  where the depth will be  $h_2$ , given that the right-hand side of Eq. (3.78) is only a function of  $h_1$  and  $h_2$ . This method is called *direct step method* and was originally devised by Bélanger (1828). A limitation is that it can only be used for prismatic channels, and that it does not permit to get the solution for the flow depth at selected locations, which is the usual case in practice. Thus, aside from its academic interest, is not a practical method.

### 3.5.6 Euler's Method

For the solution of the GVF-ODE [Eq. (3.49)], the computational domain is divided into a number of reaches of length  $\Delta x$  (Fig. 3.21). If the spatial derivative of the flow depth is discretized using a forward finite-difference

$$\frac{dh}{dx} = \frac{h_{i+1} - h_i}{\Delta x}, \quad (3.79)$$

**Fig. 3.21** Discretization of computational domain for solution of GVF-ODE

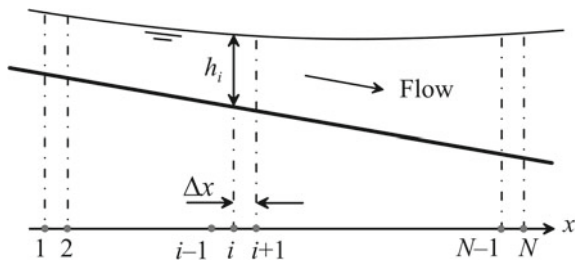
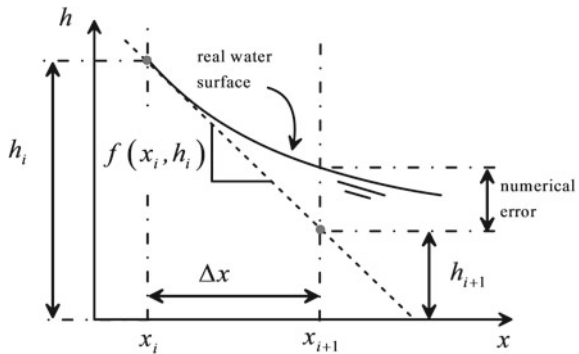


**Fig. 3.22** Sketch of the Euler scheme



the algebraic expression approximating Eq. (3.49) reads (Chaudhry 2008)

$$h_{i+1} = h_i + f(x_i, h_i)\Delta x = h_i + \left( \frac{S_o - S_f}{1 - F^2} \right)_i \Delta x. \quad (3.80)$$

Thus, the flow solution is computed on the basis of the tangent to the known point  $(x_i, h_i)$  (Fig. 3.22). This equation has the advantage of being extremely simple to apply, but the truncation error is  $O(\Delta x^2)$ , and it can destroy the solution if  $\Delta x$  is large. It is noted that we are including in the solution only the terms of power  $\Delta x$  of a Taylor series, e.g.,

$$h_{i+1} = h_i + \left( \frac{dh}{dx} \right)_i \Delta x + \left( \frac{d^2 h}{dx^2} \right)_i \frac{1}{2} (\Delta x)^2 + \left( \frac{d^3 h}{dx^3} \right)_i \frac{1}{6} (\Delta x)^3 + \dots \quad (3.81)$$

The scheme is therefore first-order accurate only. It applies in practice, but extreme care is needed to avoid an unacceptable growth of the numerical error in the solution.

### 3.5.7 Fourth-Order Runge–Kutta Method

The family of Runge–Kutta schemes considers the Taylor series Eq. (3.81), substituting the use of derivatives of order higher than one by more evaluations of the first derivative within the interval. These schemes use an updating explicit formula of type

$$h_{i+1} = h_i + \bar{f} \Delta x, \quad (3.82)$$

where the average value of  $f$  is determined differently, depending on the order of the scheme, and, thus, of the number of terms considered in the Taylor series. A fourth-order scheme yields (Apelt 1971; Chaudhry 2008)

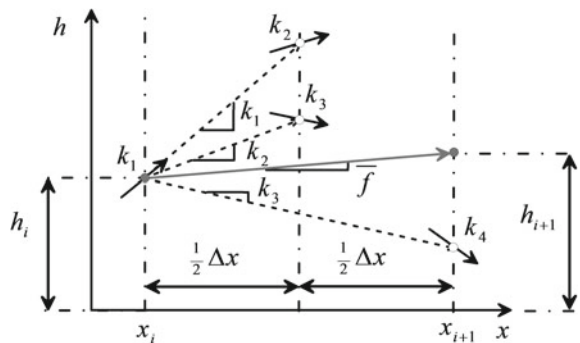
$$\bar{f} = \frac{1}{6}(k_1 + 2k_2 + 2k_3 + k_4), \quad (3.83)$$

with

$$\begin{aligned} k_1 &= f(x_i, h_i), \\ k_2 &= f\left(x_i + \frac{1}{2}\Delta x, h_i + \frac{1}{2}k_1\Delta x\right), \\ k_3 &= f\left(x_i + \frac{1}{2}\Delta x, h_i + \frac{1}{2}k_2\Delta x\right), \\ k_4 &= f(x_i + \Delta x, h_i + k_3\Delta x). \end{aligned} \quad (3.84)$$

The computational process is depicted in Fig. 3.23, where the four evaluations of the slope are seen. The truncation error of the scheme is  $O(\Delta x^5)$  (Apelt 1971). This scheme is suitable for open channel flows (Katopodes 2019). Apelt (1971) found that this is an accurate and stable method to integrate Eq. (3.49) in the up- and downstream directions regardless of whether the flow is subcritical or supercritical. Equation (3.80) is simply the first-order Runge–Kutta method.

**Fig. 3.23** Fourth-order Runge–Kutta scheme [adapted from Chapra and Canale (2010)]



### 3.5.8 Predictor–Corrector Method

Another relevant method uses the integral form of the GVF-ODE, e.g.,

$$h_{i+1} = h_i + \int_{x_i}^{x_{i+1}} f(x, h) dx. \quad (3.85)$$

The problem is to evaluate the integral numerically. Using the trapezoidal rule, one gets the implicit equation in the depth  $h_{i+1}$  as (Apelt 1971; Chaudhry 2008)

$$h_{i+1} = h_i + \frac{1}{2} \Delta x [f(x_i, h_i) + f(x_{i+1}, h_{i+1})]. \quad (3.86)$$

The following predictor–corrector scheme is therefore feasible (Apelt 1971):

*Predictor step* (explicit)

The predictor step is given by the Euler method, that is,

$$h_{i+1}^0 = h_i + \Delta x f(x_i, h_i). \quad (3.87)$$

This value is used to initiate the iterative corrector cycle, described below.

*Corrector step* (iterative)

With  $k$  as the recursion index, Eq. (3.86) can be written as the iterative formula

$$h_{i+1}^{k+1} = h_i + \frac{1}{2} \Delta x [f(x_i, h_i) + f(x_{i+1}, h_{i+1}^k)]. \quad (3.88)$$

Iteration of  $h_{i+1}$  in the corrector cycle is stopped once the solution accuracy is within a prescribed tolerance for two successive values of the iterated flow depths, that is,

$$\left| \frac{h_{i+1}^{k+1} - h_{i+1}^k}{h_{i+1}^k} \right| \leq 10^{-6}. \quad (3.89)$$

This predictor–corrector method is known as the trapezoidal method, and its truncation error is  $O(\Delta x^3)$  (Apelt 1971).

## 3.6 Applications

### 3.6.1 Test of High-Resolution Method

In this section, the fourth-order Runge–Kutta scheme is evaluated using Bresse’s analytical solution. Thus, a wide rectangular channel is adopted and the flow in a transition from mild to steep slope is used as test case (Fig. 3.17). The fourth-order Runge–Kutta scheme for this test is implemented in the file *Bresse\_RungeKutta4order.xls* available from Chap. 12, whereas Bresse’s analytical solution is available on the file *Bresse\_analytical.xls*.

As application example consider a rectangular channel of width  $b = 5$  m and  $C = 100 \text{ sm}^{-1/2}$  discharging  $Q = 15 \text{ m}^3/\text{s}$  on a slope  $S_o = 0.0001$ . An increase in the slope to  $S_o = 0.1$  is introduced abruptly. The critical depth is  $h_c = 0.972$  m, whereas the normal depths are 2.08 m and 0.208 m for the mild and steep reaches, respectively. Sub- and supercritical profiles were computed in the up- and downstream directions, respectively, using the fourth-order Runge–Kutta scheme with  $\Delta x = 0.5$  m. The boundary conditions at the slope break ( $x = 0$  m) are taken slightly above and below  $h_c$  for the sub- and supercritical profiles, namely 1 m and 0.93 m, respectively. The results are compared in Fig. 3.24 with Bresse’s analytical solution, showing an excellent match.

### 3.6.2 Comparative of Numerical Methods

Once the accuracy of the fourth-order Runge–Kutta scheme is established, it is used in this section to produce reference solutions for channels of arbitrary  $R_h$  to test other numerical schemes.

Consider as test case a rectangular channel of  $b = 2$  m and  $n = 0.015 \text{ sm}^{-1/3}$  discharging  $Q = 15 \text{ m}^3/\text{s}$  on a slope  $S_o = 0.001$ . The critical and normal depths are

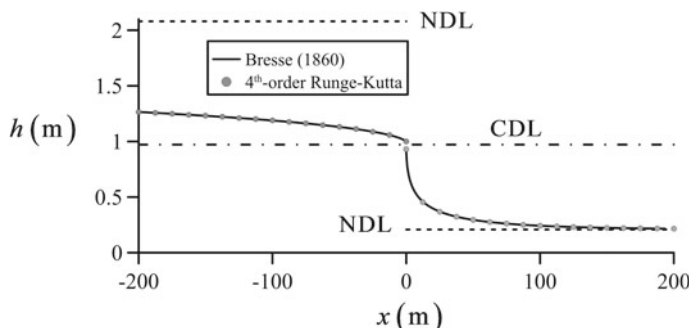


**Fig. 3.24** Evaluation of fourth-order Runge–Kutta scheme in transition from mild to steep slope

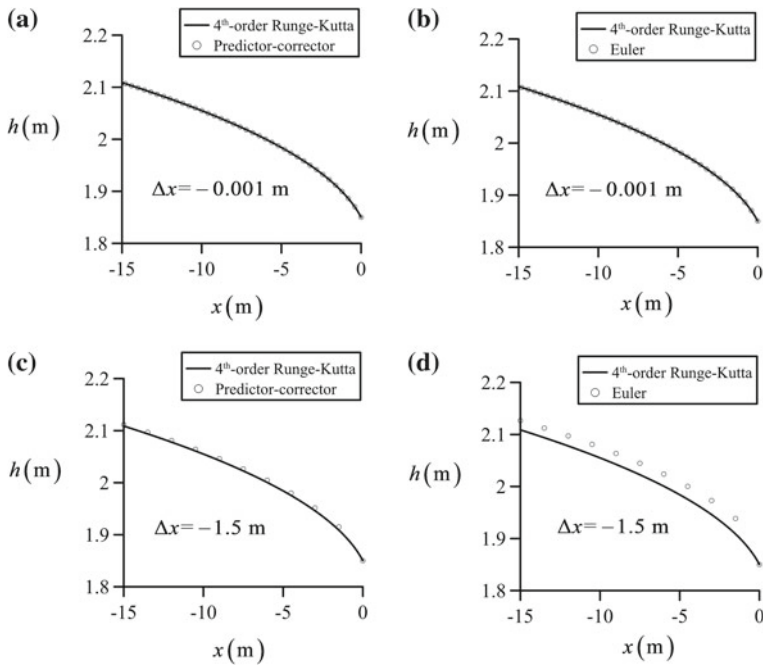


**Fig. 3.25** Comparison of various numerical schemes to solve the GVF-ODE using an M2 profile

$h_c = 1.79 \text{ m}$  and  $h_N = 4.11 \text{ m}$ . An M2 profile will be used to test various numerical schemes taking as boundary condition  $h_o = 1.85 \text{ m}$  at  $x_o = 0 \text{ m}$ . The fourth-order Runge–Kutta scheme was implemented in the file *watersurfaceprofiles\_RungeKutta4order.xls* available from Chap. 12. It is compared in Fig. 3.25a with the trapezoidal rule, available on the file *watersurfaceprofiles\_trapezoidalrule.xls*, using  $\Delta x = -0.001 \text{ m}$ . Note that the match of the two schemes is excellent. A comparison of the fourth-order Runge–Kutta scheme with Euler’s scheme, available on the file *watersurfaceprofiles\_Euler.xls*, is accomplished in Fig. 3.25b, showing likewise a very good match. As previously stated, Euler’s scheme is simple, producing good results if the truncation error is controlled with a small  $\Delta x$ . The test was repeated using  $\Delta x = -1.5 \text{ m}$ , with the corresponding results for the trapezoidal rule and Euler’s schemes presented in Fig. 3.25c and d, respectively. Note that the trapezoidal rule method is still producing good results, whereas Euler’s scheme has notable deviations. This is due to the truncation error, which is  $O(\Delta x^2)$  for Euler’s scheme but  $O(\Delta x^3)$  for the trapezoidal rule method.

The fourth-order Runge–Kutta scheme is compared with the standard step method, available on the file *Flowprofiles\_NR.xls*, in Fig. 3.26a using  $\Delta x = -1.5 \text{ m}$  for the latter. Note that there is an excellent match without any appreciable deviation. The test was repeated using  $\Delta x = -2.5 \text{ m}$  in Fig. 3.26b, and deviations are

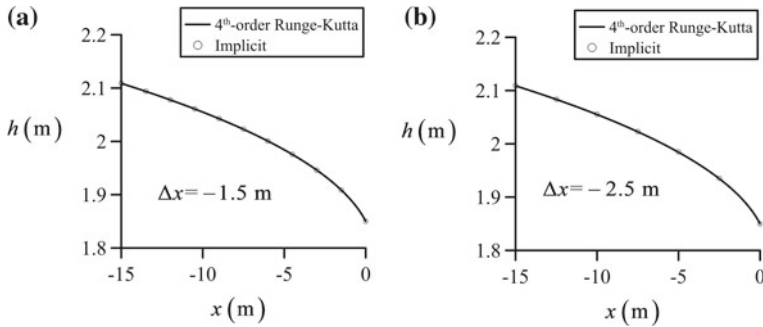


**Fig. 3.26** Evaluation of standard step method using an M2 profile

still small. This is one advantage of the standard step method, namely the possibility of using larger space steps given its implicit character.

### 3.6.3 Flow on Mild Slope

The fourth-order Runge–Kutta scheme is compared in this section with experimental data for mild slope channels (Lee et al. 1952). The test flume was rectangular with  $b = 0.2032$  m,  $S_o = 0.001$ , and  $n = 0.0092 \text{ sm}^{-1/3}$ . A subcritical M1 profile for  $Q = 0.004984 \text{ m}^3/\text{s}$  was numerically computed using as boundary condition the experimental point ( $x_o = 87.7824$  m,  $h_o = 0.14478$  m). The profile was computed from this section in the upstream direction using  $\Delta x = -0.05$  m in the Runge–Kutta solver. A comparison with experiments by Lee et al. (1952) in Fig. 3.27a shows excellent agreement. A subcritical M2 profile for  $Q = 0.009798 \text{ m}^3/\text{s}$  was computed using as boundary condition the experimental point ( $x_o = 34.1376$  m,  $h_o = 0.08128$  m) with  $\Delta x = -0.05$  m. A comparison with experiments in Fig. 3.26b shows again a very good agreement.

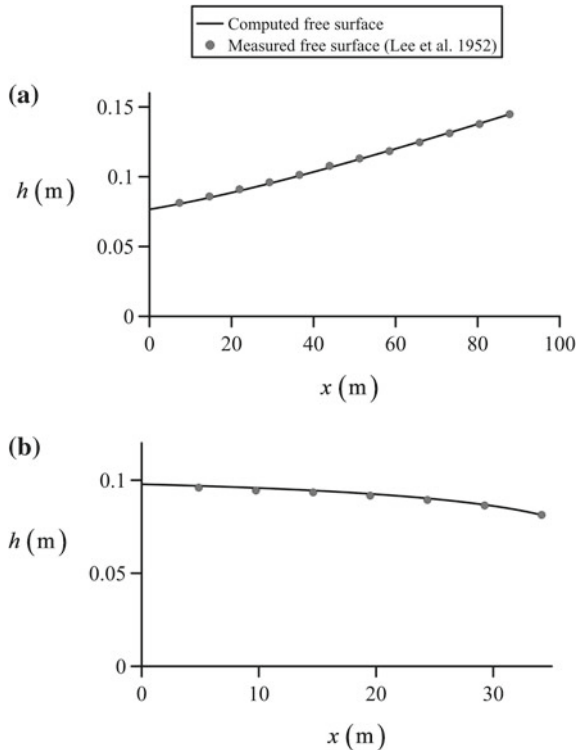
### 3.6.4 Flow on Steep Slope

The GVF equation for a rectangular channel of steep slope is [Eq. (1.151)]

$$\frac{dh}{dx} = \frac{S_o - C_f F^2 (1 + S_o^2)^2}{1 - F^2 (1 + S_o^2)} = \frac{S_o - C_f \frac{q^2}{gh^3} (1 + S_o^2)^2}{1 - \frac{q^2}{gh^3} (1 + S_o^2)}, \quad (3.90)$$

where  $C_f$  is the skin friction coefficient. Note that under the small slope assumption  $1 + S_o^2 \approx 1$ , so that Eq. (3.90) simplifies to Eq. (3.47). A steep physical slope is

**Fig. 3.27** Evaluation of fourth-order Runge–Kutta scheme with experimental data on mild slopes for the **a** M1 curve, **b** M2 curve



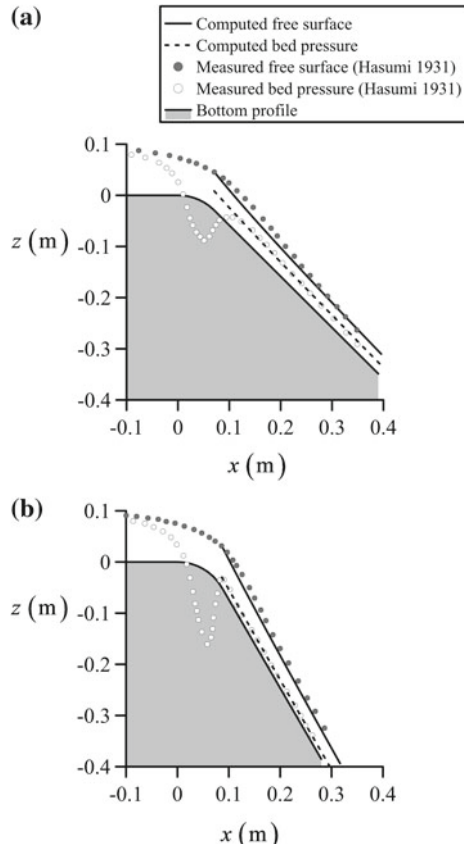
thus different from a “hydraulically steep slope” as given by comparing with Eq. (3.38). The main feature of a steep slope  $1 + S_o^2 > 1$  is that the bottom fluid pressure becomes non-hydrostatic, given by [Eq. (1.136)]

$$\frac{p_b}{\rho g} = \frac{h}{1 + S_o^2}. \quad (3.91)$$

The test data of Hasumi (1931) for slopes of  $S_o = 1$  and  $1.732$  were used to check predictions by Eqs. (3.90) and (3.91). Equation (3.90) was solved with the fourth-order Runge–Kutta scheme, available from the file *steepslope\_RungeKutta4order.xls* in Chap. 12. The slope transition is composed of a horizontal reach followed by a circular-shaped transition profile of  $R = 0.1$  m that finishes in the steep slope reach of  $45^\circ$  or  $60^\circ$  inclination angles. The channel width is  $b = 0.402$  m and the discharge  $Q = 0.04$   $\text{m}^3/\text{s}$ . A value of  $C_f = 0.001$  was used in the simulations.

The first test for  $S_o = 1$  is presented in Fig. 3.28a, where the boundary condition taken to integrate Eq. (3.90) was the experimental point at the start of the flat slope reach ( $x_o = 0.070711$  m,  $h_o = 0.075$  m). The elevation at this point is  $z_o = -0.02929$  m. The computed free surface profile is compared with the

**Fig. 3.28** Comparison of gradually-varied flow theory on steep slope with experiments for  $S_o = \mathbf{a} 1$ , **b** 1.732

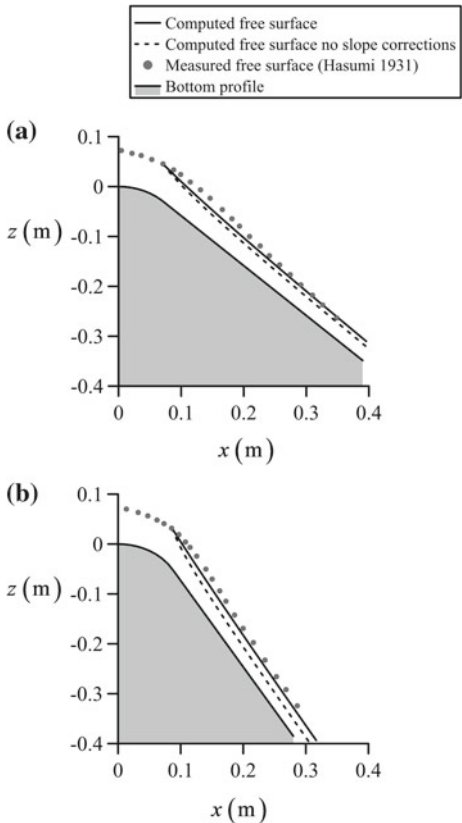


experiments by Hasumi (1931), showing a fair agreement down the slope. Once the free surface is determined, the bottom pressure head was computed from Eq. (3.91), showing again good agreement with experiments down the slope. The second test for  $S_o = 1.732$  is presented in Fig. 3.28b, with the boundary condition set as the experimental point at the start of the flat slope reach ( $x_o = 0.086602$  m,  $h_o = 0.081$  m,  $z_o = -0.05$  m). A comparison of numerical predictions and experimental observations in Fig. 3.28b shows again a good agreement down the slope.

The importance of the mild slope assumption  $1 + S_o^2 \approx 1$  is tested in Fig. 3.29, where the tests are repeated this time including the solution of Eq. (3.90) neglecting the slope corrections. The effect of the correction on the free surface for the  $45^\circ$  slope is moderate (Fig. 3.29a), but obviously, the bottom pressure is poorly predicted, given that for the mild slope case it is

$$\frac{P_b}{\rho g} = h. \quad (3.92)$$

**Fig. 3.29** Evaluation of slope correction effect on the free surface profile for  $S_o = \mathbf{a} 1, \mathbf{b} 1.732$



Bottom pressures are not considered in Fig. 3.29, therefore. The impact of the slope correction on the free surface for the  $60^\circ$  slope is depicted in Fig. 3.29b, showing in that case important deviations.

### 3.7 Compound Channels

In a compound channel, the cross-section is composed of a main channel and a flood plain (Fig. 3.30). For low flows, the main channel operates and conveys all discharge, whereas an overbank flow occurs for high floods and the flood plain transports part of the stream. The roughness values are different in the main channel and the flood plain, thereby inducing a lateral variation of the depth-averaged velocity. Dividing the cross-section into  $N$  subsections of area  $A_i$ , each with a different value of the roughness coefficient, and using Manning's equation, one can define the following velocity for each subsection

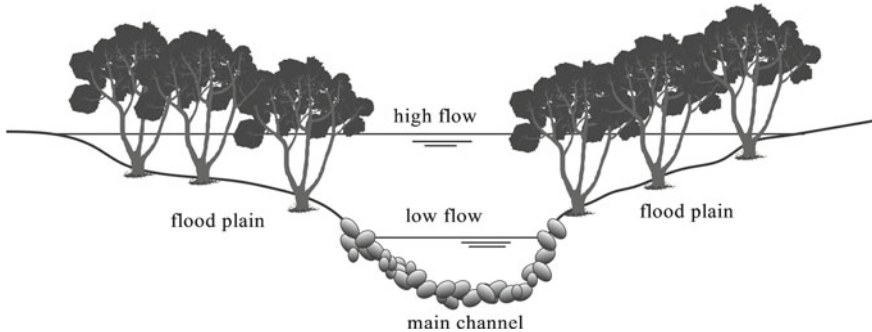


**Fig. 3.30** Compound channel flow

$$U_i = \frac{S_f^{1/2}}{n_i} R_{hi}^{2/3}. \quad (3.93)$$

To compute the hydraulic radius of a subsection, only solid perimeters are considered. The free surface profile is determined from the integral energy balance as (Jain 2001)

$$z_{b1} + h_1 + \alpha_1 \frac{Q^2}{2gA_1^2} = z_{b2} + h_2 + \alpha_2 \frac{Q^2}{2gA_2^2} + \frac{1}{2} (S_{f1} + S_{f2}) \Delta x, \quad (3.94)$$

where the friction slope  $S_f$  and Coriolis coefficient  $\alpha$  shall be determined at each section. The total discharge in the cross-section is (Chow 1959; Jain 2001)

$$Q = \sum_{i=1}^N U_i A_i = S_f^{1/2} \sum_{i=1}^N K_i = K S_f^{1/2}, \quad (3.95)$$

where

$$K_i = \frac{1}{n_i} A_i R_{hi}^{2/3}. \quad (3.96)$$

Equation (3.95) permits to express  $S_f$  as a function of  $Q$  and flow depth in each sub-section. Using Eq. (3.93), the energy velocity correction coefficient is (Sturm 2001; Jain 2001)

$$\alpha = \frac{\int_A u^3 dA}{U^3 A} = \frac{\left(\sum_{i=1}^N A_i\right)^2}{\left(\sum_{i=1}^N K_i\right)^3} \sum_{i=1}^N \frac{K_i^3}{A_i^2}. \quad (3.97)$$

Inserting Eqs. (3.95) and (3.97) in Eq. (3.94), it can be solved by the standard step method (Jain 2001). The determination of control sections, especially critical depth controls, is a complex task, given the multiple critical depths in the specific energy diagram (Sturm 2001). Further, various theoretically possible free surface profiles in compound channel flow are not yet experimentally verified.

## References

- Apelt, C. J. (1971). Numerical integration of the equation of gradually varied and spatially varied flow. In: *Proceedings of 4th Australasian Conference on Hydraulics and Fluid Mechanics*, Monash University, Melbourne, Australia (pp. 146–153).
- Bakhmeteff, B. A. (1912). *О неравномерном движении жидкости в открытом русле* [Varied flow of liquids in open channels]. St Petersburg, Russia (in Russian).
- Bakhmeteff, B. A. (1932). *Hydraulics of open channels*. New York: McGraw-Hill.
- Bélanger, J. B. (1828). *Essai sur la solution numérique de quelques problèmes relatifs au mouvement permanent des eaux courantes* [On the numerical solution of some steady water flow problems]. Carilian-Goeury, Paris (in French).
- Bresse, J. (1860). *Cours de mécanique appliquée*, 2<sup>ème</sup> partie: Hydraulique [Lecture notes on applied mechanics, Part 2, Hydraulics]. Paris: Mallet-Bachelier (in French).
- Brunner, G. W. (2016). *HEC-RAS River Analysis System Hydraulic Reference Manual*. Report CPD69, Version 5.0, US Army Corps of Engineers, Hydrologic Engineering Center (HEC), Davis, CA.
- Chanson, H. (2004). *The hydraulics of open channel flows: An introduction*. Oxford, UK: Butterworth-Heinemann.
- Chapra, S. C., & Canale, R. P. (2010). *Numerical methods for engineers* (6th ed.). New York: McGraw-Hill.
- Chaudhry, M. H. (2008). *Open-channel flow* (2nd ed.). New York: Springer.
- Chow, V. T. (1959). *Open channel hydraulics*. New York: McGraw-Hill.
- Fenton, J. D. (2010). Calculating resistance to flow in open channels. Technical Report, Alternative Hydraulics Paper 2, Vienna University of Technology, Vienna, Austria.
- Fread, D. L., & Harbaugh, T. E. (1971). Open-channel profiles by Newton's iteration technique. *Journal of Hydrology*, 13, 78–80.
- Hager, W. H. (2010). *Wastewater hydraulics: Theory and practice* (2nd ed.). Berlin: Springer.
- Hasumi, M. (1931). Untersuchungen über die Verteilung der hydrostatischen Drücke an Wehrkronen und -Rücken von Überfallwehren infolge des abstürzenden Wassers [Studies on the distribution of hydrostatic pressure distributions at overflows due to water flow]. *Journal of the Department of Agriculture*, Kyushu Imperial University 3(4), 1–97 (in German).
- Henderson, F. M. (1966). *Open channel flow*. New York: MacMillan Co.
- Hoffman, J. D. (2001). *Numerical methods for engineers and scientists* (2nd ed.). New York: Marcel Dekker.
- Jaeger, C. (1956). *Engineering fluid mechanics*. Edinburgh: Blackie and Son.
- Jain, S. C. (2001). *Open channel flow*. New York: Wiley.
- Jan, C.-D. (2014). *Gradually-varied flow profiles in open channels: Analytical solutions by using Gaussian hypergeometric function*. Advances in Geophysical and Environmental Mechanics and Mathematics. Berlin: Springer.
- Jeppson, R. (2011). *Open channel flow: Numerical methods and computer applications*. Boca Raton: CRC Press.
- Katopodes, N. D. (2019). *Free surface flow: Shallow-water dynamics*. Oxford, UK: Butterworth-Heinemann.

- Lee, M. T., Babbitt, H. E., & Baumann, E. R. (1952). *Gradually varied flow in uniform channels on mild slopes*. Engineering Experiment Station Bulletin N° 404, University of Illinois at Urbana Champaign, College of Engineering, Engineering Experiment Station.
- Montes, J. S. (1998). *Hydraulics of open channel flow*. Reston, VA: ASCE.
- Puertas, J., & Sánchez, M. (2001). *Apuntes de Hidráulica de canales* [Open channel hydraulics lecture notes]. Civil Engineering School, University da Coruña, Spain (in Spanish).
- Rouse, H. (1938). *Fluid mechanics for hydraulic engineers*. New York: McGraw-Hill.
- Rouse, H. (1950). *Engineering hydraulics*. New York: Wiley.
- Rouse, H. (1965). Critical analysis of open-channel resistance. *Journal of the Hydraulics Division, ASCE*, 91(HY4), 1–25.
- Sturm, T. W. (2001). *Open channel hydraulics*. New York: McGraw-Hill.
- Subramanya, K. (1986). *Flow in open channels*. New Delhi: Tata McGraw-Hill.
- White, F. M. (1991). *Viscous fluid flow*. New York: McGraw-Hill.
- White, F. M. (2003). *Fluid mechanics*. New York: McGraw-Hill.
- Woodward, S. M., & Posey, C. J. (1941). *Hydraulics of steady flow in open channels*. New York: Wiley.
- Yen, B. C. (1973). Open-channel flow equations revisited. *Journal of the Engineering Mechanics Division, ASCE*, 99(EM5), 979–1009.
- Yen, B. C. (1991). Hydraulic resistance in open channels. In B. C. Yen (Ed.), *Channel flow resistance: Centennial of Manning's formula* (pp. 1–135). Highlands Ranch, USA: Water Resources Publications.
- Yen, B. C. (2002). Open channel flow resistance. *Journal of Hydraulic Engineering*, 128(1), 20–39.

# Chapter 4

## Computation of Steady Transcritical Open Channel Flows



### 4.1 Introduction

There are two possible transitional open channels flows, as described in Chap. 2: the transition from subcritical ( $F < 1$ ) to supercritical ( $F > 1$ ) flows, and the transition from supercritical ( $F > 1$ ) to subcritical ( $F < 1$ ) flows. Both of these flow types are fundamentally different. The transition from subcritical to supercritical flows is smooth and continuous, as, for example, in weir flow (Fig. 4.1a). The transition from supercritical to subcritical flows, however, is abrupt, encompassing a highly turbulent free surface profile (Fig. 4.1b). This chapter details the computation of transitional flow profiles. Computations are then illustrated and compared with experimental observations.

### 4.2 Transition from Sub- to Supercritical Flow

#### 4.2.1 Formation of Singular Points in Free Surface Flows

The critical depth in a prismatic channel is a mathematically impossible value for the flow profile, given that  $dh/dx \rightarrow \infty$  (vertical flow profile) is regained from the gradually varied flow equation (see Chap. 3). However, natural channels like rivers are non-prismatic, for which the cross-sectional geometry and the bed slope vary with the streamwise  $x$ -coordinate. Man-made channels, as weirs, may be also non-prismatic. Consider the transition from a mild to a steep bottom slope with a gradual bottom transition curve (Fig. 4.2), the problem investigated by Massé

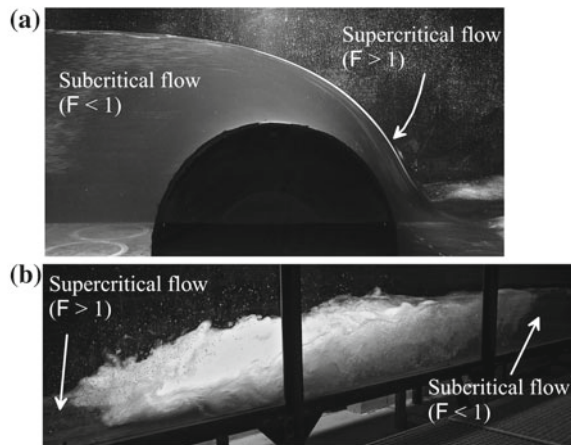


**Fig. 4.1** Transitions from **a** subcritical ( $F < 1$ ) to supercritical ( $F > 1$ ) flows over a weir, **b** supercritical ( $F > 1$ ) to subcritical ( $F < 1$ ) flow in a hydraulic jump, with  $F$  as the Froude number

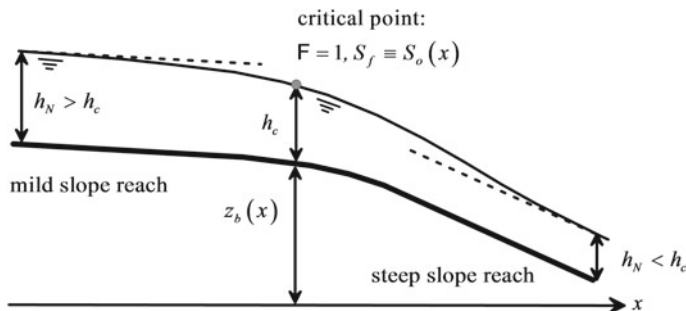


**Fig. 4.2** Transition from a mild to a steep bottom slope with a gradual bottom transition curve: Formation of a critical point, where the flow depth equals the critical depth and the friction slope is exactly equal to the bottom slope at this section

(1938), recently reviewed by Hager and Castro-Orgaz (2016). Between these two reaches, the transitional bed profile is assumed to be smooth and continuous up to second derivatives. The gradually varied flow equation is thus for a rectangular, prismatic channel (Henderson 1966).



**Pierre Massé** was born on January 13, 1898, in Paris, passing away there aged nearly 90 years old on December 15, 1987. He obtained in 1928 the civil engineering degree from *Ecole des Ponts et Chaussées*, entering subsequently in the electric industry of France, today's *Électricité de France* (EDF). He submitted in 1935 his Ph.D. thesis on variable regimes in fluvial hydraulics, in which his mathematical knowledge was developed. Further works are related to tidal flows and flows in mountainous rivers, in which aspects of supercritical flow are fundamental, including the transition to subcritical flow. His important work on the hydraulic jump and the free surface profile in channels of variable bottom slope published in 1938 was awarded the *Prix Caméré* from the French *Académie des Sciences*. He in parallel was active in the hydropower industry, collaborating with the great French dam designer André Coyne (1891–1960) on the *Portillon* Dam in the French Pyrenees, or the *Chastang* Dam on Dordogne River in Southern France. He was appointed in 1946 EDF Director of equipment, and in 1948 Vice-Director EDF, presiding from 1965 to 1969 the EDF Administrative Council. He became in 1955 *Commandeur* of the French *Légion d'Honneur* and was in 1977 elected Member of *Académie des Sciences*. The latter distinction is normally given to scientists only, shedding thus light on his great career both in theoretical and applied engineering.

$$\frac{dh}{dx} = \frac{-\frac{dz_b}{dx} - S_f}{1 - \frac{q^2}{gh^3}} = \frac{S_o(x) - S_f}{1 - F^2}, \quad (4.1)$$

where  $h$  is the flow depth,  $g$  the gravity acceleration,  $q$  the discharge per unit width,  $F = q/(gh^3)^{1/2}$  the Froude number,  $S_f$  the friction slope, and  $S_o$  the bed slope, defined as

$$S_o = -\frac{dz_b}{dx}. \quad (4.2)$$

If there are not gates, weirs, or, in general, any other channel control along the channel reach, the only possible singularity provoking a variation in the flow conditions is the variable slope reach  $z_b = z_b(x)$ . Far upstream and downstream along the uniform slopes, asymptotic conditions will be settled, with the flow depth approaching the corresponding uniform flow depth  $h_N$ . The flow gradually adjusts from the upstream subcritical uniform depth ( $h_N > h_c$ ) to the downstream supercritical uniform depth ( $h_N < h_c$ ). The free surface profile will thus cut somewhere the critical depth line to change from sub- to supercritical conditions. The flow conditions at the critical flow section are investigated following Massé (1938) and Henderson (1966). Rewrite Eq. (4.1) as

$$\frac{dh}{dx} (1 - F^2) = S_o - S_f. \quad (4.3)$$

If  $F = 1$  is set into Eq. (4.3), then  $S_o = S_f$ . As the flow gradually changes from upstream subcritical flow to downstream supercritical flow,  $dh/dx \neq 0$ . Thus, at the section where the flow depth equals the critical flow depth, the friction slope equals the local bottom slope, and, obviously, the water surface slope at this section is different from zero (Henderson 1966; Hager and Castro-Orgaz 2016). The point satisfying these conditions is referred to as singular point, acting as a control section of the flow. Starting at the singular point, the subcritical branch of the free surface profile is computed in the upstream direction, whereas the supercritical portion is computed in the downstream direction. A particular case of notable interest is the transition from an adverse to a steep slope; it is the case occurring in weir flow (Fig. 4.3) (Puertas and Sánchez 2001).

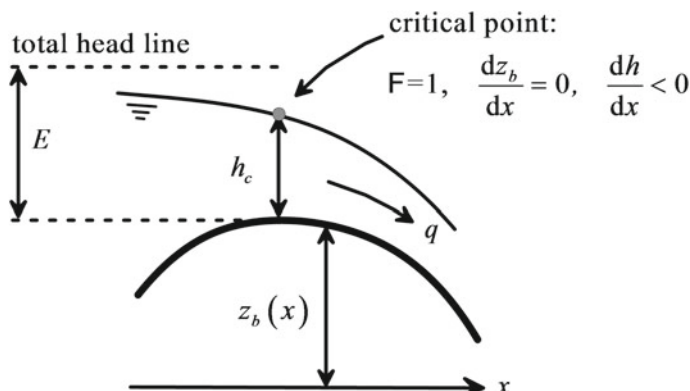


**Fig. 4.3** Formation of a critical point in ideal fluid flow along the transition from an adverse to a steep positive slope (adapted from Puertas and Sánchez 2001)

The fluid flow is assumed to be ideal given the short transitional length, and, thus,  $S_f = 0$ . Equation (4.3) then produces

$$\frac{dh}{dx} (1 - F^2) = S_o. \quad (4.4)$$

Focus on the weir crest, where  $S_o = 0$ . Inserting this in Eq. (4.4) yields

$$\frac{dh}{dx} (1 - F^2) = 0. \quad (4.5)$$

This identity is verified for the obvious case  $dh/dx = 0$ . This case is described in Chap. 2 and corresponds to either fully sub- or supercritical flows over the weir profile. However, the identity is also verified with  $F = 1$ , corresponding to critical flow at the weir crest with  $dh/dx < 0$ , given that the water accelerates from sub- to supercritical flows, so that the flow depth must decrease in the flow direction (Fig. 4.3).

#### 4.2.2 Determination of Water Surface Slope at Critical Point

If  $F = 1$ , then Eq. (4.4) produces the indetermination  $dh/dx = 0/0$  at the weir crest. This singularity in the equation of motion is removed by applying L'Hospital's rule to Eq. (4.4) (Massé 1938; Escoffier 1958; Hager and Castro-Orgaz 2016). This technique to remove flow depth gradients of the kind 0/0 on the shallow water steady-state equations is known as the singular point method in open channel hydraulics (Chow 1959; Montes 1998; Hager 1985, 2010). It originates from the work of Poincaré (1881) on ODE equations and was applied to open channel transition flow problems by Massé (1938), Escoffier (1958), Iwasa (1958), Wilson (1969), and Chen and Dracos (1996). However, this method is questioned in the literature given that the argument still prevails that Eq. (4.4) is invalid for  $h = h_c$  given the existence of non-hydrostatic pressure distribution. The gradually varied flow model is mathematically valid at the critical depth, but, physically, it is inaccurate if the free surface curvature is high, given that then the hydrostatic pressure approximation is inadequate (Montes 1998; Castro-Orgaz and Chanson 2016). The singular point method is rarely explained in open channel flow books, with Chow (1959), Henderson (1966) and Montes (1998) as notable exceptions. However, mathematical books often describe it for general application in engineering (i.e., von Kármán and Biot 1940).

Consider the weir flow depicted in Fig. 4.3. The boundary condition to integrate Eq. (4.4) is the critical depth at the weir crest,  $h(x = 0) = h_c = (q^2/g)^{1/3}$ , with the origin of the  $x$ -coordinate at the weir crest. To integrate the ODE in the up- and downstream directions using the Runge–Kutta method, the value of the free surface

slope  $dh/dx$  at the crest must be determined (Chen and Dracos 1996). However, this value is unknown, given the mathematical indetermination existing there. Equation (4.4) is a steady-state version of the SWE momentum equation. However, in steady gradually varied flow, it is also obtained by differentiation of the total energy head  $H = z_b + h + q^2/(2gh^2)$  as

$$\frac{d}{dx} \left( z_b + h + \frac{q^2}{2gh^2} \right) = 0, \quad (4.6)$$

where energy losses are neglected given the short transitional reach. Its first differential is

$$\frac{dz_b}{dx} + \frac{dh}{dx} - \frac{q^2}{gh^3} \frac{dh}{dx} = 0, \quad (4.7)$$

which is obviously equivalent to Eq. (4.4), as stated. A second differential of  $H$  is obtained from Eq. (4.7) as

$$\frac{d^2z_b}{dx^2} + \frac{d^2h}{dx^2} - \frac{q^2}{gh^3} \frac{d^2h}{dx^2} + 3 \frac{q^2}{gh^4} \left( \frac{dh}{dx} \right)^2 = 0. \quad (4.8)$$

Inserting into Eq. (4.8) the singular point conditions at the weir crest

$$\frac{q^2}{gh_c^3} = 1, \quad \frac{dz_b}{dx} = 0, \quad (4.9)$$

the following identity is regained [Eq. (2.37)]

$$\frac{d^2z_b}{dx^2} + \frac{3}{h_c} \left( \frac{dh}{dx} \right)^2 = 0. \quad (4.10)$$

The water surface slope at the weir crest is thus

$$\left( \frac{dh}{dx} \right)_c = \pm \left( -\frac{h_c}{3} \frac{d^2z_b}{dx^2} \right)^{1/2}. \quad (4.11)$$

Note from this finding that the physically correct result implies a minus sign in front of the square root function, corresponding to accelerating flow at the weir crest. Further, given that  $h_c$  is positive, imaginary numbers originate as a solution for  $dh/dx$  if  $d^2z_b/dx^2$  is positive, meaning that a concave free surface profile is not compatible with weir flow. Only a convex bottom profile ( $d^2z_b/dx^2 < 0$ ) produces a transcritical free surface profile passing from sub- to supercritical flows, therefore. The mathematical problem is thus the solution of the following ODE with critical flow as the boundary condition:

$$\left[ \begin{array}{l} \text{ODE:} \quad \frac{dh}{dx} = \begin{cases} -\frac{dz_b}{dx} & \text{if } x \neq 0, \\ 1 - \frac{q^2}{gh^3} & \\ -\left( -\frac{h_c}{3} \frac{d^2 z_b}{dx^2} \right)^{1/2} & \text{if } x = 0; \end{cases} \\ \text{Boundary condition:} \quad h(x=0) = h_c = \left( \frac{q^2}{g} \right)^{1/3}. \end{array} \right] \quad (4.12)$$

## 4.3 Transition from Super- to Subcritical Flows

### 4.3.1 Control Volume Equation for Hydraulic Jump

The transition from super- to subcritical flows is rapidly varied and, thus, cannot be handled using the gradually varied flow theory. The pressure distribution can be considered hydrostatic, but the velocity distribution is markedly non-uniform, Reynolds stresses are extremely high and air entrainment provokes a two-phase flow rather than a clear water flow (Fig. 4.1b). The flow is definitely not gradually varied within a hydraulic jump, so Eq. (4.1) cannot be integrated to predict the free surface profile of the hydraulic jump. Resort to more advanced approaches is necessary for this task (Castro-Orgaz and Hager 2009), which is beyond the scope of this book. The hydraulic jump is treated here using control volume equations, with the purpose of relating the values of depth and velocity at the boundary sections, where the flow is gradually varied (Fig. 4.4a).

Although the equation describing a hydraulic jump is presented in Chap. 2, some developments are repeated here for convenience to introduce the hydraulic jump as an element of free surface profile computations. Consider the hydraulic jump in a horizontal and rectangular channel depicted in Fig. 4.4a; the control volume with boundary sections 1 and 2, where the flow is super- and subcritical, respectively, is used to formulate integral balances. At these boundaries, pressure is hydrostatic and velocity uniform. Reynolds' transport theorem states the conservation of mass and momentum as (Liggett 1994; Sturm 2001; Chaudhry 2008),

$$\frac{d}{dt} \iiint_{CV} \rho dv + \iint_{CS} \rho (\mathbf{V} \cdot \mathbf{n}) dA = 0, \quad (4.13)$$

$$\sum \mathbf{f} = \frac{d}{dt} \iiint_{CV} \rho \mathbf{V} dv + \iint_{CS} \rho \mathbf{V} (\mathbf{V} \cdot \mathbf{n}) dA. \quad (4.14)$$

Here,  $\mathbf{V}$  is the velocity vector,  $\mathbf{f}$  a fluid force component,  $\mathbf{n}$  the unit vector normal to the control area  $A$ ,  $v$  the volume, and  $\rho$  the water density.  $CV$  and  $CS$  are the

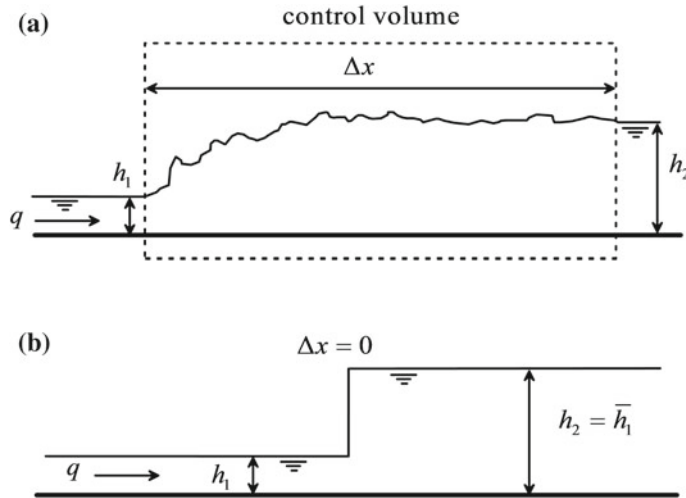


**Fig. 4.4** Hydraulic jump in a horizontal channel **a** control volume for application of Reynolds' transport theorem, **b** approximate representation of hydraulic jump as a local discontinuity ( $\Delta x = 0$ ) in the shallow water hydraulics theory

control volume and its surrounding control surface. The boundary limits of SC are flow sections 1 and 2. For steady 1D flow, these reduce to

$$q = U_1 h_1 = U_2 h_2 , \quad (4.15)$$

$$\sum F_x = \rho q(U_1 - U_2), \quad (4.16)$$

where  $U$  is the depth-averaged velocity and  $F_x$  represents the  $x$ -component of any external force acting on the control surface. The hydraulic jump involves highly turbulent flow where a large amount of energy is dissipated. Further, the control volume length  $\Delta x$  is of the order of only  $6(h_2 - h_1)$ , an experimentally determined length of the jump profile. Therefore, shear forces are usually neglected, reducing the external forces acting on the control surface to the hydrostatic forces. Equation (4.16) reduces then to

$$\frac{1}{2} \rho g (h_2^2 - h_1^2) = \rho q (U_1 - U_2). \quad (4.17)$$

After basic algebraic manipulation, Eq. (4.17) is alternatively written as

$$h_2 = \bar{h}_1 = \frac{h_1}{2} \left[ -1 + (1 + 8F_1^2)^{1/2} \right], \quad F_1^2 = \frac{q^2}{gh_1^3}. \quad (4.18)$$

This relation is known as Bélanger's equation for the hydraulic jump (Bélanger 1849). The water depth  $\bar{h}_1$  is called sequent depth of  $h_1$ . From Eq. (4.18), it is easily verified that a decrease of  $h_1$  implies an increase of  $\bar{h}_1$ . Note also that the sequent or conjugate depth of the critical depth is itself.



**Jean-Baptiste Bélanger** was born on April 4, 1790, at Valenciennes, and passed away aged 84 years on May 8, 1874, at Neuilly. He left *Ecole Polytechnique* in 1813 as member of the *Corps des Ponts et Chaussées*. His classmate Gaspard Coriolis (1792–1843) lectured later also with him. After several years of service in the French army, Bélanger gradually taught at *Ecole Centrale*, then at *Ecole Polytechnique* and finally at *Ecole des Ponts et Chaussées*, i.e., the major French engineering schools, all located in Paris. He retired in 1864 but continued to publish in scientific journals.

He worked in general mechanics and stressed the methods developed, the technical language selected, and the correct style of presentation. In hydraulics, he is particularly known for his *Essai* written in 1828 where he presented the gradually varied flow equation and its first numerical solution. The Bélanger equation correctly applies the momentum principle for the ratio of the so-called sequent depths up- and downstream of a classical hydraulic jump. His equation was systematically applied only about 100 years later when verified by hydraulic experiments. He also presented a thorough approach for backwater curves, as described by Adhémar Barré de Saint-Venant (1797–1886), and subsequently developed by Pierre Vauthier (1784–1847), Gaspard Coriolis (1792–1843), and Joseph Boussinesq (1842–1929).

Within the context of the shallow water hydraulic theory, the effect of length of the hydraulic jump is neglected ( $\Delta x = 0$ ). The hydraulic jump is therefore treated as a discontinuity determined by Eq. (4.18) (Fig. 4.4b). Physically, the difference between the transition from sub- to supercritical and that from super- to subcritical flows is easily appreciated (Fig. 4.1): The former is smooth and continuous,

whereas the latter is abrupt and highly turbulent. Mathematically, this is also stated by the shallow water hydraulics theory: Ideal weir flow results in a mathematical indetermination producing a smooth solution, whereas the hydraulic jump is mathematically a discontinuity accompanied with significant energy losses.

For a given discharge  $q$  and supercritical flow depth  $h_1$ , Eq. (4.18) defines the required value of  $h_2$ , namely  $\bar{h}_1$ , to produce a steady hydraulic jump. If given  $h_1$ , for example, the actual tailwater level  $h_2$  is less than  $\bar{h}_1$ , the shock front ( $h_2 - h_1$ ) will move in the downstream direction. The physical reason is that the momentum plus pressure force of the incoming supercritical flow is larger than that at the tailwater section. Thus, pressure forces and momentum are not in equilibrium, and the unbalanced residual provokes an unsteady motion removing the shock in the downstream direction. Only if  $h_2 \equiv \bar{h}_1$ , the jump is steady. The momentum equation of the hydraulic jump is rewritten as

$$\frac{h_1^2}{2} + \frac{q^2}{gh_1} = \frac{h_2^2}{2} + \frac{q^2}{gh_2}, \quad (4.19)$$

or using the definition of the momentum function  $S$

$$S_1 = S_2, \quad S = \frac{h^2}{2} + \frac{q^2}{gh}. \quad (4.20)$$

Equation (4.20) applies to physically explain the conditions triggering the location of a hydraulic jump at a given channel position. Conceptually, the supercritical inflow can be considered a jet-like flow, with the momentum  $qU_1$  as the important component of  $S$ . In turn, the tailwater flow can be considered a downstream water wall, with the hydrostatic force  $(1/2)gh_2^2$  as the important component of  $S$  (Puertas and Sánchez 2001). These conceptual simplifications are now used to explain the formation of surges, a topic to be described mathematically in Chap. 5. Here, only a conceptual introduction is attempted. If the momentum of the inflow jet is much larger than the hydrostatic force of the downstream water wall, then the shock front will move to the right, forming a moving hydraulic jump, that is, a traveling surge with  $h_1 < h_2$  (Jain 2001) (Fig. 4.5a), which is an unsteady flow. If the momentum of the jet is on the contrary much lower than the tailwater hydrostatic force, then the traveling surge will move to the left (Fig. 4.5b). If  $S_1$  and  $S_2$  are exactly in balance, the surge is not moving, forming a steady hydraulic jump (Fig. 4.5c), satisfying Eq. (4.20). This relation therefore serves to determine the position of a hydraulic jump. It is easily verified that the energy loss due to the hydraulic jump is [Eq. (2.136)]

$$\Delta H = \left( h_1 + \frac{q^2}{2gh_1^2} \right) - \left( h_2 + \frac{q^2}{2gh_2^2} \right) = \frac{(h_2 - h_1)^3}{4h_1 h_2}. \quad (4.21)$$

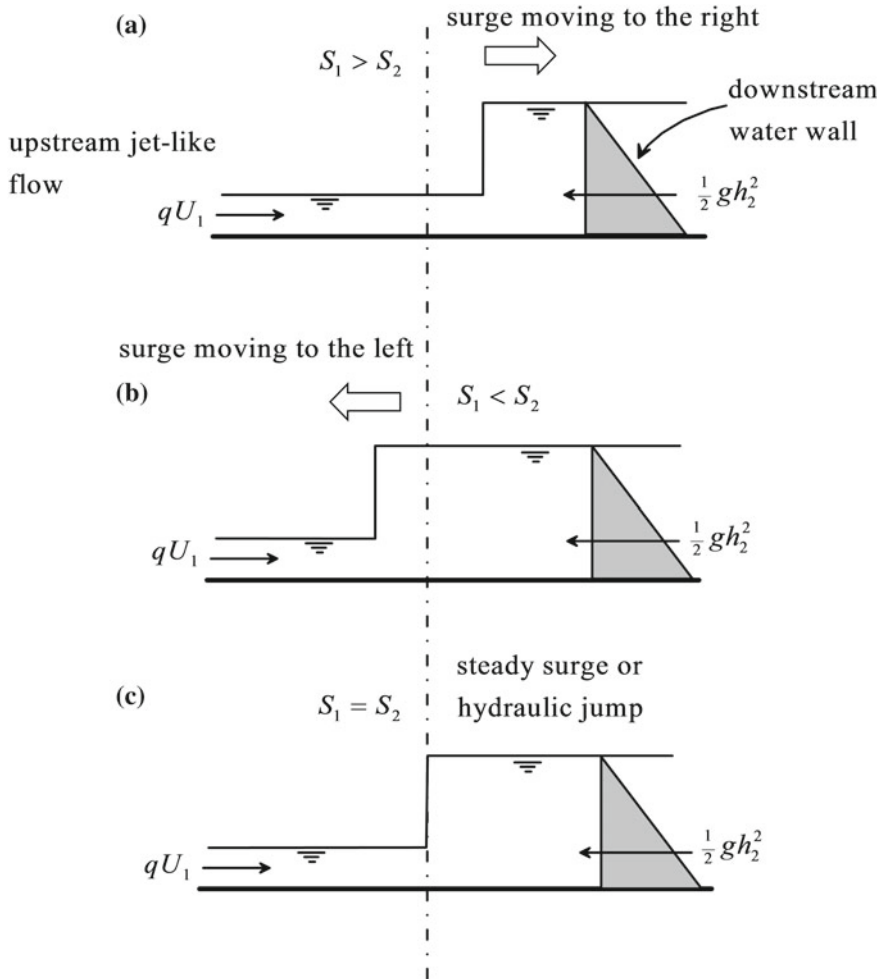


**Fig. 4.5** Moving hydraulic jump, or surge with  $h_1 < h_2$ , displacing in: **a** the downstream direction, **b** the upstream direction, **c** with no displacement, that is, under steady conditions (adapted from Puertas and Sánchez 2001)

### 4.3.2 Determination of Hydraulic Jump Position

It is now explained how to use Eq. (4.18) to determine the position of a hydraulic jump in a free surface profile using a practical example. Consider a sluice gate upstream of a free overfall in a mild slope channel. Two flow profiles are possible, each determined by a different channel control: subcritical flow profile computed in the upstream direction assuming critical flow at the brink section; supercritical flow profile computed in the downstream direction imposed by a gate opening below the

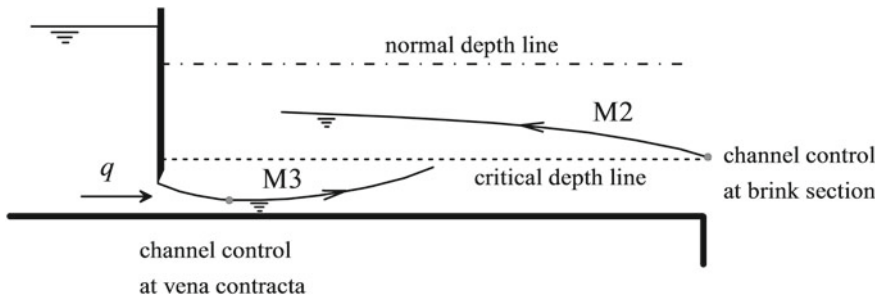


**Fig. 4.6** Sub- and supercritical free surface profiles beyond a sluice gate

critical depth (Fig. 4.6). It must be determined which of the two profiles is the actual physically valid solution, depending on which control is active, or, if both controls are active (the brink section and the gate), the super- and subcritical profiles must be assembled through a hydraulic jump. The computational process encompasses the following steps:

- (i) Compute the supercritical M3 curve  $h = h(x)$  starting at the gate section, or at the *vena contracta* assuming  $C_c = 0.61$ , if contraction effects are accounted for. The distance from the gate to the *vena contracta* is small and therefore neglected in gradually varied flow computations. The computation must be stopped ahead of reaching the critical depth line  $h_c$ , given that  $dh/dx \rightarrow \infty$ .
- (ii) After computation of the supercritical M3 profile, for each supercritical depth  $h$  of this curve, compute the corresponding sequent depth from Bélanger's equation

$$\bar{h}(x) = \frac{h(x)}{2} \left[ -1 + (1 + 8F^2)^{1/2} \right], \quad F^2 = \frac{q^2}{g[h(x)]^3}. \quad (4.22)$$

Physically, this sequent depth is the tailwater depth necessary to produce a hydraulic jump at section  $x$  where the supercritical depth is  $h(x)$ . Note that the hydraulic jump is treated as a local discontinuity.

- (iii) Compute the subcritical M2 curve starting at the brink section, with the boundary flow depth close but not identical to the critical depth, given that  $dh/dx \rightarrow \infty$  otherwise.
- (iv) If the sequent depth curve  $\bar{M}3$  of the supercritical M3 profile intersects at any point the subcritical profile M2 computed from the brink section, a hydraulic jump appears at this section. The hydraulic jump is therefore a discontinuity located at the intersection of the M2 profile with the  $\bar{M}3$  profile in this example (Fig. 4.7).

If the sequent depth curve  $\bar{M}3$  of the M3 profile is below the M2 curve in all the channel reach (Fig. 4.8), no hydraulic jump is formed; the momentum function of the M2 profile is larger than that of the M3 profile for all the channel sections.

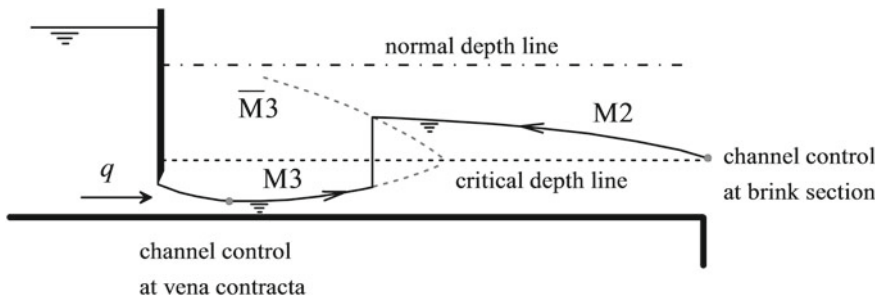


**Fig. 4.7** Free surface profile beyond a sluice gate with the formation of a hydraulic jump

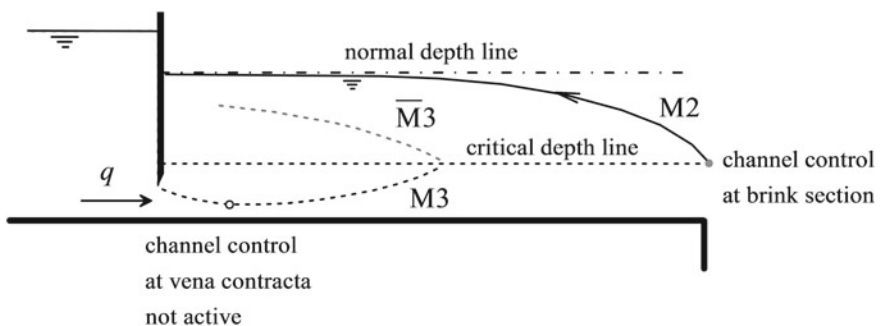


**Fig. 4.8** Subcritical free surface profile beyond a sluice gate: the gate is drowned

Therefore, the gate is drowned and the real free surface profile is the M2 curve, with subcritical flow along the channel. In this case, the only active channel control is the brink section. This case may occur if the channel beyond the sluice gate is long and the normal depth is relatively high.

If the conjugate depth curve  $\bar{M}3$  of the M3 profile is above the M2 curve along the entire channel reach (Fig. 4.9), no hydraulic jump is formed; the momentum function of the M3 profile is larger than that for the M2 profile for all the channel sections. Therefore, the hydraulic jump is fully removed from the channel and the real free surface profile is the supercritical M3 curve. In this case, the only active channel control is the gate, given that the flow is forced to exit from the channel at the brink section at a high speed, and critical flow conditions cannot be settled there, deactivating this as control. This case may occur if the channel beyond the gate is short and the M3 curve is not reaching the critical depth line.

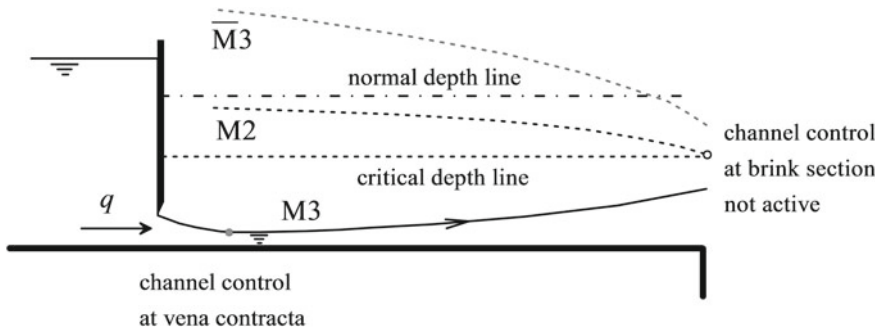


**Fig. 4.9** Supercritical free surface profile beyond a sluice gate: the hydraulic jump is rejected from the channel reach

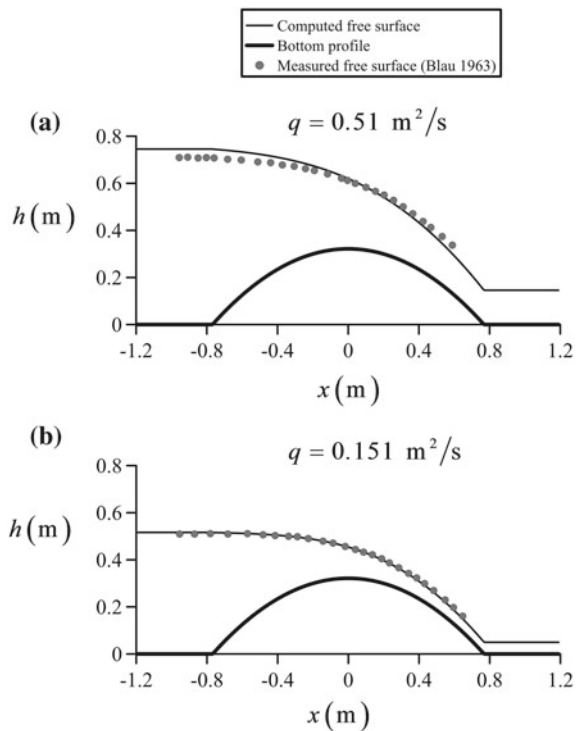
## 4.4 Computational Examples

### 4.4.1 Flow over Round-Crested Weirs

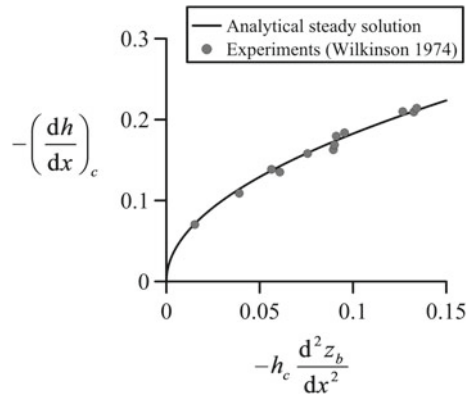
The steady transcritical free surface profile over a parabolic weir of bed shape  $z_b = 0.3216 - 0.54525x^2$  (m) was computed using Eq. (4.12). The numerical model is implemented in the file *parabolicweir\_transcritical.xls* of Chap. 12. Equation (4.12) was solved using the fourth-order Runge–Kutta method (see Chap. 3), and the corresponding sub- and supercritical branches of the free surface profile were computed in the up- and downstream directions, respectively. Theoretical predictions are compared in Fig. 4.10a, b with experimental data of Blau (1963) for two runs corresponding to  $q = 0.51$  and  $0.151 \text{ m}^2/\text{s}$ , respectively. In the first test, slight deviations between experiments and simulations are evident given the effect of the non-hydrostatic pressure distribution, not accounted for by the gradually varied flow theory. In the second run, however, predictions are in excellent agreement with observations. At the weir crest, Eq. (4.11) was used to remove the singularity of the equations of motion. This equation is compared in Fig. 4.11 with the experimental measurements of Wilkinson (1974), confirming that the result is not only theoretically sound, but also in agreement with experimental observations (Castro-Orgaz and Chanson 2016).

Figure 4.12 contains the experimental data of Sivakumaran et al. (1983) for a Gaussian hump of profile  $z_b = 20 \exp[-0.5(x/24)^2]$  (cm) for two test cases. Simulations were conducted using Eq. (4.12) as previously described for the parabolic weir. This test is implemented in the file *Gaussianhump\_transcritical.xls* in Chap. 12. The computed solution is presented for both cases and compared in Fig. 4.12a, b with the experiments. The departure between simulations and

**Fig. 4.10** Transcritical flow over parabolic weir profile. Comparison with experimental data (Blau 1963) for  $q = \mathbf{a} 0.51 \text{ m}^2/\text{s}$ , **b**  $0.151 \text{ m}^2/\text{s}$

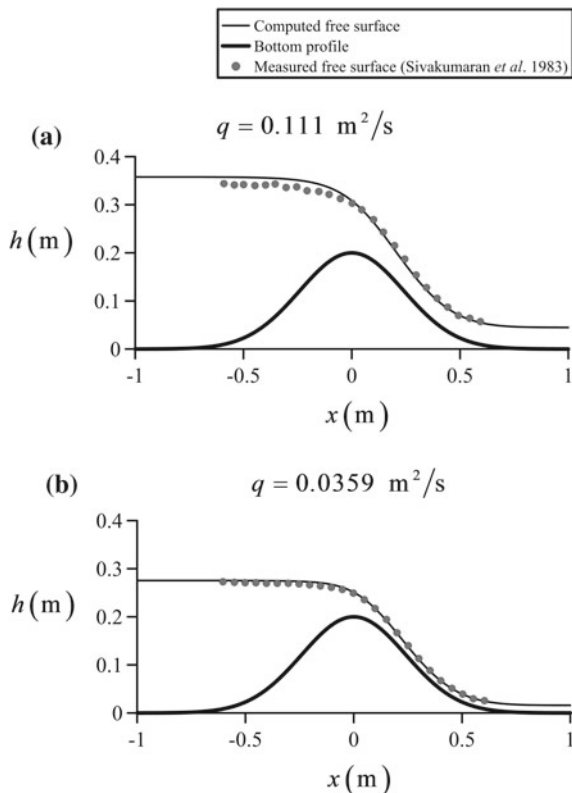


**Fig. 4.11** Free surface slope at the crest section of a parabolic weir profile. Comparison with experimental data (Wilkinson 1974)



experiments for the test case of Fig. 4.12a ( $q = 0.111 \text{ m}^2/\text{s}$ ) indicates that the effect of the non-hydrostatic pressure is notable as the flow passes from sub- to super-critical. For the test case of Fig. 4.12b ( $q = 0.0359 \text{ m}^2/\text{s}$ ), deviations between numerical results and experiments are small.

**Fig. 4.12** Transcritical flow over Gaussian weir profile. Comparison with experimental data (Sivakumaran et al. 1983) for  $q = \mathbf{a} 0.111 \text{ m}^2/\text{s}$ , **b**  $0.0359 \text{ m}^2/\text{s}$



#### 4.4.2 Hydraulic Jump Beyond a Sluice Gate

Gharangik and Chaudhry (1991) conducted measurements of steady hydraulic jumps in a horizontal flume 0.46 m wide and 14 m long. Consider a test conducted for an inflow Froude number  $F_1 = 7$ . The upstream boundary section was located at  $x = 0.305$  m from the gate, and the depth and unit discharge there resulting from experimentation were  $h = 0.031$  m and  $q = 0.118 \text{ m}^2/\text{s}$ . The tailwater level was set to  $h = 0.265$  m. The experimental measurements for this test are displayed in Fig. 4.13.

This test is available in the file *sluicegate\_hydraulicjump.xls* of Chap. 12. The predictions using Eq. (4.1) were conducted using  $\Delta x = 0.01$  m and  $n = 0.008 \text{ m}^{-1/3}\text{s}$ . The upstream boundary condition for the computation of the H3 supercritical free surface profile was taken from the experiments, and the conjugate depth curve of the H3 profile was determined applying Eq. (4.18). From the tailwater boundary condition, a subcritical flow profile was computed. The intersection of this subcritical profile with

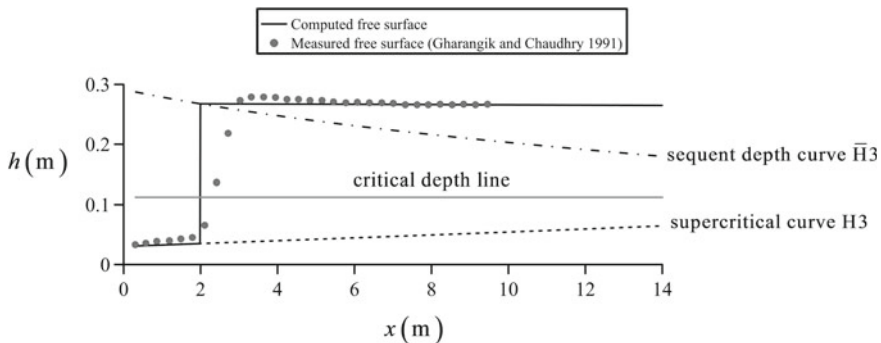


**Fig. 4.13** Comparison of numerical simulation with experimental results (Gharangik and Chaudhry 1991) for flow profile with steady hydraulic jump

the sequent depth curve fixes the position of the hydraulic jump. The computational results are displayed in Fig. 4.13. A comparison of the transcritical free surface profile with experimental data by Gharangik and Chaudhry (1991) in Fig. 4.13 shows good agreement. Note that the finite length of the jump produced by turbulence is a feature not accounted for in the theoretical predictions.

## References

- Bélanger, J. B. (1849). *Notes sur le Cours d'Hydraulique* (Notes on the Course in Hydraulics). Mém. Ecole Nat. Ponts et Chaussées, Paris, France, session 1849–1850, 222 p (in French).
- Blau, E. (1963). Der Abfluss und die hydraulische Energieverteilung über einer parabelförmigen Wehrschwelle [Distributions of discharge and energy over a parabolic-shaped weir]. Mitteilung, 7, 5–72 Forschungsanstalt für Schifffahrt, Wasser- und Grundbau, Berlin (in German).
- Castro-Orgaz, O., & Hager, W. H. (2009). Classical hydraulic jump: Basic flow features. *Journal of Hydraulic Research*, 47(6), 744–754.
- Castro-Orgaz, O., & Chanson, H. (2016). Minimum specific energy and transcritical flow in unsteady open channel flow. *Journal Irrigation and Drainage Engineering*, 142(1), 04015030.
- Chaudhry, M. H. (2008). *Open-channel flow* (2nd ed.). New York: Springer.
- Chen, J., & Dracos, T. (1996). Water surface slope at critical controls in open channel flow. *Journal of Hydraulic Research*, 34(4), 517–536.
- Chow, V. T. (1959). *Open channel hydraulics*. New York: McGraw-Hill.
- Escoffier, F. F. (1958). Transition profiles in nonuniform channels. *Transactions ASCE*, 123, 43–56.
- Gharangik, A. M., & Chaudhry, M. H. (1991). Numerical simulation of hydraulic jump. *Journal of Hydraulic Engineering*, 117(9), 1195–1211.
- Hager, W. H. (1985). Critical flow condition in open channel hydraulics. *Acta Mechanica*, 54(3–4), 157–179.
- Hager, W. H. (2010). *Wastewater hydraulics: Theory and practice* (2nd ed.). Berlin: Springer.
- Hager, W. H., & Castro-Orgaz, O. (2016). Critical flow in open channel hydraulics: From Boess to De Marchi. *Journal of Hydraulic Engineering*, 142(1), 02515003.
- Henderson, F. M. (1966). *Open channel flow*. New York: MacMillan.

- Iwasa, Y. (1958). Hydraulic significance of transitional behaviours of flows in channel transitions and controls. *Memoires of the Faculty of Engineering, Kyoto University*, 20(4), 237–276.
- Jain, S. C. (2001). *Open channel flow*. New York: Wiley.
- Liggett, J. A. (1994). *Fluid mechanics*. New York: McGraw-Hill.
- Massé, P. (1938). Ressaut et ligne d'eau dans les cours à pente variable [Hydraulic jump and free surface profile in channels of variable slope]. *Revue Générale de l'Hydraulique*, 4(19), 7–11; 4(20), 61–64 (in French).
- Montes, J. S. (1998). *Hydraulics of open channel flow*. Reston, VA: ASCE.
- Poincaré, H. (1881). Mémoire sur les courbes définies par une équation différentielle [Memoir on the defined curves of a partial differential equation]. *Journal de mathématiques pures et appliquées*, 7, 375–422 (in French).
- Puertas, J., & Sánchez, M. (2001). *Apuntes de Hidráulica de canales* [Open channel hydraulics lecture notes]. Spain: Civil Engineering School, University da Coruña (in Spanish).
- Sivakumaran, N. S., Tingsanchali, T., & Hosking, R. J. (1983). Steady shallow flow over curved beds. *Journal of Fluid Mechanics*, 128, 469–487.
- Sturm, T. W. (2001). *Open channel hydraulics*. New York: McGraw-Hill.
- von Kármán, T., & Biot, M. A. (1940). *Mathematical methods in engineering: An introduction to mathematical treatment of engineering problems*. New York: McGraw-Hill.
- Wilkinson, D. L. (1974). Free surface slopes at controls in channel flow. *Journal of the Hydraulics Division, ASCE*, 100(8), 1107–1117.
- Wilson, E. H. (1969). Surface profiles in non-prismatic rectangular channels. *Water Power*, 21 (11), 438–443.

# Chapter 5

## Unsteady Open Channel Flows: Basic Solutions



### 5.1 Introduction

Flow conditions in rivers are usually unsteady (Cunge et al. 1980; Sturm 2001; Chaudhry 2008), even though steady flow computations are conducted in engineering applications, as for determining an inundation area in hydrological studies. Further, the operation of man-made canals to control the water released from reservoirs implies unsteady maneuvers resulting in transient open channel flows (Chaudhry 2008). Therefore, real flow computations in canals and rivers require the solution of the Saint-Venant equations or the shallow water equations (SWE). In this chapter, these are presented and their basic continuous and discontinuous unsteady flow solutions are discussed.

### 5.2 Shallow Water Equations

Unsteady free surface flow is mathematically determined by the two-dimensional (2D) SWE, which are given by (see Chap. 1)

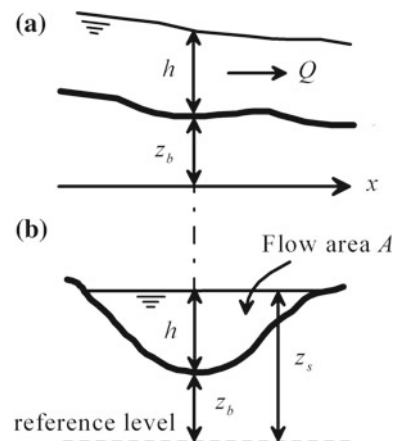
$$\begin{aligned}\frac{\partial h}{\partial t} + \frac{\partial(Uh)}{\partial x} + \frac{\partial(Vh)}{\partial y} &= 0, \\ \frac{\partial(Uh)}{\partial t} + \frac{\partial}{\partial x}(U^2h) + \frac{\partial}{\partial y}(UVh) &= -gh\frac{\partial z_s}{\partial x} - \frac{1}{\rho}(\tau_{xz})_b, \\ \frac{\partial(Vh)}{\partial t} + \frac{\partial}{\partial y}(V^2h) + \frac{\partial}{\partial x}(VUh) &= -gh\frac{\partial z_s}{\partial y} - \frac{1}{\rho}(\tau_{yz})_b.\end{aligned}\quad (5.1)$$

Here,  $(U, V)$  are the depth-averaged velocity components in the  $(x, y)$  horizontal directions,  $h$  is the flow depth,  $z_s$  the free surface elevation,  $g$  the gravity acceleration,  $\rho$  the water density, and  $\tau$  denotes here tangential stresses. Most river flows can be considered one-dimensional (1D), given that the  $x$ -direction is predominant (Fig. 5.1). Therefore, the transverse water surface slope can be assumed horizontal. To obtain 1D flow equations for an arbitrary cross section, the vertically averaged continuity and  $x$ -momentum equations are laterally integrated in the  $y$ -direction (see Chap. 1). The 2D depth-averaged model is then reduced to a 1D, sectional integrated formulation. The river is therefore basically treated as a 1D stream tube. Using Leibniz's rule and imposing that the free surface slope is independent of the  $y$ -direction (horizontal water surface), the lateral integration of Eqs. (5.1)<sub>1</sub> and (5.1)<sub>2</sub> produces the 1D Saint-Venant equations (De Saint-Venant 1871) for an arbitrary cross section (see Chap. 1)

$$\begin{aligned}\frac{\partial A}{\partial t} + \frac{\partial Q}{\partial x} &= 0, \\ \frac{\partial Q}{\partial t} + \frac{\partial}{\partial x} \left( \frac{Q^2}{A} \right) &= -gA \frac{\partial z_s}{\partial x} - gA \frac{\bar{\tau}_o}{\rho g R_h}.\end{aligned}\quad (5.2)$$

Here,  $Q$  is the discharge,  $A$  the flow area,  $R_h = A/p$  the hydraulic radius,  $p$  the wetted perimeter, and  $\bar{\tau}_o$  the average boundary shear stress acting on the wetted perimeter. The free surface elevation  $z_s(x, t)$  corresponds at any vertical line of the cross section to the sum of the bed elevation and the local water depth. The standard approach is to use the thalweg (lowest point) to define the flow depth  $h$  and bed elevation of the longitudinal river profile (Cunge et al. 1980) (Fig. 5.1). If the channel is prismatic, Eq. (5.2) can be recast as (Sturm 2001; Jain 2001; Chaudhry 2008)

**Fig. 5.1** One-dimensional unsteady river flow **a** profile view, **b** cross section



$$\begin{aligned}\frac{\partial A}{\partial t} + \frac{\partial Q}{\partial x} &= 0, \\ \frac{\partial Q}{\partial t} + \frac{\partial}{\partial x} (QU + gA\bar{h}) &= gA \left( -\frac{\partial z_b}{\partial x} - S_f \right),\end{aligned}\tag{5.3}$$

where  $U = Q/A$ ,  $h$  is the flow depth along the thalweg,  $S_f = \bar{\tau}_o/(\rho g R_h)$  the friction slope, bars indicate the depth of centroid below the free surface, and  $\partial z_b/\partial x$  is the longitudinal slope taking as reference the thalweg.

The  $x$ -coordinate is usually curvilinear, following the thalweg path in the horizontal plane ( $x, y$ ). Therefore, a river must not have severe curvatures in plan to apply Eq. (5.3). Otherwise, curvature terms must be introduced to transform the Cartesian system to curvilinear coordinates following the river plan, e.g., at river meanders. For the basic case of a rectangular cross section, and with  $q = Q/b$  as the unit discharge and  $b$  as the channel width, Eq. (5.3) reduces to

$$\begin{aligned}\frac{\partial h}{\partial t} + \frac{\partial q}{\partial x} &= 0, \\ \frac{\partial q}{\partial t} + \frac{\partial}{\partial x} \left( \frac{q^2}{h} + g \frac{h^2}{2} \right) &= gh \left( -\frac{\partial z_b}{\partial x} - S_f \right).\end{aligned}\tag{5.4}$$

Equation (5.4) is widely used in this book to introduce numerical methods. Note that the differential form of the SWE only applies to zones of the  $(x, t)$  plane where the dependent variables  $U(x, t)$  and  $h(x, t)$  are single-valued and smooth (Cunge et al. 1980).

## 5.3 Discontinuous Solutions: Basic Equations of a Positive Surge

### 5.3.1 Introduction

A special feature of the Saint-Venant equations is that they admit both continuous or gradually varied flow solutions, as well as discontinuous solutions (rapidly varied flow zones), involving abrupt changes in the flow variables, even if initial and boundary conditions are continuous (Cunge et al. 1980). Using shock-capturing methods (Toro 2001), it is possible to simulate with accuracy both continuous and discontinuous waves, where flow variables are not single-valued. To catch these discontinuous solutions, the integral form of the SWE must be used (Cunge et al. 1980; Toro 2001). This is equivalent to apply the Reynolds transport theorem (Chaudhry 2008, 2014; White 2009) to the fluid properties mass and momentum in a finite control volume.

An important discontinuous unsteady open channel flow is the surge (Fig. 5.2), corresponding to a traveling wave separating abruptly two open channel flow portions of different depth and velocity. In this section, positive surges are

**Fig. 5.2** Surge moving in a hydropower canal (Seton Canal, Vancouver, Canada) **a** general view, **b** detail of wave front (reprinted from Chaudhry 2014). Note secondary undulations (Favre waves) linked to non-hydrostatic pressure distribution of non-breaking central portion of the surge. Wave is propagating in the upstream direction after load rejection

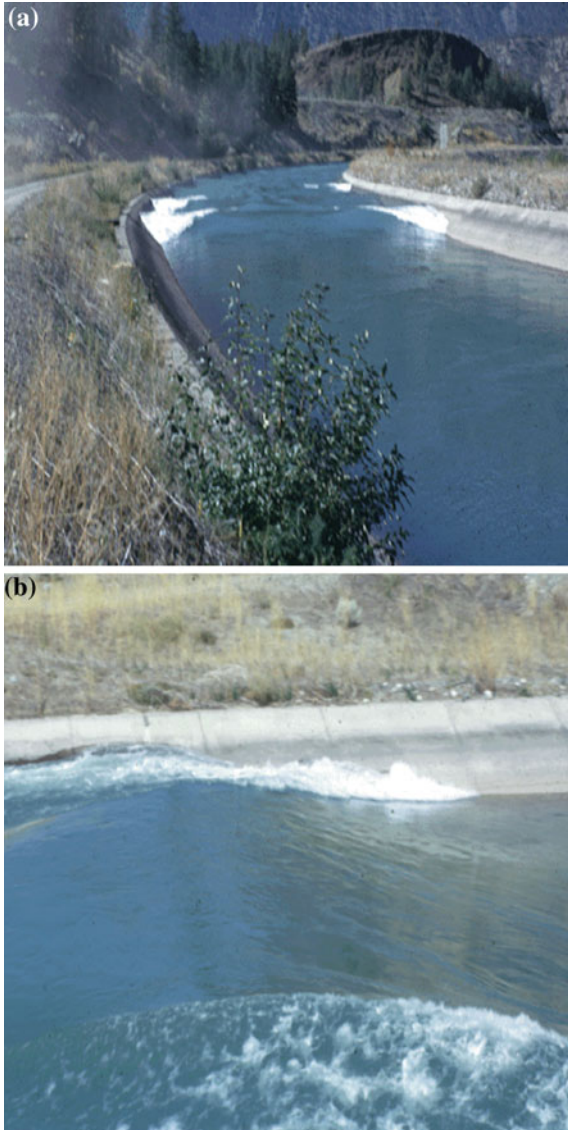


**Fig. 5.3** Undular surge with wave breaking (photograph by late Prof. D. H. Peregrine)



considered, implying a zone of deeper waters propagating over shallower waters,<sup>1</sup> either in the up- or downstream directions. A surge is generated by a sudden increase of discharge in the channel (Favre 1935; Chow 1959; Henderson 1966). Near the front of a positive surge, the fluid pressure is in reality non-hydrostatic, a feature beyond the capabilities of the SWE (see Chaps. 1 and 11). The surge, in fact, is undular due to non-hydrostatic pressure for small surge heights (Favre 1935; Peregrine 1966; Cunge 1975; Cunge et al. 1980). This leads to the so-called secondary waves or Favre waves (Fig. 5.2). However, once the undular wave breaks (Fig. 5.3), the SWE provide an excellent estimate of the shock height, celerity, and energy dissipation (Cunge 1975; Toro 2001). If a surge breaks, the length of the discontinuity is small and can be neglected. The positive surge of tidal origin is called bore (Chanson 2004) (Fig. 5.4).

### 5.3.2 Reynolds Transport Theorem

The celerity of wave propagation in gradually varied flow zones, where solutions are smooth and continuous, is  $c = (gh)^{1/2}$  (see Chap. 2). This is the celerity of an elementary gravity wave in a hydrostatic field. However, in a surge, the wave height is finite, resulting in a different propagation celerity. As will be demonstrated, a surge or bore can even propagate into the upstream direction in a supercritical flow, something impossible within the framework of small gravity waves. Here, the basic equations governing the movement of a surge will be developed considering

---

<sup>1</sup>In computational fluid dynamics (CFD), the analogous discontinuous wave stemming from the Euler equations for gas dynamics is called shock wave (Toro 2001, 2009; LeVeque 2002), although there are also contact or shear waves. The hydraulic shock wave is simply referred to as positive surge (Jain 2001; Chanson 2004; Chaudhry 2008).

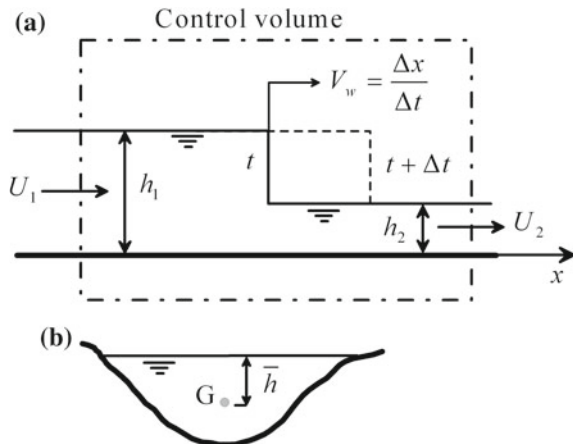


**Fig. 5.4** A tidal bore on Qiantang River at Yanguan, China, on 7/Sept/2013. Note the breaking front propagating upstream (Photo courtesy of Prof. H. Chanson)

unsteady flow computations. An alternative approach is possible by reducing the unsteady flow to a steady flow problem in moving axes propagating with the velocity of the surge  $V_w$ , which is a constant. This development will be presented in Chap. 6.

Consider a positive surge conceptually simplified to a translation wave of permanent shape with a discontinuity in depth and velocity, as sketched in Fig. 5.5. The channel is horizontal and the fluid ideal. The strategy is to insert this discontinuous solution  $\mathbf{U}(x, t)$  into the integral mass and momentum balances to obtain the

**Fig. 5.5** Positive surge moving in downstream direction **a** profile view, **b** cross section



relations defining the surge height and velocity. The movement of the surge is considered with respect to a fixed control volume in space and time, where Reynolds' transport theorem (Chow et al. 1988; Chaudhry 2008) is applied. It states the conservation of any system property within a finite control volume. For mass and momentum, these statements are, respectively (Liggett 1994; Chaudhry 2008),

$$\frac{d}{dt} \iiint_{CV} \rho dv + \iint_{CS} \rho (\mathbf{V} \cdot \mathbf{n}) dA = 0, \quad (5.5)$$

$$\sum \mathbf{f} = \frac{d}{dt} \iiint_{CV} \rho \mathbf{V} dv + \iint_{CS} \rho \mathbf{V} (\mathbf{V} \cdot \mathbf{n}) dA. \quad (5.6)$$

Here,  $\mathbf{V}$  is the velocity vector,  $\mathbf{f}$  a fluid force component,  $\mathbf{n}$  the unit vector normal to the control area  $A$ ,  $v$  the volume, and  $\rho$  the water density.  $CV$  and  $CS$  are the control volume and its surrounding control surface. The boundary limits of  $SC$  are flow sections 1 and 2. The rate of temporal variation of water mass stored in the control volume is after time  $\Delta t$

$$\frac{d}{dt} \iiint_{CV} \rho dv = \rho \frac{d}{dt} \iiint_{CV} dv = \rho \frac{dv}{dt} = \rho V_w (A_2 - A_1), \quad (5.7)$$

where  $A_1$  and  $A_2$  are the flow areas at sections 1 and 2. The net mass flow across the contour of the control volume is

$$\iint_{CS} \rho (\mathbf{V} \cdot \mathbf{n}) dA = \iint_{CS} \rho U dA = \rho U_1 A_1 - \rho U_2 A_2. \quad (5.8)$$

Thus, from Eq. (5.5), one obtains

$$\rho V_w (A_2 - A_1) + \rho U_1 A_1 - \rho U_2 A_2 = 0, \quad (5.9)$$

or

$$A_1 (U_1 - V_w) = A_2 (U_2 - V_w). \quad (5.10)$$

On inspecting Eq. (5.10), it is noted that the continuity equation across a surge is simply obtained by superimposing a constant velocity ( $-V_w$ ) to the unsteady flow velocities. The unsteady translation of the surge is thus reduced to a steady problem in moving axes at the absolute surge velocity. Likewise, the fluid force balance projected in the  $x$ -direction of surge propagation in the control volume of Fig. 5.5 reads

$$\sum f_x = \rho g (\bar{h}_2 A_2 - \bar{h}_1 A_1). \quad (5.11)$$

This is simply a hydrostatic pressure balance. The temporal rate of momentum change  $\rho \mathbf{V}$  within the control volume, projected in the  $x$ -direction, is

$$\frac{d}{dt} \iiint_{CV} \rho \mathbf{V} dV \Rightarrow \rho \frac{d}{dt} \iiint_{CV} U dV = \rho V_w (A_2 U_2 - A_1 U_1), \quad (5.12)$$

whereas the net momentum flux across the control surface is

$$\iint_{CS} \rho \mathbf{V} (\mathbf{V} \cdot \mathbf{n}) dA \Rightarrow \iint_{CS} \rho U^2 dA = \rho U_1^2 A_1 - \rho U_2^2 A_2. \quad (5.13)$$

Inserting Eqs. (5.11)–(5.13) into Eq. (5.6) produces

$$\rho g (\bar{h}_2 A_2 - \bar{h}_1 A_1) = \rho V_w (A_2 U_2 - A_1 U_1) + \rho U_1^2 A_1 - \rho U_2^2 A_2. \quad (5.14)$$

This relation is rewritten as

$$\begin{aligned} \rho g (\bar{h}_2 A_2 - \bar{h}_1 A_1) &= V_w A_2 U_2 - U_2^2 A_2 - V_w A_1 U_1 + U_1^2 A_1 \\ &= A_1 U_1 (U_1 - V_w) - A_2 U_2 (U_2 - V_w). \end{aligned} \quad (5.15)$$

This identity demonstrates that the momentum balance across a surge can also be reduced to a steady flow balance by superimposing the constant velocity ( $-V_w$ ) to the unsteady flow velocities. From Eq. (5.10), one gets

$$(U_2 - V_w) = \frac{A_1}{A_2} (U_1 - V_w). \quad (5.16)$$

Inserting into Eq. (5.15) yields

$$\begin{aligned} \rho g (\bar{h}_2 A_2 - \bar{h}_1 A_1) &= A_1 U_1 (U_1 - V_w) - A_2 U_2 \frac{A_1}{A_2} (U_1 - V_w) \\ &= A_1 U_1 (U_1 - V_w) - A_1 U_2 (U_1 - V_w) \\ &= A_1 (U_1 - V_w)(U_1 - U_2). \end{aligned} \quad (5.16)$$

From Eq. (5.10), the surge celerity is

$$V_w = \frac{U_1 A_1 - U_2 A_2}{A_1 - A_2}, \quad (5.17)$$

which, inserted in Eq. (5.16), produces

$$(U_2 - U_1)^2 = g \frac{(\bar{h}_1 A_1 - \bar{h}_2 A_2)}{A_1 A_2} (A_1 - A_2). \quad (5.18)$$

Using this relation to eliminate  $(U_1 - U_2)$  in Eq. (5.16) results in

$$(U_1 - V_w)^2 = g \frac{A_2}{A_1} \frac{(\bar{h}_2 A_2 - \bar{h}_1 A_1)}{(A_2 - A_1)}, \quad (5.19)$$

from which the surge velocity is

$$V_w = U_1 \pm \left[ g \frac{A_2}{A_1} \frac{(\bar{h}_2 A_2 - \bar{h}_1 A_1)}{(A_2 - A_1)} \right]^{1/2}. \quad (5.20)$$

A surge propagating in the downstream direction is generated by selecting the sign “+” in Eq. (5.20). Jain (2001) discussed all the possible types of surges upon algebraic analysis of Eq. (5.20). The surge celerity  $c$  is the velocity of the wave relative to that of the fluid that is propagating, e.g., the body of water moving at speed  $U_1$ . Thus,

$$c = V_w - U_1 = \pm \left[ g \frac{A_2}{A_1} \frac{(\bar{h}_2 A_2 - \bar{h}_1 A_1)}{(A_2 - A_1)} \right]^{1/2}. \quad (5.21)$$

For a rectangular cross section, it reduces to

$$c = V_w - U_1 = \pm \left[ \frac{g h_2}{2 h_1} (h_1 + h_2) \right]^{1/2}. \quad (5.22)$$

This result shows that a finite discontinuity travels with a celerity different from that of small gravity waves

$$c = \pm (gh)^{1/2}. \quad (5.23)$$

Both equations only agree if  $h_1 = h_2 = h$ , e.g., if the discontinuity is an infinitesimal perturbation. Thus, a positive surge of small height propagates at  $V_w \approx U + (gh)^{1/2}$ . This issue is of paramount relevance and must be carefully accounted for when developing open channel flow solutions involving both continuous and discontinuous portions. Equations (5.17) and (5.20) are a system of two equations determining the flow depth behind the surge  $h_1$  and its absolute velocity  $V_w$  if the initial conditions ( $h_2$ ,  $U_2$ ) and the upstream discharge  $Q_1$  producing the surge are known. The formation of a surge is physically explained by considering a smooth, gradually varied wave profile implying a zone of deeper water invading shallower water, progressively steepening due to a larger value of  $c = (gh)^{1/2}$  in deep water (Cunge 1975). As the wave evolves, the small hydrostatic waves progressively collapse, until they form a finite surge. Mathematically, this process is described with the theory of characteristics, explained in Sect. 5.5. For details, see Cunge (1975) and Montes (1998).

### 5.3.3 Positive Surges Moving Upstream in Supercritical Flow

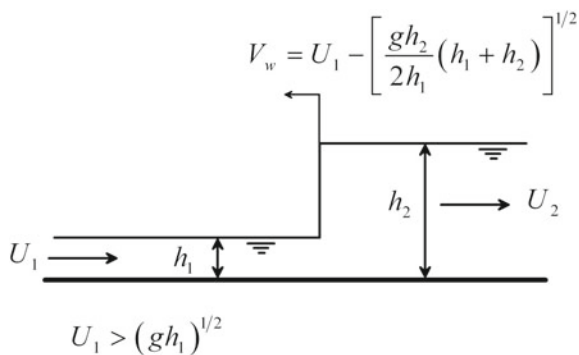
An important feature of surges is that they can run up in a supercritical current. For a surge propagating in the upstream direction (Fig. 5.6), the sign of  $V_w$  by application of the fundamental Eq. (5.22) must be negative.

Consider Eq. (5.22) rewritten as

$$V_w = U_1 \pm \left[ \frac{gh_2}{2h_1} (h_1 + h_2) \right]^{1/2}. \quad (5.24)$$

To obtain values of  $V_w < 0$ , the “−” sign must be selected. Let us define the surge jump as  $\Delta h = h_2 - h_1$  and the dimensionless jump height as  $\varepsilon = \Delta h/h_1$ . Using these definitions, Eq. (5.24) yields

**Fig. 5.6** Surge moving in upstream direction over a supercritical current



$$V_w = U_1 - \left[ g \frac{h_1 + \Delta h}{2h_1} (h_1 + h_1 + \Delta h) \right]^{1/2} = U_1 - \left[ gh_1 \frac{1+\varepsilon}{2} (2+\varepsilon) \right]^{1/2}, \quad (5.25)$$

or

$$V_w = U_1 - (gh_1)^{1/2} \left[ (1+\varepsilon) \left( 1 + \frac{\varepsilon}{2} \right) \right]^{1/2}. \quad (5.26)$$

This implies with  $F_1 = U_1/(gh_1)^{1/2}$  as the approach flow Froude number

$$\frac{V_w}{(gh_1)^{1/2}} = F_1 - \left( 1 + \frac{3}{2}\varepsilon + \frac{\varepsilon^2}{2} \right)^{1/2}. \quad (5.27)$$

Equation (5.27) shows that in a supercritical current with  $F_1 > 1$ , the surge will move upstream ( $V_w < 0$ ) if the surge jump height  $\varepsilon$  is large enough. The minimum height  $\varepsilon_{\min}$  for a given  $F_1$  above which the surge begins to move in the upstream direction is from Eq. (5.27), by setting  $V_w = 0$ , determined by

$$F_1^2 = 1 + \frac{3}{2}\varepsilon_{\min} + \frac{\varepsilon_{\min}^2}{2}. \quad (5.28)$$

For an infinitesimal surge height  $\varepsilon \rightarrow 0$ , Eq. (5.27) yields

$$\frac{V_w}{(gh_1)^{1/2}} = F_1 - 1. \quad (5.29)$$

This is always positive for  $F_1 > 1$ , implying that these infinitesimal surges cannot travel in the upstream direction in supercritical flows. For a small amplitude  $\varepsilon \ll 1$ , Eq. (5.27) reads

$$\frac{V_w}{(gh_1)^{1/2}} = F_1 - \left( 1 + \frac{3}{2}\varepsilon \right)^{1/2}. \quad (5.30)$$

This equation was presented by De Saint-Venant (1870). Using it, surges propagating in the upstream are generated. However, the resulting values of  $\varepsilon$  are not of small amplitude and thus nonlinear terms. In this case, better revert to the general Eq. (5.27). The limiting case  $V_w = 0$  corresponds to a steady surge or hydraulic jump (Fig. 5.7).



**Adhémar Barré de Saint-Venant** was born on August 23, 1797, at Filliers, France, and passed away aged 89 years at Saint-Ouen on January 6, 1886. He was educated at Ecole Polytechnique, entering the *Corps des Ponts et Chaussées* (Corps of Bridges and Roads), where he stayed for the next 25 years. He conducted works relating to harbors, navigation canals, and roads. A memoir on agricultural hydraulics was honoured by the Agricultural Society in 1849. He was named professor at *Institut Agronomique de Versailles* in 1850 and lectured also at *Ecole des Ponts et Chaussées*. de Saint-Venant left Paris city services in 1848 to devote himself exclusively to sciences, starting in 1852. His main first works related to elasticity, following Poncelet's approach. In 1868, de Saint-Venant was elected Member of *Académie des Sciences*, Paris.

The de Saint-Venant equations relate to one-dimensional unsteady flows; these are currently also referred to as the shallow water equations. A set of partial differential equations for flow depth and cross-sectional velocity as a function of space and time was established in 1871. These equations are based on hydrostatic pressure and uniform velocity distributions and serve currently for the prediction of flood flows, either in one or in two dimensions. de Saint-Venant also proposed in 1851 an equation for the loss of head in pressurized conduit flows using a power function. This paper introduces early ideas on the effect of fluid turbulence. It was recently proposed that the current Froude number should be referred to the name of de Saint-Venant, given the latter's enormous developments in this field of hydraulics.

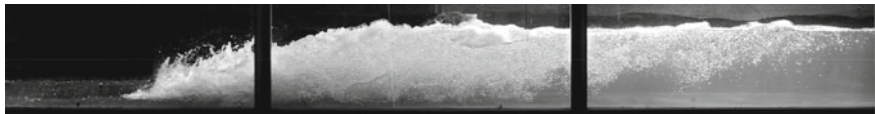


**Fig. 5.7** Hydraulic jump or steady surge (photograph VAW, ETH Zurich)

From Eq. (5.28),  $\varepsilon_{\min}$  is

$$\varepsilon_{\min} = \frac{h_2}{h_1} - 1 = -\frac{3}{2} \pm \left[ \frac{9}{4} - 2(1 - F_1^2) \right]^{1/2} = -\frac{3}{2} \pm \left[ \frac{1}{4} + 2F_1^2 \right]^{1/2}. \quad (5.31)$$

Solving Eq. (5.31) for the sequent depth ratio  $h_2/h_1$  produces Bélanger's equation for the hydraulic jump presented in Chap. 4 as [Eq. (4.18)]

$$\frac{h_2}{h_1} = \frac{1}{2} \left[ (1 + 8F_1^2)^{1/2} - 1 \right]. \quad (5.32)$$

### 5.3.4 Formulation Used in Finite Volume Methods

The general equation for a shock wave [Eq. (5.22)] moving to the right direction is

$$V_w = U_1 + \left[ \frac{gh_2}{2h_1} (h_1 + h_2) \right]^{1/2}. \quad (5.33)$$

It will be rewritten in a form widely used in CFD applications based on finite volume upwind methods with flux computations using Riemann solvers (Toro 2001; see Chap. 9). Equation (5.18) for a rectangular cross section is

$$(U_2 - U_1)^2 = \frac{g}{2} \frac{(h_1 - h_2)}{h_1 h_2} (h_1 + h_2), \quad (5.34)$$

which coupled with Eq. (5.33) yields  $V_w$  as function of the tailwater velocity  $U_2$

$$V_w = U_2 + \left[ \frac{gh_1}{2h_2} (h_1 + h_2) \right]^{1/2}. \quad (5.35)$$

Using the definition  $c_2 = (gh_2)^{1/2}$  one gets from this last expression

$$V_w = U_2 + (gh_2)^{1/2} \left[ \frac{h_1}{2h_2^2} (h_1 + h_2) \right]^{1/2} = U_2 + Kc_2. \quad (5.36)$$

Here,  $K$  is a dimensionless factor accounting for the finite surge height,

$$K = \left[ \frac{h_1}{2h_2^2} (h_1 + h_2) \right]^{1/2}. \quad (5.37)$$

Equation (5.36) is a “signal” celerity used to propagate shocks in the finite volume method, to be described in Chap. 9.

## 5.4 Methods of Solution

### 5.4.1 Shock-Capturing Methods

A shock-capturing method permits to compute the solution of a hyperbolic system of conservation laws including continuous and discontinuous waves without any special shock treatment (Cunge 1975; Toro 2001). The differential form of the 1D SWE, Eq. (5.4), can be written in vector notation as

$$\frac{\partial \mathbf{U}}{\partial t} + \frac{\partial \mathbf{F}}{\partial x} = \mathbf{S}. \quad (5.38)$$

Here,  $\mathbf{U}$  is the vector of unknowns,  $\mathbf{F}$  the flux vector, and  $\mathbf{S}$  the source term vector, given with  $C_f$  as a friction coefficient by

$$\mathbf{U} = \begin{pmatrix} h \\ Uh \end{pmatrix}, \quad \mathbf{F} = \begin{pmatrix} Uh \\ U^2 h + \frac{1}{2} gh^2 \end{pmatrix}, \quad \mathbf{S} = \begin{pmatrix} 0 \\ -gh \frac{\partial \varepsilon_b}{\partial x} - C_f U |U| \end{pmatrix} \quad (5.39)$$

This is called conservative form of the SWE (Toro 2001; Chaudhry 2008). This system of PDEs is only valid for the computation of continuous solutions, where  $h$  and  $q$  are smooth and single-valued in the  $(x, t)$  plane. The solution  $\mathbf{U}(x, t)$  of Eq. (5.38) must be differentiable with respect to  $x$  and  $t$ . To compute discontinuous flows, the PDEs must be integrated over a control volume to obtain its integral form (Cunge 1975). This fact was already used in Sect. 5.3.2 to obtain the basic relations of a surge. Here, the integral form is reproduced by integrating the conservative form of the SWE over a control volume. For simplicity, source terms are dropped, resulting in the inviscid version of the SWE over horizontal terrain, that is

$$\frac{\partial \mathbf{U}}{\partial t} + \frac{\partial \mathbf{F}}{\partial x} = \mathbf{0}. \quad (5.40)$$

This equation is now integrated over an arbitrary control volume  $CV$ , resulting in

$$\iiint_{CV} \left( \frac{\partial \mathbf{U}}{\partial t} + \frac{\partial \mathbf{F}}{\partial x} \right) dv = \mathbf{0}, \quad (5.41)$$

or,

$$\iiint_{CV} \left( \frac{\partial \mathbf{U}}{\partial t} + \nabla \cdot \mathbf{F} \right) dv = \mathbf{0}. \quad (5.42)$$

Applying Gauss's divergence theorem to the flux term in Eq. (5.42) results in

$$\iiint_{CV} \frac{\partial \mathbf{U}}{\partial t} dv + \iint_{CS} (\mathbf{F} \cdot \mathbf{n}) dA = \mathbf{0}. \quad (5.43)$$

After elementary manipulations, Eq. (5.43) becomes equivalent to Reynolds' transport theorem as used in Sect. 5.3.2. While Eq. (5.40) only applies to compute continuous flows, Eq. (5.43) describes any type of solution, both continuous and discontinuous.<sup>2</sup> The solution  $\mathbf{U}(x, t)$  of Eq. (5.43) must be integrable, but it is not necessary that it be continuous. Equation (5.43) is the basic relation used to construct shock-capturing numerical methods (Toro 2001); it conserves mass and momentum in a fluid system: If the system is discretized into control volumes which are in contact, fluxes leaving a control volume enter into the adjacent control volume across the contact surface. Overall, there is no net gain or loss of mass and momentum in the entire system, corresponding to the so-called conservative property (Roache 1972). The formulation of the SWE as presented in Eq. (5.40) is the so-called conservative form, where the conserved variables in the fluid system are  $h$  and  $(Uh)$  (Toro 2001). The non-conservative or primitive formulation of the SWE is regained by formulating the PDEs in terms of  $h$  and  $U$ , yielding (Jain 2001)

---

<sup>2</sup>In applied mathematics, the solutions of the integral form of a system of conservation laws are called *weak solutions* of the differential form, even though they may or may not be the traditional solutions of it (Cunge 1975; Macdonald 1995). This is simply a notation criterion to avoid having to refer to the integral form, but, clearly, the integral form is linked to the concept of weak solution. If a weak solution is continuous, then it is a solution of the differential form and it is called *genuine solution*.

$$\begin{aligned}\frac{\partial h}{\partial t} + h \frac{\partial U}{\partial x} + U \frac{\partial h}{\partial x} &= 0, \\ \frac{\partial U}{\partial t} + U \frac{\partial U}{\partial x} + g \frac{\partial h}{\partial x} &= 0.\end{aligned}\tag{5.44}$$

This form of the SWE generally applies only to compute continuous solutions. A shock-capturing method based on Eq. (5.43) can resolve without any special treatment surges and continuous waves, but, if applied to Eq. (5.44), will produce shocks of erroneous celerity (Cunge 1975; Toro 2001) (see Sect. 5.8). An alternative is to use the so-called shock tracking methods: in these techniques, Eq. (5.44) are used to solve the continuous portions of the solution (usually resorting to the method of characteristics, see below), and the shocks are tracked and characterized with the surge conditions as internal boundary conditions (Lai 1986; Cunge et al. 1980; Montes 1998). These techniques are not in use, given that in the presence of multiple shocks computations are extremely tedious. Thus, shock tracking methods are not further considered here.

#### 5.4.2 Outline of Solution Methods

*Method of Characteristics (MC):* The SWE are transformed to ODEs, as will be shown in the next section. In simple cases, it is possible to find analytical solutions, but in most cases, a numerical solution is required using finite difference methods (FDMs). It is an important method to understand the boundary conditions needed to solve the SWE. It is also relevant for the development of analytical solutions while solving the Riemann problem, the key ingredient of the finite volume method (FVM). The numerical solutions of the SWE using the MC and finite differences tend to be not used. For a detailed treatment, see Lai (1986) and Chaudhry (2008). Analytical considerations emerging from the MC are described below.

*Finite difference methods (FDMs):* The SWE are solved in differential form approximating the partial derivatives by finite differences using Taylor series (Chaudhry 2008). These methods are described in Chap. 7.

*Finite volume methods (FVMs):* The SWE are solved in integral form, as given by Reynolds' transport theorem, in a number of control volumes on which the domain is discretized (Toro 2001). It is a technique widely used. These methods are described in Chap. 9.

*Finite element methods (FEMs):* The solution of SWE is approximated by assuming functions in a number of finite elements on which the domain is discretized. For a detailed treatment, see Hicks and Steffler (1990) and Katopodes (2019).

*Discontinuous method of Galerkin:* Hybrid method coupling finite volume computation of fluxes resorting to Riemann solvers with discontinuous finite elements. It is described and applied to open channel flows by Khan and Lai (2014).

## 5.5 Method of Characteristics

### 5.5.1 SWE in Characteristic Form

The MC is important to understand physically how a perturbation propagates in a free surface flow. A perturbation over an initially steady flow generates a variation in depth and velocity at a given position over its equilibrium values. The method is also important to understand the boundary and initial conditions needed to solve the SWE. Simple analytical solutions of the SWE are available using the MC. The SWE in non-conservative form are, after expanding Eq. (5.3) (Jain 2001; Chaudhry 2008),

$$\begin{aligned} \frac{\partial h}{\partial t} + D \frac{\partial U}{\partial x} + U \frac{\partial h}{\partial x} &= 0, \\ \frac{1}{g} \frac{\partial U}{\partial t} + \frac{U}{g} \frac{\partial U}{\partial x} + \frac{\partial h}{\partial x} &= S_o - S_f. \end{aligned} \quad (5.45)$$

Here,  $S_o = -\partial z_b / \partial x$  is the bottom slope,  $S_f$  the friction slope and  $D = A/B$  the hydraulic depth, with  $B$  as free surface width. Summing of the two equations, after multiplying the continuity equation by an undetermined variable  $\lambda$  yields, after re-arrangement,

$$\left[ \frac{\partial U}{\partial t} + (U + \lambda D) \frac{\partial U}{\partial x} \right] + \lambda \left[ \frac{\partial h}{\partial t} + \left( U + \frac{g}{\lambda} \right) \frac{\partial h}{\partial x} \right] = g(S_o - S_f). \quad (5.46)$$

The total differentials of the functions  $U = U(x, t)$  and  $h = h(x, t)$  are defined as

$$\begin{aligned} \frac{DU}{Dt} &= \frac{\partial U}{\partial t} + \frac{\partial U}{\partial x} \frac{dx}{dt}, \\ \frac{Dh}{Dt} &= \frac{\partial h}{\partial t} + \frac{\partial h}{\partial x} \frac{dx}{dt}. \end{aligned} \quad (5.47)$$

Comparing with Eq. (5.46), the terms inside the brackets are exact total differentials only if

$$\frac{dx}{dt} = U + \lambda D = U + \frac{g}{\lambda}. \quad (5.48)$$

From this identity,  $\lambda$  is given by the expression

$$\lambda = \pm \left( \frac{g}{D} \right)^{1/2}. \quad (5.49)$$

Therefore, using this value of  $\lambda$ , one can write

$$\frac{dx}{dt} = U \pm c, \quad (5.50)$$

where  $c$  is the celerity of propagation of a small gravity perturbation

$$c = (gD)^{1/2}. \quad (5.51)$$

After mathematical manipulations, one finds

$$\frac{D}{Dt}(U + \omega) = g(S_o - S_f), \quad (5.52)$$

provided that

$$\frac{dx}{dt} = U + c, \quad (5.53)$$

and

$$\frac{D}{Dt}(U - \omega) = g(S_o - S_f), \quad (5.54)$$

if

$$\frac{dx}{dt} = U - c. \quad (5.55)$$

Here, Escoffier's stage variable  $\omega$  is defined by (Jain 2001)

$$\omega = \int_0^h \lambda dh. \quad (5.56)$$

For a rectangular cross section, the reduced equations are after elementary manipulations

$$\begin{aligned}\frac{D}{Dt}(U - 2c) &= g(S_o - S_f) \quad \text{along} \quad \frac{dx}{dt} = U - c, \\ \frac{D}{Dt}(U + 2c) &= g(S_o - S_f) \quad \text{along} \quad \frac{dx}{dt} = U + c.\end{aligned}\tag{5.57}$$

Mathematically, this system of equations states that the total material derivatives of  $(U \pm 2c)$  are equal to  $g(S_o - S_f)$ , but only along the paths in the  $x$ - $t$  plane described by the integrals of the ODEs  $dx/dt = U \pm c$ . Therefore, the original SWE, a system of PDEs valid at any point of the  $x$ - $t$  plane, has been transformed into a system of ODEs valid only along the paths given by the ODEs  $dx/dt = U \pm c$ . Note that space derivatives are no more in the equations, given that the  $x$ -coordinate is linked to time by the integrals of  $dx/dt = U \pm c$ .

Consider the case for which the source term is zero, that is,  $S_o = S_f = 0$ , resulting in

$$\begin{aligned}\frac{D}{Dt}(U - 2c) &= 0 \quad \text{along} \quad \frac{dx}{dt} = U - c, \\ \frac{D}{Dt}(U + 2c) &= 0 \quad \text{along} \quad \frac{dx}{dt} = U + c.\end{aligned}\tag{5.58}$$

For inviscid flow over horizontal topography, the so-called Riemann invariants  $(U \pm 2c)$  are conserved along the paths in the  $x$ - $t$  plane obtained upon integration of the ODEs  $dx/dt = U \pm c$ . These ODEs in the  $x$ - $t$  plane are known as characteristic curves. The family of curves given by the ODE  $dx/dt = U + c$  are known as forward characteristics, while those given by  $dx/dt = U - c$  are known as backward characteristics. In subcritical flow  $U < c$  ( $F < 1$ ), the forward and backward characteristics curves in the  $x$ - $t$  plane have positive and negative slopes, respectively (Fig. 5.8a). In supercritical flow  $U > c$  ( $F > 1$ ), both the forward and backward characteristics curves in the  $x$ - $t$  plane have positive slopes (Fig. 5.8b). For critical flow  $U = c$  ( $F = 1$ ), the backward characteristic in the  $x$ - $t$  plane is a vertical line (Fig. 5.8c).

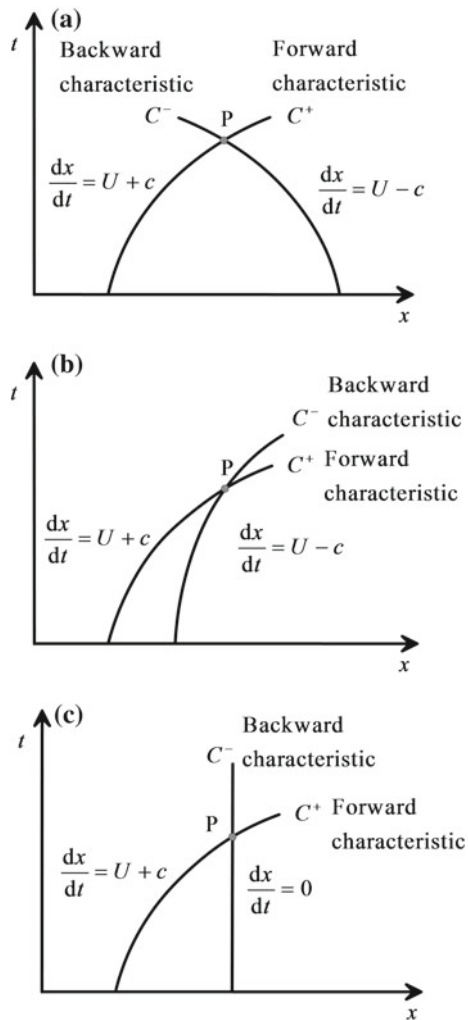
Along the points on a forward characteristic,

$$\frac{D}{Dt}(U + 2c) = 0 \Rightarrow U + 2c = \text{const. along } \frac{dx}{dt} = U + c,\tag{5.59}$$

whereas along the points on a backward characteristic results

$$\frac{D}{Dt}(U - 2c) = 0 \Rightarrow U - 2c = \text{const. along } \frac{dx}{dt} = U - c.\tag{5.60}$$

**Fig. 5.8** Characteristics in  
**a** subcritical flow,  
**b** supercritical flow, **c** critical flow



Physically, this means that a perturbation generated at any point  $x$  at a given instant of time  $t$  will propagate along the forward and backward characteristics curves conserving along these paths the corresponding Riemann invariant. The propagation of any perturbation is therefore a transmission of information along the characteristics: The non-equilibrium values  $h$  and  $U$  generated at the origin of the perturbation will generate new non-equilibrium values at other sections at different instants of time. In general,  $h$  and  $U$  are variable along the characteristics, which are thus curved lines.

### 5.5.2 Initial and Boundary Conditions

Consider forward and backward characteristics curves in subcritical flow originating at points 1 and 4 and intersecting at point 10 (Fig. 5.9). Additional characteristics may be drawn from other initial points, e.g., from points 2 and 3. A curvilinear net of characteristics is formed. Consider first only points 1, 4, and 10. Riemann invariants are conserved along the corresponding characteristics connecting 1–10 and 4–10. One may write along the forward characteristic

$$U_1 + 2c_1 = U_{10} + 2c_{10}, \quad (5.61)$$

and along the backward characteristic

$$U_4 - 2c_4 = U_{10} - 2c_{10}. \quad (5.62)$$

Conditions at points 1 and 4 are assumed to be known (depth and velocity), resulting in a system of two equations and two unknowns at point 10 (depth and velocity). The same process may be applied to the other interior grid points if additional characteristics are drawn, forming points 5, 6, 7, 8, and 9. Conditions at 5, 6, and 7 are first computed based on known conditions at 1, 2, 3, and 4. Then, conditions at points 8 and 9 are determined based on known results at 5, 6, and 7. Finally, conditions at point 10 are determined based on points 8 and 9. Note that the flow conditions in the curvilinear domain 1–4–10 influence the conditions at point 10 itself. This zone is known as domain of dependence of point 10. In Fig. 5.10, the domain of dependence of point 3 is plotted as a dark gray shadow. During the computational process described above, it is well noted that the flow conditions at point 2 “are felt” in the curvilinear triangle between the backward and forward characteristics emerging from it. This zone is known as domain of influence of point 2 (Fig. 5.10).

The SWE are a system of 2 hyperbolic PDEs for the unknowns  $U(x, t)$  and  $h(x, t)$ . To solve the equations in a given channel reach, it is needed to prescribe an initial condition. It is given by steady values of depth and velocity along the

**Fig. 5.9** Characteristics net for subcritical flow

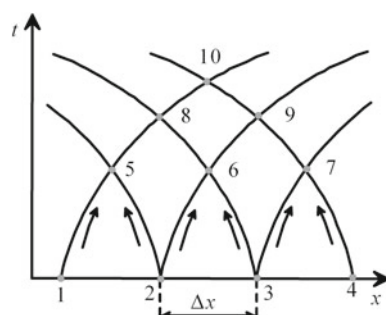
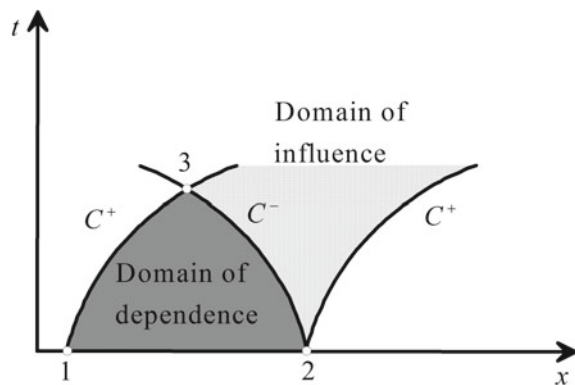


**Fig. 5.10** Domains of influence and dependence for subcritical flow



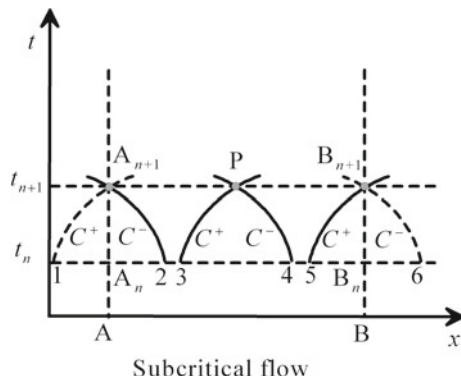
channel. Typically, the discharge is constant and the variation of water depth in space is computed by solving the steady-state version of the momentum equation (see Chap. 3)

$$\frac{dq}{dx} = 0 \Rightarrow q = q_o = \text{const.},$$

$$\frac{dh}{dx} = \frac{S_o - S_f}{1 - \frac{q^2}{c^2}} = \frac{S_o - S_f}{1 - F^2}. \quad (5.63)$$

Here,  $F$  is the Froude number and  $q_o$  the inflow discharge. Further, two boundary conditions are needed. These are the evolution of depth or velocity with time at boundary sections of the channel reach. The sections to apply the boundary conditions are different depending on whether the flow is sub- or supercritical. Consider first the channel reach A–B (Fig. 5.11) with subcritical flow conditions throughout. At the initial instant of time  $t_n$ , flow conditions at points  $A_n$ , 2, 3, 4, 5, and  $B_n$  are known. Inside the reach A–B, the forward and backward characteristics emerging from points 3 and 4, respectively, intersect at point P. Conditions there are

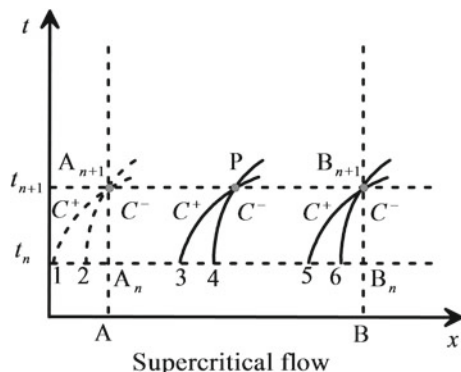
**Fig. 5.11** Boundary conditions for subcritical flow



determined mathematically based on points 3 and 4 on the  $t_n$  time line, as previously explained. Now, consider point  $A_{n+1}$  at time level  $t_{n+1}$ . The backward characteristic lies inside the physical reach A–B, but the forward characteristic is outside the upstream boundary section of the channel reach. At point  $A_{n+1}$ , the unknowns are  $U_{A_{n+1}}$  and  $h_{A_{n+1}}$ , but only one equation is available, stating the conservation of the Riemann invariant along  $C^-$ , that is,  $U_{A_{n+1}} - 2c_{A_{n+1}} = U_2 - 2c_2$ . At point  $A_{n+1}$ , therefore, a known value of either  $U_{A_{n+1}}$  or  $h_{A_{n+1}}$  has to be prescribed. This known value needed is called boundary condition. Following the same arguments, at point  $B_{n+1}$ , given that the backward characteristic is outside the physical channel reach, we need to prescribe one boundary condition, either  $U_{B_{n+1}}$  or  $h_{B_{n+1}}$ . In subcritical flow, one boundary condition is required at the upstream section and another at the downstream section of the reach. The subcritical flow is thus said to be controlled from up- and downstream. A steady-state flow is determined based on suitable unsteady computations, as explained by Stoker (1957). The basic idea is to abandon the formulation of steady flow based on Eq. (5.63) in favor of the solution of the SWE involving appropriate initial conditions and then allowing for the unsteady flow to reach the limit in the solutions as  $t \rightarrow \infty$ . If a steady flow exists, then it should be the result of unsteady computations for  $t \rightarrow \infty$ . Suitable boundary conditions must be prescribed in the initial value problem compatible with the existence of a steady flow solution (Macdonald 1995).

Consider now the channel reach A–B with supercritical flow conditions throughout (Fig. 5.12). At a generic point P inside the reach, the forward and backward characteristics intersect, so flow conditions there are determined mathematically based on points 3 and 4 at the  $t_n$  time level. Now, consider point  $A_{n+1}$  at time level  $t_{n+1}$ . The backward and forward characteristic lines passing through this point lie outside the upstream boundary section of the channel reach. At point  $A_{n+1}$ , the unknowns are  $U_{A_{n+1}}$  and  $h_{A_{n+1}}$ , but there are no equations available to undertake computations. At point  $A_{n+1}$ , therefore, known values of  $U_{A_{n+1}}$  and  $h_{A_{n+1}}$  have to be prescribed; that is, two boundary conditions are needed. At point  $B_{n+1}$ , the backward and forward characteristics lie inside the physical channel reach, and its flow conditions are therefore mathematically determined based on known conditions at

**Fig. 5.12** Boundary conditions for supercritical flow



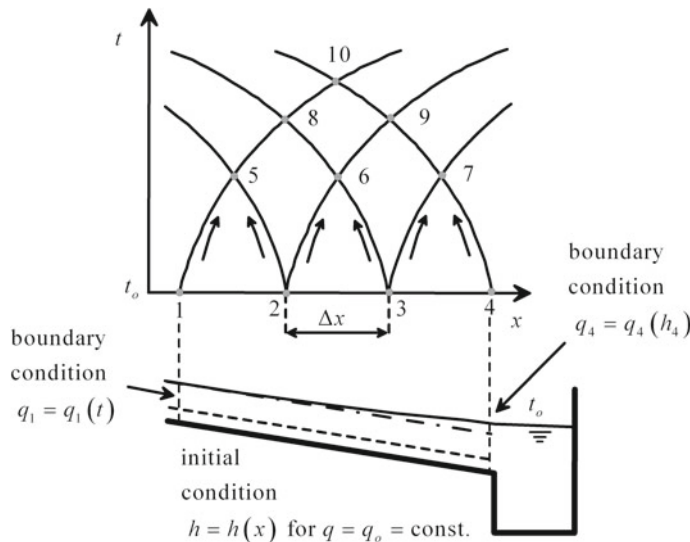


**Fig. 5.13** Example of initial and boundary condition requirements for subcritical flow

points 5 and 6. Thus, we do not need to prescribe any boundary condition at that section. In supercritical flow, two boundary conditions are required at the upstream section of the reach, and the flow is said to be controlled from upstream.

For illustrative purposes of initial and boundary data requirements, consider an initially steady subcritical flow profile of type M1 shown in Fig. 5.13, formed at the transition from a canal to a reservoir at its downstream end. Note that normal depth is larger than the critical depth in this flow profile, as explained in Chap. 3. The boundary sections of the canal reach are points 1 and 4. The initial condition needed to solve the SWE is given by the M1 backwater profile, computed by integration of Eq. (5.63). The typical boundary condition upstream of a subcritical stream is the inflow discharge hydrograph, e.g., the function  $q = q(t)$  at point 1. Likewise, a typical boundary condition at the downstream section of a subcritical stream (point 4) is the water depth  $h$  in the form of rating curve  $q = q(h)$ . This rating curve may be determined by critical flow conditions, uniform flow conditions, or a hydraulic element, e.g., a gate or a weir (see Chap. 2 for details of governing equations for each boundary condition), depending on the physical characteristics of the boundary. In our case, the water depth function in the reservoir is assumed to be known. This relation is inverted to produce  $h = h(q)$ , and, with computed values of  $q(t)$  at point 4, the function  $h_4 = h_4(t)$  is described. With these initial and boundary conditions (discharge upstream, water depth

downstream), the SWE are numerically solved along the characteristics until a new steady-state condition originates if the boundary conditions permit this equilibrium solution.<sup>3</sup>

Thus, a subcritical flow is controlled from both up- and downstream, given that perturbations at boundary sections propagate both up-and downstream of the reach. The conditions at both boundary sections thus affect the flow inside of the computational reach. A typical boundary condition at the upstream section is the discharge, e.g., a flood wave entering gradually into the reach or a sudden discharge increase from one steady discharge to a new steady discharge. A typical boundary condition at the downstream section is the water depth, controlled, for example, with man-made structures, e.g., a gate or a weir. During unsteady flow, both boundary conditions may depend on time, as explained. If a steady flow solution is physically permitted by the boundary conditions, it is the asymptotic state produced by unsteady computations based on the SWE (Macdonald 1995). For a steady subcritical flow, the upstream boundary condition  $q = q(t)$  reduces to  $q_o = \text{const.}$  in the entire channel reach (given that the continuity equation is  $dq/dx = 0$ ), whereas the downstream boundary condition  $h = h(t)$  transforms to  $h = \text{const.}$  at that section.

The steady form of the SWE is a first-order ODE, so only one boundary condition is needed. This condition is, therefore, the downstream tailwater depth. The upstream boundary condition of the SWE equations reduces simply to constant discharge; i.e., the upstream constant discharge is conserved along the entire channel reach. Based on this physical reasoning originating from the unsteady SWE, it is possible to find a justification for the traditional rule stating “*subcritical steady flows are controlled from downstream*”: Subcritical unsteady flows are controlled from both up- and downstream, but in steady state, the upstream control is “switched off.” Mathematically, the ODE for steady flow is a first-order equation to be solved once a boundary condition is prescribed. From a mathematical standpoint, this boundary condition is set either at the up- or downstream boundary sections of the reach. Physically, a more logic choice in agreement with unsteady SWE computations is to take the downstream boundary section. The same steady computational rule states that “*supercritical steady flows are controlled from upstream*”: Supercritical unsteady flows are controlled fully from upstream, but in steady state, one of the upstream controls is “switched off.” At the upstream section, both discharge and depth must be prescribed in the SWE. Following the former discussion, in steady state, the discharge is a constant, so this is the boundary condition that is automatically eliminated from the mathematical problem. The water depth at the upstream boundary section of the reach remains as boundary condition, in agreement with the steady-state computational rule.

---

<sup>3</sup>Steady flow solutions can be generated using Eq. (5.63). To be of practical relevance, a steady flow solution must be stable in time; that is, if the steady state is slightly perturbed, the flow conditions must tend back again to the original steady state (Macdonald 1995). An example of unstable steady flow solutions is presented when setting uniform flow on steep chutes, where roll waves are generated (Stoker 1957).

**Fig. 5.14** Effect of obstacle in subcritical stream initially as steady uniform flow

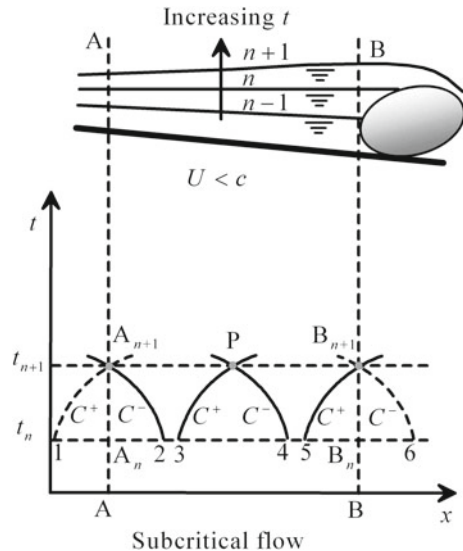
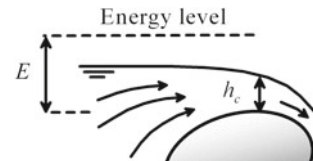


**Fig. 5.15** Stone acting as control section setting critical flow conditions



The mathematical tools are now available to better understand the effect of a stone (obstacle) inserted in an initially uniform and steady stream presented in Chap. 2, given that it is in reality an unsteady gradually varied flow process. The obstacle inserted into the initially uniform subcritical stream produces a gradual variation of water levels (Fig. 5.14) (rapidly varied flow effects are overlooked for the sake of simplicity). The upstream boundary condition at section A is the constant discharge  $q_o$  flowing initially in the uniform stream. The flow depths and velocities within the reach evolve in time, but the discharge in the reach at section A remains unaltered.

The downstream boundary condition at the vicinity of the stone (point B) is zero discharge as long as the water depth is below the top of the stone. As the water begins to pass over the stone, it acts like a round-crested weir, with critical depth somewhere on the stone surface, close to the top of its round-crested surface (Fig. 5.15).

Let  $q$  be the discharge at section B at any instant of time, the discharge equation of the flow over the stone is with  $E$  as the specific energy over the crest

$$q = \left(\frac{2}{3}\right)^{3/2} (gE^3)^{1/2}. \quad (5.64)$$

If  $h$  is the flow depth at point B and  $D$  the stone height, then

$$E = D + h + \frac{q^2}{2gh^2}. \quad (5.65)$$

Combining Eqs. (5.64) and (5.65), the nonlinear implicit equation is

$$q - \left(\frac{2}{3}\right)^{3/2} \left[ g \left( D + h + \frac{q^2}{2gh^2} \right)^3 \right]^{1/2} = 0. \quad (5.66)$$

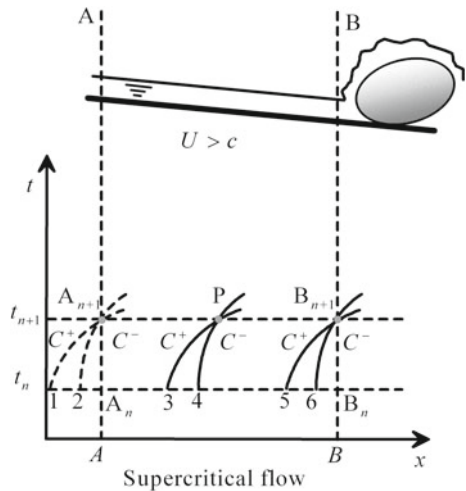
Thus, the boundary condition at point B is the function  $h = h(q)$  if  $h > D$ , obtained by numerically inverting Eq. (5.66) using, e.g., the Newton–Raphson method. For  $h < D$ , the boundary condition is simply  $q = 0$ .

With this reasoning, boundary conditions at points A and B are determined. The net of characteristics is as shown in Fig. 5.14. Consider the backward characteristic 4-P. It transmits back in space, and forward in time, information on the perturbation generated at point B. This information is transmitted back and back in space until at a given instant of time the upstream water levels at A start to increase, in response to this “information feedback.” After some time, a steady backwater profile is set within the reach. Note that the discharge at section A was a constant during the unsteady flow and that all the perturbation process was controlled by water levels at B. Discharge at B is zero until the water begins to flow over the stone. Later, it gradually increases until reaching the steady-state value  $q_o$  that is the boundary condition at the upstream section A. Therefore, the analogy with steady backwater computations is evident: The discharge in the system is  $q_o$ , and we set as boundary condition at the tailwater section the depth  $h$  satisfying Eq. (5.66) for steady state, that is,

$$q_o - \left(\frac{2}{3}\right)^{3/2} \left[ g \left( D + h + \frac{q_o^2}{2gh^2} \right)^3 \right]^{1/2} = 0. \quad (5.67)$$

For the supercritical case (Fig. 5.16), the upstream boundary condition is the constant discharge  $q_o$  flowing initially in the uniform stream. The other upstream boundary condition needed is the uniform flow depth of the initial stream. There is not any mathematical way of transmitting to the inlet (back in space) the perturbation generated by the stone at the tailwater section, as demonstrated by the characteristics plotted in Fig. 5.16. The flow profile within the channel reach is uniform and steady, until it impacts the stone, jumping above it.

**Fig. 5.16** Effect of obstacle for supercritical stream initially in steady uniform flow



### 5.5.3 Wave Celerity

Consider the propagation of a flood wave of hydrograph  $q_o(t)$  over an initially non-uniform flow in subcritical flow conditions at instant  $t_o$  (Fig. 5.17). The flow is assumed to be frictionless and the bottom slope small, so that both effects are neglected. The flow solutions are thus governed by Eqs. (5.59) and (5.60). In general, given that the initial steady flow is non-uniform, all the characteristics will be curved lines.

Consider the free surface profile at a time  $t_o$ : At sections 1 and 2 separated by a distance  $\Delta x$ , the flow depths  $h(x, t)$  and velocities  $U(x, t)$  are known. After a time  $\Delta t$ , the free surface profile will move to a new position in response to the flooding produced by  $q_o(t)$ . The forward and backward characteristics originating from points 1 and 2 at time  $t$  intersect in point P at time  $t_o + \Delta t$ , located within the reach  $\Delta x$ . Physically, the perturbations originating at points 1 and 2 at time  $t$  propagate along the characteristics during  $\Delta t$  and finally meet at point P. There,  $h$  and  $U$  are determined on the basis of flow conditions at points 1 and 2 by using the Riemann invariants. The derivative  $dx/dt$  is physically the absolute velocity of propagation of the perturbations along the paths in the  $x-t$  plane where Riemann invariants are conserved. This example shows that this derivative is in fact the rate at which information is transmitted, but it is not a “wave velocity,” with the usual meaning; there is no “visible wave profile” displacing in the physical plane at rate  $dx/dt$ . Figure 5.17 highlights that point P of the free surface profile at time  $t_o + \Delta t$  cannot be visualized by observing the temporal evolution of the free surface during the interval  $\Delta t$ . Its spatial coordinate at time  $t_o + \Delta t$  can only be determined mathematically, as explained above. Neither depth nor velocity is constant along the characteristics in general, so there are not observable perturbations of  $h$  or  $U$  traveling at rate  $\pm(gh)^{1/2}$  relative to water flow. This is due to

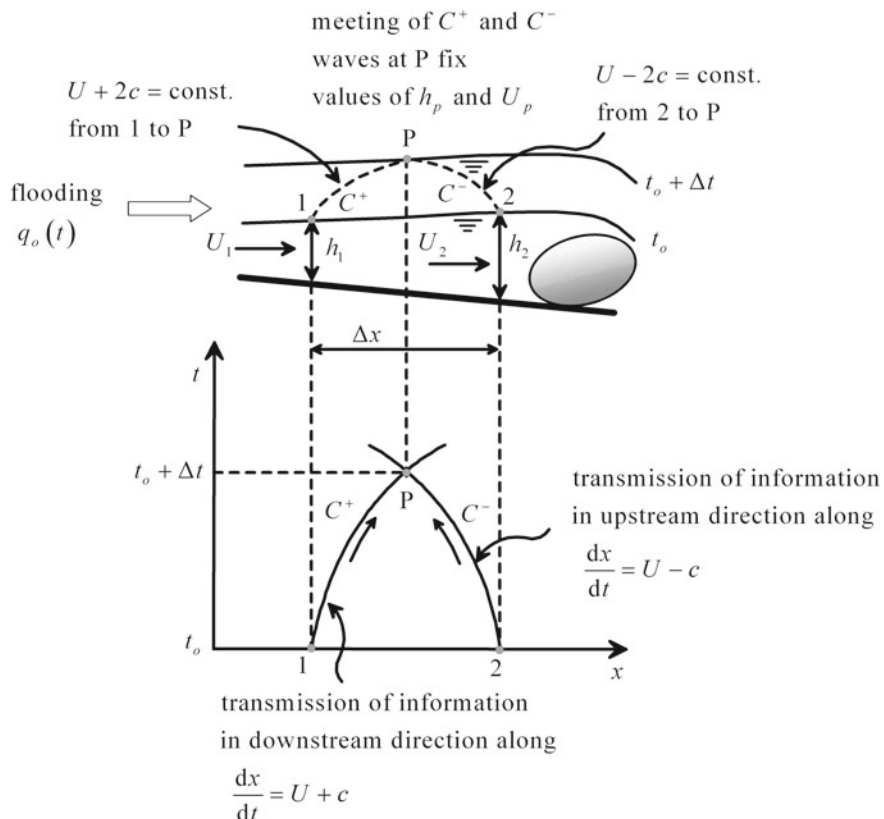


**Fig. 5.17** Physical meaning of  $dx/dt$  in method of characteristics for a perturbation propagating over initially steady non-uniform flow

the fact that the initial steady flow was non-uniform; in this case, the magnitude  $dx/dt$  is not giving the velocity of propagation of a “visual” wave. It is, however, the mathematical velocity at which the information of the perturbations in depth and velocity travels along the characteristic lines. In specific cases,  $dx/dt$  can yield a “visual” wave. It was demonstrated that a surge of infinitesimal height propagates with celerity  $(gh)^{1/2}$  relative to the water flow. Thus, a surge of small height will be visually observable traveling at a velocity close to this value. In this case, in fact, both  $h$  and  $U$  remain constant along the characteristic lines. For a negative surge propagating over an initially uniform flow, to be described below, it will be shown that  $dx/dt$  also yields the wave celerity which can be visually observed.

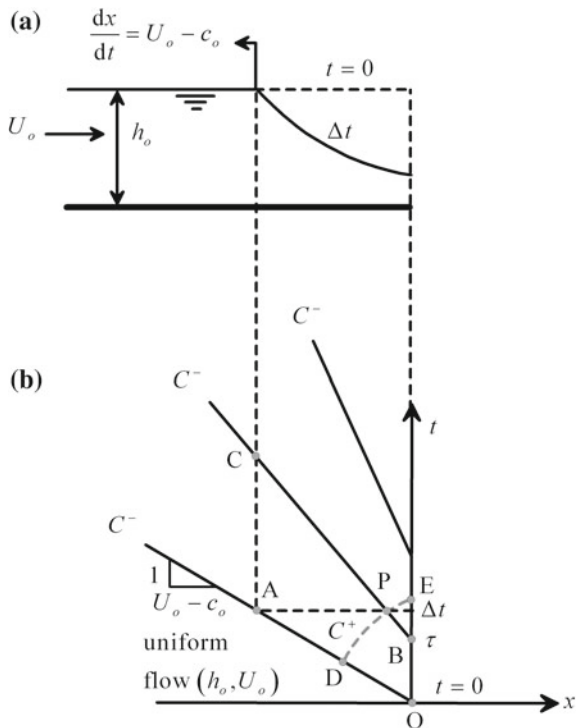
## 5.6 Simple Wave Problem: Basic Equations of Rarefaction Waves

### 5.6.1 The Simple Wave

The method of characteristics applies to obtain closed-form analytical solutions for an important type of continuous wave called simple wave. It is a smooth and continuous wave (values of depth and velocity across the wave are single-valued) solution of the SWE propagating over an initially steady and uniform stream of depth  $h_o$  and velocity  $U_o$  (Fig. 5.18). The channel is assumed to be horizontal and the flow frictionless, leading to Eqs. (5.59) and (5.60) as governing equations. The flow is perturbed at  $x = 0$  in the form of a prescribed variation of the water depth with time, or, equivalently,  $c(0, t) = g(t)$ , where the function  $g(t)$  is decreasing with time. The reduction of water depth with time at  $x = 0$  will produce a perturbation in the initial equilibrium values  $(h_o, U_o)$ , which propagates in the negative  $x$ -direction at velocity

$$\frac{dx}{dt} = U_o - c_o \equiv \frac{x}{t}. \quad (5.68)$$

**Fig. 5.18** Simple wave solution **a** physical plane, **b** characteristic plane  $(x, t)$



This characteristic is a straight line given that both depth and velocity in the undisturbed flow zone are constants. It can be demonstrated that if a member of a  $C$ -family is a straight line, then all members of this family are also straight lines (Liggett 1994; Jain 2001). Thus, for all  $C^-$  characteristics, it can be stated that

$$\frac{dx}{dt} = U - c = \text{const.} \quad (5.69)$$

Along the  $C^-$  lines, conservation of the Riemann invariant yields

$$U - 2c = \text{const.} \quad (5.70)$$

Thus, coupling Eqs. (5.69) and (5.70), it is seen that along the straight backward characteristics both velocity and celerity are constants, e.g., (Fig. 5.18)

$$U = \text{const.}, c = \text{const. along } \overline{BC}. \quad (5.71)$$

Thus, one can write, taking as reference the point at the intersection of a  $C^-$  line with the  $t$ -axis (e.g., point B in Fig. 5.18), where time is  $\tau$ ,

$$U = U_B = U(0, \tau), \quad (5.72)$$

$$c = c_B = c(0, \tau). \quad (5.73)$$

Along a generic  $C^+$  characteristic, one can write based on conservation of the Riemann invariant (Fig. 5.18)

$$U_D + 2c_D = U_P + 2c_P. \quad (5.74)$$

But point D belongs to the undisturbed flow region, implying

$$\begin{aligned} U_D &= U_o, \\ c_D &= c_o. \end{aligned} \quad (5.75)$$

Also, based on Eq. (5.71),

$$\begin{aligned} U_P &= U_B, \\ c_P &= c_B, \end{aligned} \quad (5.76)$$

resulting from Eq. (5.74) after consideration of Eqs. (5.75) and (5.76) in

$$U_o + 2c_o = U(0, \tau) + 2c(0, \tau). \quad (5.77)$$

This relation states that the Riemann invariant  $U + 2c$  is a constant in the entire  $(x, t)$  plane for the simple wave, that is,

$$U(x, t) + 2c(x, t) = \text{const.} \equiv U_o + 2c_o. \quad (5.78)$$

Along the  $C^-$  characteristic BC, it is verified that

$$\frac{dx}{dt} = U(0, \tau) - c(0, \tau), \quad (5.79)$$

which, coupled with Eq. (5.77), produces

$$\frac{dx}{dt} = U_o + 2c_o - 3c(0, \tau). \quad (5.80)$$

As the  $C^-$  lines are straight, it is possible to write

$$\frac{dx}{dt} = \frac{x}{t - \tau}. \quad (5.81)$$

Inserting in Eq. (5.80) yields for the  $C^-$  lines

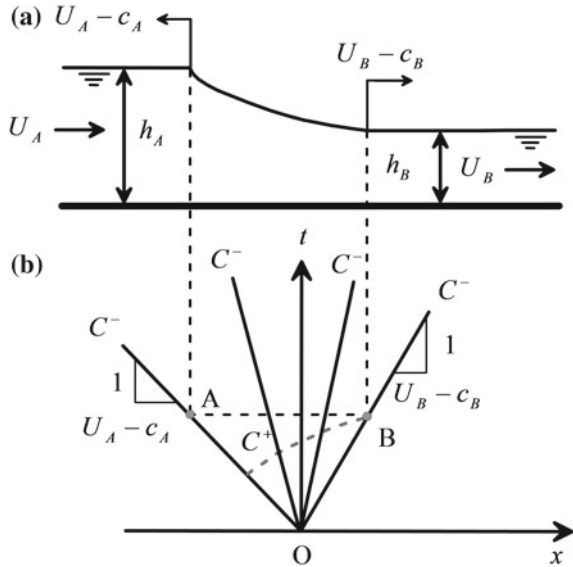
$$\frac{x}{t - \tau} = U_o + 2c_o - 3c(0, \tau). \quad (5.82)$$

As observed,  $dx/dt$  in this problem gives the velocity of propagation of a “visible” wave at the interface of the uniform flow and the negative wave.

### 5.6.2 Rarefaction Wave: A Negative Surge

Consider a particular case of the simple wave problem. We seek a smooth wave connecting two constant flow states A and B (Fig. 5.19). The simple wave solution will be applied assuming the particular case where all  $C^-$  characteristics are centered at the origin O, resulting in  $\tau = 0$ . The two edges of the wave will move at velocities given by the corresponding backward characteristics. This wave is referred to as rarefaction wave (Toro 2001), and it is a centered simple wave solution of the SWE (Stoker 1957; Jain 2001). In hydraulics, it is also called negative surge (Montes 1998; Chanson 2004), implying shallow waters invading deeper waters. Its fundamental equation is thus

**Fig. 5.19** Left-going rarefaction wave: a centered simple wave **a** physical plane, **b** characteristic plane  $(x, t)$



$$U(x, t) + 2c(x, t) = \text{const.} \equiv U_A + 2c_A \equiv U_B + 2c_B. \quad (5.83)$$

The free surface profile is easily determined as follows. Along the  $C^-$  characteristics

$$\frac{x}{t} = U - c = \text{const.} \quad (5.84)$$

From Eq. (5.83), taking the left state as reference, one can write

$$U + 2c = U_A + 2c_A. \quad (5.85)$$

The simultaneous solution of Eqs. (5.84) and (5.85) yields

$$c = \frac{1}{3} \left( U_A + 2c_A - \frac{x}{t} \right), \quad (5.86)$$

or

$$h(x, t) = \frac{1}{9g} \left( U_A + 2c_A - \frac{x}{t} \right)^2, \quad (5.87)$$

and

$$U(x, t) = \frac{1}{3} \left( U_A + 2c_A + \frac{2x}{t} \right). \quad (5.88)$$

## 5.7 Simplified Models: The Kinematic Wave

The SWE have simplified forms, upon neglecting specific terms of the momentum equation, widely used in hydrology. Based on the terms retained, dynamic, diffusive, and kinematic waves are defined as follows (Chow et al. 1988)

$$\underbrace{\frac{\partial U}{\partial t} + U \frac{\partial U}{\partial x} + g \frac{\partial h}{\partial x}}_{\text{dynamic wave}} - \underbrace{g(S_o - S_f)}_{\substack{\text{kinematic wave} \\ \text{diffusive wave}}} = 0. \quad (5.89)$$

With the actual power of computational methods, the dynamic wave model is by far the dominant approach. Only the kinematic wave is, however, still used in hydrological models. Given this fact and the conceptual interest of kinematic waves, this simplified model is described here. The kinematic wave equations are, for a rectangular channel, the continuity equation

$$\frac{\partial h}{\partial t} + \frac{\partial q}{\partial x} = 0, \quad (5.90)$$

and a simplified momentum equation stating balance of gravity and friction forces,

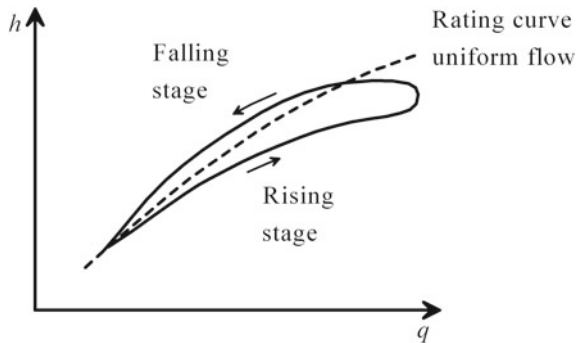
$$S_o - S_f = 0. \quad (5.91)$$

The kinematic wave implies that: (i) The flow is not significantly accelerated, and (ii) the variation of flow depth with distance in a given instant of time is small with a negligible pressure gradient. The friction slope is assumed to produce a relation of the type

$$h = \alpha q^\beta. \quad (5.92)$$

For example, using Manning's equation for a wide rectangular channel, the following result in conformity with Eq. (5.92) is generated

**Fig. 5.20** Rating curve for (—) dynamic and (---) kinematic waves (adapted from Henderson 1966)



$$h = \left( \frac{n^2}{S_o} \right)^{3/10} q^{3/5}. \quad (5.93)$$

Here,  $n$  is Manning's roughness coefficient. A basic hypothesis of the kinematic wave theory is that the flow is from instant to instant locally uniform. Unsteadiness is introduced by the continuity equation. This implies that the rating curve  $h-q$  is singled-valued in kinematic waves (Fig. 5.20). However, in a dynamic wave, the rating curves are looped, with different branches for the rising and falling limbs of the flood wave (Henderson 1966).

While solving the SWE, a unique head–discharge rating curve can be prescribed at the downstream section of a reach based on uniform flow. It is physically equivalent to set a kinematic-like downstream boundary condition to solve a dynamic wave model. Thus, from a computational viewpoint, the flow is considered kinematic at the downstream end and dynamic in all other sections. To circumvent this deficiency, this boundary condition is moved to far downstream from the originally selected downstream boundary section, allowing thus in the entire reach of interest for dynamic loop ratings (Abbott 1975).

Inserting Eq. (5.92) into Eq. (5.90) yields

$$\alpha\beta q^{\beta-1} \frac{\partial q}{\partial t} + \frac{\partial q}{\partial x} = 0. \quad (5.94)$$

Accordingly, kinematic waves are fully determined by changes in discharge  $q = q(x, t)$ . The total differential of  $q$  is

$$dq = \frac{\partial q}{\partial t} dt + \frac{\partial q}{\partial x} dx, \quad (5.95)$$

which is rewritten as

$$\frac{Dq}{Dt} = \frac{\partial q}{\partial t} + \frac{\partial q}{\partial x} \frac{dx}{dt}. \quad (5.95)$$

Comparing Eqs. (5.94) and (5.95), both are identical if

$$\frac{Dq}{Dt} = 0, \quad (5.96)$$

$$\frac{dx}{dt} = \frac{1}{\alpha \beta q^{\beta-1}}. \quad (5.97)$$

This is the characteristic form of the kinematic wave model. It implies that the discharge  $q$  is a constant along the paths in the  $(x, t)$  plane defined by Eq. (5.97). These paths are forward characteristics, thereby implying that in this type of wave, information of a perturbation cannot be transmitted forward in time and back in space. Basically, this means that only one boundary condition upstream of the river reach is necessary for kinematic wave routing, e.g., the inflow hydrograph  $q = q(0, t)$ . Note by differentiation of Eq. (5.92) that

$$\frac{dh}{dq} = \alpha \beta q^{\beta-1}. \quad (5.98)$$

Thus, the kinematic wave characteristics are given with  $c_k$  as the kinematic wave celerity (Chow et al. 1988) by

$$\frac{dx}{dt} = \frac{dq}{dh} = c_k. \quad (5.99)$$

If the inflow discharge is known at the upstream end of the reach, a specific value  $q = q(0, t)$  of the discharge at a time  $t$  will appear at a position  $L$  at the end of the reach (Fig. 5.21) at time  $\tau$  given by

$$\tau = t + \int_0^L \frac{dx}{c_k(q)} = t + \frac{L}{c_k[q(0, t)]}. \quad (5.100)$$

Note that information of the upstream perturbation (variation in discharge) is only propagated in the downstream direction. The characteristic curves are straight, given that  $q = \text{const.}$  along each line. The value of  $c_k$  and hence the slope of a characteristic is fully determined by the upstream hydrograph at time level  $t$ . A kinematic wave does not subside, therefore, so the peak discharge  $q_{\max}$  remains

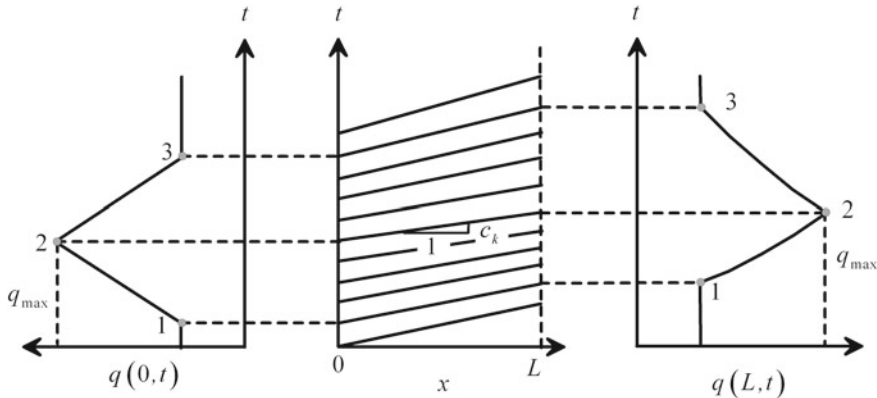


**Fig. 5.21** Kinematic wave routing (adapted from Chow et al. 1988)

unaltered and the wave profile simply suffers a deformation (Fig. 5.21) (Henderson 1966). This deformation implies a steepening of the tailwater face, eventually leading to the formation of a kinematic shock (Lighthill and Whitham 1955). However, this issue is debatable, as shown by Henderson (1966), given that the steepening is accompanied by an increase in the importance of free surface slope terms neglected in the kinematic wave model. These terms may become important at the threshold of formation of a kinematic surge, given that they introduce diffusion and attenuation. If they are strong enough, the kinematic surge formation may be counterbalanced and a smooth wave profile of permanent shape traveling at constant speed finally forms. This smooth wave solution is called monoclonal wave (Sturm 2001; Jain 2001). In the more complex case of flow with rainfall, a source term must be added to the continuity equation and the characteristic lines are then curved (Chow et al. 1988; Jain 2001).

The kinematic wave celerity can be written as

$$c_k = \frac{dq}{dh} = \frac{d(Uh)}{dh} = U + h \frac{dU}{dh}. \quad (5.101)$$

Using Manning's equation for a wide rectangular channel

$$U = \frac{S_o^{1/2}}{n} h^{2/3} \quad (5.102)$$

results in

$$\frac{dU}{dh} = \frac{2 S_o^{1/2}}{3 n} h^{-1/3}. \quad (5.103)$$

Inserting into Eq. (5.101) produces

$$c_k = \frac{5}{3} U. \quad (5.104)$$

Comparing Eq. (5.104) with the absolute celerity  $c_d$  of the dynamic wave traveling downstream

$$c_d = U + (gh)^{1/2}, \quad (5.105)$$

the ratio of both signals results in

$$\frac{c_k}{c_d} = \frac{\frac{5}{3} U}{U + (gh)^{1/2}} = \frac{5}{3 F + 1}. \quad (5.106)$$

Lighthill and Whitham (1955) demonstrated that in a flood wave propagating over initially uniform flow, both kinematic and dynamic waves coexist. Consider a smooth and continuous flood wave propagating over an initially steady and uniform stream. They argued that the main body of the flood behaves, essentially, like a kinematic wave, whereas the wave fronts are basically governed by the dynamic wave model. If  $F < 1.5$ , then Eq. (5.106) yields  $c_k < c$ , implying that the main body of the flood wave travels slower than the front advancing at velocity  $U_o + (gh_o)^{1/2}$ . In reality, close to, but slightly above  $F \approx 1$ , the flow is non-hydrostatic, with undular features, a characteristic beyond the scope of the SWE. Thus, for a subcritical stream with  $F < 1$ , which is clearly the most usual case in river flows, the main body of the wave can in fact propagate at celerity  $c_k$  as found by Lighthill and Whitham (1955), whereas the leading positive front would propagate at speed  $U_o + (gh_o)^{1/2}$  (Fig. 5.22) implying that there is a “dynamic wave ahead the main kinematic wave.” They also showed that in the domain of solution where the dynamic wave is the governing model, there is no appreciable variation of flow depth and velocity. Of course, this is likely to be linked to the assumption of initially uniform flow. The strongest variations in both are accomplished once the main (kinematic) bulk of the wave arrives (Henderson 1966) (Fig. 5.22).

## 5.8 Use of Non-conservative Form of SWE

As previously explained, Eq. (5.44) are the non-conservative form of the SWE. Manipulation permits to write this system as (Cunge 1975; Toro 2001)

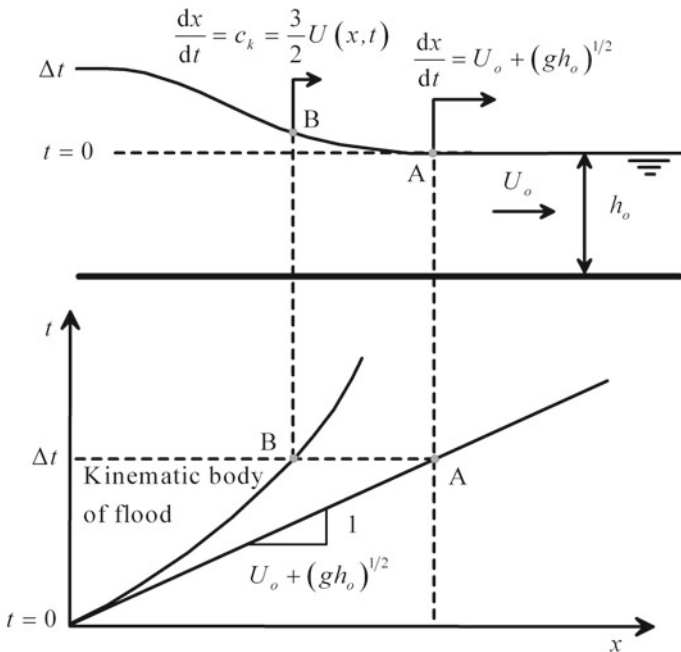


**Fig. 5.22** Kinematic and dynamic waves (adapted from Stoker 1957; Henderson 1966)

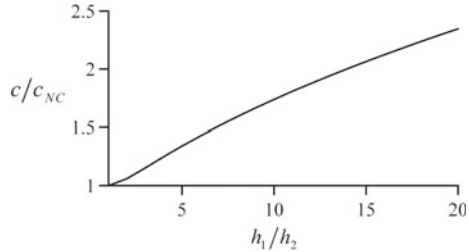
$$\frac{\partial}{\partial t} \begin{pmatrix} h \\ U \end{pmatrix} + \frac{\partial}{\partial x} \begin{pmatrix} Uh \\ \frac{1}{2}U^2 + gh \end{pmatrix} = \begin{pmatrix} 0 \\ 0 \end{pmatrix}. \quad (5.107)$$

Mathematically, Eq. (5.107) is written in conservative form, yet physically, the fluid velocity  $U$  is not a conserved quantity. Equation (5.107) state conservation of mass and energy. Equation (5.107) apply to produce solutions of the SWE only if they are smooth or gradually varied, e.g., as for a river flood wave or a negative surge in a hydropower canal. However, shock waves are not well reproduced by Eq. (5.107), to be shown. The celerity of a right-going positive surge is, based on the conservative form of the SWE [Eq. (5.35)],

$$c = \left[ \frac{gh_1}{2h_2} (h_1 + h_2) \right]^{1/2}. \quad (5.108)$$

This equation is generally in good agreement with experiments for breaking positive surges (Cunge 1975). The integral form of Eq. (5.107) yields as celerity of the shock wave (Cunge 1975; Toro 2001)

**Fig. 5.23** Ratio of conservative to non-conservative positive surge celerity as function of surge height



$$c_{NC} = \left[ \frac{2gh_1^2}{(h_1 + h_2)} \right]^{1/2}. \quad (5.109)$$

The ratio of both celerities is then (Fig. 5.23)

$$\frac{c}{c_{NC}} = \frac{1}{2} \frac{\left(1 + \frac{h_1}{h_2}\right)}{\left(h_1/h_2\right)^{1/2}}, \quad (5.110)$$

This ratio is only equal to unity in the trivial case  $h_1 = h_2$ , e.g., for smooth solutions. However, Eq. (5.110) shows in Fig. 5.23 that for  $h_1/h_2 < 2$ , the errors of Eq. (5.107) predicting the celerity of a positive surge are small. Thus, the non-conservative form of the SWE applies to compute smooth or continuous solutions, as previously done using the method of characteristics, and for weak shock waves. Physically, Eq. (5.109) is based on conservation of mass and energy across a shock wave. Clearly, a shock wave is a highly dissipative phenomenon, and, thus, a solution based on energy conservation is incorrect. For weak shocks, however, energy dissipation is small, explaining why Eq. (5.109) is acceptable for small surge heights. Thus, it is necessary to write the conservation laws in conservative form to obtain weak solutions, but, also, the conserved variables should have a physical meaning in the problem being simulated (Cunge 1975).

A physical shock implies characteristics converging from both sides of the shock path in the  $(x, t)$  plane (Cunge 1975; Toro 2001). It is possible to mathematically obtain non-physical shocks due to the entropy-violating conditions, where characteristics diverge (Toro 2001; Katopodes 2019). Obviously, these weak solutions of the SWE must be discarded.

## 5.9 Limitations of SWE

Limitations of SWE computational results are discussed with an illustrative example. As previously explained, the integral form of the SWE applies to produce steady flow solutions prescribing suitable initial and boundary conditions. For unsteady 1D flow, the integral form of the SWE is

$$\iint_{CV} \frac{\partial \mathbf{U}}{\partial t} dx dt + \oint (\mathbf{F} \cdot \mathbf{n}) ds = \iint_{CV} \mathbf{S} dx dt. \quad (5.111)$$

Here, the control volume  $CV$  is an area of the  $(x, t)$  plane, and the flux integral is extended along the closed contour line which defines the  $CV$ , with  $s$  as the curvilinear arch length. Consider the spillway depicted in Fig. 5.24. Static water at the upstream face of the weir is considered as initial condition. Boundary conditions are physically a constant discharge supplied at the upstream inlet, and a prescribed tailwater flow depth obtained by regulation of a gate. After transient flow, the steady flow profile shown in Fig. 5.24 is generated.

SWE produce a continuous steady flow solution at the weir crest, where the flow changes from sub- to supercritical conditions. Somewhere in the tailwater, a hydraulic jump is formed to allow for transitional flow from super- to subcritical conditions forced with a gate. Both types of transcritical flows are therefore obtained as solutions of SWE [Eqs. (5.111)] (numerical computations to be detailed in Chap. 9). However, these mathematical results might not be an accurate representation of the physical phenomena being simulated: If the fluid pressure is in reality non-hydrostatic, then the mathematical solution of the SWE is meaningless (see Chap. 11). Roughly, for example, the continuous flow solution of the SWE at a weir crest is only accurate if the ratio of crest specific energy to bottom curvature is below 0.25 (Castro-Orgaz and Chanson 2016). The hydraulic jump is correctly predicted by the SWE only if a roller is formed (Castro-Orgaz and Hager 2009). If the hydraulic jump is undular, say for inflow Froude numbers below 1.7 (Montes and Chanson 1998), then the prediction of the SWE is not in conformity with experimental observations.

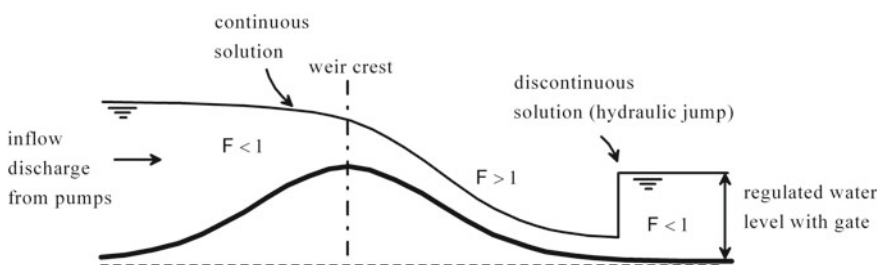


**Fig. 5.24** Steady transcritical flow as solution of unsteady computations using SWE

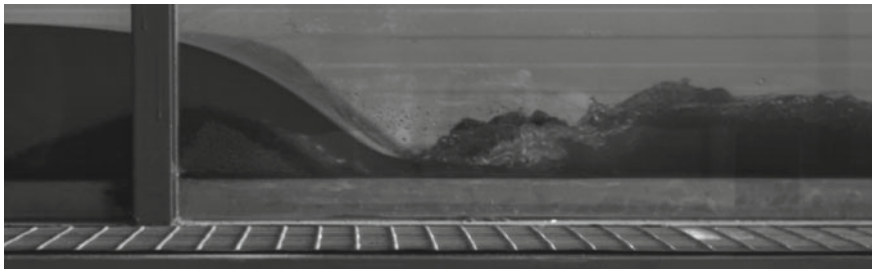


**Fig. 5.25** Dike erosion test showing continuous weir flow surface over eroded dike and hydraulic jump in tailwater (test at experimental flume of IAS-CSIC, Córdoba; photograph by O. Castro-Orgaz)

The continuous flow solution at a weir crest and a moving hydraulic jump (positive surge propagating upstream) can be observed in many unsteady environmental flows. A prominent example is the gradual erosion of dikes (Fig. 5.25). These flows are simulated using extended versions of the SWE accounting for the suspended and bed-load sediment transport modes (Wu 2008) (see Chap. 10). Limitations of predictions based on these families of models are essentially those described above; e.g., the fluid pressure shall be hydrostatic, in addition to those related to empirical sediment transport formulae.

## 5.10 Hydrologic Routing

### 5.10.1 Reservoir Routing

There exist cases where the flood routing procedure can be accomplished by ignoring dynamic effects, e.g., neglecting the momentum equation in the SWE and solving the continuity equation alone. An important example involves the passage of a flood wave across a reservoir (Fig. 5.26), given that the reservoir water surface remains nearly horizontal. Consider here a reservoir with an overflow structure consisting of a standard spillway crest without gates.

The continuity equation is

$$\frac{\partial A}{\partial t} + \frac{\partial Q}{\partial x} = 0. \quad (5.112)$$

Integrating between a section upstream of the reservoir (subscript  $e$ ) and a section on the spillway crest (subscript  $s$ ) yields

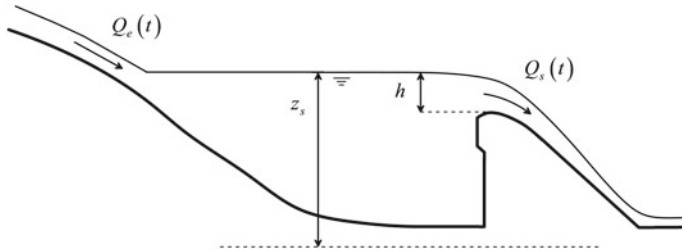


**Fig. 5.26** Reservoir routing

$$Q_e - Q_s = \frac{d}{dt} \int_{x_e}^{x_s} A dx. \quad (5.113)$$

The volume stored in the reservoir  $\forall$  is defined as

$$\forall = \int_{x_e}^{x_s} A dx, \quad (5.114)$$

which permits to rewrite Eq. (5.113) as

$$\frac{d\forall}{dt} = Q_e - Q_s. \quad (5.115)$$

The inflow hydrograph is typically a function of time, e.g.,  $Q_e = Q_e(t)$ , whereas the spillway rating curve is of the form

$$Q_s = C_d L (2g E^3)^{1/2} \approx [C_d (2g)^{1/2}] L h^{3/2} = C L h^{3/2}. \quad (5.116)$$

Here,  $E$  is the energy head on the weir crest, approximated to the approach flow depth above the spillway invert  $h$ ,  $L$  is the spillway width, and  $C_d$  is the discharge coefficient. Note that the  $C$  coefficient used in hydrological computations is not dimensionless. For a known inflow hydrograph and given spillway, Eq. (5.115) must be numerically solved to compute the outflow hydrograph.

First, the *modified Puls method* (Chow et al. 1988) is presented here. It is an implicit finite difference method which is based on the integral form of Eq. (5.115) over a time period  $\Delta t = t_{i+1} - t_i$ , that is,

$$\int_{S_i}^{S_{i+1}} dS = \int_{t_i}^{t_{i+1}} (Q_e - Q_s) dt. \quad (5.117)$$

Here,  $i$  represents the time subscript, and  $S$  is the storage volume above the spillway crest. Using the trapezoidal rule, Eq. (5.117) yields

$$S_{i+1} - S_i = \frac{\Delta t}{2} [(Q_e - Q_s)_{i+1} + (Q_e - Q_s)_i], \quad (5.118)$$

or re-arranged

$$\frac{2S_{i+1}}{\Delta t} + Q_{si+1} = (Q_{ei} + Q_{ei+1}) + \frac{2S_i}{\Delta t} - Q_{si}. \quad (5.119)$$

To apply Eq. (5.119), the inflow hydrograph  $Q_e = Q_e(t)$  and discharge rating curve  $Q_s = Q_s(h)$  are known in advance. However, to produce the output  $Q_s = Q_s(t)$  as solution of Eq. (5.119), a function relating  $S$  to the actual value of  $h$  is additionally needed. This information results from topographic data of the reservoir by evaluating the integral

$$S(h) = \int_0^h F(h) dh. \quad (5.120)$$

Here,  $F(h)$  is the plan area of the water surface at elevation  $h$  relative to the spillway crest. The function  $F = F(h)$  is known from constant elevation contour lines in the reservoir, taken from available planimetric information. In general, the volume integral must be numerically solved using a low order method, thereby introducing errors in the estimation (Fenton 1992). Once  $S = S(h)$  is available, the numerical procedure is as follows:

1. As initial condition, the water surface elevation is assumed to be at the spillway invert when the inflow hydrograph reaches the upstream reservoir section. Then, both  $S$  and  $Q_s$  are zero at  $t = 0$ . Of course, other scenarios are possible. The quantity  $2S/\Delta t - Q_s$  is thus zero. The sum  $Q_{ei} + Q_{ei+1}$  is known from the inflow hydrograph for all values of  $i$ .
2. A routing interval  $\Delta t$  is selected. The function  $2S/\Delta t + Q_s$  versus  $Q_s$  is constructed using the functions  $Q_s = Q_s(h)$  and  $S = S(h)$ : For a given  $h$ ,  $S$  and  $Q_s$  are determined and thus  $2S/\Delta t + Q_s$ .
3. The variable  $2S/\Delta t + Q_s$  at  $i + 1$  is computed from Eq. (5.119).
4. Using the function  $2S/\Delta t + Q_s$  versus  $Q_s$ , the outflow discharge  $Q_{si+1}$  is computed from the known value  $(2S/\Delta t + Q_s)_{i+1}$ .

5. Apply the identity  $2S/\Delta t - Q_s = (2S/\Delta t + Q_s) - 2Q_s$  to generate the initial data for the next time step.
6. Go back to Step 3 if the final time is not yet reached.

An alternative to use the integral Eq. (5.117) is to directly solve Eq. (5.115), which is a first-order ODE (Chow et al. 1988; Ayuso 1990; Fenton 1992). The change in water storage for an infinitesimal change in surface elevation  $dz_s$  is

$$dV = F dz_s. \quad (5.121)$$

Inserting Eq. (5.121) in Eq. (5.115) produces

$$\frac{dz_s}{dt} = \frac{Q_e - Q_s}{F}, \quad (5.122)$$

or,

$$\frac{dh}{dt} = \frac{Q_e(t) - Q_s(h)}{F(h)} \equiv f(t, h). \quad (5.123)$$

This is the equation describing the temporal variation of the reservoir level  $h = h(t)$ . Equation (5.123) can be solved using any method to solve ODEs. If the time derivative is discretized using a forward in time finite-difference

$$\frac{dh}{dt} = \frac{h_{i+1} - h_i}{\Delta t}, \quad (5.124)$$

the algebraic expression approximating Eq. (5.123) reads

$$h_{i+1} = h_i + f_i \Delta t = h_i + \frac{Q_e(t_i) - Q_s(h_i)}{F(h_i)} \Delta t. \quad (5.125)$$

This equation has the advantage of being extremely simple to apply. Given its explicit character, the time step  $\Delta t$  must be limited to assure numerical stability. However, as demonstrated by Fenton (1992), this is not a real limitation in practical computations. Equation (5.125) is the so-called Euler equation, a first-order Runge–Kutta method. Runge–Kutta schemes are explicit, using an updating formula of the type (see Chap. 3)

$$h_{i+1} = h_i + \bar{f} \Delta t, \quad (5.126)$$

where the average value of  $f$  is determined differently, depending on the order of the scheme. Chow et al. (1988) proposed a third-order Runge–Kutta method, whereas Ayuso (1990) used a fourth-order scheme. For this last option, the average slope is

$$\bar{f} = \frac{1}{6}(k_1 + 2k_2 + 2k_3 + k_4), \quad (5.127)$$

with

$$\begin{aligned} k_1 &= f(t_i, h_i), \\ k_2 &= f\left(t_i + \frac{1}{2}\Delta t, h_i + \frac{1}{2}k_1\Delta t\right), \\ k_3 &= f\left(t_i + \frac{1}{2}\Delta t, h_i + \frac{1}{2}k_2\Delta t\right), \\ k_4 &= f(t_i + \Delta t, h_i + k_3\Delta t). \end{aligned} \quad (5.128)$$

Following Fenton (1992), a comparison of the modified *Puls* method, the Euler method, and the fourth-order Runge–Kutta method is shown in Fig. 5.27. The inflow hydrograph considered is plotted in the figure; note that the peak discharge is  $120 \text{ m}^3/\text{s}$  and the base time about 6 h. The reservoir is prismatic with a constant horizontal area of  $50,000 \text{ m}^2$ . The spillway for this test has a width  $L = 100 \text{ m}$  with a (hydrological) discharge coefficient  $C = 2.037 \text{ m}^{1/2}/\text{s}$ . A time step  $\Delta t = 0.1 \text{ h}$  was adopted. The codes prepared for the computations are implemented in the files “Euler.xls,” “Puls.xls,” and “rk4.xls,” available in Chap. 12. The code for the fourth-order Runge–Kutta method was adapted from the Fortran code *PRAVEM* available from Ayuso (1990).

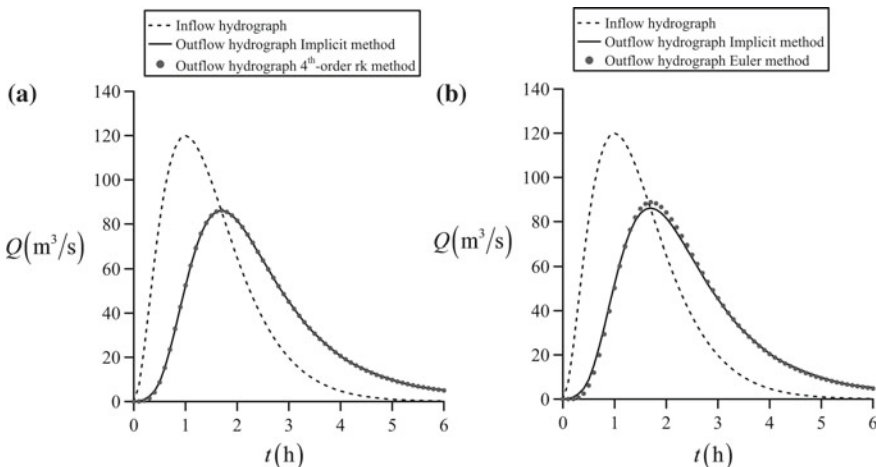


**Fig. 5.27** Comparison of numerical methods for reservoir routing

Comparing the implicit (*Puls*) method with the explicit fourth-order Runge–Kutta (rk4) method in Fig. 5.27a shows excellent agreement, thereby highlighting that either of the two is a good selection. The Puls and the Euler methods are compared in Fig. 5.27b, indicating reasonable agreement of the two. Note the small distortion in the ascending outflow hydrograph branch predicted by Euler method, as well as the overprediction of the peak discharge. However, despite these inaccuracies, the simple implementation of this method supports its use at minimum for teaching purposes (Fenton 1992).

Hager et al. (1984) experimentally determined the flood routing process in a laboratory scale reservoir. The inflow hydrographs followed the smooth equation

$$q = T^n \exp[n(1 - T)], \quad (5.129)$$

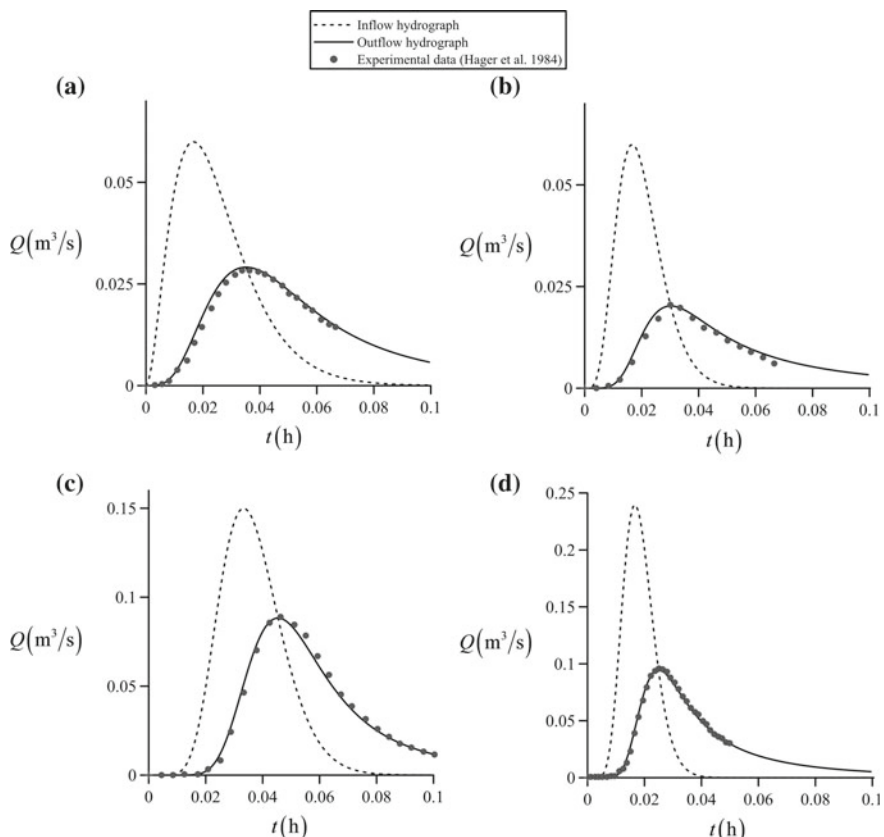


**Fig. 5.28** Comparison of reservoir routing solution with experiments involving smooth inflow hydrographs with  $(Q^*, t^*, n, C_d) =$  **a**  $(60 \text{ l/s}, 60 \text{ s}, 2, 0.463)$ , **b**  $(60 \text{ l/s}, 60 \text{ s}, 5, 0.46)$ , **c**  $(150 \text{ l/s}, 120 \text{ s}, 10, 0.48)$ , **d**  $(240 \text{ l/s}, 60 \text{ s}, 10, 0.49)$

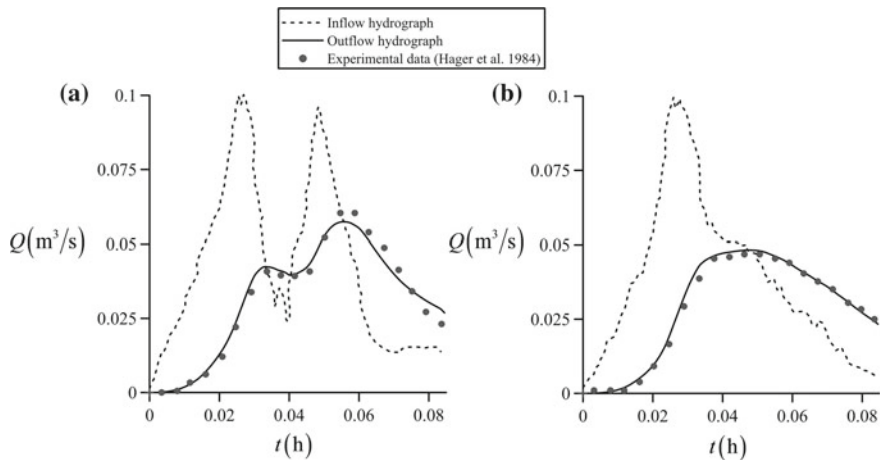


**Fig. 5.29** Comparison of reservoir routing solution with experiments involving real inflow hydrographs with  $C_d = \mathbf{a} 0.471, \mathbf{b} 0.475$

where the normalized variables are  $q = Q/Q^*$  and  $T = t/t^*$ ; \* denotes a reference quantity, and  $n$  is a parameter. Experiments for four tests are plotted in Fig. 5.28, along with the values for  $(Q^*, t^*, n, C_d)$  in each run. The reservoir is prismatic in elevation, with a constant plan area of  $F = 39.7 \text{ m}^2$ , and the spillway width is  $L = 0.54 \text{ m}$ .

The rk4 solver was run using  $\Delta t = 0.0005 \text{ h}$  (1.8 s); the results are presented in Fig. 5.28 superimposed with the inflow hydrograph and the measured outflows. Note that the agreement is good, supporting the accuracy of Eq. (5.123) to describe reservoir routing processes.

To further test the rk4 solver, an additional comparison with experiments is made in Fig. 5.29, where the inflow hydrographs are irregular, aimed at describing real flood events. The numerical simulation produces again a fair approximation to the experiments, faithfully following the shape of the measured outflow discharge curves.

### 5.10.2 Muskingum Channel Routing

The Muskingum method is a hydrologic routing technique for canals based on the solution of the continuity equation. To match the backwater effects in a reach of a canal or river, the storage function is composed of two terms, one representing the backwater storage and the other representing a level (reservoir) storage, e.g. (Chow et al. 1988)

$$S = \underbrace{kx(I - Q)}_{\text{backwaterstorage}} + \underbrace{kQ}_{\text{levelstorage}}. \quad (5.130)$$

Here,  $I$  is the inflow hydrograph and  $Q$  the outflow hydrograph. The parameters  $k$  and  $x$  are empirical and must be therefore calibrated with data. Parameter  $x$  is a weighting factor ranging from 0 to 0.5, controlling the wave attenuation, while  $k$  has the dimension of time. It is usually estimated as the travel time of the peak discharge. Using Eq. (5.130),

$$\begin{aligned} S_i &= k[xI_i + (1 - x)Q_i], \\ S_{i+1} &= k[xI_{i+1} + (1 - x)Q_{i+1}]. \end{aligned} \quad (5.131)$$

Inserting into Eq. (5.118) produces

$$S_{i+1} - S_i = \frac{Q_{ei} + Q_{ei+1}}{2} \Delta t - \frac{Q_{si} + Q_{si+1}}{2} \Delta t \quad (5.132)$$

or,

$$Q_{si+1} = C_0 Q_{ei+1} + C_1 Q_{ei} + C_2 Q_{si} \quad (5.133)$$

where the routing coefficients are

$$\begin{aligned} C_0 &= \frac{\Delta t - 2kx}{2k(1 - x) + \Delta t}, \\ C_1 &= \frac{\Delta t + 2kx}{2k(1 - x) + \Delta t}, \\ C_2 &= \frac{2k(1 - x) - \Delta t}{2k(1 - x) + \Delta t}. \end{aligned} \quad (5.134)$$

Note that  $C_0 + C_1 + C_2 = 1$ . For  $\Delta t = k$  and  $x = 1/2$  results,  $C_0 = 0$ ,  $C_1 = 1$  and  $C_2 = 0$ , e.g.,  $Q_{si+1} = Q_{ei}$ ; that is, the flood is moving with a pure translation without any attenuation.

## References

- Abbott, M. B. (1975). Computational hydraulics: A short pathology. *Journal of Hydraulic Research*, 14(4), 271–285.  
 Ayuso, J. L. (1990). *Circulación de flujos: métodos de cálculo usuales en el diseño de canales y embalses en pequeñas cuencas* [Flood routing: Usual methods in the design of canals and reservoirs in small drainage basins]. Córdoba, Spain: University of Córdoba Press (in Spanish).

- Castro-Orgaz, O., & Chanson, H. (2016). Minimum specific energy and transcritical flow in unsteady open channel flow. *Journal of Irrigation and Drainage Engineering*, 142(1), 04015030.
- Castro-Orgaz, O., & Hager, W. H. (2009). Classical hydraulic jump: Basic flow features. *Journal of Hydraulic Research*, 47(6), 744–754.
- Chanson, H. (2004). *The hydraulics of open channel flows: An introduction*. Oxford, UK: Butterworth-Heinemann.
- Chaudhry, M. H. (2008). *Open-channel flow* (2nd ed.). New York: Springer.
- Chaudhry, M. H. (2014). *Applied hydraulic transients* (3rd ed.). New York: Springer.
- Chow, V. T. (1959). *Open channel hydraulics*. New York: McGraw-Hill.
- Chow, V. T., Maidment, D. R., & Mays, L. W. (1988). *Applied hydrology*. New York: McGraw-Hill.
- Cunge, J. A. (1975). Rapidly varying flow in power and pumping canals (Chap. 14). In K. Mahmood & V. Yevjevich (Eds.), *Unsteady flow in open channels*, 2, 539–586. Fort Collins, CO, USA: Water Resources Publications.
- Cunge, J. A., Holly, F. M., & Verwey, A. (1980). *Practical aspects of computational river hydraulics*. London: Pitman.
- De Saint-Venant, A. B. (1870). Démonstration élémentaire de la formule de propagation d'une onde ou d'une intumescence dans un canal prismatique; et remarques sur les propagations du son et da la lumière sur les ressauts, ainsi que sur la distinction des rivières et des torrents [Elementary demonstration of the formula of propagation of a wave or a disturbance in a prismatic channel; and remarks on the propagations of sound, light, and bores, as also on the distinction between a river and a torrent: Part 1]. *Comptes Rendus de l'Académie des Sciences*, 71, 186–195 (in French).
- De Saint-Venant, A. B. (1871). Théorie du mouvement non permanent des eaux, avec application aux crues des rivières et à l'introduction des marées dans leur lit [Theory of unsteady water movement, applied to floods in rivers and the effect of tidal flows: Part 2]. *Comptes Rendus de l'Académie des Sciences*, 73, 147–154 (in French).
- Favre, H. (1935). *Etude théorique et expérimentale des ondes de translation dans les canaux découverts* [Theoretical and experimental study of travelling surges in open channels]. Paris, France: Dunod (in French).
- Fenton, J. D. (1992). Reservoir routing. *Hydrological Sciences Journal*, 37(3), 233–246.
- Hager, W. H., Sinniger, R., & Regamey, J.-M. (1984). Reservoir storage equation experimentally verified. *Water Power and Dam Construction*, 36(11), 44–48.
- Henderson, F. M. (1966). *Open channel flow*. New York: MacMillan.
- Hicks, F. E., & Steffler, P. M. (1990). *Finite element modelling of open channel flow*. Water Resources Engineering Report 90-6. Canada: University of Alberta.
- Jain, S. C. (2001). *Open channel flow*. New York: Wiley.
- Katopodes, N. D. (2019). *Free surface flow: Computational methods*. Oxford, UK: Butterworth-Heinemann.
- Khan, A. A., & Lai, W. (2014). *Modeling shallow water flows using the discontinuous Galerkin method*. New York: CRC Press, Taylor and Francis.
- Lai, C. (1986). Numerical modelling of unsteady open-channel flow. *Advances in Hydroscience*, 14, 161–333.
- LeVeque, R. J. (2002). *Finite volume methods for hyperbolic problems*. New York: Cambridge University Press.
- Lighthill, M. J., & Whitham, G. B. (1955). On kinematic waves: Flood movement in long rivers. *Proceedings Royal Society London*, A, 229, 281–345.
- Liggett, J. A. (1994). *Fluid mechanics*. New York: McGraw-Hill.
- Macdonald, I. (1995). *Analysis and computation of steady open channel flow* (Ph.D. thesis). University of Reading, UK.
- Montes, J. S. (1998). *Hydraulics of open channel flow*. Reston, VA: ASCE.
- Montes, J. S., & Chanson, H. (1998). Characteristics of undular hydraulic jumps: Results and calculations. *Journal of Hydraulic Engineering*, 124(2), 192–205.

- Peregrine, D. H. (1966). Calculations of the development of an undular bore. *Journal of Fluid Mechanics*, 25, 321–330.
- Roache, P. J. (1972). *Computational fluid dynamics*. Albuquerque: Hermosa publishers.
- Stoker, J. J. (1957). *Water waves: The mathematical theory with applications*. New York: Interscience publishers.
- Sturm, T. W. (2001). *Open channel hydraulics*. New York: McGraw-Hill.
- Toro, E. F. (2001). *Shock-capturing methods for free-surface shallow flows*. Singapore: Wiley.
- Toro, E. F. (2009). *Riemann solvers and numerical methods for fluid dynamics*. London: Springer.
- White, F. M. (2009). *Fluid mechanics*. New York: McGraw-Hill.
- Wu, W. (2008). *Computational river dynamics*. London, U.K.: Taylor & Francis.

# Chapter 6

## Ideal Dam Break Waves



### 6.1 Introduction

The dam break of an ideal fluid stored in an infinite reservoir in a rectangular, prismatic, and horizontal channel will be considered in this chapter. Solutions for both dry (Ritter 1892) and wet (Stoker 1957) tailwater conditions will be considered. Though these analytical solutions are ideal and too simplistic, they are relevant for several reasons. These analytical solutions are illustrative examples of computations involving the shallow water equations (SWE) where both continuous and discontinuous waves are formed (Henderson 1966; Jain 2001; Chanson 2004). Thus, this is an important material to learn basic aspects of unsteady open channel flows. Further, these are reference solutions to test the behavior of numerical schemes for the solution of the SWE (Toro 2001). The dam break problem is a particular case of a more general initial value problem in fluid dynamics, known as the “Riemann problem” (see Chap. 8) (Toro 2001, 2009). It represents the key physical ingredient in the development of numerical solutions using the finite volume method (FVM) for solving hyperbolic equations, to be presented in Chap. 9. Thus, it is fundamental to master the dam break problem to properly understand the basis of the FVM.

Historically, the first solution to the ideal dam break wave was given by Ritter (1892) for dry tailwater conditions. However, it was only until World War II that its study gained impulse (Ré 1946) given the consideration of the Allied Command to anticipate the effects of a possible destruction of the large dams on Rhine River in northwestern Germany (Chow 1959). Examples of catastrophic dam breaks by bombs of the Allied Forces are the Möhne and Eder Dams on Ruhr Valley (Kirschmer 1949) (Fig. 6.1).

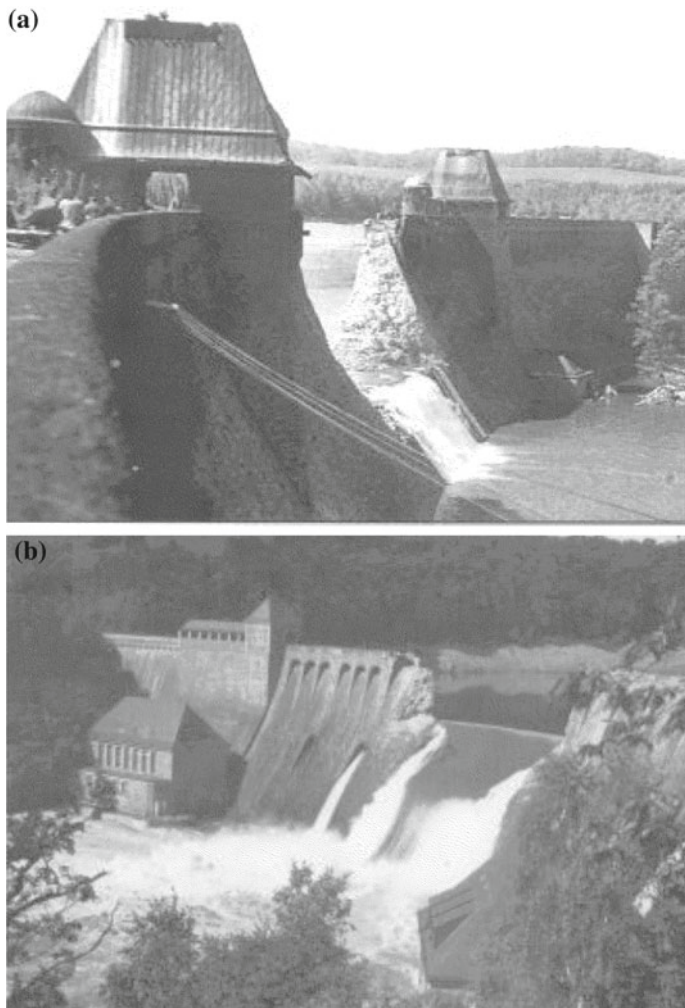
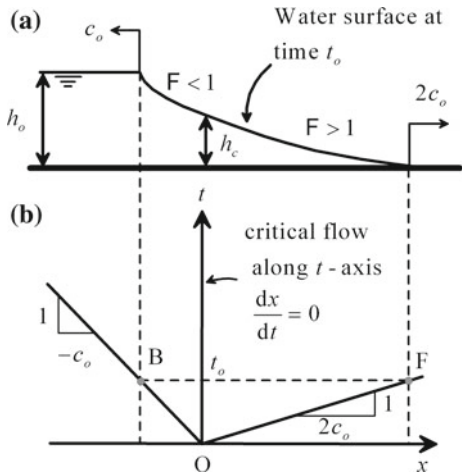


**Fig. 6.1** Dam breaks of **a** Möhne Dam, **b** Eder Dam. Photographs taken from the webpage <http://www.thedambusters.org.uk/>

## 6.2 Dam Break Wave Under Dry Tailwater Conditions

Consider the dam break generated by instantaneously removing a vertical gate at location “O” in a dry channel containing an initially motionless ideal fluid upstream of the gate ( $U_o = 0$ ) of depth  $h_o$  (Fig. 6.2). The basic equations to study these waves of an inviscid fluid propagating over a horizontal channel are, in characteristic form (Henderson 1966; Jain 2001) (see Chap. 5),

**Fig. 6.2** Dry-bed dam break  
wave **a** physical plane,  
**b**  $(x, t)$  plane



$$\begin{aligned} \frac{D}{Dt}(U - 2c) &= 0 && \text{if } \frac{dx}{dt} = U - c, \\ \frac{D}{Dt}(U + 2c) &= 0 && \text{if } \frac{dx}{dt} = U + c. \end{aligned} \quad (6.1)$$

Here,  $U$  is the water velocity,  $c = (gh)^{1/2}$  the shallow water wave celerity,  $g$  the gravity acceleration,  $h$  the water depth,  $x$  the space coordinate, and  $t$  time.

After dam break initiation, a negative wave spreads back into the reservoir, while a wave front of zero depth travels forward over the dry channel bed. Line OB represents the border of the negative wave, which is always in contact with still water where the water depth equals  $h_o$ . Thus, this is a straight backward  $C^-$  characteristic; all other  $C^-$  characteristics are also straight lines (Stoker 1957; Jain 2001). Its equation is

$$\frac{dx}{dt} = U_o - c_o = \frac{x}{t} = -(gh_o)^{1/2}. \quad (6.2)$$

The dry front is a discontinuity of zero water depth. Therefore, it is simultaneously a backward and forward characteristic, determined with  $U_F$  as the absolute wet-dry front velocity by

$$\frac{dx}{dt} = U_F. \quad (6.3)$$

Consider a forward characteristic connecting a point on the backward characteristic representing the negative wave edge, given by Eq. (6.2), and the dry front. The following identity applies, based on conservation of the corresponding Riemann invariant,

$$U_o + 2c_o = U_F + 2c_F. \quad (6.4)$$

Given that  $U_o = 0$  (fluid at rest), and that  $c_F = 0$  (zero depth at dry front), Eq. (6.4) yields

$$2c_o = U_F. \quad (6.5)$$

When inserted into Eq. (6.3), it produces

$$\frac{dx}{dt} = \frac{x}{t} = 2c_o = 2(gh_o)^{1/2}. \quad (6.6)$$

Accordingly, the dry front propagating over dry terrain moves at double speed of the negative wave edge. As the slope determined by Eq. (6.6) is constant, the dry front path is a straight line passing across origin O. From the simple wave problem, the solution obtained from Eq. (6.1) for the  $C^-$  characteristics is (see Chap. 5) [Eq. (5.82)]

$$\frac{x}{t - \tau} = U_o + 2c_o - 3[gh(0, \tau)]^{1/2}. \quad (6.7)$$

Here,  $h(0, \tau)$  is the flow depth at the point of intersection of the  $C^-$  characteristic with the  $t$ -axis. In the dam break problem  $U_o = 0$ , simplifying Eq. (6.7) to

$$\frac{x}{t - \tau} = 2c_o - 3[gh(0, \tau)]^{1/2}. \quad (6.8)$$

At the dam axis,  $x = 0$ . Thus, given that  $(t - \tau) > 0$ , one must have for all values of  $t$

$$2c_o - 3[gh(0, \tau)]^{1/2} = 0. \quad (6.9)$$

From this relation, the depth at the dam axis is a constant, given by

$$h = \frac{4c_o^2}{9g} = \frac{4}{9}h_o, \quad (6.10)$$

or,

$$c = \frac{2}{3}c_o. \quad (6.11)$$

The basic equation of the simple wave (Chap. 5) is written for the dam break problem as

$$U(x, t) + 2c(x, t) = \text{const.} \equiv 2c_o. \quad (6.12)$$

Applying Eq. (6.12) to the dam axis, the corresponding velocity is a constant given by

$$U + \frac{4}{3}c_o = 2c_o \Rightarrow U = \frac{2}{3}c_o. \quad (6.13)$$

The slope of the  $C^-$  characteristic at the dam axis is thus determined by

$$\frac{dx}{dt} = U - c = \frac{2}{3}c_o - \frac{2}{3}c_o = 0. \quad (6.14)$$

Equation (6.14) reveals that the  $t$ -axis is a  $C^-$  characteristic corresponding to the critical flow condition. It further implies that the other  $C^-$  characteristics cannot cross the  $t$ -axis, given that otherwise an intersection of members of the same family would result in the development of a surge, which is excluded here. This reasoning is analogous to set  $\tau = 0$  in Eq. (6.8). The instantaneous free surface profile is, using Eq. (6.12)

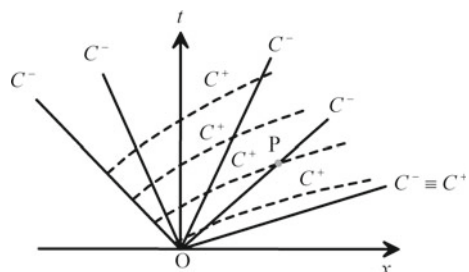
$$\frac{x}{t} = U - c = (2c_o - 2c) - c = 2c_o - 3c = 2(gh_o)^{1/2} - 3(gh)^{1/2}, \quad (6.15)$$

or, with  $h = h(x, t)$  as the flow depth at an arbitrary point P

$$h(x, t) = \frac{1}{9g} \left[ 2(gh_o)^{1/2} - \frac{x}{t} \right]^2. \quad (6.16)$$

Note also that along the  $C^-$  characteristics both  $h$  and  $U$  are constant by virtue of the simple wave features (Chap. 5). The SWE along the wet-dry interface degenerates from the hyperbolic to the parabolic type (Dressler 1952). Given that all the  $C^-$  characteristics are straight lines passing across the origin O, the  $C^+$  lines are of necessity curved (Stoker 1957; Jain 2001). The network of resulting characteristic curves is depicted in Fig. 6.3.

**Fig. 6.3** Net of characteristics for dry-bed dam break wave (adapted from Dressler 1952)





**August Ritter** was born on 11 December, 1826 at Lüneburg, in today's Germany, and there passed away aged 82 years on 26 February, 1908. He studied at the Hannover Polytechnic School and at Göttingen University. Once having obtained the degree as mechanical engineer and the PhD title in 1853, he worked at Hannover, Chemnitz, Leipzig, and Lüneburg in machinery workshops and lectured at the Hannover Polytechnic School from 1859. Ritter was appointed professor of mechanics at Aachen Technical University in 1870. He authored books in analytical and technical mechanics, including chapters relating to hydraulics. He explored the laws of heat flow, based on the theory of Robert Julius Mayer. After retirement in 1899, he moved to his native city, and was active in the local society for natural sciences.

Ritter is well known in hydraulics for two papers published in 1892 and 1895, the first relating to the dam break wave and the second to the hydraulic jump. Both works are not in his general field of work, yet the dam break paper was the first approach to a phenomenon that has currently much impact on dam safety. The so-called Ritter dam break wave describes perfect fluid flow once a body of water in a prismatic rectangular channel is released by instantaneously removing a vertical gate. Ritter introduced both the negative wave front propagating into the reservoir, and the positive wave front moving downstream over a frictionless horizontal bed. His approach is fundamental, although the effects of friction and bottom slope are excluded. Ritter was awarded the honorary doctorate from Technical University of Dresden in 1903.

In the dry-bed dam break problem for  $x < 0$ , the backward characteristics has a negative slope, so the flow is subcritical ( $F < 1$ ; with  $F = U/(gh)^{1/2}$  as the Froude number). At the dam axis, the flow is critical with a backward characteristic coincident with the  $t$ -axis. For  $x > 0$ , the backward characteristics has a positive

slope, so the flow is supercritical ( $F > 1$ ). Consider a forward characteristic connecting a point on the backward characteristic corresponding to the leading edge of the negative wave, and an arbitrary point P on the  $x$ - $t$  plane (Fig. 6.3). Conservation of the corresponding Riemann invariant along the forward characteristic gives

$$U_P = 2c_o - 2c_P. \quad (6.17)$$

Inserting the result for the free surface profile, Eq. (6.15), produces for the velocity as function of time and space

$$U_P = U(x, t) = \frac{2}{3} \left[ \frac{x}{t} + c_o \right] = \frac{2}{3} \left[ \frac{x}{t} + (gh_o)^{1/2} \right]. \quad (6.18)$$

Equations (6.16) and (6.18) are the original solutions to the dry-bed dam break problem of Ritter (1892). The local and convective accelerations from his solution are, respectively,

$$\frac{\partial U}{\partial t} = -\frac{2}{3} \frac{x}{t^2}, \quad (6.19)$$

and

$$U \frac{\partial U}{\partial x} = \frac{4}{9t} \left[ (gh_o)^{1/2} + \frac{x}{t} \right]. \quad (6.20)$$

Further, the pressure force gradient for this wave is

$$g \frac{\partial h}{\partial x} = -\frac{2}{9t} \left[ 2(gh_o)^{1/2} - \frac{x}{t} \right]. \quad (6.21)$$

An interesting issue on inspecting Eqs. (6.19)–(6.21) is that the local acceleration exactly balances the sum of the convective acceleration plus the pressure force gradient. It implies that Ritter's unsteady dam break wave is largely governed by local acceleration effects, a matter rarely emphasized. It can be easily verified by the reader that the use of Eqs. (6.19)–(6.21) satisfies the non-conservative or primitive formulation of the momentum balance

$$\frac{\partial U}{\partial t} + U \frac{\partial U}{\partial x} + g \frac{\partial h}{\partial x} = 0. \quad (6.22)$$

An analogous verification can be conducted by the reader for the continuity equation. At the origin of the dam axis, the flow is critical and steady in Ritter's solution. Thus, with  $h_c$  as the critical depth and  $q$  the unit discharge (see Chap. 2)

$$F = \frac{U}{(gh)^{1/2}} = 1 \Rightarrow h = h_c = \left(\frac{q^2}{g}\right)^{1/3}. \quad (6.23)$$

Using Eqs. (6.10) and (6.13), the steady discharge is

$$q = Uh = \left(\frac{2}{3}c_o\right)\left(\frac{4}{9}h_o\right) = \frac{8}{27}g^{1/2}h_o^{3/2}. \quad (6.24)$$

Inserting Eq. (6.24) into Eq. (6.23) produces for the critical depth

$$h_c = \left(\frac{8^2}{27^2}h_o^3\right)^{1/3} = \left[\left(\frac{2^3}{3^3}\right)^2\right]^{1/3}h_o = \frac{4}{9}h_o. \quad (6.25)$$

This verifies that the water depth at the dam axis corresponds to the critical flow depth. Given that the solution at the dam axis is steady, the specific energy concept applies. There,  $E$  is a minimum given by

$$E = h + \frac{q^2}{2gh^2} = \frac{3}{2}h_c. \quad (6.26)$$

Inclusion of hydraulic resistance notably modifies the flow behavior in the vicinity of the dry front,<sup>1</sup> yet the conditions near the dam axis and the negative front are not greatly affected.

### 6.3 Dam Break Wave Under Wet Tailwater Conditions

A finite water depth is now considered in the downstream channel (Fig. 6.4a). Ritter's parabolic profile cannot be simply connected to the stillwater layer, given that the velocity is then discontinuous at the assembling point B (finite at the parabolic edge, zero at the still water). Physically, the only possibility to account for a velocity discontinuity is the formation of a surge of finite height, where both velocity and depth are discontinuous (Fig. 6.4b) (Stoker 1957; Henderson 1966). The structure of a dam break wave under wet tailwater conditions implies, therefore, a rarefaction wave connected to a surge advancing over the still water (Fig. 6.5).

---

<sup>1</sup>The effect of hydraulic resistance on dam break waves is a complex problem which was notably tackled using analytical developments by Dressler (1952, 1954) and Whitham (1955), and experimentally by Schoklitsch (1917). However, no general analytical solution is yet known to the problem. Thus, this topic will be presented within a numerical framework in Chap. 9 using finite volume solvers of the SWE.

**Fig. 6.4** Wet-bed dam break wave physically **a** erroneous, **b** correct solution

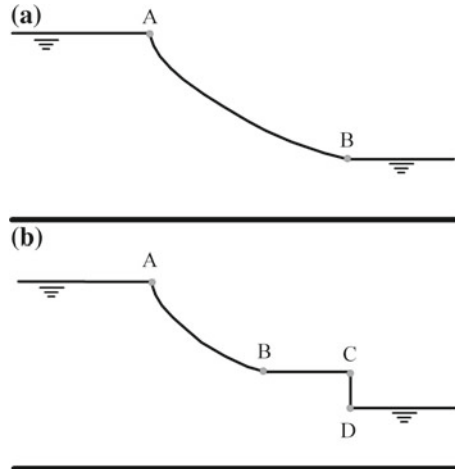
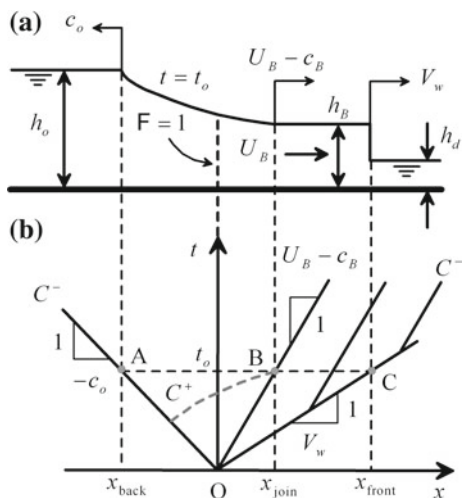


**Fig. 6.5** Wet-bed dam break wave for  $h_d/h_o < 0.138$   
**a** physical plane, **b**  $(x, t)$  plane. Critical flow ( $F = 1$ ) is at the  $t$ -axis (this wave produces an instantaneous transcritical flow profile with both continuous and discontinuous portions)



Thus, we have to determine the surge front and ensemble it to Ritter's parabolic wave profile. The new unknowns are the water depth and velocity in the surge zone ( $U_B, h_B$ ), and the surge front velocity  $V_w$  (Montes 1998). At this point, it is illustrative to detail an alternative method to the Reynolds transport theorem (see Chap. 5) to obtain the surge control-volume equations. The surge is a discontinuity in depth and velocity that propagates at constant speed  $V_w$ . Therefore, its shape is not deformed as it moves, so it is possible to transform the SWE PDEs (see Chap. 5),

$$\frac{\partial \mathbf{U}}{\partial t} + \frac{\partial \mathbf{F}}{\partial x} = \mathbf{0}, \quad (6.27)$$

to moving axes with the surge using a Galilei coordinate transformation, where  $\mathbf{U} = (h, Uh)^T$  and  $\mathbf{F} = (Uh, gh^2/2 + U^2h)^T$  are the vectors of unknowns and fluxes, respectively. The space coordinate  $X$  in moving axes is related to the absolute longitudinal coordinate  $x$  by  $X = x - V_w t$ . Therefore, basic calculus permits to write the identities

$$\frac{\partial \mathbf{U}}{\partial t} = \frac{\partial \mathbf{U}}{\partial X} \frac{\partial X}{\partial t} = \frac{\partial \mathbf{U}}{\partial X} (-V_w), \quad (6.28)$$

$$\frac{\partial \mathbf{F}}{\partial x} = \frac{\partial \mathbf{F}}{\partial X} \frac{\partial X}{\partial x} = \frac{\partial \mathbf{F}}{\partial X} (+1). \quad (6.29)$$

The SWE are now transformed for a wave traveling with constant speed and shape to

$$\frac{\partial \mathbf{U}}{\partial t} + \frac{\partial \mathbf{F}}{\partial x} = -V_w \frac{\partial \mathbf{U}}{\partial X} + \frac{\partial \mathbf{F}}{\partial X} = \mathbf{0}, \quad (6.30)$$

that is, to the system of ODEs

$$\frac{d}{dX} (\mathbf{F} - V_w \mathbf{U}) = \mathbf{0}. \quad (6.31)$$

These ODEs do not apply at the discontinuity of a surge. Therefore, its integral form is

$$\int_{X_B}^{X_d} \frac{d}{dX} (\mathbf{F} - V_w \mathbf{U}) dX = \mathbf{0}, \quad (6.32)$$

which yields the following solution as a function of the states ahead and behind the shock

$$\frac{\mathbf{F}_B - \mathbf{F}_d}{\mathbf{U}_B - \mathbf{U}_d} = V_w. \quad (6.33)$$

This vector equation states the so-called Rankine–Hugoniot jump conditions for a shock wave. Therefore, the two equations to be satisfied are the mass and momentum balances across the surge, given, respectively, from the Rankine–Hugoniot jump conditions Eq. (6.33)

$$V_w(h_B - h_d) = U_B h_B, \quad (6.34)$$

$$V_w(U_B h_B) = \left( g \frac{h_B^2}{2} + U_B^2 h_B \right) - \left( g \frac{h_d^2}{2} \right). \quad (6.35)$$

After algebraic manipulation, these equations are rewritten as

$$h_B(V_w - U_B) = V_w h_B, \quad (6.36)$$

and

$$\frac{h_B^2}{2} + h_B \frac{(V_w - V_B)^2}{g} = \frac{h_d^2}{2} + \frac{h_d V_w^2}{g}. \quad (6.37)$$

An alternative form of Eq. (6.37) presented in Chap. 5 is

$$V_w = \left[ \frac{g h_B}{2 h_d} (h_B + h_d) \right]^{1/2}. \quad (6.38)$$

Equations (6.36) and (6.38) are identical to those found by applying Reynolds' transport theorem in a fixed reference system (see Chap. 5). The three unknowns to fully determine the wave structure are  $U_B$ ,  $h_B$ , and  $V_w$ . A third equation needed to mathematically close the system originates from conserving the Riemann invariant along a forward characteristic  $C^+$  connecting the joint point of the parabolic and surge portions (point B in Fig. 6.5), with a point on the negative front. The resulting equation is given by

$$U_B + 2c_B = 2c_o. \quad (6.39)$$

The computational process involves the solution of a system of three non-linear equations for the unknowns  $U_B$ ,  $h_B$ , and  $V_w$  [Eqs. (6.36), (6.38), and (6.39)]. First, these are coupled to produce a single equation in the depth  $h_B$  inserting  $V_w$  from Eq. (6.38) and  $U_B$  from Eq. (6.39) into Eq. (6.36) (Jain 2001)

$$\left[ \frac{g h_B}{2 h_d} (h_B + h_d) \right]^{1/2} - \frac{h_B \left[ 2(g h_o)^{1/2} - 2(g h_B)^{1/2} \right]}{(h_B - h_d)} = 0. \quad (6.40)$$

Its solution to find the root  $h_B$  is easily implemented using the Newton–Raphson method as follows. Equation (6.40) is rewritten for convenience as

$$f(h_B) \equiv (h_B - h_d) \left[ \frac{g (h_B + h_d)}{2 h_d h_B} \right]^{1/2} + 2 \left[ (g h_B)^{1/2} - (g h_o)^{1/2} \right] = 0. \quad (6.41)$$

A better approximation to the root of Eq. (6.41) is based on the Newton–Raphson method with  $k$  as the recursion index by (Hoffman 2001)

$$h_B^{k+1} = h_B^k - \frac{f^k}{(df/dh_B)^k}. \quad (6.42)$$

The derivative term needed in Eq. (6.42) is

$$\frac{df}{dh_B} = g(gh_B)^{-1/2} + \left[ \frac{g}{2} \frac{(h_B + h_d)}{h_d h_B} \right]^{1/2} - g \frac{(h_B - h_d)}{4h_B^2} \left[ \frac{g}{2} \frac{(h_B + h_d)}{h_d h_B} \right]^{-1/2}. \quad (6.43)$$

A good initial value for  $h_B$  to initialize the algorithm is

$$h_B = \frac{1}{g} \left[ \frac{(gh_o)^{1/2} + (gh_d)^{1/2}}{2} \right]^2. \quad (6.44)$$

Once  $h_B$  is computed,  $V_w$  follows from the momentum balance applying Eq. (6.38), and  $U_B$  is given from Eq. (6.39) stating the Riemann invariant along the  $C^+$  characteristic by

$$U_B = 2(gh_o)^{1/2} - 2(gh_B)^{1/2}. \quad (6.45)$$

The computational sequence is as follows:

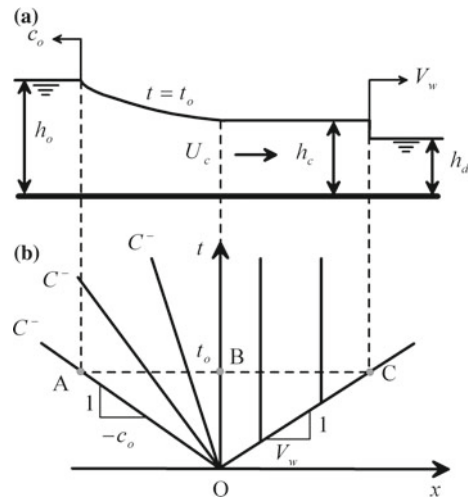
- (1) For given values of  $h_o$  and  $h_d$  compute  $U_B$ ,  $h_B$ , and  $V_w$  as described above.
- (2) For a given instant of time  $t$ , the position of the negative front is  $x_{\text{back}} = -c_o t$ , of the surge front is  $x_{\text{front}} = V_w t$ , and of the assembling point of the parabolic profile with the constant state behind the surge is  $x_{\text{join}} = (U_B - c_B)t$ .
- (3) Compute the free surface and velocity profiles applying the rarefaction wave Eqs. (6.16) and (6.18) if  $x_{\text{back}} < x < x_{\text{join}}$ . The constant state values behind the surge apply if  $x_{\text{join}} < x < x_{\text{front}}$ .

As the tailwater depth  $h_d$  increases, the velocity  $U_B$  decreases. For a particular value of  $h_d$ , the limit  $U_B = c_B$  can occur, implying that point B becomes the critical flow section, coincident thus with the  $t$ -axis (Fig. 6.6). In this case, the entire constant flow zone behind the surge is under critical flow. From Eq. (6.10), the critical flow depth is  $h_c = (4/9)h_o$ . To find this limiting value of  $h_d$ ,  $U_B = c_B$  is set into Eq. (6.40), resulting in

$$\left[ \frac{g}{2} \frac{h_B}{h_d} (h_B + h_d) \right]^{1/2} - \frac{h_B c_B}{(h_B - h_d)} = 0, \quad (6.46)$$

**Fig. 6.6** Wet-bed dam break wave for  $h_d/h_o = 0.138$ 

**a** physical plane,  
**b**  $(x, t)$  plane. Entire water body behind the surge is under critical flow condition. This case is likely to be theoretical but not realistic. Under critical or near-critical flow conditions, waves exhibit undular flow features in response to non-hydrostatic fluid pressure ( $F = 1$ )



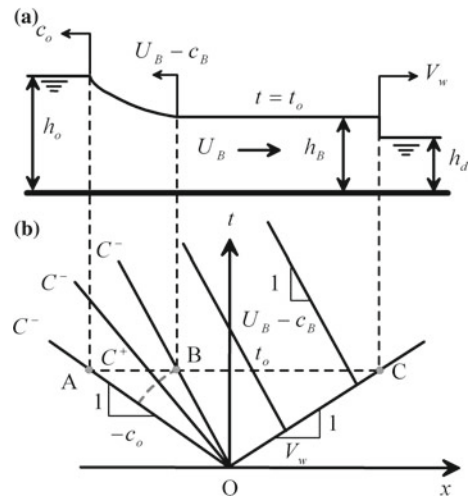
or,

$$\left[ \frac{1}{2} \frac{1}{h_d/h_B} \left( 1 + \frac{h_d}{h_B} \right) \right]^{1/2} - \frac{1}{(1 - h_d/h_B)} = 0. \quad (6.47)$$

The solution of this implicit equation produces  $h_d/h_B \approx 0.3105$ . Thus, the limiting ratio of water depths is  $h_d/h_o = 0.3105 \cdot (4/9) = 0.138$ . For  $h_d > 0.138h_o$ , the wave structure is as depicted in Fig. 6.7, with subcritical flow throughout.

**Fig. 6.7** Wet-bed dam break wave for  $h_d/h_o > 0.138$ 

**a** physical plane, **b**  $(x, t)$  plane. Subcritical flow occurs through the wave ( $F < 1$ )



## 6.4 Computational Examples

The solution for the ideal dry and wet dam break waves described above is implemented in a source code available in the sheet *DamBreakAnalytical.xls* (Chap. 12). An example using this code is presented here, applying it to simulate the ideal dam break of the Möhne Dam. The maximum water depth in the reservoir was  $h_o = 32$  m (Kirschmer 1949). It was observed that a surge of about 10 m height propagated in the tailwater. Simulations were conducted assuming  $h_d = 1.5$  m. The numerical solution gave  $h_B = 9.7$  m,  $U_B = 15.93$  m/s, and  $V_w = 18.84$  m/s. The computed free surface and velocity profiles 1 h after the dam break are plotted in Fig. 6.8. Note that the surge height is close to that observed. The relative wave celerity is  $c_w = V_w - U_B = 2.9$  m/s, which is also in fair agreement with estimations available; an average value of 2.88 m/s is quoted by Kirschmer (1949). This computation gives an impression of the tremendous magnitude of the flow variables after breaking of a real dam.

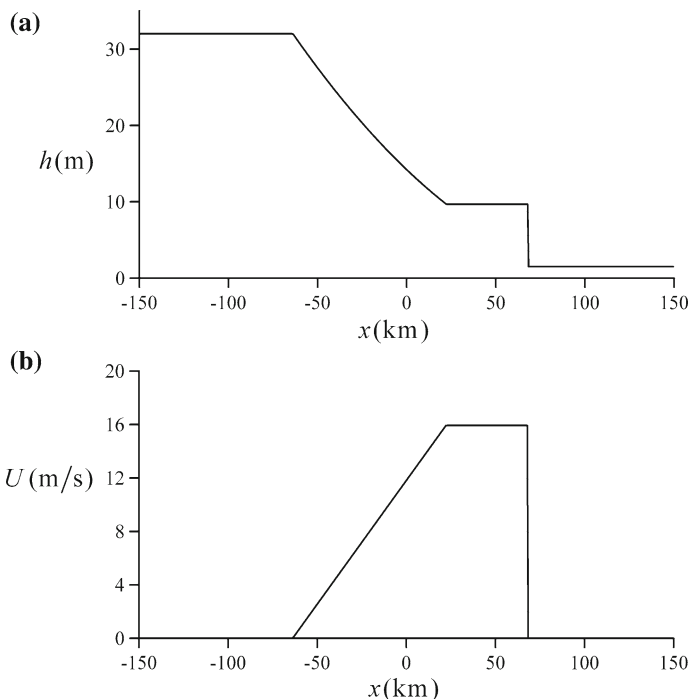


**Fig. 6.8** Ideal dam break wave of Möhne Dam for 1.5 m in the tailwater, after 1 h of routing

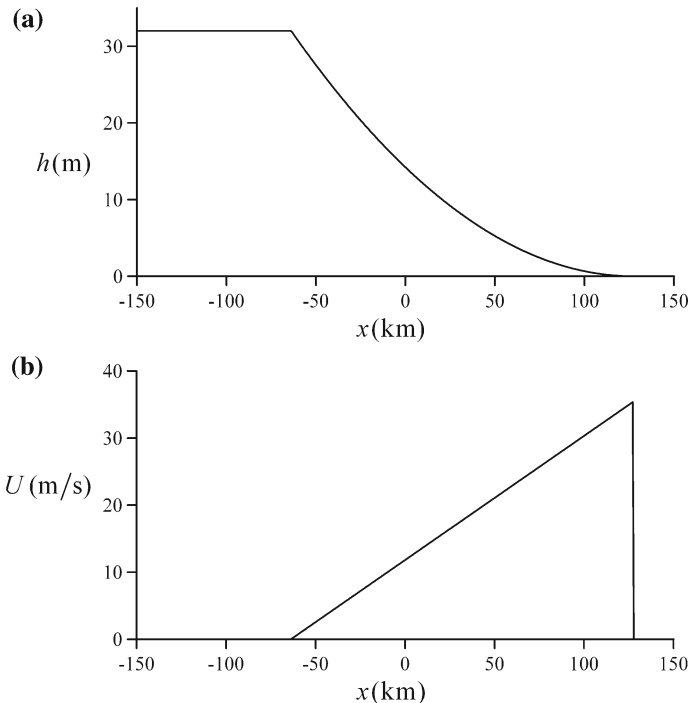
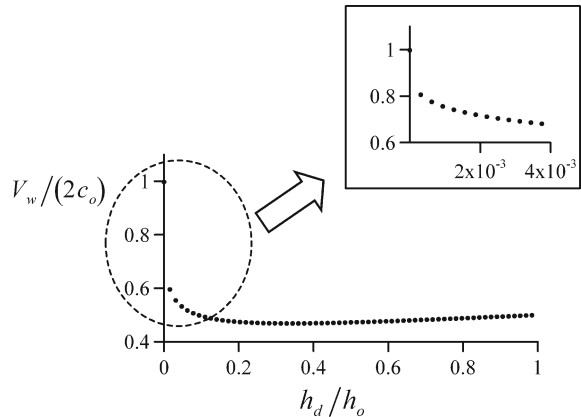


**Fig. 6.9** Ideal dam break wave of Möhne Dam for dry tailwater after 1 h of routing

**Fig. 6.10** Ratio  $V_w/(2c_o)$  of wet to dry front celerities as function of depth ratio  $h_d/h_o$



The same computation was repeated for the dry-bed condition ( $h_d = 0$ ), resulting in the profiles plotted in Fig. 6.9. As observed, the increase of velocity at the positive front is considerable. Comparing these two sets of simulations for the Möhne Dam results in  $V_w/(2c_o) = 18.84/35.43 = 0.531$ . This shows the tremendously decelerating effect of wetting the tailwater. A plot of  $V_w/(2c_o)$  as a function of the depth ratio  $h_d/h_o$  is presented in Fig. 6.10, to show with more generality the behavior of the front celerity as a function of tailwater wetting conditions. Note that the deceleration effect occurs fast just after a minimal wetting of the tailwater (see detail in Fig. 6.10). The positive front velocity ratio then becomes nearly constant with values around  $V_w/(2c_o) = 0.47$ , and then slightly increases when  $h_d/h_o$  raises above 0.34.

The quality of Ritter's solution to predict dry-bed dam break waves is examined in Fig. 6.11, where the free surface predictions using Eq. (6.16) are compared with the experimental data of Ozmen-Cagatay and Kocaman (2010) at different normalized times  $T = t(g/h_o)^{1/2}$  starting at abrupt gate removal. The shape of the dam break wave curves of Fig. 6.11 is similar to those previously measured by Dressler (1954) and by Lauber and Hager (1998). The upstream water depth in the experiments by Ozmen-Cagatay and Kocaman (2010) was  $h_o = 0.25$  m. Note that the parabolic shape predicted by Ritter is in fair agreement with observations for this dataset. For a more general prediction of dry-bed dam break waves, non-hydrostatic and friction effects have to be accounted for. Castro-Orgaz and Chanson (2017) found that the negative wave celerity and the wave profile are accurately predicted if non-hydrostatic effects are considered in a depth-averaged model, whereas friction effects for laboratory data are confined to the narrow front tip which behaves essentially like a diffusive wave.

Computations for wet-bed dam break waves are compared with laboratory data for  $h_d/h_o < 0.138$  and  $h_d/h_o > 0.138$  in Figs. 6.12 and 6.13, respectively. During wave initiation, the wave profile is affected by the non-hydrostatic flow condition, a feature beyond the capabilities of the SWE, and, thus, agreement with experiments is not expected during this process (see Chap. 11). For a wet-bed dam break wave of shallow tailwater (Fig. 6.12), supercritical flow occurs in a part of the wave profile. As shown by experiments, the turbulence and wave breaking are strong in these flows, producing an irregular free surface that is not in precise agreement with the theoretical prediction. However, the overall position of the surge front is reasonably predicted.

For the subcritical dam break wave ( $h_d/h_o > 0.138$ ), turbulence effects are less stringent, and once the wave breaks, the prediction of the SWE is in excellent agreement with experiments (see Fig. 6.13 at  $T = 6.51$  and 6.89).

**Fig. 6.11** Comparison of theoretical dry-bed dam break prediction  $h/h_o[x/h_o]$  at various times  $T$  with laboratory data

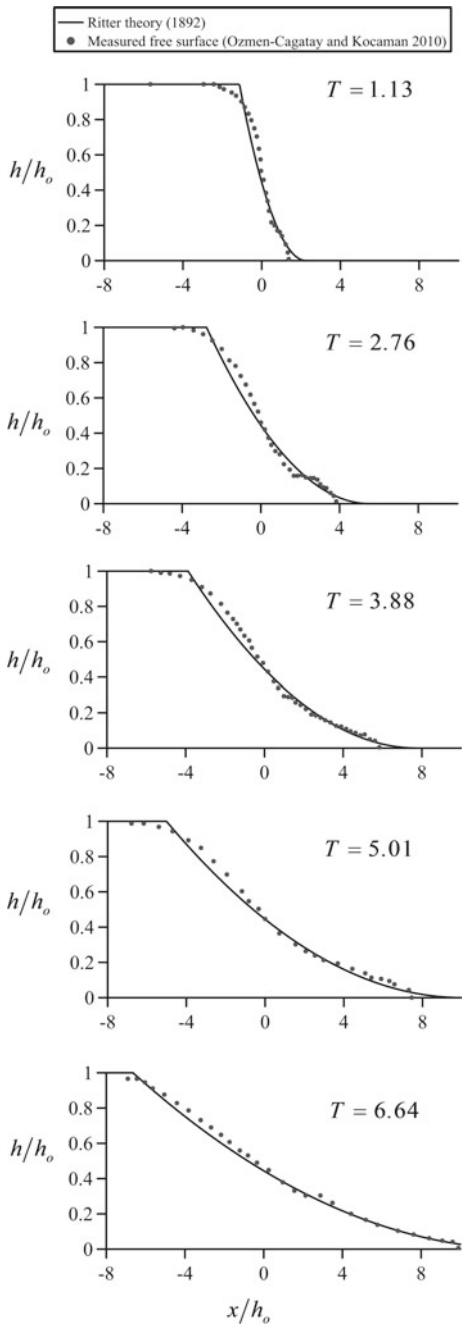


**Fig. 6.12** Comparison of theoretical wet-bed dam break prediction  $h/h_o[x/h_o]$  at various times  $T$  for  $h_d/h_o < 0.138$  with laboratory data

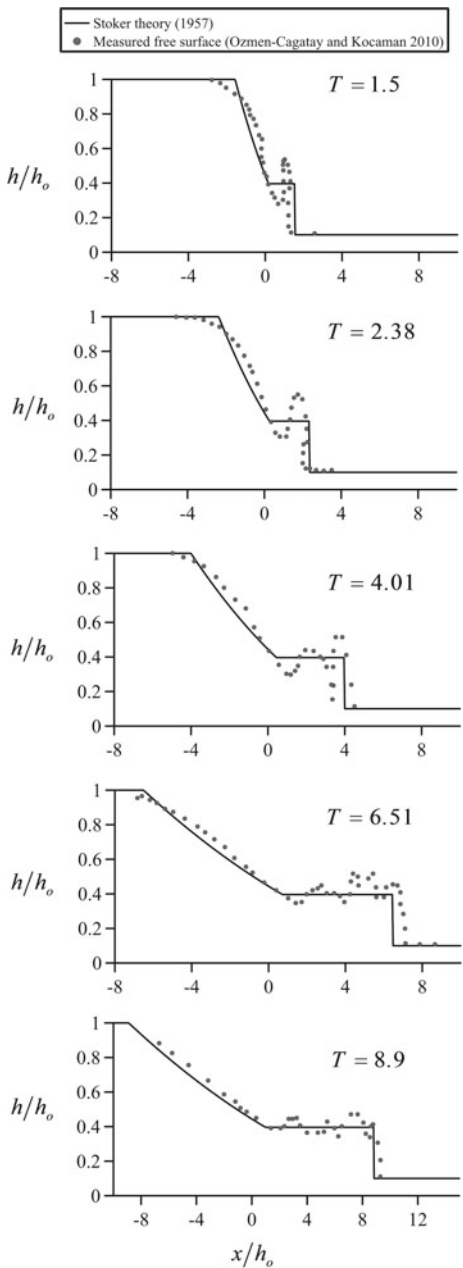
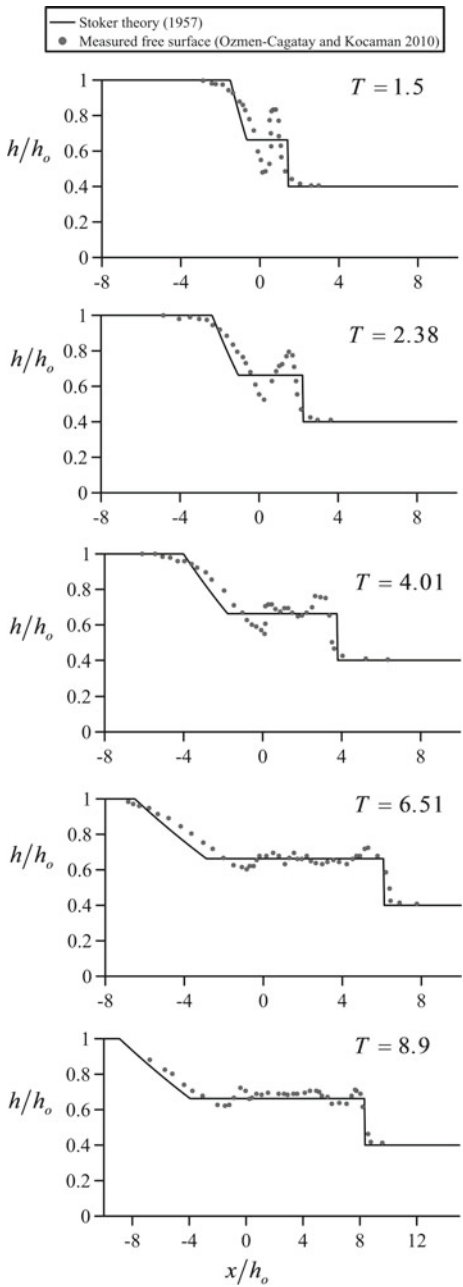


**Fig. 6.13** Comparison of theoretical wet-bed dam break prediction  $h/h_o[x/h_o]$  at various times  $T$  for  $h_d/h_o > 0.138$  with laboratory data



## References

- Castro-Orgaz, O., & Chanson, H. (2017). Ritter's dry-bed dam-break flows: Positive and negative wave dynamics. *Environmental Fluid Mechanics*, 17(4), 665–694.
- Chanson, H. (2004). *The hydraulics of open channel flows: An introduction*. Oxford, UK: Butterworth-Heinemann.
- Chow, V. T. (1959). *Open channel hydraulics*. New York: McGraw-Hill.
- Dressler, R. F. (1952). Hydraulic resistance effect upon the dambreak functions. *Journal of Research, National Bureau of Standards*, 49(3), 217–225.
- Dressler, R. (1954). Comparison of theories and experiments for the hydraulic dam-break wave. *Proceedings of the International Association Scientific Hydrology, Assemblée Générale*, 3(38), 319–328, Rome, Italy.
- Henderson, F. M. (1966). *Open channel flow*. New York: MacMillan Co.
- Hoffman, J. D. (2001). *Numerical methods for engineers and scientists* (2nd ed.). New York: Marcel Dekker.
- Jain, S. C. (2001). *Open channel flow*. New York: Wiley.
- Kirschner, O. (1949). Zerstörung von Talsperren und Dämmen [Destruction of dams and dikes]. *Schweizerische Bauzeitung*, 67(20), 277–281 (in German).
- Lauber, G., & Hager, W. H. (1998). Experiments to dambreak wave: Horizontal channel. *Journal of Hydraulic Research*, 36(3), 291–307.
- Montes, J. S. (1998). *Hydraulics of open channel flow*. Reston VA: ASCE.
- Ozmen-Cagatay, H., & Kocaman, S. (2010). Dam-break flows during initial stage using SWE and RANS approaches. *Journal of Hydraulic Research*, 48(5), 603–611.
- Ré, R. (1946). Étude du lacher instantané d'une retenue d'eau dans un canal par la méthode graphique [Study of instantaneous release of water in a channel using the graphical method]. *La Houille Blanche*, 1(3), 181–188 (in French).
- Ritter, A. (1892). Die Fortpflanzung von Wasserwellen [Propagation of water waves]. *Zeitschrift Verein Deutscher Ingenieure*, 36(2), 947–954 (in German).
- Schoklitsch, A. (1917). Über Dammbruchwellen [On dam break waves]. Kaiserliche Akademie der Wissenschaften, Wien, Mathematisch-Naturwissenschaftliche Klasse. *Sitzungberichte IIa*, 126, 1489–1514 (in German).
- Stoker, J. J. (1957). *Water waves: The mathematical theories with applications*. New York: Wiley.
- Toro, E. F. (2001). *Shock-capturing methods for free-surface shallow flows*. Singapore: Wiley.
- Toro, E. F. (2009). *Riemann solvers and numerical methods for fluid dynamics*. London: Springer.
- Whitham, G. B. (1955). The effects of hydraulic resistance in the dam-break problem. *Proceedings of the Royal Society of London*, A, 227, 399–407.

# Chapter 7

## Finite Difference Methods



### 7.1 Introduction

The SWE are a system of two nonlinear hyperbolic PDEs that must be numerically solved to describe the time evolution of the fluid velocity and water depth in the entire computational domain. Finite-difference methods to obtain approximate numerical solutions are described in this chapter. First, basic numerical aspects are presented. The implementation of boundary conditions for continuous and discontinuous flows is then discussed, and various schemes widely used are explained in detail. The performance of these schemes is assessed using analytical solutions and experimental data for selected test cases.

### 7.2 Basic Numerical Aspects

#### 7.2.1 Remark on Basic Numerical Concepts

Some basic concepts linked to the numerical solution of hyperbolic conservation laws to be used in this chapter are (Hoffman 2001):

*Accuracy:* The truncation errors are an accuracy measure of the finite-difference (FD) scheme. These result from approximating the derivatives by FDs. In general, the accuracy of a numerical scheme is impaired by both truncation errors and (machine) round-off errors. However, the latter are usually negligible, given their smallness.

*Convergence:* Reference is made to the relation between the solution produced by the FD scheme and the solution of the original differential equation. Convergence is reached if the FD solution approaches the solution of the differential equation as the spatial and temporal steps,  $\Delta x$  and  $\Delta t$ , tend to zero.

*Consistency:* This refers to the relation between the algebraic equation produced by the FD scheme and the original differential equation. Consistency is reached if the FD equation approaches the original differential equation as  $\Delta x$  and  $\Delta t$  tend to zero. Consistency is needed to have a convergent solution, but it is not a sufficient condition.

*Stability:* A numerical scheme is stable if the solution remains bounded as it evolves in time. An unstable solution becomes unbounded due to the accumulation of errors and may result in a crashing of computations.

### 7.2.2 Finite-Difference Approximations

The SWE for a rectangular cross section, written in conservative form, are

$$\frac{\partial \mathbf{U}}{\partial t} + \frac{\partial \mathbf{F}}{\partial x} = \mathbf{S}. \quad (7.1)$$

Here,  $\mathbf{U}$  is the vector of unknowns,  $\mathbf{F}$  the flux vector, and  $\mathbf{S}$  the source term vector, with  $h$  as the water depth,  $U$  the fluid velocity,  $z_b$  the bed elevation,  $x$  the longitudinal coordinate,  $t$  the time,  $g$  the gravity acceleration, and  $C_f$  as a friction coefficient, given by

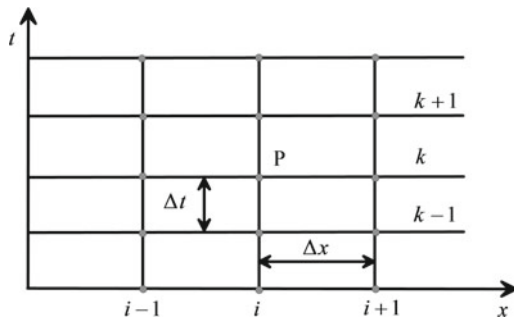
$$\mathbf{U} = \begin{pmatrix} h \\ Uh \end{pmatrix}, \quad \mathbf{F} = \begin{pmatrix} Uh \\ U^2 h + \frac{1}{2} g h^2 \end{pmatrix}, \quad \mathbf{S} = \begin{pmatrix} 0 \\ -gh \frac{\partial z_b}{\partial x} - C_f U |U| \end{pmatrix}. \quad (7.2)$$

To compute the variables  $U(x, t)$  and  $h(x, t)$ , a discretization of the governing equations is required. The partial derivatives (or integrals) in the governing equations are then replaced by discrete numbers. Discretization of the partial differential equations, Eq. (7.1), leads to *finite difference methods* (FDM). In turn, the discretization of integral equations as

$$\iint_{CV} \frac{\partial \mathbf{U}}{\partial t} dx dt + \oint (\mathbf{F} \cdot \mathbf{n}) ds = \iint_{CV} \mathbf{S} dx dt, \quad (7.3)$$

leads to the so-called *finite volume methods* (FVM) (Anderson 1995; Hoffmann 2001; Toro 2009), with  $CV$  as the control volume in the  $(x, t)$  plane,  $\mathbf{n}$  as the unit vector normal to the closed contour of  $CV$ , and  $s$  as the curvilinear coordinate. Here, FDM are considered, where the PDEs are approximated by algebraic relations obtained by replacing the partial derivatives by finite-differences.

**Fig. 7.1** Finite-difference grid in the  $(x, t)$  plane



Consider a finite-difference grid in the  $x$ - $t$  plane (Fig. 7.1), where nodes are defined by uniform steps  $\Delta x$  and  $\Delta t$  in the  $x$ - and  $t$ -directions, respectively. The objective is to replace the original PDEs, valid at any point on the  $x$ - $t$  plane, by algebraic expressions that apply only to the grid points  $(i, k)$  of the mesh, with  $i$  and  $k$  as the node indices in the  $x$ - and  $t$ -directions, respectively.

Finite-difference representations of derivatives are based on Taylor series expansions (Sturm 2001; Chaudhry 2008). For example, for vector  $\mathbf{F}$ , a Taylor expansion in the  $x$ -direction at point  $i + 1$  and time level  $k$  reads (Hoffman 2001)

$$\mathbf{F}_{i+1}^k = \mathbf{F}_i^k + \left(\frac{\partial \mathbf{F}}{\partial x}\right)_i^k \Delta x + \left(\frac{\partial^2 \mathbf{F}}{\partial x^2}\right)_i^k \frac{(\Delta x)^2}{2} + \left(\frac{\partial^3 \mathbf{F}}{\partial x^3}\right)_i^k \frac{(\Delta x)^3}{6} + \dots \quad (7.4)$$

Solving for the first derivative of  $\mathbf{F}$  from the former expression results in

$$\left(\frac{\partial \mathbf{F}}{\partial x}\right)_i^k = \underbrace{\frac{\mathbf{F}_{i+1}^k - \mathbf{F}_i^k}{\Delta x}}_{\text{Finite difference approximation}} - \underbrace{\left(\frac{\partial^2 \mathbf{F}}{\partial x^2}\right)_i^k \frac{\Delta x}{2} - \left(\frac{\partial^3 \mathbf{F}}{\partial x^3}\right)_i^k \frac{(\Delta x)^2}{6} + \dots}_{\text{Truncation error}} \quad (7.5)$$

If the first derivative in Eq. (7.5) is taken as the finite-difference approximation, the remaining part of the equation is the so-called truncation error, thus

$$\left(\frac{\partial \mathbf{F}}{\partial x}\right)_i^k \approx \frac{\mathbf{F}_{i+1}^k - \mathbf{F}_i^k}{\Delta x}. \quad (7.6)$$

The partial derivative of a continuous magnitude,  $\mathbf{F}$ , is replaced by the algebraic difference. As the neglected truncation error is proportional to  $\Delta x$ , this approximation is first-order accurate. Mathematically, this is expressed as the so-called forward finite-difference

$$\left(\frac{\partial \mathbf{F}}{\partial x}\right)_i^k = \frac{\mathbf{F}_{i+1}^k - \mathbf{F}_i^k}{\Delta x} + O(\Delta x). \quad (7.7)$$

A Taylor expansion at point  $(i - 1, k)$  about the point  $(i, k)$  reads

$$\mathbf{F}_{i-1}^k = \mathbf{F}_i^k + \left(\frac{\partial \mathbf{F}}{\partial x}\right)_i^k (-\Delta x) + \left(\frac{\partial^2 \mathbf{F}}{\partial x^2}\right)_i^k \frac{(-\Delta x)^2}{2} + \left(\frac{\partial^3 \mathbf{F}}{\partial x^3}\right)_i^k \frac{(-\Delta x)^3}{6} + \dots \quad (7.8)$$

From similar arguments, one finds for the so-called backward finite-difference

$$\left(\frac{\partial \mathbf{F}}{\partial x}\right)_i^k = \frac{\mathbf{F}_i^k - \mathbf{F}_{i-1}^k}{\Delta x} + O(\Delta x). \quad (7.9)$$

In applications, the first-order accuracy is often insufficient. Simply subtracting the two Taylor series, Eqs. (7.4) and (7.8), results in (Hoffman 2001)

$$\mathbf{F}_{i+1}^k - \mathbf{F}_{i-1}^k = 2\left(\frac{\partial \mathbf{F}}{\partial x}\right)_i^k \Delta x + 2\left(\frac{\partial^3 \mathbf{F}}{\partial x^3}\right)_i^k \frac{(\Delta x)^3}{6} + \dots \quad (7.10)$$

From Eq. (7.10), the so-called central finite-difference approximation becomes

$$\left(\frac{\partial \mathbf{F}}{\partial x}\right)_i^k = \frac{\mathbf{F}_{i+1}^k - \mathbf{F}_{i-1}^k}{2\Delta x} + O(\Delta x^2), \quad (7.11)$$

which is second-order space accurate. Forward, backward, and central finite-differences can also be formed for the time derivative  $\partial \mathbf{U}/\partial t$ .

*Remark:* A logic choice for the finite-difference quotient to use in the discretization of spatial gradients is based on the concept of *upwinding*. Most field equations in environmental physics contain terms representing advection and diffusion processes, as

$$\frac{\partial f}{\partial t} + \underbrace{u \frac{\partial f}{\partial x}}_{\text{convective term}} = \underbrace{D \frac{\partial^2 f}{\partial x^2}}_{\text{diffusion term}}. \quad (7.12)$$

Here,  $f$  is a property advected and diffused, e.g., concentration of a scalar,  $D$  is a diffusion coefficient, and  $u$  is the advection speed (Roache 1972). Neglecting diffusion, Eq. (7.12) reduces to

$$\frac{\partial f}{\partial t} + u \frac{\partial f}{\partial x} = 0. \quad (7.13)$$

While the obvious choice for discretization of the time derivative to advance in time starting at known time level is the forward finite-difference

$$\frac{\partial f}{\partial t} = \frac{f_i^{k+1} - f_i^k}{\Delta t} + O(\Delta t), \quad (7.14)$$

the best choice for the spatial gradient is not so evident. The following options are mathematically possible:

Forward finite-difference

$$\frac{\partial f}{\partial x} = \frac{f_{i+1}^k - f_i^k}{\Delta x} + O(\Delta x), \quad (7.15)$$

Backward finite-difference

$$\frac{\partial f}{\partial x} = \frac{f_i^k - f_{i-1}^k}{\Delta x} + O(\Delta x), \quad (7.16)$$

Central finite-difference

$$\frac{\partial f}{\partial x} = \frac{f_{i+1}^k - f_{i-1}^k}{2\Delta x} + O(\Delta x^2). \quad (7.17)$$

These finite-difference quotients take information on the perturbation propagation in different ways. The backward difference takes information at a node from its upstream side, the forward difference from the downstream side, and the central difference from both. An upwind model uses information available about the wave propagation to select the proper numerical discretization of the spatial derivatives in the PDE. An upwind approximation for Eq. (7.13) is designed by taking information at a node from the side to which the perturbation approaches while propagating. The simple first-order upwind model for the convection equation is then

$$\begin{aligned} \frac{f_i^{k+1} - f_i^k}{\Delta t} + u \frac{f_i^k - f_{i-1}^k}{\Delta x} &= 0 && \text{if } u > 0, \\ \frac{f_i^{k+1} - f_i^k}{\Delta t} + u \frac{f_{i+1}^k - f_i^k}{\Delta x} &= 0 && \text{if } u < 0. \end{aligned} \quad (7.18)$$

This scheme, due to Courant et al. (1952), is conditionally stable. Other choices based on central [Eq. (7.17)], or one-sided finite-differences in the same direction as  $u$  (down-winding schemes), are unconditionally unstable (Roache 1972; Anderson 1995). A useful one-sided scheme is only obtained by accounting for the sign of the

wave propagation speed  $u$ . This is the utility of up-winding. The centered scheme based on Eq. (7.17) is not good, given the unstable behavior. Note that the upwind differences are related to the central difference by

$$\begin{aligned}\frac{f_i^k - f_{i-1}^k}{\Delta x} &= \frac{f_{i+1}^k - f_{i-1}^k}{2\Delta x} - \left(\frac{\Delta x}{2}\right) \frac{f_{i+1}^k - 2f_i^k + f_{i-1}^k}{(\Delta x)^2} && \text{if } u > 0, \\ \frac{f_{i+1}^k - f_i^k}{\Delta x} &= \frac{f_{i+1}^k - f_{i-1}^k}{2\Delta x} + \left(\frac{\Delta x}{2}\right) \frac{f_{i+1}^k - 2f_i^k + f_{i-1}^k}{(\Delta x)^2} && \text{if } u < 0.\end{aligned}\quad (7.19)$$

Therefore, upwind methods introduce numerical diffusion into the centered scheme to make it stable. The diffusion is numerical with  $D = \Delta x/2$ .

Returning to the SWE, a possible model for the discretization of Eq. (7.1) written without source terms,

$$\frac{\partial \mathbf{U}}{\partial t} + \frac{\partial \mathbf{F}}{\partial x} = \mathbf{0}, \quad (7.20)$$

is with accuracy  $O(\Delta t, \Delta x^2)$

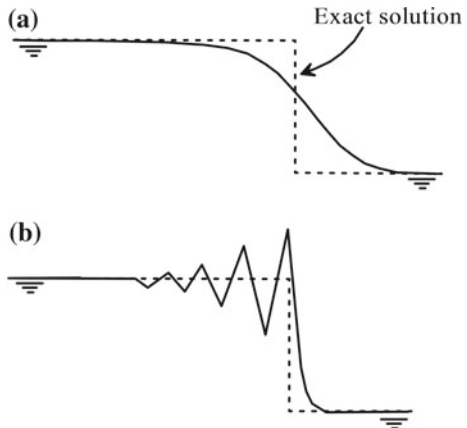
$$\frac{\mathbf{U}_i^{k+1} - \mathbf{U}_i^k}{\Delta t} + \frac{\mathbf{F}_{i+1}^k - \mathbf{F}_{i-1}^k}{2\Delta x} = \mathbf{0}. \quad (7.21)$$

In spite of the second-order spatial accuracy, this finite-difference model is not suitable, given its instability (Liggett and Cunge 1975; Cunge et al. 1980; Montes 1998; Sturm 2001; Chaudhry 2008), as also explained with Eq. (7.13). Therefore, the proper selection of an FD model should not rely on producing small truncation errors simply by increasing the order of the scheme. The lesson to be learnt is: Not all mathematically permissible discretizations are necessarily a good approximation for the physical problem to be simulated.

### 7.2.3 Shock-Capturing Schemes

Conservative and non-conservative forms of the SWE apply to simulate continuous and smooth wave fields. However, the celerity of positive surges is poorly predicted by the non-conservative form (Chap. 5). Thus, in this chapter, only the conservative form is considered. The SWE in differential form are valid only for continuous flows, excluding the generation of discontinuities. Thus, logic would dictate to abandon Eq. (7.1) and any FD approximation of this model when dealing with discontinuous flows. Practice, however, reveals that shock-capturing models can be constructed based on Eq. (7.1) (Cunge 1975). The reason for this apparently contradictory success is as follows: The finite-difference algebraic equations representing the original PDEs have shock-capturing ability because they mimic (or

**Fig. 7.2** Computed shock solutions contaminated by  
**a** diffusion errors and  
**b** dispersion errors



approximate) the discrete form of the integral conservation laws (to be derived for the FVM in Chap. 9). Therefore, some finite-difference schemes approximating the original PDEs as  $\Delta \mathbf{U}/\Delta t + \Delta \mathbf{F}/\Delta x = \mathbf{S}$  are interpreted as particular discretizations of the integral Eq. (7.3). In this chapter, only shock-capturing finite-difference schemes are considered.

Two typical numerical errors appear in shock-capturing schemes. First-order finite-difference schemes introduce numerical diffusion, smearing the shock front (Fig. 7.2a). Second-order schemes introduce numerical dispersion errors. These produce high-frequency oscillations near sharp gradients, as close to a shock (Fig. 7.2b). In general, the second-order schemes are preferred in practice, given the sharp resolution of shocks. The dispersion errors are locally controlled by adding limited numerical diffusion.

Some finite-difference schemes mimic the integral form of the conservation laws and thus produce shocks in the solution, as explained. However, not all shock-capturing schemes produce physical shocks in the solution. To reproduce a physical shock in the solution, the following entropy condition must be satisfied (Lax 1954; Lax and Wendroff 1960; Toro 2001)

$$\lambda(\mathbf{U}_L) \geq S \geq \lambda(\mathbf{U}_R). \quad (7.22)$$

Here,  $\lambda(\mathbf{U}) = U + (gh)^{1/2}$  are the eigenvalues associated with the  $C^+$  characteristics for the right-going shock depicted in Fig. 7.3, and  $L$  and  $R$  denote states at the left and right sides of the shock displacing with velocity  $S$ . Equation (7.22) implies that the characteristic curves converge to the path of the shock in the  $(x, t)$  plane (Fig. 7.3). If Eq. (7.22) is not satisfied, the finite-difference scheme may produce a non-physical jump (Bhallamudi 2002). Upwind models for the SWE use the eigenvalues to detect the direction of signal propagation and thus the adequate finite-difference representation of spatial gradients. At a critical point [ $U = (gh)^{1/2}$ ], the eigenvalue corresponding to the backward characteristic vanishes. Then, some

**Fig. 7.3** Sketch of discontinuity in the physical plane and conditions for a physical shock in  $(x, t)$  plane

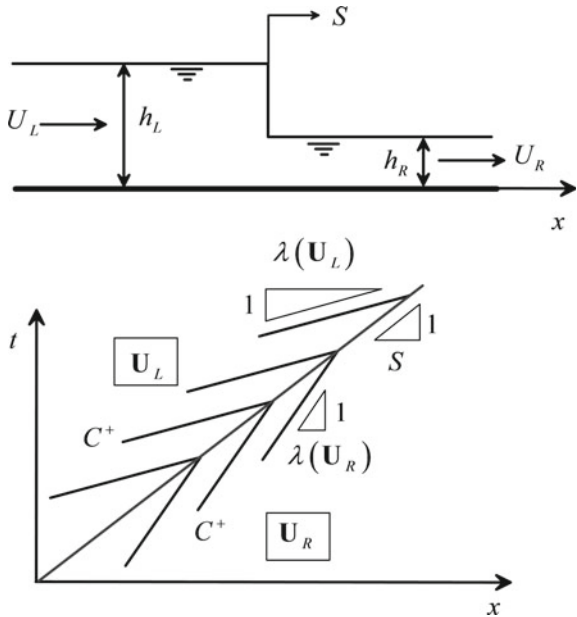
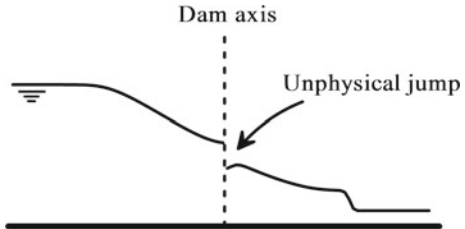


**Fig. 7.4** Unphysical shock in transcritical dam break wave



schemes are unable to distinguish a rarefaction wave crossing smoothly a critical point from a shock (Bhallamudi 2002; Zoppou and Roberts 2003). These models need an entropy fix to produce meaningful results. Without this correction, a prediction with an unphysical jump as in Fig. 7.4 is produced.

#### 7.2.4 Explicit and Implicit Schemes: Stability

In Eq. (7.21), the vector  $\mathbf{U}$  at the new time level  $k + 1$  is computed based on data at time level  $k$ , where all information is known. It permits to evaluate  $\mathbf{F}$  at all nodes of the mesh. Values of  $\mathbf{U}$  at each node  $i$  for time  $t + \Delta t$  are therefore explicitly solved. This type of model is referred to as explicit. However, it is possible to evaluate  $\mathbf{F}$  at time level  $k + 1$ , resulting in

$$\frac{\mathbf{U}_i^{k+1} - \mathbf{U}_i^k}{\Delta t} + \frac{\mathbf{F}_{i+1}^{k+1} - \mathbf{F}_{i-1}^{k+1}}{2\Delta x} = \mathbf{0}. \quad (7.23)$$

Note that  $\mathbf{F} = \mathbf{F}(\mathbf{U})$ , e.g.,

$$\frac{\partial \mathbf{U}}{\partial t} + \frac{\partial \mathbf{F}(\mathbf{U})}{\partial x} = \mathbf{0}, \quad (7.24)$$

with

$$\mathbf{U} = \begin{pmatrix} h \\ Uh \end{pmatrix} = \begin{pmatrix} U_1 \\ U_2 \end{pmatrix}, \quad \mathbf{F} = \begin{pmatrix} Uh \\ U^2 h + \frac{1}{2} g h^2 \end{pmatrix} = \begin{pmatrix} U_2 \\ \frac{U_1^2}{U_1} + \frac{1}{2} g U_1^2 \end{pmatrix}. \quad (7.25)$$

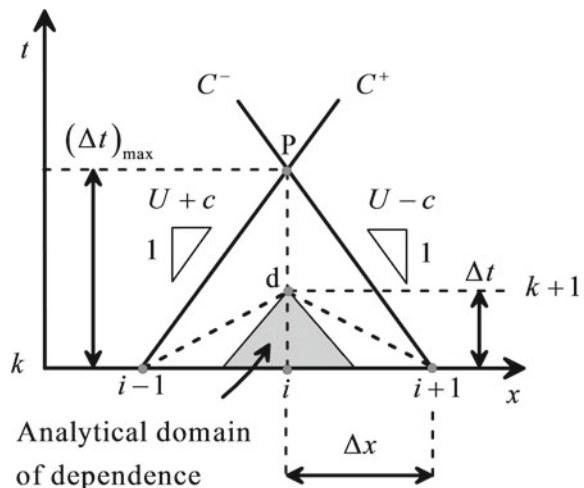
Thus, Eq. (7.23) cannot be directly solved for  $\mathbf{U}$  at the new time level  $k + 1$ . Rather, it is an implicit equation to be solved numerically to compute the vector  $\mathbf{U}$  at time level  $k + 1$ . The equation at a node is thus

$$\frac{\mathbf{U}_i^{k+1} - \mathbf{U}_i^k}{\Delta t} + \frac{\mathbf{F}_{i+1}^{k+1}(\mathbf{U}_{i+1}^{k+1}) - \mathbf{F}_{i-1}^{k+1}(\mathbf{U}_{i-1}^{k+1})}{2\Delta x} = \mathbf{0}. \quad (7.26)$$

This type of model is said to be implicit. The implicit method results in a system of nonlinear implicit equations, to be simultaneously solved for all nodes. They are unconditionally stable (Chaudhry 2008). The selection of the type of scheme, implicit or explicit, is by no means a rigid decision (Anderson 1995). The implicit methods are applied to large time steps, given the unconditional stability. However, the solution at each time level involves a more complex numerical method, which obviously implies more coding work. Additionally, even if computations being stable for any time step are an advantage, the use of a large step may deteriorate the quality of the computed transient wave solution due to its contamination by truncation errors. The explicit methods involve simple computations for each new time level, with the corresponding simplicity of coding. However, to be stable, the time step cannot be arbitrary. Rather, a physical constraint must be added, as explained below, to limit the largest permissible time step. Due to coding simplicity, and if the main interest is the computation of an accurate wave pattern which is likely to evolve fast, as in a dam break wave, explicit schemes are a good practical choice (Zoppou and Roberts 2003). In this chapter, the attention is thus restricted to these techniques. To implement implicit schemes, see Sturm (2001) or Chaudhry (2008).

In an explicit method, the time step  $\Delta t$  for a size of cell  $\Delta x$  is limited to the time needed by perturbations originating at adjacent nodes to propagate and interact. Consider a node  $i$ , surrounded by nodes  $i - 1$  and  $i + 1$  in a finite-difference mesh (Fig. 7.5). Assume that the flow is subcritical in the entire computational domain and that  $\Delta x$  is fixed. If  $\Delta x$  is small, it is permissible to assume that the forward and backward characteristics originating at nodes  $i - 1$  and  $i + 1$ , respectively, are

**Fig. 7.5** Stable time stepping: analytical domain of dependence at the computational point d of the finite-difference mesh lies inside the numerical domain of dependence [Adapted from Anderson (1995)]



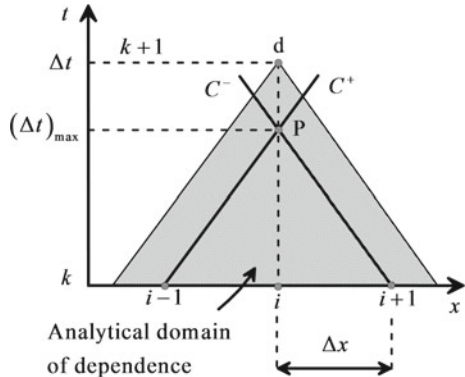
approximately straight lines, intersecting at point P. For simplicity's sake, it is assumed that flow conditions at time level  $k$  are uniform. The numerical domain of dependence is the triangle defined by points P,  $i + 1$ , and  $i - 1$ . Flow conditions at point P are influenced by those in the area defining the numerical domain of dependence. In this domain, with  $c = (gh)^{1/2}$  as the shallow water wave celerity, the maximum time step  $(\Delta t)_{\max}$  to stick inside it is

$$(\Delta t)_{\max} = \frac{\Delta x}{U \pm c}. \quad (7.27)$$

Consider that the time step  $\Delta t$  selected for computations in our finite-difference mesh is less than this value, resulting in point d at the new time level. The points on the  $x$ -axis at the actual time level  $k$  influencing this node lie between  $i - 1$  and  $i + 1$ . Computationally, the analytical domain of dependence defined by the characteristics at point d ( $i, k + 1$ ) (shaded area in Fig. 7.5) thus lies inside the numerical domain of dependence (triangle  $i - 1, d, i + 1$ ) produced by the mesh. In this case, computations are stable (Anderson 1995).

Consider now that the time step selected in the finite-difference mesh is greater than the maximum value fixed by the numerical domain of dependence of point P (Fig. 7.6). Therefore, the computational point d at the new time level  $k + 1$  is above point P. The points on the  $x$ -axis at the actual time level  $k$  influencing this node lie outside the interval  $(i - 1, i + 1)$ . The analytical domain of dependence at point d, triggering the state of node  $i$  at the new time level  $k + 1$ , then lies outside the numerical domain of dependence. This implies that at the new time level our finite-difference model is demanding information about the propagation of perturbations to nodes located outside the computational portion  $(i - 1, i + 1)$ . This information is not actually arriving at node d, so computations will become unstable. The production of computations is thus forced at time  $\Delta t$  after the meeting of perturbations originating from nodes  $i - 1$  and  $i + 1$ , occurring at time  $(\Delta t)_{\max}$ .

**Fig. 7.6** Unstable time stepping: analytical domain of dependence at the computational point  $d$  of the finite-difference mesh lies outside the numerical domain of dependence [Adapted from Anderson (1995)]



As a consequence, the “computations arrive late in time,” by which the model loses the information generated at nodes  $i - 1$  and  $i + 1$  “in the immediate past.” That is, we demand our model to do computations at a time when all the relevant information regarding perturbation propagation already passed through this spatial location just a moment ago. From this, reasoning originates the stability condition for explicit methods, stating that the Courant–Friedrichs–Lewy number **CFL** must satisfy (Courant et al. 1928)

$$\text{CFL} = (U \pm c) \frac{\Delta t}{\Delta x} \leq 1. \quad (7.28)$$

It assures that the analytical domain of dependence at a node lies within the numerical domain of dependence (Anderson 1995). In other words, let a time step be small enough to advance in time “catching” the information of perturbations before it leaves a portion of the computational domain. From a practical viewpoint, a common  $\Delta t$  for all nodes to “jump” to the new time level  $k + 1$  is determined. Therefore, the smallest  $\Delta t$  possible is selected, that is (Toro 2001; Chaudhry 2008),

$$\Delta t = \frac{\text{CFL} \cdot \Delta x}{\max(|U_i| + c_i)}. \quad (7.29)$$

For practical computations,  $\text{CFL} = 0.9$  is typically used (Toro 2001; Chaudhry 2008).



**Richard Courant** was born on January 8, 1888, at Lublinitz, formerly in Germany and today in Poland, passing away at age 84 on January 27, 1972, at New Rochelle, NY, USA. He started studies in mathematics at Breslau (currently Wrocław) University, moving in 1905 to University of Zurich and later to University of Göttingen, Germany, becoming a collaborator of David Hilbert (1862–1943) and earning his Ph.D. title in 1910. He continued his research during a two-year period at the University of Münster as Professor of mathematics, founding there its Mathematical Institute, which he directed from 1928 to 1933. He left Germany in 1933 due to his Jewish background, moving to University of Cambridge in the UK. In 1936, he accepted a professorship at New York University, New York City, NY, founding an institute for graduate studies in applied mathematics. It was renamed in 1964 Courant Institute of Mathematical Sciences, gradually developing in the foremost centers of applied mathematics .

Courant and Hilbert authored in 1924 the textbook *Methods in Mathematical Physics*, several times revised and widely used by mathematicians, physicists, and engineers. The book deals mainly with methods to numerically solve both ordinary and partial differential equations using finite-differences. Courant also is the namesake for the Courant–Friedrichs–Lewy (CFL) condition in fluid mechanics, establishing a necessary condition for convergence of hyperbolic partial differential equations, as are, e.g., the shallow water equations, arising in the numerical analysis of explicit time integration schemes. He also was strongly related to the advances in the finite element method, a numerical method for solving problems of engineering and mathematical physics. Given that most equations in fluid mechanics and hydraulics do not have analytical solutions, the role of Courant in advancing the solution methods is outstanding.

#### Remark: *Lax equivalence theorem*

This fundamental theorem in the analysis of finite-difference equations was formulated by Lax and Richtmeyer (1956) stating that, for a well-posed linear initial

value problem, a consistent finite-difference approximation will produce a convergent solution if there is stability. This theorem is important because if stability and consistency are satisfied (which are simple to analyze), convergence is assured (which is difficult to analyze directly). Obviously, the SWE are nonlinear and most of the practical applications are not amenable for simplified linearized solutions, but the theorem is also accepted for more general problems.

## 7.3 Boundary and Initial Conditions

### 7.3.1 Initial Conditions

To compute the transient wave solution of the SWE, it is necessary to know the values of depth and velocity in all the spatial nodes of the mesh. These values cannot be arbitrary: If these data are not compatible with the SWE, then spurious waves will be generated in the system after initiation of the transient computations, masking the real waves. Thus, physically realistic initial conditions must be determined. Typically, one of the two following options is possible:

*System initially static:* The free surface is horizontal, and the fluid velocity is zero in all nodes. Dry areas may be included in the computational domain.

*System initially under steady flow:* Depth and velocity must be determined using the steady-state techniques (Chaps. 2–4). The solution involves the numerical solution of the ODE for gradually varied or continuous steady flows (Henderson 1966; Jain 2001)

$$\frac{dh}{dx} = \frac{-\frac{\partial z_b}{\partial x} - S_f}{1 - \frac{q^2}{gh^3}}, \quad (7.30)$$

where  $h$  is water depth,  $q$  unit discharge,  $z_b$  bed elevation, and  $S_f$  the friction slope. For rapidly varied or discontinuous steady flows (hydraulic jumps), Bélanger's equation is used (Henderson 1966; Jain 2001)

$$\frac{h_2}{h_1} = \frac{1}{2} \left[ \left( 1 + 8F_1^2 \right)^{1/2} - 1 \right]. \quad (7.31)$$

Here,  $h_1$  and  $h_2$  are the sequent depths and  $F_1 = (q^2/gh_1^3)^{1/2}$  is the inflow Froude number at the supercritical section.

### 7.3.2 Boundary Conditions for Continuous Flows

The flow state at the up- or downstream ends of the reach determines the nature of the boundary conditions required there. For subcritical flow, one boundary condition is needed at each end of the reach, either the flow depth or the discharge or a function relating both (rating curve). In continuous flows, the SWE in characteristic form are applied to determine the other unknown flow variable there. For a rectangular cross section, and with  $S_o$  as the bottom slope, the SWE in characteristic form are (Jain 2001; Chaudhry 2008)

$$\frac{D}{Dt}(U - 2c) = g(S_o - S_f) \quad \text{if} \quad \frac{dx}{dt} = U - c, \quad (7.32)$$

$$\frac{D}{Dt}(U + 2c) = g(S_o - S_f) \quad \text{if} \quad \frac{dx}{dt} = U + c, \quad (7.33)$$

or,

$$\frac{DU}{Dt} - \frac{g}{c} \frac{Dh}{Dt} = g(S_o - S_f) \quad \text{if} \quad \frac{dx}{dt} = U - c, \quad (7.34)$$

$$\frac{DU}{Dt} + \frac{g}{c} \frac{Dh}{Dt} = g(S_o - S_f) \quad \text{if} \quad \frac{dx}{dt} = U + c. \quad (7.35)$$

At an upstream boundary section with subcritical flow, discretization of Eq. (7.34) yields (Fig. 7.7a)

$$(U_1^{k+1} - U_p^k) - \frac{g}{c_p^k} (h_1^{k+1} - h_p^k) = g(S_o - S_f)_p^k \Delta t. \quad (7.36)$$

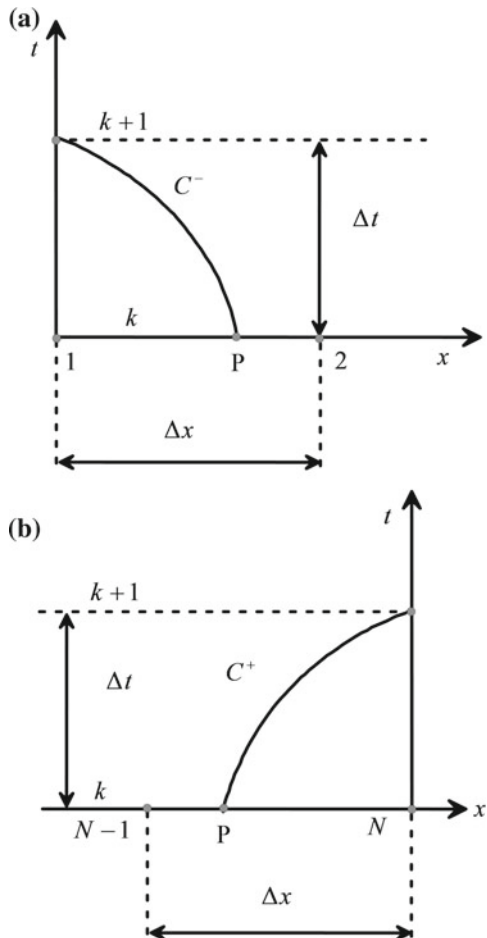
Assuming that flow conditions at point P are approximated by those of node 2, to avoid interpolations, the result is (Chaudhry 2008)

$$U_1^{k+1} = U_2^k + \frac{g}{c_2^k} (h_1^{k+1} - h_2^k) + g(S_o - S_f)_2^k \Delta t. \quad (7.37)$$

For a more rigorous computation, the exact coordinate of point P is determined by the backward characteristic (García-Navarro and Saviron 1992). At a downstream boundary section with subcritical flow, discretization of Eq. (7.35) yields (Fig. 7.7b)

$$(U_N^{k+1} - U_p^k) + \frac{g}{c_p^k} (h_N^{k+1} - h_p^k) = g(S_o - S_f)_p^k \Delta t, \quad (7.38)$$

**Fig. 7.7** Characteristics in subcritical flow at **a** upstream boundary and **b** downstream boundary



which is similarly simplified to (Gharangik and Chaudhry 1991; Chaudhry 2008)

$$U_N^{k+1} = U_{N-1}^k - \frac{g}{c_{N-1}^k} (h_N^{k+1} - h_{N-1}^k) + g(S_o - S_f)_{N-1}^k \Delta t. \quad (7.39)$$

If the flow is supercritical at the upstream boundary section, two boundary conditions must be supplied. If the flow is supercritical at the downstream boundary section, both Eqs. (7.34) and (7.35) are discretized to determine  $(h, U)$  at point  $(N, k + 1)$  based on data at point  $(N-1, k)$ .

### 7.3.3 Boundary Conditions for Discontinuous Flows

If the flow at a boundary section is discontinuous, Eqs. (7.34) and (7.35) cannot be used (Terzidis and Strelkoff 1970; García-Navarro and Sáviro 1992). Then, the Rankine–Hugoniot jump conditions stating the mass and the momentum conservation equations across a shock wave apply, namely [Eqs. (5.17) and (5.35)]

$$V_w = \frac{U_1 h_1 - U_2 h_2}{h_1 - h_2}, \quad (7.40)$$

$$V_w = U_2 + \left[ \frac{g h_1}{2 h_2} (h_1 + h_2) \right]^{1/2}. \quad (7.41)$$

Here,  $V_w$  is the absolute surge velocity and subscripts 1 and 2 indicate conditions upstream and downstream of the shock front. Equations (7.40)–(7.41) contain five variables ( $h_1$ ,  $h_2$ ,  $U_1$ ,  $U_2$ , and  $V_w$ ), so they apply to produce boundary conditions provided that three are known. If a flow starts at  $i = 1$  as discontinuous supercritical flow due to a sudden (known) increase of discharge, the equations can be used to generate the value of the unknown water depth there if the tailwater conditions ( $h_2$ ,  $U_2$ ) are given.

## 7.4 Explicit Schemes

### 7.4.1 FTCS Scheme

The forward in time, centered in space scheme is possibly the simplest FD scheme, but, as demonstrated by Liggett and Cunge (1975), it is unstable. It is therefore called “unstable scheme.” The fluxes  $\mathbf{F}$  are evaluated at the time level  $k$  where the vector  $\mathbf{U}$  is completely known, using central finite differences. The conservative formula is then

$$\mathbf{U}_i^{k+1} = \mathbf{U}_i^k - \frac{\Delta t}{2\Delta x} (\mathbf{F}_{i+1}^k - \mathbf{F}_{i-1}^k) + \mathbf{S}_i^k \Delta t. \quad (7.42)$$

This model appears to work under extremely low values of CFL in combination with artificial viscosity to dampen oscillations. However, the scheme is of no practical value.



**Peter David Lax** was born on May 1, 1926, in Budapest, Hungary. His Jewish parents both were physicists. They left Hungary in 1941, traveling via Lisbon to New York, NY, USA. He started his studies in mathematics in 1944 at New York University (NYU). During World War II, the army sent him to Texas A&M University, then to the Oak Ridge National Laboratory, and soon afterward to the Manhattan Project at Los Alamos, NM, where he began working as a calculator operator, but eventually moved on to higher-level mathematics. After World War II, he remained with the army at Los Alamos for another year, while taking courses at the University of New Mexico, and then studied at Stanford University for a semester with the Hungarian mathematicians Szegő and Pólya. He returned to NYU in 1946, obtaining his graduation and earning the Ph.D. title in 1949 under the supervision of Kurt O. Friedrichs (1901–1982).

Lax made remarkable contributions early in his career continuing to produce research, which changed the direction of many areas of mathematics. In 1957, he published the important paper Asymptotic solutions of oscillating initial value problems, laying the beginnings of the theory of Fourier integral operators. Asked what was so novel about the viewpoint that made the ideas able to enjoy such wide application, he replied: “It is a micro-local description of what is going on. It combines looking at the problem in the large and in the small. The numerical implementation of the micro-local point of view is by wavelets and similar approaches, which are powerful numerically.” He thrived in the Courant Institute of Mathematical Sciences, NYU, where applied mathematics was studied alongside relevant pure mathematics in an exciting mix of ideas, which led to great progress. He was appointed Institute Director in 1972, continuing until 1980. It was a particularly difficult time to take on this role since NYU had just closed down their School of Engineering, moving the mathematicians from there into the Courant Institute. This produced friction when these people wanted to set up their own computing department while a new Computer Science Department had just been founded. He succeeded in ensuring that there were not two rival

departments in the Institute, but the politics involved was difficult. His most important works include Nonlinear partial differential equations in applied science (1983), Hyperbolic systems of conservation laws and the mathematical theory of shock waves (1987), or his Hyperbolic partial differential equations (2006). He has received numerous awards and honors for his mathematical researches and his advances in the field of computational mathematics.

#### 7.4.2 Lax' Diffusive Scheme

The Lax diffusive method is a one-step finite-difference method with shock-capturing ability, but numerically diffusive. It is a variant of the unstable scheme. The scheme is given by the updating formula

$$\mathbf{U}_i^{k+1} = \frac{(\mathbf{U}_{i-1}^k + \mathbf{U}_{i+1}^k)}{2} - \frac{\Delta t}{2\Delta x} (\mathbf{F}_{i+1}^k - \mathbf{F}_{i-1}^k) + \mathbf{S}_i^k \Delta t. \quad (7.43)$$

It is conditionally stable, and the time step  $\Delta t$  is restricted by the CFL condition (Hirsch 1988, 1990; Hoffman 2001). The Lax diffusive method depends on the value of CFL, as highlighted below. An FD scheme is said to be consistent if the finite-difference form tends to the original PDE if both  $\Delta x$  and  $\Delta t \rightarrow 0$ . The following space and time Taylor expansions around the node  $(i, k)$  are formed

$$\mathbf{U}_i^{k+1} = \mathbf{U}_i^k + \left( \frac{\partial \mathbf{U}}{\partial t} \right)_i^k \Delta t + \left( \frac{\partial^2 \mathbf{U}}{\partial t^2} \right)_i^k \frac{(\Delta t)^2}{2} + \dots, \quad (7.44)$$

$$\mathbf{U}_{i+1}^k = \mathbf{U}_i^k + \left( \frac{\partial \mathbf{U}}{\partial x} \right)_i^k \Delta x + \left( \frac{\partial^2 \mathbf{U}}{\partial x^2} \right)_i^k \frac{(\Delta x)^2}{2} + \dots, \quad (7.45)$$

$$\mathbf{U}_{i-1}^k = \mathbf{U}_i^k - \left( \frac{\partial \mathbf{U}}{\partial x} \right)_i^k \Delta x + \left( \frac{\partial^2 \mathbf{U}}{\partial x^2} \right)_i^k \frac{(\Delta x)^2}{2} + \dots, \quad (7.46)$$

$$\mathbf{F}_{i+1}^k = \mathbf{F}_i^k + \left( \frac{\partial \mathbf{F}}{\partial x} \right)_i^k \Delta x + \left( \frac{\partial^2 \mathbf{F}}{\partial x^2} \right)_i^k \frac{(\Delta x)^2}{2} + \dots, \quad (7.47)$$

$$\mathbf{F}_{i-1}^k = \mathbf{F}_i^k - \left( \frac{\partial \mathbf{F}}{\partial x} \right)_i^k \Delta x + \left( \frac{\partial^2 \mathbf{F}}{\partial x^2} \right)_i^k \frac{(\Delta x)^2}{2} + \dots \quad (7.48)$$

Inserting Eqs. (7.44)–(7.48) into Eq. (7.43) produces

$$\begin{aligned} \mathbf{U}_i^k + \left(\frac{\partial \mathbf{U}}{\partial t}\right)_i^k \Delta t + \left(\frac{\partial^2 \mathbf{U}}{\partial t^2}\right)_i^k \frac{(\Delta t)^2}{2} &= \frac{1}{2} \left[ 2\mathbf{U}_i^k + \left(\frac{\partial^2 \mathbf{U}}{\partial x^2}\right)_i^k (\Delta x)^2 \right] \\ &\quad - \frac{\Delta t}{2\Delta x} \left[ 2\left(\frac{\partial \mathbf{F}}{\partial x}\right)_i^k \Delta x \right] + \mathbf{S}_i^k \Delta t, \end{aligned} \quad (7.49)$$

or

$$\frac{\partial \mathbf{U}}{\partial t} + \frac{\partial \mathbf{F}}{\partial x} = \frac{1}{2} \frac{(\Delta x)^2}{\Delta t} \frac{\partial^2 \mathbf{U}}{\partial x^2} - \frac{1}{4} \frac{\partial^2 \mathbf{U}}{\partial t^2} \Delta t + \mathbf{S}. \quad (7.50)$$

For  $\Delta x$  and  $\Delta t \rightarrow 0$ , it reduces to

$$\frac{\partial \mathbf{U}}{\partial t} + \frac{\partial \mathbf{F}}{\partial x} = \frac{1}{2} D \frac{\partial^2 \mathbf{U}}{\partial x^2} + \mathbf{S}. \quad (7.51)$$

This is the equation modeled by the Lax scheme, where  $D$  is a numerical mesh diffusion-like coefficient given by

$$D = \frac{(\Delta x)^2}{\Delta t}. \quad (7.52)$$

The Lax scheme is thus not consistent. Therefore, for a fixed value of  $\Delta x$ , if the value of CFL is reduced, computations are performed with a smaller value of  $\Delta t$ . Accordingly,  $D$  increases and the solution experiences greater diffusion. This diffusive scheme has mesh-dependent features, therefore.

### 7.4.3 MacCormack Predictor–Corrector Scheme

The MacCormack (1969) method is a two-step predictor–corrector finite-difference scheme with shock-capturing ability. In the predictor step, the fluxes  $\mathbf{F}$  are evaluated at the time level  $k$  using forward finite-differences

$$\mathbf{U}_i^{\text{pred}} = \mathbf{U}_i^k - \frac{\Delta t}{\Delta x} (\mathbf{F}_{i+1}^k - \mathbf{F}_i^k) + \mathbf{S}_i^k \Delta t. \quad (7.53)$$

This step gives an estimation of the flow conditions at the new time level  $k + 1$ , denoted as predicted values. In the corrector step, the fluxes  $\mathbf{F}$  are evaluated with the estimated vector  $\mathbf{U}$  at time level  $k + 1$ , using backward finite-differences, resulting in

$$\mathbf{U}_i^{\text{corr}} = \mathbf{U}_i^k - \frac{\Delta t}{\Delta x} \left( \mathbf{F}_i^{\text{pred}} - \mathbf{F}_{i-1}^{\text{pred}} \right) + \mathbf{S}_i^{\text{pred}} \Delta t. \quad (7.54)$$

The final value is taken as average of estimations in predictor and corrector steps, e.g.,

$$\mathbf{U}_i^{k+1} \equiv \mathbf{U}_i^{\text{ave}} = \frac{\mathbf{U}_i^{\text{pred}} + \mathbf{U}_i^{\text{corr}}}{2}. \quad (7.55)$$

It is possible to construct a variant of the scheme using backward finite-differences in the predictor step and forward finite-differences in the corrector. Both variants of the scheme can also cyclically be applied during computations (Chaudhry 2008). Practice indicates that the best results occur if the discretization in the predictor step is in the direction of shock wave propagation. Accordingly, the scheme presented here would be more adequate for a right-going shock wave in the positive  $x$ -direction. MacCormack's scheme is the second-order accuracy in both space and time (Hoffman 2001), and is conditionally stable and thus constrained by the CFL condition.

*Remark: Gibbs phenomenon and Godunov's theorem*

The Godunov theorem states that any numerical scheme of order higher than one cannot be monotone (Hirsch 1988, 1990). The immediate consequence is that higher-order schemes will produce non-physical oscillations in zones of high gradients of  $\mathbf{U}$ , as near a shock wave, e.g., the surge front of a dam break wave. These oscillations are known as the Gibbs phenomenon and are the result of dispersive errors contaminating the solution.

Given that the MacCormack scheme is second-order accurate in time and space  $O(\Delta x^2, \Delta t^2)$ , it exhibits spurious oscillations near a shock. First-order schemes do not suffer from unphysical oscillations, but at the price of excessive diffusion smearing the shock front along a large number of computational nodes. In the second-order schemes, there is no numerical diffusion, and the shock front is sharply resolved within only a few computational nodes. Thus, in practice, the second-order schemes are used and the strategy to control non-physical oscillations is to introduce locally an amount of numerical diffusion if needed (Hirsch 1988, 1990).

#### 7.4.4 MacCormack Scheme with Calibrated Artificial Viscosity

Unphysical oscillations in the MacCormack scheme are reduced by introducing artificial diffusion in the scheme. Consider Eq. (7.51) as the governing equation.

After application of predictor and corrector steps, incorporation of artificial viscosity is given by solving the additional problem

$$\frac{\partial \mathbf{U}}{\partial t} = \varepsilon \frac{(\Delta x)^2}{\Delta t} \frac{\partial^2 \mathbf{U}}{\partial x^2}. \quad (7.56)$$

Here,  $\varepsilon$  is a diffusion coefficient introduced to control the amount of dissipation in the scheme. If  $\varepsilon$  is taken constant, and the spatial derivative of the diffusive term is discretized with a second-order central finite-difference, the updating formula is

$$\mathbf{U}_i^{k+1} = \mathbf{U}_i^{\text{ave}} + \varepsilon (\mathbf{U}_{i+1}^{\text{ave}} - 2\mathbf{U}_i^{\text{ave}} + \mathbf{U}_{i-1}^{\text{ave}}). \quad (7.57)$$

The method by Jameson et al. (1981) follows this idea, and it is simple to implement. The variant of Eq. (7.57) used is

$$\mathbf{U}_i^{k+1} = \mathbf{U}_i^{\text{ave}} + \varepsilon_{i+1/2} (\mathbf{U}_{i+1}^{\text{ave}} - \mathbf{U}_i^{\text{ave}}) - \varepsilon_{i-1/2} (\mathbf{U}_i^{\text{ave}} - \mathbf{U}_{i-1}^{\text{ave}}), \quad (7.58)$$

where

$$\varepsilon_{i+1/2} = K \max(\varepsilon_{i+1}, \varepsilon_i), \quad (7.59)$$

and  $\varepsilon_i$  is a parameter computed based on the water surface profile as

$$\varepsilon_i = \frac{|h_{i+1} - h_i + h_{i-1}|}{|h_{i+1}| - |h_i| + |h_{i-1}|}. \quad (7.60)$$

It is closely related to the water surface curvature at node  $i$ , discretized with a second-order central finite-difference.  $K$  is the coefficient of artificial viscosity, which must be calibrated. It varies typically between 0.5 and 3 (Zoppou and Roberts 2003). This scheme has been used by Fennema and Chaudhry (1986) and Gharangik and Chaudhry (1991). It introduces numerical diffusion only in zones of the solution where oscillations develop, but leaves other portions of the profile unaffected.

#### 7.4.5 TVD MacCormack Scheme

The “total variation diminishing (TVD)” schemes are of high order, thereby producing a sharp resolution of shocks, but introduce a bounding of the solution to avoid spurious oscillations. The total variation  $TV$  of a function  $f$  is defined as (Hirsch 1988, 1990)

$$TV(f) = \sum_{i=-\infty}^{\infty} |f_{i+1} - f_i|, \quad (7.61)$$

and a scheme for the conservation laws that satisfies

$$TV(f^{k+1}) \leq TV(f^k) \quad (7.62)$$

is said to be TVD. A TVD scheme is second-order accurate in smooth regions and reduces to first-order accurate near discontinuities to suppress spurious oscillations where sharp gradients are detected. The numerical dispersion of the second-order scheme is then suppressed by the numerical diffusion introduced where necessary by switching to a first-order accurate scheme. Here, the TVD version of the MacCormack scheme developed by García-Navarro et al. (1992) is presented. The final values are computed adding a dissipation step given by

$$\mathbf{U}_i^{k+1} = \mathbf{U}_i^{\text{ave}} + \frac{\Delta t}{\Delta x} \left( \mathbf{D}_{i+1/2}^k - \mathbf{D}_{i-1/2}^k \right), \quad (7.63)$$

where the diffusive term  $\mathbf{D}_{i+1/2}$  is given by

$$\mathbf{D}_{i+1/2}^k = \frac{1}{2} \sum_{n=1}^2 \alpha_{i+1/2}^n \psi_{i+1/2}^n \left( 1 - \frac{\Delta t}{\Delta x} \left| \lambda_{i+1/2}^n \right| \right) \left( 1 - \phi_{i+1/2}^n \right) \mathbf{e}_{i+1/2}^n. \quad (7.64)$$

The various terms in Eq. (7.64) are systematically presented below for implementation. First, the average values of velocity and celerity are determined from

$$U_{i+1/2} = \frac{U_i \sqrt{h_i} + U_{i+1} \sqrt{h_{i+1}}}{\sqrt{h_i} + \sqrt{h_{i+1}}}, \quad c_{i+1/2} = \left( g \frac{h_i + h_{i+1}}{2} \right)^{1/2}. \quad (7.65)$$

The eigenvalues  $\lambda_i^{1,2}$  and average eigenvalues  $\lambda_{i+1/2}^{1,2}$  are given by

$$\lambda_i^{1,2} = U_i \pm c_i, \quad \lambda_{i+1/2}^{1,2} = U_{i+1/2} \pm c_{i+1/2}. \quad (7.66)$$

The eigenvectors are determined from

$$\mathbf{e}_{i+1/2}^{1,2} = \begin{pmatrix} 1 \\ \lambda_{i+1/2}^{1,2} \end{pmatrix}. \quad (7.67)$$

The function  $\psi$  is an entropy fix to avoid unphysical jumps in rarefaction waves, given by

$$\psi_{i+1/2}^{1,2} = \begin{cases} \left| \lambda_{i+1/2}^{1,2} \right| & \text{if } \left| \lambda_{i+1/2}^{1,2} \right| \geq \varepsilon_{i+1/2}^{1,2}, \\ \varepsilon_{i+1/2}^{1,2} & \text{else} \end{cases}, \quad (7.68)$$

where

$$\varepsilon_{i+1/2}^{1,2} = \max\left(0, \lambda_{i+1/2}^{1,2} - \lambda_i^{1,2}, \lambda_{i+1}^{1,2} - \lambda_{i+1/2}^{1,2}\right). \quad (7.69)$$

The jump projections in the values of  $\mathbf{U}$  between nodes  $i$  and  $i + 1$  onto the eigenvectors  $\mathbf{e}_{i+1/2}^{1,2}$  are

$$\alpha_{i+1/2}^{1,2} = \frac{1}{2c_{i+1/2}^1} \left[ \mp \lambda_{i+1/2}^{2,1} (h_{i+1} - h_i) \pm (q_{i+1} - q_i) \right]. \quad (7.70)$$

The function  $\phi$  is a flux limiter taken here as (Hseng and Chu 2000)

$$\phi_{i+1/2}^{1,2} = \frac{r_{i+1/2}^{1,2} + \left(r_{i+1/2}^{1,2}\right)^2}{1 + \left(r_{i+1/2}^{1,2}\right)^2}, \quad (7.71)$$

where

$$r_{i+1/2}^{1,2} = \frac{\alpha_{i+1/2-s}^{1,2}}{\alpha_{i+1/2}^{1,2}}, \quad (7.72)$$

and

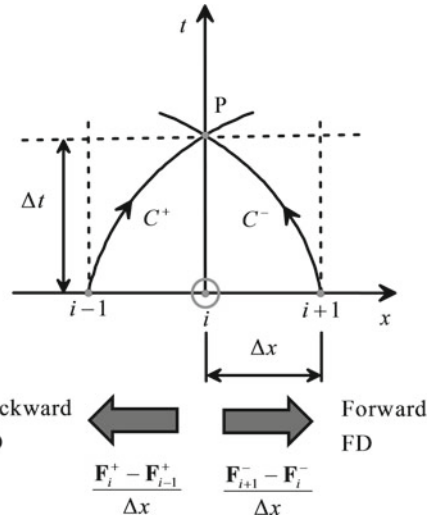
$$s = \text{sign}\left(\lambda_{i+1/2}^{1,2}\right). \quad (7.73)$$

A useful feature of this scheme is that it is free from calibration parameters.

#### 7.4.6 Upwind Scheme

In upwind methods, the discretization of the flux gradient  $\partial\mathbf{F}/\partial x$  is sensitive to the sign of the eigenvalues. This aims at capturing numerically the propagation of perturbations by correctly identifying transmission up- or downstream. To illustrate concepts, consider subcritical flow (Fig. 7.8). For perturbations propagating

**Fig. 7.8** Upwind discretization of fluxes in subcritical flow



downstream, the flux contribution is denoted by  $\mathbf{F}^+$ , whereas for those propagating upstream the associated flux is denoted by  $\mathbf{F}^-$ . These are linked to the eigenvalues  $U + (gh)^{1/2}$  and  $U - (gh)^{1/2}$ , respectively. The flux  $\mathbf{F}$  is then split as (Hirsch 1988, 1990)

$$\mathbf{F} = \mathbf{F}^+ + \mathbf{F}^- \quad (7.74)$$

This definition permits to formulate the SWE as<sup>1</sup>

$$\frac{\partial \mathbf{U}}{\partial t} + \frac{\partial \mathbf{F}^+}{\partial x} + \frac{\partial \mathbf{F}^-}{\partial x} = \mathbf{0}. \quad (7.75)$$

An upwind discretization of  $\partial \mathbf{F}^+ / \partial x$  uses backward finite-differences to detect the propagation of perturbations in the downstream direction along the  $C^+$  characteristics. Likewise, an upwind discretization of  $\partial \mathbf{F}^- / \partial x$  uses forward finite-differences to detect the propagation of perturbations in the upstream direction along the  $C^-$  characteristics (Fig. 7.8) (Steger and Warming 1981). The result is thus

$$\mathbf{U}_i^{k+1} - \mathbf{U}_i^k + \frac{\Delta t}{\Delta x} (\mathbf{F}_i^+ - \mathbf{F}_{i-1}^+) + \frac{\Delta t}{\Delta x} (\mathbf{F}_{i+1}^- - \mathbf{F}_i^-) = \mathbf{0}. \quad (7.76)$$

<sup>1</sup>For simplicity's sake, source terms are not considered here. It is possible to treat  $\mathbf{S}$  using an upwind method (Toro 2001).

It is necessary to develop the expressions determining  $\mathbf{F}^+$  and  $\mathbf{F}^-$ . Following the Bermudez and Vazquez-Cendon (1994) upwind scheme, consider matrix  $\mathbf{G}$  that satisfies the identity

$$\mathbf{F} = \mathbf{GU}. \quad (7.77)$$

Zoppou and Roberts (2003) demonstrated that the desired matrix is

$$\mathbf{G} = \mathbf{P}\Lambda\mathbf{P}^{-1} = \begin{pmatrix} 0 & 1 \\ \frac{1}{2}gh - U^2 & 2U \end{pmatrix}, \quad (7.78)$$

where

$$\mathbf{P} = \begin{pmatrix} 1 & 1 \\ U + \frac{c}{\sqrt{2}} & U - \frac{c}{\sqrt{2}} \end{pmatrix}, \quad (7.79)$$

and

$$\mathbf{P}^{-1} = \frac{1}{2c} \begin{pmatrix} c - U\sqrt{2} & \sqrt{2} \\ c + U\sqrt{2} & -\sqrt{2} \end{pmatrix}. \quad (7.80)$$

The matrix  $\Lambda$  contains the eigenvalues  $\lambda_1$  and  $\lambda_2$  of  $\mathbf{G}$  as

$$\Lambda = \begin{pmatrix} \lambda_1 & 0 \\ 0 & \lambda_2 \end{pmatrix} = \begin{pmatrix} U + \frac{c}{\sqrt{2}} & 0 \\ 0 & U - \frac{c}{\sqrt{2}} \end{pmatrix}. \quad (7.81)$$

Now,  $\Lambda$  is decomposed in positive and negative components as

$$\Lambda = \Lambda^+ + \Lambda^-, \quad (7.82)$$

where

$$\Lambda^+ = \begin{pmatrix} \lambda_1^+ & 0 \\ 0 & \lambda_2^+ \end{pmatrix}, \quad (7.83)$$

and

$$\Lambda^- = \begin{pmatrix} \lambda_1^- & 0 \\ 0 & \lambda_2^- \end{pmatrix}. \quad (7.84)$$

In these matrices, the positive and negative components of the eigenvalues are defined by the expressions

$$\lambda_{1,2}^+ = \frac{\lambda_{1,2} + |\lambda_{1,2}|}{2}, \quad \lambda_{1,2}^- = \frac{\lambda_{1,2} - |\lambda_{1,2}|}{2}. \quad (7.85)$$

From these relation results the identity

$$|\Lambda| = \Lambda^+ - \Lambda^-, \quad (7.86)$$

where

$$|\Lambda| = \begin{pmatrix} \left|U + \frac{c}{\sqrt{2}}\right| & 0 \\ 0 & \left|U - \frac{c}{\sqrt{2}}\right| \end{pmatrix}. \quad (7.87)$$

The following transformation of the flux  $\mathbf{F}$  is then conducted

$$\begin{aligned} \mathbf{F} &= \mathbf{GU} = (\mathbf{P}\Lambda\mathbf{P}^{-1})\mathbf{U} = [\mathbf{P}(\Lambda^+ + \Lambda^-)\mathbf{P}^{-1}]\mathbf{U} = [\mathbf{P}\Lambda^+\mathbf{P}^{-1} + \mathbf{P}\Lambda^-\mathbf{P}^{-1}]\mathbf{U} \\ &= [\mathbf{G}^+ + \mathbf{G}^-]\mathbf{U} = \mathbf{F}^+ + \mathbf{F}^-, \end{aligned} \quad (7.88)$$

thereby demonstrating the flux decomposition stated in Eq. (7.74). Also,

$$\begin{aligned} \mathbf{F}^+ &= \mathbf{G}^+\mathbf{U} = (\mathbf{P}\Lambda^+\mathbf{P}^{-1})\mathbf{U} = [\mathbf{P}(|\Lambda| + \Lambda^-)\mathbf{P}^{-1}]\mathbf{U} = [\mathbf{P}|\Lambda|\mathbf{P}^{-1} + \mathbf{P}\Lambda^-\mathbf{P}^{-1}]\mathbf{U} \\ &= [|\mathbf{G}| + \mathbf{G}^-]\mathbf{U} = |\mathbf{F}| + \mathbf{F}^-. \end{aligned} \quad (7.89)$$

From this result emerge the definitions

$$|\mathbf{F}| = |\mathbf{G}|\mathbf{U}, \quad (7.90)$$

and

$$|\mathbf{G}| = \mathbf{P}|\Lambda|\mathbf{P}^{-1}. \quad (7.91)$$

Using Eqs. (7.88) and (7.89) produces

$$\mathbf{F}^+ = \frac{\mathbf{F} + |\mathbf{F}|}{2}, \quad (7.92)$$

Similarly, one obtains for  $\mathbf{F}^-$

$$\mathbf{F}^- = \frac{\mathbf{F} - |\mathbf{F}|}{2}. \quad (7.93)$$

After elementary matrix operations,  $|\mathbf{G}|$  is given by

$$|\mathbf{G}| = \mathbf{P}|\mathbf{A}|\mathbf{P}^{-1} = \begin{pmatrix} G_{11} & G_{12} \\ G_{21} & G_{22} \end{pmatrix}, \quad (7.94)$$

where

$$G_{11} = \left(-\frac{\sqrt{2}}{2c}\right) \left[ \left|U + \frac{c}{\sqrt{2}}\right| \left(U - \frac{c}{\sqrt{2}}\right) - \left|U - \frac{c}{\sqrt{2}}\right| \left(U + \frac{c}{\sqrt{2}}\right) \right], \quad (7.95)$$

$$G_{12} = \left(-\frac{\sqrt{2}}{2c}\right) \left[ -\left|U + \frac{c}{\sqrt{2}}\right| + \left|U - \frac{c}{\sqrt{2}}\right| \right], \quad (7.96)$$

$$G_{21} = \left(-\frac{\sqrt{2}}{2c}\right) \left[ \left|U + \frac{c}{\sqrt{2}}\right| \left(U - \frac{c}{\sqrt{2}}\right) \left(U + \frac{c}{\sqrt{2}}\right) - \left|U - \frac{c}{\sqrt{2}}\right| \left(U - \frac{c}{\sqrt{2}}\right) \left(U + \frac{c}{\sqrt{2}}\right) \right], \quad (7.97)$$

$$G_{22} = \left(-\frac{\sqrt{2}}{2c}\right) \left[ -\left|U + \frac{c}{\sqrt{2}}\right| \left(U + \frac{c}{\sqrt{2}}\right) + \left|U - \frac{c}{\sqrt{2}}\right| \left(U - \frac{c}{\sqrt{2}}\right) \right]. \quad (7.98)$$

Inserting Eqs. (7.92) and (7.93) into Eq. (7.76) yields

$$\begin{aligned} \mathbf{U}_i^{k+1} - \mathbf{U}_i^k + \frac{\Delta t}{\Delta x} \left[ \left( \frac{\mathbf{F} + |\mathbf{F}|}{2} \right)_i - \left( \frac{\mathbf{F} + |\mathbf{F}|}{2} \right)_{i-1} \right] \\ + \frac{\Delta t}{\Delta x} \left[ \left( \frac{\mathbf{F} - |\mathbf{F}|}{2} \right)_{i+1} - \left( \frac{\mathbf{F} - |\mathbf{F}|}{2} \right)_i \right] = \mathbf{0}, \end{aligned} \quad (7.99)$$

or

$$\mathbf{U}_i^{k+1} = \underbrace{\mathbf{U}_i^k - \frac{\Delta t}{2\Delta x} (\mathbf{F}_{i+1}^k - \mathbf{F}_{i-1}^k)}_{\text{unstable scheme}} + \underbrace{\frac{\Delta t}{2\Delta x} (|\mathbf{F}|_{i+1}^k - 2|\mathbf{F}|_i^k + |\mathbf{F}|_{i-1}^k)}_{\text{diffusive term}}. \quad (7.100)$$

Here,  $|\mathbf{F}|$  is given by

$$|\mathbf{F}| = \begin{pmatrix} G_{11}U_1 + G_{12}U_2 \\ G_{21}U_1 + G_{22}U_2 \end{pmatrix}. \quad (7.101)$$

Note that the upwind scheme introduces a diffusive term into the updating equation of the unstable scheme [see Eq. (7.18) for the advection of a scalar]. The method presented here is called flux splitting.

## 7.5 Computational Examples

### 7.5.1 Subcritical Dam Break Wave with Wet Tailwater

Consider a subcritical dam break wave of depth ratio  $h_d/h_u = 0.4$  and upstream water depth  $h_u = 1$  m. Simulations conducted with the unstable scheme using  $\text{CFL} = 0.1$  are displayed at time  $t = 2$  s in Fig. 7.9a, b, and compared with the analytical solution of Stoker (1957). The numerical model is implemented in the code available on the file “*Dambreak\_Unstable.xls*” (Chap. 12). Note the large instabilities generated, showing the poor performance of the scheme for resolving rarefaction and shock waves in free surface flows. The small value of  $\text{CFL}$  used was needed to obtain a computational result. For larger values, computations failed. Attempts to use this scheme are found in the literature. A possible way to find an “apparent” stable result is to introduce a large amount of dissipation in the scheme. This is revealed in Fig. 7.9c, d, where the artificial viscosity method by Jameson et al. (1981) was applied. Note that oscillations are suppressed, but this is no indication that the scheme correctly works; simply, a numerical artifact was used to force a solution.

Simulations conducted for the same test using the Lax diffusive scheme and  $\text{CFL} = 1$  are presented in Fig. 7.10a, b. As expected, the shock and rarefaction waves are smeared due to the diffusion term introduced by this scheme. The numerical model is implemented in the code available on the file “*Dambreak\_Diffusive.xls*” (Chap. 12). The same simulation was conducted using  $\text{CFL} = 0.2$ , with the results shown in Fig. 7.10c, d. The low  $\text{CFL}$  value introduced an unacceptable amount of numerical diffusion.

The simulation results from the MacCormack scheme are shown in Fig. 7.11a, b. Spurious oscillations in the shock front and at the toe of the rarefaction wave are present, albeit more visible in the velocity profile. These oscillations result from dispersive errors. Applying the artificial viscosity method of Jameson et al. (1981) as presented by Chaudhry (2008) with a calibrated  $K = 2$ , the oscillations are almost suppressed, as noted from Fig. 7.11c, d. The numerical model is implemented in the code available from “*Dambreak\_MacCormack\_Jameson.xls*” (Chap. 12). Applying the MacCormack TVD scheme results in Fig. 7.12a, b.

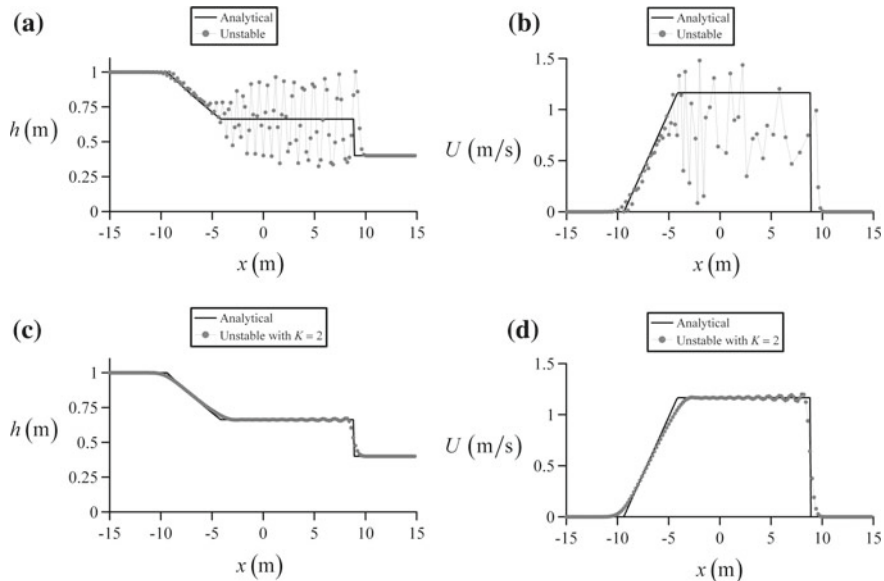


**Fig. 7.9** Subcritical dam break wave for  $h_d/h_u = 0.4$  computed with the unstable scheme using  $CFL = 0.1$  showing effect of artificial viscosity coefficient  $K$

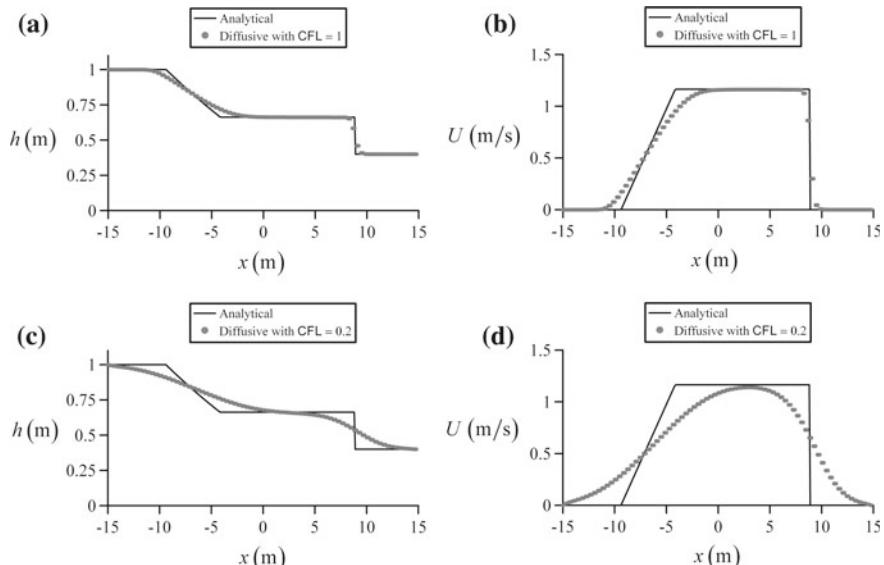


**Fig. 7.10** Subcritical dam break wave for  $h_d/h_u = 0.4$  computed with diffusive scheme highlighting effect of  $CFL$

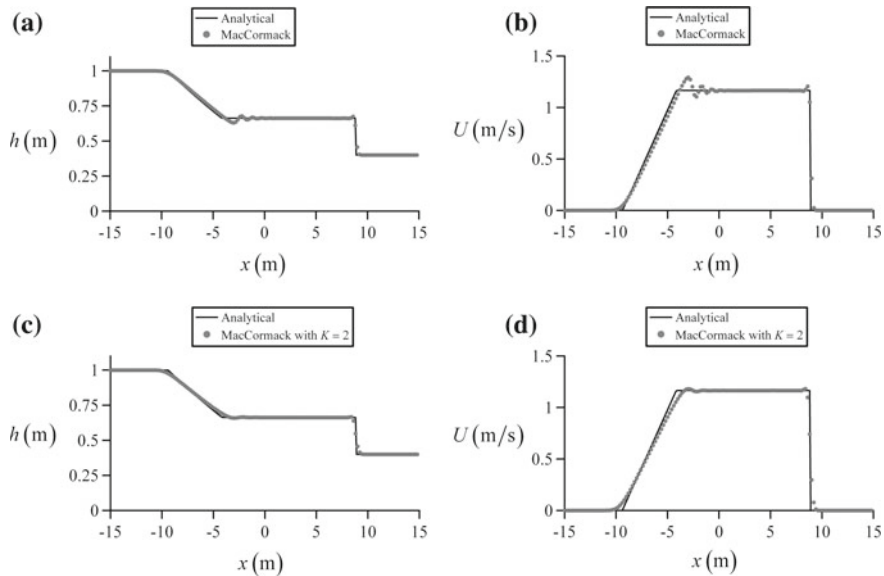


**Fig. 7.11** Subcritical dam break wave for  $h_d/h_u = 0.4$  computed with MacCormack scheme using  $CFL = 0.9$  showing effect of artificial viscosity coefficient  $K$

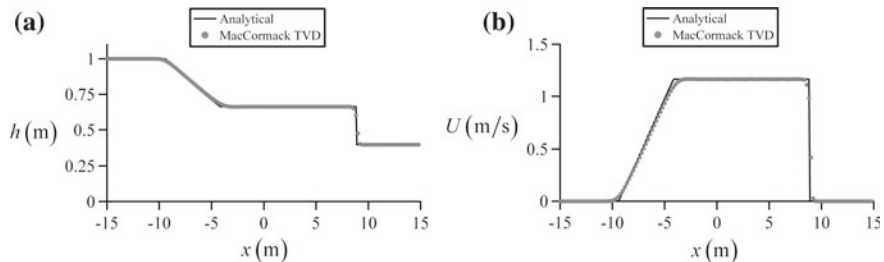


**Fig. 7.12** Subcritical dam break wave for  $h_d/h_u = 0.4$  computed with TVD MacCormack scheme using  $CFL = 0.9$

Spurious oscillations in the shock front and at the toe of the rarefaction wave are suppressed without the need of using any calibration parameter, which is a remarkable advantage. The numerical model is implemented in the code available on the file “*Dambreak\_MacCormack\_TVD.xls*” (Chap. 12). The simulation results obtained using the upwind scheme are shown in Fig. 7.13a, b. Note that the diffusion of the scheme, as in other first-order schemes, is present. The numerical model is implemented in the code available on the file “*Dambreak\_Upwind.xls*” (Chap. 12).

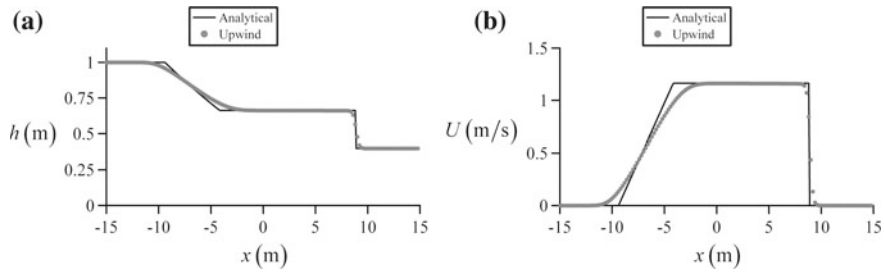


**Fig. 7.13** Subcritical dam break wave for  $h_d/h_u = 0.4$  computed with upwind scheme using  $CFL = 0.9$

### 7.5.2 Transcritical Dam Break Wave with Wet Tailwater

The subcritical dam break wave is not a severe test case (Zoppou and Roberts 2003). A transcritical dam break wave was thus generated using a depth ratio  $h_d/h_u = 0.001$  and  $h_u = 1$  m. Critical flow establishes at the dam axis in a point of the rarefaction wave. Only the TVD MacCormack, upwind, and Lax diffusive schemes were able to generate computational results, which are displayed in Fig. 7.14 for  $t = 2$  s.

The results of the MacCormack TVD scheme are excellent, as shown in Fig. 7.14a, b. The upwind method, however, produces an unphysical jump at the dam axis related to a violation of the entropy condition. The Lax diffusive scheme produces results not in precise agreement neither for the rarefaction nor for the shock waves.

### 7.5.3 Subcritical Surge

In this section, the propagation of a subcritical positive surge is considered. Its analytical solution is with  $V_w$  as the absolute surge velocity and subscripts 1 and 2 denoting conditions behind and in front of the surge,

$$\mathbf{U}(x, t) = \begin{cases} \mathbf{U}_1 & \text{if } x \leq V_w t \\ \mathbf{U}_2 & \text{if } x \geq V_w t \end{cases}. \quad (7.102)$$

The discontinuity is located at  $x = 0$  for  $t = 0$ . The surge mass conservation states [Eq. (7.40)]

$$V_w = \frac{U_1 h_1 - U_2 h_2}{h_1 - h_2}, \quad (7.103)$$

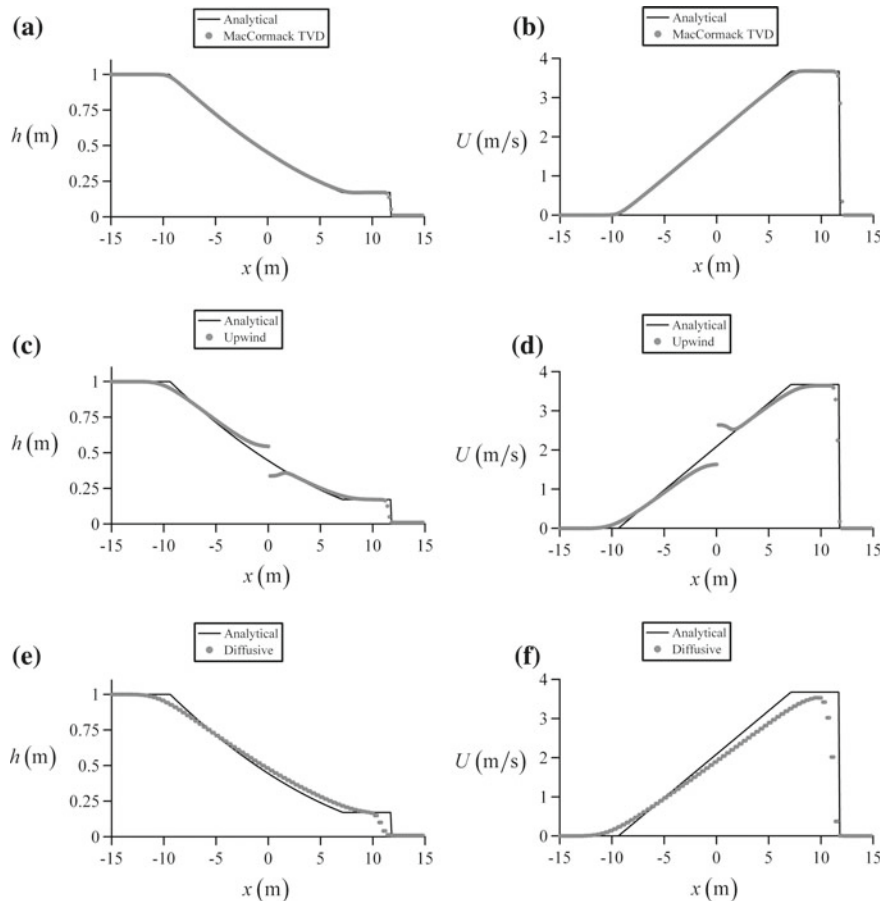


**Fig. 7.14** Transcritical dam break wave for  $h_d/h_u = 0.001$  computed using  $\text{CFL} = 0.9$  with (a, b) MacCormack TVD scheme, (c, d) upwind scheme, (e, f) Lax diffusive scheme

whereas the momentum equation is [Eq. (7.41)]

$$V_w = U_2 + \left[ \frac{g}{2} \frac{h_1}{h_2} (h_1 + h_2) \right]^{1/2}. \quad (7.104)$$

Combining Eqs. (7.103) and (7.104), and using the definition of unit discharge  $q = Uh$ , results in

$$\frac{q_1 - q_2}{h_1 - h_2} = U_2 + \left[ \frac{g}{2} \frac{h_1}{h_2} (h_1 + h_2) \right]^{1/2}, \quad (7.105)$$

or

$$q_1 = U_2 h_1 + (h_1 - h_2) \left[ \frac{g}{2} \frac{h_1}{h_2} (h_1 + h_2) \right]^{1/2}. \quad (7.106)$$

This is an implicit equation to be solved for  $h_1$ , once the values of  $q_1$ ,  $h_2$ , and  $U_2$  are prescribed, e.g.,

$$f(h_1) \equiv U_2 h_1 + (h_1 - h_2) \left[ \frac{g}{2} \frac{h_1}{h_2} (h_1 + h_2) \right]^{1/2} - q_1 = 0. \quad (7.107)$$

A better approximation to the root of Eq. (7.107) is based on the Newton–Raphson method with  $z$  as the recursion index by Hoffman (2001)

$$h_1^{z+1} = h_1^z - \frac{f^z}{(df/dh_1)^z}. \quad (7.108)$$

The derivative term needed in Eq. (7.108) is

$$\frac{df}{dh_1} = U_2 + g(h_1 - h_2) \frac{2h_1 + h_2}{4h_2} \left[ \frac{g}{2} \frac{h_1}{h_2} (h_1 + h_2) \right]^{-1/2} + \left[ \frac{g}{2} \frac{h_1}{h_2} (h_1 + h_2) \right]^{1/2}. \quad (7.109)$$

A good initial value for  $h_1$  to initialize the algorithm is

$$h_1 = h_2 + \frac{q_1 - q_2}{V_w} = h_2 + \frac{q_1 - q_2}{U_2 + (gh_2)^{1/2}}. \quad (7.110)$$

Once  $h_1$  is determined,  $V_w$  follows from Eqs. (7.103) or (7.104), and the profile given by Eq. (7.102) is determined. The solution is implemented in a code available on the file “SurgeAnalytical.xls” (Chap. 12).

The MacCormack TVD scheme was used to simulate a subcritical surge propagating over initially still water of depth 0.205 m. A sudden increase of discharge at the inflow section of  $0.028 \text{ m}^3/\text{s}$  was supplied in a channel 0.42 m wide. These are the test conditions for surge experiments conducted by Favre (1935). Consider now ideal surges ( $n = 0 \text{ m}^{1/3}/\text{s}$ ). At the first time step, the water depth at the upstream section was determined with the boundary conditions for discontinuous flows, to apply then the method of characteristics for the remaining time steps with Eq. (7.37) as

$$U_1^{k+1} = U_2^k + \frac{g}{c_2^k} (h_1^{k+1} - h_2^k) + g(S_o - S_f)_2^k \Delta t. \quad (7.111)$$

Equation (7.111) yields the quadratic function for  $h_1^{k+1}$

$$\frac{g}{c_2^k} (h_1^{k+1})^2 + \left[ U_2^k - \frac{g}{c_2^k} h_2^k + g(S_o - S_f)_2^k \Delta t \right] h_1^{k+1} - q_1^{k+1} = 0. \quad (7.112)$$

The numerical solution is implemented in the code “Favre\_FDM\_TVD\_BoundaryDiscont\_Subcrit.xls” (Chap. 12). The program output at  $t = 40$  s is shown in Fig. 7.15a, b. Note the excellent agreement with the analytical solution. Computations were repeated implementing the boundary condition at the upstream section using only the method of characteristics. The numerical solution is

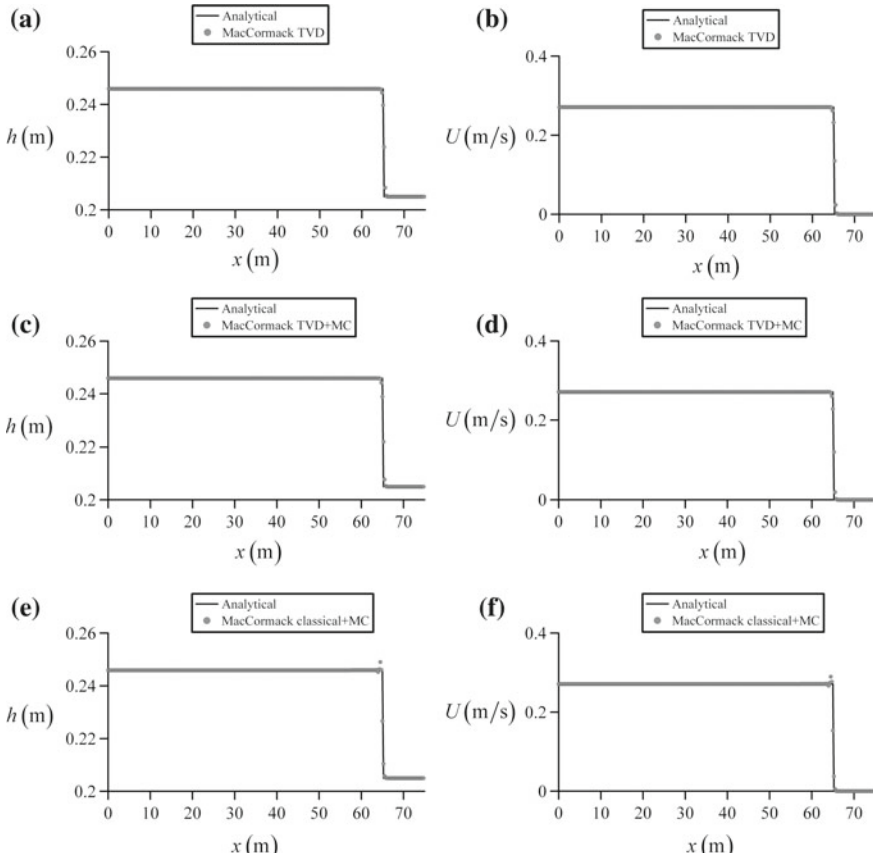


**Fig. 7.15** Subcritical surge computed with MacCormack scheme

implemented in the code “*Favre\_FDM\_TVD*” (Chap. 12). Results are displayed in Fig. 7.15c, d, not showing an evident variation of the former results. However, it is better to properly treat the boundary conditions as discontinuous when they involve jumps. The use of the classic MacCormack scheme with the boundary condition at the upstream section determined using the method of characteristics yields the results of Fig. 7.15e, f. A spurious oscillation appears at the shock front, but, overall, this computation is also acceptable. The numerical solution is implemented in the code “*Favre\_FDM\_Jameson*” (Chap. 12).

### 7.5.4 Supercritical Surge

A test suggested by García-Navarro and Sáviro (1992) is considered. A supercritical surge is generated with a discharge increase of  $1400 \text{ m}^3/\text{s}$  in a horizontal and frictionless flume 1 m wide and 2 m of initial static water. As the flow is supercritical, both depth and velocity must be prescribed at the inflow section. The water depth is thus computed using the jump conditions, and the values of  $h$  and  $Q$  are fixed along the simulation. The numerical solution is implemented in the code “*Favre\_FDM\_TVD\_BoundaryDiscont\_Super.xls*” (Chap. 12). Computational results are displayed in Fig. 7.16a, b, showing good agreement with

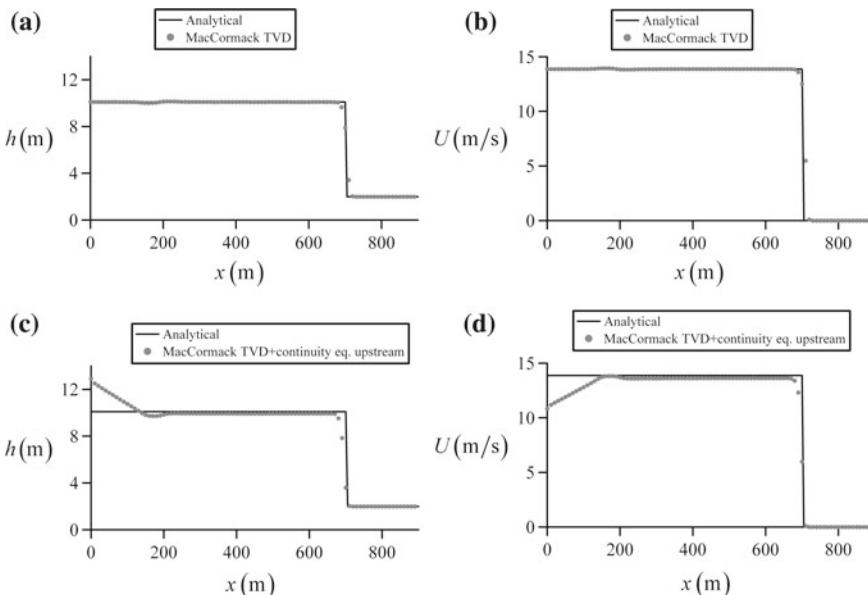


**Fig. 7.16** Supercritical surge computed with MacCormack scheme

the analytical solution except for a small hump numerically generated during the initial simulation instants. To evidence the importance of correct implementation of boundary conditions, we demonstrate the result of implementing naive approximations. It is tempting to assume that a boundary section is just another computational point, treating  $\partial\mathbf{F}/\partial x$  using either backward or forward finite-differences. In our case, the idea may be to generate the unknown water depth at the inflow section by discretizing the continuity equation using forward finite-differences. That is,

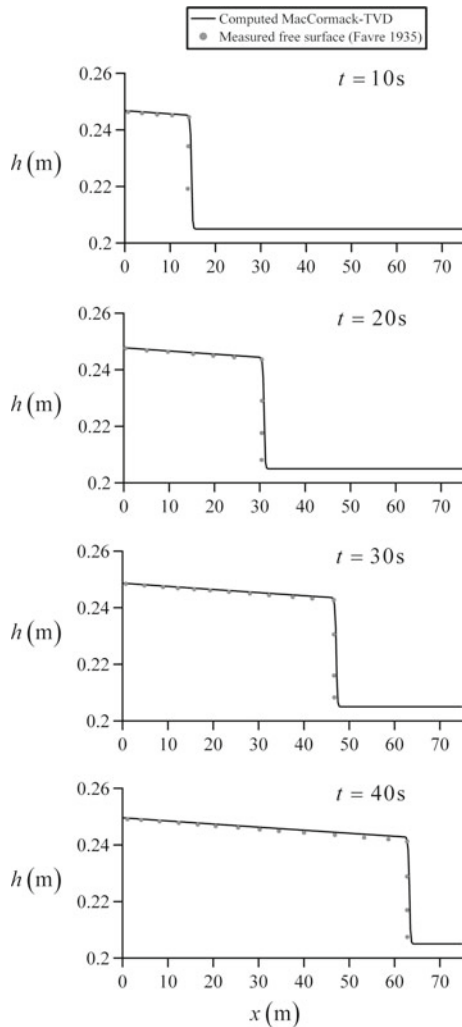
$$h_1^{k+1} = h_1^k - \frac{\Delta t}{\Delta x} (q_2^k - q_1^k). \quad (7.113)$$

This naive determination of the unknown water depth at the inflow section was implemented, and the poor results generated are shown in Fig. 7.16c, d, as found by García-Navarro and Sáviron (1992). This demonstrates the importance of the correct implementation of boundary conditions. The numerical solution is implemented in the code “*Favre\_FDM\_TVD\_BoundaryDiscont\_Super\_Cont.xls*” (Chap. 12).

### 7.5.5 Positive Surge with Friction

Favre (1935) measured a subcritical surge propagating over initially still water of depth 0.205 m. The discharge increase at the inlet section was  $0.028 \text{ m}^3/\text{s}$ , and the channel width was 0.42 m. Manning’s coefficient for this flume was  $n = 0.01 \text{ m}^{1/3}/\text{s}$  (Favre 1935; Terzidis and Strelkoff 1970). Computational results generated with the TVD MacCormack scheme along with a discontinuous-continuous implementation of the upstream boundary condition were generated at several instants of time. Results are displayed in Fig. 7.17 and compared with experimental data. The time needed to switch on the pumps and generate into the flume the discharge pulse was computationally accounted for as a time lag of 1 s, given that the generation of the discharge pulse is instantaneous in the mathematical model. Comparing profiles at two different instants of time, the absolute velocity of the surge predicted by the numerical model is in excellent agreement with that indicated by the experiments. The numerical solution is implemented in the code “*Favre\_FDM\_TVD\_BoundaryDiscont\_Subcrit.xls*” (Chap. 12).

**Fig. 7.17** Comparison of computational results with Favre's subcritical surge experiments



In general, the MacCormack TVD scheme by García-Navarro et al. (1992) was found to work well in all test cases; given its simple implementation, it is thus recommended.

## References

- Anderson, J. D. (1995). *Computational fluid dynamics: The basics with applications*. McGraw-Hill, New York.  
 Bermudez, A., & Vazquez, M. E. (1994). Upwind methods for hyperbolic conservation laws with source terms. *Computers & Fluids*, 23(8), 1049–1071.

- Bhallamudi, S. M. (2002). Computation of open-channel flows with shocks: an overview. In R. Prasad & S. Vedula (Eds.), *Research perspectives in hydraulics and water resources engineering* (pp. 89–130). London, UK: World Scientific.
- Chaudhry, M. H. (2008). *Open-channel flow* (2nd ed.). New York: Springer.
- Courant, R., Friedrichs, K., & Lewy, H. (1928). Über die partiellen Differenzengleichungen der mathematischen Physik [On the partial differential equations in Mathematical physics]. *Mathematische Annalen*, 100(1), 32–74 (in German).
- Courant, R., Isaacson, E., & Rees, M. (1952). On the solution of nonlinear hyperbolic differential equations by finite differences. *Communications on Pure and Applied Mathematics*, 5(3), 243–255.
- Cunge, J. A. (1975). Rapidly varying flow in power and pumping canals. In K. Mahmood & V. Yevjevich (Eds.), *Unsteady flow in open channels* (Chap. 14, pp. 539–586). Fort Collins, CO: Water Resources Publications.
- Cunge, J. A., Holly, F. M., & Verwey, A. (1980). *Practical aspects of computational river hydraulics*. London: Pitman.
- Favre, H. (1935). *Etude théorique et expérimentale des ondes de translation dans les canaux découverts*. [Theoretical and experimental study of travelling surges in open channels]. Dunod, Paris, France (in French).
- Fennema, R. J., & Chaudhry, M. H. (1986). Explicit numerical schemes for unsteady free-surface flows with shocks. *Water Resources Research*, 22(13), 1923–1930.
- Garcia-Navarro, P., Alcrudo, F., & Saviron, J. M. (1992). 1-D open-channel flow simulation using TVD-McCormack scheme. *Journal of Hydraulic Engineering*, 118(10), 1359–1372.
- Garcia-Navarro, P., & Saviron, J. M. (1992). McCormack's method for the numerical simulation of one-dimensional discontinuous unsteady open-channel flow. *Journal of Hydraulic Research*, 30(1), 95–105.
- Gharangik, A. M., & Chaudhry, M. H. (1991). Numerical simulation of hydraulic jump. *Journal of Hydraulic Engineering*, 117(9), 1195–1211.
- Henderson, F. M. (1966). *Open channel flow*. New York: MacMillan Co.
- Hirsch, C. (1988). *Numerical computation of internal and external flows, vol. 1: Fundamentals of numerical discretization*. Chichester: Wiley.
- Hirsch, C. (1990). *Numerical computation of internal and external flows, vol. 2: computational methods for inviscid and viscous flows* (Vol. 2). Chichester: Wiley.
- Hoffman, J. D. (2001). *Numerical methods for engineers and scientists* (2nd ed.). New York: Marcel Dekker.
- Hseng, M., & Chu, C. R. (2000). The simulation of dam-break flows by an improved predictor-corrector TVD scheme. *Advances in Water Resources*, 23(6), 637–643.
- Jain, S. C. (2001). *Open channel flow*. New York: Wiley.
- Jameson, A., Schmidt, W., & Turkel, E. (1981). Numerical solutions of the Euler equations by finite volume methods using Runge-Kutta time-stepping schemes. American Institute of Aeronautics and Astronautics, *Fluid and Plasma Dynamics Conf.*, Palo Alto CA, AIAA-81-1259.
- Lax, P. (1954). Weak solutions of nonlinear hyperbolic equations and their numerical computation. *Communications on Pure and Applied Mathematics*, 7, 159–193.
- Lax, P. D., & Richtmyer, R. D. (1956). Survey of the stability of linear finite difference equations. *Communications on Pure and Applied Mathematics*, 9, 267–293.
- Lax, P., & Wendroff, B. (1960). System of conservation laws. *Communications on Pure and Applied Mathematics*, 13(2), 217–237.
- Liggett, J. A., & Cunge, J. A. (1975). Numerical methods of solution of the unsteady flow equations. In K. Mahmood & V. Yevjevich (Eds.), *Unsteady flow in open channels* (Chap. 4, pp. 89–179). Fort Collins, CO: Water Resources Publications.
- MacCormack, R. W. (1969). The effect of viscosity in hypervelocity impact cratering. *American Institute Aeronautics and Astronautics*, Paper 69–354.
- Montes, J. S. (1998). *Hydraulics of open channel flow*. Reston, VA: ASCE.
- Roache, P. J. (1972). *Computational fluid dynamics*. Albuquerque, NM: Hermosa Publishers.

- Steger, J. L., & Warming, R. F. (1981). Flux vector splitting of the inviscid gas dynamic equations with application to finite-difference methods. *Journal of Computational Physics*, 40(2), 263–293.
- Stoker, J. J. (1957). *Water waves: The mathematical theory with applications*. New York: Interscience Publishers.
- Sturm, T. W. (2001). *Open channel hydraulics*. New York: McGraw-Hill.
- Terzidis, G., & Strelkoff, T. (1970). Computation of open channel surges and shocks. *Journal of the Hydraulics Division*, ASCE, 96(HY12), 2581–2610.
- Toro, E. F. (2001). *Shock-capturing methods for free-surface shallow flows*. Singapore: Wiley.
- Toro, E. F. (2009). *Riemann solvers and numerical methods for fluid dynamics*. London: Springer.
- Zoppou, C., & Roberts, S. (2003). Explicit schemes for dam-break simulations. *Journal of Hydraulic Engineering*, 129(1), 11–34.

# Chapter 8

## The Riemann Problem



### 8.1 Introduction

In fluid dynamics, the classical Riemann problem (Riemann 1860) is an initial-value problem for a set of homogeneous PDEs in which the initial data consist of two constant states forming a discontinuity (Toro 1997, 2001; LeVeque 2002; Guinot 2003) (Fig. 8.1). It is a generalization of the dam break problem (Stoker 1957) described in Chap. 6. The Riemann problem is important for a number of reasons. First, it is the simplest initial-value problem for the shallow water equations (SWEs), with a solution including both smooth and discontinuous waves. The understanding of this fundamental wave problem is of paramount importance to assimilate how waves propagate in shallow water. Despite its apparent simplicity, it represents the practical case of instantaneous gate maneuvers in open channels (Henderson 1966; Jain 2001; Jeppson 2011; Katopodes 2019). Another important aspect is that the Riemann problem yields an exact solution of the SWE; thus, it applies to check the performance of numerical schemes. Finally, it is a fundamental component of a class of numerical schemes known as finite volume Godunov-type methods (Godunov 1959), to be described in Chap. 9.

Let subscripts  $L$  and  $R$  denote conditions at the left- and right-hand sides of the discontinuity at time  $t = 0$ ; the initial conditions then are

$$\mathbf{U}(x, 0) = \begin{cases} \mathbf{U}_L & \text{if } x < 0, \\ \mathbf{U}_R & \text{if } x > 0, \end{cases} \quad (8.1)$$

where  $x$  is the spatial coordinate and the discontinuity is located initially at  $x = 0$ . The solution  $\mathbf{U}(x, t)$  subject to Eq. (8.1) is to be determined from

$$\frac{\partial \mathbf{U}}{\partial t} + \frac{\partial \mathbf{F}}{\partial x} = 0. \quad (8.2)$$

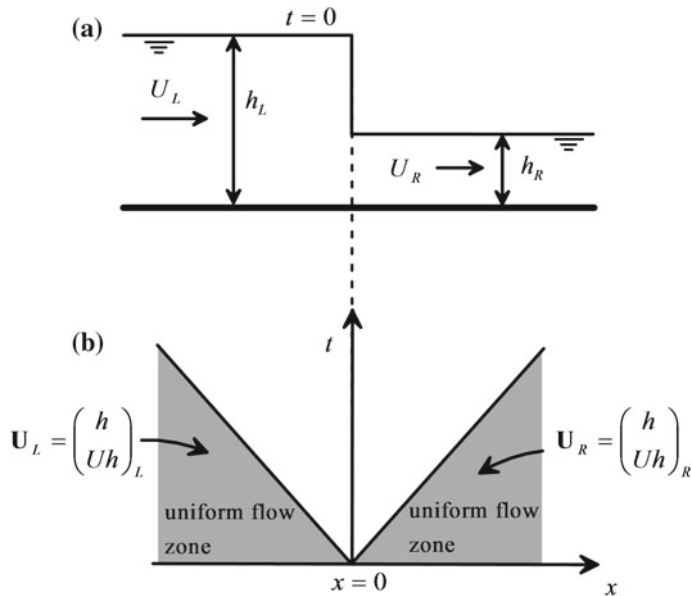


**Fig. 8.1** Initial conditions of Riemann problem for the SWE **a** physical plane, **b**  $x$ - $t$  plane

Here,  $\mathbf{U}$  is the vector of unknowns and  $\mathbf{F}$  is the flux vector given, with  $h$  as the water depth and  $U$  as the depth-averaged velocity, by

$$\mathbf{U} = \begin{pmatrix} h \\ Uh \end{pmatrix}, \quad \mathbf{F} = \begin{pmatrix} Uh \\ U^2 h + \frac{1}{2} g h^2 \end{pmatrix}. \quad (8.3)$$

The fundamental difference with the dam break problem stems from the possibility of having nonvanishing initial values of  $U$  at each side of the discontinuity. The basic wave solutions are those described in Chaps. 5 and 6, namely shock waves and rarefaction waves. Previous relations are then first generalized to accommodate arbitrary initial data, and then, the solution strategy of the wave structure for wet-bed conditions is detailed. The computation of the complete wave profile is presented. The dry-bed Riemann solver is subsequently explained, and finally, the instantaneous gate operations in open channels are analyzed in detail using the theory presented.

## 8.2 Wet-Bed Exact Riemann Solver

### 8.2.1 Wave Relations

As previously discussed, the basic wave solutions of Eqs. (8.1), (8.2) are shocks and rarefaction waves. The type of wave generated at each side of the discontinuity for  $t > 0$  is not known in advance, demanding for an iterative solution of the wave field starting with an assumed wave pattern. In general, four cases may arise:

- (1) Left wave is a rarefaction, and right wave is a shock.
- (2) Left wave is a rarefaction, and right wave is a rarefaction.
- (3) Left wave is a shock, and right wave is a shock.
- (4) Left wave is a shock, and right wave is a rarefaction.

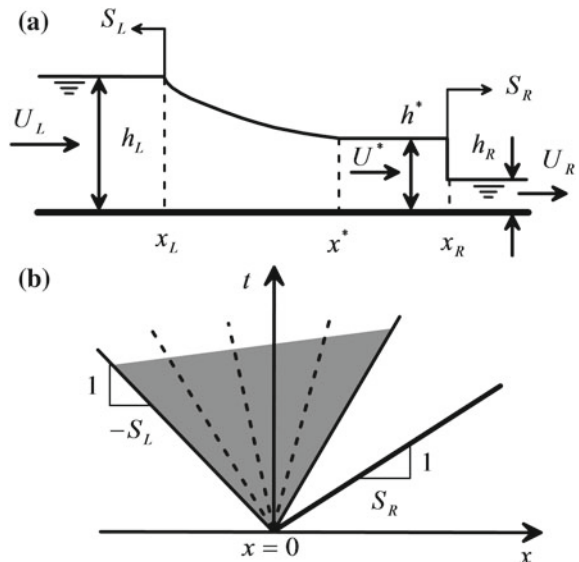
Consider case 1, with a left-going rarefaction wave and a right-going shock (Fig. 8.2). The basic equation for a left rarefaction wave results from the relation stating conservation of the Riemann invariant  $U + 2c$  within the wave, that is, with  $c = (gh)^{1/2}$  [Eq. (5.78)]

$$U(x, t) + 2c(x, t) = \text{const.} \quad (8.4)$$

Direct application yields

$$U^* + 2c^* = U_L + 2c_L, \quad (8.5)$$

**Fig. 8.2** Wave pattern of Riemann problem for left-going rarefaction wave and right-going shock wave  
**a** physical plane, **b**  $x$ - $t$  plane (gray shadow depicts the rarefaction wave  $x$ - $t$  domain, and the thick black line represents the shock front path)



or,

$$U^* = U_L - 2(c^* - c_L) = U_L - 2[(gh^*)^{1/2} - (gh_L)^{1/2}]. \quad (8.6)$$

This equation states the conditions at the star region as function of initial conditions at the left side of the discontinuity. It is therefore an equation “connecting” the constant state zone with the left-side initial conditions. Following Toro (2001), we define a left-side function  $f_L$  as

$$\begin{aligned} U^* &= U_L - f_L, \\ f_L &= 2[(gh^*)^{1/2} - (gh_L)^{1/2}]. \end{aligned} \quad (8.7)$$

The propagation speed  $S_R$  of a right-going shock wave is given from the Rankine–Hugoniot jump conditions by [Eq. (5.35)]

$$S_R = U_R + \left[ \frac{gh^*}{2h_R} (h^* + h_R) \right]^{1/2}. \quad (8.8)$$

This relation is now expressed as a function of the depth-averaged velocity at the star region. Using the mass conservation equation in moving axes, namely

$$h_R(U_R - S_R) = h^*(U^* - S_R), \quad (8.9)$$

it is possible to write

$$(h^* - h_R)(S_R - U_R) = h^*(U^* - U_R). \quad (8.10)$$

Inserting into Eq. (8.8) produces

$$U^* = U_R + (h^* - h_R) \left[ \frac{g}{2h^*h_R} (h^* + h_R) \right]^{1/2}. \quad (8.11)$$

This relation is also written as

$$\begin{aligned} U^* &= U_R + f_R, \\ f_R &= (h^* - h_R) \left[ \frac{g}{2h^*h_R} (h^* + h_R) \right]^{1/2}. \end{aligned} \quad (8.12)$$

Here,  $f_R$  is a function “connecting” the constant state zone with the right-side conditions. Equating the velocity in the star region from Eqs. (8.7) and (8.12) produces

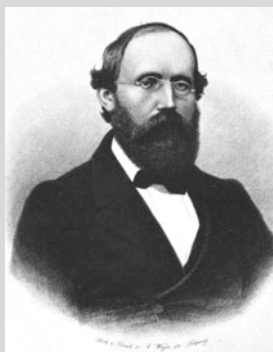
$$f(h^*) = U_R - U_L + f_R(h^*, h_R) + f_L(h^*, h_L) = 0. \quad (8.13)$$

This is an equation that must be numerically solved to determine the water depth at the star region  $h^*$ . Once done,  $U^*$  is computed either from Eqs. (8.7) or (8.12). The important aspect at this stage is that the Riemann problem produces an equation where the constant state zone is linked to initial data via left- and right-hand functions. Note that the type of function is different for shock and rarefaction waves, thereby indicating that it is necessary to discriminate in advance which type of wave originates at each side of the discontinuity. Note further that the left-going rarefaction wave produces a depression of water depths ( $h^* < h_L$ ), whereas the right-going shock involve an increase in water level ( $h^* > h_R$ ). An important issue is that Eq. (8.13) is general, as verified by repeating this analysis for the other three types of wave patterns. It implies formulating the equations for a left-going shock using the Rankine–Hugoniot jump conditions, and the continuous solution of the right-going smooth wave, basically implying conservation of the Riemann invariant  $U(x, t) - 2c(x, t)$  across the rarefaction (Jain 2001; Toro 2001). The repetition process is elementary and is left to the reader. The results for  $f_R$  and  $f_L$ , depending on whether they are linked to rarefactions or shocks, are summarized as (Toro 2001)

$$f_L = \begin{cases} 2\left[(gh^*)^{1/2} - (gh_L)^{1/2}\right] & \text{if } h^* \leq h_L \quad (\text{rarefaction wave}) \\ (h^* - h_L)\left[\frac{g}{2h^*h_L}(h^* + h_L)\right]^{1/2} & \text{if } h^* > h_L \quad (\text{shock wave}) \end{cases}, \quad (8.14)$$

$$f_R = \begin{cases} 2\left[(gh^*)^{1/2} - (gh_R)^{1/2}\right] & \text{if } h^* \leq h_R \quad (\text{rarefaction wave}) \\ (h^* - h_R)\left[\frac{g}{2h^*h_R}(h^* + h_R)\right]^{1/2} & \text{if } h^* > h_R \quad (\text{shock wave}) \end{cases}. \quad (8.15)$$

Note that in a given Riemann problem, once the value of  $h^*$  is adopted, the types of waves generated at the right and left sides are automatically determined.



**Bernhard Riemann** was born on September 17, 1826, at Breselenz, in today's Germany, passing away almost aged 40 years on July 20, 1866, at Selasca, Italy. He initiated studies in 1846 in theology and philology at Göttingen University, but soon turned to mathematics. One year later, he moved to Berlin University submitting, from Göttingen in 1850, a thesis on the Theory of functions with a complex variable. This work was praised by Gauss and led the foundations for his work in the following decade. In 1859, he moved to Göttingen, where Gauss had been Professor until 1855. The struggle to survive on the casual fees of a private teacher had undermined his health such that he passed away at young age.

Riemann introduced in mathematics the many-leafed Riemann surfaces whose sheets are connected around the branch points of the function, on which the latter can be defined as single value. He demonstrated how to treat the function as a conformal map of a simply connected domain, described essentially by the point singularities of the function and the shape of the map along the boundary of the domain. He also laid the foundations to the non-Euclidian geometry. Throughout this subject, he was motivated by his studies in mathematical physics. Riemann computed in hydromechanics two-dimensional outflow from a large tank by the hodograph method and determined the contraction coefficient from an infinitely small orifice. His method was generalized by Richard von Mises (1883–1953) some fifty years later and served as a starting point of plane inviscid flow analyses in the twentieth century. Riemann also worked on the propagation characteristics of waves in air.

### 8.2.2 *Solution of Star Region*

The solution process is iterative, starting with an initial guess of  $h^*$ . This value, upon comparison with  $h_L$  and  $h_R$ , determines which types of waves generate at the

left- and right-hand sides. In general, the initial guess  $h_o^*$  does not satisfy Eq. (8.13), producing

$$U_R - U_L + f_R(h_o^*, h_R) + f_L(h_o^*, h_L) \neq 0. \quad (8.16)$$

A better approximation to the root of Eq. (8.13) involves the Newton–Raphson method with  $k$  as the recursion index as (Hoffman 2001; Toro 2001)

$$(h^*)^{k+1} = (h^*)^k - \frac{f^k}{(df/dh^*)^k}. \quad (8.17)$$

With this new value of  $h^*$ , the types of waves at  $L$  or  $R$  may change, therefore. Thus, the wave field is iteratively updated in the solution process. The derivative term needed in Eq. (8.17) is

$$\frac{df}{dh^*} = \frac{df_L}{dh^*} + \frac{df_R}{dh^*}, \quad (8.18)$$

where

$$\frac{df_L}{dh^*} = \begin{cases} g(gh^*)^{-1/2} & \text{if } h^* \leq h_L, \\ \left[ \frac{g}{2h^*h_L} (h^* + h_L) \right]^{1/2} - g \frac{(h^* - h_L)}{4h^{*2}} \left[ \frac{g}{2h^*h_L} (h^* + h_L) \right]^{-1/2} & \text{if } h^* > h_L, \end{cases} \quad (8.19)$$

and

$$\frac{df_R}{dh^*} = \begin{cases} g(gh^*)^{-1/2} & \text{if } h^* \leq h_R, \\ \left[ \frac{g}{2h^*h_R} (h^* + h_R) \right]^{1/2} - g \frac{(h^* - h_R)}{4h^{*2}} \left[ \frac{g}{2h^*h_R} (h^* + h_R) \right]^{-1/2} & \text{if } h^* > h_R. \end{cases} \quad (8.20)$$

Following Toro (2001), a good initial estimate of  $h^*$  is given by the so-called two-rarefaction approximation. For two rarefaction waves, inserting the corresponding  $f_L$  and  $f_R$  functions into Eq. (8.13), results in

$$f(h^*) = U_R - U_L + 2[(gh^*)^{1/2} - (gh_R)^{1/2}] + 2[(gh^*)^{1/2} - (gh_L)^{1/2}] = 0, \quad (8.21)$$

whose analytical solution is (Toro 2001)

$$h^* = \frac{1}{g} \left[ \frac{(gh_L)^{1/2} + (gh_R)^{1/2}}{2} - \frac{1}{4}(U_R - U_L) \right]^2. \quad (8.22)$$

The wave relation across the left rarefaction implies conservation of the Riemann invariant  $U + 2c$ , resulting in

$$U^* + 2c^* = U_L + 2c_L. \quad (8.23)$$

Across the right rarefaction wave,  $U - 2c$  is conserved, from which

$$U^* - 2c^* = U_R - 2c_R. \quad (8.24)$$

Summing the two equations yields for  $U^*$

$$U^* = \frac{1}{2}(U_R + U_L) + (c_L - c_R). \quad (8.25)$$

### 8.2.3 Complete Wave Profiles

#### *Left shock wave*

For a left shock wave, the signal speed is (Toro 2001)

$$\begin{aligned} S_L &= U_L - \lambda_L(gh_L)^{1/2}, \\ \lambda_L &= \left[ \frac{1}{2} \frac{(h^* + h_L)h^*}{h_L^2} \right]^{1/2}. \end{aligned} \quad (8.26)$$

This is needed to track the position of the shock front at any instant of time. The depth and velocity within the shock wave are simply  $h^*$  and  $U^*$ .

#### *Left rarefaction wave*

For a left rarefaction wave, the signal speeds of its edge and tail are, respectively,

$$\begin{aligned} S_L &= U_L - (gh_L)^{1/2}, \\ S_L^* &= U^* - (gh^*)^{1/2}. \end{aligned} \quad (8.27)$$

Between the edge and the tail of the rarefaction, the spatial variations of depth and velocity for any instant of time are given by solving  $x/t = U - c$  and  $U + 2c = \text{const.}$  for  $U(x, t)$  and  $c(x, t)$  by

$$\begin{aligned} (gh)^{1/2} &= \frac{1}{3} \left[ U_L + 2(gh_L)^{1/2} - \frac{x}{t} \right], \\ U &= \frac{1}{3} \left[ U_L + 2(gh_L)^{1/2} + 2\frac{x}{t} \right]. \end{aligned} \quad (8.28)$$

### *Right shock wave*

For a right shock wave, the signal speed is, from the Rankine–Hugoniot jump conditions

$$\begin{aligned} S_R &= U_R + \lambda_R (gh_R)^{1/2}, \\ \lambda_R &= \left[ \frac{1}{2} \frac{(h^* + h_R)h^*}{h_R^2} \right]^{1/2}, \end{aligned} \quad (8.29)$$

which is similarly needed to track the position of the shock front at any instant of time. The depth and velocity within the shock wave are simply  $h^*$  and  $U^*$ .

### *Right rarefaction wave*

For a right rarefaction wave, the signal speeds of its edge and tail are, respectively,

$$\begin{aligned} S_R &= U_R + (gh_R)^{1/2}, \\ S_R^* &= U^* + (gh^*)^{1/2}. \end{aligned} \quad (8.30)$$

Between the rarefaction edge and tail, the spatial variations of depth and velocity for any instant of time are given by

$$\begin{aligned} (gh)^{1/2} &= \frac{1}{3} \left[ -U_R + 2(gh_R)^{1/2} + \frac{x}{t} \right], \\ U &= \frac{1}{3} \left[ U_R - 2(gh_R)^{1/2} + 2\frac{x}{t} \right]. \end{aligned} \quad (8.31)$$

#### **8.2.4 Possible Wave Patterns and Computation of Fluxes**

For the four cases previously reported, there are a number of subcases depending on the relative position of each wave with respect to the  $t$ -axis, determined by the signs of  $S_L$ ,  $S_L^*$ ,  $S_R$  and  $S_R^*$ . The 16 possible cases are plotted in Figs. 8.3, 8.4, 8.5, and 8.6 (Zoppou and Roberts 2003; Roberts 2013).

As stated at the start of this chapter, the Riemann problem is a key ingredient used in Godunov-type finite volume methods. Here, it is advanced that a fundamental quantity to be determined is the value of the flux vector  $\mathbf{F}$  at coordinate  $x = 0$ , i.e., the flux crossing the plane where the discontinuity in  $\mathbf{U}$  was initially generated. Using the definitions of  $\mathbf{U}$  and  $\mathbf{F}$ , it is elementary to demonstrate that

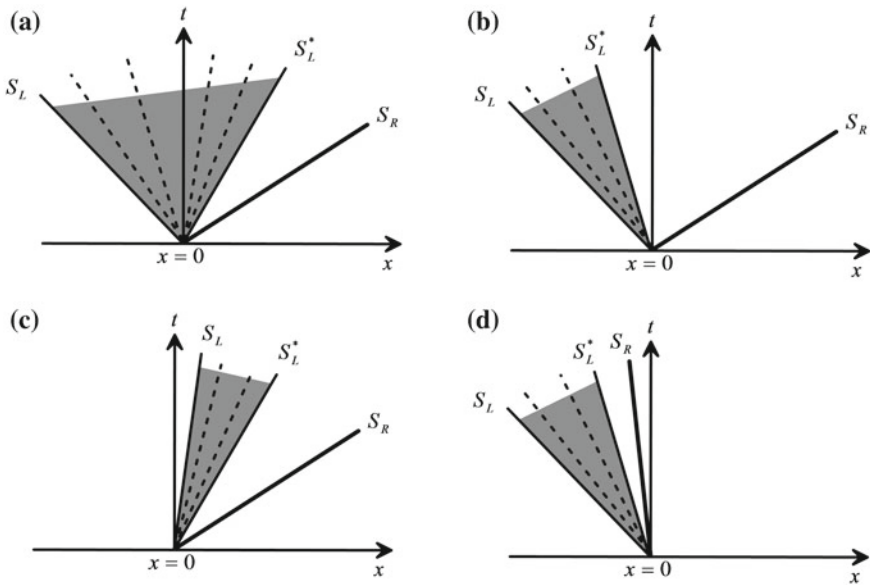


**Fig. 8.3** Wave patterns of Riemann problem for left rarefaction wave and right shock wave (case 1) (adapted from Roberts 2013)

$$\mathbf{U} = \begin{pmatrix} h \\ Uh \end{pmatrix} = \begin{pmatrix} U_1 \\ U_2 \end{pmatrix}, \quad \mathbf{F} = \mathbf{F}(\mathbf{U}) = \begin{pmatrix} U_2 \\ \frac{U_2^2}{U_1} + \frac{1}{2}gU_1^2 \end{pmatrix}. \quad (8.32)$$

This means that the value of  $\mathbf{F}$  is fully determined by  $\mathbf{U}$ . Thus, the value of  $\mathbf{F}(x = 0)$  is given by the solution of the Riemann problem at  $x = 0$ , namely  $\mathbf{U}(x = 0)$ . Depending on the specific wave pattern,  $\mathbf{U}(x = 0)$  may equal  $\mathbf{U}_L$ ,  $\mathbf{U}_R$ ,  $\mathbf{U}^*$ , or a value  $\mathbf{U}_c$  to be determined using the rarefaction wave equations, corresponding to critical flow. The computation of the value of  $\mathbf{F}(x = 0)$  for the 16 possible cases depicted in Figs. 8.3, 8.4, 8.5 and 8.6 is summarized in Table 8.1. Note that some cases are equivalent in terms of computation of  $\mathbf{F}(x = 0)$ , despite the different complete wave patterns. If a finite volume scheme is constructed using the exact solution of the Riemann problem, it is said to use an “exact Riemann solver.” This nomenclature should be understood as the use of the numerical solution originating from the consideration of the complete Riemann problem. “Exact Riemann solver” should not be confused with having closed-form analytical solutions in a Riemann solver. In fact, this is only true for the two-rarefaction case. To the authors’ knowledge, exact analytical solutions are unknown for the rest of wave patterns.

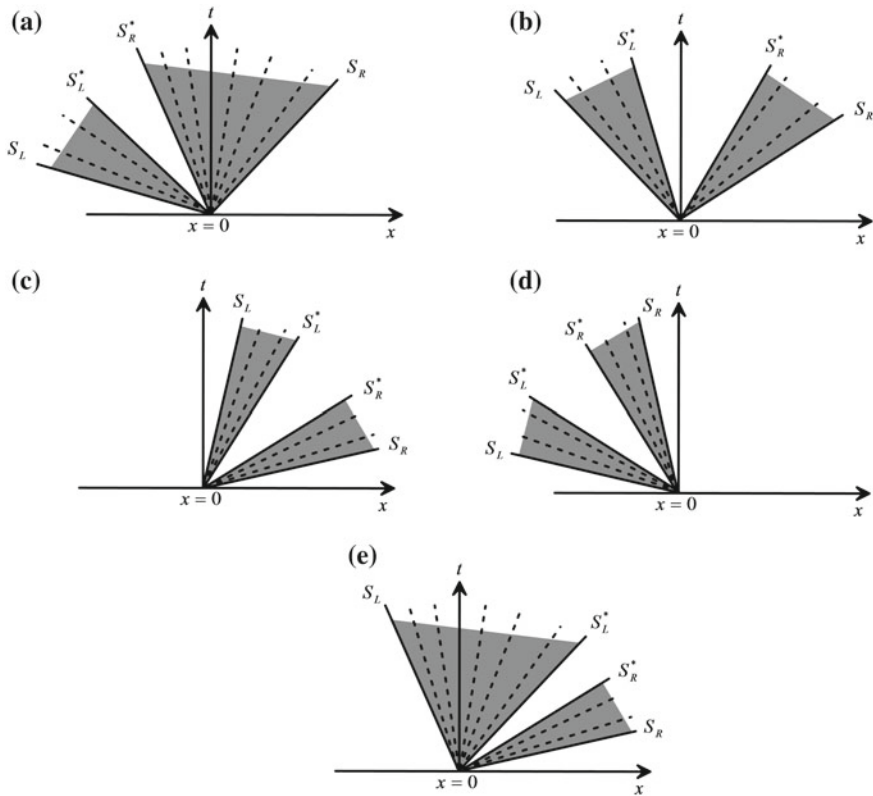


**Fig. 8.4** Wave patterns of Riemann problem for left and right rarefaction waves (case 2) (adapted from Roberts 2013)

### 8.2.5 Computational Examples

In this section, computational examples are presented to illustrate the propagation of waves originating from the solution of the Riemann problem under wet-bed conditions. Test conditions for the examples are summarized in Table 8.2.

The first example is presented in Fig. 8.7, simulating a flume with initially static water and a gate closed at left. The gate is suddenly opened at time  $t = 0$ , and the wave motion shown in Fig. 8.7 is generated after 2 s of routing. The wave pattern is composed of two shocks propagating to the right. Given that  $S_L < S_R$ , the width of the star region progressively increases with time. The computational output is summarized in Table 8.3. The results were generated with a code in which the described solution of the wet-bed Riemann problem was implemented. This code was inserted into the file “*ExactRiemannSolver\_wetbed.xls*”, available in Chap. 12.

The program was also used to run the test presented in Fig. 8.8, originally due to Toro (2001). It consists of two identical rarefaction waves traveling in opposite

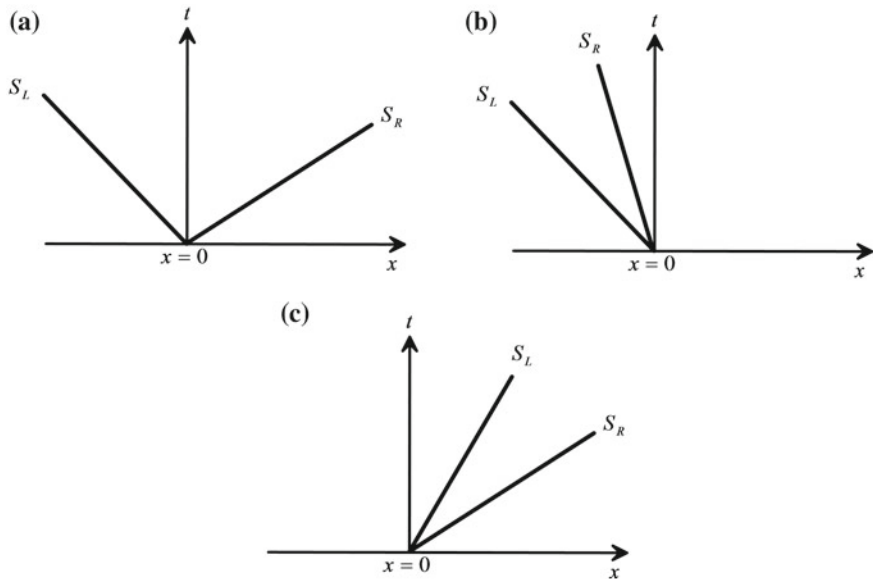


**Fig. 8.5** Wave patterns of Riemann problem for left and right shock waves (case 3) (adapted from Roberts 2013)

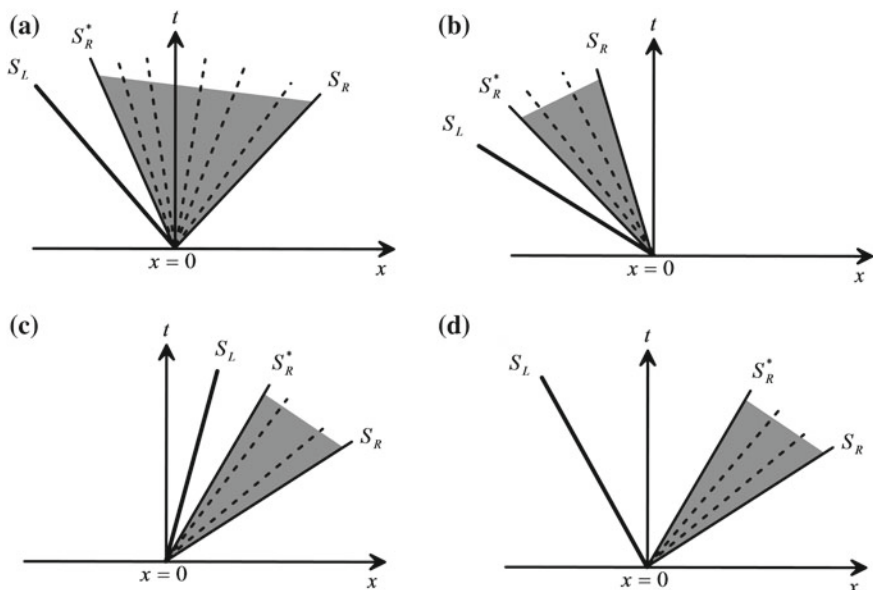


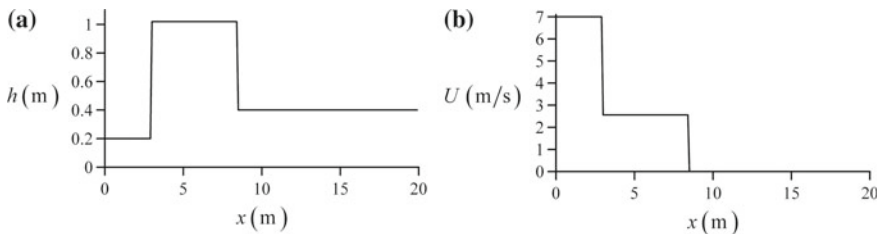
**Fig. 8.6** Wave patterns of Riemann problem for left shock wave and right rarefaction wave (case 4) (adapted from Roberts 2013)

**Table 8.1** Evaluation of the flux  $\mathbf{F}$  in the Riemann problem (see Figs. 8.3, 8.4, 8.5, and 8.6)

Case	Subcase	$\mathbf{F}(x = 0)$
1	a	$\mathbf{F}(\mathbf{U}_c)$ ; critical flow at left rarefaction
1	b	$\mathbf{F}(\mathbf{U}^*)$
1	c	$\mathbf{F}(\mathbf{U}_L)$
1	d	$\mathbf{F}(\mathbf{U}_R)$
2	a	$\mathbf{F}(\mathbf{U}_c)$ ; critical flow at right rarefaction
2	b	$\mathbf{F}(\mathbf{U}^*)$
2	c	$\mathbf{F}(\mathbf{U}_L)$
2	d	$\mathbf{F}(\mathbf{U}_R)$
2	e	$\mathbf{F}(\mathbf{U}_c)$ ; critical flow at left rarefaction
3	a	$\mathbf{F}(\mathbf{U}^*)$
3	b	$\mathbf{F}(\mathbf{U}_R)$
3	c	$\mathbf{F}(\mathbf{U}_L)$
4	a	$\mathbf{F}(\mathbf{U}_c)$ ; critical flow at right rarefaction
4	b	$\mathbf{F}(\mathbf{U}_R)$
4	c	$\mathbf{F}(\mathbf{U}_L)$
4	d	$\mathbf{F}(\mathbf{U}^*)$

**Table 8.2** Test conditions for examples of wave solutions of the Riemann problem

Test	Time (s)	$h_L$ (m)	$h_R$ (m)	$U_R$ (m/s)	$U_L$ (m/s)
Figure 8.7	2	0.2	0.4	0	7
Figure 8.8	2	1	1	5	-5
Figure 8.9	2	1	0.2	2.5	0.5

**Fig. 8.7** Riemann solution of test with two right-going shocks for **a** free surface profile  $h(x)$  and **b** depth-averaged velocity  $U(x)$ **Table 8.3** Test results for examples of wave solutions of Riemann problem. The discontinuity is located at  $x = 0$ ,  $t = 0$ 

Test	Time (s)	$S_R$ (m/s)	$S_L$ (m/s)	$h^*$ (m)	$U^*$ (m/s)
Figure 8.7	2	4.213	1.477	1.02	2.56
Figure 8.8	2	8.132	-8.132	0.041	0
Figure 8.9	2	4.5	-2.632	0.317	3.238

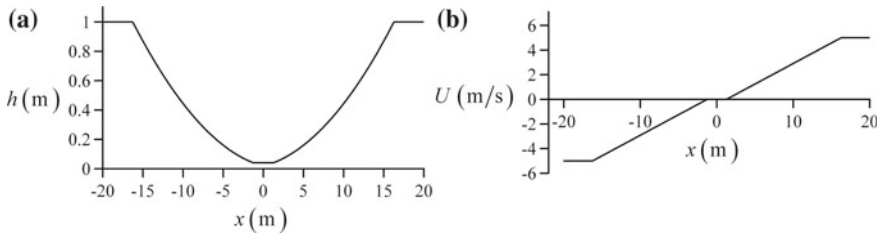


**Fig. 8.8** Riemann solution of test with left- and right-going rarefaction waves for **a** free surface profile  $h(x)$  and **b** depth-averaged velocity  $U(x)$

directions. The interest of this type of test is that the interaction of the rarefaction waves produces a star region of static water where the bed may become dry under certain conditions. The mathematical conditions for two identical rarefaction waves traveling in opposite directions are  $h_R = h_L$  and  $U_L = -U_R$ . Inserting these into Eq. (8.22) produces

$$h^* = \frac{1}{g} \left[ \frac{2(gh_R)^{1/2}}{2} - \frac{1}{4}(2U_R) \right]^2 = \frac{1}{g} \left[ (gh_R)^{1/2} - \frac{1}{2}U_R \right]^2. \quad (8.33)$$

This is rewritten with the Froude number  $F_R = U_R/c_R$  as

$$h^* = h_R \left( 1 - \frac{1}{2}F_R \right)^2. \quad (8.34)$$

Thus, for the limiting case  $F_R = 2$ , a dry-bed condition  $h^* = 0$  is generated. The velocity at the star region is from Eq. (8.25)

$$U^* = \frac{1}{2}(U_R - U_R) + (c_R - c_R) = 0. \quad (8.35)$$

The water there is thus stagnant for all values of  $F_R$ .

The last example is presented in Fig. 8.9, where the results include a rarefaction wave traveling to the left, and a shock to the right. The tailwater depth is small, so that the rarefaction wave crosses the initial position of the discontinuity ( $x = 0$ ), and critical flow  $F = 1$  is thus settled there. Transcritical flow is established along the rarefaction wave, which is connected to a supercritical bore along the right portion of the wave profile.

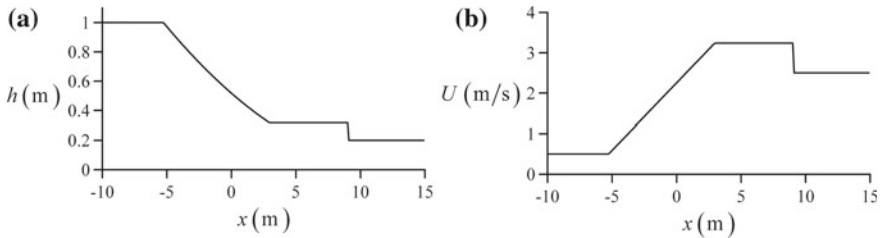


**Fig. 8.9** Riemann solution of test with left-going rarefaction wave and right-going shock for **a** free surface profile  $h(x)$  and **b** depth-averaged velocity  $U(x)$

## 8.3 Dry-Bed Exact Riemann Solver

### 8.3.1 Wet–Dry Interface

The wave structure of the Riemann problem changes drastically if a portion of the computational domain is dry. Before presenting the corresponding wave solutions, consider Toro (2001), who demonstrated that a shock wave cannot connect the wet–dry portions. Let  $\mathbf{U}_L$  represent the initial wet-bed data, and  $\mathbf{U}_R$  the data of the dry-bed region. Obviously,  $h_R = 0$ . Assume that a shock wave propagating with velocity  $S$  connects the two states. The Rankine–Hugoniot jump conditions are then

$$S = \frac{h_L U_L - h_R U_R}{h_L - h_R} = \frac{h_L U_L^2 + \frac{1}{2} g h_L^2 - h_R U_R^2 - \frac{1}{2} g h_R^2}{h_L U_L - h_R U_R}. \quad (8.36)$$

Setting  $h_R = 0$ , the first identity yields  $S = U_L$ . Substitution in the second identity yields

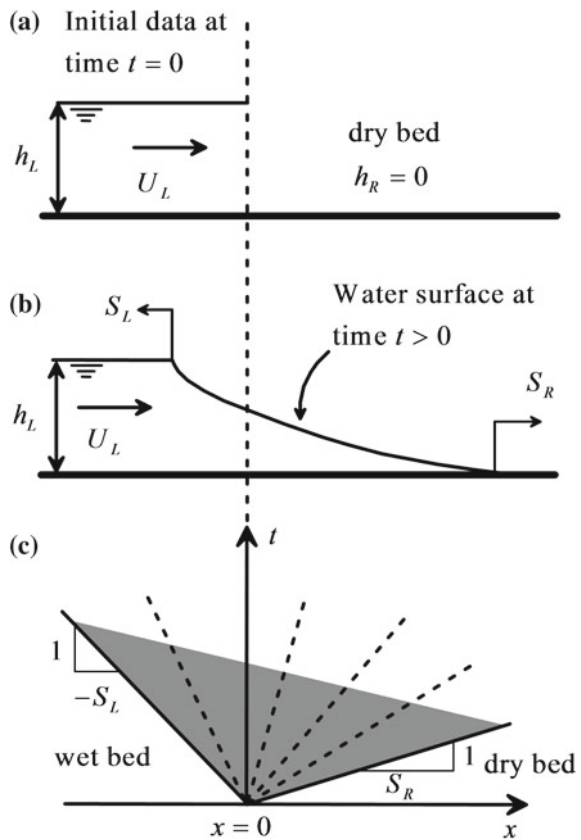
$$S = \frac{h_L U_L^2 + \frac{1}{2} g h_L^2}{h_L U_L} \equiv U_L \Rightarrow h_L = 0, \quad (8.37)$$

which is obviously in contradiction with the initial assumption  $h_L > 0$ . Thus, a shock wave cannot physically exist at the wet–dry interface. At this interface, the depth is simply zero, and there is a jump in velocity, which is zero in the dry terrain, and finite at the wave edge.

### 8.3.2 Possible Wave Patterns

Consider first wet-bed conditions on the left, corresponding to the initial data (Fig. 8.10)

**Fig. 8.10** Dry-bed conditions of the right a initial data, b free surface profile  $h(x)$ , and c  $x-t$  plane



$$\mathbf{U}(x, 0) = \begin{cases} \mathbf{U}_L & \text{if } x < 0 \\ \mathbf{0} & \text{if } x > 0 \end{cases} \quad (8.38)$$

A rarefaction wave is formed, with the left edge propagating at velocity

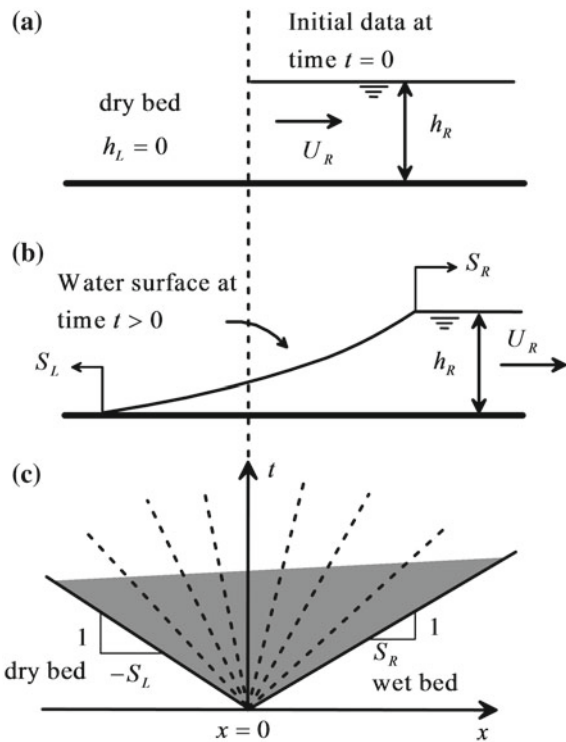
$$S_L = U_L - (gh_L)^{1/2}. \quad (8.39)$$

The velocity of propagation of the right-going wet-dry interface is determined using the basic equation of the rarefaction wave, namely

$$U_R + 2c_R = U_L + 2c_L. \quad (8.40)$$

At the dry front  $h_R = 0$ , so that from Eq. (8.40)

**Fig. 8.11** Dry-bed conditions of the left **a** initial data, **b** free surface profile  $h(x)$ , and **c**  $x-t$  plane



$$S_R = U_R = U_L + 2c_L. \quad (8.41)$$

The depth and velocity within the rarefaction wave are thus given by (Toro 2001)

$$\begin{aligned} (gh)^{1/2} &= \frac{1}{3} \left[ U_L + 2(gh_L)^{1/2} - \frac{x}{t} \right], \\ U &= \frac{1}{3} \left[ U_L + 2(gh_L)^{1/2} + 2\frac{x}{t} \right]. \end{aligned} \quad (8.42)$$

For wet-bed conditions on the right side (Fig. 8.11), the corresponding initial data are

$$\mathbf{U}(x, 0) = \begin{cases} \mathbf{0} & \text{if } x < 0 \\ \mathbf{U}_R & \text{if } x > 0 \end{cases}. \quad (8.43)$$

A rarefaction wave is formed, with the right edge propagating at velocity

$$S_R = U_R + (gh_R)^{1/2}. \quad (8.44)$$

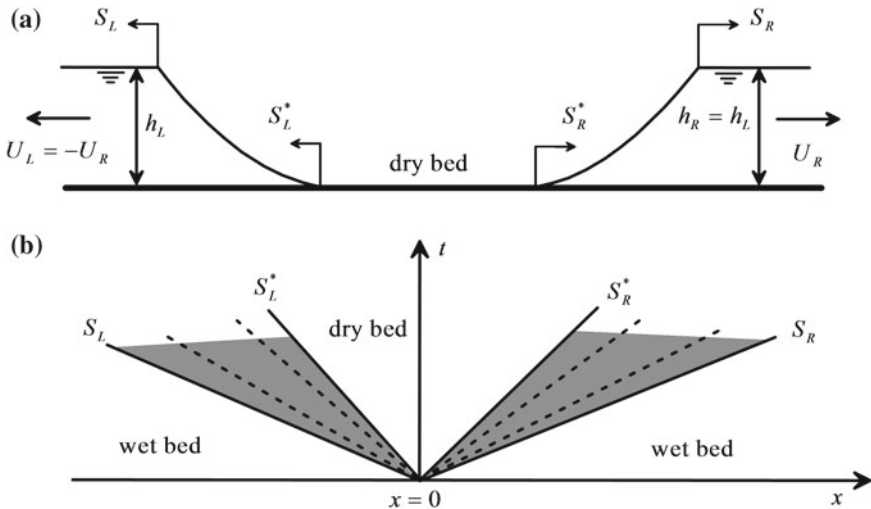


**Fig. 8.12** Dry-bed conditions along center of two rarefactions **a** free surface profiles  $h(x)$  and **b**  $x$ - $t$  plane

The propagation velocity of the left-going wet–dry interface is determined using the basic equation of the rarefaction wave, namely

$$U_R - 2c_R = U_L - 2c_L. \quad (8.45)$$

At the dry front  $h_L = 0$ , so that from Eq. (8.45)

$$S_L = U_L = U_R - 2c_R. \quad (8.46)$$

The depth and velocity within the rarefaction wave are thus given by (Toro 2001)

$$\begin{aligned} (gh)^{1/2} &= \frac{1}{3} \left[ -U_R + 2(gh_R)^{1/2} + \frac{x}{t} \right], \\ U &= \frac{1}{3} \left[ U_R - 2(gh_R)^{1/2} + 2\frac{x}{t} \right]. \end{aligned} \quad (8.47)$$

A third case occurs in relation to the two-rarefaction wave case previously studied for the wet-bed Riemann solver. The solution of the wet-bed Riemann problem yields Eq. (8.33). If  $F_R > 2$ , a dry bed is generated within the two rarefaction waves (Fig. 8.12). The wave solution then changes; the celerity of the dry fronts is given by

$$S_L^* = U_L + 2c_L \quad (8.48)$$

for the left rarefaction wave and

$$S_R^* = U_R - 2c_R \quad (8.49)$$

for the right rarefaction wave.

From Eq. (8.21), the celerity in the star region is

$$c^* = (gh^*)^{1/2} = \frac{(gh_L)^{1/2} + (gh_R)^{1/2}}{2} - \frac{1}{4}(U_R - U_L). \quad (8.50)$$

Given that  $c^*$  must be positive to generate real values of  $h^*$ , the depth-positivity condition is thus, for arbitrary data (Toro 2001),

$$c^* = \frac{1}{2} \left[ (gh_L)^{1/2} + (gh_R)^{1/2} \right] - \frac{1}{4}(U_R - U_L) \geq 0. \quad (8.51)$$

For given initial data in a Riemann problem, a preliminary check is conducted to decide whether a wet-bed or dry-bed Riemann solver applies. If  $h_R = 0$ , or  $h_L = 0$ , or  $c^* < 0$ , the dry-bed Riemann solver is selected, whereas the wet-bed Riemann solver must be used otherwise.



**Eleuterio Francisco Toro** was born on July 16, 1946, at Capitan Pastene, Chile. He started, in 1967, his career as Teacher of primary education at Victoria, Chile, continuing studies of mathematical pedagogy, obtaining the B.Sc. degree in pure mathematics in 1977 at the University of Warwick, UK, and in 1978 the M.Sc. degree in applied mathematics from University of Dundee, UK. He obtained the PhD degree in 1982 in computational mathematics from the University of Teesside, Middlesbrough UK. From 1983 until 2001, he was Lecturer and Senior Lecturer in computational fluid mechanics at Cranfield University, UK, and Professor of applied mathematics at the Manchester Metropolitan University. From 2002 to 2016, he was Full

Professor of numerical analysis at DICAM, University of Trento, Italy, from when he there is Emeritus Professor.

His research was and still is focused on the construction of computational methods for solving partial differential equations, thereby particularly dealing with the hyperbolic equations, as these of the shallow water equations. The ADER framework launched in 2001 allows for the construction of one-step, nonlinear numerical methods of arbitrary order of accuracy in both space and time. This method results in a huge efficiency gain, thereby increasing the power of mathematical modeling and simulation for solving practical problems in science and engineering. This technique is relevant in many applications including aero-acoustics, shock waves, tsunami wave propagation, meteorology, biology, and medicine. He is famous in the scientific community for having written two books dealing with Riemann solvers and the finite volume technology; the first, *Riemann solvers and numerical methods in fluid dynamics*, is dedicated to the solution of the Euler equations in gas dynamics. The second, *Shock-capturing methods for shallow free surface flows*, is devoted to the solution of the Saint Venant equations for water flows. The two books are supported by the NUMERICA library, a collection of source codes for teaching, research and practice, where the details of the methods presented in the books are explained in detail. The book readers are encouraged to download this library from the Web site of Prof. Toro: <https://eleuterotoro.com/>.

## 8.4 Application: Gate Maneuvers in Open Channels

### 8.4.1 Complete Gate Opening

Consider steady flow at a gate (Fig. 8.13), where subcritical approach flow (state  $L$ ) is transformed into supercritical flow<sup>1</sup> (state  $R$ ). Contraction effects are overlooked in the present shallow water analysis (Jain 2001). These were accounted for by Cozzolino et al. (2015) for both complete and partial gate openings.

If the gate is fully opened, the initial data correspond to the Riemann problem stated in Fig. 8.1, with  $U_L h_L = U_R h_R = \text{const.}$  as the initial discharge. Figure 8.2 shows the wave profile for a transcritical rarefaction after full gate opening. The computational example presented in Fig. 8.9 represents thus a full gate opening.

---

<sup>1</sup>We will analyze instantaneous (partial or full) sluice gate openings and closures for supercritical conditions downstream of the gate. Submerged flows are not considered; the gate acts thus as a control section in all cases.

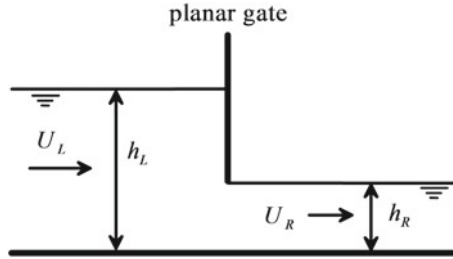


**Fig. 8.13** Planar gate in open channel forming a discontinuity between two uniform flow zones. Contraction effects are overlooked in the SWE analysis

#### 8.4.2 Partial Gate Opening

Consider initially steady gate flow as sketched in Fig. 8.14a, with subscripts  $u$  and  $R$  referring to the up- and downstream zones of the gate. For given values of  $h_u$  and  $h_R$ , the values of  $U_u$  and  $U_R$  are determined with the known initial discharge. For partial gate opening ( $w > h_R$  and  $w < h_L$ ) (Fig. 8.14b), a depression of depth  $h_d$  and velocity  $U_d$  is formed upstream of the gate, propagating in the upstream direction via a rarefaction wave. The unknowns in the upstream flow portion are thus  $h_d$ ,  $U_d$  and the velocity at the gate opening  $U_L$ . Across the rarefaction, one may write the identity

$$U_u + 2c_u = U_d + 2c_d. \quad (8.52)$$

Two additional equations are needed. One involves energy conservation across the gate

$$h_d + \frac{U_d^2}{2g} = w + \frac{U_L^2}{2g}, \quad (8.53)$$

while the other is the mass conservation equation

$$U_L w = U_d h_d. \quad (8.54)$$

Using Eqs. (8.54), (8.52) is rewritten as

$$U_u + 2c_u = \frac{w}{h_d} U_L + 2(gh_d)^{1/2}. \quad (8.55)$$

From Eq. (8.53), one gets with Eq. (8.54)

$$\frac{U_L^2}{2g} = h_d - w + \frac{U_d^2}{2g} = h_d - w + \frac{w^2}{h_d^2} \frac{U_L^2}{2g}, \quad (8.56)$$

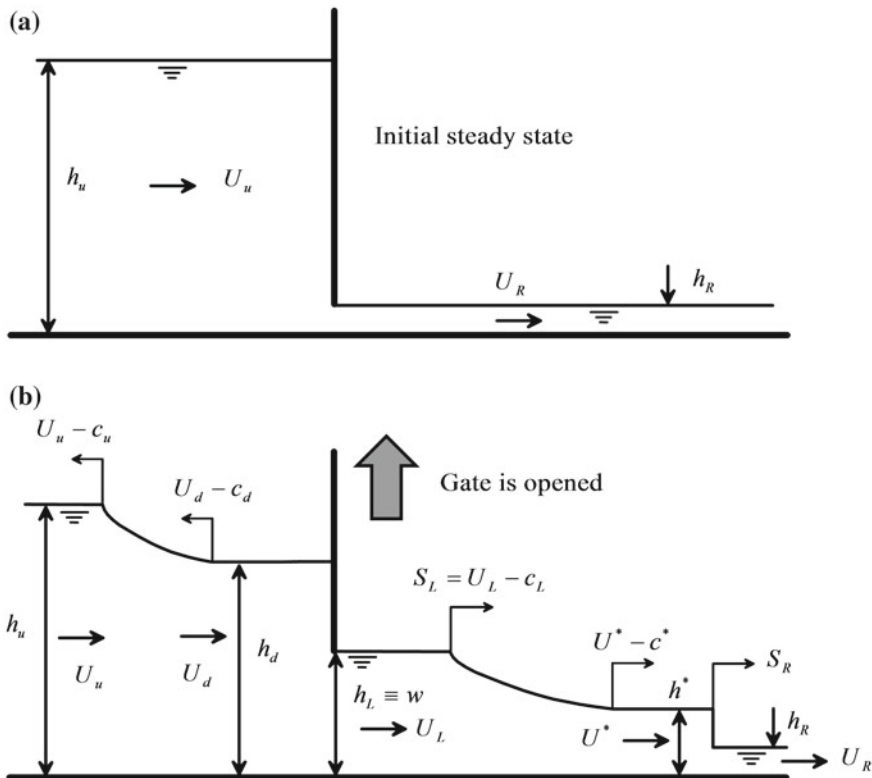


**Fig. 8.14** Partial gate opening **a** initial steady state, **b** generation of transient motion (flow downstream of the gate corresponds to case c of Fig. 8.3) (adapted from Montuori and Greco 1973)

or

$$U_L = [2g(h_d - w)]^{1/2} \left( 1 - \frac{w^2}{h_d^2} \right)^{-1/2}. \quad (8.57)$$

Inserting Eq. (8.57) into Eq. (8.55) yields the nonlinear implicit equation for  $h_d$

$$f(h_d) = w(2g)^{1/2}(h_d + w)^{-1/2} + 2(gh_d)^{1/2} - U_u - 2c_u = 0. \quad (8.58)$$

This is easily solved using the Newton–Raphson method. Once  $h_d$  is computed,  $U_L$  is determined from Eq. (8.57) and  $U_d$  from Eq. (8.54). In the downstream gate zone, a wave pattern as shown in Fig. 8.14b may be generated, involving a rarefaction and a shock wave. The solution of this flow portion corresponds essentially

to the computation of a Riemann problem with a right-going rarefaction wave and a right-going shock. Obviously, other wave patterns are in principle possible depending on the initial data of the Riemann problem posed on the right gate side. Montuori (1968) presents a notable discussion of possible wave solutions. The solution to the partial gate opening was implemented in a code, inserted in the file “*Partialgateopening.xls*”, available in Chap. 12. To use this code:

- (1) There must be a gate opening  $w > h_R$  because results are meaningless otherwise, given that it is assumed that a rarefaction wave is formed upstream of the gate.
- (2) The left wave in the Riemann problem downstream of the gate must be right going.

A computational example is summarized in Table 8.4, and the profiles downstream of the gate are plotted in Fig. 8.15. This type of solution was described by Jain (2001).

If the flow depth  $h_R$  is very shallow, the right wave may be a rarefaction wave instead of a shock (Fig. 8.16a). There is still another possible flow profile downstream of the gate, composed of two shocks (Fig. 8.16b). This situation occurs if  $w$  is not large as compared to  $h_R$ ; we consider it here for illustrative purposes. Suppose the limiting case  $h_L = h_R$ , with  $U_L > U_R$ . Equation (8.13) yields for a two-shock case if  $h_L = h_R$ ,

**Table 8.4** Example of partial gate opening. Initial discharge is  $0.5 \text{ m}^2/\text{s}$  and new gate opening  $w = 0.4 \text{ m}$

Flow	$h_u$ (m)	$U_u$ (m/s)	$h_d$ (m)	$U_d$ (m/s)	$U_L$ (m/s)
Upstream	1	0.5	0.645	1.733	2.795
	$h_R$ (m)	$U_R$ (m/s)	$h^*$ (m)	$U^*$ (m/s)	
Downstream	0.2	2.5	0.316	3.234	

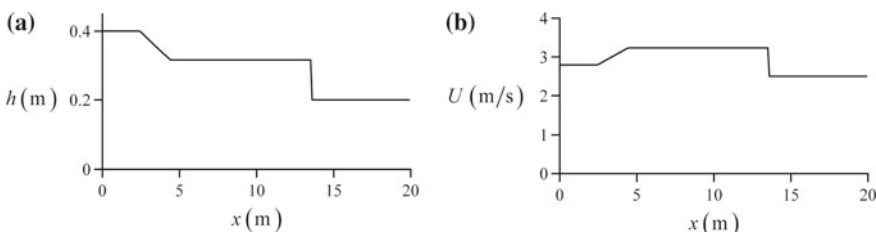


**Fig. 8.15** Riemann solution of partial gate opening test for flow downstream of the gate plane with **a** free surface profile  $h(x)$  and **b** depth-averaged velocity  $U(x)$ . Details see Table 8.4

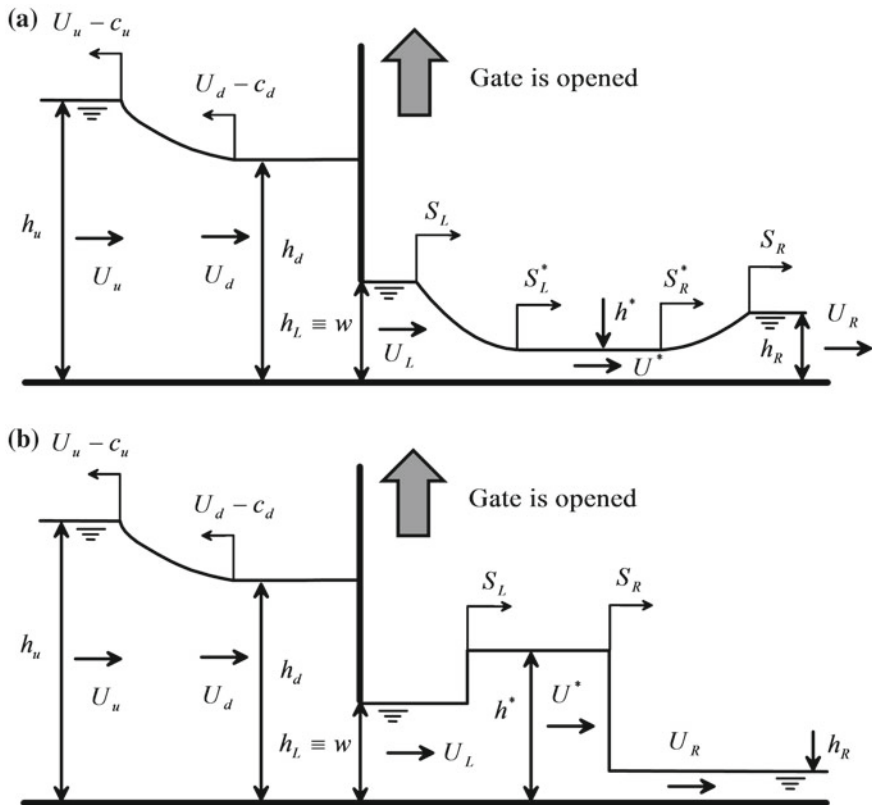


**Fig. 8.16** Partial gate opening **a** transient motion with two rarefactions beyond the gate, corresponding to case c in Fig. 8.4, **b** transient with two shocks beyond the gate, corresponding to case c in Fig. 8.5 (adapted from Montuori and Greco 1973)

**Table 8.5** Example of partial gate opening. Initial discharge is  $0.5 \text{ m}^2/\text{s}$  and new gate opening  $w = 0.25 \text{ m}$

Flow	$h_u$ (m)	$U_u$ (m/s)	$h_d$ (m)	$U_d$ (m/s)	$U_L$ (m/s)
Upstream	1	0.5	0.827	1.066	3.53
	$h_R$ (m)	$U_R$ (m/s)	$h^*$ (m)	$U^*$ (m/s)	
Downstream	0.2	2.5	0.307	3.185	

$$2(h^* - h_R) \left[ \frac{g}{2h^*h_R} (h^* + h_R) \right]^{1/2} = U_L - U_R. \quad (8.59)$$

Note that the right-hand side of Eq. (8.59) is positive; to have a compatible positive left-hand side, of necessity then  $h^* > h_R$ , implying that the two-shock

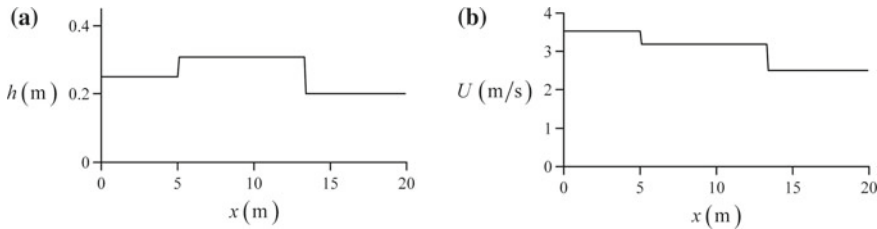


**Fig. 8.17** Riemann solution of partial gate opening test for flow downstream of the gate plane with **a** free surface profile  $h(x)$  and **b** depth-averaged velocity  $U(x)$ . Details see Table 8.5

assumed wave pattern, is the correct solution. Another simulation was conducted based on the example presented in Table 8.4, but using the smaller gate opening  $w = 0.25$  m. Results are summarized in Table 8.5, with the flow profiles downstream of the gate presented in Fig. 8.17.

#### 8.4.3 Complete Gate Closure

Consider the case of a complete gate closure (Fig. 8.18). Upstream of the gate, a shock wave traveling to the left, is formed. The unknowns in this portion of the computational domain are the velocity  $U_d$ , the flow depth  $h_d$ , and the surge velocity  $S$  (Jain 2001). By definition of gate closure,  $U_d = 0$ . Thus, the two remaining unknowns are determined using the mass and momentum conservation equations across the surge, e.g., the Rankine–Hugoniot jump conditions, which are, respectively,

$$h_u(U_u - S) = -h_dS, \quad (8.60)$$

$$S = U_u - \left[ \frac{gh_d}{2h_u} (h_u + h_d) \right]^{1/2}. \quad (8.61)$$

The solution of this system of equations entails no difficulty. On the downstream gate side, the flow solution admits two possible wave patterns. If the downstream Froude number is  $F_R < 2$ , the channel is wet beyond the gate and the water is static there, with a rarefaction wave traveling to the right (Fig. 8.18a). This case is computationally equivalent to the two-rarefaction Riemann problem for wet-bed conditions. However, if  $F_R > 2$ , the channel is dry beyond the gate, while there is still a rarefaction wave traveling to the right, yet of nonvanishing celerity at the wet-dry interface (Fig. 8.18b).

A computational example is presented in Fig. 8.19. The test data and the results are shown in Table 8.6. The first test case corresponds to a two-rarefaction Riemann problem with wet-bed conditions. The profiles for  $h(x)$  and  $U(x)$  at  $t = 3$  s are plotted in Fig. 8.19a, b only for  $x > 0$ , given that the rest of the profiles are

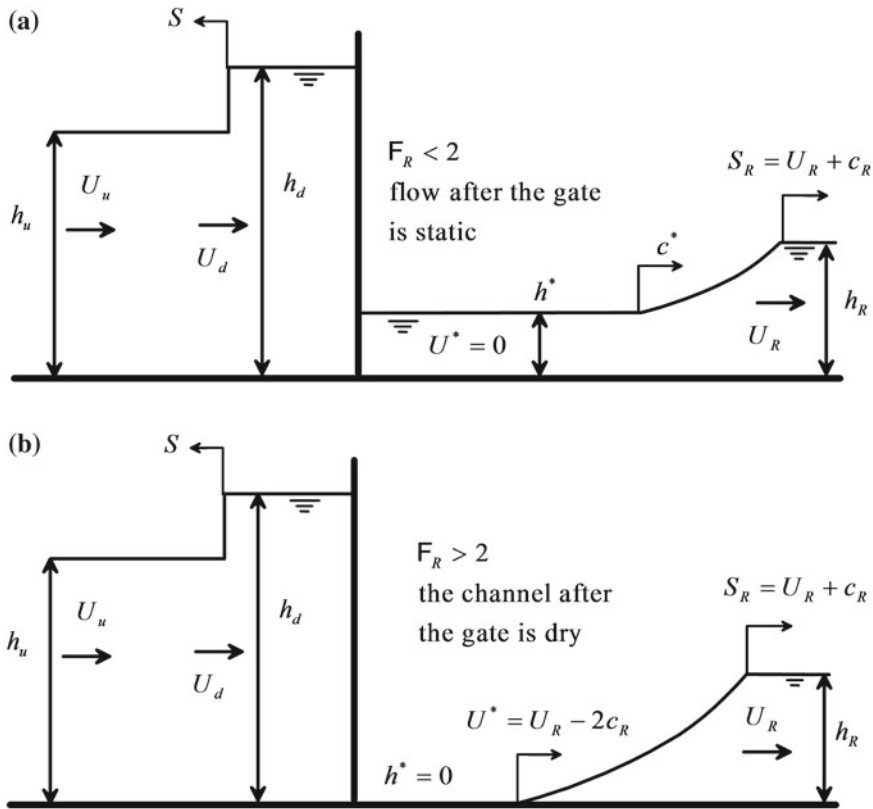
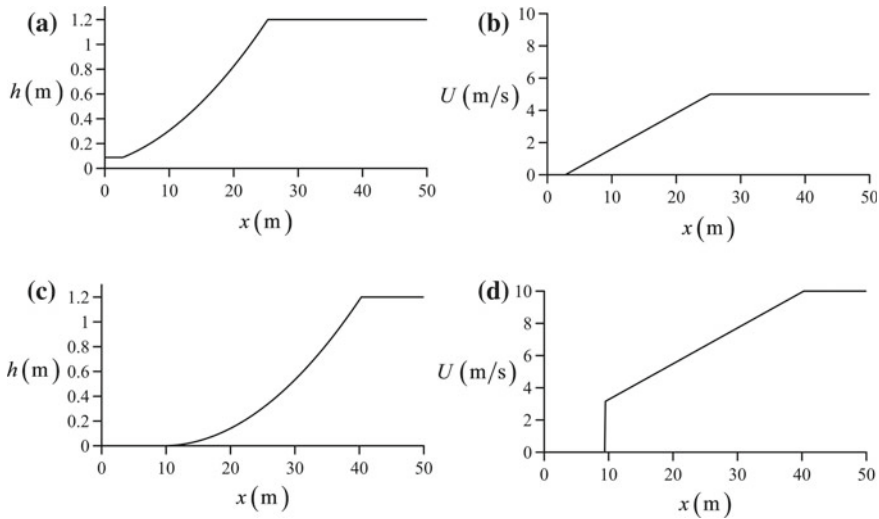


Fig. 8.18 Complete gate closure **a** wet bed beyond the gate, **b** dry bed beyond the gate

meaningless. The simulations were conducted with the wet-bed Riemann solver available on the file “*ExactRiemannSolver\_wetbed.xls*”. A second test was conducted by increasing the velocity at the tailwater section to produce a Froude number in excess of 2. A dry-bed two-rarefaction approach was used to model the flow, with the profiles for  $x > 0$  plotted in Fig. 8.19c, d. The results were generated with a dry-bed Riemann solver available on the file “*ExactRiemannSolver\_drybed.xls*”.

#### 8.4.4 Partial Gate Closure

For the case of a partial gate closure, a surge propagates in the upstream direction within the approach flow to the gate (Fig. 8.20). The unknowns in this flow portion are  $S$ ,  $h_d$ ,  $U_d$ , and  $U_L$ . The equations available are the continuity equation across the surge



**Fig. 8.19** Riemann solution for full gate closure test: flow downstream of the gate with **a, b** free surface profile  $h(x)$  and depth-averaged velocity  $U(x)$  for wet-bed conditions, **c, d** idem for dry-bed conditions. Details see Table 8.6

**Table 8.6** Examples of complete gate closure using the two-rarefaction Riemann problem

Test	$h_L$ (m)	$h_R$ (m)	$U_L$ (m/s)	$U_R$ (m/s)	$h^*$ (m)	$U^*$ (m/s)
Wet-bed	1.2	1.2	-5	5	0.088	0
Dry-bed	1.2	1.2	-10	10	0	3.138

$$h_u(U_u - S) = h_d(U_d - S), \quad (8.62)$$

the momentum equation across the surge

$$S = U_u - \left[ \frac{gh_d}{2h_u} (h_u + h_d) \right]^{1/2}, \quad (8.63)$$

conservation of energy at the gate

$$h_d + \frac{U_d^2}{2g} = w + \frac{U_L^2}{2g}, \quad (8.64)$$

and conservation of mass at the gate

$$U_L w = U_d h_d. \quad (8.65)$$

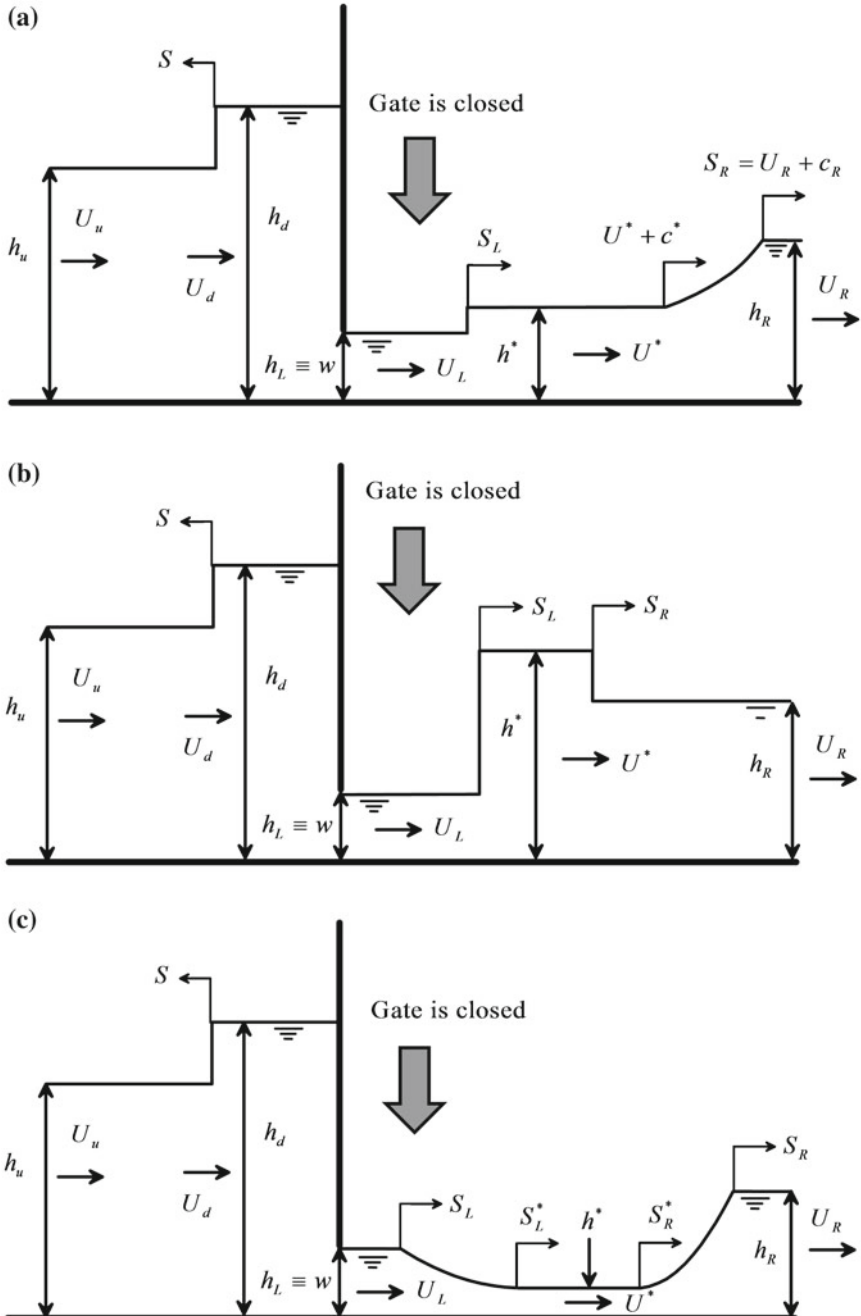


**Fig. 8.20** Partial gate closure **a** shock–rarefaction waves, see case c in Fig. 8.6, **b** two shock waves, see case c in Fig. 8.5, **c** two rarefaction waves, see case c in Fig. 8.4 (adapted from Montuori and Greco 1973)

Once this system of four equations and four unknowns is solved (Jain 2001), the flow downstream of the gate is computed as a Riemann problem. The case involving a shock wave followed by a rarefaction wave is plotted in Fig. 8.20a. Depending on the initial data of the Riemann problem, a number of wave profiles may be generated beyond the gate. The cases of two shocks and two rarefaction waves are sketched in Fig. 8.20b, c, respectively.

These scenarios are illustrated with a numerical example using the code available in “*ExactRiemannSolver\_wetbed.xls*”. Data for this example are taken from Jain (2001, example 7-6). The initial discharge is  $q_o = 7.92 \text{ m}^2/\text{s}$ ,  $h_R = 1 \text{ m}$ ,  $U_R = q_o/h_R = 7.92 \text{ m/s}$  and the gate opening is set to  $w = 0.7 \text{ m}$ . Solving the equations upstream of the gate yields  $U_L = 8.63 \text{ m/s}$  (Jain 2001). The downstream flow profiles for this test are plotted in Fig. 8.21a, b, and computations are summarized in Table 8.7. Note that the wave patterns involve a left shock and right rarefaction. Henceforth, we keep  $w$  fixed. Given that the gate acts as a control, flow conditions upstream of the gate remain unaltered for fixed  $w$ . Now, raise  $h_R$  up to 1.2 m, computing the corresponding  $U_R$  to satisfy the initial data. As observed from Figs. 8.21c, d and Table 8.7, the wave patterns in this case correspond to two shocks. If the analysis is repeated this time lowering  $h_R$  to 0.8 m, two rarefaction waves travel to the right of the gate (Fig. 8.21e, f and Table 8.7). As illustrated in this example, the treatment of the gate maneuvers within the context of a Riemann problem permits to identify all possible wave patterns without the need of preliminary assumptions.

#### 8.4.5 Comparison with Experiments

The experimental investigation by Montuori and Greco (1973) is used to test the overall quality of the theory presented against experiments. Two experiments are selected, with experimental data for the Riemann problem posed beyond the gate listed in Table 8.8, as well as visual observations reported with photographs by Montuori and Greco (1973). Computations of the star region values using the wet-bed Riemann solver are included in the same table. In the comparison undertaken below, the left conditions of the Riemann problem are taken as the experimental conditions at the new vena contracta after the gate movement. Thus, contraction effects are accounted for here.

The first experiment is reproduced computationally in Fig. 8.22. Wave results are plotted in Fig. 8.22 after 5 s of routing. Note that the experimental data for the Riemann problem produce computationally a two-shock wave pattern, in concordance with the visual observations by Montuori and Greco (1973). Table 8.9 compares the theory with available experimental measurements, indicating fair agreement.

The second experiment is reproduced computationally in Fig. 8.23. Wave results are plotted in Fig. 8.23 after 5 s of routing. The experimental data for the Riemann problem in this test produce computationally a shock–rarefaction wave pattern, in

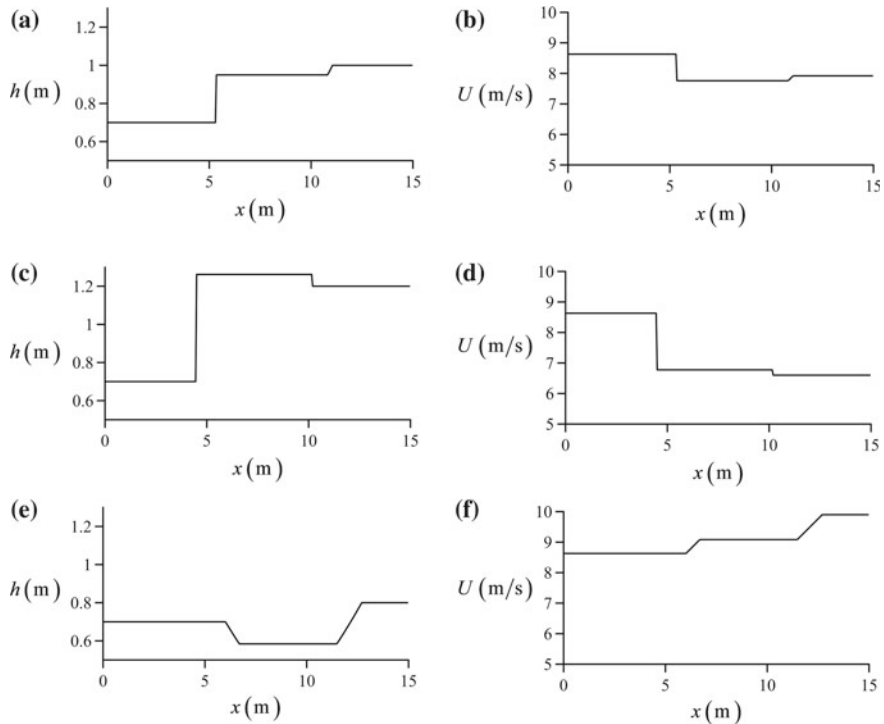


**Fig. 8.21** Partial gate closure. Generation of different wave patterns keeping  $w$  fixed and varying  $h_R$  (and  $U_R = q_o/h_R$ ). See Table 8.7 for test conditions of each plot

**Table 8.7** Examples of Riemann problems downstream of gate after partial gate closure

Test	Waves	$h_R$ (m)	$U_R$ (m/s)	$h^*$ (m)	$U^*$ (m/s)
Figure 8.21a, b	Shock–rarefaction	1	7.92	0.95	7.76
Figure 8.21c, d	Two shocks	1.2	6.6	1.26	6.77
Figure 8.21e, f	Two rarefactions	0.8	9.9	0.58	9.08

Test conditions are:  $q_o = 7.92 \text{ m}^2/\text{s}$ ,  $h_L = w = 0.7 \text{ m}$ ,  $U_L = 8.63 \text{ m/s}$ ,  $q_{new} = U_L w = 6.041 \text{ m}^2/\text{s}$

**Table 8.8** Experiments of Montuori and Greco (1973): data of Riemann problem beyond the gate and computed values of star region using wet-bed Riemann solver

Test	Wave pattern experimentally observed	$h_L$ (m)	$h_R$ (m)	$U_L$ (m/s)	$U_R$ (m/s)	$h^*$ (m)	$U^*$ (m/s)
Figure 8.22	Two bores	0.057	0.1	1.844	0.11	0.165	0.685
Figure 8.23	A bore followed by smooth wave	0.0248	0.093	2.513	1.955	0.073	1.733

Subscript  $L$  indicates conditions at the new vena contracta after gate movement, and  $R$  indicates tailwater conditions existing before moving the gate

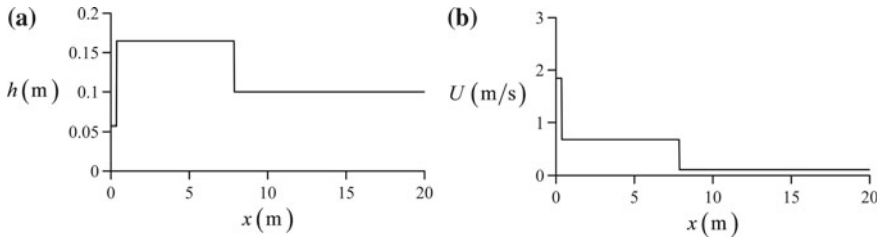


**Fig. 8.22** Computational reproduction of a two-shock wave pattern beyond a gate generated experimentally by Montuori and Greco (1973). For details, see Table 8.9

**Table 8.9** Comparison of theory and experiments by Montuori and Greco (1973) for the Riemann problem presented in Fig. 8.22

	$S_L$ (m/s)	$S_R$ (m/s)	$h^*$ (m)
Simulation	0.072	1.573	0.165
Experiment	0.1	1.45	0.165

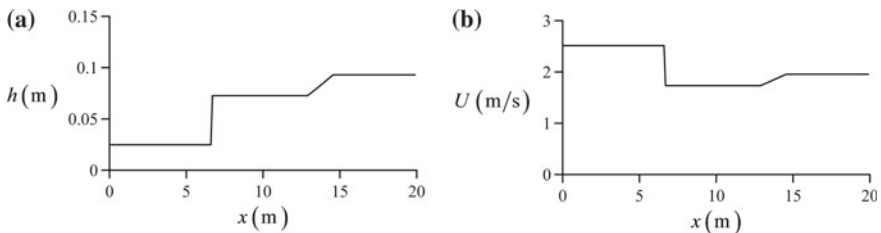


**Fig. 8.23** Computational reproduction of a shock–rarefaction wave pattern beyond a gate generated experimentally by Montuori and Greco (1973). For details, see Table 8.10

**Table 8.10** Comparison of theory and experiments by Montuori and Greco (1973) for the Riemann problem presented in Fig. 8.23

	$S_L$ (m/s)	$h^*$ (m)
Simulation	1.329	0.073
Experiment	1.45	0.065

concordance with the visual observations by Montuori and Greco (1973). A comparison of theory with the available experimental measurements is reported in Table 8.10, showing again fair agreement of the Riemann solution with experiments.

*Remark:* Lax entropy condition for shocks

While presenting surges and depression waves in Chap. 5, the usual case was explained, namely the shock as a discontinuous increase in depth and the rarefaction wave as a gradual depression in depth. In the literature, the depression shock (see wave propagation at rate  $S_L$  in Fig. 8.20a, for example) tends to be overlooked. While it is certainly true that it is not the usual case while describing surges of tidal origin, it is a realistic flow profile in the context of gate maneuvers in open channels. It was first described by Montuori and Greco (1973) based on conservation of mass and momentum and verified experimentally. In recent open channel flow books, it is an accepted solution (e.g. Fig. 8.20a) (Jain 2001 page 222; Jeppson 2011 page 920; Katopodes 2019 page 768). We will now demonstrate that the experiments of Montuori and Greco (1973) satisfy Lax' entropy condition, and thus, the depression shock of Fig. 8.23 is physically realistic.

Let the eigenvalues be

$$\lambda_1(\mathbf{U}) = U - (gh)^{1/2}, \quad \lambda_2(\mathbf{U}) = U + (gh)^{1/2}, \quad (8.66)$$

a discontinuity separating states  $\mathbf{U}_L$  and  $\mathbf{U}_R$  and propagating at speed  $S$  satisfies Lax entropy condition if there is a  $p$  index such that (LeVeque 2002, page 268)

$$\lambda_p(\mathbf{U}_L) > S > \lambda_p(\mathbf{U}_R). \quad (8.67)$$

In this case, the  $p$ -characteristics are impinging on the discontinuity, while the other characteristics are crossing it,

$$\begin{aligned} \lambda_i(\mathbf{U}_L) &< S & \text{and} & \lambda_i(\mathbf{U}_R) < S & \text{for } i < p, \\ \lambda_i(\mathbf{U}_L) &> S & \text{and} & \lambda_i(\mathbf{U}_R) > S & \text{for } i > p. \end{aligned} \quad (8.68)$$

In our case,  $p$  can be 1 or 2, so one of the following set of identities shall be verified by the depression shock:

*Conditions for  $p = 2$*

$$\begin{aligned} \lambda_2(\mathbf{U}_L) &> S > \lambda_2(\mathbf{U}_R), \\ \lambda_1(\mathbf{U}_L) &< S, \\ \lambda_1(\mathbf{U}_R) &< S. \end{aligned} \quad (8.69)$$

It can be easily verified that this set of statements is coherent with Fig. 7.3 and Eq. (7.22).

*Conditions for  $p = 1$*

$$\begin{aligned} \lambda_1(\mathbf{U}_L) &> S > \lambda_1(\mathbf{U}_R), \\ \lambda_2(\mathbf{U}_L) &> S, \\ \lambda_2(\mathbf{U}_R) &> S. \end{aligned} \quad (8.70)$$

**Table 8.11** Verification of Lax entropy condition for depression shock in Fig. 8.23 ( $S_L = 1.329$  m/s), using data in Table 8.8

Test	$\lambda_1(\mathbf{U}_L)$ (m/s)	$\lambda_1(\mathbf{U}^*)$ (m)	$\lambda_2(\mathbf{U}_L)$ (m/s)	$\lambda_2(\mathbf{U}^*)$ (m/s)
Figure 8.23	2.02	0.889	3.007	2.578

This is the set of identities verified by the depression shock in Fig. 8.23. To analyze this shock, the left state is that of the Riemann problem and the right state corresponds to the star region. Therefore, we will check the identities

$$\begin{aligned}\lambda_1(\mathbf{U}_L) &> S_L > \lambda_1(\mathbf{U}^*), \\ \lambda_2(\mathbf{U}_L) &> S_L, \\ \lambda_2(\mathbf{U}^*) &> S_L.\end{aligned}. \quad (8.71)$$

This work is accomplished in Table 8.11 using previous information of Table 8.8, resulting that Eq. (8.71) is verified, and therefore, the depression shock in Fig. 8.23 is a correct physical solution, as also observed experimentally by Montuori and Greco (1973).

The described exact solutions apply to analyze instantaneous gate operations. If the gate maneuvers are not instantaneous, or if source terms are introduced into the SWE to account, for example, for frictional effects, the theory described is invalid and a numerical solution is then required.

## References

- Cozzolino, L., Cimorelli, L., Covelli, C., Della Morte, R., & Pianese, D. (2015). The analytic solution of the shallow-water equations with partially open sluice-gates: The dam-break problem. *Advances in Water Resources*, 80(6), 90–102.
- Godunov, S. K. (1959). A difference method for numerical calculation of discontinuous solutions of the equations of hydrodynamics. *Matematicheskiy Sbornik*, 47(3), 271–306 (in Russian).
- Guinot, V. (2003). *Godunov-type schemes: An introduction for Engineers*. Amsterdam, Boston: Elsevier science.
- Henderson, F. M. (1966). *Open channel flow*. New York: MacMillan Co.
- Hoffman, J. D. (2001). *Numerical methods for engineers and scientists* (2nd ed.). New York: Marcel Dekker.
- Jain, S. C. (2001). *Open channel flow*. New York: Wiley.
- Jeppson, R. (2011). *Open channel flow: Numerical methods and computer applications*. CRC Press, Taylor and Francis, New York.
- Katopodes, N. D. (2019). *Free surface flow: Computational methods*. Oxford, UK: Butterworth-Heinemann.
- LeVeque, R. J. (2002). *Finite volume methods for hyperbolic problems*. New York: Cambridge University Press.
- Montuori, C. (1968). Brusca immissione di una corrente ipercritica a tergo di altra preesistente [Sudden perturbation of a supercritical flow over the pre-existing flow]. *L'Energia Elettrica*, 45(3), 174–187 (in Italian).

- Montuori, C., & Greco, V. (1973). Fenomeno di moto vario a valle di una paratoia piana [Varied flow phenomena beyond a plane gate]. *L'Energia Elettrica*, 50(2), 73–88 (in Italian).
- Riemann, B. (1860). Über die Fortpflanzung ebener Luftwellen von endlicher Schwingungsweite [On the propagation of plane air waves of finite amplitude]. *Abhandlungen der Königlichen Gesellschaft der Wissenschaften zu Göttingen*, 8, 43–65 (in German).
- Roberts, S. (2013). *Numerical solution of conservation laws applied to the shallow water equations*. Lecture notes. Australia: Mathematical Sciences Institute, Australian National University.
- Stoker, J. J. (1957). *Water waves: The mathematical theory with applications*. New York: Interscience publishers.
- Toro, E. F. (1997). *Riemann solvers and numerical methods for fluid dynamics*. London: Springer.
- Toro, E. F. (2001). *Shock-capturing methods for free-surface shallow flows*. Singapore: Wiley.
- Zoppou, C., & Roberts, S. (2003). Explicit schemes for dam-break simulations. *Journal of Hydraulic Engineering*, 129(1), 11–34.

# Chapter 9

## Finite Volume Methods



### 9.1 Introduction

The one-dimensional shallow water equations (SWE), or Saint-Venant equations, are a system of nonlinear hyperbolic conservation laws (Toro 2001). The mathematical meaning behind these “surnames” linked to the development of Saint-Venant is clearly elucidated by the definitions (Karni 2011; Vazquez-Cendón 2015):

Conservation is a fundamental principle of the physical world. Matter may move around and redistribute but it does not appear or disappear. Hyperbolicity means that news that happen at a given point A, take time before they may affect affairs at another point B. Nonlinear means the manner in which news propagate depends on what type of news it is. This makes the subject of nonlinear conservation laws fascinating, rich and challenging to study.

The SWE are solved in this chapter using finite volume methods for hyperbolic conservation laws, where the space–time plane is divided into control volumes or simply finite volumes. The presentation focuses on Godunov-type methods, in which the solution of a number of local Riemann problems between each pair of adjacent cells is used. The constructed numerical method satisfies locally the conservation laws, so that wave propagation information is generated at the cell interfaces. This wave information is used to construct the numerical scheme and then evolve the solution in time, representing therefore an upwind scheme. First, Godunov-type methods are stated for the homogeneous SWE, after which approximate Riemann solvers are presented. The treatment of dry beds is discussed, as well as the inclusion of source terms including the discretization of the bed slope term to produce a well-balanced scheme. The treatment of bed friction is explained in detail. The one-sided first-order method is presented, as well as the second-order Total Variation Diminishing (TVD) MUSCL (Monotonic Upstream Centered Schemes for Conservation Laws)-Hancock scheme. Numerical computations for selected test cases are finally compared with exact solutions and experimental observations to highlight the quality of computations.

## 9.2 Godunov-Type Schemes

### 9.2.1 Conservative Formula

The SWE are written in vector conservative form as

$$\frac{\partial \mathbf{U}}{\partial t} + \frac{\partial \mathbf{F}}{\partial x} = \mathbf{S}. \quad (9.1)$$

Here,  $\mathbf{U}$  is the vector of the conserved variables,  $\mathbf{F}$  the flux vector and  $\mathbf{S}$  the source term vector, given for a rectangular channel by

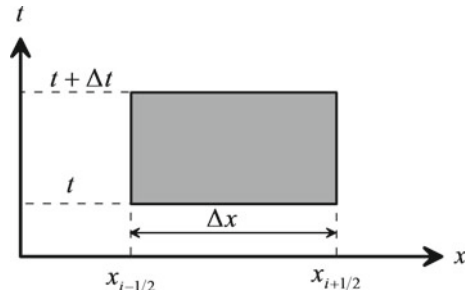
$$\mathbf{U} = \begin{pmatrix} h \\ hU \end{pmatrix}, \quad \mathbf{F} = \begin{pmatrix} hU \\ hU^2 + \frac{1}{2}gh^2 \end{pmatrix}, \quad \mathbf{S} = \begin{pmatrix} 0 \\ -gh \frac{\partial z_b}{\partial x} - ghS_f \end{pmatrix}, \quad (9.2)$$

with  $h$  as the water depth,  $U$  the depth-averaged velocity,  $z_b$  the bed elevation,  $g$  the gravity acceleration and  $S_f$  the friction slope. The differential Eq. (9.1) is valid in zones of the computational domain with smooth or continuous solutions, but it does not apply at discontinuous portions as shocks. Therefore, Eq. (9.1) is integrated over a control volume in the  $x$ - $t$  plane, resulting in

$$\iint \left( \frac{\partial \mathbf{U}}{\partial t} + \frac{\partial \mathbf{F}}{\partial x} \right) dx dt = \iint \mathbf{S} dx dt. \quad (9.3)$$

The integral Eq. (9.3) allows for the computation of both continuous and discontinuous solutions. It is the fundamental relation of the finite volume method. For the rectangular control volume in the  $x$ - $t$  plane depicted in Fig. 9.1, one can write (Toro 2001, 2009)

**Fig. 9.1** Control volume in  $x$ - $t$  plane



$$\int_t^{t+\Delta t} \int_{x_{i-1/2}}^{x_{i+1/2}} \left( \frac{\partial \mathbf{U}}{\partial t} + \frac{\partial \mathbf{F}}{\partial x} \right) dx dt = \int_{x_{i-1/2}}^{x_{i+1/2}} dx \int_t^{t+\Delta t} \frac{\partial \mathbf{U}}{\partial t} dt + \int_t^{t+\Delta t} dt \int_{x_{i-1/2}}^{x_{i+1/2}} \frac{\partial \mathbf{F}}{\partial x} dx = \int_{x_{i-1/2}}^{x_{i+1/2}} \int_t^{t+\Delta t} \mathbf{S} dx dt. \quad (9.4)$$

Here,  $i$  is the cell index in the  $x$ -direction, and  $i + 1/2$  the interface between cells  $i$  and  $i + 1$ . Equation (9.4) generates after elementary integration (Toro 2001, 2009)

$$\begin{aligned} & \int_{x_{i-1/2}}^{x_{i+1/2}} [\mathbf{U}(x, t + \Delta t) - \mathbf{U}(x, t)] dx + \int_t^{t+\Delta t} [\mathbf{F}(x_{i+1/2}, t) - \mathbf{F}(x_{i-1/2}, t)] dt \\ &= \int_{x_{i-1/2}}^{x_{i+1/2}} \int_t^{t+\Delta t} \mathbf{S} dx dt. \end{aligned} \quad (9.5)$$

Let the temporal and spatial average values be defined as

$$\begin{aligned} \mathbf{F}_{i+1/2} &= \frac{1}{\Delta t} \int_t^{t+\Delta t} \mathbf{F}(x_{i+1/2}, t) dt, \\ \mathbf{F}_{i-1/2} &= \frac{1}{\Delta t} \int_t^{t+\Delta t} \mathbf{F}(x_{i-1/2}, t) dt, \\ \mathbf{U}_i^{k+1} &= \frac{1}{\Delta x} \int_{x_{i-1/2}}^{x_{i-1/2} + \Delta x} \mathbf{U}(x, t + \Delta t) dx, \\ \mathbf{U}_i^k &= \frac{1}{\Delta x} \int_{x_{i-1/2}}^{x_{i-1/2} + \Delta x} \mathbf{U}(x, t) dx, \\ \mathbf{S}_i &= \frac{1}{\Delta x \Delta t} \int_{x_{i-1/2}}^{x_{i+1/2}} \int_t^{t+\Delta t} \mathbf{S} dx dt. \end{aligned} \quad (9.6)$$

Inserting Eq. (9.6) into Eq. (9.5) results in the exact conservative formula

$$\mathbf{U}_i^{k+1} = \mathbf{U}_i^k - \frac{\Delta t}{\Delta x} (\mathbf{F}_{i+1/2} - \mathbf{F}_{i-1/2}) + \Delta t \mathbf{S}_i. \quad (9.7)$$

This is the fundamental equation of the schemes to be presented here. The computational domain in the finite volume method is divided into a number of control

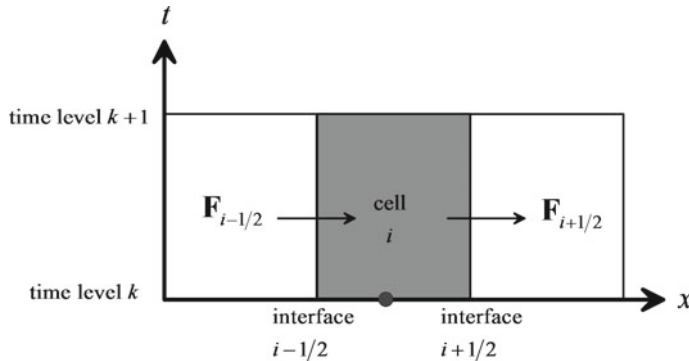


**Fig. 9.2** Intercell fluxes

volumes in the  $x$ - $t$  plane (Fig. 9.2), where Eq. (9.7) is applied. Here,  $\mathbf{F}_{i+1/2}$  is the numerical flux across the interface between cells  $i$  and  $i + 1$ . No numerical approximations are introduced in Eq. (9.7), although it looks like a finite-difference equation. Until stating the contrary, the homogeneous version of the SWE is focused by dropping the source terms, e.g., setting  $\mathbf{S}_i = \mathbf{0}$  in Eq. (9.7).

### 9.2.2 *Conservative Property: Definition of Numerical Discharge*

Note that in the conservative formula (9.7), the flux leaving cell  $i$  through the interface  $i + 1/2$  is identical to the flux entering into cell  $i + 1$  across this common interface. Let us write the conservative formula for updating the conserved variables at cell  $i - 1$ ,

$$\mathbf{U}_{i-1}^{k+1} = \mathbf{U}_{i-1}^k - \frac{\Delta t}{\Delta x} (\mathbf{F}_{i-1/2} - \mathbf{F}_{i-3/2}). \quad (9.8)$$

Summing it with Eq. (9.7) produces, with  $\mathbf{S}_i = \mathbf{0}$ ,

$$\mathbf{U}_i^{k+1} + \mathbf{U}_{i-1}^{k+1} = \mathbf{U}_i^k + \mathbf{U}_{i-1}^k - \frac{\Delta t}{\Delta x} (\mathbf{F}_{i+1/2} - \mathbf{F}_{i-3/2}). \quad (9.9)$$

It indicates that the total variation of  $\mathbf{U}$  is determined by the fluxes entering and leaving the extreme interfaces of the block formed by the adjacent cells  $i - 1$  and  $i$ . If the computational domain is divided into  $N$  cells, the summation of the updating equation for all the cells yields

$$\sum_{i=1}^N \mathbf{U}_i^{k+1} = \sum_{i=1}^N \mathbf{U}_i^k - \frac{\Delta t}{\Delta x} (\mathbf{F}_{N+1/2} - \mathbf{F}_{1/2}). \quad (9.10)$$

In this case, the total variation of  $\mathbf{U}$  in the computational domain is determined by the fluxes entering and leaving the boundary sections. This is the so-called conservative property (Roache 1972; Toro 1992, 2001; LeVeque 1992, 2002; Vazquez-Cendón 2015).

The numerical discharge is the first component of the numerical flux vector, e.g.,

$$q_{i+1/2} = \mathbf{F}_{i+1/2}(1) = \frac{1}{\Delta t} \int_t^{t+\Delta t} q(x_{i+1/2}, t) dt, \quad (9.11)$$

corresponding to a time average of the discharge crossing the interface  $i + 1/2$ . This definition of discharge satisfies the conservative property, for the reasons stated above. However, the numerical discharge can also be defined as the second component of the vector  $\mathbf{U}$ ; it is a spatial average value at the time level  $k + 1$ ,

$$q_i^{k+1} = \mathbf{U}_i^{k+1}(2) = \frac{1}{\Delta x} \int_{x_{i-1/2}}^{x_{i-1/2} + \Delta x} q(x, t + \Delta t) dx. \quad (9.12)$$

This definition of the numerical discharge does not satisfy the conservative property, however. Whether Eq. (9.11) or (9.12) for the numerical discharge is used to represent the true physical discharge is open to debate. In some steady flow problems ( $q = \text{const.}$ ), like the hydraulic jump, the steady-state solution generated by the SWE using certain numerical schemes for transient computations experience unphysical jumps in  $q_i^{k+1}$ , whereas  $q_{i+1/2}$  attains a constant steady value due to the conservative property (Ying and Wang 2008). This last definition of numerical discharge may be then more useful to approximate the true physical discharge (Ying and Wang 2008). In practice, computational schemes are not affected by the choice; it is only a matter on which variable is taken as the output numerical discharge once the solution is determined.

### 9.2.3 Godunov Upwind Numerical Flux

The conservative Eq. (9.7) with  $\mathbf{S}_i = \mathbf{0}$  applies to update the solution of the space-averaged values  $\mathbf{U}_i$  once the numerical flux  $\mathbf{F}_{i+1/2}$  is estimated. This step transforms the exact Eq. (9.7) approximate for a particular computation. The exact solution  $\mathbf{U}(x, t)$  within a cell can be written in the form of a Taylor series as

$$\mathbf{U}(x) = \mathbf{U}(x_i) + (x - x_i) \left( \frac{\partial \mathbf{U}}{\partial x} \right)_i + \frac{(x - x_i)^2}{2} \left( \frac{\partial^2 \mathbf{U}}{\partial x^2} \right)_i + \dots \quad (9.13)$$

In the Godunov upwind method, the actual solution  $\mathbf{U}(x)$  at time  $t$  is approximated by the space-averaged values within each cell (Fig. 9.3)

$$\mathbf{U}(x) = \mathbf{U}(x_i) = \mathbf{U}_i. \quad (9.14)$$

The piecewise constant data representations produce a scheme first-order accurate in space and time. Between each two adjacent cells, a discontinuity in  $\mathbf{U}$  is formed generating a sequence of local Riemann problems along the computational domain (Fig. 9.4). Godunov-type methods incorporate the solution of the Riemann problem (exact or approximate) into the conservative formula

$$\mathbf{U}_i^{k+1} = \mathbf{U}_i^k - \frac{\Delta t}{\Delta x} (\mathbf{F}_{i+1/2} - \mathbf{F}_{i-1/2}). \quad (9.15)$$

**Fig. 9.3** Cell-averaged values  $\mathbf{U}_i$  as approximation of the exact solution  $\mathbf{U}(x)$  at time  $t$ . The plot represents the typical distribution of a single component of  $\mathbf{U} = (U_1, U_2)^T$

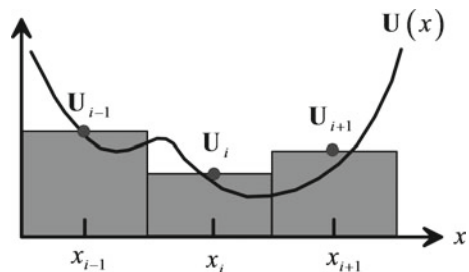
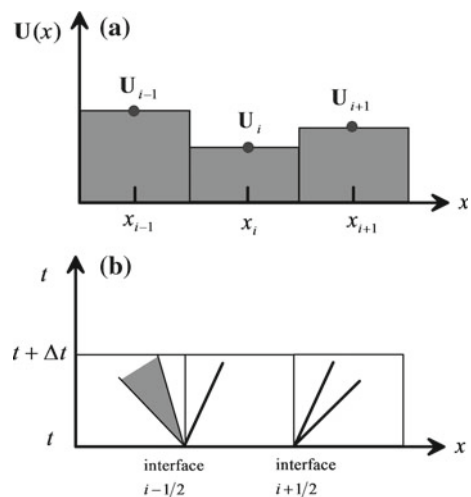


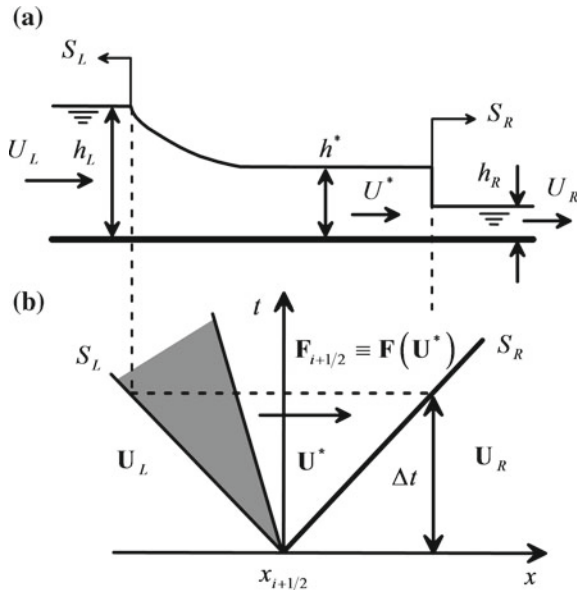
**Fig. 9.4** Godunov upwind method. **a** Piecewise constant data representation and **b** local Riemann problems formed along computational domain



Consider two initial states  $\mathbf{U}_L$  and  $\mathbf{U}_R$  at a generic interface  $i + 1/2$  between cells  $i$  and  $i + 1$ . This is by definition a local Riemann problem, from which a number of wave patterns may result. The typical case with a left-going rarefaction wave and right-going shock is presented in Fig. 9.5. The shock and rarefaction waves propagate with signal speeds  $S_R$  and  $S_L$ , respectively. The exact Riemann solution presented in Chap. 8 thus applies here, taking the role of a component of the numerical scheme. The complete Riemann solution is constructed assembling rarefaction and shock waves. Thus, it is noted that the solution of the Riemann problem is self-similar, e.g.,  $\mathbf{U}_{i+1/2}(x/t)$ . At the original position of the discontinuity ( $x = 0$ ), the solution of the Riemann problem is thus independent of  $t$  and therefore steady. The constant state region behind the shock front (star region) depicted in Fig. 9.5 is denoted as  $\mathbf{U}^*$ . The numerical flux crossing the original discontinuity at  $x = x_{i+1/2}$  is  $\mathbf{F}_{i+1/2}$ , which is needed to apply Eq. (9.15). The star region in the Riemann problem is a steady-state zone where the conserved variables are  $\mathbf{U}^*$ . This is part of the total (local) Riemann solution  $\mathbf{U}_{i+1/2}$ . Therefore, the numerical flux crossing the  $t$ -axis in the Riemann problem is also a constant, so that the intercell flux is exactly evaluated based on the Riemann solution at  $x = x_{i+1/2}$  as

$$\begin{aligned}\mathbf{F}_{i+1/2} &= \underbrace{\frac{1}{\Delta t} \int_{t_k}^{t_{k+1}} \mathbf{F}(x = x_{i+1/2}, t) dt}_{\text{global system of reference}} = \underbrace{\frac{1}{\Delta t} \int_0^{\Delta t} \mathbf{F}(x = 0, t) dt}_{\text{local system of reference}} \\ &= \mathbf{F}(x = 0) = \mathbf{F}[\mathbf{U}_{i+1/2}(x = 0)].\end{aligned}\quad (9.16)$$

**Fig. 9.5** Riemann problem solution at interface  $i + 1/2$  for left-going rarefaction wave and right-going shock under subcritical flow. **a** Free surface profile, **b**  $x$ - $t$  plane



This is the Godunov upwind numerical flux, namely the physical flux function evaluated using the solution of the Riemann problem at the location of the interface in question. Note that in local coordinates, the origin of the discontinuity is taken at  $x = 0$ .

For the case depicted in Fig. 9.5, the vector  $\mathbf{U}_{i+1/2}(x = 0)$  is  $\mathbf{U}^*$ . Thus,

$$\mathbf{F}_{i+1/2} \equiv \mathbf{F}(\mathbf{U}^*). \quad (9.17)$$

The value of  $\mathbf{U}^*$  is determined solving the exact Riemann problem for wet-bed conditions. If the left rarefaction wave crosses the  $t$ -axis, critical flow occurs along it, producing the values of  $c$  and  $U$  after setting  $dx/dt = U - c = 0$  (Toro 2001),

$$c_c = (gh_c)^{1/2} = U_c = \frac{1}{3}(U_L + 2c_L). \quad (9.18)$$

The critical depth  $h_c$  is thus from Eq. (9.18)

$$h_c = \frac{1}{9g}(U_L + 2c_L)^2. \quad (9.19)$$

Using Eq. (9.18), the numerical (critical) flux is then

$$\mathbf{F}_{i+1/2} = \mathbf{F}(\mathbf{U}_c) = \begin{pmatrix} h_c U_c \\ h_c U_c^2 + \frac{1}{2}gh_c^2 \end{pmatrix} = \begin{pmatrix} g^{1/2}h_c^{3/2} \\ \frac{3}{2}gh_c^2 \end{pmatrix}. \quad (9.20)$$

This is also a steady vector. For a right-going rarefaction the flow is simply negative. Thus, critical flow is obtained setting  $dx/dt = U + c = 0$ , resulting in (Toro 1992, 2001)

$$c_c = (gh_c)^{1/2} = -U_c = \frac{1}{3}(-U_R + 2c_R), \quad (9.21)$$

with the critical depth  $h_c$  given by

$$h_c = \frac{1}{9g}(-U_R + 2c_R)^2. \quad (9.22)$$

The numerical (critical) flux is then

$$\mathbf{F}_{i+1/2} = \mathbf{F}(\mathbf{U}_c) = \begin{pmatrix} h_c U_c \\ h_c U_c^2 + \frac{1}{2}gh_c^2 \end{pmatrix} = \begin{pmatrix} -g^{1/2}h_c^{3/2} \\ \frac{3}{2}gh_c^2 \end{pmatrix}, \quad (9.23)$$

which is obviously identical to Eq. (9.20) but with a flow reversal. If the left-state values reach the  $t$ -axis, the numerical flux is

$$\mathbf{F}_{i+1/2} = \mathbf{F}(\mathbf{U}_L) = \begin{pmatrix} h_L U_L \\ h_L U_L^2 + \frac{1}{2} g h_L^2 \end{pmatrix}. \quad (9.24)$$

Likewise, if the right-state values are propagated to the  $t$ -axis

$$\mathbf{F}_{i+1/2} = \mathbf{F}(\mathbf{U}_R) = \begin{pmatrix} h_R U_R \\ h_R U_R^2 + \frac{1}{2} g h_R^2 \end{pmatrix}. \quad (9.25)$$

The solution of the Riemann problem may be conducted exactly, as described here, or approximately, based on a simplified representation of the wave structure. A summary of all possible wave patterns is presented in Chap. 8 (see Figs. 8.3-8.6 and Table 8.1), as well as a discussion of the possible dry-bed cases. This method, first-order accurate in both space and time, is essentially the Godunov first-order upwind method (Godunov 1959). In this method, the waves computed at each interface satisfy locally the conservation equations, and this wave propagation information generated is used to evolve the solution in time, and thus, the numerical method constructed is of upwind type. High-order accuracy is sometimes needed (Harten 1983; Sweby 1984), and to obtain second-order accuracy, data representation within a cell must be changed, using linear approximations.

### 9.2.4 Stability Condition

Consider the right wave from the Riemann problem formed at interface  $i - 1/2$  and the left wave from Riemann problem formed at interface  $i + 1/2$ , both propagating within cell  $i$  (Fig. 9.6). Consider that the wave of maximum speed  $S_{\max}$  within the data is the left wave emanating from interface  $i + 1/2$ . For stability of the explicit Godunov scheme, the Courant–Friedrichs–Lewy number  $\text{CFL}$  must be limited. The time step  $\Delta t$  is determined at time level  $k$  using the equation

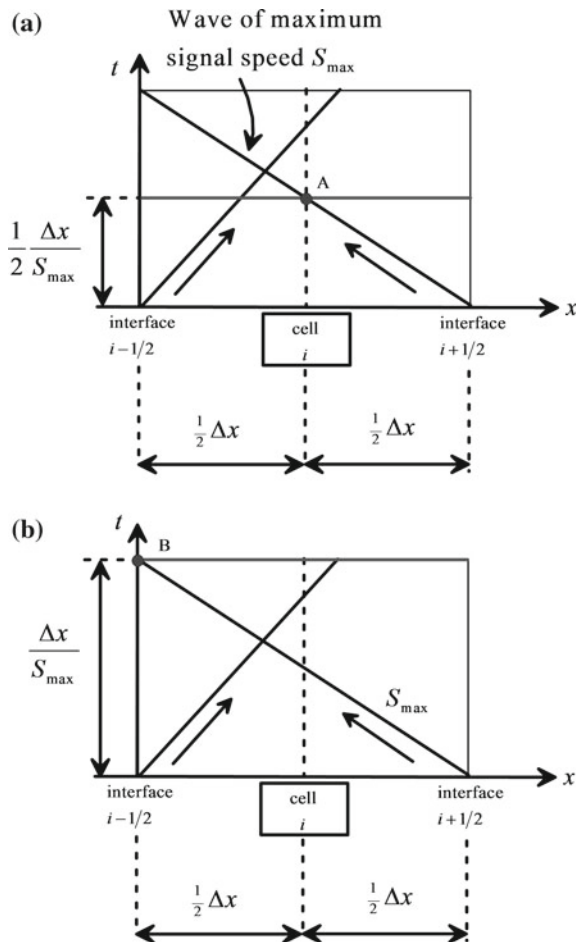
$$\Delta t = \frac{\Delta x}{S_{\max}} \text{CFL}. \quad (9.26)$$

At first glance, stability of the scheme may be thought to be imposed by avoiding the interaction of waves within a cell (Fig. 9.6a). The limiting time step is thus given by  $\text{CFL} = 1/2$ , resulting in

$$\Delta t = \frac{1}{2} \frac{\Delta x}{S_{\max}}. \quad (9.27)$$

This time step avoids that during time  $\Delta t$ , the fastest signal crosses more than half of the cell width (see point A in Fig. 9.6a). However, a careful inspection of the conservative Eq. (9.15) and the Godunov numerical flux Eq. (9.16) reveal that computations are only a function of the numerical flux  $\mathbf{F}_{i+1/2}$ , which, in turn, is not a

**Fig. 9.6** Propagation of waves in Godunov scheme with  $\text{CFL} = \mathbf{a}$  1/2 there is no wave interaction within the cell, **b** 1; there is wave interaction within the cell, yet the Riemann problem at interface  $i + 1/2$ , from which the wave of maximum speed  $S_{\max}$  ensues, does not influence the state at interface  $i - 1/2$ , and, thus, the numerical flux  $\mathbf{F}_{i-1/2}$  resulting from the Riemann problem there is not contaminated



function of the entire Riemann solution, but rather of the particular value at  $x_{i+1/2}$ . Thus, the detailed Riemann solution is not important at all, and wave interaction within a cell can be permitted as long as the waves originating from a discontinuity are not affecting the solution of the Riemann problem at the adjacent discontinuities. The stability condition of the scheme is thus  $\text{CFL} = 1$ , providing a maximum time step of (Fig. 9.6b, point B)

$$\Delta t = \frac{\Delta x}{S_{\max}}. \quad (9.28)$$

In practice,  $\text{CFL} = 0.9$  is usually adopted. One may estimate  $S_{\max}$  using the eigenvalues available at time  $k$ , e.g.,

$$\Delta t = \frac{\Delta x}{S_{\max}} \text{CFL} = \frac{\Delta x}{\max \left[ |U_i^k| + (gh_i^k)^{1/2} \right]} \text{CFL}. \quad (9.29)$$

Under the presence of dry fronts, whose speeds are much faster than the eigenvalues, the scheme may turn unstable, so care is required. In these cases, a lower value of CFL may be necessary to produce stable results.



**Sergei Konstantinovich Godunov** was born on July 17, 1929, at Moscow. He was from 1946 to 1951 at the Department of Mechanics and Mathematics of the Moscow State University, from where he obtained in 1951 the M.S. diploma. He became in 1954 Candidate (Ph.D.), and in 1965 Doctor of Physical and Mathematical Sciences D.Sc. He was elected Corresponding Member of the USSR Academy of Sciences in 1976, and Member of the Russian Academy of Sciences in 1994. In 1997, he was awarded Honorary Professor at the University of Michigan, Ann Arbor, MI. He was further awarded the State Lenin Prize in 1959, the A. N. Krylov Prize in 1972, and in 1993 the M. A. Lavrentiev Prize.

His most influential work is in the area of applied and numerical mathematics, with a major impact on science and engineering, particularly in the development of methodologies used in computational fluid dynamics (CFD). His scheme is a conservative method for solving partial differential equations. Therein, the conservative variables are considered as piecewise constant over the mesh cells at each time step, and the time evolution is determined by the exact solution of the Riemann (shock tube) problem at the intercell

boundaries. His theorem formulated in 1959 states that linear numerical schemes for solving partial differential equations, having the property of not generating new extrema (monotone scheme), can be at most first-order accuracy.

He was from 1951–1953 Scientific Researcher at the Steklov Institute of Mathematics (Moscow), from 1953–1962 Scientific Researcher at the Keldysh Institute of Applied Mathematics (Moscow), followed from 1962–1969 as Head of Laboratory, Keldysh Institute of Applied Mathematics, then from 1969–1980 Head of Laboratory, Computing Center of the Siberian Branch of the USSR Academy of Sciences (Novosibirsk), 1980–2000 Head of Laboratory and Vice-President (1981–1986) of the Sobolev Institute of Mathematics, the Siberian Branch of the Russian Academy of Sciences (Novosibirsk), from when he is their Counsellor.

### 9.2.5 Computational Sequence for Godunov First-Order Scheme

The implementation of Godunov's first-order scheme encompasses the following steps:

1. Start at time level  $k$  with known data of the cell-averaged values  $\mathbf{U}_i$  in the entire computational domain
2. Solve exactly the Riemann problem  $R(\mathbf{U}_i, \mathbf{U}_{i+1})$  formed at interface  $i + 1/2$  between cells  $i$  and  $i + 1$ , and compute the numerical flux  $\mathbf{F}_{i+1/2}$ . Repeat for all computational cells. Approximate solutions of the Riemann problem are applied also, as presented below
3. Use Eq. (9.29) to determine a stable time step  $\Delta t$ , with  $CFL < 1$
4. Apply the conservative formula Eq. (9.15) to obtain the cell-averaged values  $\mathbf{U}_i$  at the new time level  $k + 1$  for all computational cells
5. Go to step 1, and repeat the computational cycle until reaching the final target time.

It is necessary for this computational sequence to set the boundary conditions at the extremes of the computational domain. This issue is detailed in Sect. 9.8.1.

The scheme previously described is the version of Godunov's method that prevails in practice. However, the original scheme (Godunov 1959) is a variant in which the complete Riemann solution is used to evolve the solution. The version of the scheme is given by the following steps (Toro 2001, 2009):

1. Start at time level  $k$  with known data of the cell-averaged values  $\mathbf{U}_i$  in the entire computational domain

2. Solve exactly the Riemann problem  $R(\mathbf{U}_i, \mathbf{U}_{i+1})$  formed at interface  $i + 1/2$  between cells  $i$  and  $i + 1$ . The complete solution  $\mathbf{U}_{i+1/2}(x/t)$  of each Riemann problem will be used. The numerical flux is not determined. Repeat for all computational cells
3. Use Eq. (9.29) to determine a stable time step  $\Delta t$ , with  $CFL < 1/2$ , given that the complete solution of the Riemann problem will be used. This limit avoids that the waves emanating from an interface interact with waves originated at adjacent interfaces. Interaction of Riemann problems is not considered in the scheme, given that each interface is treated in an isolated way
4. At each cell  $i$ , determine the new cell-averaged values at time level  $k + 1$  averaging the solutions  $\mathbf{U}_{i+1/2}$  and  $\mathbf{U}_{i-1/2}$ , e.g.,

$$\mathbf{U}_i^{k+1} = \frac{1}{\Delta x} \int_0^{\frac{1}{2}\Delta x} \mathbf{U}_{i-1/2}(x, \Delta t) dx + \frac{1}{\Delta x} \int_{-\frac{1}{2}\Delta x}^0 \mathbf{U}_{i+1/2}(x, \Delta t) dx. \quad (9.30)$$

Note that  $x$  is the local coordinate for the interface in question. The updated cell-averaged conservative variables at the new time level are thus a spatial average of the solution of two Riemann problems solved locally at the two interfaces of each finite volume. Note that the solution of each Riemann problem is evaluated at time  $\Delta t$ , and that each solution is determined within half of the cell width. For this reason, interaction of the waves from the Riemann problems is prohibited and  $CFL$  cannot exceed  $1/2$  in this version of the scheme.

5. Go to step 1, and repeat the computational cycle until reaching the final target time.

Figure 9.7 presents schematically a snapshot of computational cell  $i$  after time  $\Delta t$ . Within it, three waves are propagated: a right-going shock generated at interface  $i - 1/2$  and two left-going shocks coming from interface  $i + 1/2$ . The value of  $CFL < 1/2$ , so that waves are not interacting within the cell. This simple case illustrates how to evaluate Eq. (9.30); solving the integrals at time level  $k + 1$  from point A to B (Fig. 9.7), one finds

$$\begin{aligned} \mathbf{U}_i^{k+1} \Delta x &= \underbrace{\mathbf{U}_{i-1/2}^* S_{Ri-1/2} \Delta t + \mathbf{U}_i^k \left( \frac{1}{2} \Delta x - S_{Ri-1/2} \Delta t \right)}_{\text{Integration of Riemann problem from } i-1/2} \\ &\quad + \underbrace{\mathbf{U}_i^k \left( S_{Li+1/2} \Delta t - \frac{1}{2} \Delta x \right) + \mathbf{U}_{i+1/2}^* (S_{Ri+1/2} \Delta t - S_{Li+1/2} \Delta t) - \mathbf{U}_{i+1}^k S_{Ri+1/2} \Delta t}_{\text{Integration of Riemann problem from } i+1/2}. \end{aligned} \quad (9.31)$$

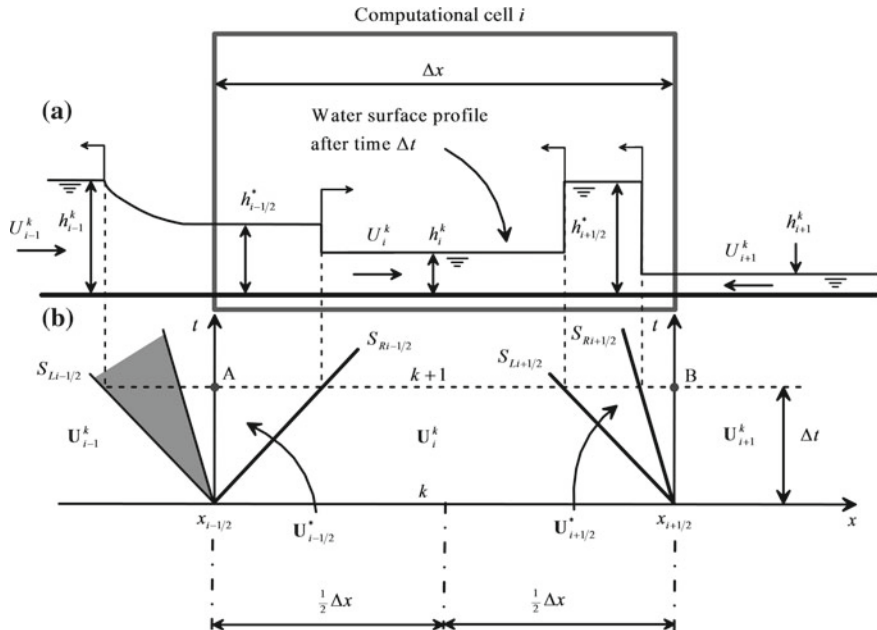


**Fig. 9.7** Riemann solutions at cell  $i$  for  $\text{CFL} < 1/2$ : with left-going rarefaction and right-going shock generated at interface  $i - 1/2$ , and two left-going shocks generated at interface  $i + 1/2$ . **a** Free surface profile at local time  $\Delta t$ , **b**  $x$ - $t$  plane

As shown with this simple example, the updating process may be tedious, especially if a rarefaction wave is present in the solution at time level  $k + 1$ . Further, the restrictive stability condition  $\text{CFL} < 1/2$  is another disadvantage of this version of Godunov's scheme. It is thus not further considered.

Applying Godunov's scheme based on Eq. (9.15), the numerical fluxes are

$$\mathbf{F}_{i-1/2} = \mathbf{F}(\mathbf{U}_{i-1/2}^*), \quad (9.32)$$

and

$$\mathbf{F}_{i+1/2} = \mathbf{F}(\mathbf{U}_{i+1}^k). \quad (9.33)$$

Equation (9.15) yields then

$$\mathbf{U}_i^{k+1} = \mathbf{U}_i^k - \frac{\Delta t}{\Delta x} [\mathbf{F}(\mathbf{U}_{i+1}^k) - \mathbf{F}(\mathbf{U}_{i-1/2}^*)]. \quad (9.34)$$

As shown, Eq. (9.34) is simpler to apply than Eq. (9.31), and the maximum time step  $\Delta t$  could be multiplied by two.

### 9.3 Approximate Riemann Solvers

#### 9.3.1 HLL Riemann Solver

Harten et al. (1983) developed an approximate Riemann solver, named Harten–Lax–van Leer (HLL). The fundamental idea to simplify the Riemann problem is to assume that the rarefaction waves (continuous waves of finite extension) can be replaced by discontinuous waves (infinitely thin waves). Consider the exact Riemann problem depicted in Fig. 9.8a, with a left-going rarefaction wave and a right-going shock. The simplified wave structure according to the HLL principle is as shown in Fig. 9.8b: The constant initial states  $\mathbf{U}_L$  and  $\mathbf{U}_R$  are separated by a single constant state  $\mathbf{U}_{HLL}$ . The first issue is thus to find an equation describing this constant state zone.

Following Toro (2009), consider the control volume sketched in Fig. 9.9 with a gray shadow. The integral form of the homogeneous conservation laws yields there [Eq. (9.5)]

$$\int_{x_L}^{x_R} [\mathbf{U}(x, T) - \mathbf{U}(x, 0)] dx + \int_0^T [\mathbf{F}(x_R, t) - \mathbf{F}(x_L, t)] dt = \mathbf{0}. \quad (9.35)$$

For the simplified HLL wave structure, Eq. (9.35) yields after elementary integration

$$\int_{x_L}^{x_R} \mathbf{U}(x, T) dx = x_R \mathbf{U}_R - x_L \mathbf{U}_L + T(\mathbf{F}_L - \mathbf{F}_R) dt. \quad (9.36)$$

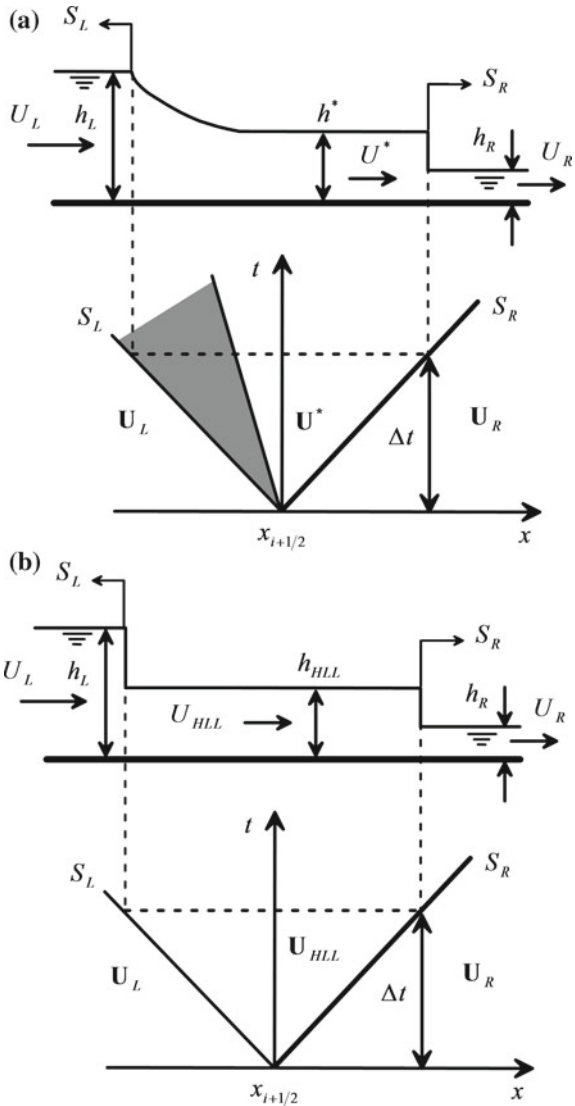
The undetermined integral in Eq. (9.36) is expanded as follows

$$\int_{x_L}^{x_R} \mathbf{U}(x, T) dx = \int_{x_L}^{TS_L} \mathbf{U}(x, T) dx + \int_{TS_L}^{TS_R} \mathbf{U}(x, T) dx + \int_{TS_R}^{x_R} \mathbf{U}(x, T) dx. \quad (9.37)$$

Two of the integrals in Eq. (9.37) are immediate, resulting in

$$\int_{x_L}^{x_R} \mathbf{U}(x, T) dx = (TS_L - x_L) \mathbf{U}_L + (x_R - TS_R) \mathbf{U}_R + \int_{TS_L}^{TS_R} \mathbf{U}(x, T) dx. \quad (9.38)$$

**Fig. 9.8** Riemann problem with left-going rarefaction wave and right-going shock.  
**a** Exact wave structure and  
**b** simplified HLL wave structure

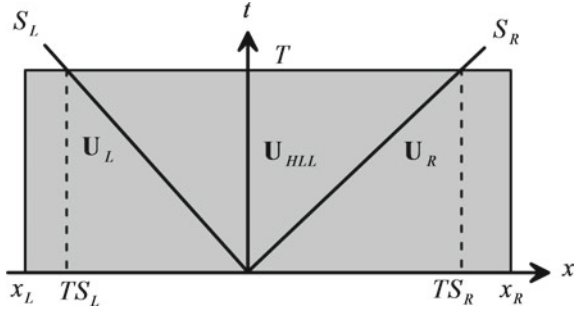


Equating Eqs. (9.36) and (9.38) generates

$$\int_{TS_L}^{TS_R} \mathbf{U}(x, T) dx = T(S_R \mathbf{U}_R - S_L \mathbf{U}_L + \mathbf{F}_L - \mathbf{F}_R), \quad (9.39)$$

from which the average state is

**Fig. 9.9** Control volume for the development of HLL Riemann solver



$$\mathbf{U}_{HLL} = \frac{1}{T(S_R - S_L)} \int_{TS_L}^{TS_R} \mathbf{U}(x, T) dx = \frac{S_R \mathbf{U}_R - S_L \mathbf{U}_L + \mathbf{F}_L - \mathbf{F}_R}{S_R - S_L}. \quad (9.40)$$

Both the rarefaction waves and shocks are discontinuous waves in the HLL approximation (see example in Fig. 9.8b). Thus, the Rankine–Hugoniot jump conditions apply across both, resulting in

$$\frac{\mathbf{F}_{HLL} - \mathbf{F}_L}{\mathbf{U}_{HLL} - \mathbf{U}_L} = S_L, \quad (9.41)$$

and

$$\frac{\mathbf{F}_{HLL} - \mathbf{F}_R}{\mathbf{U}_{HLL} - \mathbf{U}_R} = S_R. \quad (9.42)$$

Using the value of  $\mathbf{U}_{HLL}$  in either of the two jump conditions, the HLL numerical flux is

$$\mathbf{F}_{HLL} = \frac{S_R \mathbf{F}_L - S_L \mathbf{F}_R + S_R S_L (\mathbf{U}_R - \mathbf{U}_L)}{S_R - S_L}. \quad (9.43)$$

The possible cases for the numerical flux are thus (Toro 2001)

$$\mathbf{F}_{i+1/2} = \begin{cases} \mathbf{F}_L & \text{if } S_L \geq 0 \\ \frac{S_R \mathbf{F}_L - S_L \mathbf{F}_R + S_R S_L (\mathbf{U}_R - \mathbf{U}_L)}{S_R - S_L} & \text{if } S_L \leq 0 \leq S_R. \\ \mathbf{F}_R & \text{if } S_R \leq 0 \end{cases} \quad (9.44)$$

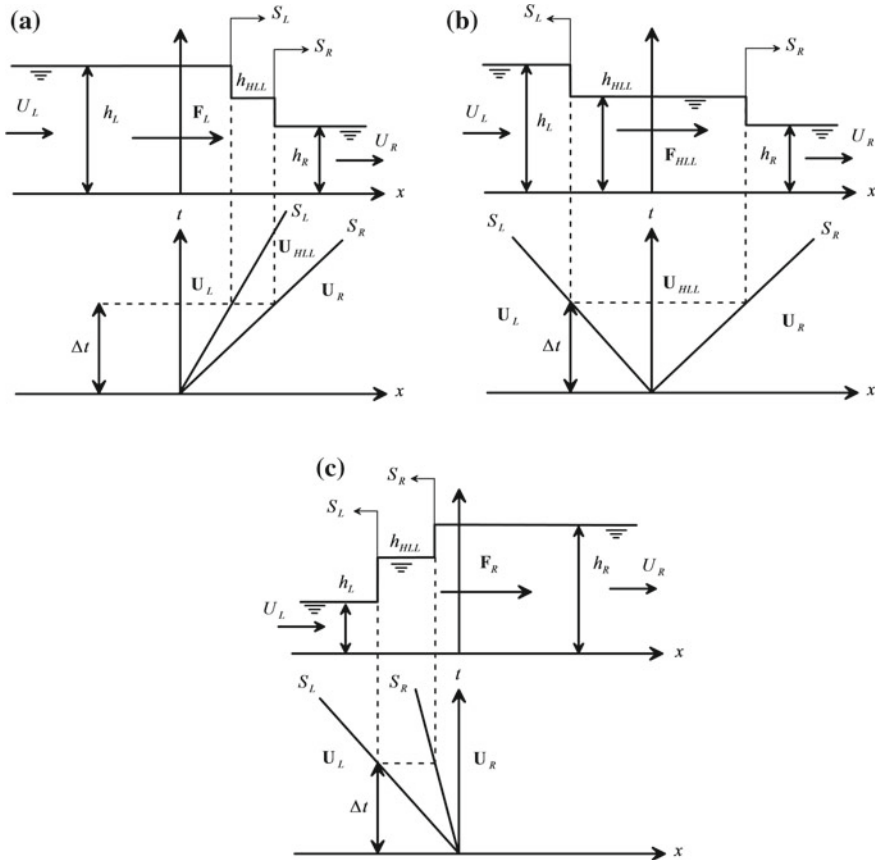


**Fig. 9.10** Example of possible wave cases in HLL approximate Riemann solver [corresponding to Eq. (9.44)]. **a** Two right-going waves, **b** left- and right-going waves, **c** two left-going waves

These are sketched in Fig. 9.10. To apply Eq. (9.44), a reliable estimate of both  $S_R$  and  $S_L$  is needed. For wet-bed conditions, these are given as used in the exact Riemann solver by (Toro 2001)

$$S_L = U_L - c_L \lambda_L, \quad S_R = U_R + c_R \lambda_R. \quad (9.45)$$

Here,  $c = (gh)^{1/2}$  is the celerity, and the corrector factor to distinguish between the celerity of shock propagation, and that of a rarefaction wave given by the corresponding eigenvalue, is ( $K = L, R$ )

$$\lambda_K = \begin{cases} \left[ \frac{1}{2} \left( \frac{h^*(h^* + h_K)}{h_K^2} \right) \right]^{1/2} & h^* > h_K \text{(shock wave on } K\text{)}, \\ 1 & h^* \leq h_K \text{(rarefaction wave on } K\text{)}. \end{cases} \quad (9.46)$$

Obviously, an estimate of the flow depth in the star region of the exact Riemann problem is needed. The two-rarefaction result is used here following Toro (2001) [Eq. (8.22)]

$$h^* = \frac{1}{g} \left[ \frac{1}{2} (c_L + c_R) + \frac{1}{4} (U_L - U_R) \right]^2. \quad (9.47)$$

For the dry-bed case on the right ( $h_R = 0$ )

$$S_L = U_L - c_L; \quad S_R = U_L + 2c_L, \quad (9.48)$$

whereas for the dry-bed case on the left ( $h_L = 0$ )

$$S_L = U_R - 2c_R; \quad S_R = U_R + c_R. \quad (9.49)$$

### 9.3.2 Lax Numerical Flux

The Lax diffusive method (Lax 1954; Lax and Wendroff 1960) is a finite-difference scheme with artificial viscosity (see Chap. 7). It is a variant of the unstable scheme, given by the updating formula (Cunge 1975; Cunge et al. 1980)

$$\mathbf{U}_i^{k+1} = \frac{(\mathbf{U}_{i-1}^k + \mathbf{U}_{i+1}^k)}{2} - \frac{\Delta t}{2\Delta x} (\mathbf{F}_{i+1}^k - \mathbf{F}_{i-1}^k). \quad (9.50)$$

It is pertinent at this stage to provide an interpretation of the Lax diffusive method within the context of finite volume methods and the solution of the Riemann problem. Consider a finite-difference mesh where the nodes are coincident with the cell centers in a finite volume setup. Nodal values of the finite difference scheme are thus equal to the cell-averaged values. The equation modeled by the Lax scheme is (Chaudhry 2008) [see Eq. (7.51)]

$$\frac{\partial \mathbf{U}}{\partial t} + \frac{\partial \mathbf{F}}{\partial x} = \frac{1}{2} D \frac{\partial^2 \mathbf{U}}{\partial x^2}, \quad (9.51)$$

with  $D$  as an artificial viscosity coefficient given by

$$D = \frac{(\Delta x)^2}{\Delta t}. \quad (9.52)$$

An issue of the Lax scheme is its inconsistency, given that a source term with artificial viscosity is added to obtain numerical stability. The integral solution of Eq. (9.51) will be worked out as follows; rewrite it using basic calculus as

$$\frac{\partial \mathbf{U}}{\partial t} + \frac{\partial}{\partial x} \left( \mathbf{F} - \frac{1}{2} D \frac{\partial \mathbf{U}}{\partial x} \right) = \mathbf{0}, \quad (9.53)$$

or with  $\mathbf{f}$  as a flux function affected by artificial viscosity

$$\frac{\partial \mathbf{U}}{\partial t} + \frac{\partial \mathbf{f}}{\partial x} = \mathbf{0}. \quad (9.54)$$

Its integral form over a control volume in the  $x$ - $t$  plane is thus

$$\mathbf{U}_i^{k+1} = \mathbf{U}_i^k - \frac{\Delta t}{\Delta x} (\mathbf{f}_{i+1/2} - \mathbf{f}_{i-1/2}). \quad (9.55)$$

The numerical flux  $\mathbf{f}_{i+1/2}$  at interface  $i + 1/2$  is exactly

$$\begin{aligned} \mathbf{f}_{i+1/2} &= \frac{1}{\Delta t} \int_t^{t+\Delta t} \mathbf{f}(x_{i+1/2}, t) dt \\ &= \frac{1}{\Delta t} \int_t^{t+\Delta t} \left( \mathbf{F} - \frac{1}{2} D \frac{\partial \mathbf{U}}{\partial x} \right)_{i+1/2} dt \\ &= \frac{1}{\Delta t} \int_t^{t+\Delta t} \mathbf{F}(x_{i+1/2}, t) dt - \frac{1}{\Delta t} \int_t^{t+\Delta t} \frac{1}{2} D \frac{\partial \mathbf{U}}{\partial x} dt \\ &= \mathbf{F}_{i+1/2} - \frac{1}{2} D \left( \frac{\partial \mathbf{U}}{\partial x} \right)_{i+1/2}. \end{aligned} \quad (9.56)$$

Approximations are now introduced into the general Eq. (9.56). The numerical flux  $\mathbf{F}_{i+1/2}$  is simply approximated by averaging the physical flux function evaluated at the initial states of the Riemann problem at interface  $i + 1/2$ , whereas the derivative of  $\mathbf{U}$  is approximated by a finite difference, resulting in

$$\mathbf{f}_{i+1/2} = \frac{\mathbf{F}_i^k + \mathbf{F}_{i+1}^k}{2} - \frac{1}{2} D \left( \frac{\mathbf{U}_{i+1}^k - \mathbf{U}_i^k}{\Delta x} \right) = \frac{\mathbf{F}_i^k + \mathbf{F}_{i+1}^k}{2} - \frac{1}{2} \frac{\Delta x}{\Delta t} (\mathbf{U}_{i+1}^k - \mathbf{U}_i^k). \quad (9.57)$$

Developing the corresponding expression for  $\mathbf{f}_{i-1/2}$ , and inserting the results into Eq. (9.55), Eq. (9.50) is regained. In the finite volume interpretation of the Lax scheme, the solution of the local Riemann problems is avoided by adding artificial viscosity, thereby forcing numerical stability. The numerical flux of the Lax method is usually defined as (Toro 2001)

$$\mathbf{F}_{i+1/2} = \frac{\mathbf{F}_L + \mathbf{F}_R}{2} - \frac{1}{2} \frac{\Delta x}{\Delta t} (\mathbf{U}_R - \mathbf{U}_L), \quad (9.58)$$

to be used into

$$\mathbf{U}_i^{k+1} = \mathbf{U}_i^k - \frac{\Delta t}{\Delta x} (\mathbf{F}_{i+1/2} - \mathbf{F}_{i-1/2}). \quad (9.59)$$

The price of avoiding the solution of the local Riemann problems is to add artificial viscosity. If the artificial viscosity term is dropped, the numerical flux is

$$\mathbf{F}_{i+1/2} = \frac{\mathbf{F}_i^k + \mathbf{F}_{i+1}^k}{2}, \quad (9.60)$$

resulting in the unstable formula (Hoffman 2001; Hirsch 1988, 1990; LeVeque 2002)

$$\mathbf{U}_i^{k+1} = \mathbf{U}_i^k - \frac{\Delta t}{2\Delta x} (\mathbf{F}_{i+1} - \mathbf{F}_{i-1}). \quad (9.61)$$

Thus, not solving the Riemann problem and taking the numerical flux as an average of estimates based on initial data is not a good choice.

An alternative interpretation of Eq. (9.58) is given by Toro (2001) as follows. Consider the HLL numerical flux given by Eq. (9.44) with the signal speeds approximated as

$$S_R = -S_L = S_{\max}, \quad (9.62)$$

where  $S_{\max}$  is to be determined. The numerical flux is then

$$\begin{aligned} \mathbf{F}_{i+1/2} &= \frac{S_{\max} \mathbf{F}_L + S_{\max} \mathbf{F}_R - S_{\max}^2 (\mathbf{U}_R - \mathbf{U}_L)}{2S_{\max}} \\ &= \frac{\mathbf{F}_L + \mathbf{F}_R}{2} - \frac{1}{2} S_{\max} (\mathbf{U}_R - \mathbf{U}_L). \end{aligned} \quad (9.63)$$

Using Eq. (9.29) with  $\text{CFL} = 1$  yields

$$S_{\max} = \frac{\Delta x}{\Delta t}, \quad (9.64)$$

which inserted into Eq. (9.63) yields Eq. (9.58). Therefore, the Lax–Friedrichs scheme can be alternatively understood as a Godunov-type method with the HLL Riemann solver using the simplest possible choice for the signal speeds.

### 9.3.3 Roe Riemann Solver

Roe (1981) developed an approximate Riemann solver for the Euler equations later applied by Glaister (1987) to the SWE. The homogeneous version of Eq. (9.1) can be written as

$$\frac{\partial \mathbf{U}}{\partial t} + \mathbf{A}(\mathbf{U}) \frac{\partial \mathbf{U}}{\partial x} = \mathbf{0}, \quad (9.65)$$

where  $\mathbf{A}$  is the Jacobian matrix

$$\mathbf{A} = \frac{\partial \mathbf{F}}{\partial \mathbf{U}}. \quad (9.66)$$

With  $\tilde{\mathbf{A}}$  as a matrix of constant coefficients used to approximate matrix  $\mathbf{A}$ , Roe transformed the nonlinear Eq. (9.65) into the linear system

$$\frac{\partial \mathbf{U}}{\partial t} + \tilde{\mathbf{A}} \frac{\partial \mathbf{U}}{\partial x} = \mathbf{0}. \quad (9.67)$$

This matrix is defined locally in terms of the initial data of the Riemann problem at a generic interface, e.g.,  $\tilde{\mathbf{A}} = \tilde{\mathbf{A}}(\mathbf{U}_L, \mathbf{U}_R)$ . Using the solution to the Riemann problem for the linear system and resorting to the integral form of the conservation laws result in the Roe numerical flux (Toro 2001, 2009; Khan and Lai 2014)

$$\mathbf{F}_{i+1/2}^{Roe} = \frac{\mathbf{F}_L + \mathbf{F}_R}{2} - \frac{1}{2} \sum_{j=1}^2 \tilde{\alpha}_j |\tilde{\lambda}_j| \tilde{\mathbf{k}}_j. \quad (9.68)$$

Here, the wave strengths are

$$\tilde{\alpha}_1 = \frac{1}{2} \left( \Delta h - \frac{\tilde{h} \Delta U}{\tilde{c}} \right), \quad \tilde{\alpha}_2 = \frac{1}{2} \left( \Delta h + \frac{\tilde{h} \Delta U}{\tilde{c}} \right), \quad (9.69)$$

whereas the average eigenvalues are

$$\tilde{\lambda}_1 = \tilde{U} - \tilde{c}, \quad \tilde{\lambda}_2 = \tilde{U} + \tilde{c}, \quad (9.70)$$

and right eigenvectors

$$\tilde{\mathbf{K}}_1 = \begin{pmatrix} 1 \\ \tilde{U} - \tilde{c} \end{pmatrix}, \quad \tilde{\mathbf{K}}_2 = \begin{pmatrix} 1 \\ \tilde{U} + \tilde{c} \end{pmatrix}. \quad (9.71)$$

The jumps in  $h$  and  $U$  are defined by

$$\Delta h = h_R - h_L, \quad \Delta U = U_R - U_L, \quad (9.72)$$

and the Roe averages are given by

$$\tilde{h} = (h_R h_L)^{1/2}, \quad (9.73)$$

$$\tilde{c} = \left[ \frac{g}{2} (h_R + h_L) \right]^{1/2}, \quad (9.74)$$

$$\tilde{U} = \frac{h_L^{1/2} U_L + h_R^{1/2} U_R}{h_L^{1/2} + h_R^{1/2}}. \quad (9.75)$$

The Roe solver as stated above is not entropy satisfying. Thus, an entropy fix is needed to avoid unphysical jumps in transcritical rarefactions.

## 9.4 Dry-Bed Treatment

Computationally we must decide whether cells are wet or dry, even though conceptually they could be partially filled with water. This is a practical case when solving the SWE, given that the position of a shoreline usually lies between cell centers. Thus, cells can be fully wet, partially wet (partially dry) or dry, but computationally we must define only wet and dry cells (Brocchini and Dodd 2008).

If the numerical flux is computed using the exact Riemann solver, the dry-bed cases are automatically considered. The HLL Riemann solver previously exposed also applies to dry-bed conditions if the correct signal speeds  $S_L$  and  $S_R$  for the dry-bed problem are accounted for, as given by Eqs. (9.48) and (9.49). This permits reasonably well to compute the numerical flux for dry-bed problems (Toro 2001). To identify a dry bed in the computational domain, consider a small threshold depth  $\varepsilon$  (Sanders 2001; Khan and Lai 2014). For a generic interface  $i + 1/2$ , the following cases are possible:

- (i) If  $h_L > \varepsilon$  and  $h_R \leq \varepsilon$ , the numerical flux  $\mathbf{F}_{i+1/2}$  is computed assuming a dry bed on the right
- (ii) If  $h_R > \varepsilon$  and  $h_L \leq \varepsilon$ , the numerical flux  $\mathbf{F}_{i+1/2}$  is computed assuming a dry bed on the left
- (iii) If  $h_R \leq \varepsilon$  and  $h_L \leq \varepsilon$ , the numerical flux  $\mathbf{F}_{i+1/2}$  is set to zero.

After each time loop, a check of computed cell-averaged water depths  $h_i^{k+1}$  is conducted to identify the formation of new dry-bed conditions within the computational domain. Two methods are used in practice:

- (a) *Dry nodes are defined with zero water depth*: The following conditions are implemented in the code

$$\text{If } h_i^{k+1} \leq \varepsilon \Rightarrow U_i^{k+1} = 0. \quad (9.76)$$

$$\text{If } h_i^{k+1} < 0 \Rightarrow U_i^{k+1} = 0, \quad h_i^{k+1} = 0. \quad (9.77)$$

In this method, the depth is clearly zero at the dry nodes. Thus, physical functions divided by  $h$  must be also checked in the code to reset the values to zero under dry-bed conditions, e.g., the function  $q^2/(gh)$  or the friction slope  $S_f = n^2 q^2 / (h^{10/3})$ , with  $n$  as Manning's roughness coefficient.

- (b) *Dry nodes are not defined with zero water depth*: The following conditions are implemented in the code

$$\text{If } h_i^{k+1} \leq \varepsilon \Rightarrow U_i^{k+1} = 0, \quad h_i^{k+1} = \varepsilon. \quad (9.78)$$

This method can generate unphysical fluxes over uneven beds, so that method (a) is preferred (Khan and Lai 2014). A typical value used is  $\varepsilon = 10^{-16}$  m.

Care is needed during assignation of  $\mathbf{U}$  values at the interface of a wet and a dry cell, e.g., during the tracking of a shoreline. Suppose an interface with a wet cell on the left and a dry cell on the right, that is, the shoreline is inside the (computationally) dry cell, which is in reality a partially-filled cell. Now assume water is static on a slope. At this interface  $h_L \neq 0$  from the wet cell, but  $h_R = 0$  from the dry cell, thereby generating unphysical numerical flux. Thus, in this event  $h_R$ , is set equal to  $h_L$  and  $q_R = -q_L$  to avoid unphysical flux (Bradford and Sanders 2002).

## 9.5 Source Terms

### 9.5.1 Splitting Technique

The problem posed now is the solution of the SWE with a source term  $\mathbf{S} = \mathbf{S}(\mathbf{U})$ , e.g.,

$$\frac{\partial \mathbf{U}}{\partial t} + \frac{\partial \mathbf{F}}{\partial x} = \mathbf{S}(\mathbf{U}). \quad (9.79)$$

The friction slope is parametrized for a wide channel with  $C_f$  as a friction coefficient as

$$S_f = C_f \frac{U|U|}{gh}, \quad (9.80)$$

so that the source term of the SWE is

$$\mathbf{S} = \mathbf{S}(\mathbf{U}) = \begin{pmatrix} 0 \\ -gh \frac{\partial z_b}{\partial x} - gh S_f \end{pmatrix} = \begin{pmatrix} 0 \\ -g U_1 \frac{\partial z_b}{\partial x} - C_f \frac{U_2}{U_1} \left| \frac{U_2}{U_1} \right| \end{pmatrix}, \quad (9.81)$$

where  $\mathbf{U} = (U_1, U_2) = (h, q)$ . This source term is reaction-like, given that terms with  $\mathbf{U}$  derivatives are missing. Here, a splitting scheme following Toro (2001) is presented. An alternative to splitting is up-winding the source terms (Bermudez and Vazquez-Cendón 1994). Our problem is thus to find the vector  $\mathbf{U}$  at time level  $k + 1$  including the effect of the source terms, that is,

$$\left. \begin{array}{l} \text{PDEs: } \frac{\partial \mathbf{U}}{\partial t} + \frac{\partial \mathbf{F}}{\partial x} = \mathbf{S}(\mathbf{U}) \\ \text{Initial cond.: } \mathbf{U}(x, t) = \mathbf{U}_i^k \end{array} \right\} \Rightarrow \mathbf{U}_i^{k+1}(x_i, t^{k+1}). \quad (9.82)$$

In the splitting approach, the problem given by Eq. (9.82) is solved in two consecutive steps as follows:

*Step 1* Solve the homogeneous part of Eq. (9.82) using the Godunov-type scheme,

$$\left. \begin{array}{l} \text{PDEs: } \frac{\partial \mathbf{U}}{\partial t} + \frac{\partial \mathbf{F}}{\partial x} = \mathbf{0} \\ \text{Initial cond.: } \mathbf{U}(x, t) = \mathbf{U}_i^k \end{array} \right\} \Rightarrow \mathbf{U}_i^{\text{adv}}(x_i, t^{k+1}). \quad (9.83)$$

In this first step, the effects of advection are accounted for. This step may be regarded as a predictor part to compute an approximate solution at time level  $k + 1$  overlooking source terms effects. From the viewpoint of open channel hydraulics, this advection step forces the so-called “*pseudo-uniform flow condition*” (bed-slope effects in equilibrium with friction). The solution of the advection step is given by

$$\mathbf{U}_i^{\text{adv}} = \mathbf{U}_i^k - \frac{\Delta t}{\Delta x} (\mathbf{F}_{i+1/2} - \mathbf{F}_{i-1/2}), \quad (9.84)$$

which was already described in the preceding sections.

*Step 2* Update the solution including the effect of the source terms,

$$\left. \begin{array}{l} \text{ODEs: } \frac{d\mathbf{U}}{dt} = \mathbf{S}(\mathbf{U}) \\ \text{Initial cond.: } \mathbf{U}(x, t) = \mathbf{U}_i^{\text{adv}} \end{array} \right\} \Rightarrow \mathbf{U}_i^{k+1}(x_i, t^{k+1}). \quad (9.85)$$

A variety of ODE solvers apply in this step. It may be regarded as a correction step to deviate the advection solution from pseudo-uniformity. An integral form of the ODEs is

$$\mathbf{U}_i^{k+1} = \mathbf{U}_i^{\text{adv}} + \int_t^{t+\Delta t} \mathbf{S}_i(\mathbf{U}) dt. \quad (9.86)$$

This equation highlights that the vector  $\mathbf{S}_i(\mathbf{U})$  may be evaluated at different states during the time integration depending on how the integral is discretized. This fact is important and may affect the quality of the computed solution. Obviously, this source term  $\mathbf{S}_i(\mathbf{U})$  shall be regarded as a cell-averaged value.

### 9.5.2 ODE Solvers

There is a great variety of ODE solvers to be used in Eq. (9.86); see, for example, Hoffman (2001). Here, the most widely employed are summarized.

#### *First-order forward Euler scheme*

The integral in Eq. (9.86) is evaluated taking the value of  $\mathbf{S}(\mathbf{U})$  at a specified time level, resulting in an explicit scheme. Using the value of  $\mathbf{S}(\mathbf{U}_i^k)$  yields the not best possible choice (Toro 2001)

$$\mathbf{U}_i^{k+1} = \mathbf{U}_i^{\text{adv}} + \mathbf{S}(\mathbf{U}_i^k) \Delta t. \quad (9.87)$$

A better approximation is

$$\mathbf{U}_i^{k+1} = \mathbf{U}_i^{\text{adv}} + \mathbf{S}(\mathbf{U}_i^{\text{adv}}) \Delta t, \quad (9.88)$$

where the source terms include the effects of advection.

#### *First-order backward Euler scheme*

The integral in Eq. (9.86) is evaluated taking the value of  $\mathbf{S}(\mathbf{U})$  at the unknown time level  $k + 1$ , resulting in an implicit scheme. The updating formula is then

$$\mathbf{U}_i^{k+1} = \mathbf{U}_i^{\text{adv}} + \mathbf{S}(\mathbf{U}_i^{k+1}) \Delta t. \quad (9.89)$$

### Second-order TVD Runge–Kutta scheme

The updating sequence is given by the two explicit steps (Gottlieb and Shu 1998; Khan and Lai 2014)

$$\mathbf{U}_i^{(1)} = \mathbf{U}_i^{\text{adv}} + \mathbf{S}(\mathbf{U}_i^{\text{adv}}) \Delta t, \quad (9.90)$$

$$\mathbf{U}_i^{k+1} = \frac{1}{2} \mathbf{U}_i^{\text{adv}} + \frac{1}{2} \mathbf{U}_i^{(1)} + \frac{1}{2} \mathbf{S}[\mathbf{U}_i^{(1)}] \Delta t. \quad (9.91)$$

### Third-order TVD Runge–Kutta scheme

The updating sequence is given by the three explicit steps (Gottlieb and Shu 1998; Khan and Lai 2014)

$$\mathbf{U}_i^{(1)} = \mathbf{U}_i^{\text{adv}} + \mathbf{S}(\mathbf{U}_i^{\text{adv}}) \Delta t, \quad (9.92)$$

$$\mathbf{U}_i^{(2)} = \frac{3}{4} \mathbf{U}_i^{\text{adv}} + \frac{1}{4} \mathbf{U}_i^{(1)} + \frac{1}{4} \mathbf{S}[\mathbf{U}_i^{(1)}] \Delta t, \quad (9.93)$$

$$\mathbf{U}_i^{k+1} = \frac{1}{3} \mathbf{U}_i^{\text{adv}} + \frac{2}{3} \mathbf{U}_i^{(2)} + \frac{2}{3} \mathbf{S}[\mathbf{U}_i^{(2)}] \Delta t. \quad (9.94)$$

### 9.5.3 Well-Balanced Schemes

The discretization applied to the bed-slope source term has an important impact on the quality of the steady-state solutions generated by the unsteady flow solver, an

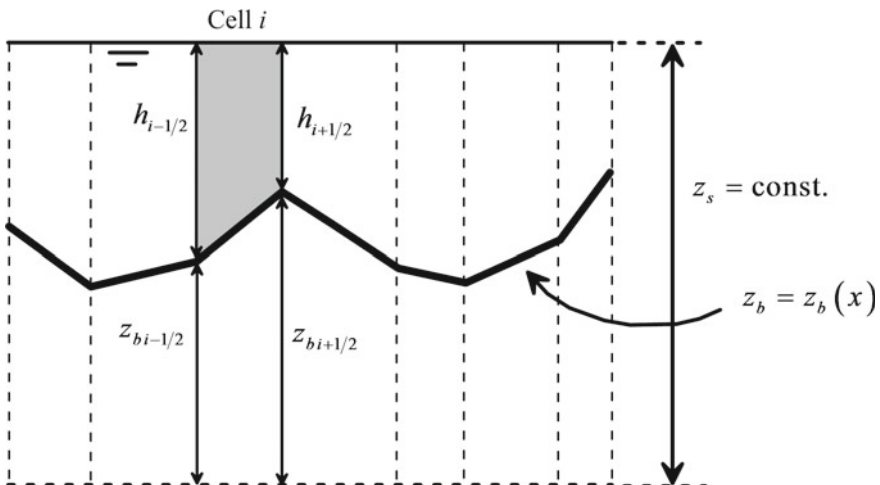


**Fig. 9.11** Static water over variable topography ( $z_s = \text{const.}$ ,  $q = 0$ )

issue demonstrated as follows. Consider static water over a variable bed profile  $z_b = z_b(x)$  (Fig. 9.11), for which the conservation laws reduce to

$$\frac{\partial \mathbf{F}}{\partial x} = \mathbf{S}, \quad (9.95)$$

or

$$\frac{\partial}{\partial x} \left( \frac{gh^2}{2} \right) = -gh \frac{\partial z_b}{\partial x}. \quad (9.96)$$

The integral form of Eq. (9.95) over a cell is

$$(\mathbf{F}_{i+1/2} - \mathbf{F}_{i-1/2}) - \Delta x \mathbf{S}_i = \mathbf{0}, \quad (9.97)$$

or,

$$g \frac{h_{i+1/2}^2 - h_{i-1/2}^2}{2} = -\Delta x \left( gh \frac{\partial z_b}{\partial x} \right)_i. \quad (9.98)$$

To preserve this identity, the average source term contribution within a cell must be compatible with the discretization scheme of the numerical fluxes. Otherwise, artificial waves originating from the numerical scheme may appear, breaking down static conditions. Topography is defined at cell interfaces, and within a cell, the bed profile is assumed to vary linearly. The bed source term may be discretized as

$$\left( gh \frac{\partial z_b}{\partial x} \right)_i = g \frac{h_{i+1/2} + h_{i-1/2}}{2} \frac{z_{bi+1/2} - z_{bi-1/2}}{\Delta x}. \quad (9.99)$$

The imbalance of numerical fluxes at cell  $i$  is given by the hydrostatic forces as

$$g \frac{(h_{i+1/2}^2 - h_{i-1/2}^2)}{2} = g \frac{(h_{i+1/2} + h_{i-1/2})(h_{i+1/2} - h_{i-1/2})}{2}. \quad (9.100)$$

Given that the water is static, e.g.,

$$h(x) + z_b(x) = \text{const.} \quad (9.101)$$

Equation (9.100) transforms into

$$g \frac{(h_{i+1/2}^2 - h_{i-1/2}^2)}{2} = -g \frac{(h_{i+1/2} + h_{i-1/2})(z_{bi+1/2} - z_{bi-1/2})}{2}. \quad (9.102)$$

Inserting Eqs. (9.99) and (9.102) into Eq. (9.98), the identity is preserved, so the scheme is said to be well-balanced, or to satisfy the C-property (Bermudez and Vazquez-Cendón 1994). As noted in this illustrative example, the hydrostatic forces ( $gh^2/2$ ) contained inside the flux gradient  $\partial\mathbf{F}/\partial x$  are responsible for the potential imbalance with the bed-slope source term if Eq. (9.99) is not used.

For partially filled cells, e.g. with static water on a slope, the bed jump  $z_{bi+1/2} - z_{bi-1/2}$  in Eq. (9.99) shall be modified (Brufau et al. 2002). If  $h_{i+1/2} = 0$  then  $z_{bi+1/2} - z_{bi-1/2}$  is replaced by  $h_{i-1/2}$ , whereas for  $h_{i-1/2} = 0$  it is substituted by  $h_{i+1/2}$ .

An alternative to circumvent this problem is to reformulate the SWE as follows

$$\frac{\partial \mathbf{U}}{\partial t} + \frac{\partial \mathbf{F}}{\partial x} = \mathbf{S}, \quad (9.103)$$

where  $\mathbf{U}$  is the vector of the conserved variables,  $\mathbf{F}$  the flux vector, and  $\mathbf{S}$  the source term vector, given in this case by (Ying et al. 2004)

$$\mathbf{U} = \begin{pmatrix} h \\ hU \end{pmatrix}, \quad \mathbf{F} = \begin{pmatrix} hU \\ hU^2 \end{pmatrix}, \quad \mathbf{S} = \begin{pmatrix} 0 \\ -gh \frac{\partial z_s}{\partial x} - ghS_f \end{pmatrix}. \quad (9.104)$$

As noted, the hydrostatic forces are no more contained in  $\mathbf{F}$ ; in the source term, the bed-slope source term is substituted by a free surface elevation ( $z_s = z_b + h$ ) gradient term. For static water, the integral form of Eq. (9.103) reduces to

$$-\Delta x \left( gh \frac{\partial z_s}{\partial x} \right)_i = 0. \quad (9.105)$$

Using Eq. (9.101), the scheme is seen to be automatically well-balanced.

#### 9.5.4 Treatment of Friction

Consider the bed-slope source term overlooked temporarily. In this case, and with  $f$  as the Darcy–Weisbach friction factor ( $C_f = f/8$ ) (White 2009), Eq. (9.85) is reduced to the scalar ODE, assuming a wide rectangular channel and positive  $U$

$$\frac{dq}{dt} = -ghS_f = -\frac{f}{8}U^2. \quad (9.106)$$

For wet-bed conditions, the forward Euler discretization is acceptable, resulting in the updating formula

$$q_i^{k+1} = q_i^{\text{adv}} - \frac{f}{8} (U_i^{\text{adv}})^2 \Delta t. \quad (9.107)$$

However, near wet–dry fronts the explicit discretization may generate instabilities, so that an alternative method is explained here. Using backward Euler discretization [Eq. (9.89)], Eq. (9.106) yields

$$q_i^{k+1} = q_i^{\text{adv}} - \frac{f}{8} (U_i^{k+1})^2 \Delta t, \quad (9.108)$$

or

$$U_i^{k+1} = \frac{q_i^{\text{adv}}}{h_i^{k+1}} - \frac{f}{8h_i^{k+1}} (U_i^{k+1})^2 \Delta t. \quad (9.109)$$

Equation (9.109) is a quadratic function solved at each time step to obtain the cell-averaged velocity  $U_i^{k+1}$  accounting for frictional effects. Note that the friction force might stop the flow in the extreme; e.g., a flow reversal cannot be numerically permitted. Thus, the following condition must be verified by numerical computations

$$q_i^{k+1} q_i^{\text{adv}} \geq 0. \quad (9.110)$$

Other flow resistance formulae like Manning’s equation are frequently used in river flow computations (Henderson 1966; Cunge et al. 1980; Khan and Lai 2014). A semi-implicit approach is also used in some models.

## 9.6 One-Sided First-Order Upwind Scheme

In this section, the first-order upwind finite volume method of Ying et al. (2004) is described. In this model, the SWE are used in the form given by Eqs. (9.103) and (9.104), so the scheme is well-balanced. The updating formula is given by the integral equation

$$\mathbf{U}_i^{k+1} = \mathbf{U}_i^k - \frac{\Delta t}{\Delta x} (\mathbf{F}_{i+1/2} - \mathbf{F}_{i-1/2}) + \Delta t \mathbf{S}_i. \quad (9.111)$$

The numerical flux is evaluated with the one-sided upwind method as (Ying et al. 2004)

$$\mathbf{F}_{i+1/2} = \left[ \begin{array}{c} q_{i+j}^k \\ \frac{(q_{i+j}^k)^2}{h_{i+j}^k} \end{array} \right]. \quad (9.112)$$

Here  $j = 0$  if  $q_i$  and  $q_{i+1} > 0$ ,  $j = 1$  if  $q_i$  and  $q_{i+1} < 0$ , and  $j = 1/2$  for any other case; subscript  $i + 1/2$  means in that case average values between  $i$  and  $i + 1$  cell-averaged values. The water surface gradient cannot be evaluated with a central difference, given that non-physical jumps are then formed within rarefaction waves (Ying et al. 2004). Thus, an average between up- and downwind gradients is formed as (Ying et al. 2004)

$$gh \frac{\partial z_s}{\partial x} = gh_i^{k+1} \left( w_1 \frac{z_{s,i+1-j}^{k+1} - z_{s,i-j}^{k+1}}{\Delta x} + w_2 \frac{z_{s,i+j}^{k+1} - z_{s,i-1+j}^{k+1}}{\Delta x} \right). \quad (9.113)$$

Note that the water depths used in Eq. (9.113) are those at time  $k + 1$ , after solving the advection step for the continuity equation. The weighting factors are

$$w_1 = 1 - \frac{\Delta t}{\Delta x} \frac{U_{i+1-j}^k + U_{i-j}^k}{2} \quad \text{and} \quad w_2 = \frac{\Delta t}{\Delta x} \frac{U_{i+j}^k + U_{i-1+j}^k}{2}. \quad (9.114)$$

The computational sequence to apply the scheme encompasses the following steps:

- (1) Start with known cell-averaged values of  $\mathbf{U}$  at a time level  $k$ .
- (2) Determine a stable time step  $\Delta t$  using the CFL condition, e.g., typically with  $\text{CFL} = 0.9$ , using Eq. (9.29).
- (3) Compute the numerical fluxes  $\mathbf{F}_{i+1/2}$  using Eq. (9.112).
- (4) Compute the water depths solving the advection step for the continuity equation

$$h_i^{k+1} = h_i^k - \frac{\Delta t}{\Delta x} (q_{i+1/2} - q_{i-1/2}). \quad (9.115)$$

- (5) Evaluate the water surface gradient source term using Eq. (9.113).
- (6) Compute the discharge at the new time level including the effects of source terms as

$$\begin{aligned} q_i^{k+1} &= q_i^k \\ &- \frac{\Delta t}{\Delta x} \left[ \frac{q_{i+j}^2 - q_{i-j}^2}{h_{i+j}} \right] - gh_i^{k+1} \left( w_1 \frac{z_{s,i+1-j}^{k+1} - z_{s,i-j}^{k+1}}{\Delta x} + w_2 \frac{z_{s,i+j}^{k+1} - z_{s,i-1+j}^{k+1}}{\Delta x} \right) \Delta t \\ &- \frac{f}{8} U_i^k |U_i^k| \Delta t. \end{aligned} \quad (9.116)$$

- (7) Go to step (1), and repeat the cycle until reaching the final time of computations.

## 9.7 MUSCL-Hancock Second-Order TVD Scheme

### 9.7.1 MUSCL Reconstruction

van Leer introduced a second-order version of the Godunov (1959) scheme (van Leer 1979). The scheme is called MUSCL (Monotonic Upstream Centered Schemes for Conservation Laws). Second-order accuracy is regained by reconstructing the solution  $\mathbf{U}(x)$  within the cells. The idea is to replace data representation using the constant cell-averaged value  $\mathbf{U}_i$  by a function  $\mathbf{U}(x_{i-1/2} < x < x_{i+1/2})$  that approximates the exact solution within a cell. The function used for the reconstruction must preserve the cell-averaged value regained from the conservative formula. That is, the latest cell-averaged values available obtained by applying the time stepping are used in the reconstruction of the solution at the actual time level. In van Leer's scheme, the reconstruction of the solution within a cell is linear (Fig. 9.12a, b), but parabolic approximations also apply (Colella and Woodward 1984). The linear reconstruction of the solution  $\mathbf{U}(x)$  within a cell gives

$$\mathbf{U}_i(x) = \mathbf{U}_i^k + (x - x_i) \frac{\Delta \mathbf{U}_i}{\Delta x}. \quad (9.117)$$

Note that the slope vector is constant for a given cell, but each conserved variable will have a different scalar slope contained therein. To compute the slope vector for the reconstructed solution,  $\Delta \mathbf{U}_i / \Delta x$ , up- and downstream jumps are first defined as

$$\Delta \mathbf{U}_{i-1/2} = \mathbf{U}_i^k - \mathbf{U}_{i-1}^k, \quad \Delta \mathbf{U}_{i+1/2} = \mathbf{U}_{i+1}^k - \mathbf{U}_i^k. \quad (9.118)$$

Taking an average slope, with the averaging coefficient  $-1 < \omega < 1$ , produces (Toro 2001)

$$\Delta \mathbf{U}_i = \frac{1}{2} [(1 - \omega) \Delta \mathbf{U}_{i+1/2} + (1 + \omega) \Delta \mathbf{U}_{i-1/2}]. \quad (9.119)$$

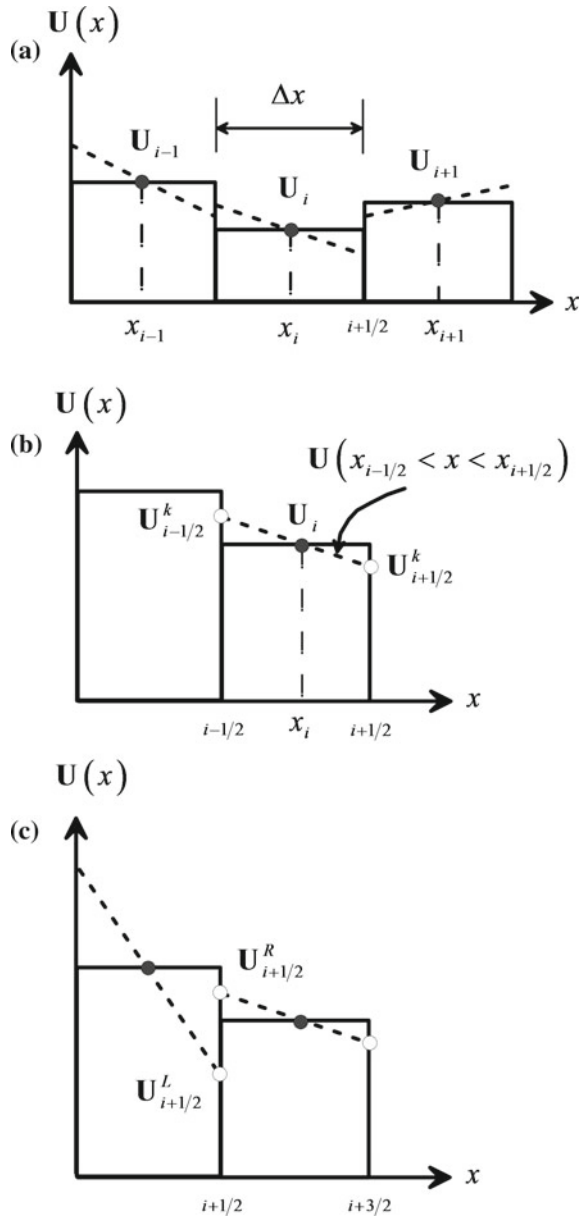
A typical value is  $\omega = 0$ . The boundary extrapolated values at each cell face are thus (Fig. 9.12b)

$$\mathbf{U}_{i-1/2}^k = \mathbf{U}_i^k - \frac{1}{2} \Delta \mathbf{U}_i, \quad \mathbf{U}_{i+1/2}^k = \mathbf{U}_i^k + \frac{1}{2} \Delta \mathbf{U}_i. \quad (9.120)$$

Thus, the solution of a Riemann problem at a generic interface  $i + 1/2$  is now conducted based on extrapolated values at the left and right sides of each interface (Fig. 9.12c)

$$\mathbf{U}_{i+1/2}^L = \mathbf{U}_i^k + \frac{1}{2} \Delta \mathbf{U}_i, \quad \mathbf{U}_{i+1/2}^R = \mathbf{U}_{i+1}^k - \frac{1}{2} \Delta \mathbf{U}_{i+1}. \quad (9.121)$$

**Fig. 9.12** MUSCL reconstruction. **a** Linear approximation within cells, **b** definition of extrapolated values at cell faces [the figure represents the typical reconstruction of a component of the vector  $\mathbf{U} = (U_1, U_2)^T$ ], and **c** formation of local Riemann problem at interface  $i + 1/2$





**Bram van Leer** was born on November 26, 1942, at Surabaya, Netherlands East Indies. He obtained the Ph.D. degree from Leiden State University in 1970. He made seminal contributions to computational fluid dynamics (CFD) in his 5-part article series “Towards the ultimate conservative difference scheme” published from 1972 to 1979, where he extended Godunov’s finite volume scheme to second order (MUSCL), developed non-oscillatory interpolation using limiters, an approximate Riemann solver, and discontinuous Galerkin schemes for unsteady advection. Since joining the University of Michigan’s Aerospace Engineering Department in 1986, he has worked on convergence acceleration by local preconditioning and multigrid relaxation for Euler and Navier–Stokes problems, unsteady adaptive grids, space-environment modeling, atmospheric flow modeling, extended hydrodynamics for rarefied flows, and discontinuous Galerkin methods. He retired in 2012. His research interests were in CFD, fluid dynamics, and numerical analysis.

He obtained in 1996 the College of Engineering Research Award (University of Michigan), was elected in 1995 AIAA Fellow, was awarded in 1990 and 1992 the NASA Langley Group Achievement Award, in 1992 the Department of Aerospace Engineering Research Award (University of Michigan), the Honorary Doctorate from the Vrije Universiteit Brussels in 1990, and the C. J. Kok Prize of Leiden State University in 1978. He is a Fellow of the American Institute of Aeronautics and Astronautics (AIAA) and Member of the Society for Industrial and Applied Mathematics (SIAM).

### 9.7.2 Slope Limiting

The reconstruction process previously exposed produces spurious numerical oscillations in zones with sharp variations of  $\mathbf{U}$ , as at a shock wave front (Toro 2009). Gibbs’ phenomenon must be controlled, therefore. This control is achieved

using the so-called total variation diminishing (TVD) schemes. They suppress Gibbs' phenomenon by degradation of the scheme to first-order accuracy in zones with sharp variations of  $\mathbf{U}$ , while keeping second-order accuracy in smooth portions of the solution. Spurious oscillations are suppressed by limiting the slope in the reconstruction stage. Thus, the reconstruction of the solution reads now with  $\overline{\Delta \mathbf{U}_i}/\Delta x$  as the limited slope vector

$$\begin{aligned}\mathbf{U}_i(x) &= \mathbf{U}_i^k + (x - x_i) \frac{\overline{\Delta \mathbf{U}_i}}{\Delta x}, \\ \mathbf{U}_{i+1/2}^L &= \mathbf{U}_i^k + \frac{1}{2} \overline{\Delta \mathbf{U}_i}, \quad \mathbf{U}_{i+1/2}^R = \mathbf{U}_{i+1}^k - \frac{1}{2} \overline{\Delta \mathbf{U}_{i+1}}.\end{aligned}\tag{9.122}$$

The idea is to limit the slopes obtained in the reconstruction stage by applying a limiter function. A widely used limiting function is the so-called minmod limiter, which for two numbers  $a$  and  $b$  is

$$\text{Minmod}(a, b) = \text{sign}(a) \max[0, \min(|a|, \text{sign}(a) \cdot b)].\tag{9.123}$$

Expanding the function, the possible cases are summarized as:

$$\text{Minmod}(a, b) = \begin{cases} a & \text{if } |a| < |b| \text{ and } a \cdot b > 0 \\ b & \text{if } |a| > |b| \text{ and } a \cdot b > 0 \\ 0 & \text{if } a \cdot b < 0 \end{cases}.\tag{9.124}$$

The minmod function gives the smallest modulus if all arguments have the same sign and is zero otherwise. For the MUSCL scheme, the minmod limiter is thus

$$\overline{\Delta \mathbf{U}_i} = \text{sign}(\Delta \mathbf{U}_{i+1/2}) \max[0, \min(|\Delta \mathbf{U}_{i+1/2}|, \text{sign}(\Delta \mathbf{U}_{i+1/2}) \cdot \Delta \mathbf{U}_{i-1/2})].\tag{9.125}$$

The three possible cases are depicted in Fig. 9.13. If the jumps have the same sign (Fig. 9.13a, b), the solution is monotone. Therefore, the limited jump is nonzero, and equal to the smaller one in absolute value. If the jumps change their signs, the up- and downslopes have different signs (Fig. 9.13c), thereby implying a solution  $\mathbf{U}(x)$  of certain curvature (oscillation). The propagation of these non-physical undulations is constrained turning to first-order accuracy the scheme by setting the limited jump to zero. Thus, the linear reconstruction is not done in these cases. Therefore, the TVD scheme is adaptive; it decides the regions of the computational domain where the scheme has to be second-order accurate and those where the linear reconstructions must

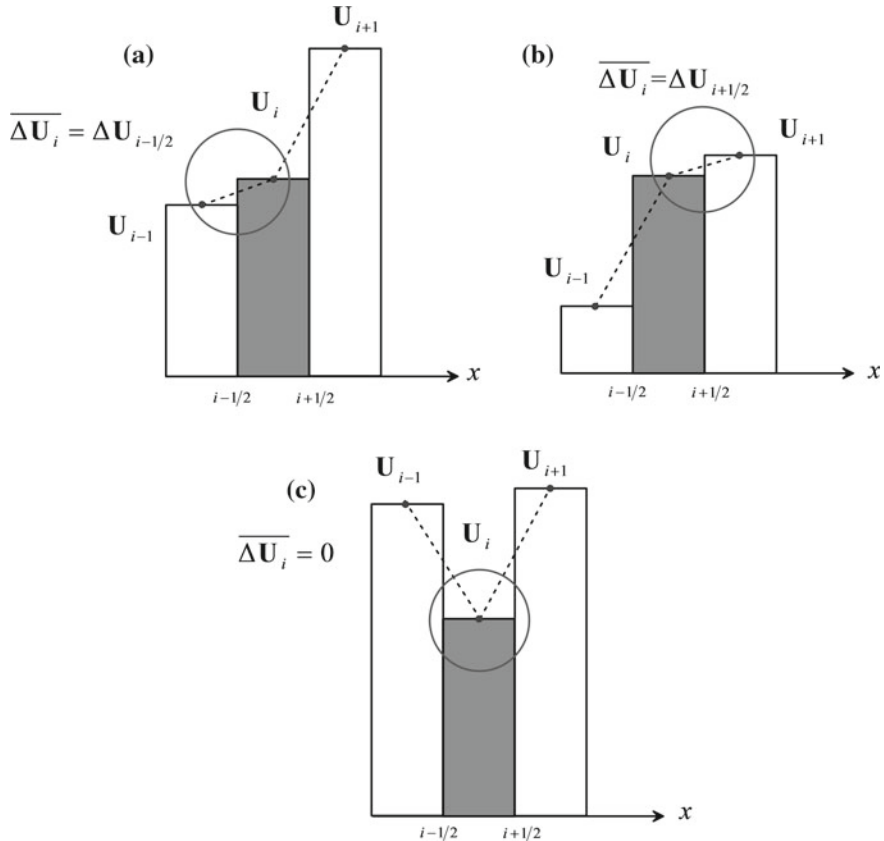


**Fig. 9.13** Effect of minmod slope limiter. **a** Limited jump is the upstream jump, **b** Limited jump is the downstream jump, and **c** limited jump is zero [the figure represents a component of the vector  $\mathbf{U} = (U_1, U_2)^T$ ]

be switched off, thereby reducing to Godunov's first-order scheme. A family of limiters is formulated as (Bradford and Sanders 2005)

$$\overline{\Delta \mathbf{U}_i} = \begin{cases} \text{sign}(\Delta \mathbf{U}_{i+1/2}) \min[\min(|\Delta \mathbf{U}_{i+1/2}|, |\Delta \mathbf{U}_{i-1/2}|), \beta \cdot \min(|\Delta \mathbf{U}_{i+1/2}|, |\Delta \mathbf{U}_{i-1/2}|)] & \text{if } \Delta \mathbf{U}_{i+1/2} \cdot \Delta \mathbf{U}_{i-1/2} > 0 \\ 0 & \text{else.} \end{cases} \quad (9.126)$$

For  $\beta = 2$  results the Superbee limiter; for  $\beta = 1$ , it simplifies to the minmod limiter, whereas  $\beta = 0$  reduces the scheme to first order. The Superbee limiter is less diffusive than minmod, thus producing a sharper resolution of shocks. The reconstructed flow depths at the cell interface shall not become negative, to be assured prior to compute the numerical flux (Sanders 2001).

### 9.7.3 Hancock Step

The MUSCL scheme (van Leer 1979) described is second-order accurate in space, but only first-order accurate in time. It was simplified and improved by Hancock (1980) while developing the PISCES industrial simulation code (Van Leer 2006). The method would have remained unnoticed in the manual of this code, but it was rescued by van Albada et al. (1982) and applied for the simulation of cosmic gas dynamics. The idea of Hancock's predictor–corrector scheme is remarkably simple: A first-order upwind method transforms into second-order time accuracy by evolving the cell boundary values used to compute the numerical flux, and the source terms, by half the time step (Sweby 1999). Thus, to regain second-order accuracy in both time and space, the vector  $\mathbf{U}$  is expanded using a Taylor series within a cell as follows. The cell interface value evolved a time  $\Delta t/2$ ,  $\mathbf{U}_{i+1/2}^{k+1/2} = \mathbf{U}(\frac{1}{2}\Delta x, \frac{1}{2}\Delta t)$ , can be expressed as a function of the cell-averaged value at time  $k$  using a Taylor series for two variables as (Sweby 1999)

$$\mathbf{U}_{i+1/2}^{k+1/2} = \mathbf{U}_i^k + \frac{1}{2}\Delta x \left( \frac{\partial \mathbf{U}}{\partial x} \right)_i^k + \frac{1}{2}\Delta t \left( \frac{\partial \mathbf{U}}{\partial t} \right)_i^k + O(\Delta x^2, \Delta t^2). \quad (9.127)$$

Note that the value of  $\mathbf{U}$  at the cell center at time  $k$  is the cell-averaged value, as assured by the MUSCL linear reconstruction at time level  $k$ . The time derivative of  $\mathbf{U}$  is from the differential form of the SWE

$$\frac{\partial \mathbf{U}}{\partial t} = -\frac{\partial \mathbf{F}}{\partial x} + \mathbf{S}. \quad (9.128)$$

Inserting Eq. (9.128) into Eq. (9.127) produces

$$\begin{aligned} \mathbf{U}_{i+1/2}^{k+1/2} &= \mathbf{U}_i^k + \frac{1}{2}\Delta x \left( \frac{\partial \mathbf{U}}{\partial x} \right)_i^k + \frac{1}{2}\Delta t \left( -\frac{\partial \mathbf{F}}{\partial x} + \mathbf{S} \right)_i^k \\ &= \mathbf{U}_i^k + \frac{1}{2}\Delta x \left( \frac{\partial \mathbf{U}}{\partial x} \right)_i^k - \frac{1}{2}\Delta t \left( \frac{\partial \mathbf{F}}{\partial x} \right)_i^k + \frac{1}{2}\Delta t \mathbf{S}_i^k. \end{aligned} \quad (9.129)$$

Based on the MUSCL reconstruction, the slope is

$$\left( \frac{\partial \mathbf{U}}{\partial x} \right)_i^k = \frac{\mathbf{U}_{i+1/2}^k - \mathbf{U}_{i-1/2}^k}{\Delta x}. \quad (9.130)$$

Approximating the gradient of fluxes by a first-order finite-difference as

$$\left( \frac{\partial \mathbf{F}}{\partial x} \right)_i^k \approx \frac{\mathbf{F}(\mathbf{U}_{i+1/2}^k) - \mathbf{F}(\mathbf{U}_{i-1/2}^k)}{\Delta x}, \quad (9.131)$$

and noting that

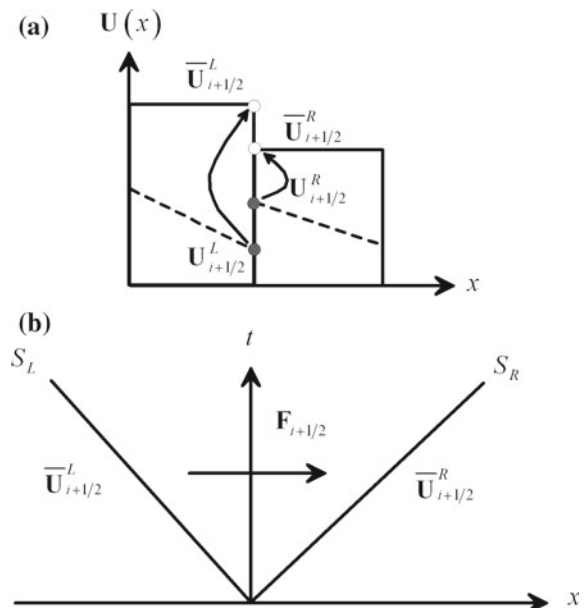
$$\mathbf{S}_i^k = \mathbf{S}(\mathbf{U}_i^k), \quad (9.132)$$

the relations needed in Eq. (9.129), namely Eqs. (9.130)–(9.132), are available. Inserting these, one gets

$$\begin{aligned} \mathbf{U}_{i+1/2}^{k+1/2} &= \mathbf{U}_i^k + \underbrace{\frac{1}{2}\Delta x \frac{\mathbf{U}_{i+1/2}^k - \mathbf{U}_{i-1/2}^k}{\Delta x}}_{\text{MUSCL reconstruction}} - \frac{1}{2}\Delta t \frac{\mathbf{F}(\mathbf{U}_{i+1/2}^k) - \mathbf{F}(\mathbf{U}_{i-1/2}^k)}{\Delta x} + \frac{1}{2}\Delta t \mathbf{S}(\mathbf{U}_i^k) \\ &= \mathbf{U}_{i+1/2}^k - \frac{\Delta t}{2\Delta x} [\mathbf{F}(\mathbf{U}_{i+1/2}^k) - \mathbf{F}(\mathbf{U}_{i-1/2}^k)] + \frac{\Delta t}{2} \mathbf{S}(\mathbf{U}_i^k). \end{aligned} \quad (9.133)$$

This is Hancock's step to regain second-order time accuracy: The MUSCL reconstructed interface values  $\mathbf{U}_{i+1/2}^k$  at time  $k$  are evolved half the time step to obtain an improved data representation given by  $\mathbf{U}_{i+1/2}^{k+1/2}$ . Looking to an interface rather than to a single cell, Hancock's step amounts to evolve the interface values  $\mathbf{U}_{i+1/2}^L$  and  $\mathbf{U}_{i+1/2}^R$  to regain second-order accuracy in time to  $\overline{\mathbf{U}}_{i+1/2}^L$  and  $\overline{\mathbf{U}}_{i+1/2}^R$  (Fig. 9.14a). These are given by Hancock's scheme from Eq. (9.133) as

**Fig. 9.14** Hancock's step. **a** Evolution of boundary extrapolated value at interface  $i + 1/2$  half the time step and **b** formation of new local Riemann problem at interface  $i + 1/2$  with evolved values at the interface



$$\begin{aligned}\bar{\mathbf{U}}_{i+1/2}^L &= \mathbf{U}_{i+1/2}^L - \frac{\Delta t}{2\Delta x} \left[ \mathbf{F}\left(\mathbf{U}_{i+1/2}^L\right) - \mathbf{F}\left(\mathbf{U}_{i-1/2}^R\right) \right] + \frac{\Delta t}{2} \mathbf{S}_i, \\ \bar{\mathbf{U}}_{i+1/2}^R &= \mathbf{U}_{i+1/2}^R - \frac{\Delta t}{2\Delta x} \left[ \mathbf{F}\left(\mathbf{U}_{i+3/2}^L\right) - \mathbf{F}\left(\mathbf{U}_{i+1/2}^R\right) \right] + \frac{\Delta t}{2} \mathbf{S}_{i+1},\end{aligned}\quad (9.134)$$

forming a new local Riemann problem. With these evolved boundary extrapolated variables  $\bar{\mathbf{U}}_{i+1/2}^L$  and  $\bar{\mathbf{U}}_{i+1/2}^R$  defining states  $L$  and  $R$ , the numerical flux is computed using the HLL approximate Riemann solver (Fig. 9.14b). Once this flux is determined, the computation of the transient flow is conducted as described previously. Note that this predictor step considers the source terms. The bed-slope effect is typically accounted for (Zhou et al. 2001; Aureli et al. 2008). It is evaluated based on interface data at cell  $i$  as [see Eq. (9.99)]

$$\left(gh\frac{\partial z_b}{\partial x}\right)_i = g \frac{\left(\bar{h}_{i+1/2}^L + \bar{h}_{i-1/2}^R\right)}{2} \frac{(z_{bi+1/2} - z_{bi-1/2})}{\Delta x}. \quad (9.135)$$

Friction is treated in a final splitting step using an implicit treatment (Aureli et al. 2008) to increase stability in the vicinity of wet-dry interfaces.

#### 9.7.4 Computational Sequence

The computational process is summarized in the following steps:

- (1) Start at time level  $k$  with the cell-averaged values  $\mathbf{U}_i$ .
- (2) Apply the CFL condition [Eq. (9.29)] to select a stable time step.
- (3) Reconstruct the solution using the TVD MUSCL scheme: Get a limited slope applying the minmod limiter [Eq. (9.125)] to suppress spurious oscillations. Other limiters are possible.
- (4) Compute values at cell interfaces using the limited slopes [Eq. (9.122)].
- (5) Evolve the interface values half the time step using Hancock's method [Eq. (9.134)].
- (6) Solve the Riemann problem at each interface using the evolved interface values typically with the HLL approximate Riemann solver. Other methods to compute the numerical flux are possible, as the exact Riemann solver.
- (7) Apply the conservative equation to resolve the advection step

$$\mathbf{U}_i^{\text{adv}} = \mathbf{U}_i^k - \frac{\Delta t}{\Delta x} \left[ \mathbf{F}_{i+1/2} \left( \bar{\mathbf{U}}_{i+1/2}^L, \bar{\mathbf{U}}_{i+1/2}^R \right) - \mathbf{F}_{i-1/2} \left( \bar{\mathbf{U}}_{i-1/2}^L, \bar{\mathbf{U}}_{i-1/2}^R \right) \right]. \quad (9.136)$$

- (8) Include the effect of the bed-slope source terms using the values obtained at time  $k + 1/2$  with Hancock's method, e.g.,

$$\tilde{\mathbf{U}}_i = \mathbf{U}_i^{\text{adv}} - \left[ 0, \frac{\Delta t}{2\Delta x} g(\bar{h}_{i+1/2}^L + \bar{h}_{i-1/2}^R)(z_{bi+1/2} - z_{bi-1/2}) \right]^T. \quad (9.137)$$

Combining Eqs. (9.136) and (9.137) yields (Mingham and Causon 1998; Aureli et al. 2008)

$$\begin{aligned} \tilde{\mathbf{U}}_i = & \mathbf{U}_i^k - \frac{\Delta t}{\Delta x} \left[ \mathbf{F}_{i+1/2} \left( \bar{\mathbf{U}}_{i+1/2}^L, \bar{\mathbf{U}}_{i+1/2}^R \right) - \mathbf{F}_{i-1/2} \left( \bar{\mathbf{U}}_{i-1/2}^L, \bar{\mathbf{U}}_{i-1/2}^R \right) \right] \\ & - \left[ 0, \frac{\Delta t}{2\Delta x} g(\bar{h}_{i+1/2}^L + \bar{h}_{i-1/2}^R)(z_{bi+1/2} - z_{bi-1/2}) \right]^T. \end{aligned} \quad (9.138)$$

This is only a function of the predicted values at  $k + 1/2$  obtained with Hancock's method.

- (9) Include the effect of friction using an implicit Euler scheme

$$\mathbf{U}_i^{k+1} = \tilde{\mathbf{U}}_i - \Delta t \left[ 0, \frac{f}{8} U_i^{k+1} |U_i^{k+1}| \right]^T. \quad (9.139)$$

A semi-implicit trapezoidal rule also applies (Aureli et al. 2008).

- (10) Go to step (1), and repeat the cycle until reaching the target time.

### 9.7.5 Surface Gradient Method

The MUSCL reconstruction process of the vector  $\mathbf{U} = (h, q)^T$  (step 3 in the sequence above) is called depth gradient method (DGM) (Zhou et al. 2001); it may lead to unphysical discharges over uneven topography; given that for static water, the reconstruction of variable  $h$  will produce jumps in water depths at cell interfaces and thus a water movement even if the water is initially at rest. Figure 9.15 depicts the application of DGM to an uneven profile, from where is seen that

$$h_i^k \neq h_{i+1}^k \neq h_{i+2}^k. \quad (9.140)$$

A linear reconstruction yields a local Riemann problem at each cell involving left and right states

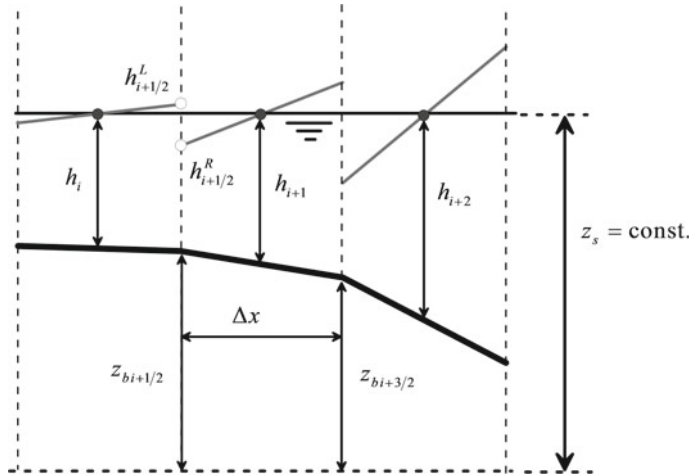


**Fig. 9.15** Generation of jump in water depths at cell interfaces by the depth gradient method over uneven topography

$$\mathbf{U}_{i+1/2}^L = \begin{pmatrix} h_{i+1/2}^L \\ q_{i+1/2}^L = 0 \end{pmatrix}, \quad \mathbf{U}_{i+1/2}^R = \begin{pmatrix} h_{i+1/2}^R \\ q_{i+1/2}^R = 0 \end{pmatrix}. \quad (9.141)$$

Assume to compute now the first time step of the transient flow, starting with zero discharge in the system and a horizontal free surface. Reconstruction of the depth profile yields the momentum equation

$$q_i^{k+1} = -g \frac{\Delta t}{\Delta x} \frac{\left(F_{i+1/2}^R\right)^2 - \left(F_{i-1/2}^R\right)^2}{2} - g \Delta t \frac{\left(h_{i+1/2}^L + h_{i-1/2}^R\right)}{2} \frac{(z_{bi+1/2} - z_{bi-1/2})}{\Delta x} \neq 0. \quad (9.142)$$

In this equation,  $F_{i+1/2}^R$  is the momentum function obtained at the interface  $i + 1/2$  solving the Riemann problem formed there. Obviously, the discharge is in general not zero, indicating the generation of an unphysical discharge. If  $h_{i+1/2}^L = h_{i+1/2}^R = h_{i+1/2}$ , Eq. (9.142) reduces to

$$q_i^{k+1} = -g \frac{\Delta t}{\Delta x} \frac{\left(h_{i+1/2}^2 - h_{i-1/2}^2\right)}{2} - g \Delta t \frac{h_{i+1/2} + h_{i-1/2}}{2} \frac{(z_{bi+1/2} - z_{bi-1/2})}{\Delta x} = 0, \quad (9.143)$$

which is zero by virtue of the condition  $z_s = \text{const.}$  Thus, to avoid unphysical discharge it is necessary to block the formation of jumps in water depths at cell faces during the reconstruction stage.

Based on this result, an alternative is to reconstruct the free surface elevation  $z_s$  and discharge  $q$ , and, once done, the water depths are deduced at the intercell faces (Nujic 1995; Zhou et al. 2001). The reconstructed interface values are then

$$\mathbf{Q}_{i-1/2}^k = \mathbf{Q}_i^k - \frac{1}{2}\overline{\Delta \mathbf{Q}_i}, \quad \mathbf{Q}_{i+1/2}^k = \mathbf{Q}_i^k + \frac{1}{2}\overline{\Delta \mathbf{Q}_i}, \quad (9.144)$$

where

$$\mathbf{Q} = \begin{pmatrix} z_s \\ q \end{pmatrix} = \begin{pmatrix} z_b + h \\ q \end{pmatrix}. \quad (9.145)$$

Once the interface values are determined with the limited slopes, the water depths at the cell faces are

$$h_{i-1/2}^k = (z_s)_{i-1/2}^k - (z_b)_{i-1/2}, \quad h_{i+1/2}^k = (z_s)_{i+1/2}^k - (z_b)_{i+1/2}. \quad (9.146)$$

With this technique, the identity given by Eq. (9.143) is preserved, and thus, unphysical discharge is not generated, given that the flow depths at the cell faces are unique for static conditions. This technique is referred to as the surface gradient method (SGM). This reconstruction, however, can lead to small, even negative water depths near dry-wet fronts (Aureli et al. 2008). DGM, in contrast, is more robust for bore front tracking. Aureli et al. (2008) propose a hybrid reconstruction combining the good capabilities of the SGM and DGM, called weighted surface-depth gradient method.

## 9.8 Boundary and Initial Conditions

### 9.8.1 Boundary Conditions

The computational domain is typically divided into  $N$  cells (Fig. 9.16a) of width  $\Delta x$ , e.g., with the initial data

$$\mathbf{U}_i^k, \quad i = 1, 2, \dots, N-1, N. \quad (9.147)$$

The conservative Eq. (9.7) is used to evolve the vector  $\mathbf{U}$  as

$$\mathbf{U}_i^{k+1} = \mathbf{U}_i^k - \frac{\Delta t}{\Delta x} (\mathbf{F}_{i+1/2} - \mathbf{F}_{i-1/2}) + \Delta t \mathbf{S}_i, \quad i = 1, 2, \dots, N-1, N. \quad (9.148)$$

On inspecting Eq. (9.148), two issues are noted:

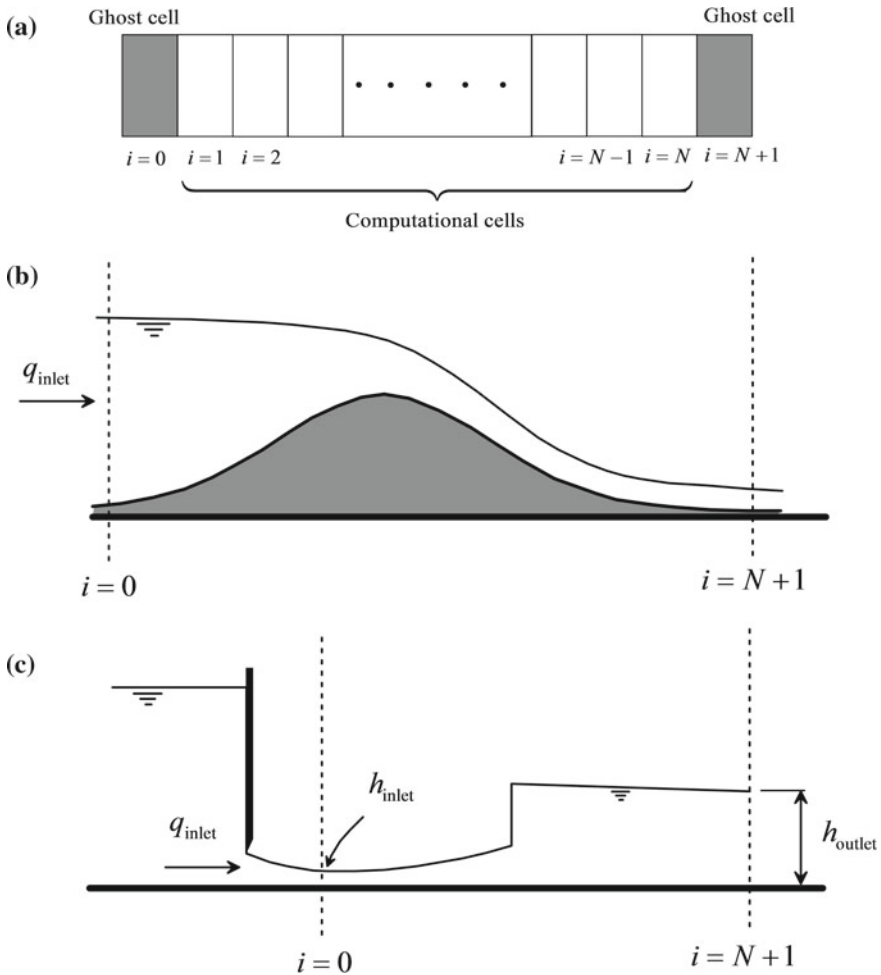


**Fig. 9.16** Boundary conditions. **a** Definition of ghost cells in the computational domain, ghost cells in **(b)** weir flow, **c** gate flow

(i) The updating equation for cell  $i = 1$  is

$$\mathbf{U}_1^{k+1} = \mathbf{U}_1^k - \frac{\Delta t}{\Delta x} (\mathbf{F}_{3/2} - \mathbf{F}_{1/2}) + \Delta t \mathbf{S}_1. \quad (9.149)$$

In this formula, the numerical flux entering into the left face of cell  $i = 1$ , namely  $\mathbf{F}_{1/2}$ , is needed. However, there is no initial data defined to form a Riemann problem at this interface and thus compute the numerical flux.

(ii) The updating equation for cell  $i = N$  is

$$\mathbf{U}_N^{k+1} = \mathbf{U}_N^k - \frac{\Delta t}{\Delta x} (\mathbf{F}_{N+1/2} - \mathbf{F}_{N-1/2}) + \Delta t \mathbf{S}_N. \quad (9.150)$$

In this formula, the numerical flux leaving the right face of cell  $i = N$ , namely  $\mathbf{F}_{N+1/2}$ , is needed. However, there is no initial data defined to form a Riemann problem at this interface and thus compute the numerical flux.

From the above arguments, it is necessary to incorporate two additional cells at the left and right ends of the computational domain, called ghost cells (LeVeque 2002; Toro 2009) (Fig. 9.16a). Physical boundary conditions are transmitted to the computational model through these cells, which in turn are used to form two additional Riemann problems needed to compute the missing numerical fluxes and thus evolve in time cells  $i = 1$  and  $N$ . Here, the simplest way of implementing boundary conditions is exposed using ghost cells with a zero-order extrapolation from the interior solution. Care should be taken to ensure that spurious waves are not generated when implementing boundary conditions (LeVeque 2002).

#### *Subcritical inflow section*

At a subcritical inflow section, one boundary condition must be prescribed, as known from the method of characteristics, explained in Chap. 5 (Henderson 1966; Jain 2001). This is typically the inlet discharge for weir flow (Fig. 9.16b). The other variable needed at the ghost cell is obtained approximately by extrapolation from the interior solution (LeVeque 2002). The vector  $\mathbf{U}$  at the ghost cell  $i = 0$  is thus given by

$$\begin{aligned} q_o^{k+1} &= q_{\text{inlet}}, \\ h_o^{k+1} &= h_1^{k+1}. \end{aligned} \quad (9.151)$$

For a more rigorous computation of  $h_o^{k+1}$  the characteristic  $C^+$  shall be used (see Chaps. 5 and 7; Eq. 7.37).

#### *Subcritical outflow section*

At a supercritical outflow section, boundary conditions are not needed (see Chap. 5). The other variable required at the ghost cell is obtained approximately by extrapolation from the interior solution (LeVeque 2002). This is typical for supercritical flow at the tailwater portion of weir flow (Fig. 9.16b). The vector  $\mathbf{U}$  at the ghost cell  $i = N + 1$  is thus given by

$$\begin{aligned} q_{N+1}^{k+1} &= q_N^{k+1}, \\ h_{N+1}^{k+1} &= h_{\text{outlet}}. \end{aligned} \quad (9.152)$$

For a more rigorous computation of  $q_{N+1}^{k+1}$  the characteristic  $C^+$  shall be used (see Chaps. 5 and 7; Eq. 7.39).

### *Supercritical inflow section*

At a supercritical inflow section, two boundary conditions must be prescribed (see Chap. 5). This is typical for supercritical flow issued from a sluice (Fig. 9.16c). The vector  $\mathbf{U}$  at the ghost cell  $i = 0$  is thus given by

$$\begin{aligned} q_o^{k+1} &= q_{\text{inlet}}, \\ h_o^{k+1} &= h_{\text{inlet}}. \end{aligned} \quad (9.153)$$

Here, inlet conditions refer to the *vena contracta* conditions.

### *Supercritical outflow section*

At a supercritical outflow section, boundary conditions are not needed (see Chap. 5). The two variables required at the ghost cell are obtained by extrapolation from the interior solution (LeVeque 2002). This is typical for supercritical flow at the tailwater portion of weir flow (Fig. 9.16b). The vector  $\mathbf{U}$  at the ghost cell  $i = N + 1$  is thus given by

$$\begin{aligned} q_{N+1}^{k+1} &= q_N^{k+1}, \\ h_{N+1}^{k+1} &= h_N^{k+1}. \end{aligned} \quad (9.154)$$

After application of the conservative equation in a given time loop, the following data are generated:

$$\mathbf{U}_i^{k+1}, \quad i = 1, 2, \dots, N-1, N. \quad (9.155)$$

Once this step finished,  $\mathbf{U}$  at the ghost cells is determined depending on the type of flow section as exposed above and summarized here as:

$$\begin{aligned} \mathbf{U}_o^{k+1} &= \begin{pmatrix} h \\ q \end{pmatrix}_o^{k+1} \\ &= \begin{cases} \text{one boundary condition, one value extrapolated from } i = 1 & \text{if } F_1 < 1 \\ \text{two boundary conditions} & \text{if } F_1 > 1, \end{cases} \\ \mathbf{U}_{N+1}^{k+1} &= \begin{pmatrix} h \\ q \end{pmatrix}_{N+1}^{k+1} \\ &= \begin{cases} \text{one boundary condition, one value extrapolated from } i = N & \text{if } F_N < 1 \\ \text{two values extrapolated from } i = N & \text{if } F_N > 1. \end{cases} \end{aligned} \quad (9.156)$$

### 9.8.2 Initial Conditions

The initial conditions are the values of vector  $\mathbf{U}$  at the computational cells at the initial instant at which transient computations start, e.g.,

$$\mathbf{U}_i^0 = \begin{pmatrix} h \\ q \end{pmatrix}_i^0, \quad i = 1, 2, \dots, N-1, N. \quad (9.157)$$

If the water is initially static over a variable bottom profile of constant elevation  $z_s$ , the vector is

$$\mathbf{U}_i^0 = \begin{pmatrix} h \\ q \end{pmatrix}_i^0 = \begin{pmatrix} z_s - z_{bi} \\ 0 \end{pmatrix}, \quad i = 1, 2, \dots, N-1, N. \quad (9.158)$$

This is a wet-bed initial vector. For dry-bed portions of the computational domain, the vector reads

$$\mathbf{U}_i^0 = \begin{pmatrix} h \\ q \end{pmatrix}_i^0 = \begin{pmatrix} 0 \\ 0 \end{pmatrix}, \quad i = 1, 2, \dots, N-1, N. \quad (9.159)$$

The water may be also under steady-state conditions, once changes in boundary conditions are introduced. Then, the initial discharge is a constant  $q_o$  in the absence of sources/sinks, e.g., infiltration, side weirs, or precipitation. The water depth profile is varied,  $h_o = h_o(x)$ , and it has to be determined with the steady-state techniques of Chaps. 3 and 4, or taken from the steady asymptotic state of a previous unsteady flow computation. The initial vector then reads

$$\mathbf{U}_i^0 = \begin{pmatrix} h \\ q \end{pmatrix}_i^0 = \begin{pmatrix} h_o = h_o(x) \\ q_o = \text{const.} \end{pmatrix}, \quad i = 1, 2, \dots, N-1, N. \quad (9.160)$$

## 9.9 Computational Examples

### 9.9.1 Ideal Dam Break Waves

The MUSCL-Hancock scheme using the HLL approximate Riemann solver was coded and implemented in the file *DamBreakWave.xls* available in Chap. 12. The code can be run with friction, and the selected value of  $\beta$  in the limiter [Eq. (9.126)] fixes the use of minmod ( $\beta = 1$ ), Superbee ( $\beta = 2$ ) or changes the second-order scheme to the Godunov first-order scheme if  $\beta = 0$ . In this section, ideal fluid flow computations in a horizontal channel using the minmod slope limiter are conducted.

If the limiter is deactivated inside the code, spurious oscillations remain un suppressed contaminating numerical solutions.

A subcritical dam break wave of depth ratio  $h_d/h_u = 0.4$  and upstream water depth  $h_u = 1$  m is considered in Fig. 9.17a, b. Numerical simulations were conducted using  $CFL = 0.9$  and  $\Delta x = 0.1$  m, with computational results displayed at time  $t = 3$  s. In the same figure, the exact solution of Stoker (1957), detailed in Chap. 6, is plotted. The MUSCL-Hancock scheme is shown to produce an excellent oscillation-free solution of the wave profiles, including the correct shock strength and position. A most stringent test case is generated in Figs. 9.17c, d using a depth ratio  $h_d/h_u = 0.01$ ,  $h_u = 1$  m and identical values of computational parameters. Critical flow establishes at the dam axis  $x = 0$  in a point of the rarefaction wave. As depicted in the comparison of the numerical solution with the exact results, the MUSCL-Hancock scheme produces a highly accurate resolution of transcritical flow near the dam axis. Therefore, the scheme is entropy preserving and unphysical jumps are avoided. Finally, a dry-bed dam break wave is considered in Figs. 9.17e, f. Dry beds were handled in the numerical model using Eqs. (9.76) and (9.77), and the computational results show good agreement with Ritter's analytical solution (Ritter 1892). Note that the dry front in Fig. 9.16e is faster than the shock fronts in Figs. 9.16a, c. A more detailed study of numerical schemes applied to the dam break problem is available (Zoppou and Roberts 2003).

### 9.9.2 Dam Break Waves with Friction

The MUSCL-Hancock scheme implemented in the file *DamBreakWave.xls* permits simulation of real fluid flows based on Manning's equation for the friction slope

$$S_f = n^2 \frac{U^2}{R_h^{4/3}}, \quad (9.161)$$

where  $n$  is Manning's roughness coefficient and  $R_h$  the hydraulic radius. For an explicit treatment of friction, the updating after the advection step is conducted using

$$q_i^{k+1} = q_i^{\text{adv}} - (ghS_f)_i^{\text{adv}} \Delta t = q_i^{\text{adv}} - gn^2 \left( h \frac{U^2}{R_h^{4/3}} \right)_i^{\text{adv}} \Delta t. \quad (9.162)$$

For an implicit treatment, the updating equation is

$$q_i^{k+1} = q_i^{\text{adv}} - (ghS_f)_i^{k+1} \Delta t = q_i^{\text{adv}} - gn^2 \left( h \frac{U^2}{R_h^{4/3}} \right)_i^{k+1} \Delta t, \quad (9.163)$$

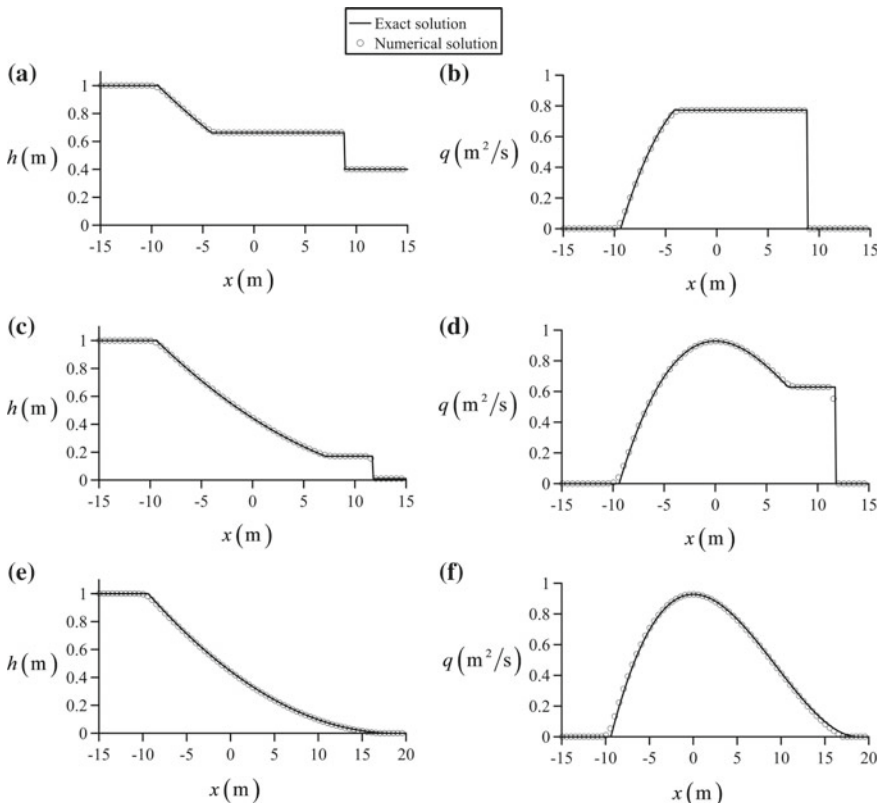


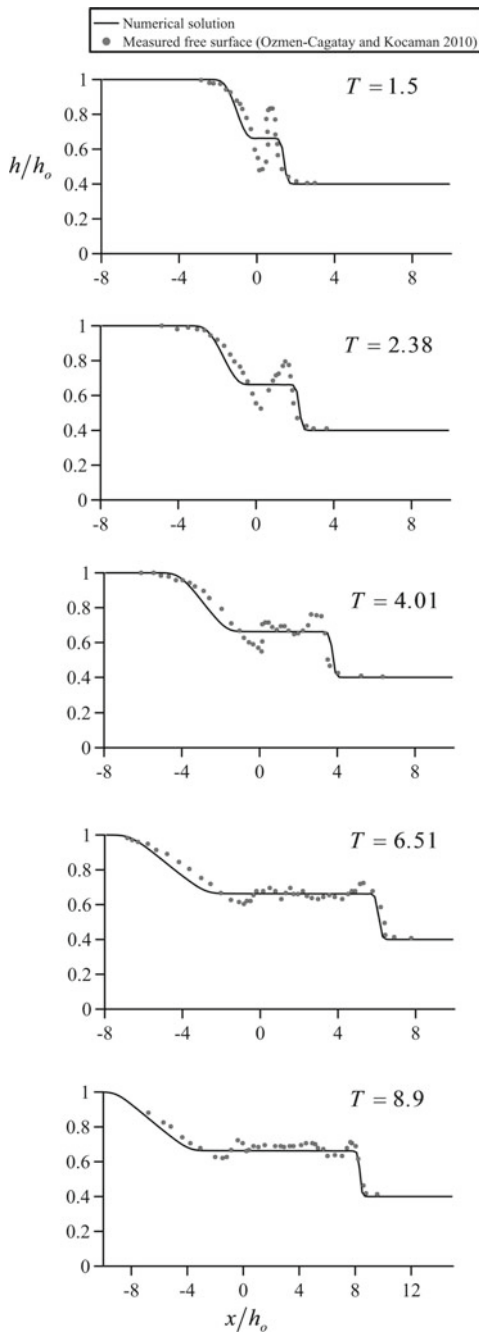
**Fig. 9.17** Ideal dam break wave simulations: comparison of numerical simulations using the MUSCL-Hancock scheme with exact solutions for **a**, **b** subcritical wet-bed test, **c**, **d** transcritical wet-bed test, **e**, **f** dry-bed test

or

$$U_i^{k+1} = \frac{q_i^{\text{adv}}}{h_i^{k+1}} - gn^2 \frac{(U_i^{k+1})^2}{(R_{hi}^{k+1})^{4/3}} \Delta t. \quad (9.164)$$

The experimental data of Ozmen-Cagatay and Kocaman (2010) at various normalized times  $T = t(g/h_o)^{1/2}$  starting at abrupt gate removal are considered in Fig. 9.18 for a subcritical dam break wave test ( $h_d/h_o > 0.138$ ) in a horizontal channel. Their upstream water depth was  $h_o = 0.25$ , the flume width 0.3 m, and the downstream water depth for this series  $h_d = 0.1$  m. Simulations were conducted with the MUSCL-Hancock scheme using  $\text{CFL} = 0.9$  and  $\Delta x = 0.05$  m. Manning's roughness coefficient was set to  $n = 0.005 \text{ m}^{-1/3}\text{s}$ , with an implicit treatment of the

**Fig. 9.18** Comparison of numerical simulations using the MUSCL-Hancock scheme with experimental data (Ozmen-Cagatay and Kocaman 2010) for a subcritical dam break wave



friction source term and the minmod slope limiter. During initiation of motion, the wave profile is affected by non-hydrostatic flow effects (Castro-Orgaz and Chanson 2017), so that precise agreement of experiments with simulations based on the SWE is not expected. The overall position of the surge front is reasonably predicted, but the detailed wave shape is affected by turbulence, a feature not accounted for in the mathematical model. Experiments (Ozmen-Cagatay and Kocaman 2010) and numerical simulations using the MUSCL-Hancock scheme for a transcritical dam break wave test ( $h_d/h_o < 0.138$ ) are considered in Fig. 9.19, with  $h_d = 0.025$  m. For this test, the position of the surge is reasonably well predicted, but the effects of turbulence are strong in the supercritical portion of the wave profile. A dry-bed dam break wave is examined in Fig. 9.20, showing a reasonable agreement of numerical predictions with experimental data by Ozmen-Cagatay and Kocaman (2010). The shape of the experimental curves of Fig. 9.20 is similar to those previously measured by Dressler (1954) or Lauber (1997).

The experiments by Schoklitsch (1917) for a dam break wave in a dry, rectangular, horizontal flume are considered as an additional test case. The flume was 0.093 m wide, 0.08 m high, and 20 m long. The dam was located at  $x = 10$  m, and the removal was considered instantaneous. The tailwater flume portion was initially dry, and the water depth at the dam 0.074 m. Experimental data recorded by Schoklitsch (1917) for two times after dam removal, namely  $t = 3.75$  s and  $t = 9.4$  s, are plotted in Fig. 9.21a, b, respectively. The predictions using the MUSCL-Hancock scheme were conducted using  $CFL = 0.9$ ,  $\Delta x = 0.1$  m, and  $n = 0.008 \text{ m}^{-1/3}$  s. A comparison of simulations and data shows good agreement. The effect of flow resistance in this dataset is significant for the wave front, as observed from the comparison of the numerical simulation with Ritter's solution plotted in the same figure.

### 9.9.3 Positive Surge with Friction

Favre (1935) conducted measurements of a subcritical surge propagating in a horizontal flume 0.42 m wide with initially static water of depth 0.205 m. The surge was generated by setting a discharge increase at the inlet section of  $0.028 \text{ m}^3/\text{s}$ . Manning's coefficient for this flume was  $n = 0.01 \text{ m}^{-1/3}$  s (Favre 1935; Terzidis and Strelkoff 1970). The time needed to switch on the pumps and generate the discharge pulse into the flume was computationally accounted for as a time lag of 1 s, given that the generation of the discharge pulse is instantaneous in the mathematical model, as explained in Chap. 7. The predictions using the MUSCL-Hancock scheme were conducted using  $CFL = 0.9$ ,  $\Delta x = 0.25$  m and an explicit treatment of the friction source term. This test is available in the file *FavreWave.xls* in Chap. 12. A comparison of simulations and test data in Fig. 9.22 shows good agreement. Comparing wave profiles at two different instants of time, the absolute velocity of the surge predicted by the MUSCL-Hancock scheme is in excellent agreement with that indicated by the data.

**Fig. 9.19** Comparison of numerical simulations using the MUSCL-Hancock scheme with experimental data (Ozmen-Cagatay and Kocaman 2010) for a transcritical dam break wave

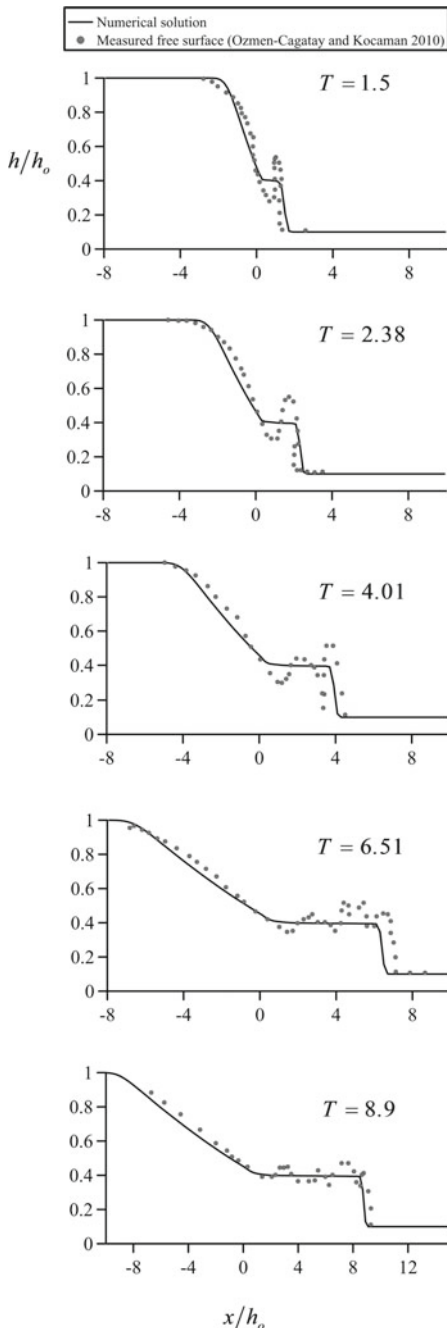


**Fig. 9.20** Comparison of numerical simulations using the MUSCL-Hancock scheme with experimental data (Ozmen-Cagatay and Kocaman 2010) for a dry-bed dam break wave

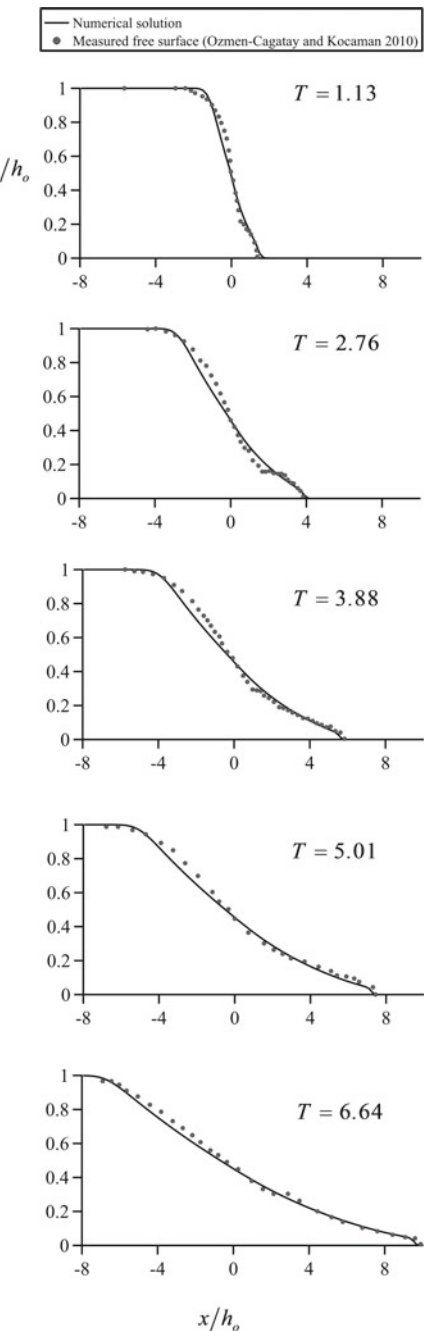
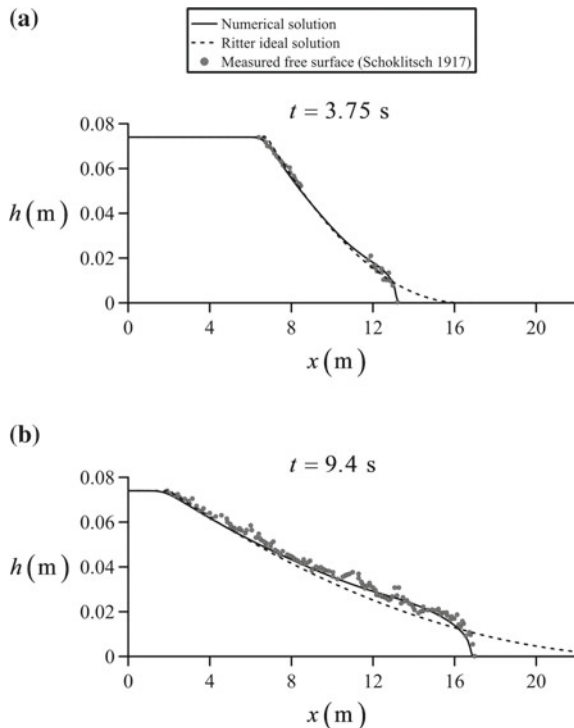


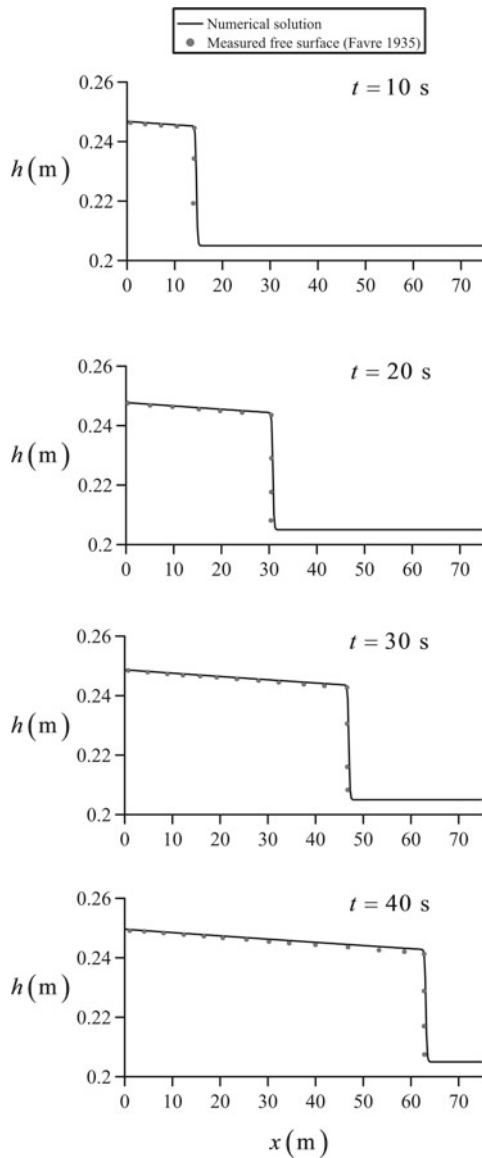
**Fig. 9.21** Comparison of numerical simulations using the MUSCL-Hancock scheme with experimental data of Schoklitsch (1917) for a dry-bed dam break wave and **a**  $t = 3.75$  s, **b**  $t = 9.4$  s



#### 9.9.4 Hydraulic Jump Beyond a Sluice Gate

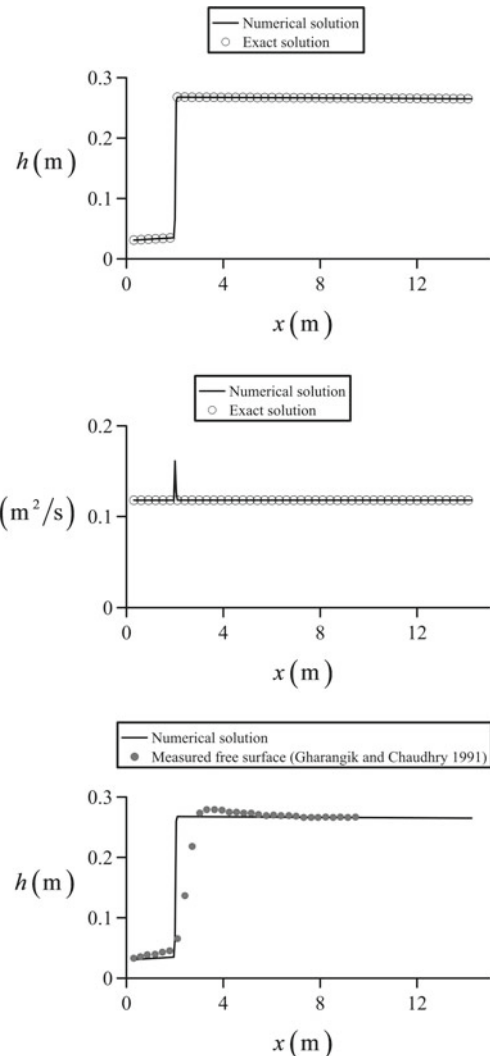
Gharangik and Chaudhry (1991) conducted measurements of steady hydraulic jumps in a horizontal flume 0.46 m wide and 14 m long. A supercritical profile was initially generated in the flume using a gate at the inlet, and the hydraulic jump was thereafter generated raising the tailwater level with another gate (Fig. 9.16c). Consider a test conducted for an inflow Froude number  $F_1 = 7$ . The upstream boundary section was located at  $x = 0.305$  m from the gate, and the depth and unit discharge there resulting from experimentation are  $h = 0.031$  m and  $q = 0.118$  m<sup>2</sup>/s. The tailwater level was set to  $h = 0.265$  m. This test is available in the file *Hydraulicjump\_gate.xls* of Chap. 12. The predictions using the MUSCL-Hancock scheme were conducted using  $CFL = 0.5$ ,  $\Delta x = 0.05$  m and an explicit treatment of the friction source term with  $n = 0.008$  m<sup>-1/3</sup>s. The initial condition was a static layer of 0.1 m along the flume. Upstream boundary conditions were then settled, and, after 15 s of routing, the tailwater level was raised instantaneously to 0.265 m. The model was run up to  $t = 1500$  s to ensure steady flow conditions. A comparison of simulations and data in Fig. 9.23a shows good agreement of the steady wave profile with the exact result obtained by solving the steady-state flow equations of Chap. 4. The numerical model confines the jump to three computational cells only, but ideally this jump length should be zero. The numerical discharge of Fig. 9.23b attains a constant value, except just at the jump, where a peak

**Fig. 9.22** Comparison of numerical simulations using the MUSCL-Hancock scheme with experimental data (Favre 1935) for a positive surge



is detected, given the use of Eq. (9.12). This is purely a numerical issue common to many numerical schemes (Khan and Lai 2014). A comparison of the water surface profile with experimental data by Gharangik and Chaudhry (1991) in Fig. 9.23c shows good agreement, although the finite length of the jump produced by turbulence is not a feature tractable with the numerical model of the SWE.

**Fig. 9.23** Comparison of numerical simulation using the MUSCL-Hancock scheme with exact and experimental results (Gharangik and Chaudhry 1991) for a steady hydraulic jump



### 9.9.5 Flow over Round-Crested Weirs

An important transcritical open channel flow feature is the passage from sub- ( $F < 1$ ) to supercritical ( $F > 1$ ) flow over a round-crested weir (Fig. 9.16b). Here, this steady transcritical flow is simulated using the MUSCL-Hancock scheme assuming ideal fluid flow. An initial steady free surface profile over the weir, for which  $q_o = \text{const.}$  and  $h_o = h_o(x)$  are known, must be prescribed to initiate unsteady computations [Eq. (9.160)]. Assuming  $S_f = 0$ , Eq. (9.1) reduces for steady flow to (Henderson 1966)

$$\frac{dh}{dx} = \frac{-\frac{\partial z_b}{\partial x} - S_f}{1 - F^2} = \frac{-\frac{\partial z_b}{\partial x}}{1 - \frac{q^2}{gh^3}}. \quad (9.165)$$

In this test, Eq. (9.165) was used to produce an initial free surface profile over the weir. The profile was numerically computed using the fourth-order Runge–Kutta method (Chaudhry 2008), as described in Chaps. 3 and 4. Computations started at the crest section where the flow is critical ( $F = 1$ ); that is,  $h = h_c = (q^2/g)^{1/3}$ . If  $F = 1$ , then Eq. (9.165) must equal the indeterminate identity  $dh/dx = 0/0$ . This singularity is removed by applying L'Hospital's rule to Eq. (9.165), resulting in (see Chap. 4)

$$\left(\frac{dh}{dx}\right)_c = -\left(-\frac{h_c}{3} \frac{\partial^2 z_b}{\partial x^2}\right)^{1/2}. \quad (9.166)$$

At the crest section, Eq. (9.166) was implemented in the Runge–Kutta solver, and the corresponding sub- and supercritical branches of the water surface profile were computed in the up- and downstream directions, respectively.

For unsteady transcritical flow over a weir, one boundary condition must be prescribed at the subcritical section on the upstream weir side, whereas no boundary conditions need to be prescribed at the supercritical outlet section. The inlet boundary condition is given by an instantaneous rise in the discharge, which is kept constant during all transient flow. Unknown values of conserved variables at boundary sections are then computed using ghost cells by extrapolation of values at adjacent interior cells (LeVeque 2002), as previously explained. The steady water surface profile over a weir of bed shape  $z_b = 0.2 - 0.01x^2$  (m) was computed using the MUSCL-Hancock method with the HLL approximate Riemann solver and the DGM for reconstruction, for a target discharge of  $q = 0.2$  m<sup>3</sup>/s. It was settled instantaneously at the inlet, once transient computations were initiated, and kept constant during all the routing. The initial free surface profile was computed for the steady discharge  $q_o = 0.05$  m<sup>3</sup>/s.

This particular weir is widely used to test unsteady numerical models (i.e., Zhou et al. 2001; Ying et al. 2004; Castro-Orgaz and Chanson 2016). In this test case,  $\Delta x = 0.05$  m and  $CFL = 0.9$  were used. The code is available in the file *Weir\_DGM\_parabolic.xls*. In the code *Weir\_DGM\_parabolic\_MC.xls*, the upstream water depth is determined by using a backward characteristic, showing variations at initiation of motion only ( $t < 0.05$  s). Some snapshots of the unsteady flow motion are presented in Fig. 9.24, from where it is observed how a shock wave passes over the weir (Fig. 9.24a–c). Once it disappears, e.g., at  $t = 3$  s (Fig. 9.24d), the unsteady free surface flow profile is smooth and gradually adjusts to the disequilibrium in discharge along the weir profile. The results of Fig. 9.24e involve a simulation time of  $t = 350$  s to ensure that steady-state conditions are reached. The steady water surface profiles computed using Eqs. (9.165) and (9.166) are presented in the same figure (labeled as exact solution), showing the excellent agreement of the finite volume computations with these results. Note further that the discharge is well conserved by the unsteady flow model. The same computations conducted

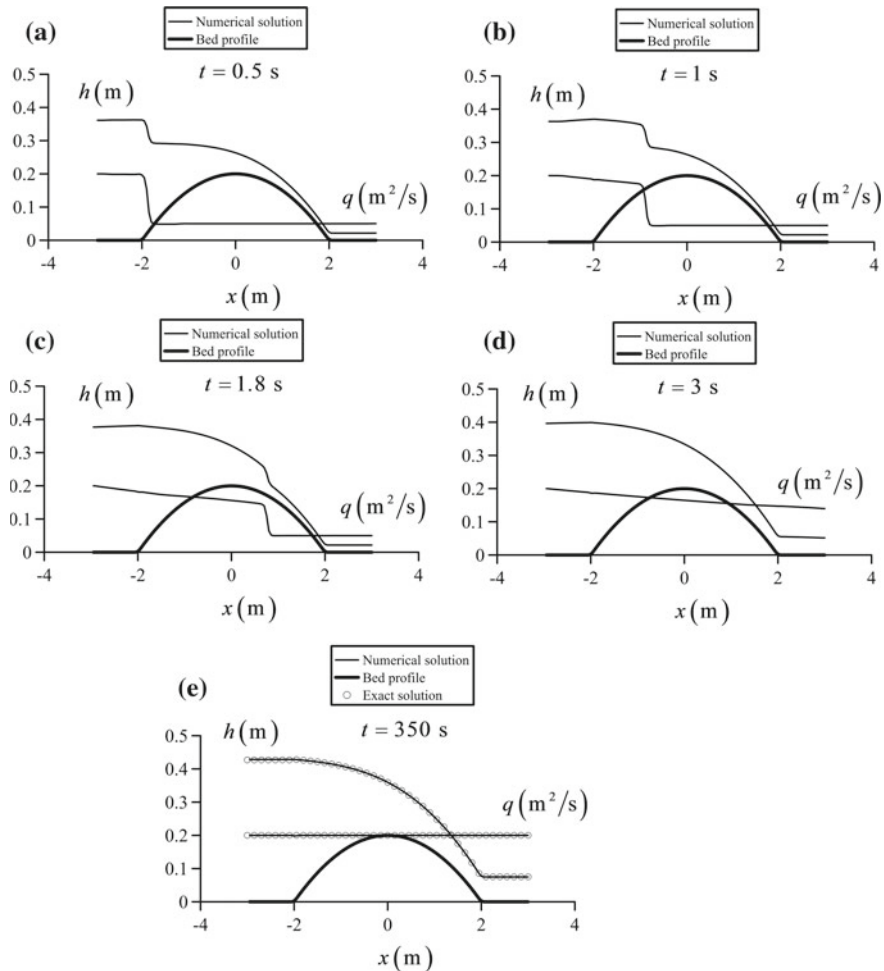


**Fig. 9.24** Unsteady transcritical flow using the MUSCL-Hancock scheme: evolution of bore passage over a weir profile and comparison of steady-state solution with exact results

using the one-sided upwind finite volume method yield results almost identical (Castro-Orgaz and Chanson 2016) (the two profiles deviate only in the third digit). This numerical model is implemented in the file *Weir\_upwind.xls* of Chap. 12. The code *Weir\_dry\_SGM-DGM\_MC.xls* permits to simulate this steady flow and allows for flooding over dry terrain.

Figure 9.25 contains the experimental data of Sivakumaran et al. (1983) for a Gaussian hump of profile  $z_b = 20\exp[-0.5(x/24)^2]$  (cm) for two test cases. This weir test is implemented in the file *Weir\_DGM\_Sivakumaran.xls* in Chap. 12. The computed solution using the MUSCL-Hancock scheme is presented for both cases and compared in Fig. 9.25a, c with the exact steady solution obtainable using Eqs. (9.165) and (9.166). Steady solutions obtained with the MUSCL-Hancock

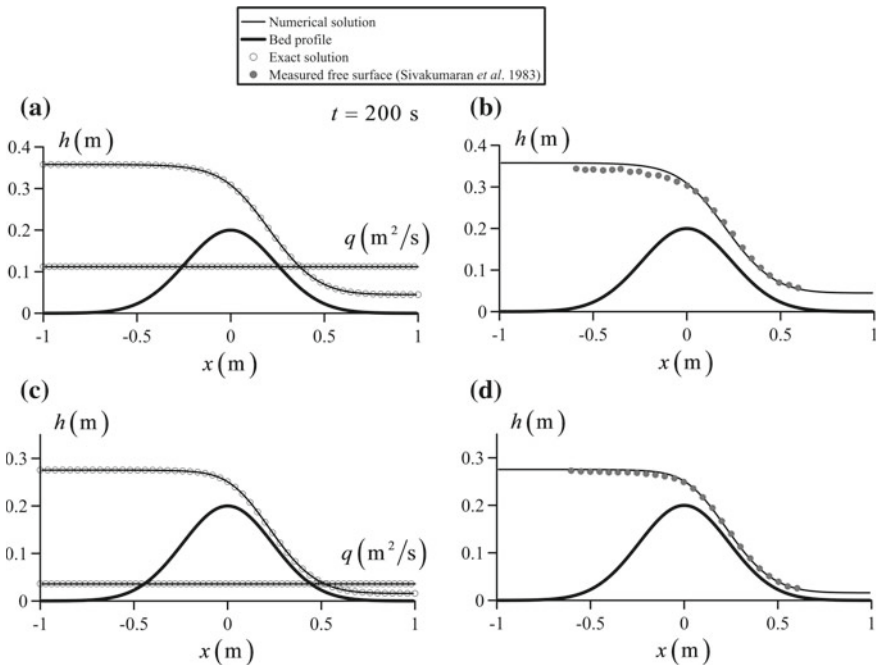


**Fig. 9.25** Transcritical flow over Gaussian weir profile using the MUSCL-Hancock scheme. Comparison of steady-state solutions with exact results and experimental data (Sivakumaran et al. 1983) for  $q$  = **a**, **b**  $0.111 \text{ m}^2/\text{s}$ , **c**, **d**  $0.0359 \text{ m}^2/\text{s}$

scheme are in excellent agreement with exact results (Fig. 9.25a, c). The departure between simulations and experiments for the test case of Fig. 9.25b ( $q = 0.111 \text{ m}^2/\text{s}$ ) indicates that the effect of the vertical acceleration as the flow passes from sub- to supercritical is notable, so that the solution of the SWE does not fully agree with physical experiments due to non-hydrostatic effects. For the test case of Fig. 9.25d ( $q = 0.0359 \text{ m}^2/\text{s}$ ), deviations between numerical results and experiments are small.

The SWE produce realistic free surface profile solutions across the critical depth using shock-capturing numerical methods. The computation of a steady flow profile using an unsteady flow computation produces a solution that automatically crosses the critical depth. This unsteady flow computation is performed without any further special treatment at the critical point, as the unsteady computation does not suffer from any mathematical indetermination. However, the steady gradually-varied flow equation has a mathematical indetermination at critical flow conditions resolved with L'Hopital's rule. The unsteady computation produces a singular point at the weir crest automatically as the steady state is asymptotically reached (Castro-Orgaz and Chanson 2016).

### 9.9.6 Dam Break Wave Evolution over a Bottom Sill

Consider the experimental tests of Ozmen-Cagatay and Kocaman (2011) for a dam break wave propagated over a trapezoidal sill. The upstream water depth was  $h_o = 0.25$  m, the flume width was 0.3 m, and the downstream channel was dry. A trapezoidal bottom sill 0.075 m high, of 0.3 m crest length, with up- and downstream slopes of 7.5/35, was inserted 1.53 m downstream of the gate used to simulate the dam section. The upstream flume portion was used to store the water and simulate a reservoir, over a length of 4.65 m. This test was modeled with the one-sided first-order finite volume method (Ying et al. 2004). Simulations were conducted using  $CFL = 0.9$  and  $\Delta x = 0.01$  m assuming ideal fluid flow. The downstream boundary conditions were modeled as transmissive boundary conditions (Toro 2001), e.g.,

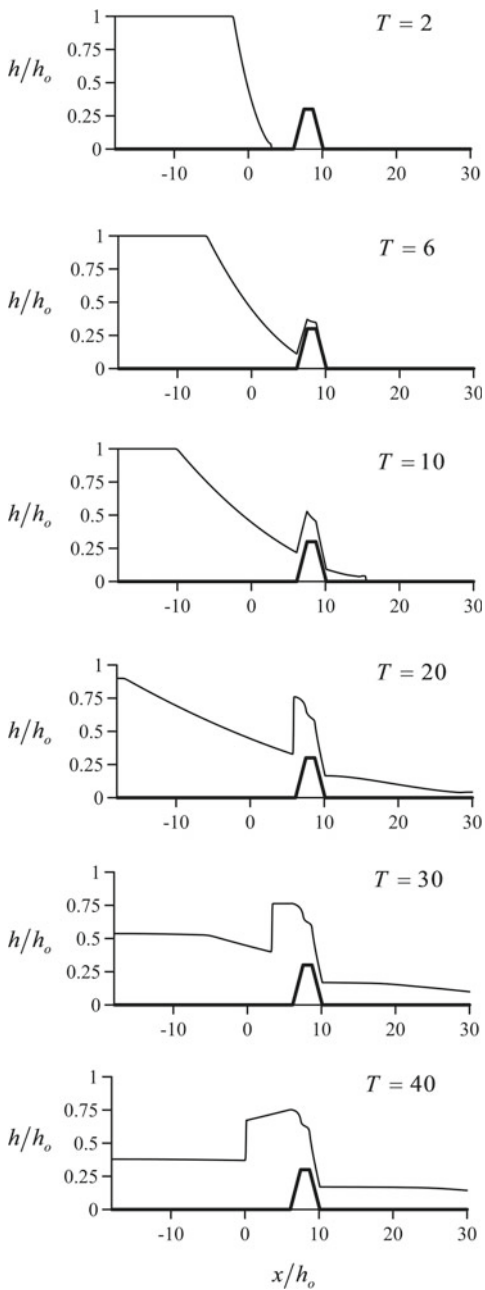
$$\begin{aligned} q_{N+1}^{k+1} &= q_N^{k+1}, \\ h_{N+1}^{k+1} &= h_N^{k+1}. \end{aligned} \quad (9.167)$$

These are also the conditions used to model supercritical flow at an outlet. The upstream portion of the computational domain is a solid wall, which must be modeled using reflective boundary conditions (Toro 2001)

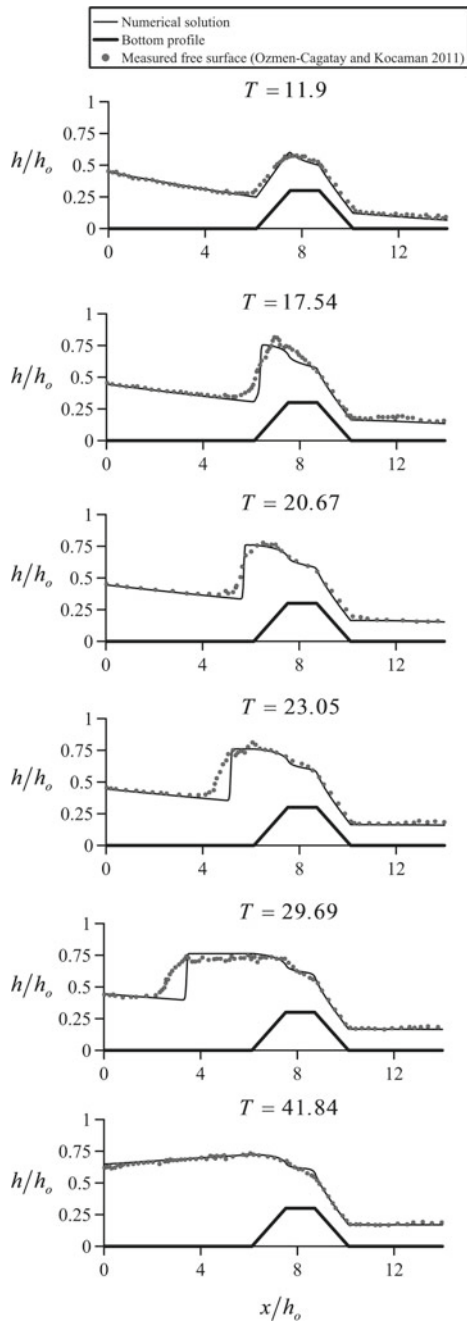
$$\begin{aligned} q_o^{k+1} &= -q_1^{k+1}, \\ h_o^{k+1} &= h_1^{k+1}. \end{aligned} \quad (9.168)$$

The physical effect of this condition is to represent what actually happens at a solid wall: There is no mass flow, and there is a hydrostatic thrust acting on the wall. Instead of using Eq. (9.168) it is possible to fix the numerical flux directly. The computational model is available in the code of the file “*Dambreak\_sill.xls*”, Chap. 12. The evolution of this flow is observed in Fig. 9.26, showing the initial run-up of a supercritical current over the trapezoidal sill, and its subsequent drowning with wave breaking and bore propagation in the upstream direction. The experimental data of Ozmen-Cagatay and Kocaman (2011) at different normalized times  $T = t(g/h_o)^{1/2}$  are considered in Fig. 9.27, where computational results at the same times are also included. Note that the SWE produce an excellent representation of the supercritical flow passage over the trapezoidal sill and adequately represent wave breaking and formation of the bore propagating in the upstream direction at later times. The precise shape of the upstream bore is not well predicted, given that the SWE are unable to model the finite bore length due to turbulence, but the overall position of the bore is in good agreement with computations. The propagation of a supercritical flow over a sill and subsequent wave breaking and propagation of an upstream bore is a beautiful hydraulic feature (Fig. 9.28) to be handled with satisfactory results using the SWE.

**Fig. 9.26** Evolution of a dam break wave over a trapezoidal bottom sill computed with the one-sided first-order finite volume scheme (Ying et al. 2004), for the experimental setup of Ozmen-Cagatay and Kocaman (2011)



**Fig. 9.27** Evolution of a dam break wave over a trapezoidal bottom sill computed with the one-sided first-order finite volume scheme (Ying et al. 2004) for the experimental setup of Ozmen-Cagatay and Kocaman (2011): comparison of experiments and simulations



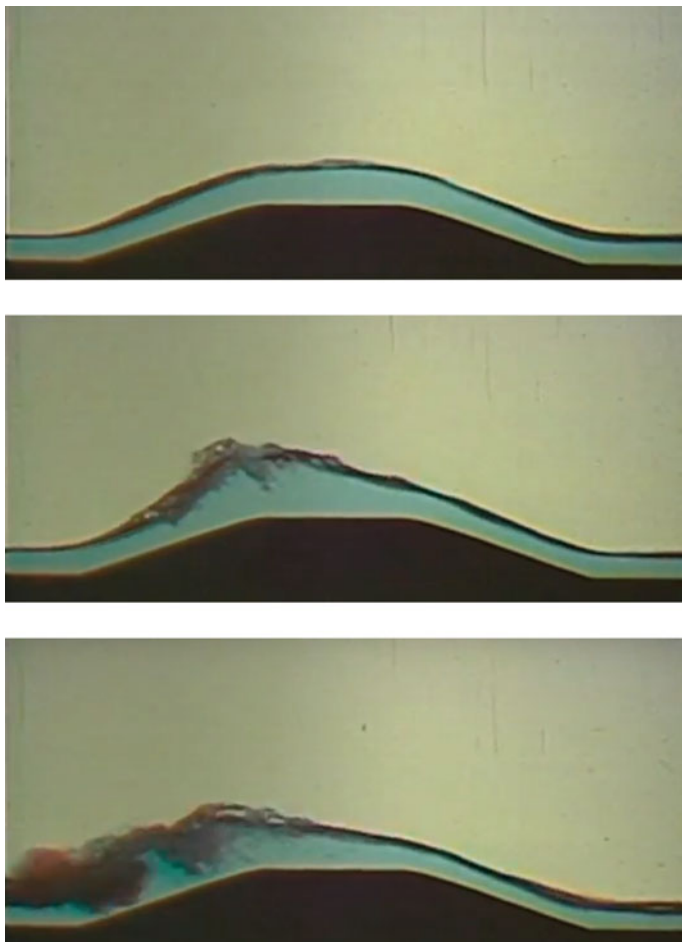


**Fig. 9.28** Supercritical flow over a sill resulting in wave breaking and a surge propagating in the upstream direction (flow is from left to right) [Taken from movie Fluid motion in a gravitational field, by Rouse (1961), IIHR-Hydroscience & Engineering, The University of Iowa]

### 9.9.7 Solitary Wave Run-Up on a Plane Beach

Synolakis (1986) conducted a series of laboratory experiments for incident solitary waves on a plane beach of slope 1:19.85. The crest of the initial solitary wave solution is placed at half a wavelength from the toe of the plane beach (located at  $x = 0$  m), which is approximately given by

$$L = \left( \frac{4h_o}{3H} \right)^{1/2} \operatorname{arcosh} \left( \sqrt{\frac{1}{0.05}} \right), \quad (9.169)$$

where  $h_o = 1$  m is the still water depth and  $H$  the solitary wave amplitude. A test for non-breaking solitary wave run-up with  $H/h_o = 0.04$  is presented in Fig. 9.29 to check the predictions of the SWE. The initial condition is given by the solitary wave solution

$$\eta(x, 0) = H \operatorname{sech}^2 \left[ \left( \frac{3H}{4h_o^3} \right)^{1/2} (x + L) \right], \quad (9.170)$$

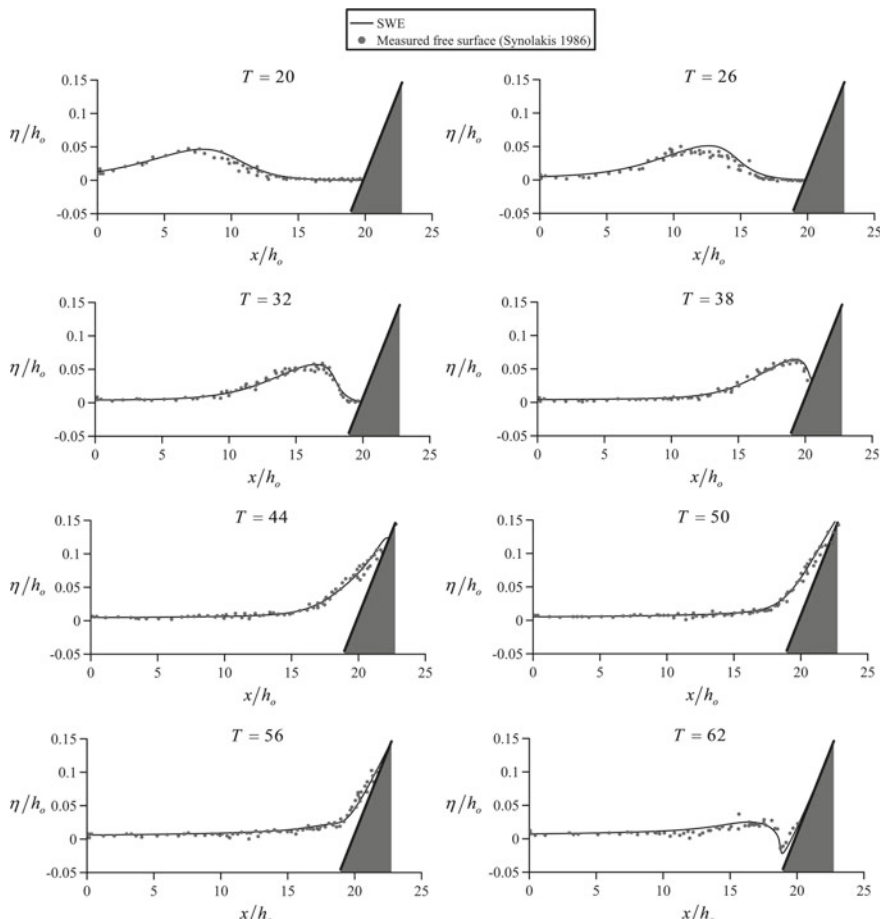


**Fig. 9.29** Non-breaking solitary wave run-up on a plane beach for  $H/h_o = 0.04$  at various normalized times  $T = t(g/h_o)^{1/2}$

$$U(x, 0) = \eta(x, 0) \left( \frac{g}{h_o} \right)^{1/2}, \quad (9.171)$$

where  $\eta = h - h_o$  is the free surface displacement. Solutions were obtained with the MUSCL-Hancock scheme using an implicit treatment of the friction effects. Computations were conducted using  $CFL = 0.4$  and  $\Delta x = 0.1$  m. The depth gradient method was used for reconstruction of the solution, along with a wetting-drying procedure to track the position of the shoreline. To simulate the bed roughness effects during both the run-up and the drawdown, a Manning's coefficient  $n = 0.01$  m<sup>1/3</sup>/s was used, assuming wide channel conditions, the scheme is implemented in the file *solitarywaverunup.xls* in Chap. 12. Simulations at different normalized times  $T = t(g/h_o)^{1/2}$  are considered in Fig. 9.29, where the experimental data of Synolakis (1986) at identical times are also included. The SWE produce an excellent representation of the wave run-up and drawdown features, including the formation of the hydraulic jump.

A test for the breaking solitary wave run-up with  $H/h_o = 0.3$  is presented in Fig. 9.30, where the predictions of the SWE are compared with experimental data of Synolakis (1986). The numerical solution disagrees with the experimental data at  $T = 10$  and 15, given that non-hydrostatic effects are significant, not accounted for by the SWE. Wave breaking is observed at  $T = 20$  and 25. Once the wave is broken, the SWE satisfactorily reproduce the run-up characteristics. At  $T = 30, 35$ , and 40, the SWE predictions are in good agreement with the experimental data during the run-up process. From  $T = 45$  to 60, a moving hydraulic jump is progressively formed, linked to the drawdown process. Overall, the bore propagation is satisfactorily predicted by the SWE model. Further research on this topic was presented by Hafsteinsson et al. (2017). A sequence of photographs during a model test is shown in Fig. 9.31, where the run-up flow front and the formation of a moving hydraulic jump during the drawdown are observed.

As highlighted in this chapter, the finite volume solutions of the 1D SWE produce results in conformity with exact and experimental results for a variety of flows, including cases with subcritical, transcritical, and supercritical conditions, the existence of wet–dry interfaces, uneven topography, steady conditions, and propagation of bores.

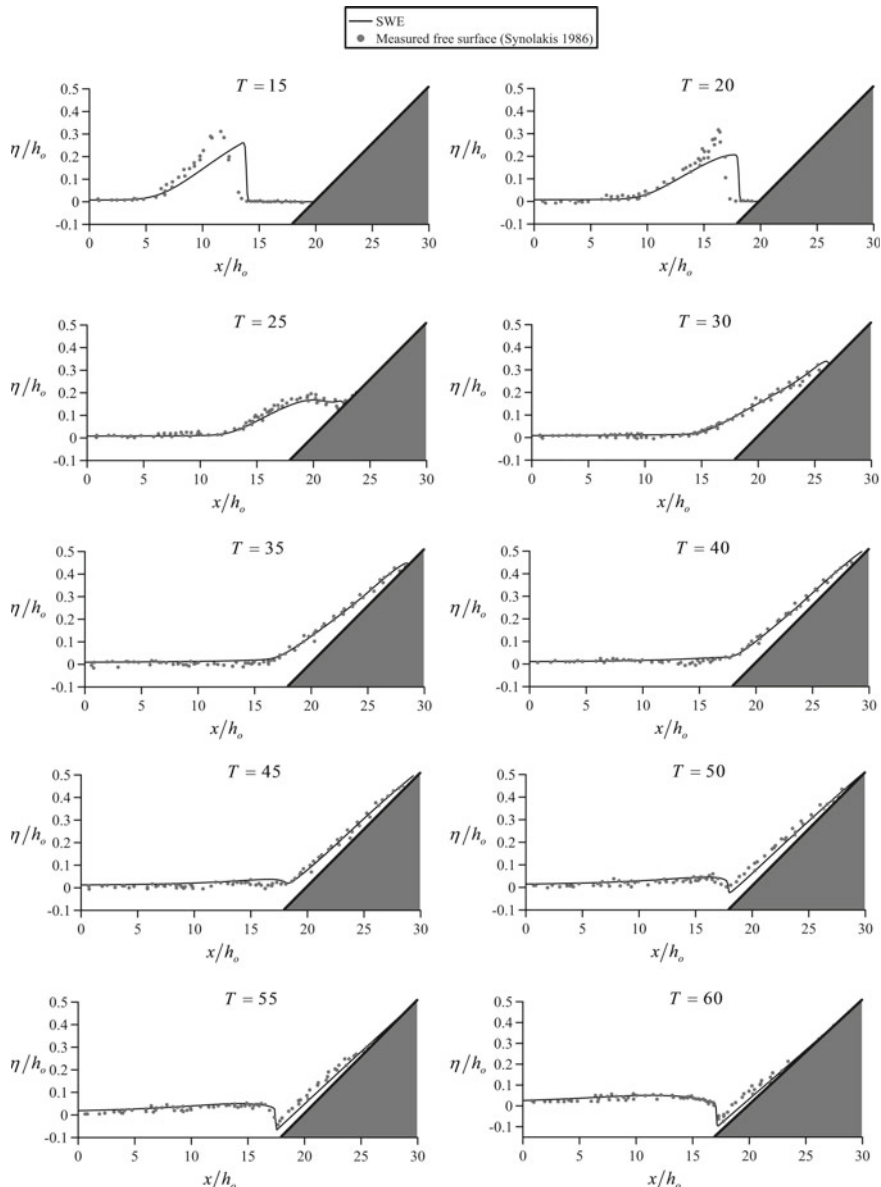


**Fig. 9.30** Breaking solitary wave run-up on a plane beach for  $H/h_o = 0.3$  at various normalized times  $T = t(g/h_o)^{1/2}$

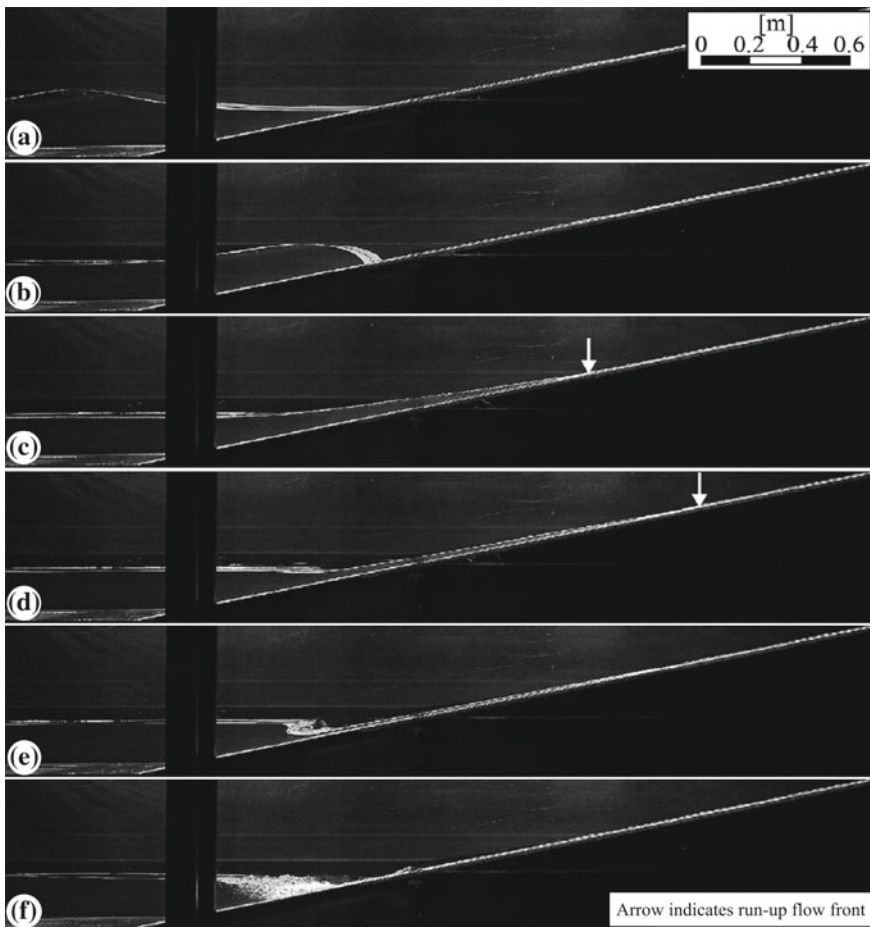


**Fig. 9.31** Model tests of non-breaking solitary wave run-up on slope (VAW photographs)

## References

- Aureli, F., Maranzoni, A., Mignosa, P., & Ziveri, C. (2008). A weighted surface-depth gradient method for the numerical integration of the 2D shallow water equations with topography. *Advances in Water Resources*, 31(7), 962–974.
- Bermudez, A., & Vazquez-Cendón, M. E. (1994). Upwind methods for hyperbolic conservation laws with source terms. *Computers & Fluids*, 23(8), 1049–1071.
- Bradford, S. F., & Sanders, B. F. (2002). Finite-volume model for shallow-water flooding of arbitrary topography. *Journal of Hydraulic Engineering*, 128(3), 289–298.
- Bradford, S. F., & Sanders, B. F. (2005). Performance of high-resolution, nonlevel bed, shallow-water models. *Journal of Engineering Mechanics*, 131(10), 1073–1081.
- Brocchini, M., & Dodd, N. (2008). Nonlinear shallow water equation modeling for coastal engineering. *Journal of Waterway, Port, Coastal, and Ocean Engineering*, 134(2), 104–120.

- Brufau, P., Vázquez-Cendón, M. E., & García-Navarro, P. (2002). A numerical model for the flooding and drying of irregular domains. *International Journal for Numerical Methods in Fluids*, 39(3), 247–275.
- Castro-Orgaz, O., & Chanson, H. (2016). Minimum specific energy and transcritical flow in unsteady open channel flow. *Journal of Irrigation and Drainage Engineering*, 142(1), 04015030.
- Castro-Orgaz, O., & Chanson, H. (2017). Ritter's dry-bed dam-break flows: Positive and negative wave dynamics. *Environmental Fluid Mechanics*, 17(4), 665–694.
- Chaudhry, M. H. (2008). *Open-channel flow* (2nd ed.). New York: Springer.
- Colella, P., & Woodward, P. (1984). The piecewise-parabolic method (PPM) for gas dynamical simulations. *Journal of Computational Physics*, 54(1), 174–201.
- Cunge, J. A. (1975). Rapidly varying flow in power and pumping canals. In K. Mahmood & V. Yevjevich (Eds.), *Unsteady flow in open channels*, 14, 539–586. Fort Collins, CO, USA: Water Resources Publications.
- Cunge, J. A., Holly, F. M., & Verwey, A. (1980). *Practical aspects of computational river hydraulics*. London: Pitman.
- Dressler, R. (1954). Comparison of theories and experiments for the hydraulic dam-break wave. In *Proceedings of International Association of Scientific Hydrology*, 3(38), 319–328. Rome, Italy: Assemblée Générale.
- Favre, H. (1935). *Etude théorique et expérimentale des ondes de translation dans les canaux découverts* [Theoretical and experimental study of travelling surges in open channels]. Dunod, Paris, France (in French).
- Gharangik, A. M., & Chaudhry, M. H. (1991). Numerical simulation of hydraulic jump. *Journal of Hydraulic Engineering*, 117(9), 1195–1211.
- Glaister, P. (1987). *Difference schemes for the shallow water equations* (Numerical Analysis Report 9/87). UK: Department of Mathematics, University of Reading.
- Godunov, S. K. (1959). A difference method for numerical calculation of discontinuous solutions of the equations of hydrodynamics. *Matematicheskiy Sbornik*, 47(3), 271–306 (in Russian).
- Gottlieb, S., & Shu, C. W. (1998). Total variation diminishing Runge-Kutta schemes. *Mathematics of Computation*, 67(221), 73–85.
- Hafsteinsson, H. J., Evers, F. M., & Hager, W. H. (2017). Solitary wave run-up: wave breaking and bore propagation. *Journal of Hydraulic Research*, 55(6), 787–798.
- Hancock, S. L. (1980). *PISCES industrial simulation code manual*. Physics International.
- Harten, A. (1983). High resolution schemes for hyperbolic conservation laws. *Journal of Computational Physics*, 49(3), 357–393.
- Harten, A., Lax, P., & van Leer, B. (1983). On upstream differencing and Godunov-type scheme for hyperbolic conservation laws. *Society for Industrial and Applied Mathematics*, 25(1), 35–61.
- Henderson, F. M. (1966). *Open channel flow*. New York: MacMillan Co.
- Hirsch, C. (1988). *Numerical computation of internal and external flows, 1: Fundamentals of numerical discretization*. Chichester, England: Wiley.
- Hirsch, C. (1990). *Numerical computation of internal and external flows, 2: Computational methods for inviscid and viscous flows*. Chichester, England: Wiley.
- Hoffman, J. D. (2001). *Numerical methods for engineers and scientists* (2nd ed.). New York: Marcel Dekker.
- Jain, S. C. (2001). *Open channel flow*. New York: Wiley.
- Karni, S. (2011). Nonlinear hyperbolic conservation laws-a brief informal introduction. *Lecture notes on numerical methods for hyperbolic equations: short book course*. London: Taylor and Francis.

- Khan, A. A., & Lai, W. (2014). *Modeling shallow water flows using the discontinuous Galerkin method*. Taylor and Francis, New York: CRC Press.
- Lauber, G. (1997). *Experimente zur Talsperrenbruchwelle im glatten geneigten Rechteckkanal* [Experiments to the dam break wave in smooth sloping rectangular channel]. Ph.D. thesis, ETH Zurich, Zürich, Switzerland (in German).
- Lax, P. (1954). Weak solutions of nonlinear hyperbolic equations and their numerical computation. *Communications on Pure and Applied Mathematics*, 7, 159–193.
- Lax, P. D., & Wendroff, B. (1960). Systems of conservation laws. *Communications in Pure and Applied Mathematics*, 13(2), 217–237.
- LeVeque, R. J. (1992). *Numerical methods for conservation laws*. Basel, Switzerland: Birkhäuser.
- LeVeque, R. J. (2002). *Finite volume methods for hyperbolic problems*. New York: Cambridge University Press.
- Mingham, C. G., & Causon, D. M. (1998). High-resolution finite-volume method for shallow water flows. *Journal of Hydraulic Engineering*, 124(6), 605–614.
- Nujic, M. (1995). Efficient implementation of non-oscillatory schemes for the computation of free-surface flows. *Journal of Hydraulic Research*, 33(1), 100–111.
- Ozmen-Cagatay, H., & Kocaman, S. (2010). Dam-break flows during initial stage using SWE and RANS approaches. *Journal of Hydraulic Research*, 48(5), 603–611.
- Ozmen-Cagatay, H., & Kocaman, S. (2011). Dam-break flow in the presence of obstacle: Experiment and CFD simulation. *Engineering Applications of Computational Fluid Mechanics*, 5(4), 541–552.
- Ritter, A. (1892). Die Fortpflanzung von Wasserwellen [Propagation of water waves]. *Zeitschrift Verein Deutscher Ingenieure*, 36(2), 947–954 (in German).
- Roache, P. J. (1972). *Computational fluid dynamics*. Albuquerque NM: Hermosa Publishers.
- Roe, P. L. (1981). Approximate Riemann solvers, parameter vectors, and difference schemes. *Journal of Computational Physics*, 43(2), 357–372.
- Rouse, H. (1961). *Fluid motion in a gravitational field*. IIHR film, The University of Iowa, Iowa.
- Sanders, B. F. (2001). High-resolution and non-oscillatory solution of the St. Venant equations in non-rectangular and non-prismatic channels. *Journal of Hydraulic Research*, 39(3), 321–330.
- Schoklitsch, A. (1917). Über Dammbruchwellen [On dam break waves]. Kaiserliche Akademie der Wissenschaften, Wien, Mathematisch-Naturwissenschaftliche Klasse. *Sitzungberichte IIa*, 126, 1489–1514 (in German).
- Sivakumaran, N. S., Tingsanchali, T., & Hosking, R. J. (1983). Steady shallow flow over curved beds. *Journal of Fluid Mechanics*, 128, 469–487.
- Stoker, J. J. (1957). *Water waves: The mathematical theory with applications*. New York: Interscience Publishers.
- Sweby, P. K. (1984). High resolution schemes using flux limiters for hyperbolic conservation laws. *Journal of the Society for Industrial and Applied Mathematics, Series B Numerical Analysis*, 21(5), 995–1011.
- Sweby, P. K. (1999). *Godunov methods* (Numerical Analysis Report 7/99), UK: Department of Mathematics, University of Reading.
- Synolakis, C. E. (1986). *The runup of long waves* (Ph.D. thesis). California Institute of Technology, California.
- Terzidis, G., & Strelkoff, T. (1970). Computation of open channel surges and shocks. *Journal of the Hydraulics Division, ASCE*, 96(HY12), 2581–2610.
- Toro, E. F. (1992). Riemann problems and the WAF method for solving the two-dimensional shallow water equations. *Philosophical Transactions of the Royal Society of London, Series A*, 338, 43–68.
- Toro, E. F. (2001). *Shock-capturing methods for free-surface shallow flows*. Singapore: Wiley.

- Toro, E. F. (2009). *Riemann solvers and numerical methods for fluid dynamics: A practical introduction*. Berlin, Germany: Springer.
- van Albada, G. D., van Leer, B., & Roberts, W. W. (1982). A comparative study of computational methods in cosmic gas dynamics. *Astronomy & Astrophysics*, 108(1), 76–84.
- van Leer, B. (1979). Towards the ultimate conservative difference scheme, V: A second-order sequel to Godunov's method. *Journal of Computational Physics*, 32, 101–136.
- van Leer, B. (2006). Upwind and high-resolution methods for compressible flow: From Donor cell to residual distribution schemes. *Computer Physics Communications*, 172(2), 192–206.
- Vazquez-Cendón, M. E. (2015). *Solving hyperbolic equations with finite volume methods*. New York: Springer.
- White, F. M. (2009). *Fluid mechanics*. New York: McGraw-Hill.
- Ying, X., Khan, A., & Wang, S. (2004). Upwind conservative scheme for the Saint Venant equations. *Journal of Hydraulic Engineering*, 130(10), 977–987.
- Ying, X., & Wang, S. (2008). Improved implementation of the HLL approximate Riemann solver for one-dimensional open channel flows. *Journal of Hydraulic Research*, 46(1), 21–34.
- Zhou, J. G., Causon, D. M., Mingham, C. G., & Ingram, D. M. (2001). The surface gradient method for the treatment of source terms in the shallow water equations. *Journal of Computational Physics*, 168(1), 1–25.
- Zoppou, C., & Roberts, S. (2003). Explicit schemes for dam-break simulations. *Journal of Hydraulic Engineering*, 129(1), 11–34.

# Chapter 10

## Sediment Transport and Movable Beds



### 10.1 Introduction

Transportation of sediment is an important and frequent phenomenon in rivers. Sediment is mobilized as bed-load with particles sliding, saltating and rolling over the river bed, or as a suspended-load, where particles move with the turbulent water flow away from the bed. The dynamic processes of sediment erosion and deposition modify the average density of the river fluid and reshape the river contours, which are the physical boundaries conveying the flow. The study of sediment transport in free surface flow is subject matter for a complete book. The works of Wu (2008) and Dey (2014) are recommended for a comprehensive study. The purpose of this chapter is to introduce how sediment transport is accounted for in shallow water models by introducing the fluid–sediment mixture density and the river bed deformation. The two-layer model of Wu and Wang (2007, 2008) is used for this task and solved with the first-order upwind method. The problems of dam break waves over an erodible bed and dike erosion due to overtopping are used as test cases.

### 10.2 Flow Equations

#### 10.2.1 Shallow Water Equations

Consider 1D unsteady free surface flow over an erodible bed in a vertical plane (Fig. 10.1). The elevation of the static erodible sediment bed is  $z_b(x, t)$ , and the fluid flow above is composed of a mixture of water and sediment. The dynamic flow above the bed is composed of a bed-load layer, whose flux per unit width is  $q_b$ , and a suspended-load layer. The latter flow depth is  $h(x, t)$ , the discharge per unit width

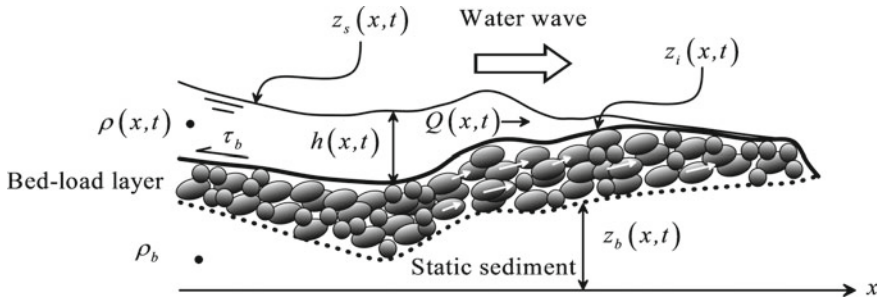


**Fig. 10.1** One-dimensional two-layer flow over erodible bed

is  $q(x, t)$  and the depth-averaged velocity in  $x$ -direction is  $U(x, t) = q/h$ . The depth-averaged hydrostatic mass and momentum conservation equations for the suspended-load layer are, when integrating the RANS equations [see Eqs. (1.161) and (1.181)],

$$\frac{\partial}{\partial t}(\rho A) + \frac{\partial}{\partial x}(\rho Q) + \rho_i \frac{\partial A_i}{\partial t} = 0, \quad (10.1)$$

$$\frac{\partial}{\partial t}(\rho Q) + \frac{\partial}{\partial x}\left(\rho \frac{Q^2}{A}\right) = -\rho g A \frac{\partial z_s}{\partial x} - \rho g A S_f - \frac{1}{2} g \frac{\partial \rho}{\partial x} h_p A. \quad (10.2)$$

Here,  $Q(x, t)$  = discharge,  $A(x, t)$  = flow area,  $S_f$  = friction slope,  $A_i$  = transverse bed sediment area taking the interface of suspended and bed-load layers as reference,  $\rho(x, t)$  = mass density of the water–sediment mixture in the suspended-load layer,  $t$  = time, and  $x$  = streamwise coordinate.

Consider the thickness of the bed-load layer negligible as compared to  $h$ , which is thereby approximated as the thickness of the suspended plus the bed-load layers. The flow density is thus computed in terms of the total sediment concentration as  $\rho = \rho_w(1 - C_t) + \rho_s C_t$ , where  $\rho_w$  = clear water mass density,  $\rho_s$  = sediment mass density,  $C_t(x, t)$  = depth-averaged total sediment concentration in the fluid layer of thickness  $h$  (suspended plus bed-load layers),  $\rho_i \approx \rho_b$  = mass density of static bed layer, defined as  $\rho_b = \rho_w p_m + \rho_s(1 - p_m)$  and  $p_m$  = sediment porosity. For a rectangular section, Eqs. (10.1)–(10.2) reduce with  $z_s \approx z_b + h$  to

$$\frac{\partial}{\partial t}(\rho h) + \frac{\partial}{\partial x}(\rho h U) = -\rho_i \frac{\partial z_i}{\partial t} \approx -\rho_b \frac{\partial z_b}{\partial t}, \quad (10.3)$$

$$\frac{\partial}{\partial t}(\rho h U) + \frac{\partial}{\partial x}(\rho h U^2) = -\rho g h \frac{\partial z_s}{\partial x} - \frac{1}{2} g h^2 \frac{\partial \rho}{\partial x} - \tau_b. \quad (10.4)$$

The bed shear stress is computed with  $n$  = Manning's roughness coefficient and  $R_h$  = hydraulic radius from

$$\tau_b = \rho g \frac{n^2 U |U|}{R_h^{1/3}}. \quad (10.5)$$

### 10.2.2 Sediment Transport Layers and Bed Deformation

The sediment transport phenomenon is included in the vertically integrated flow equations [Eqs. (10.3)–(10.4)] as highlighted by the presence of the functions  $\rho(x, t)$  and  $z_b(x, t)$ . These flow variables are related to the bed- and suspended-load fluxes, thereby implying that additional transport equations are needed. Here, the sediment transport model of Wu and Wang (2007) is used to complete the system of governing equations. The 1D depth-averaged mass conservation equation for the *suspended* sediment is (Wu and Wang 2007; Wu 2008)

$$\frac{\partial}{\partial t}(hC_s) + \frac{\partial}{\partial x}(hUC_s) = E - D. \quad (10.6)$$

Here,  $C_s(x, t)$  = depth-averaged suspended sediment concentration; and  $E(x, t)$  and  $D(x, t)$  = entrainment and depositional rates of sediment across the interface of suspended- and bed-load layers. The mass balance in the *bed-load* layer is (Wu and Wang 2007; Wu 2008)

$$\frac{\partial}{\partial t}(h_b C_b) + \frac{\partial q_b}{\partial x} + (1 - p_m) \frac{\partial z_b}{\partial t} = D - E, \quad (10.7)$$

where  $h_b(x, t)$  = thickness of bed-load layer,  $C_b(x, t)$  = depth-averaged bed-load sediment concentration, and  $q_b(x, t)$  = bed-load flux. The evolution of the static sediment bed can be determined from the mass balance equation (Wu 2008)

$$\frac{\partial z_b}{\partial t} = \frac{1}{1 - p_m} \left( D - E + \frac{q_b - q_{b^*}}{L} \right), \quad (10.8)$$

where  $L$  = non-equilibrium adaptation length of total-load transport and  $q_{b^*}(x, t)$  = equilibrium bed-load flux. In unsteady flows, a certain distance is required to reach the equilibrium condition of sediment transport. This length  $L$  is defined as the non-equilibrium adaptation length. Inserting Eq. (10.8) into Eq. (10.7), the bed-load mass balance equation is rewritten as

$$\frac{\partial}{\partial t}(h_b C_b) + \frac{\partial q_b}{\partial x} = \frac{q_{b^*} - q_b}{L}. \quad (10.9)$$

Note that  $q_b = h_b U_b C_b$ , where  $U_b$  = bed-load velocity, approximated here as  $U$  (Wu and Wang 2007).

### 10.2.3 Modified Flow Equations

For numerical implementation, it is recommended to remove the density  $\rho$  from the temporal and flux terms of the shallow water equations, forming an additional source term (Cao et al. 2004). Inserting the definitions  $\rho = \rho_w(1 - C_t) + \rho_s C_t$  and  $C_t = C_s + q_b/(hU)$  into Eqs. (10.3)–(10.4), the system of conservation laws is rewritten as

$$\frac{\partial h}{\partial t} + \frac{\partial}{\partial x}(hU) = \frac{1}{1 - p_m} \left( E - D + \frac{q_{b^*} - q_b}{L} \right), \quad (10.10)$$

$$\begin{aligned} \frac{\partial}{\partial t}(hU) + \frac{\partial}{\partial x}(hU^2) &= -gh \frac{\partial z_s}{\partial x} - \frac{\tau_b}{\rho} - \frac{1}{2} \frac{g}{\rho} h^2 \frac{\partial \rho}{\partial x} \\ &\quad - \frac{\rho_b - \rho}{\rho} \frac{U}{1 - p_m} \left( E - D + \frac{q_{b^*} - q_b}{L} \right), \end{aligned} \quad (10.11)$$

where the mixture density at the bed is  $\rho_b = \rho_s(1 - p_m) + \rho_w p_m$ .

### 10.2.4 Total-Load Equation

Rather than using Eqs. (10.6)–(10.7), it is possible to define a transport equation for the total load if separate computations for each load are of no interest. Summing Eqs. (10.6)–(10.7) produces

$$\frac{\partial}{\partial t}(hC_s + h_b C_b) + \frac{\partial}{\partial x}(hUC_s + q_b) + (1 - p_m) \frac{\partial z_b}{\partial t} = 0. \quad (10.12)$$

Using the definition of the total-load concentration  $C_t = C_s + q_b/(hU)$ , and resorting to Eq. (10.8), the total sediment transport mass conservation equation is (Wu and Wang 2007, 2008)

$$\frac{\partial}{\partial t}(hC_t) + \frac{\partial}{\partial x}(hUC_t) = - \left( D - E + \frac{q_b - q_{b^*}}{L} \right). \quad (10.13)$$

We now define the source term of Eq. (10.13) as function of the total load as (Wu 2008)

$$D - E + \frac{q_b - q_{b^*}}{L} \equiv \psi = \frac{q_t - q_{t^*}}{L}, \quad (10.14)$$

where  $q_{t^*}$  = total-load sediment transport capacity rate,  $q_t = qC_t$  = actual total-load sediment transport rate, and  $L$  = non-capacity adaptation length of the total-load sediment transport.

### 10.2.5 Sediment Transport Closure

According to Wu et al. (2004),  $L$  is given as the larger adaptation lengths of bed-load ( $L_b$ ) and suspended-load ( $L_s$ ). It is with  $\alpha$  = non-capacity adaptation coefficient of suspended-load

$$L = \max[L_b, L_s] = \max\left[L_b, \frac{U}{\alpha\omega_s}\right], \quad (10.15)$$

calculated with  $\alpha_0 = 2$  as (Wu 2008)

$$\alpha = \min[\alpha_0, (1 - p_m)/C_t]. \quad (10.16)$$

The settling velocity of sediment particles in turbid water  $\omega_s$  is determined from the Richardson–Zaki formula with  $m = 4$  (Wu 2008)

$$\omega_s = \omega_o(1 - C_t)^m, \quad (10.17)$$

where the settling velocity of a single particle in clear water is with  $d$  as the particle diameter and  $v$  the kinematic viscosity of water (Wu 2008)

$$\omega_o = \left[ (13.95v/d)^2 + 1.09[(\rho_s/\rho) - 1]gd \right]^{0.5} - 13.95v/d. \quad (10.18)$$

The actual total load is  $q_t = hUC_t$ , while the total-load capacity is determined as the contribution of both the suspended-load and the bed-load as

$$q_{t^*} = q_{s^*} + q_{b^*}. \quad (10.19)$$

Here,  $q_{s^*}$  and  $q_{b^*}$  = suspended- and bed-load sediment transport capacity rates, respectively, computed using Wu et al.'s (2000) formulas. To compute the equilibrium bed-load flux  $q_{b^*}$ , alternative empirical formulations could be considered, including the classical equations by Meyer-Peter and Müller, Yalin and van Rijn (Dey 2014).



**Eugen Meyer-Peter** was born on February 25, 1883, at Herisau, Switzerland, and passed away aged 86 years on June 18, 1969, at Zürich, Switzerland. He received the ETH civil engineering diploma in 1905, joining then the consulting firm of Conradin Zschokke (1842–1918), an expert in hydraulic engineering, with Meyer-Peter eventually becoming an expert in caisson foundation. The latter was involved in harbor works at Dieppe (France) and Venice (Italy), as also in the Rhine power plant Augst-Wyhlen. In 1920, he took over as ETH professor of hydraulic engineering and in parallel aimed to set up a hydraulic laboratory. Financial constraints postponed its inauguration until 1930.

He set out with excellent collaborators, including Henry Favre (1901–1966), Charles Jaeger (1901–1989), Hans-Albert Einstein (1904–1973), and Robert Müller (1908–1987). Next to contract work, a number of important research projects were initiated, such as on surges in tailrace tunnels, unsteady free surface flows, scour due to plunging jets, and spatially varied flows. His name remains related to his researches pertaining to sediment transport, with a first formula for the bed-load transport of uniform sediment in 1934, and the Meyer-Peter-Müller (MPM) formula in 1948, currently mainly applied for relatively steep rivers, such as in the Alpine Rhine environment. He was also involved in the prediction of future river degradation. He was awarded honorary doctorates from Zürich University in 1933 and the University of Grenoble in 1950. He is considered a great organizer of research campaigns and was the founder or co-founder of various institutes at ETH Zurich.

According to Wu et al. (2000), both capacity rates can be determined by using

$$q_{s^*} = 0.0000262 \left[ \left( \frac{\rho_s}{\rho_w} - 1 \right) g d^3 \right]^{1/2} \left[ \left( \frac{\tau}{\tau_c} - 1 \right) \frac{U}{\omega_s} \right]^{1.74}, \quad (10.20)$$

$$q_{b^*} = 0.0053 \left[ \left( \frac{\rho_s}{\rho_w} - 1 \right) g d^3 \right]^{1/2} \left[ \left( \frac{n'}{n} \right)^{3/2} \frac{\tau_b}{\tau_c} - 1 \right]^{2.2}, \quad (10.21)$$

where  $d$  = single sediment size diameter,  $\tau$  = shear stress on the wetted perimeter of the cross-section,  $\tau_b$  = bed shear stress tangent to sediment–fluid interface,  $\tau_c$  = critical bed shear stress determining the threshold for incipient sediment motion,  $n'$  = Manning's coefficient corresponding to the grain roughness for a movable bed ( $= d^{1/6}/20$ ), and  $n$  = Manning's roughness coefficient for the channel bed, with  $d$  in [m] and  $n$  in [ $\text{sm}^{-1/3}$ ]. Assuming a channel width larger than the flow depth,  $\tau \approx \tau_b$ . By numerical experimentation in shallow water flows, it was found that the last assumption does not reduce the accuracy of the solution. The critical shear stress is calculated with  $\Theta$  = Shields parameter = 0.03 as (Wu 2008)

$$\tau_c = \Theta(\rho_s - \rho)gd. \quad (10.22)$$

To apply Eqs. (10.20)–(10.21), the following ratio needs to be determined

$$\frac{\tau_b}{\tau_c} = \frac{\rho u_*^2}{\rho (u_*^2)_c}. \quad (10.23)$$

The bed shear stress yields the shear velocity as

$$u_* = n \frac{g^{1/2} U}{R_h^{1/6}}, \quad (10.24)$$

whereas the critical shear velocity is from Eq. (10.22)

$$(u_*)_c = \left[ \Theta \left( \frac{\rho_s}{\rho} - 1 \right) g d \right]^{1/2} = \left[ \Theta \left( \frac{s}{K} - 1 \right) g d \right]^{1/2}. \quad (10.25)$$

Here,  $s = \rho_s/\rho_w$  is the particle submerged density ratio and

$$K = \frac{\rho}{\rho_w} = (1 - C_t) + sC_t. \quad (10.26)$$

Note that  $K$  is based on the depth-averaged mixture density. Fraccarollo and Capart (2002) observed extremely high sediment concentration near the bed in geomorphic dam break flows. Thus, for dam break waves, the empirically enhanced version of  $K$  used is

$$K \approx \frac{\rho_b}{\rho_w} = [(1 - C_t) + sC_t]_b. \quad (10.27)$$

The near-bed value for dam break waves over erodible beds considered below is  $C_t = 0.6$ .

## 10.3 Numerical Scheme

### 10.3.1 Conservation Laws

Equations (10.10), (10.11), (10.13), and (10.8) can be written as (Cao et al. 2004; Wu and Wang 2008)

$$\frac{\partial \mathbf{U}}{\partial t} + \frac{\partial \mathbf{F}}{\partial x} = \mathbf{S}, \quad (10.28)$$

where

$$\mathbf{U} = \begin{pmatrix} h \\ hU \\ hC_t \\ z_b \end{pmatrix}, \quad \mathbf{F} = \begin{pmatrix} hU \\ hU^2 \\ hUC_t \\ 0 \end{pmatrix}, \quad \mathbf{S} = \begin{pmatrix} -\frac{\psi}{1-p_m} \\ -gh \frac{\partial z_s}{\partial x} - \frac{\tau_b}{\rho} - \frac{1}{2} \frac{g}{\rho} h^2 \frac{\partial \rho}{\partial x} \\ + \frac{\rho_b - \rho}{\rho} \frac{U}{1-p_m} \psi \\ \frac{-\psi}{1-p_m} \end{pmatrix}. \quad (10.29)$$

Here,  $\mathbf{U}$  is the dependent variable vector,  $\mathbf{F}$  the flux in the  $x$ -direction, and  $\mathbf{S}$  the source term. Note that the thickness of the bed-load layer is not resolved by this model, as originally assumed, that is,  $z_s = z_b + h$ .

### 10.3.2 First-Order Upwind Finite Volume Method

Consider a rectangular finite volume mesh in the  $x-t$  plane. Cell  $i$  is limited by both cell interfaces  $i - 1/2$  and  $i + 1/2$ . In the  $t$ -axis, the control volumes are delimited by the time levels  $k$  and  $k + 1$ . Integration of Eq. (10.28) over a control volume yields exactly (Toro 2001) [see Eq. (9.7)]

$$\mathbf{U}_i^{k+1} = \mathbf{U}_i^k - \frac{\Delta t}{\Delta x} (\mathbf{F}_{i+1/2} - \mathbf{F}_{i-1/2}) + \Delta t \mathbf{S}_i, \quad (10.30)$$

where  $k$  = time level,  $\Delta t$  = time step, and  $\Delta x$  = grid step. According to Ying et al. (2004), the one-sided upwind method is used to evaluate the intercell fluxes in Eq. (10.30) as

$$\mathbf{F}_{i+1/2} = \begin{pmatrix} h \\ hU^2 \\ hUC_t \\ 0 \end{pmatrix}_{i+1/2}^k. \quad (10.31)$$

Here,  $l$  = operator determining the upwind direction as function of the discharge  $q = Uh$  sign as:  $l = 0$  if  $q_i > 0$  and  $q_{i+1} > 0$ ,  $l = 1$  if  $q_i < 0$  and  $q_{i+1} < 0$ , and  $l = 1/2$  in other cases, where  $l = 1/2$  refers to an average of the flow variable between its value at  $i$  and  $i + 1$ .

### 10.3.3 Source Terms

To increase model robustness, the flow depth in the momentum topographic source term is evaluated at the time level  $k + 1$ , given that it is available by previously solving the continuity equation. To ensure numerical stability of the one-sided first-order upwind method, the water surface gradient in Eq. (10.30) is evaluated following Ying et al. (2004) by using a weighted average of the downwind and the upwind gradients as

$$\left( gh \frac{\partial z_s}{\partial x} \right)_i \approx gh_i^{k+1} \left( w_1 \frac{z_{s,i+1}^{k+1} - z_{s,i}^{k+1}}{\Delta x} + w_2 \frac{z_{s,i}^{k+1} - z_{s,i-1}^{k+1}}{\Delta x} \right). \quad (10.32)$$

The weighting factors are

$$w_1 = 1 - \frac{\Delta t}{\Delta x} \frac{U_{i+1-l}^k + U_{i-l}^k}{2} \quad \text{and} \quad w_2 = \frac{\Delta t}{\Delta x} \frac{U_{i+l}^k + U_{i-1+l}^k}{2}. \quad (10.33)$$

The sediment transport source term in the momentum equation is discretized in the numerical model as

$$\left( -\frac{1}{2} \frac{g}{\rho} h^2 \frac{\partial \rho}{\partial x} + \frac{\rho_b - \rho}{\rho} \frac{U}{1 - p_m} \psi \right)_i \approx -\frac{1}{2} \frac{g}{\rho_i} h_i^2 \frac{\rho_{i+1} - \rho_{i-1}}{2\Delta x} + \frac{\rho_b - \rho_i}{\rho_i} \frac{U_i}{1 - p_m} \psi_i, \quad (10.34)$$

and  $\tau_b/\rho$  is computed from Eq. (10.5).

### 10.3.4 Stability Condition

For stability of an explicit scheme, the Courant–Friedrichs–Lowy number must be  $\text{CFL} < 1$  (Toro 2001). Given the value of  $\text{CFL}$ ,  $\Delta t$  is determined at time level  $k$  from [Eq. (9.29)]

$$\Delta t = \text{CFL} \left[ \frac{\Delta x}{\max \left| U_i^k + (gh_i^k)^{1/2} \right|} \right]. \quad (10.35)$$

The maximum value for  $\text{CFL}$  was determined by trial-and-error numerical experiments. The value was typically less than 0.5.

### 10.3.5 Computational Sequence

The process of the numerical solution is as follows:

1. A longitudinal finite volume mesh of cell width  $\Delta x$  is defined.
2. The initial conditions are set.
3. The value of  $\Delta t$  is computed by applying Eq. (10.35).
4. The first-order upwind method is applied to compute  $\mathbf{F}_{i+1/2}$ .
5. The sediment transport computations are conducted to evaluate  $\psi$  at each cell.
6. The water depth at time  $h^{k+1}$  is computed from the first component of Eq. (10.30).
7. The source terms in the momentum equation due to the friction slope, free surface slope, and sediment transport are evaluated.
8. The discharge  $q^{k+1}$  is computed from the second component of Eq. (10.30).
9. The total sediment load  $(hC_t)^{k+1}$  is computed from the third component of Eq. (10.30).
10. The bed profile is updated using the fourth component of Eq. (10.30).
11. If the actual time equals the final, then stop.
12. Boundary conditions are set.
13. Go back to step 3 for a new time loop.

## 10.4 Test Cases

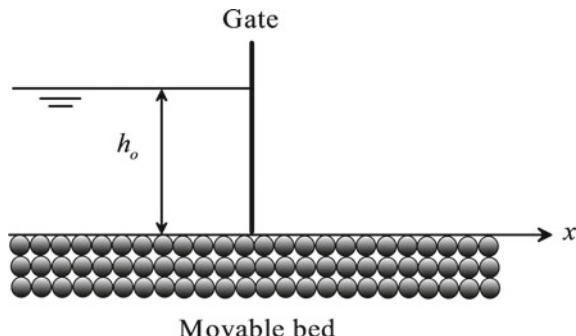
### 10.4.1 Dam Break Wave over Movable Bed

Dam break flow is a topic of continued research interest given its highly detrimental effects. The usual engineering approach to predict these flows relies on the use of

depth-averaged shallow water wave models based on a hydrostatic pressure distribution (Wu 2008). In recent years, hydrostatic shallow water flow models were extensively studied. Wu and Wang (1999, 2007, 2008) developed Saint-Venant-type mixture flow equations for dam break flows over erodible beds. Fraccarollo and Capart (2002) proposed a two-layer movable bed dam break flow model with separate simulations of clear water and mixture sediment–water layers. Capart and Young (1998, 2002) and Cao et al. (2004) developed models for dam break waves over erodible bed considering non-equilibrium sediment transport conditions. Geomorphic shallow water flows, as dam break waves over an erodible bed, require consideration of fluid motion and erosion/deposition of particles. It is accepted that the shallow water flow approximation with hydrostatic pressure produces a reasonable balance between computational efforts and accuracy of results (Pontillo et al. 2010; Greco et al. 2012).

In this section, dam break waves over an erodible bed generated under laboratory conditions (Fig. 10.2) are considered, where the movable bed is made of uniform particles, the tailwater portion of the flume is dry, and the dam is simulated with a gate. The experimental data included in Figs. 10.3 and 10.4 are taken from the Taipei and Louvain test cases (Capart and Young 1998; Fraccarollo and Capart 2002). Both sets correspond to laboratory observations, where the flow depth upstream of the dam was  $h_o = 0.1$  m and the tailwater portion of the flume was dry. Values of  $\Delta x = 0.01$  m and  $CFL = 0.3$  are set in the numerical model implemented in the file *Movablebed\_DamBreak.xls*, available in Chap. 12. According to Wu and Wang (2007),  $C_{tb} = 0.6$ ,  $L_b = 0.25$  m,  $\alpha_0 = 2$ , and  $n = 0.025$  s/m $^{1/3}$  are used as simulation data for both test cases. The bed sediment layer porosities are  $p_m = 0.28$  and 0.30 for the Taipei and Louvain tests, respectively. The dry downstream bed is simulated by adopting a minute flow depth of 0.0005 m. This technique is accepted for dam break flow simulations (Wu 2008), although this is conceptually incorrect (Toro 2001). Alternatively, a zero tailwater depth can be prescribed if an algorithm to preserve positivity in the computed water depths near the wet–dry front is implemented (Wu 2008). The computational domain was selected so that waves do not reach the boundaries.

**Fig. 10.2** Laboratory setup to generate a dam break flow over erodible bed



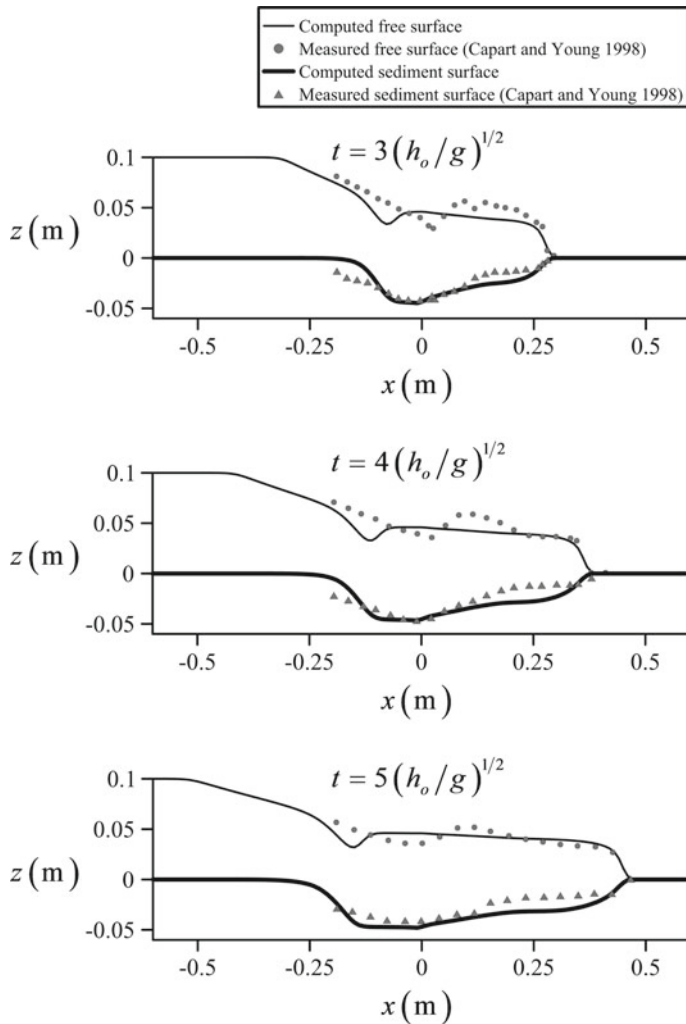


**Fig. 10.3** Water and bed surfaces at different times for the Taipei test case

In Fig. 10.3, the Taipei experiment (Capart and Young 1998) is simulated by solving Eqs. (10.28)–(10.29) at times  $t = 3t_o$ ,  $4t_o$ , and  $5t_o$  after the dam failure, where the time scaling is  $t_o = (h_o/g)^{1/2} \approx 0.1$  s. The sediment particles used were artificial pearls covered with a shiny white coating, having  $d = 6.1$  mm,  $\rho_s = 1048$  kg/m<sup>3</sup>, and  $\omega_o = 7.6$  cm/s. The flume was sufficiently long and deep with  $b = 0.2$  m. The model produces a bed profile eroded by the dam break flow in overall agreement with the experiments. The experimental free surface profile is composed of a negative smooth wave, followed by a train of undulations above the

scour hole, ending in a positive wave where its edge is a wet–dry front propagating in the positive  $x$ -direction. Note that the experimental data show free surface undulations at the vicinity of the positive wave portion, not predicted by hydrostatic computations. However, the position of the wet–dry front predicted by the hydrostatic model is in agreement with the experimental data. The overall wave features are thus well predicted by the SWE.

The study of the Louvain test experiment at times  $t = 5t_o$ ,  $7.5t_o$ , and  $10t_o$  after the dam break is presented in Fig. 10.4. In this experiment, Fraccarollo and Capart

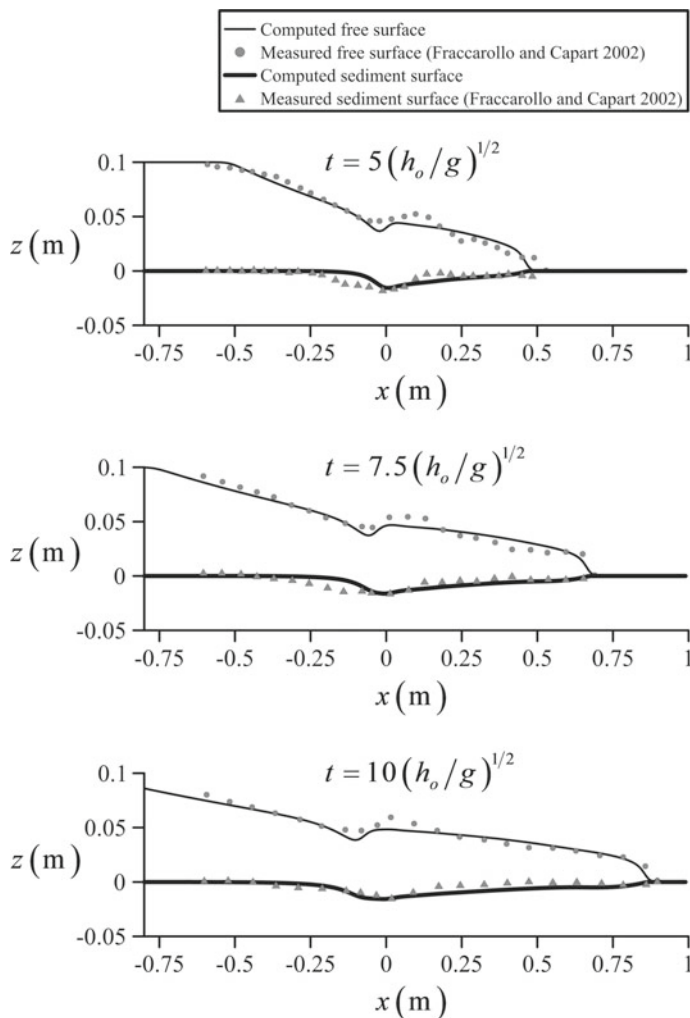


**Fig. 10.4** Water and bed surfaces at different times for Louvain test case

(2002) used cylindrical PVC pellets as sediment particles, having  $d = 3.5$  mm,  $\rho_s = 1540$  kg/m<sup>3</sup>, and  $\omega_o = 18$  cm/s. The flume had a width  $b = 0.10$  m. The hydrostatic model produces simulations of the eroded bed profiles with some divergence from the experimental results, but in overall agreement. The free surface profile predicted is in fair agreement with observations, but the undulations due to non-hydrostatic pressure are not reproduced (Cantero-Chinchilla et al. 2016).

### 10.4.2 Dike Erosion due to Overtopping

Dike breach experiments of Schmocker (2011) were selected for comparison purposes with numerical simulations using Eq. (10.30). Figure 10.5 shows a definition sketch of his experimental setup. Tests 42 and 55 were selected, involving variations in sediment diameter (non-cohesive material) and discharge. The tests features are summarized in Table 10.1. The dike erosion process produces a round-crested weir-like profile (Fig. 10.6), with features different from the dam break wave problem.

The experimental data of Test 42 are compared in Fig. 10.7 with the numerical solution resulting from Eq. (10.30). Values of  $\Delta x = 0.025$  m and  $CFL = 0.25$  were set in the numerical model, which is implemented in the file *Movablebed\_Dikebreaching.xls*, available in Chap. 12. For the simulations  $K = 1$  [see Eq. (10.26)],  $L = 0.01$  m,  $\omega_s = \omega_o$ , and  $n = 0.018$  s/m<sup>1/3</sup> were used. The bed sediment layer porosity  $p_m$  is calculated from (Wu and Wang 2008)

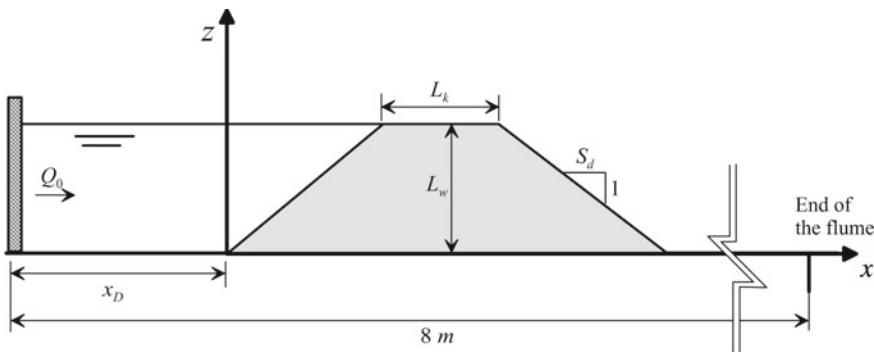


**Fig. 10.5** Definition sketch of experimental setup (Schmocker 2011), subscript “0” defines the inflow conditions

**Table 10.1** Dike test characteristics

Test	$d$ (mm)	$L_k$ (m)	$b$ (m)	$x_D$ (m)	$S_d$ (—)	$Q_0$ (m <sup>3</sup> s <sup>-1</sup> )
42	1.0	0.1	0.2	1.0	1:2	0.006
55	2.0	0.1	0.2	1.0	1:2	0.016



**Fig. 10.6** Dike erosion test (photograph O. Castro-Orgaz)

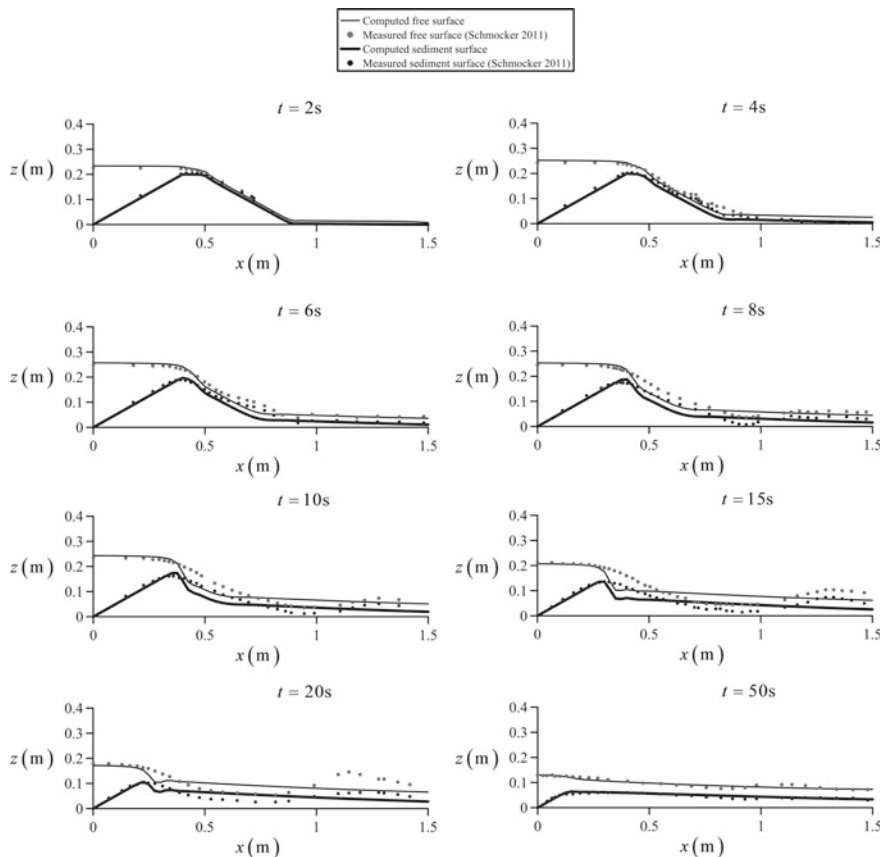


**Fig. 10.7** Water and bed surfaces at different times for dike erosion Test 42

$$p_m = 0.13 + \frac{0.21}{[d(\text{mm}) + 0.002]^{0.21}}. \quad (10.36)$$

The dry bed was simulated by adopting the minute flow depth 0.0001 m. The upstream discharge was implemented in the numerical model as an instantaneous pulse in a ghost cell, whereas the upstream water depth at the ghost cell was determined by extrapolating the interior solution at the previous instant. At the downstream section, transmissive boundary conditions were implemented in a ghost cell (Toro 2001). For Test 42, the discharge is low, and non-hydrostatic effects are expected to be small. This is in turn verified by comparing simulations with measurements in Fig. 10.7, from where it is observed that the water level upstream of the dike crest is in conformity with the theory. Beyond the dike crest, the numerical model predicts excessive erosion on the downstream slope, thereby diverging theory from experimental results.

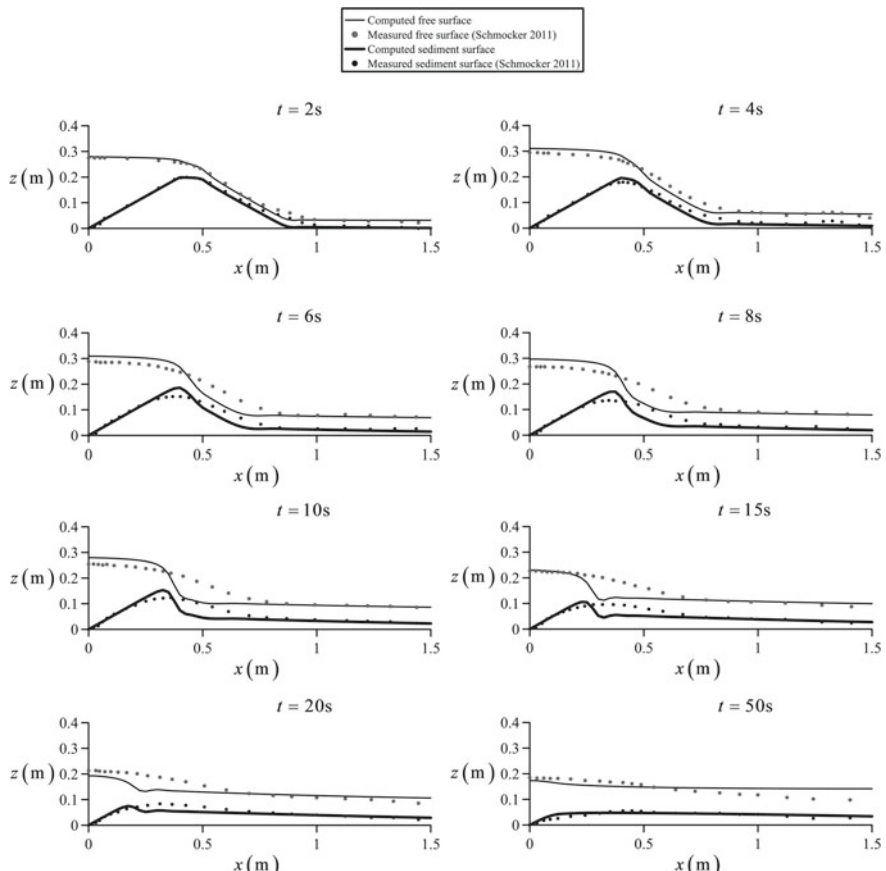


**Fig. 10.8** Water and bed surfaces at different times for dike erosion Test 55

The experimental and computational results for Test 55 are presented in Fig. 10.8, whose particle size and inflow discharge are larger than for Test 42. Note that the upstream flow depth is systematically overestimated resulting from the hydrostatic pressure assumption. The model produces in this test again an overestimation of erosion in the supercritical flow portion. The entire process is highly complex and still not fully understood. Recent results suggest that non-hydrostatic pressures shall be introduced in shallow water models to produce a more accurate flow profile up to the dike crest, whereas for simulating the tailwater portion the displacement of the granular dike has a non-negligible effect (Cantero-Chinchilla et al. 2018, 2019).

In this chapter, the extended shallow water equations for geomorphic flows are presented and solved by using an upwind finite volume scheme. Applications to dam break waves over erodible beds and dike failures due to overtopping highlight that the physical processes involved are extremely complex and still not fully accounted for in these families of computational models.

## References

- Cantero-Chinchilla, F., Castro-Orgaz, O., Dey, S., & Ayuso, J. L. (2016). Nonhydrostatic dam break flows II: One-dimensional depth-averaged modelling for movable bed flows. *Journal of Hydraulic Engineering*, 142(12), 04016069.
- Cantero-Chinchilla, F. N., Castro-Orgaz, O., Schmocker, L., Hager, W. H., & Dey, S. (2018). Depth-averaged modelling of granular dike overtopping. *Journal of Hydraulic Research*, 56(4), 537–550.
- Cantero-Chinchilla, F. N., Castro-Orgaz, O., Dey, S. (2019). Prediction of overtopping dike failure: A sediment transport and dynamic granular bed deformation model. *Journal of Hydraulic Engineering*, 145(6), 04019021.
- Cao, Z., Pender, G., Wallis, S., & Carling, P. (2004). Computational dam-break hydraulics over erodible sediment bed. *Journal of Hydraulic Engineering*, 130(7), 689–703.
- Capart, H., & Young, D. L. (1998). Formation of a jump by the dam-break wave over a granular bed. *Journal of Fluid Mechanics*, 372, 165–187.
- Capart, H., Young, D. L. (2002). Two-layer shallow water computations of torrential flows. In: *Proceedings of River Flow*, vol. 2, (pp. 1003–1012). Lisse, The Netherlands: Balkema.
- Dey, S. (2014). *Fluvial hydrodynamics: Hydrodynamic and sediment transport phenomena*. Berlin: Springer.
- Fraccarollo, L., & Capart, H. (2002). Riemann wave description of erosional dam break flows. *Journal of Fluid Mechanics*, 461, 183–228.
- Greco, M., Iervolino, M., Leopardi, A., & Vacca, A. (2012). A two-phase model for fast geomorphic shallow flows. *International Journal of Sediment Research*, 27(4), 409–425.
- Pontillo, M., Schmocker, L., Greco, M., & Hager, W. H. (2010). 1D numerical evaluation of dike erosion due to overtopping. *Journal of Hydraulic Research*, 48(5), 573–582.
- Schmocker, L. (2011). *Hydraulics of dike breaching*. Ph.D. thesis. Zürich, Switzerland: Swiss Federal Institute of Technology.
- Toro, E. F. (2001). *Shock-capturing methods for free-surface shallow flows*. New York: Wiley.
- Wu, W. (2008). *Computational river dynamics*. London, U.K.: Taylor and Francis.
- Wu, W., & Wang, S. S. Y. (1999). Movable bed roughness in alluvial rivers. *Journal of Hydraulic Engineering*, 125(12), 1309–1312.

- Wu, W., & Wang, S. S. Y. (2007). One-dimensional modeling of dam-break flow over movable beds. *Journal of Hydraulic Engineering*, 133(1), 48–58.
- Wu, W., & Wang, S. S. Y. (2008). One-dimensional explicit finite-volume model for sediment transport. *Journal of Hydraulic Research*, 46(1), 87–98.
- Wu, W., Wang, S. S. Y., & Jia, Y. (2000). Nonuniform sediment transport in alluvial rivers. *Journal of Hydraulic Research*, 38(6), 427–434.
- Wu, W., Vieira, D. A., & Wang, S. S. Y. (2004). One-dimensional numerical model for nonuniform sediment transport under unsteady flows in channel networks. *Journal of Hydraulic Engineering*, 130(9), 914–923.
- Ying, X., Khan, A. A., & Wang, S. S. Y. (2004). Upwind conservative scheme for the Saint Venant equations. *Journal of Hydraulic Engineering*, 130(10), 977–987.

# Chapter 11

## Numerical Modeling of Non-hydrostatic Free Surface Flows



### 11.1 Introduction

The shallow water equations (SWE) are a dispersionless system of hyperbolic PDEs obtained by assuming that the vertical flow acceleration is negligible. Under this assumption, the vertical momentum balance is reduced to the hydrostatic pressure law (Toro 2001; Castro-Orgaz and Hager 2017). This approach produces good solutions for shallow flows if the vertical length scale [ $H$ ] is negligible as compared to the horizontal length scale [ $L$ ]. In turn, this scenario is realistic in many open channel and river hydraulics problems. However, there are as well a large number of practical questions where this level of mathematical approximation is not well suited. It includes flows across hydraulic structures like weirs, intakes, overfalls, energy dissipators, and water wave motion in maritime and fluvial hydraulics, as the solitary and cnoidal waves, and the undular bore propagation in a river. In this large portfolio of problems, the vertical length scale [ $H$ ], though it can be small, is not negligible as compared to [ $L$ ] (Steffler and Jin 1993; Castro-Orgaz and Hager 2017). A non-hydrostatic vertical pressure distribution must therefore be accounted for in the depth-averaged equations. A higher-order mathematical model based on the so-called *Boussinesq equations* is a possible choice to simulate these flows. Depending on the technique and terms retained while introducing the vertical acceleration and/or turbulent stresses on the depth-averaged equations, different types of Boussinesq equations are obtained. In this chapter, we only consider inviscid flow solutions following Castro-Orgaz and Cantero-Chinchilla (2019). The non-hydrostatic flows considered are shallow, and waves are thus long and dispersion effects weak. The modeling of highly dispersive waves from deep to intermediate depths is beyond the scope of this chapter. First, steady potential open channel flow problems in a vertical plane are considered, then generalizations for inviscid unsteady flow over a 3D terrain. Illustrative problems relating to hydraulic structures and wave motion are solved using second- and higher-order numerical schemes.

## 11.2 Two-Dimensional Steady Potential Flow

### 11.2.1 Basic Equations

Consider steady two-dimensional (2D) *potential* free surface flows over a curved bed (Fig. 11.1). The governing equations are (Rouse 1938; Valentine 1969)

$$\frac{\partial u}{\partial x} + \frac{\partial w}{\partial z} = 0, \quad (11.1)$$

$$u \frac{\partial u}{\partial x} + w \frac{\partial u}{\partial z} = - \frac{1}{\rho} \frac{\partial p}{\partial x}, \quad (11.2)$$

$$u \frac{\partial w}{\partial x} + w \frac{\partial w}{\partial z} = - \frac{1}{\rho} \frac{\partial p}{\partial z} - g, \quad (11.3)$$

$$\frac{\partial u}{\partial z} - \frac{\partial w}{\partial x} = 0. \quad (11.4)$$

Here,  $u$  is the velocity component in the  $x$ -direction,  $w$  that in the vertical  $z$ -direction,  $p$  is pressure,  $g$  the gravity acceleration, and  $\rho$  the fluid density. Equation (11.1) is the continuity equation of an incompressible fluid, Eqs. (11.2) and (11.3) are the momentum equations in the  $x$ - and  $z$ -directions, and Eq. (11.4) is the irrotational flow condition. Equations (11.1)–(11.3) are the Euler equations for inviscid fluid flow.

The potential function  $\phi$  is defined by Thom and Apelt (1961), Valentine (1969)

$$u = \frac{\partial \phi}{\partial x}, \quad w = \frac{\partial \phi}{\partial z}. \quad (11.5)$$

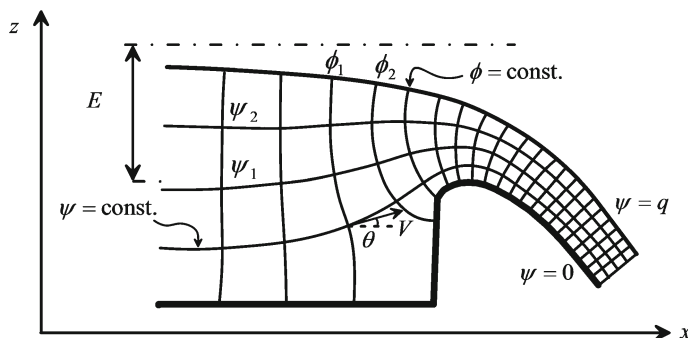


**Fig. 11.1** Potential flow over a curved bed

This flow field automatically satisfies Eq. (11.4). Inserting Eq. (11.5) in Eq. (11.1), the flow field obeys the Laplace equation for  $\phi$ ,

$$\frac{\partial^2 \phi}{\partial x^2} + \frac{\partial^2 \phi}{\partial z^2} = 0. \quad (11.6)$$

For an incompressible fluid, a stream function  $\psi$  is defined by Thom and Apelt (1961), Valentine (1969) as

$$u = -\frac{\partial \psi}{\partial z}, \quad w = \frac{\partial \psi}{\partial x}. \quad (11.7)$$

Using these relations in Eq. (11.1), the continuity equation is automatically satisfied. Using Eq. (11.7) in Eq. (11.4), the stream function satisfies the Laplace equation

$$\frac{\partial^2 \psi}{\partial x^2} + \frac{\partial^2 \psi}{\partial z^2} = 0. \quad (11.8)$$

The lines  $\psi = \text{const.}$  are streamlines, and the velocity vector, of modulus  $V = (u^2 + w^2)^{1/2}$  and inclined with respect to the  $x$ -axis by the angle  $\theta = \tan^{-1}(w/u)$ , is tangent to them. The equipotential lines  $\phi = \text{const.}$  are normal to the streamlines at intersection points, forming the so-called flow net of a potential flow (Fig. 11.1). The Cauchy–Riemann equations are derived by equaling the velocity components in Eqs. (11.5) and (11.7) as

$$u = \frac{\partial \phi}{\partial x} = -\frac{\partial \psi}{\partial z}, \quad w = \frac{\partial \phi}{\partial z} = \frac{\partial \psi}{\partial x}. \quad (11.9)$$

A final result of relevance to solve potential free surface flows is the Bernoulli equation, stating conservation of the total energy head  $H$  within the fluid domain (Valentine 1969)

$$H = z + \frac{p}{\rho g} + \frac{u^2 + w^2}{2g} = \text{const.} \quad (11.10)$$

Two-dimensional potential flow solutions are generally based on Eqs. (11.6), (11.8), (11.9), and (11.10), or variations using other mappings. The velocity ( $u, w$ ) and pressure  $p$  of the 2D potential flow can be inserted into the vertically integrated form of the momentum equations to obtain additional mathematical statements. One of great utility is the vertically integrated  $x$ -momentum balance, obtained by integration of Eq. (11.2) from the channel bottom (subscript  $b$ ) to the free surface (subscript  $s$ ), using Leibniz's rule, and imposing kinematic boundary conditions, expressing tangency of the velocity at the basal and free surfaces, namely [see Eqs. (1.13) and (1.15)]

$$w_s = u_s \frac{\partial z_s}{\partial x}, \quad w_b = u_b \frac{\partial z_b}{\partial x}. \quad (11.11)$$

The result is [see Eq. (1.126)]

$$\frac{dS}{dx} = -\frac{p_b}{\rho g} \frac{dz_b}{dx}, \quad (11.12)$$

where

$$S = \int_{z_b}^{z_b + h} \left( \frac{u^2}{g} + \frac{p}{\rho g} \right) dz \quad (11.13)$$

is the specific momentum (Jaeger 1956; Matthew 1991; Montes 1998).

### 11.2.2 Picard Iteration

An approximate 1D model to solve potential flow problems is considered here. In turn, this is a topic where a large research activity was conducted since the 1980s following Boussinesq's (1877) theory, see, e.g., Hager and Hutter (1984a, b), Hager (1985), Marchi (1992, 1993), and Matthew (1991). There is a vast amount of Boussinesq-type approximations to construct 1D models in civil, environmental, and coastal engineering [see Castro-Orgaz and Hager (2017) for a detailed review]. Here, an elegant and rigorous method developed by Matthew (1991) is presented. It is based on the Picard iteration of the full 2D potential flow equations. The idea of all 1D methods is to eliminate the  $z$ -dependence of the equations and to produce a model where the position of the free surface as function of the  $x$ -coordinate is part of the solution itself. Van Dyke (1975) discussed methods to solve systems of partial differential equations in fluid flow problems by approximations. One of the possible techniques is to iterate the solution of the equations  $\nabla^2 \phi = 0$  and  $\nabla^2 \psi = 0$  starting with an initial solution. This is the idea pursued by Matthew (1991), who iterated the Cauchy–Riemann equations [Eq. (11.9)], using uniform flow as initial solution (Matthew 1991; Castro-Orgaz and Hager 2013, 2014). The process is described by Matthew (1991) for steady flow and extensively discussed by Castro-Orgaz and Hager (2017) in their generalization for unsteady potential flow, so that only the final results are stated here. The potential velocity components approximated to second-order accuracy are

$$u = U + (2U_x \eta_x + U \eta_{xx}) \left( \frac{h}{2} - \eta \right) + U_{xx} \left( \frac{h^2}{6} - \frac{\eta^2}{2} \right), \quad (11.14)$$

$$w = -U_x \eta - U \eta_x, \quad (11.15)$$

with the variable  $\eta(x, z) = z - z_b(x)$  as the vertical distance above the channel bottom,  $U = q/h$  the depth-averaged velocity,  $h$  the vertical flow depth, and  $q$  the unit discharge. Subscripts indicate differentiation, e.g.,  $U_x = \partial U / \partial x$ ,  $U_{xx} = \partial^2 U / \partial x^2$ ,  $\eta_x = -\partial z_b / \partial x$ , and  $\eta_{xx} = -\partial^2 z_b / \partial x^2$ . For steady flow, the spatial derivatives of  $U$  and  $\eta$  take the form

$$\begin{aligned} U_x &= -\frac{qh_x}{h^2}, & U_{xx} &= -\frac{qh_{xx}}{h^2} + 2\frac{qh_x^2}{h^3}, \\ \eta_x &= -z_{bx}, & \eta_{xx} &= -z_{bx}. \end{aligned} \quad (11.16)$$

Inserting Eq. (11.16) into Eqs. (11.14) and (11.15) results in (Castro-Orgaz and Hager 2017)

$$u = \frac{q}{h} \left[ 1 + \left( z_{bx} - \frac{2h_x z_{bx}}{h} \right) \left( \frac{2\eta - h}{2} \right) + \left( \frac{h_{xx}}{2h} - \frac{h_x^2}{h^2} \right) \left( \frac{3\eta^2 - h^2}{3} \right) \right], \quad (11.17)$$

$$w = \frac{q}{h} \left[ z_{bx} + \frac{\eta}{h} h_x \right]. \quad (11.18)$$

Inserting Eqs. (11.17)–(11.18) in the Bernoulli Eq. (11.10), neglecting second-order terms, and particularizing the result for the free surface ( $p = 0$ ,  $\eta = h$ ), results in the extended Bernoulli-type equation (Matthew 1991; Castro-Orgaz and Hager 2017)

$$H = z_b + h + \frac{q^2}{2gh^2} \left( 1 + \frac{2hh_{xx} - h_x^2}{3} + hz_{bx} + z_{bx}^2 \right). \quad (11.19)$$

This theory considers the curvature effect of both the free surface and the bottom, accounted for by the inclusion of  $h_{xx} = d^2h/dx^2$  and  $z_{bx} = d^2z_b/dx^2$ ; it also considers the slope effect of the free surface and the bottom by inclusion of  $h_x = dh/dx$  and  $z_{bx} = dz_b/dx$ . The values of these slopes and curvatures are not necessarily small, given that no restriction on non-linearity was imposed. Therefore, Matthew's (1991) theory, used by Castro-Orgaz and Hager (2009), is an approximate potential flow model that includes the effects of finite curvatures and slopes. This equation was presented by Naghdi and Vongsarnpigoon (1986) based on the theory of a Cosserat surface (Green and Naghdi 1976a, b; Naghdi 1979). It is remarkable to state that this equation is the steady-state form of the well-known Serre-Green-Naghdi equations, which are widely applied in ocean research. This issue will be further exploited below. Equation (11.19) was also obtained by Marchi (1992, 1993) by expanding the stream function in power series, and by Zhu and Lawrence (1998) by using a perturbation method. It is a second-order differential equation, from which the free surface profile  $h = h(x)$  is determined. For given  $q$  and  $H = \text{const.}$ , and prescribed flow depths at two boundary sections, Eq. (11.19) is

solved numerically as a two-point boundary value problem (Zhu 1996; Castro-Orgaz and Hager 2009).

Using Bernoulli's equation, the pressure distribution to this order of accuracy is (Matthew 1991; Castro-Orgaz and Hager 2017)

$$\frac{p}{\gamma} = h - \eta + \frac{q^2}{2gh^2} \left[ (2hz_{bx} - 2h_x z_{bx}) \left(1 - \frac{\eta}{h}\right) + (hh_{xx} - h_x^2) \left(1 - \frac{\eta^2}{h^2}\right) \right]. \quad (11.20)$$

The value at the channel bottom  $p_b = p(\eta = 0)$  is [see Eq. (1.132)]

$$\frac{p_b}{\gamma} = h + \frac{q^2}{2gh^2} (2hz_{bx} + hh_{xx} - h_x^2 - 2z_{bx}h_x). \quad (11.21)$$

After having established the energy equation, the momentum principle is considered. Inserting Eqs. (11.17) and (11.20) for the distributions of  $u$  and  $p$  into Eq. (11.13), the specific momentum  $S$  is given by (Castro-Orgaz and Hager 2017) [see Eq. (1.133)]

$$S = \frac{h^2}{2} + \frac{q^2}{gh} \left( 1 + \frac{hh_{xx} - h_x^2}{3} + \frac{hz_{bx}}{2} - \frac{h_x z_{bx}}{2} \right). \quad (11.22)$$

Using Eqs. (11.21) and (11.22), the vertically integrated momentum balance [Eq. (11.12)] can be equally used to compute the free surface profile  $h = h(x)$ . It remains to delineate the connection between the energy [Eq. (11.19)] and momentum [Eqs. (11.12), (11.21) and (11.22)] models for steady potential flow over curved beds. Consider first Eq. (11.19), given that the energy head is a constant in potential flow, its differentiation with respect to  $x$  yields

$$\begin{aligned} \frac{dH}{dx} &= z_{bx} + h_x - \frac{q^2}{gh^3} h_x \left( 1 + \frac{2hh_{xx} - h_x^2}{3} + hz_{bx} + z_{bx}^2 \right) \\ &\quad + \frac{q^2}{2gh^2} \left( \frac{2hh_{xxx}}{3} + hz_{bx} + h_x z_{bx} + 2z_{bx} z_{bx} \right) = 0. \end{aligned} \quad (11.23)$$

The result is the following third-order ODE after elementary re-arrangement

$$\begin{aligned} z_{bx} + h_x - \frac{q^2}{gh^3} h_x - \frac{2}{3} \frac{q^2}{gh^2} h_x h_{xx} + \frac{1}{3} \frac{q^2}{gh^3} h_x^3 + \frac{1}{3} \frac{q^2}{gh} h_{xxx} \\ - \frac{1}{2} \frac{q^2}{gh^2} h_x z_{bx} - \frac{q^2}{gh^3} h_x z_{bx}^2 + \frac{1}{2} \frac{q^2}{gh} z_{bx} + \frac{q^2}{gh^2} z_{bx} z_{bx} = 0. \end{aligned} \quad (11.24)$$

Now, Eqs. (11.21)–(11.22) are inserted into Eq. (11.12), producing

$$\frac{d}{dx} \left[ \frac{h^2}{2} + \frac{q^2}{gh} \left( 1 + \frac{hh_{xx} - h_x^2}{3} + \frac{hz_{bxx}}{2} - \frac{h_x z_{bx}}{2} \right) \right] = - \left[ h + \frac{q^2}{2gh^2} (2hz_{bxx} + hh_{xx} - h_x^2 - 2z_{bx}h_x) \right] \frac{dz_b}{dx}. \quad (11.25)$$

Expanding the various terms in Eq. (11.25) yields Eq. (11.24). This implies that the energy and momentum balances produce the identical governing equation to this order of accuracy. Therefore, it is in principle easier to adopt Eq. (11.19), which is an integral form of Eq. (11.25). This is interesting from a numerical standpoint, given that the higher order of differentiation is reduced to second order, avoiding instability problems linked to the discretization of third-order derivatives in Boussinesq-type equations (Bonneton et al. 2011). Equation (11.25) is the steady-state version of the Serre–Green–Naghdi equations; thus, Eq. (11.19) is an integral form of these equations under steady flow. Equation (11.19) admits analytical solutions for selected problems like the flow profile upstream of a free overfall, the solitary wave, or the supercritical jet beyond a sluice gate (Castro-Orgaz and Hager 2017). However, in general, a numerical solution is required for flows over curved beds.

### 11.2.3 Spillway Crest

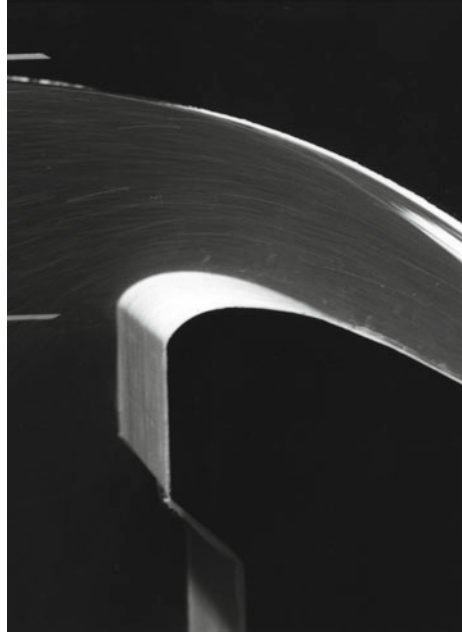
Reconsider Eq. (11.23). Imposing  $dz_b/dx = 0$  yields, after re-arrangement,

$$\frac{q^2}{gh^3} \left( 1 + \frac{2hh_{xx} - h_x^2}{3} - \frac{h^2 h_{xxx}}{3h_x} + \frac{hz_{bxx}}{2} - \frac{h^2 z_{bx}}{2h_x} \right) = 1. \quad (11.26)$$

This relation is valid at the spillway crest (Fig. 11.2); accepting a physical solution with finite free surface slope ( $h_x < 0$ ), it is the critical flow condition for curvilinear flows. This condition serves as the mathematical equation describing the critical depth in non-hydrostatic flows (Castro-Orgaz and Hager 2017). Equation (11.26) indicates that the non-hydrostatic critical flow condition does not depend on the section conditions alone, e.g., the actual value of  $h$ , but in addition on the configuration of the flow profile  $h = h(x)$  in the vicinity of the crest section, and on the local bottom geometry variation  $z_b = z_b(x)$ . The words by Rouse (1938) on p. 326 of his book state:

... Since the ratio of depth to specific energy at the true critical section is so definitely a function of the curvature imposed by the fixed boundaries, it is almost futile to expect that a simple relationship may be found expressing this ratio in terms of boundary geometry. It is to be hoped, nevertheless, that a broader understanding of true critical discharge may soon lead to definite progress in this essential field.

**Fig. 11.2** Flow over spillway crest (VAW photo)



Equation (11.26) is an advance in this line; the non-hydrostatic effects imposed by the boundary conditions are included in the critical flow statement. Equation (11.26) is an approximate solution at the weir crest to the elliptic problem posed by Laplace's equation for potential flow. Therefore, the approximation to this elliptic problem depends not only on the crest conditions, but rather on the complete flow solution, which, in turn, determines the spatial derivatives  $h_x$ ,  $h_{xx}$ , and  $h_{xxx}$ .

It is possible, however, to find approximations to these derivatives at the weir crest on the basis of the lower-order energy head equation for hydrostatic flows (Hager 1985; Matthew 1991) [Eq. (2.12)]

$$H = z_b + h + \frac{q^2}{2gh^2} = \text{const.} \quad (11.27)$$

This theory for critical curvilinear flows is presented here following Castro-Orgaz and Hager (2017). Differentiation of Eq. (11.27) produces for critical flow ( $F = 1$ ) the following approximations for  $h_x^2$  and  $hh_{xx}$  at the weir crest, with  $R$  as the crest curvature radius (Castro-Orgaz and Hager 2017),

$$h_x^2 = -\frac{hz_{bxz}}{3} = \frac{h}{3R}, \quad (11.28)$$

$$h_{xx} = -\frac{4z_{bxz}}{9} = \frac{4}{9R}. \quad (11.29)$$

The specific energy at the weir crest ( $dz_b/dx = 0$ ) is from Eq. (11.19)

$$E = h + \frac{q^2}{2gh^2} \left( 1 + \frac{2hh_{xx} - h_x^2}{3} + hz_{bxx} \right), \quad (11.30)$$

and the discharge coefficient of the spillway is defined by Poleni's equation as (Montes 1998)

$$q = C_d (gE^3)^{1/2}. \quad (11.31)$$

Inserting Eqs. (11.28)–(11.29) into Eq. (11.30), and using Eq. (11.31) produce, retaining first-order terms (Castro-Orgaz and Hager 2017)

$$C_d = \left( \frac{2}{3} \right)^{3/2} \left( 1 + \frac{22E}{81R} \right). \quad (11.32)$$

The critical depth in curvilinear motion is determined from Eq. (11.26). The third-order flow depth derivative term needed in this equation is approximated by differentiation of Eq. (11.27) as (Castro-Orgaz and Hager 2017)

$$\frac{h^2 h_{xxx}}{h_x} = -\frac{5}{9} h z_{bxx} = \frac{5h}{9R}. \quad (11.33)$$

Inserting Eqs. (11.28), (11.29), and (11.33) into Eq. (11.26) produces when retaining first-order terms (Castro-Orgaz and Hager 2017)

$$\frac{h_{\text{crest}}}{h_c} = 1 - \frac{E}{9R}. \quad (11.34)$$

The bottom pressure head at the weir crest is from Eq. (11.21)

$$\frac{p_b}{\gamma} = h + \frac{q^2}{2gh^2} (2hz_{bxx} + hh_{xx} - h_x^2), \quad (11.35)$$

where  $\gamma$  is the specific weight of fluid. Using Eqs. (11.28), (11.29), and (11.34) into Eq. (11.35) yields to first-order accuracy

$$\frac{(p_b)_{\text{crest}}}{\gamma h_c} = 1 - \frac{20E}{27R}. \quad (11.36)$$

Equations (11.32), (11.34), and (11.36) comprise the first-order solutions for the problem of critical flow in curvilinear motion. They are expected to be valid for weakly curved flows, e.g., up to  $E/R = 1$  (Castro-Orgaz and Hager 2017). This

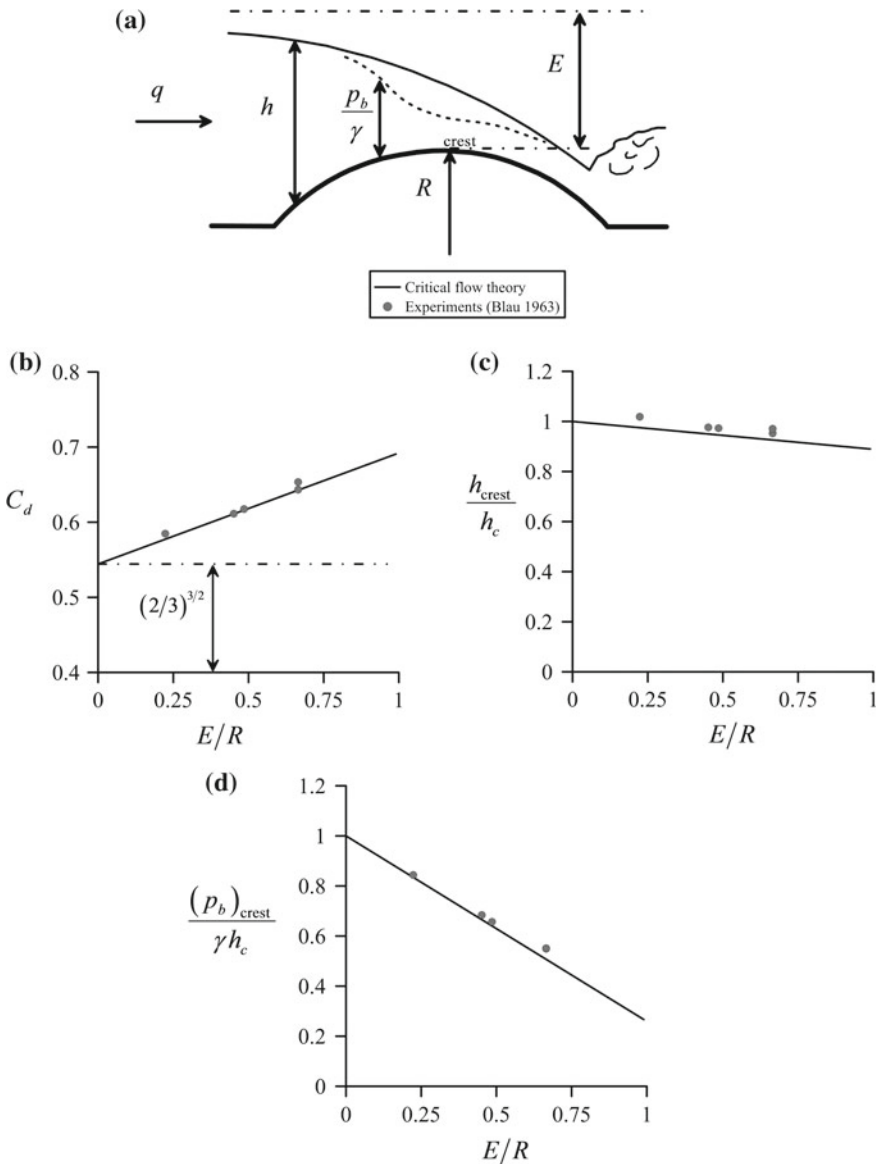


**Fig. 11.3** Critical flow at crest of a parabolic weir

theory is compared in Fig. 11.3 with the experimental data of Blau (1963) for a parabolic weir of crest radius  $R = 0.919$  m. Note that the approximate theory produces a solution in fair agreement with observations. The advantage of this type of model is that the full solution of Eq. (11.19) is avoided. The full solution  $h(x)$  of flow over curved beds can only be obtained numerically, given the lack of known exact analytical expressions.

### 11.2.4 Steep Slope

Consider flows away from a slope break, where streamline curvature effects can be neglected. The flow is gradually varied on a steep slope (Fig. 11.4), given that the variation of  $h$  with  $x$  is small, as confirmed by experiments (Castro-Orgaz and Hager 2009, 2017).

For these flows, it can be assumed that  $h_x^2 \approx h_{xx} \approx 0$ . Further, on the slope, the bed is flat, resulting in  $z_{bx} = 0$ . On this slope, however, the term  $z_{bx}$  is finite. Therefore, despite  $h_x$  will be small, the product  $(h_x \cdot z_{bx})$  remains finite. Therefore, Eqs. (11.19) and (11.21) for gradually varied, 1D potential flow on a finite slope read (Castro-Orgaz and Chanson 2016)

$$H = z_b + h + \frac{q^2}{2gh^2} (1 + z_{bx}^2), \quad (11.37)$$

$$\frac{p_b}{\gamma} = h - \frac{q^2}{2gh^2} (2z_{bx}h_x). \quad (11.38)$$

Differentiation of Eq. (11.37) produces for supercritical flow on the steep slope (large  $F$ ) the ODE (Castro-Orgaz and Hager 2009)

$$\frac{dh}{dx} = \frac{z_{bx}}{\frac{q^2}{gh^3} (1 + z_{bx}^2)}. \quad (11.39)$$

Inserting Eq. (11.39) into Eq. (11.38), the bottom pressure head is [see Eq. (1.137)]

$$\frac{p_b}{\gamma} = h - \frac{q^2}{2gh^2} (2z_{bx}h_x) = h \left( 1 - \frac{z_{bx}^2}{1 + z_{bx}^2} \right) = \frac{h}{1 + z_{bx}^2}. \quad (11.40)$$

**Fig. 11.4** Transition from a mild to a steep slope (VAW photo)



Equation (11.40) is the bottom pressure head in gradually varied flows on a steep slope, implying non-hydrostatic conditions. This is the value to which 1D computations tend on a slope using Eq. (11.19) (Castro-Orgaz and Hager 2009).

### 11.2.5 Flow over Round-Crested Weir: Numerical Method

On inspecting Eqs. (11.36) and (11.40), it can be appreciated that Matthew's (1991) theory accounts for curvature (weir crest) and slope (chute) effects in non-hydrostatic fluid pressure. The theory has the advantage that it is mathematically elaborated. Thus, the salient results are rigorous statements, without the need of artificial tuning of the final equations, based on ad hoc assumptions. A numerical method to solve Eq. (11.19) is considered in this section for the flow over a round-crested weir. The method will be presented taking as test case transcritical flow over a bell-shaped hump prescribed by

$$z_b = a \exp \left[ -b \left( \frac{x}{L} \right)^2 \right]. \quad (11.41)$$

Here,  $a$  is the maximum weir elevation,  $b$  a coefficient, and  $L$  a horizontal length scale. The hump experimentally tested by Sivakumaran et al. (1983) was designed for  $a = 0.2$  m,  $b = 0.5$ , and  $L = 0.24$  m. The computational domain is discretized using a finite-difference mesh divided in  $N$  nodes separated by  $\Delta x$  (Fig. 11.5). For a given flow rate  $q$  and known boundary flow depths  $h(i=1)$  and  $h(i=N)$ , Eq. (11.19) is a second-order ODE to be solved for the computational nodes  $i = 2, 3, \dots, N-1$ . Further, the constant  $H$  must be evaluated prior to any numerical

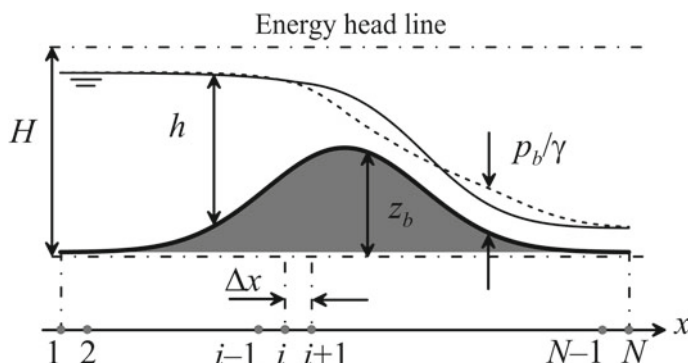


**Fig. 11.5** Finite-difference model for the solution of the steady Serre-Green-Naghdi equations [adapted from Castro-Orgaz and Cantero-Chinchilla (2019)]

solution. The nodes  $i = 1$  and  $i = N$  are located away from the hump in zones where the streamlines are parallel and the pressure is hydrostatic. Therefore,  $H$  is estimated from

$$H \approx h_1 + \frac{q^2}{2gh_1^2}. \quad (11.42)$$

However, neither  $h(i = 1)$  nor  $h(i = N)$  is known in advance for weir flow. For a transition from upstream subcritical to downstream supercritical flow, these flow depths are the alternate depths corresponding to the total head  $H$ . For a numerical solution, an iterative strategy is necessary. Equation (11.19) can be solved numerically using a shooting method transforming it into a pair of ODEs. Starting with a guessed value of  $h_1$  and setting  $dh/dx = 0$  there, given that the streamlines are parallel at the inflow section (Castro-Orgaz and Hager 2017), the flow profile is explicitly computed based on the results at the previous computational section. Once  $h_1$  is assumed, the corresponding value of  $H$  is determined by Eq. (11.42). Using a Runge–Kutta solver, the system of two ODEs is integrated along the computational domain from  $i = 1$  up to  $i = N$ , with the flow depth there determined as the final result of the numerical integration. This value of the flow depth is compared to the supercritical alternate depth of  $h_1$ , and, if they do not match within a prescribed tolerance, then  $h_1$  and thus also  $H$  are both in error; the value of  $h_1$  must be therefore corrected. This method of attack for transcritical flow over a round-crested weir was first discussed by Naghdi and Vongsarnpigoon (1986), who numerically solved Eq. (11.19) for the weir experiments of Sivakumaran et al. (1983). They found that if the value of  $h_1$  is too low, the flow profile intersects the bed profile elsewhere ( $h = 0$  at this point), and computations are thus aborted before reaching the end section. If the head is too large, an undular jump is formed at the tailwater portion of the weir. The value of  $h_1$  can be iterated, but a high precision is needed to obtain the correct physical solution. This was later discussed by Fenton (1996) and Castro-Orgaz and Hager (2017). Castro-Orgaz and Hager (2013) demonstrated that a physically correct solution for transcritical weir flow follows with this shooting technique.

An alternative method of solution is to treat Eq. (11.19) as a boundary value problem directly, discretizing the equations using finite-differences and solving the implicit system of equations iteratively. The first solution of a steady Boussinesq-type equation using an implicit finite-difference method was elaborated by Hosoda and Tada (1994) to compute the undular jump profile. For the specific case of transcritical flow over a weir, Zhu (1996) and Zhu and Lawrence (1998) solved Eq. (11.19) as a boundary value problem using a collocation method, finding excellent agreement between the numerical solution and the data of Sivakumaran et al. (1983). Onda and Hosoda (2004) solved Eq. (11.15) for flow over curved bed forms, but added terms to account for bed friction and turbulence. They used a second-order accurate central finite-difference scheme and solved the resulting equations iteratively with a technique similar to a Newton–Raphson method. Zerihun and Fenton (2006) computed transcritical flows with an implicit finite-difference scheme solved iteratively with a Newton–Raphson iteration assisted by a lower-upper (LU) decomposition of an analytical Jacobian matrix.

Castro-Orgaz and Hager (2009) applied Eq. (11.19) for the transition from a mild to a steep slope using a centered finite-difference scheme fourth-order accurate and solved the resulting implicit system of equations as an optimization problem. Here, a simpler version of the finite-difference method of Castro-Orgaz and Hager (2009) is elaborated. Following Onda and Hosoda (2004), the free surface derivatives of steady Boussinesq-type equations can be discretized using second-order central finite-differences as

$$\frac{dh}{dx} = \frac{h_{i+1} - h_{i-1}}{2\Delta x}, \quad \frac{d^2h}{dx^2} = \frac{h_{i+1} - 2h_i + h_{i-1}}{(\Delta x)^2}. \quad (11.43)$$

Inserting Eq. (11.43) into Eq. (11.19) yields the algebraic equation at node  $i$  as

$$H_i = (z_b)_i + h_i + \frac{q^2}{2gh_i^2} \left[ 1 + \frac{2h_i}{3(\Delta x)^2} (h_{i+1} - 2h_i + h_{i-1}) - \frac{(h_{i+1} - h_{i-1})^2}{12(\Delta x)^2} \right. \\ \left. + h_i(z_{bx})_i + (z_{bx}^2)_i \right]. \quad (11.44)$$

If the discrete flow depths  $h_{i-1}$ ,  $h_i$ , and  $h_{i+1}$  are an accurate representation of the true flow solution at these nodes, then the estimated head at node  $H_i$  can be considered to equal  $H$ , within a prescribed tolerance. Thus

$$H - H_i = f_i(h_{i+1}, h_i, h_{i-1}) \leq \varepsilon H. \quad (11.45)$$

Here,  $\varepsilon$  is the tolerance, typically set to  $10^{-6}$ . In this event, the problem is finished and there is no need to iterate the flow depths at the finite-difference nodes. However, the initially assumed distribution of flow depths at the nodes of the mesh is in general not accurate enough, and there is a need of iterative solutions. Thus, at each node  $i$ , the error  $e_i$  generated by the assumed solution is

$$e_i = H - H_i > \varepsilon H. \quad (11.46)$$

Now the correction strategy is elaborated. Let  $k$  be the iteration index, then the variation of the error at node  $i$  between two consecutive iterations can be expressed using a truncated Taylor series as

$$de_i = e_i^{k+1} - e_i^k = \left( \frac{\partial e_i}{\partial h_{i-1}} \right) dh_{i-1} + \left( \frac{\partial e_i}{\partial h_i} \right) dh_i + \left( \frac{\partial e_i}{\partial h_{i+1}} \right) dh_{i+1}. \quad (11.47)$$

We seek setting to zero the error after the current iteration, that is,  $e_i^{k+1} \equiv 0$ . Thus, Eq. (11.47) for the  $N - 2$  computational nodes is written in matrix form with  $\mathbf{J}$  as the Jacobian matrix as

$$-\mathbf{e}^k = \mathbf{J}^k \mathbf{d}\mathbf{h}. \quad (11.48)$$

Thanks to the second-order differences used [Eq. (11.43)] to discretize the steady Boussinesq-type equation [Eq. (11.19)], the structure of the linear system (11.48) is tridiagonal, and the vector of corrections  $\mathbf{d}\mathbf{h}$  can be efficiently determined using the Thomas algorithm (Hoffman 2001). Once this task is accomplished, the new estimation of the flow depths is given by

$$\mathbf{h}^{k+1} = \mathbf{h}^k + \mathbf{d}\mathbf{h}. \quad (11.49)$$

The non-zero elements of the Jacobian matrix  $\mathbf{J}$  are given analytically as

$$\begin{aligned} \frac{\partial e_i}{\partial h_i} = & - \left\{ 1 - \frac{q^2}{gh_i^3} \left[ 1 + \frac{2h_i}{3(\Delta x)^2} (h_{i+1} - 2h_i + h_{i-1}) - \frac{(h_{i+1} - h_{i-1})^2}{12(\Delta x)^2} + h_i(z_{bx})_i + (z_{bx}^2)_i \right] \right. \\ & \left. + \frac{q^2}{2gh_i^2} \left[ \frac{2}{3(\Delta x)^2} (h_{i+1} - 2h_i + h_{i-1}) - \frac{4h_i}{3(\Delta x)^2} + (z_{bx})_i \right] \right\}, \end{aligned} \quad (11.50)$$

$$\frac{\partial e_i}{\partial h_{i-1}} = - \frac{q^2}{2gh_i^2} \left[ \frac{2h_i}{3(\Delta x)^2} + \frac{(h_{i+1} - h_{i-1})}{6(\Delta x)^2} \right], \quad (11.51)$$

$$\frac{\partial e_i}{\partial h_{i+1}} = - \frac{q^2}{2gh_i^2} \left[ \frac{2h_i}{3(\Delta x)^2} - \frac{(h_{i+1} - h_{i-1})}{6(\Delta x)^2} \right]. \quad (11.52)$$

A reasonable initial solution must be implemented in the Newton–Raphson scheme to obtain a convergent solution. Computation of the transcritical flow profile over the weir using the hydrostatic version of Eq. (11.19) for the actual discharge  $q$ , namely

$$H = z_b + h + \frac{q^2}{2gh^2}, \quad (11.53)$$

yields an estimation of flow depths in the subcritical flow portion, which are too far away from the Boussinesq solution for some tests, however. This produces divergent numerical computations.

A different strategy was therefore adopted based on Eq. (11.53). The assumed flow depth  $h_1$  was used to estimate the head as  $H = h_1$ ; the specific energy at the weir crest is then  $E_{\min} = h_1 - a$ . The hydrostatic discharge compatible with this minimum specific energy is (Chanson 2004)

$$q_o = \left(\frac{2}{3}\right)^{3/2} (gE_{\min}^3)^{1/2}. \quad (11.54)$$

The two positive solutions of Eq. (11.53) are (Chanson 2004)

$$h = (H - z_b) \left[ \frac{1}{3} + \frac{2}{3} \cos\left(\frac{\Gamma}{3}\right) \right] \quad (11.55)$$

for subcritical flow, and

$$h = (H - z_b) \left[ \frac{1}{3} + \frac{2}{3} \cos\left(\frac{\Gamma}{3} + \frac{4\pi}{3}\right) \right] \quad (11.56)$$

for supercritical flow, where

$$\cos \Gamma = 1 - \frac{27}{4} \left( \frac{H - z_b}{h_c} \right)^{-3}, \quad (11.57)$$

with  $h_c = (q_o^2/g)^{1/3}$ . The transcritical hydrostatic flow profile computed for  $q_o$  was found to produce a reasonable initial estimate of the flow depths at the finite-difference nodes. Once the free surface profile is accurately predicted with Eq. (11.19), the result must be analyzed. If a train of standing waves is formed upstream from the weir, this points at an incorrect estimate of  $H$ . It basically indicates that the corresponding value of the discharge coefficient  $C_d$  is incorrect, with

$$C_d = \frac{q}{\left[g(H - a)^3\right]^{1/2}}. \quad (11.58)$$

For transcritical weir flow, the flow passes from upstream subcritical to downstream supercritical flow without appreciable waves on the flow profile. The relation between  $q$  and  $H$  is unique, and the value of  $C_d$  is therefore fixed. However, for a given  $q$ , other flow profiles with upstream waves are mathematically possible from Eq. (11.19) for different values of  $H$ . These are not physical solutions to the weir flow problem, however. This phenomenon is described by Zhu (1996), who also found upstream trains of standing waves while solving Eq. (11.19) as a boundary value problem using a collocation method. The head  $H$  (or  $h_1$ ) must be iterated until the upstream waves are suppressed.

The process of numerical solution is as follows:

1. Given the discharge  $q$ , a value of  $h_1$  is assumed, and  $H$  is then computed using Eq. (11.42).
2. The value of  $h_N$  is the supercritical alternate depth of  $h_1$ .

3. The flow depths  $h_1$  and  $h_N$  are set as boundary conditions.
4. An initial free surface profile is determined for the computational nodes  $h_2, h_3, \dots, h_{N-1}$  using Eqs. (11.54)–(11.57).
5. The error  $e_i$  at each computational node is determined from Eqs. (11.44) and (11.46).
6. The Jacobian matrix is formed using Eqs. (11.50)–(11.52).
7. The linear system of Eq. (11.48) is solved using the Thomas algorithm, resulting in the vector of corrections at each node, with

$$\mathbf{dh} = \begin{pmatrix} dh_2 \\ dh_3 \\ \vdots \\ dh_{N-1} \end{pmatrix} = \begin{pmatrix} h_2^{k+1} - h_2^k \\ h_3^{k+1} - h_3^k \\ \vdots \\ h_{N-1}^{k+1} - h_{N-1}^k \end{pmatrix}. \quad (11.59)$$

8. The updated values of  $\mathbf{h}$  are computed using Eq. (11.49).
9. The error  $e_i$  at each computational node is determined from Eqs. (11.44) and (11.46). If the maximum error is not within a prescribe tolerance  $\varepsilon H$ , then go back to step 6 for an improved estimation of  $\mathbf{h}$ .
10. Once the free surface profile converges, if a train of standing waves is formed at the upstream weir side, the flow depth  $h_1$  must be iterated to produce the correct discharge coefficient  $C_d$  of weir flow, which is reached when these waves are suppressed (Zhu 1996).

The numerical model described is implemented in a code available on the file “*Matthew\_SVK\_Implicit.xls*,” in Chap. 12. The selection of a reasonable value of  $h_1$  to start the cycle can be done by resorting to equations available in the literature, e.g., using the result of a third-order Boussinesq equation (Matthew 1991)

$$C_d = \left(\frac{2}{3}\right)^{3/2} \left[ 1 + \frac{22E}{81R} - 0.045 \left(\frac{E}{R}\right)^2 \right], \quad (11.60)$$

where  $E = H - a$ . For the Gaussian hump,  $d^2z_b/dx^2 = -2ab/L^2$  at the crest. If the assumed head is too far from its correct value, the numerical solution may diverge while updating  $\mathbf{h}$ . This was avoided using a relaxation factor of 0.25 in the Newton–Raphson algorithm.

Figure 11.6 displays the experimental data of Sivakumaran et al. (1983) for a symmetrical hump of shape  $z_b = 0.2 \exp[-0.5(x/0.24)^2]$  (m). The unit discharge is  $0.11197 \text{ m}^2/\text{s}$ . The up- and downstream boundary sections are located at

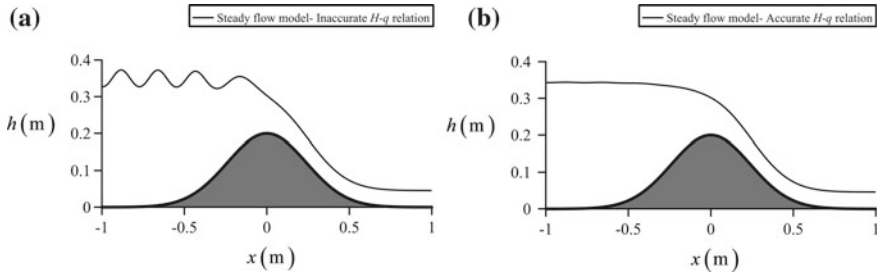


**Fig. 11.6** Iteration of upstream flow depth in transcritical non-hydrostatic flow over a weir **a** RUN 1, **b** RUN 2 (see Table 11.1) [adapted from Castro-Orgaz and Cantero-Chinchilla (2019)]

$x = \pm 1.5$  m. Equation (11.19) was numerically solved with the implicit finite-difference method described above using  $\Delta x = 0.05$  m. A first computation was conducted assuming  $h_1 = 0.35$  m, and the corresponding free surface profile and discharge coefficient are reported in Fig. 11.6a and Table 11.1 as RUN1, respectively. Note that this arbitrary  $h_1$  value, though close to experiments, produces an unacceptable variation of  $C_d$ , with the corresponding train of upstream waves (Fig. 11.6a). For RUN 2, the value of  $h_1$  after some iterations is given in Table 11.1, resulting in a smooth free surface profile (Fig. 11.6b). The predicted  $C_d$  value is now very close to the experimental value.

Once the final free surface profile is determined, the bottom pressure head is estimated from the finite-difference version of Eq. (11.21) as

$$\left( \frac{p_b}{\rho g} \right)_i = h_i + \frac{q^2}{2gh_i^2} \left[ 2h_i(z_{bx})_i + \frac{h_i}{(\Delta x)^2} (h_{i+1} - 2h_i + h_{i-1}) - \frac{(h_{i+1} - h_{i-1})^2}{4(\Delta x)^2} - (z_{bx})_i \frac{(h_{i+1} - h_{i-1})}{\Delta x} \right]. \quad (11.61)$$

The computed water surface and bottom pressure profiles are compared in Fig. 11.7 with the corresponding test data (Sivakumaran 1981; Sivakumaran et al. 1983), resulting in excellent agreement.

**Table 11.1** Iteration of  $C_d$  in weir flow ( $q = 0.11197 \text{ m}^2/\text{s}$ )

	$h_1$ (m)	$H$ (m)	$C_d$	Variation $C_d$ (%)
RUN 1	0.35	0.35521	0.584602	-5.8
RUN 2	0.343447	0.348865	0.622411	+0.29
Experiments	0.3437	0.349154	0.620603	-

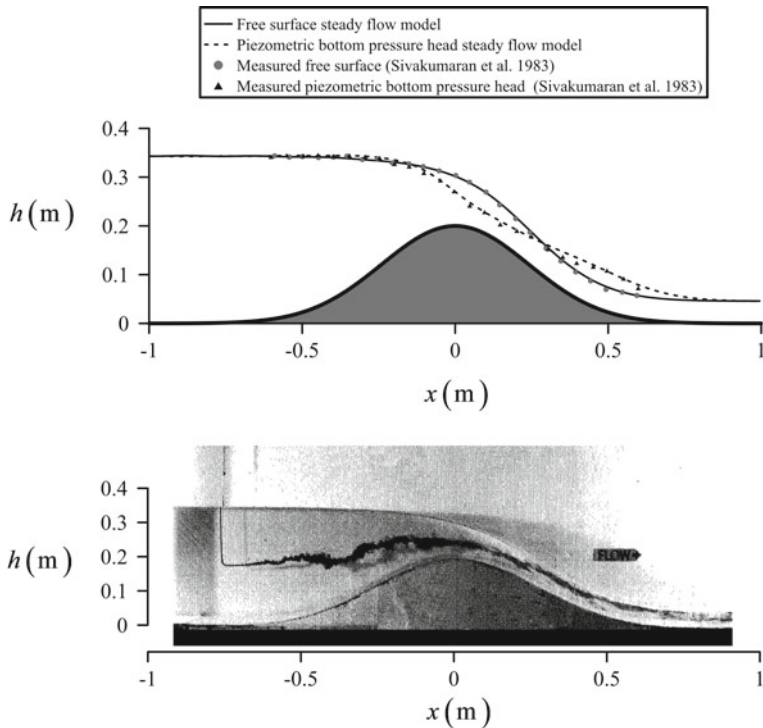
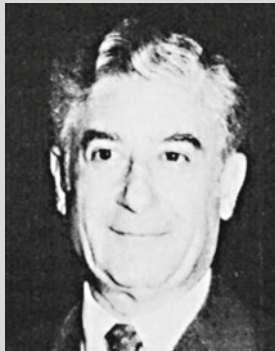


**Fig. 11.7** Comparison of computed and measured (Sivakumaran 1981; Sivakumaran et al. 1983) free surface and piezometric bottom pressure head in transcritical flow over a weir; a scaled photo from experiments (Sivakumaran 1981) is also shown



Paul Mansour **Naghdi** was born on March 29, 1924, in Tehran, Iran, and passed away on July 9, 1994, aged 70 years at Berkeley CA, USA, having been naturalized there in 1948. He made studies at the University of Michigan, Ann Arbor MI, receiving the PhD degree in 1951. He was there assistant until 1958, then associate and full professor. He moved to the University of California, Berkeley CA, as a professor of engineering science, chairing from 1964 to 1969 its Department of Applied Mechanics. He was a member of the National Academy of Engineering NAE, the American Society of Mechanical Engineers ASME, and ASME Fellow from 1969. He was the 1958 Guggenheim Fellow, recipient of the Timoshenko Medal in 1980, and was awarded ASME Honorary Membership in 1983.

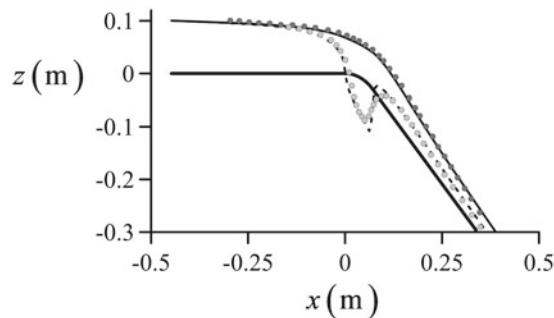
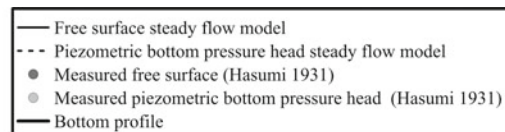
Naghdi's work on continuum mechanics extended over forty years including most aspects of the mechanical behavior of solids and fluids. He was strongly attracted by fundamental questions and always sought to treat these at the highest level of generality. He is known for his works in the areas of shell theory and plasticity, but also in viscoelasticity, fluid sheets and jets, continuum thermodynamics, and the mixture theory. His talents as a teacher were legendary. At Berkeley, he continually refined a magnificent series of courses on theoretical mechanics. These were well prepared, clearly delivered, original, and intellectually provocative. They also reflected his deep understanding of the history of mechanics and his encyclopedic knowledge of literature.

### 11.2.6 Transition from Mild to Steep Slope

Transitional flows from mild to steep bottom slopes (Fig. 11.4) involve a continuous free surface profile and a significant departure of the bottom piezometric pressure profile from the free surface (Montes 1994; Castro-Orgaz and Hager 2009).

The numerical model developed in the previous section was applied to the experimental data of Hasumi (1931) for a slope transition composed of a horizontal reach followed by a circular-shaped transition profile of  $R = 0.1$  m that finishes in a steep slope reach of  $45^\circ$  inclination. The unit discharge is  $0.0995 \text{ m}^2/\text{s}$ . The up- and downstream boundary sections were located away from the slope break using  $\Delta x = 0.005$  m and 180 nodes to model the flow. The upstream boundary flow depth was taken as the critical depth for hydrostatic flow  $h_c = (q^2/g)^{1/3}$ , resulting in the total head of the potential flow problem of  $H = 3h_c/2$ . At the downstream boundary section, the supercritical non-hydrostatic flow depth for streamlines nearly parallel to the bed was estimated to  $h_d = [(1 + S_o^2) \cdot q^2/(2gE)]^{1/2}$ , where  $E$  is the specific energy at the downstream section and  $S_o = 1$  is the chute slope for this test (Castro-Orgaz and Hager 2009). The success in the iteration process depends upon the selection of a plausible initial flow profile. In this test case, the initial flow profile was taken as a rough linear interpolation between the critical depth and the brink flow depth  $h_b = 0.7h_c$  along the horizontal reach, and between  $h_b$  and  $h_d$  along the chute portion. The code for this test is available on the file *Matthew\_slopebreak.xls*, in Chap. 12. The bed profile derivatives were obtained using second-order central finite-differences. The computed water surface and bed pressure profiles are compared in Fig. 11.8 with the experimental data, resulting in a good agreement. Note the computed pressure peak near the end of the transition circle, which is in disagreement with the experiments, resulting from the downstream bed curvature discontinuity. This computational effect can be removed by substituting the real bed profile by an approximate transition curve with a smooth curvature variation (Castro-Orgaz and Hager 2009). However, this task is not accomplished here, given that the emphasis is on the computational process rather than on improving the simulation results.

**Fig. 11.8** Comparison of computed and measured free surface and piezometric bottom head in transition from mild to steep slope



### 11.2.7 Flow over Trapezoidal Profiled Weir

Zerihun (2004) conducted steady non-hydrostatic flow tests for transcritical flow over trapezoidal profiled weirs. The steady numerical model was applied to a trapezoidal weir of up- and downstream slopes 2:1 (H:V) and crest width and height both of 0.15 m. The unit discharge is  $0.06128 \text{ m}^2/\text{s}$ . The up- and downstream boundary sections were located away from the weir using  $\Delta x = 0.01 \text{ m}$  and 300 nodes. The upstream boundary flow depth  $h_1$  was determined by iteration until the upstream undulations in the approach flow were significantly suppressed. At the downstream boundary section, the supercritical alternate depth of the upstream depth was settled in the mathematical model. For the initial free surface profile, linear variations along the weir involving the inflow depth, critical depth, brink depth, supercritical depth at the toe of the weir, and the tailwater flow depth were assumed. The code for this test is available on the file *Matthew\_embankmentweir.xls*, in Chap. 12. The bed profile derivatives were obtained using second-order central finite-differences. The computed water surface and bed pressure profiles after the iteration of  $h_1$  are compared in Fig. 11.9a with the experimental data (Zerihun 2004), resulting in a good agreement. The pressure peaks at the slope discontinuities can be removed using transition curves (Zerihun 2004), but this task is not accomplished here.

A simulation for the same weir for  $q = 0.07102 \text{ m}^2/\text{s}$  using  $\Delta x = 0.005 \text{ m}$  is presented in Fig. 11.9b, showing again a good match with experimental observations. Lesleighter et al. (2008) simulated this weir test with CFD solving the Reynolds-Averaged Navier–Stokes equations, and their results for the bottom pressure head are presented in Fig. 11.9c. Note that the experimental data of Zerihun (2004) did not reveal pressure peaks at the bed-slope breaks, but CFD simulations highlight those peaks, although they are of smaller magnitude than predicted by the 1D model. It is impossible to know the experimental magnitude of these peaks, given that no pressure taps were installed at these positions (Zerihun 2004). However, the physical model experiments conducted by Lesleighter et al. (2008) on trapezoidally profiled spillways reveal pressure peaks at slope breaks.

## 11.3 Unsteady Ideal Fluid Flow

### 11.3.1 Two-Dimensional Serre Equations

Important problems like the propagation of undular, transcritical waves over topography (Fig. 11.10) require a generalization of the results to unsteady 2D flows (Nadiga et al. 1996). The mathematical procedure to generate 2D non-hydrostatic equations consists in vertically integrating the governing equations at an arbitrary horizontal  $(x, y)$ -position from  $z_b$  to  $z_s$ , where subscripts  $b$  and  $s$ , respectively, refer to the bed and the free surface (Fig. 11.10), apply Leibniz's rule, and impose the

**Fig. 11.9** Comparison of computed and measured (Zerihun 2004) free surfaces and bottom pressure heads under transcritical flow over a trapezoidal weir for **a**  $q = 0.06128 \text{ m}^2/\text{s}$ , **b**, **c**  $q = 0.07102 \text{ m}^2/\text{s}$

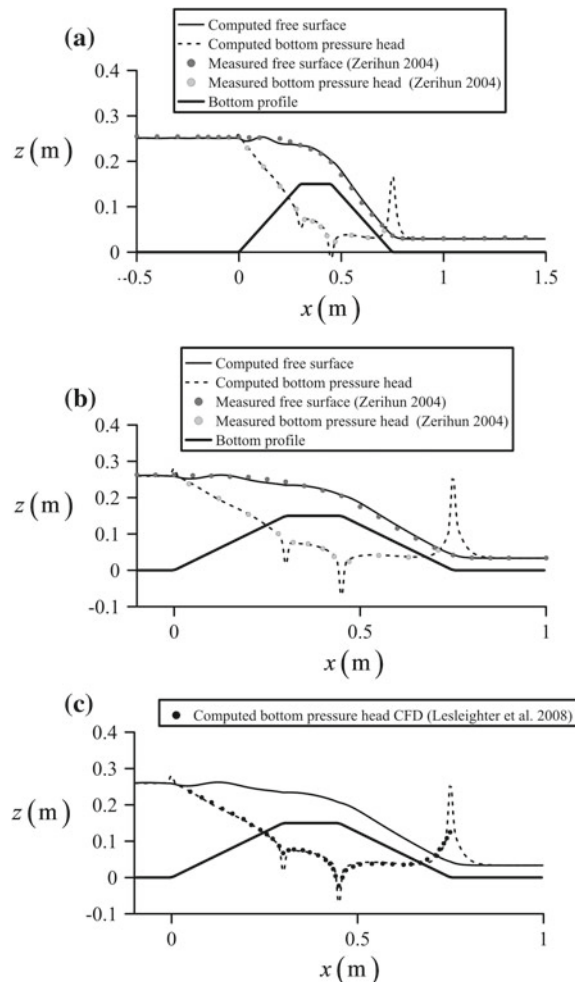
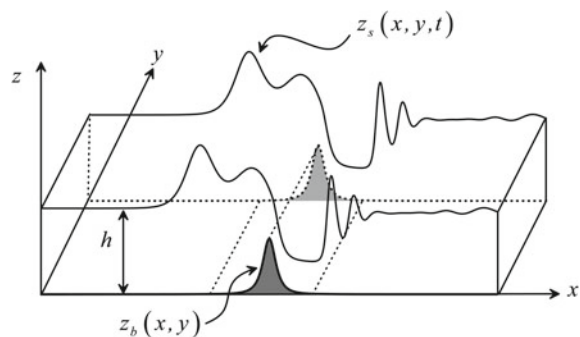


**Fig. 11.10** Undular waves over an obstacle



kinematic and dynamic boundary conditions (Castro-Orgaz et al. 2015; Castro-Orgaz and Hager 2017). For the continuity equation of clear water flow with vanishing entrainment or deposition from above and below, this process yields the exact result

$$\frac{\partial h}{\partial t} + \text{Div}(\mathbf{u}h) = 0. \quad (11.62)$$

Here,  $\mathbf{u} = (U, V)$  is the depth-averaged velocity vector with  $U$  and  $V$  as depth-averaged velocities in the  $x$ - and  $y$ -directions, respectively,  $\text{Div}() = \partial()/\partial x + \partial()/\partial y$  the two-dimensional horizontal divergence operator, and  $h$  the flow depth. The general depth-integrated momentum equations in the  $(x, y, z)$  directions are given by Castro-Orgaz et al. (2015) and Castro-Orgaz and Hager (2017). Following Serre (1953), the  $(u, v)$  velocity components in the horizontal  $(x, y)$  directions are approximated by their depth-averaged values, that is,

$$u(x, y, z, t) \approx U(x, y, t) = \frac{1}{h} \int_{z_b}^{z_s} u dz, \quad v(x, y, z, t) \approx V(x, y, t) = \frac{1}{h} \int_{z_b}^{z_s} v dz. \quad (11.63)$$

The vertical velocity is then approximately computed by integrating the continuity equation in the vertical direction, resulting in (Castro-Orgaz et al. 2015)

$$\begin{aligned} w(x, y, z, t) &= -\frac{\partial}{\partial x}[U(z - z_b)] - \frac{\partial}{\partial y}[V(z - z_b)] = -\text{Div}[\mathbf{u}(z - z_b)] \\ &= w_b - \eta(\text{Div}\mathbf{u}), \quad w_b = U \frac{\partial z_b}{\partial x} + V \frac{\partial z_b}{\partial y} = \mathbf{u} \cdot \text{Grad}(z_b), \end{aligned} \quad (11.64)$$

where  $\eta = z - z_b$  and  $w_b$  is the vertical velocity at the bed. Within this level of mathematical approximation, boundary layers are neglected, and a slip velocity at the bed is accepted for depth-averaged modeling purposes. If we replace  $u$  and  $v$  everywhere by  $U$  and  $V$  in the general depth-integrated  $(x, y)$  momentum equations of Castro-Orgaz and Hager (2017), and turbulence stresses are neglected, then the resulting inviscid equations can be expressed as a system of partial differential equations in general conservative form as (Castro-Orgaz and Hager 2017) [see Eqs. (1.24), (1.35) and (1.36)]

$$\begin{aligned} \frac{\partial \mathbf{U}}{\partial t} + \frac{\partial \mathbf{F}}{\partial x} + \frac{\partial \mathbf{G}}{\partial y} &= \mathbf{S}, \\ \mathbf{U} = \begin{pmatrix} h \\ Uh \\ Vh \end{pmatrix}, \quad \mathbf{F} = \begin{pmatrix} Uh \\ U^2 h + \frac{1}{\rho} \int_{z_b}^{z_s} p dz \\ UVh \end{pmatrix}, \quad \mathbf{G} = \begin{pmatrix} Vh \\ VUh \\ V^2 h + \frac{1}{\rho} \int_{z_b}^{z_s} p dz \end{pmatrix}, \quad \mathbf{S} = -\frac{1}{\rho} \begin{pmatrix} 0 \\ p_b \frac{\partial z_b}{\partial x} \\ p_b \frac{\partial z_b}{\partial y} \end{pmatrix}. \end{aligned} \quad (11.65)$$

In these equations,  $\mathbf{U}$  is the dependent variable vector,  $\mathbf{F}$  and  $\mathbf{G}$  are the fluxes in the  $x$ - and  $y$ -directions for non-hydrostatic pressure conditions, respectively, and  $\mathbf{S}$  is the source term. The pressure distribution  $p(z)$  is needed for model closure. The vertical pressure distribution for depth-independent horizontal velocity components and inviscid flow is given by (Castro-Orgaz et al. 2015) [see Eq. (1.60)]

$$\begin{aligned} p(x, y, z, t) &= \rho g(h - \eta) + \rho \frac{\partial}{\partial t} \int_z^{z_s} w dz + \rho \frac{\partial}{\partial x} \left[ U \int_z^{z_s} w dz \right] + \rho \frac{\partial}{\partial y} \left[ V \int_z^{z_s} w dz \right] - \rho w^2 \\ &= \rho g(h - \eta) + \rho \frac{\partial I}{\partial t} + \rho \text{Div}(I\mathbf{u}) - \rho w^2. \end{aligned} \quad (11.66)$$

The auxiliary variable  $I$  is determined using Eq. (11.64) as

$$\begin{aligned} I &= \int_z^{z_s} w(x, y, z) dz = - \int_z^{z_s} \text{Div}[\mathbf{u}(z - z_b)] dz = -\text{Div} \left( \mathbf{u} \int_z^{z_s} (z - z_b) dz \right) + \mathbf{u} h \cdot \text{Grad}(h + z_b) \\ &= -\text{Div} \left( \mathbf{u} \frac{h^2 - \eta^2}{2} \right) + \mathbf{u} h \cdot \text{Grad}(h + z_b) \\ &= -\text{Div}(\mathbf{u}) \frac{h^2 - \eta^2}{2} + (h - \eta) \mathbf{u} \cdot \text{Grad}(z_b), \end{aligned} \quad (11.67)$$

where  $\text{Grad}() = \partial() / \partial x + \partial() / \partial y$  is the 2D horizontal gradient operator. Equations (11.66) and (11.67) determine pressure at the vertical position  $z$  whenever the horizontal depth-averaged velocity components  $\mathbf{u} = (U, V)$  are known. The general system of Eqs. (11.65)–(11.67) must be manipulated to produce a form suitable for numerical implementation. Using Eq. (11.67), we may deduce (Castro-Orgaz and Cantero-Chinchilla 2019)

$$\begin{aligned} \text{Div}(I\mathbf{u}) &= \text{Div} \left[ \left\{ -\text{Div}(\mathbf{u}) \frac{h^2 - \eta^2}{2} \right\} \mathbf{u} + \mathbf{u} (h - \eta) \mathbf{u} \cdot \text{Grad}(z_b) \right] \\ &= \underbrace{\text{Div} \left[ \left\{ -\text{Div}(\mathbf{u}) \frac{h^2 - \eta^2}{2} \right\} \mathbf{u} \right]}_A + \underbrace{\text{Div}[\mathbf{u} \cdot \{(h - \eta) \mathbf{u} \cdot \text{Grad}(z_b)\}]}_B. \end{aligned} \quad (11.68)$$

The terms  $A$  and  $B$  are determined after some elementary operations by

$$\begin{aligned} A &= \text{Div} \left[ \left\{ -\text{Div}(\mathbf{u}) \frac{h^2 - \eta^2}{2} \right\} \mathbf{u} \right] = -\frac{h^2 - \eta^2}{2} \mathbf{u} \cdot \text{Grad}[\text{Div}(\mathbf{u})] - [\text{Div}(\mathbf{u})]^2 \frac{h^2 - \eta^2}{2} \\ &\quad - h \text{Div}(\mathbf{u}) \mathbf{u} \cdot \text{Grad}(h) - \eta \text{Div}(\mathbf{u}) \mathbf{u} \cdot \text{Grad}(z_b), \end{aligned} \quad (11.69)$$

and

$$B = \text{Div}[\mathbf{u} \cdot \{(h - \eta)\mathbf{u} \cdot \text{Grad}(z_b)\}] = [\text{Div}(\mathbf{u})\mathbf{u} \cdot \text{Grad}(z_b)](h - \eta) + [\mathbf{u} \cdot \text{Grad}(z_b)]\mathbf{u} \cdot \text{Grad}(h + z_b) + \{\mathbf{u} \cdot \text{Grad}[\mathbf{u} \cdot \text{Grad}(z_b)]\}(h - \eta). \quad (11.70)$$

Further, one gets from Eq. (11.64)

$$w^2 = [w_b - \eta(\text{Div}\mathbf{u})]^2 = [\mathbf{u} \cdot \text{Grad}(z_b)]^2 + [\text{Div}(\mathbf{u})]^2\eta^2 - 2[\mathbf{u} \cdot \text{Grad}(z_b)]\text{Div}(\mathbf{u})\eta, \quad (11.71)$$

and resorting again to Eq. (11.67)

$$\begin{aligned} \frac{\partial I}{\partial t} &= \frac{\partial}{\partial t} \left[ -\text{Div}(\mathbf{u}) \frac{h^2 - \eta^2}{2} \right] + \frac{\partial}{\partial t} [(h - \eta)\mathbf{u} \cdot \text{Grad}(z_b)] \\ &= -\text{Div}\left(\frac{\partial \mathbf{u}}{\partial t}\right) \frac{h^2 - \eta^2}{2} + h^2[\text{Div}(\mathbf{u})]^2 + h\text{Div}(\mathbf{u})\mathbf{u} \cdot \text{Grad}(h) \\ &\quad - \text{Div}(h\mathbf{u})\mathbf{u} \cdot \text{Grad}(z_b) + (h - \eta) \frac{\partial \mathbf{u}}{\partial t} \cdot \text{Grad}(z_b), \end{aligned} \quad (11.72)$$

in which  $\partial h / \partial t$  has been replaced by  $-\text{Div}(\mathbf{u}h)$  via Eq. (11.62). The vertical pressure distribution can now be evaluated from Eq. (11.66) collecting Eqs. (11.68)–(11.72). The result after some manipulation is

$$\begin{aligned} \frac{p}{\rho} &= g(h - \eta) + \underbrace{\left\{ [\text{Div}(\mathbf{u})]^2 - \text{Div}\left(\frac{\partial \mathbf{u}}{\partial t}\right) - \mathbf{u} \cdot \text{Grad}[\text{Div}(\mathbf{u})] \right\}}_{\zeta_1} \frac{h^2 - \eta^2}{2} \\ &\quad + \underbrace{\left\{ \frac{\partial \mathbf{u}}{\partial t} \cdot \text{Grad}(z_b) + \mathbf{u} \cdot \text{Grad}[\mathbf{u} \cdot \text{Grad}(z_b)] \right\}}_{\zeta_2} (h - \eta). \end{aligned} \quad (11.73)$$

For 2D waves propagating over horizontal terrain  $\zeta_2 = 0$  results (Hutter and Castro-Orgaz 2016)

$$\frac{p}{\rho} = g(h - \eta) + \left\{ [\text{Div}(\mathbf{u})]^2 - \text{Div}\left(\frac{\partial \mathbf{u}}{\partial t}\right) - \mathbf{u} \cdot \text{Grad}[\text{Div}(\mathbf{u})] \right\} \frac{h^2 - \eta^2}{2}. \quad (11.74)$$

For 1D waves, it reduces to the original result of Serre (1953)

$$\frac{p}{\rho} = g(h - \eta) + \left\{ \left(\frac{\partial U}{\partial x}\right)^2 - \frac{\partial^2 U}{\partial x \partial t} - U \frac{\partial^2 U}{\partial x^2} \right\} \frac{h^2 - \eta^2}{2}. \quad (11.75)$$

Using Eq. (11.73), the pressure integral is

$$\int_0^h \frac{p}{\rho} d\eta = g \frac{h^2}{2} + \zeta_1 \frac{h^3}{3} + \zeta_2 \frac{h^2}{2}, \quad (11.76)$$

and the bottom pressure becomes

$$\frac{p_b}{\rho} = gh + \zeta_1 h^2 + \zeta_2 h. \quad (11.77)$$

Inserting Eqs. (11.76)–(11.77) into Eqs. (11.65), the general 2D inviscid Serre or fully non-linear Boussinesq equations are obtained. These equations are used to model fully non-linear and weakly dispersive water waves. These results presented here are in agreement with those obtained by Nadiga et al. (1996) using a perturbation method.

### 11.3.2 One-Dimensional Serre Equations

For 1D water waves propagating over arbitrary topography, Eqs. (11.65) and (11.73) read

$$\begin{aligned} \mathbf{U} &= \begin{pmatrix} h \\ Uh \end{pmatrix}, \quad \mathbf{F} = \begin{pmatrix} Uh \\ U^2 h + \frac{1}{2} g h^2 + \frac{1}{3} \zeta_1 h^3 + \frac{1}{2} \zeta_2 h^2 \end{pmatrix}, \quad \mathbf{S} = -\frac{\partial z_b}{\partial x} \begin{pmatrix} 0 \\ gh + \zeta_1 h^2 + \zeta_2 h \end{pmatrix}, \\ \frac{\partial \mathbf{U}}{\partial t} + \frac{\partial \mathbf{F}}{\partial x} &= \mathbf{S}, \end{aligned} \quad (11.78)$$

where the 1D non-hydrostatic coefficients are

$$\begin{aligned} \zeta_1 &= \left( \frac{\partial U}{\partial x} \right)^2 - \frac{\partial^2 U}{\partial x \partial t} - U \frac{\partial^2 U}{\partial x^2}, \\ \zeta_2 &= \frac{\partial U}{\partial t} \frac{\partial z_b}{\partial x} + U^2 \frac{\partial^2 z_b}{\partial x^2} + U \frac{\partial U}{\partial x} \frac{\partial z_b}{\partial x}. \end{aligned} \quad (11.79)$$

Serre (1953) derived 1D equations for turbulent, weakly dispersive, fully non-linear water waves over nearly horizontal and flat topography. The same system was obtained by Su and Gardner (1969) for a horizontal bed applying the irrotational flow assumption and by Green and Naghdi (1976a, b) for 2D flows over arbitrary terrain using the theory of directed fluid sheets. The system is called the *Serre-Green-Naghdi* (SGN) equations in coastal engineering, but in civil and environmental engineering these are referred to as the *Serre* equations or simply *Boussinesq* equations (Soares-Frazão and Zech 2002; Soares-Frazão and Guinot 2008; Mohapatra and Chaudhry 2004; Cantero-Chinchilla et al. 2016). They apply to model a variety of fully non-linear and weakly dispersive wave phenomena, like

**Fig. 11.11** Undular bore in Severn River (courtesy of Mark Humpage; a collection of undular bore photos is available at <https://www.markhumpage.com/Mother-Nature/Severn-Bore/>)



the undular bore (Peregrine 1966, 1967, 1972) (Fig. 11.11). The equations are discussed by Barthelemy (2004), Cienfuegos et al. (2006), Dias and Milewski (2010), and Bonneton et al. (2011) for coastal engineering problems. Equations (11.78)–(11.79), the 1D inviscid Serre equations for weakly dispersive and fully non-linear water waves over topography, were derived and numerically solved by Seabra-Santos et al. (1987). The  $x$ -momentum equation in Eq. (11.78) can be rewritten as

$$\frac{\partial(Uh)}{\partial t} + \frac{\partial M}{\partial x} = -\frac{p_b}{\rho} \frac{\partial z_b}{\partial x}, \quad (11.80)$$

where  $M$  is the momentum function, given by

$$M = U^2 h + \frac{1}{2} g h^2 + \left[ \left( \frac{\partial U}{\partial x} \right)^2 - \frac{\partial^2 U}{\partial x \partial t} - U \frac{\partial^2 U}{\partial x^2} \right] \frac{1}{3} h^3 + \left[ \frac{\partial U}{\partial t} \frac{\partial z_b}{\partial x} + U^2 \frac{\partial^2 z_b}{\partial x^2} + U \frac{\partial U}{\partial x} \frac{\partial z_b}{\partial x} \right] \frac{1}{2} h^2, \quad (11.81)$$

and the bottom pressure is

$$\frac{p_b}{\rho} = gh + \left[ \left( \frac{\partial U}{\partial x} \right)^2 - \frac{\partial^2 U}{\partial x \partial t} - U \frac{\partial^2 U}{\partial x^2} \right] h^2 + \left[ \frac{\partial U}{\partial t} \frac{\partial z_b}{\partial x} + U^2 \frac{\partial^2 z_b}{\partial x^2} + U \frac{\partial U}{\partial x} \frac{\partial z_b}{\partial x} \right] h. \quad (11.82)$$

Note that  $M = gS$ . If unsteadiness is dropped, e.g.,  $\partial() / \partial t$  and  $U = q/h$  is used to transform the  $U$ -derivatives into  $h$ -derivatives, Eqs. (11.81)–(11.82) reduce to

Eqs. (11.22) and (11.21), respectively. This means that the steady version of the SGN equations derived here equals the steady Picard iteration model. The immediate implication is that Eq. (11.19), an extended Bernoulli-type equation, is the integral form of Eq. (11.78) in steady state. It has important applications for water wave flow problems. It is common practice while developing unsteady flow solvers of the SWE to test their ability to converge to steady flow solutions. The convergence to steady transcritical flow over a weir is a common and widely accepted test (see Sect. 9.9.5). This issue was exported to non-hydrostatic Boussinesq-type solvers forcing a version of these models with the dispersive terms deactivated to fight with this test and to demonstrate their convergence to the steady flow solution. However, it is more logic and stringent to test the ability of a non-hydrostatic unsteady flow solver to converge to the correct steady non-hydrostatic flow solution. This opens the path of using Eq. (11.19) as a means to generate “*exact*” steady non-hydrostatic flow solutions and to test the ability of non-hydrostatic solvers of Eq. (11.78) to converge to these solutions. We remark then that the relevance of the steady flow solver of Eq. (11.19) is therefore not only its ability to reveal the role on non-hydrostaticity in weir flow, but also their utility to generate steady flow solutions of the more general unsteady flow system.

For numerical computations, it is desirable to collect in a single vector all the terms with temporal derivatives. This task is accomplished here. Consider the following identity

$$\frac{\partial}{\partial t} \left[ \frac{h^3}{3} \frac{\partial U}{\partial x} \right] = \frac{h^3}{3} \frac{\partial^2 U}{\partial t \partial x} + h^2 \frac{\partial h}{\partial t} \frac{\partial U}{\partial x}, \quad (11.83)$$

that permits to write

$$\begin{aligned} \frac{\partial}{\partial x} \left[ \frac{h^3}{3} \frac{\partial^2 U}{\partial t \partial x} \right] &= \frac{\partial}{\partial x} \left[ \frac{\partial}{\partial t} \left( \frac{h^3}{3} \frac{\partial U}{\partial x} \right) - h^2 \frac{\partial h}{\partial t} \frac{\partial U}{\partial x} \right] \\ &= \frac{\partial^2}{\partial x \partial t} \left[ \frac{h^3}{3} \frac{\partial U}{\partial x} \right] + \frac{\partial}{\partial x} \left[ h^2 \frac{\partial(Uh)}{\partial x} \frac{\partial U}{\partial x} \right]. \end{aligned} \quad (11.84)$$

Using this identity, it is possible to split terms with temporal derivatives. Following the same strategy for the remaining terms with time derivatives in  $M$  and  $p_b$ , the following alternative form of Eq. (11.78) is obtained

$$\begin{aligned} \frac{\partial \mathbf{W}}{\partial t} + \frac{\partial \mathbf{F}}{\partial x} &= \mathbf{S} + \mathbf{S}_d, \\ \mathbf{W} &= \begin{pmatrix} h \\ \sigma \end{pmatrix}, \quad \mathbf{F} = \begin{pmatrix} Uh \\ U^2 h + \frac{1}{2} g h^2 \end{pmatrix}, \\ \mathbf{S} &= -\frac{\partial z_b}{\partial x} \begin{pmatrix} 0 \\ gh \end{pmatrix}, \quad \mathbf{S}_d = -\frac{\partial z_b}{\partial x} \begin{pmatrix} 0 \\ p_1 \end{pmatrix} - \frac{\partial D}{\partial x} \begin{pmatrix} 0 \\ 1 \end{pmatrix}, \end{aligned} \quad (11.85)$$

where

$$\sigma = Uh - \frac{1}{3}h^3 \frac{\partial^2 U}{\partial x^2} - h^2 \frac{\partial U}{\partial x} \frac{\partial h}{\partial x} + Uh \frac{\partial z_b}{\partial x} \left( \frac{\partial z_b}{\partial x} + \frac{\partial h}{\partial x} \right) + \frac{1}{2} Uh^2 \frac{\partial^2 z_b}{\partial x^2}, \quad (11.86)$$

$$D = \left[ \left( \frac{\partial U}{\partial x} \right)^2 - U \frac{\partial^2 U}{\partial x^2} \right] \frac{1}{3} h^3 + \left( U \frac{\partial U}{\partial x} \frac{\partial z_b}{\partial x} + U^2 \frac{\partial^2 z_b}{\partial x^2} \right) \frac{1}{2} h^2 + \frac{\partial(Uh)}{\partial x} \left[ U \frac{\partial z_b}{\partial x} - h \frac{\partial U}{\partial x} \right] h, \quad (11.87)$$

$$p_1 = \left[ \left( \frac{\partial U}{\partial x} \right)^2 - U \frac{\partial^2 U}{\partial x^2} \right] h^2 + \left( U \frac{\partial U}{\partial x} \frac{\partial z_b}{\partial x} + U^2 \frac{\partial^2 z_b}{\partial x^2} \right) h + \frac{\partial(Uh)}{\partial x} \left[ U \frac{\partial z_b}{\partial x} - h \frac{\partial U}{\partial x} \right]. \quad (11.88)$$

Equation (11.86) is a Helmholtz equation for the non-hydrostatic velocity field. In Eq. (11.85), all the time derivatives are collected in a single time-stepping term, and the remaining contributions originating from non-hydrostatic pressure with only spatial derivatives are treated as source term  $\mathbf{S}_d$ . The SWE are obtained from the SGN equations by setting  $\mathbf{S}_d = \mathbf{0}$  and  $\sigma = Uh$ . An alternative to the SGN model is the VAM (vertically averaged and moment equations) model (Khan and Steffler 1996a, b). The accuracy of this system for simulating water waves involving both large amplitudes and high dispersion effects was demonstrated (Cantero-Chinchilla et al. 2018). The SGN equations can be improved to model short waves using the method by Nwogu (1993). This technique is, however, beyond the scope of this chapter.

### 11.3.3 Solitary Wave

Consider waves of permanent form propagating over still water with celerity  $c$ . Using the Galilei transformation  $X = x - ct$  for a wave displacement in the positive  $x$ -direction over a horizontal bed, the Serre–Green–Naghdi equations, Eq. (11.78), take the form (Castro-Orgaz and Hager 2017)

$$-c \frac{\partial h}{\partial X} + \frac{\partial(Uh)}{\partial X} = 0, \quad (11.89)$$

$$-c \frac{\partial(Uh)}{\partial X} + \frac{\partial}{\partial X} \left[ \frac{1}{2} gh^2 + U^2 h + (U_X^2 - UU_{XX} + cU_{XX}) \frac{1}{3} h^3 \right] = 0. \quad (11.90)$$

Integration of Eq. (11.89) yields the progressive discharge  $q$

$$q = (U - c)h = \text{const.} \quad (11.91)$$

Using Eq. (11.91), (11.90) is written in the simplified form

$$-c^2 \frac{\partial h}{\partial X} + \frac{\partial}{\partial X} \left[ \frac{1}{2} gh^2 + U^2 h + (U_X^2 - (U - c)U_{XX}) \frac{1}{3} h^3 \right] = 0. \quad (11.92)$$

The solitary wave is a solution of Eq. (11.92) subject to the boundary conditions  $h \rightarrow h_o$  and  $U \rightarrow 0$  for  $x \rightarrow \pm\infty$ , with  $h_o$  as still water depth. Integrating twice, the final result is with  $F_o = q/(gh_o^3)^{1/2}$  (Serre 1953; Benjamin and Lighthill 1954; Castro-Orgaz and Hager 2017)

$$\frac{h(x, t)}{h_o} = 1 + (F_o^2 - 1) \operatorname{sech}^2 \left[ \frac{(3F_o^2 - 3)^{1/2}}{F_o} \frac{(x - ct)}{2h_o} \right]. \quad (11.93)$$

Using the conditions  $h = h_o$  and  $U = 0$  at  $x \rightarrow \pm\infty$ , the progressive discharge  $q$  verifies the identity

$$q = [U(X) - c]h(X) = -ch_o, \quad (11.94)$$

from which the depth-averaged velocity is

$$U(x, t) = c \left[ 1 - \frac{h_o}{h(x, t)} \right]. \quad (11.95)$$

The maximum flow depth at the solitary wave crest is obtained from Eq. (11.93) at  $x - ct = 0$  as

$$h_{\max} = h_o F_o^2 = h_o \frac{c^2 h_o^2}{g h_o^3} = \frac{c^2}{g}. \quad (11.96)$$

This then yields

$$c = (gh_{\max})^{1/2} = (gh_o)^{1/2} \left( \frac{h_{\max}}{h_o} \right)^{1/2} = (gh_o)^{1/2} \left( 1 + \frac{A}{h_o} \right)^{1/2}, \quad (11.97)$$

where  $A$  is the solitary wave amplitude. Another useful relation is thus

$$F_o^2 = \left( 1 + \frac{A}{h_o} \right). \quad (11.98)$$

For given values of  $h_o$  and  $A$ , the degree of non-linearity of the solitary wave is fixed. The celerity  $c$  and  $F_o$  are thus deduced from Eqs. (11.97)–(11.98), and, resorting to Eqs. (11.93) and (11.95), the functions  $h(x, t)$  and  $U(x, t)$  are fully

determined. This analytical solution is of great utility to check the quality of numerical models to solve Eq. (11.78).



Joseph Valentin **Boussinesq** was born on March 15, 1842, at St. André-de-Sangonis, France, and passed away on February 19, 1929, in Paris. He was self-taught, starting his scientific writing in 1865. He thereby took into consideration during his long career all branches of mathematical physics except for electro-magnetism. After having served as teacher at various colleges of France, he was appointed in 1873 Lecturer at the University of Lille. In 1886, Boussinesq was appointed to the chair of mechanics at the famous Sorbonne University, Paris, taking over in 1896 as professor of mathematical physics at *Collège de France*.

Boussinesq's life work in hydraulics is outstanding but extremely hard to follow, given his complicated writing style. His colleagues Alfred A. Flamant (1839–1915) or Auguste Boulanger (1866–1923) were able to present in their books a more popular approach of Boussinesq's ideas. His 1872 paper explains the observations of solitary waves of John Scott Russell (1808–1882) from a physical perspective thereby overcoming the many attempts offered in the past decades. It was noted that many hydraulic phenomena could only be explained by inclusion of the streamline curvature effects. This paper particularly attracted the interest of Adhémar Barré de Saint-Venant (1797–1886), who in 1871 had published his famous paper on the shallow water equations, yet by assuming hydrostatic pressure and uniform velocity distributions. The monumental 1877 *Essay* of Boussinesq made his name definitely known to the hydraulics community given the large number of relevant problems discussed. In the 1880s, he started in addition a close collaboration with Henry Bazin (1829–1917) on the weir flow features, for which streamline curvature effects again are significant. In hydraulics, this collaboration between the then best experimenter and scientist marked the start of engineering hydraulics, leading to the close relationship between scientists in mathematical physics and hydraulics in the twentieth century. The outstanding merits of Boussinesq were awarded by his nomination to the mechanics chair at Sorbonne, taking over the chair of his intimate colleague de Saint-Venant.

### 11.3.4 MUSCL-Hancock Scheme

The system of Eq. (11.85) is solved here using a finite volume-finite difference method based on the MUSCL-Hancock scheme, a second-order accurate model in space and time (see Sect. 9.7). Boussinesq-type water wave propagation models are solved for coastal engineering applications using fourth-order accurate schemes in space, and third-order accuracy or fourth-order accuracy in time. The reason for imposing such accuracy is that truncation errors originating from the discretization to second-order accuracy of the Saint-Venant type leading terms can induce numerical dispersion. This problem is serious for large-scale simulations using sparse time-space meshes (Wei et al. 1995). However, using a fine mesh in second-order accurate schemes, this effect disappears or is significantly limited. There are good reasons for testing a second-order non-hydrostatic scheme, however: The current knowledge of the finite volume technology for the solution of the SWE is in a state of maturity permitting the development of a large variety of 1D and 2D solvers worldwide. Research groups developed their own codes and verified them extensively. If the inclusion of non-hydrostatic effects into a solver is offered

in a simple way, implying only an improvement of an existing SWE solver, there is a great probability that this development will reach a large echo in the hydraulics community. Driven by this line of thinking, it is then logic to investigate how accurate can be a second-order non-hydrostatic module introduced in a second-order SWE solver. A numerical experiment is conducted here solving the SGN equations with the MUSCL-Hancock scheme originally developed for the SWE. The ability of the model to replicate steady flow over a weir will be investigated, and the aptness of the second-order accuracy of the scheme will be assessed against a third-order in time, fourth-order in space solver with an architecture similar to that used in Boussinesq-type models for ocean research. To solve Eq. (11.85), a splitting approach is used. First, an advection step is tackled discarding  $\mathbf{S}_d$ . For a rectangular control volume in the  $x-t$  plane, the integral form of Eq. (11.85) then reads (Toro 2001)

$$\mathbf{W}_i^{\text{adv}} = \mathbf{W}_i^k - \frac{\Delta t}{\Delta x} (\mathbf{F}_{i+1/2} - \mathbf{F}_{i-1/2}) + \Delta t \mathbf{S}_i. \quad (11.99)$$

Here,  $\Delta t$  and  $\Delta x$  are the step sizes in the  $x$  and  $t$  axes, respectively,  $k$  refers to the time level,  $i$  is the cell index in the  $x$ -direction, and  $\mathbf{F}_{i+1/2}$  is the numerical flux crossing the interface  $i + 1/2$  between cells  $i$  and  $i + 1$ . Note that the advection step as defined here includes the bed-slope source term directly. The topography source term is discretized for a well-balanced scheme as [see Eq. (9.99)]

$$\mathbf{S}_i = -g \left( h \frac{\partial z_b}{\partial x} \right)_i \begin{pmatrix} 0 \\ 1 \end{pmatrix} = -g \cdot \frac{h_{i+1/2} + h_{i-1/2}}{2} \frac{(z_{bi+1/2} - z_{bi-1/2})}{\Delta x} \begin{pmatrix} 0 \\ 1 \end{pmatrix}. \quad (11.100)$$

The solution process starts with the cell-averaged values of conserved variables at time level  $k$ ,  $\mathbf{U}_i^k$ . For second-order space accuracy, a piecewise linear reconstruction is conducted within each cell (Toro 2001). Linear slopes resulting from the reconstructed solution must be limited to avoid spurious oscillations near discontinuities. Let letters  $L$  and  $R$  denote the reconstructed variables at the left and right sides of a cell interface; the resulting values of  $\mathbf{U}$  at each of its sides are with  $\overline{\Delta \mathbf{U}_i}$  and  $\overline{\Delta \mathbf{U}_{i+1}}$  as the limited jumps (Toro 2001) [see Eqs. (9.122)–(9.125)]

$$\mathbf{U}_{i+1/2}^L = \mathbf{U}_i^k + \frac{1}{2} \overline{\Delta \mathbf{U}_i}, \quad \mathbf{U}_{i+1/2}^R = \mathbf{U}_{i+1}^k - \mathbf{U}_i^k - \frac{1}{2} \overline{\Delta \mathbf{U}_{i+1}}. \quad (11.101)$$

The surface gradient method (SGM) (Zhou et al. 2001) is adopted, consisting of the reconstruction of the free surface elevation, instead of the water depth  $h$ . The minmod limiter is used in the tests presented here. In the MUSCL-Hancock method, an evolution of boundary-extrapolated values  $\mathbf{U}_{i+1/2}^L$  and  $\mathbf{U}_{i+1/2}^R$  at interface  $i + 1/2$  over half the time step is conducted to regain second-order accuracy in time. Based on a Taylor series expansion in space and time, interface values are then given by (Toro 2001) [see Eq. (9.134)]

$$\begin{aligned}\bar{\mathbf{U}}_{i+1/2}^L &= \mathbf{U}_{i+1/2}^L - \frac{\Delta t}{2\Delta x} [\mathbf{F}(\mathbf{U}_{i+1/2}^L) - \mathbf{F}(\mathbf{U}_{i-1/2}^R)] + \frac{\Delta t}{2} \mathbf{S}_i, \\ \bar{\mathbf{U}}_{i+1/2}^R &= \mathbf{U}_{i+1/2}^R - \frac{\Delta t}{2\Delta x} [\mathbf{F}(\mathbf{U}_{i+3/2}^L) - \mathbf{F}(\mathbf{U}_{i+1/2}^R)] + \frac{\Delta t}{2} \mathbf{S}_{i+1}.\end{aligned}\quad (11.102)$$

With these evolved boundary-extrapolated variables  $\bar{\mathbf{U}}_{i+1/2}^L$  and  $\bar{\mathbf{U}}_{i+1/2}^R$  defining states  $L$  and  $R$ , the numerical flux is computed using the HLL approximate Riemann solver as (Toro 2001) [see Eq. (9.44)]

$$\mathbf{F}_{i+1/2} = \begin{cases} \mathbf{F}_L & \text{if } S_L \geq 0 \\ \frac{S_R \mathbf{F}_L - S_L \mathbf{F}_R + S_R S_L (\mathbf{U}_R - \mathbf{U}_L)}{S_R - S_L}, & \text{if } S_L \leq 0 \leq S_R. \\ \mathbf{F}_R & \text{if } S_R \leq 0 \end{cases} \quad (11.103)$$

Note that the Riemann problem corresponding to the homogeneous version of Eq. (11.85),  $\partial \mathbf{W}/\partial t + \partial \mathbf{F}/\partial x$ , implies the determination of a numerical flux  $\mathbf{F}_{i+1/2}$  as function of two states  $\mathbf{W}_L$  and  $\mathbf{W}_R$  (Montecinos et al. 2016). However, we rather assume that this numerical flux is determined by the left and right states of vector  $\mathbf{U}$ . While this is incorrect, it is a common practice in phase resolving Boussinesq-type models. Keeping this limitation in mind, the computational results will be critically looked at. Here,  $\mathbf{F}_L$  and  $\mathbf{F}_R$  are the fluxes computed at states  $L$  and  $R$ . Robust wave speed estimates  $S_L$  and  $S_R$  for a wet bed are given by (Toro 2001) [see Eqs. (9.45)–(9.46)]

$$S_L = U_L - c_L \lambda_L, \quad S_R = U_R + c_R \lambda_R, \quad (11.104)$$

where  $c = (gh)^{1/2}$ , and  $\lambda_K (K = L, R)$  is

$$\lambda_K = \begin{cases} \left[ \frac{1}{2} \left( \frac{h_*(h_* + h_K)}{h_K^2} \right) \right]^{1/2} & h_* > h_K \\ 1 & h_* \leq h_K \end{cases}. \quad (11.105)$$

The flow depth at the star region of the Riemann problem at each interface  $h_*$  is (Toro 2001) [see Eq. (9.47)]

$$h_* = \frac{1}{g} \left[ \frac{1}{2} (c_L + c_R) + \frac{1}{4} (U_L - U_R) \right]^2. \quad (11.106)$$

For the dry-bed problem, the celerity of the signals is given by [see Eqs. (9.48)–(9.49)]

$$S_L = U_R - 2c_R \quad (\text{if } h_L = 0), \quad S_R = U_L + 2c_L \quad (\text{if } h_R = 0). \quad (11.107)$$

For stability in time of the explicit scheme, the Courant–Friedrichs–Lowy number  $\text{CFL}$  must be less than unity (Toro 2001). Given the value of  $\text{CFL}$ ,  $\Delta t$  is determined at time level  $k$  from [see Eq. (9.29)]

$$\Delta t = \text{CFL} \left[ \frac{\Delta x}{\max \left| U_i^k + (gh_i^k)^{1/2} \right|} \right]. \quad (11.108)$$

Once the solution of Eq. (11.99) is available, the value obtained for the flow depth is  $h^{k+1}$ ; the auxiliary variable  $\sigma$ , however, must be updated to include the effect of  $\mathbf{S}_d$ . Here, we will use a predictor–corrector finite-difference scheme to incorporate  $\mathbf{S}_d$  in the solution. First, a predictor step is conducted as

$$\sigma_i^p = \sigma_i^{\text{adv}} + \Delta t \left[ -p_1 \frac{\partial z_b}{\partial x} - \frac{\partial D}{\partial x} \right]_i^{\text{adv}}. \quad (11.109)$$

All the spatial derivatives in the non-hydrostatic source term (linked to  $p_1$ ,  $D$ , and its gradient) are approximated using second-order central finite-differences. In general, a derivative is discretized in this work as

$$\left( \frac{\partial^m f}{\partial x^m} \right)_i = \frac{1}{\Delta x^m} \sum_{-k}^{+k} \omega_k f_k, \quad (11.110)$$

where the weights are given in Table 11.2. The only exception is the first derivative of  $U$ , which is discretized in the predictor step using a forward finite-difference as (Mohapatra and Chaudhry 2004)

$$U_x = \frac{U_{i+1} - U_i}{\Delta x}. \quad (11.111)$$

Once  $\sigma_i^p$  is determined, the predicted velocity field must be resolved. This is accomplished by solving an elliptic problem posed by Eq. (11.86). The process is explained below, given that it must be also applied after the correction step.

The corrector step is given by

$$\sigma_i^{k+1} = \sigma_i^{\text{adv}} + \Delta t \left[ -p_1 \frac{\partial z_b}{\partial x} - \frac{\partial D}{\partial x} \right]_i^p, \quad (11.112)$$

**Table 11.2** Weighting factors for discretization of spatial derivatives in non-hydrostatic terms based on Abramowitz and Stegun (1972) and Fornberg (1988)

Type of derivative	Order of derivative	Order of accuracy	Weighting factor $\omega_k$ at nodes				
			$k = -2$	$k = -1$	$k = 0$	$k = +1$	$k = +2$
Centered	1	2	0	-1/2	0	+1/2	0
Centered	1	4	1/12	-2/3	0	2/3	-1/12
Centered	2	2	0	1	-2	1	0
Centered	2	4	-1/12	4/3	-5/2	4/3	-1/12
Upwind	1	1	-	-1	1	-	-
Upwind	1	2	1/2	-2	3/2	-	-

which is adopted as the final step. The first derivative of  $U$  is discretized in the corrector step with a backward finite-difference as (Mohapatra and Chaudhry 2004)

$$U_x = \frac{U_i - U_{i-1}}{\Delta x}. \quad (11.113)$$

Once the values of  $\sigma$  are determined at each finite volume for the new time level, the following elliptic problem is stated at each cell of the computational domain

$$\sigma_i^{k+1} = d_1 U_{i-1}^{k+1} + d_2 U_i^{k+1} + d_3 U_{i+1}^{k+1}, \quad (11.114)$$

which is obtained by discretizing Eq. (11.86) using second-order central finite-differences. Here

$$\begin{aligned} d_1 &= -\frac{h_i^3}{3(\Delta x)^2} + \frac{h_i^2}{4(\Delta x)^2} (h_{i+1} - h_{i-1}), \\ d_2 &= h_i + \frac{2h_i^3}{3(\Delta x)^2} + \alpha, \\ d_3 &= -\frac{h_i^3}{3(\Delta x)^2} - \frac{h_i^2}{4(\Delta x)^2} (h_{i+1} - h_{i-1}), \\ \alpha &= h_i \frac{(z_{bi+1} - z_{bi-1})}{2\Delta x} \left[ \frac{(z_{bi+1} - z_{bi-1})}{2\Delta x} + \frac{(h_{i+1} - h_{i-1})}{2\Delta x} \right] + h_i^2 \frac{(z_{bi+1} - 2z_{bi} + z_{bi-1})}{(\Delta x)^2}. \end{aligned} \quad (11.115)$$

Equation (11.115) produces an algebraic relation containing the unknown velocity values at the new time level for the three surrounding cells  $i - 1$ ,  $i$ , and  $i + 1$ . Equation (11.115) for the cells  $i = 2$  to  $N - 1$  is assembled, producing a tridiagonal system of equations, which is easily solved using the Thomas algorithm (Hoffman 2001). Once the velocity  $U_i^{k+1}$  is determined, the cell-averaged discharge  $q_i^{k+1}$  is evaluated. It is necessary to incorporate two additional cells at the left and right ends of the computational domain, called ghost cells (LeVeque 2002; Toro 2009). Physical boundary conditions are transmitted to the computational model through these cells. Here, the simplest way of implementing boundary conditions is exposed using ghost cells with a zero-order extrapolation from the interior solution. Care should be taken to ensure that spurious waves are not generated when implementing boundary conditions (LeVeque 2002). Here, transmissive boundary conditions are implemented allowing waves to enter and leave the computational domain freely. Mignot and Cienfuegos (2009) incorporated the boundary conditions in a Serre-type model neglecting the dispersive effects at those cells by using the characteristic form of the SWE. Here, we follow the same concept but with a rather different treatment.

Given that dispersive effects will be neglected at cells  $i = 1$  and  $i = N$ , the source term there is  $\mathbf{S}_d = \mathbf{0}$ . In this way, there are no dispersive effects at those cells

influencing the solution at cells  $i = 2$  and  $i = N - 1$  through the discretization of  $\partial D/\partial x$  while solving Eq. (11.85). At the subcritical inflow section, one boundary condition must be prescribed, as known from the method of characteristics (Henderson 1966). The other variable needed at the ghost cell is obtained by extrapolation from the interior solution (LeVeque 2002). This corresponds to the inlet discharge for weir flow. Thus, we implemented in the upstream ghost cell

$$\begin{aligned} q_1^{k+1} &= q_{\text{inlet}}, \\ h_1^{k+1} &= h_2^{k+1}. \end{aligned} \quad (11.116)$$

At the outflow section  $i = N$ , a transmissive boundary condition is implemented to let the waves leave the computational domain as

$$\begin{aligned} q_N^{k+1} &= q_{N-1}^{k+1}, \\ h_N^{k+1} &= h_{N-1}^{k+1}. \end{aligned} \quad (11.117)$$

The process of numerical solution is as follows:

1. A longitudinal finite volume mesh with cell width  $\Delta x$  is defined, and the bed profile function  $z_b(x)$  is used to define the bed elevation at the cell faces. The bed elevation at the cell center is taken as the average of cell faces, consistent with a linear variation of the bed profile within the cell. The bed derivatives for the dispersive terms are evaluated using the computed coordinates at cell centers by second-order central finite-differences.
2. The initial conditions are set. These can be arbitrary provided that they generate the desired transcritical steady flow profile.
3. Boundary conditions are set using Eqs. (11.116)–(11.117).
4. The value of  $\Delta t$  is computed by Eq. (11.108).
5. The MUSCL-Hancock reconstruction is conducted using the vector  $\mathbf{U}$ .
6. With boundary-extrapolated values of  $\mathbf{U}$ , the local Riemann problems formed at cell interfaces are solved with the HLL Riemann solver, resulting in  $\mathbf{F}_{i+1/2}$ .
7. The water depth at time  $h^{k+1}$  is computed from the first component of Eq. (11.99).
8. The bed-slope source term of the momentum equation is determined from Eq. (11.100) using the definitive values of  $h$ .
9. The advection estimation of the conservative variable  $\sigma$  is determined from the second component of Eq. (11.99).
10. A predictor step is conducted to evaluate  $\mathbf{S}_d$ . Equation (11.109) is applied with a second-order estimation of the spatial derivatives.
11. Once  $\sigma_p$  is available at all cells, the tridiagonal system is solved using the Thomas algorithm to obtain the predicted velocities [see Eq. (11.114)].
12. A corrector step is conducted to evaluate  $\mathbf{S}_d$ . Equation (11.112) is applied with a second-order estimation of the spatial derivatives.

13. Once  $\sigma^{k+1}$  is available at all cells, the tridiagonal system is solved using the Thomas algorithm to obtain the final velocities [Eq. (11.114)].
14. If the actual time is equal to the final time, then stop.
15. Go back to step 3 for a new time loop.

### 11.3.5 High-Order Scheme

In this section, a high-resolution scheme in both space and time  $O(\Delta t^3, \Delta x^4)$  is developed to assess the second-order MUSCL-Hancock scheme. For the time stepping, a third-order strong stability preserving (SSP) Runge–Kutta scheme is given by (Gottlieb et al. 2001)

$$\begin{aligned} \mathbf{W}_i^{(1)} &= \mathbf{W}_i^k + L[\mathbf{U}_i^k] \Delta t + (\mathbf{S}_d)_i^{(1)} \Delta t \quad \Rightarrow \mathbf{U}_i^{(1)} = E^{-1} [\mathbf{W}_i^{(1)}], \\ \mathbf{W}_i^{(2)} &= \mathbf{W}_i^{(1)} + L[\mathbf{U}_i^{(1)}] \Delta t + (\mathbf{S}_d)_i^{(2)} \Delta t \quad \Rightarrow \mathbf{U}_i^{(2)} = E^{-1} [\mathbf{W}_i^{(2)}], \\ \mathbf{W}_i^{(3)} &= \frac{3}{4} \mathbf{W}_i^k + \frac{1}{4} \mathbf{W}_i^{(2)} \quad \Rightarrow \mathbf{U}_i^{(3)} = E^{-1} [\mathbf{W}_i^{(3)}], \\ \mathbf{W}_i^{(4)} &= \mathbf{W}_i^{(3)} + L[\mathbf{U}_i^{(3)}] \Delta t + (\mathbf{S}_d)_i^{(4)} \Delta t \quad \Rightarrow \mathbf{U}_i^{(4)} = E^{-1} [\mathbf{W}_i^{(4)}], \\ \mathbf{W}_i^{k+1} &= \frac{1}{3} \mathbf{W}_i^k + \frac{2}{3} \mathbf{W}_i^{(4)} \quad \Rightarrow \mathbf{U}_i^{k+1} = E^{-1} [\mathbf{W}_i^{(k+1)}]. \end{aligned} \quad (11.118)$$

Here,  $E[ ]$  is the elliptic operator linked to Eq. (11.114), and  $L[ ]$  is the finite volume-finite difference spatial operator

$$L[\mathbf{U}_i] = -\frac{1}{\Delta x} (\mathbf{F}_{i+1/2} - \mathbf{F}_{i-1/2}) + \mathbf{S}_i. \quad (11.119)$$

In the space operator  $L()$ ,  $\mathbf{U}$  is reconstructed with fourth-order accuracy, but the elliptic operator  $E()$  is maintained with second-order accuracy to preserve the tridiagonal structure of the linear system of equations determining the non-hydrostatic velocity field.  $\mathbf{S}_d$  must be updated with  $U$  at the corresponding time stage, so iteration is needed. A high-order total variation diminishing monotone upstream centred scheme for conservation laws (MUSCL-TVD-4th) is adopted to reconstruct the solution (Erduran et al. 2005). The local Riemann problem at each cell interface is then determined by the vector  $\mathbf{U}$  at its left ( $L$ ) and right ( $R$ ) sides from

$$\mathbf{U}_{i+1/2}^L = \mathbf{U}_i + \frac{1}{6} \left[ \varphi(r_1) \Delta^* \mathbf{U}_{i-1/2} + 2\varphi\left(\frac{1}{r_1}\right) \Delta^* \mathbf{U}_{i+1/2} \right], \quad (11.120)$$

$$\mathbf{U}_{i+1/2}^R = \mathbf{U}_{i+1} - \frac{1}{6} \left[ 2\varphi(r_2)\Delta^*\mathbf{U}_{i+1/2} + \varphi\left(\frac{1}{r_1}\right)\Delta^*\mathbf{U}_{i+3/2} \right], \quad (11.121)$$

where the operators used are defined by

$$\Delta^*\mathbf{U}_{i+1/2} = \Delta\mathbf{U}_{i+1/2} - \frac{1}{6} (\Delta\bar{\mathbf{U}}_{i+3/2} - 2\Delta\bar{\mathbf{U}}_{i+1/2} + \Delta\bar{\mathbf{U}}_{i-1/2}), \quad (11.122)$$

$$\Delta\bar{\mathbf{U}}_{i-1/2} = \text{minmod}[\Delta\mathbf{U}_{i-1/2}, \Delta\mathbf{U}_{i+1/2}, \Delta\mathbf{U}_{i+3/2}], \quad (11.123)$$

$$\Delta\bar{\mathbf{U}}_{i+1/2} = \text{minmod}[\Delta\mathbf{U}_{i+1/2}, \Delta\mathbf{U}_{i+3/2}, \Delta\mathbf{U}_{i-1/2}], \quad (11.124)$$

$$\Delta\bar{\mathbf{U}}_{i+3/2} = \text{minmod}[\Delta\mathbf{U}_{i+3/2}, \Delta\mathbf{U}_{i-1/2}, \Delta\mathbf{U}_{i+1/2}], \quad (11.125)$$

$$\Delta\mathbf{U}_{i+1/2} = \mathbf{U}_{i+1} - \mathbf{U}_i. \quad (11.126)$$

The minmod function of 3 numbers is given by

$$\text{minmod}[a, b, c] = \text{sign}(a)\max[|a|, 2\text{sign}(a)b, 2\text{sign}(a)c]. \quad (11.127)$$

The van Leer limiting function is used here

$$\varphi(r_i) = \frac{r_i + |r_i|}{1 + |r_i|}, \quad r_1 = \frac{\Delta^*\mathbf{U}_{i+1/2}}{\Delta^*\mathbf{U}_{i-1/2}}, \quad r_2 = \frac{\Delta^*\mathbf{U}_{i+3/2}}{\Delta^*\mathbf{U}_{i+1/2}}. \quad (11.128)$$

The surface gradient method is applied to reconstruct the water surface elevation. Once the reconstruction step is finished, the numerical flux  $\mathbf{F}_{i+1/2}$  is estimated with the HLL approximate Riemann solver. The dispersive source term  $\mathbf{S_d}$  (with the exception of  $U_x$ ) is discretized using fourth-order accurate central finite-differences (Table 11.2) for the cells  $i = 3$  to  $N - 2$ . At the cells  $i = 2$  and  $N - 1$ ,  $\mathbf{S_d}$  is discretized using second-order differences, and dispersive effects are deactivated at the ghost cells  $i = 1$  and  $i = N$  ( $\mathbf{S_d} = \mathbf{0}$ ) to avoid any non-hydrostatic influence transmitted to the cells  $i = 2$  and  $i = N - 1$  through the gradient  $\partial D / \partial x = (D_{i+1} - D_{i-1})/(2\Delta x)$ . The derivative  $U_x$  is computed using upwind differencing of first order at cells  $i = 2$  and  $N - 1$ , and of second order at cells  $i = 3$  to  $N - 2$  (Table 11.2).

The process of numerical solution is as follows:

1. A longitudinal finite volume mesh with cell width  $\Delta x$  is defined and the bed profile function  $z_b(x)$  is used to define the bed elevation at the cell faces. The bed elevation at the cell center is taken as the average of cell faces, consistent with a linear variation of the bed profile within the cell. The bed derivatives for the dispersive terms are evaluated using the computed coordinates at cell centers by second-order central finite-differences at cells  $i = 2$  and  $N - 1$ , and with fourth-order central differences at the other cells.

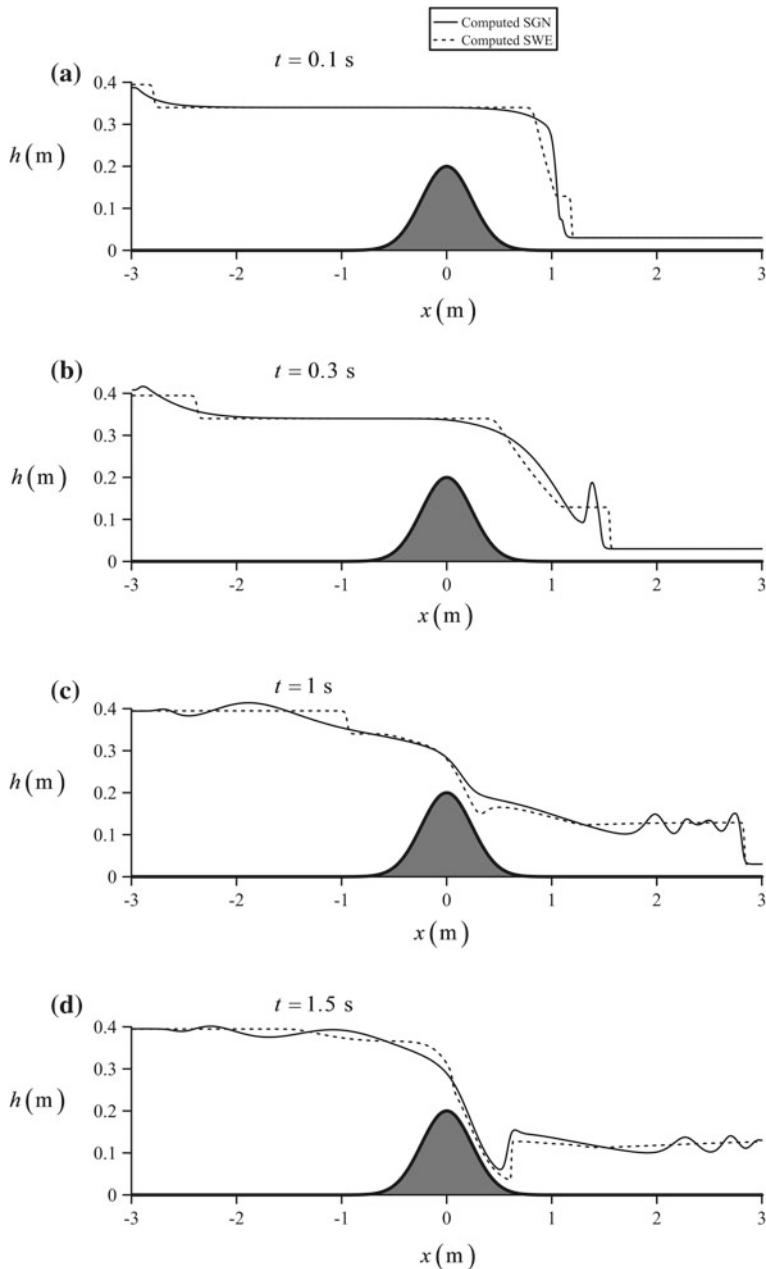
2. The initial conditions are set.
3. Boundary conditions are set using Eqs. (11.116)–(11.117).
4. The value of  $\Delta t$  is computed by Eq. (11.108).
5. The fourth-order MUSCL reconstruction is conducted using the vector  $\mathbf{U}$ .
6. With boundary-extrapolated values of  $\mathbf{U}$ , the local Riemann problems formed at cell interfaces are solved with the HLL Riemann solver, resulting in  $\mathbf{F}_{i+1/2}$ .
7. The bed-slope source term of the momentum equation is determined from Eq. (11.100).
8. The dispersive source term  $\mathbf{S}_d$  is evaluated by second-order central finite-differences at cells  $i = 2$  and  $N - 1$ , and with fourth-order central differences at the other cells.
9. The space operator  $L(\mathbf{U})$  is determined from Eq. (11.119).
10. The elliptic operator  $E(\mathbf{U})$  is inverted using Eq. (11.114).
11. Repeat steps 5–10 for the third-order SSP Runge–Kutta time stepping using Eq. (11.118), with iteration of  $\mathbf{S}_d$  at each time stage.
12. If the actual time is equal to the final time, then stop.
13. Go back to step 3 for a new cycle.

## 11.4 Unsteady Flow Test Cases

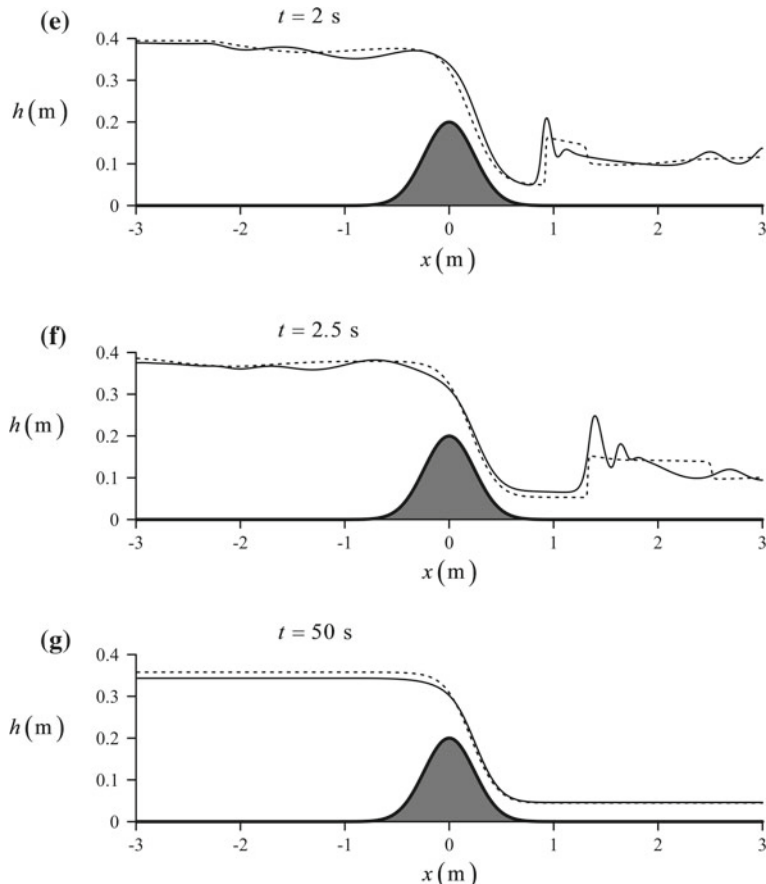
### 11.4.1 Flow over Round-Crested Weir

Figure 11.12 displays the unsteady wave evolution for the symmetrical hump of shape  $z_b = 0.2\exp[-0.5(x/0.24)^2]$  (m) according to Sivakumaran et al. (1983). The unit discharge is  $0.11197 \text{ m}^2/\text{s}$ . The up- and downstream boundary sections are located at  $x = \pm 3 \text{ m}$ . The mesh used is of  $\Delta x = 0.01 \text{ m}$  with  $\text{CFL} = 0.4$ . For comparative purposes, the same simulation was conducted solving the SWE. For the simulations shown in Fig. 11.12, a dam break numerical setup is implemented; a gate is located at coordinate  $x = 1 \text{ m}$ . The water is static, with free surface elevations of 0.34 and 0.03 m up- and downstream of the gate, respectively. The gate is removed instantaneously at time  $t = 0$ ; the steady discharge is introduced at the inlet section as a pulse and kept constant during the simulation. The numerical model used is implemented in a code available on the file “*MUSCLHancock\_weir.xls*,” in Chap. 12.

At time  $t = 0$ , the dam break initial conditions generate a downstream traveling dispersive shock wave and an upstream traveling rarefaction wave (Fig. 11.12a, b). Compare the SGN and the SWE, where a solitary wave at the shock front is predicted by the former. At the upstream section, the addition of the discharge pulse generates another wave. In Fig. 11.12c, an undular wave pattern upstream of the weir is visible, and a dam break front with undulations according to the SGN equations. The SWE predict a sharp shock front, as expected from the second-order MUSCL-Hancock scheme. In Fig. 11.12d, the upstream wave train is still active,



**Fig. 11.12** Evolution of water surface profile  $h(x)$  at various times  $t$  in unsteady weir flow [adapted from Castro-Orgaz and Cantero-Chinchilla (2019)]



**Fig. 11.12** (continued)

while supercritical flow develops along the downstream weir face, with a hydraulic jump near the toe of the weir. The undular waves of the dam break front are progressively leaving the computational domain. In Fig. 11.12e the upstream water waves continue their activity looking for equilibrium in the upstream water depths, while the hydraulic jump phenomena increase their intensity at the downstream side of the obstacle. Dispersive effects gain weight, and a large amplitude initial wave is formed at the jump front, as is typical for undular hydraulic jumps. Figure 11.12f shows that the upstream waves start to diminish in wave amplitude, and that the undular hydraulic jump is pushed out of the computational domain by the supercritical flow on the downstream weir face. Figure 11.12g finally shows the steady-state results obtained from the simulation.

Before discussing the steady flow results, the adequacy of the implemented transmissive boundary condition is assessed in Fig. 11.13. Here, the computational

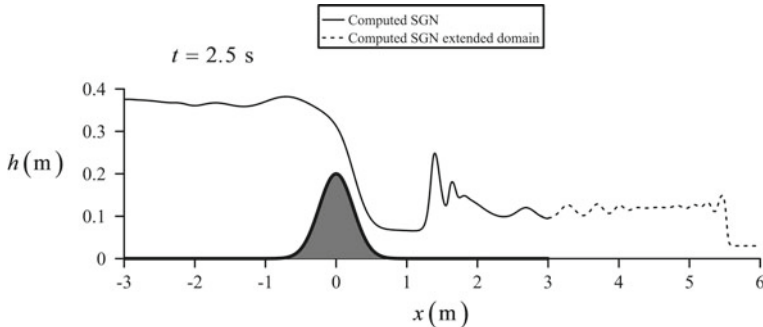


**Fig. 11.13** Evaluation of transmissive boundary condition

results are shown for  $t = 2.5$  s using a domain of double length downstream of the weir crest. Note that the waves are freely leaving the computational domain without significant alterations. A more accurate approach would require the inclusion of sponge layers at both ends of the domain (Cantero-Chinchilla et al. 2018).

The steady flow results generated by the unsteady flow solver are compared in Fig. 11.14 with the “exact” steady flow solution previously presented in Fig. 11.7. Note that the two simulations are in excellent agreement both for the free surface and the bed pressure profiles. The bed pressure head for the unsteady flow solver was determined using a finite-difference discretization of Eq. (11.82) based on the computed vector  $\mathbf{U}$  at each time  $t$ . Therefore, the proposed generalization of the MUSCL-Hancock scheme of the SWE is able to deal with this problem introducing the simple implementation of an additional source term and a tridiagonal equation solver.

It is common practice in water wave simulations for ocean research to use high-resolution schemes, typically of order  $O(\Delta t^3, \Delta x^4)$ . This is done to reduce truncation errors and to avoid numerical dispersion. A question may be well asked if this is also necessary while producing steady non-hydrostatic flow solutions. It

**Fig. 11.14** Comparison of steady and unsteady flow solvers [adapted from Castro-Orgaz and Cantero-Chinchilla (2019)]

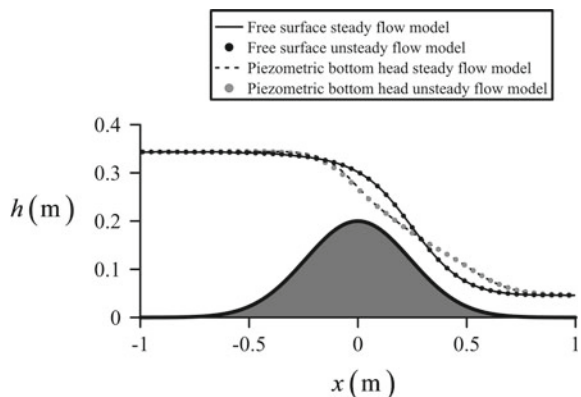
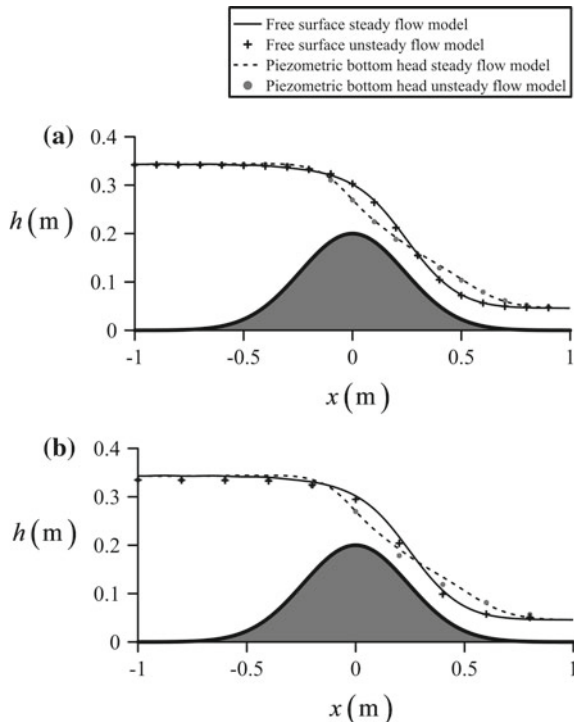


**Fig. 11.15** Comparison of steady and unsteady flow solvers using coarser meshes in the unsteady flow model [adapted from Castro-Orgaz and Cantero-Chinchilla (2019)]



is shown in Fig. 11.14 that the  $O(\Delta t^2, \Delta x^2)$  scheme produces a highly accurate steady flow solution. Now, we test if this accuracy is maintained using a coarse mesh. A new unsteady flow simulation was conducted dividing the numbers of computational cells in Fig. 11.15, e.g., using a mesh of only  $\Delta x = 0.1$  m, and imposing the maximum time step for stability by trial and error, which was found at  $CFL = 0.7$ . The results shown in Fig. 11.15a reveal that even for this coarse mesh, results are still very good. The conclusion is that second-order accuracy is enough for the simulation of steady non-hydrostatic flows, and centred discretizations produce highly accurate results both for steady and unsteady solvers. Finally, Fig. 11.15b presents the results for  $\Delta x = 0.2$  m and  $CFL = 0.25$ . With this mesh, the total number of cells is 30, and the flow over the obstacle is represented only by 9 of these cells. There is an obvious loss of accuracy for this extremely coarse mesh, but the prediction is still in fair agreement with the exact results.

A comparison of the MUSCL-Hancock scheme with the third-order RK/fourth-order MUSCL scheme at  $t = 1$  s and 2.5 s is displayed in Fig. 11.16, using the same mesh adopted to produce Fig. 11.12. The two are in good agreement, with some deviations at the undular jump on the tailwater, indicating that the mesh adopted for MUSCL-Hancock simulation is adequate, but should be refined to get more precise results. The high-resolution model is implemented in a code available on the file “rk3MUSCL4\_weir.xls,” in Chap. 12. In general, a possible practical

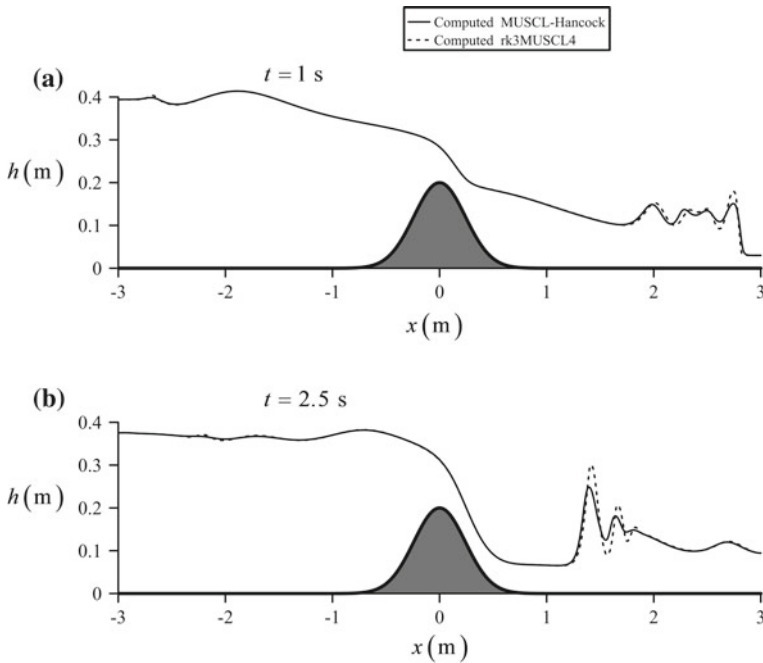


**Fig. 11.16** Comparison of MUSCL-Hancock method with the rk3MUSCL4 solver during transient flow

strategy for using an  $O(\Delta t^2, \Delta x^2)$  SWE scheme improved with dispersive terms is to run a first simulation, and, if extreme waves are expected in any portion of the computational domain, to refine locally the mesh there to increase the model resolution (Popinet 2015).

### 11.4.2 Solitary Wave Propagation

The solitary wave [Eq. (11.93)] is a solution of the SGN equations in which non-linear and dispersive effects are balanced. Non-linear effects are present in the SWE, but this model is dispersionless. The SGN are fully non-linear and weakly dispersive Boussinesq equations. Thanks to the full non-linearity in the non-hydrostatic terms, there is no limitation on the wave amplitude modeled by SGN equations. However, the equations are weakly dispersive, and, thus, only long waves are correctly propagated. A solitary wave of large amplitude is therefore a possible theoretical solution within the domain of validity of the SGN equations. However, exact balancing of non-linear and dispersive effects is necessary to produce a wave of permanent form traveling over still water. As the solitary wave is an analytical solution of Eq. (11.78) resulting from such balancing, a numerical

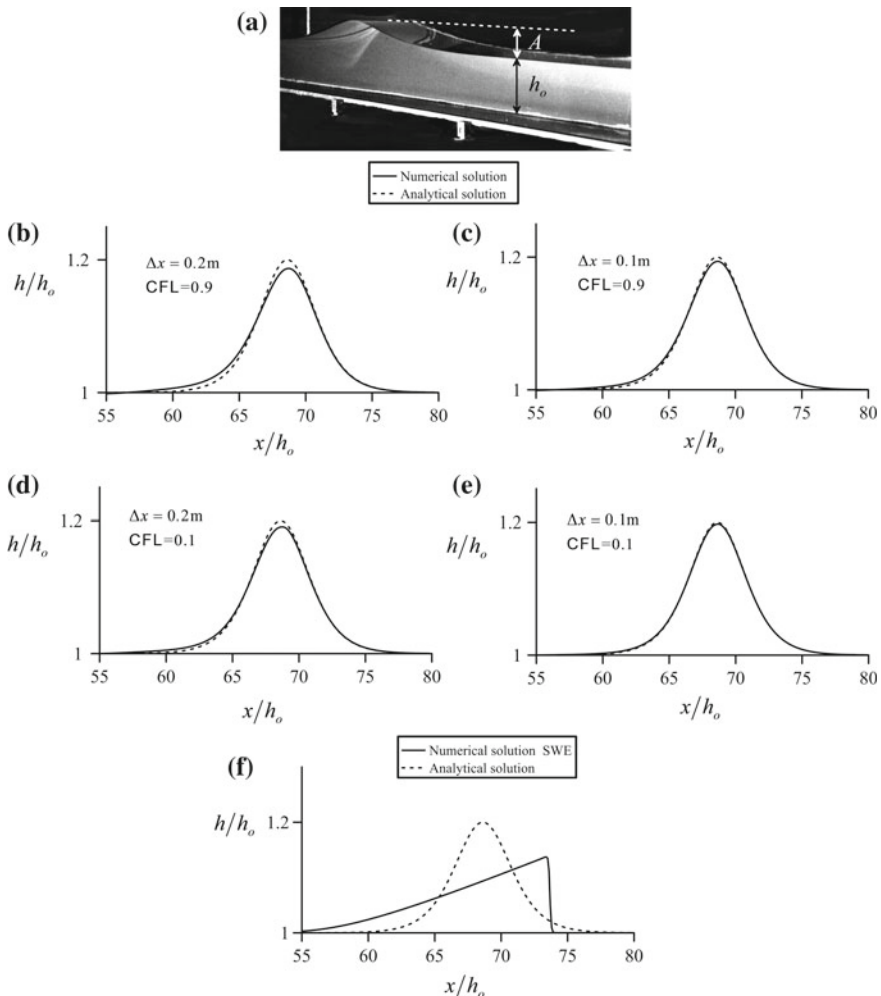


**Fig. 11.17** Propagation of solitary wave of  $A/h_o = 0.2$  and  $h_o = 1$  m using the MUSCL-Hancock scheme at  $t = 20$  s

scheme to solve them must be able to preserve this equilibrium while propagating an analytical solitary wave as input data. The ability of the MUSCL-Hancock scheme to propagate a solitary wave is investigated in Fig. 11.17. A test case involving  $h_o = 1$  m and  $A = 0.2$  m (Fig. 11.17a) is considered in Fig. 11.17b–e at  $t = 20$  s after initiation of routing. The numerical model is implemented in a code available on the file “*MUSCLHancock\_solidarywave.xls*,” in Chap. 12.

A comparison between the analytical and numerical solutions as functions of  $\Delta x$  and CFL indicates that if progressively reducing both, it is possible to find a mesh where the numerical prediction perfectly matches the theoretical expression

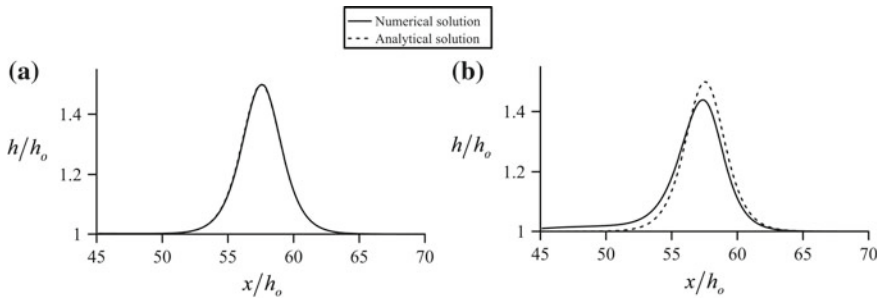


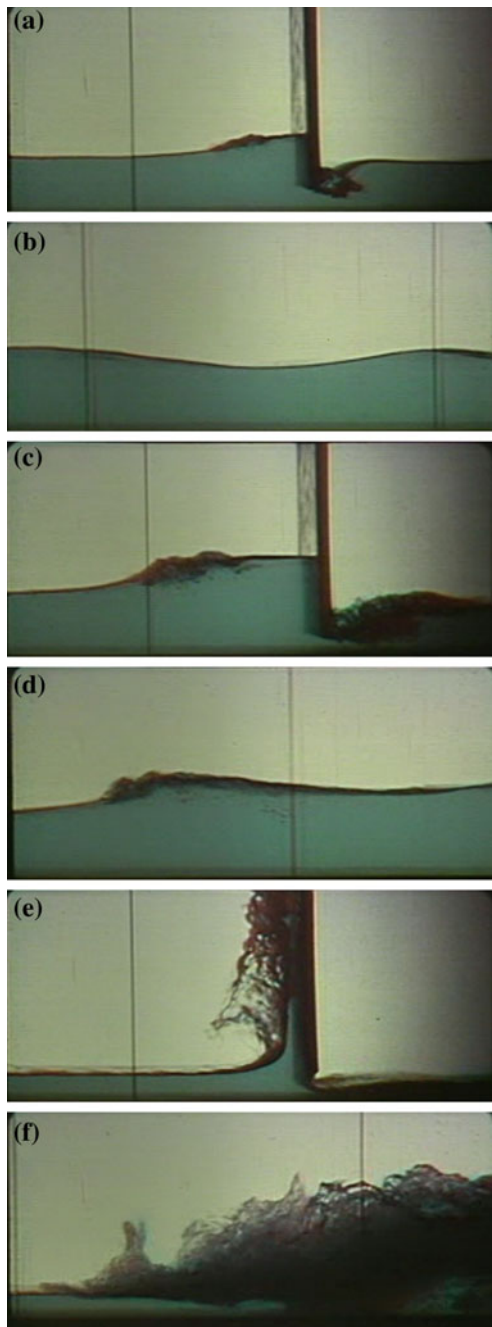
**Fig. 11.18** Comparison of **a** rk3MUSCL4 solver with **b** MUSCL-Hancock solver for solitary wave propagation

(Fig. 11.17e). The MUSCL-Hancock scheme for the SGN equations is thus able to preserve the balance between non-linear and dispersive effects. This is not the case for the same scheme applied to the SWE (Fig. 11.17f), given that dispersive effects are absent. After 20 s of routing, the SWE transform the input solitary wave into a shock.

A test case involving  $h_o = 1$  m and  $A = 0.5$  m is considered in Fig. 11.18 at  $t = 15$  s after initiation of routing. A mesh with  $\Delta x = 0.15$  m and  $CFL = 0.8$  was used in the rk3MUSCL4 numerical model, with the results shown in Fig. 11.18a. The numerical model is implemented in a code available on the file “rk3MUSCL4\_solitarywave.xls,” in Chap. 12. Note that the high-resolution model produces an excellent result. The same test with the same mesh was implemented in the MUSCL-Hancock scheme, with the results shown in Fig. 11.18b. There is an obvious distortion of the solitary wave profile for this mesh, indicating the need to refine the mesh in the  $O(\Delta t^2, \Delta x^2)$  scheme. This comparison was conducted for a high-amplitude wave,  $A/h_o = 0.5$ , which clearly reveals the benefits of an  $O(\Delta t^3, \Delta x^4)$  scheme for this extreme non-linearity.

The balance between non-linearity and dispersion in non-hydrostatic waves can experimentally be observed in surges. An abrupt gate closure generates a surge propagating in the upstream direction (Rouse 1961). If the wave amplitude is much less than the final depth, the surge is undular (Fig. 11.19a, b) (Rouse 1961), from where the quoted balance between non-linear and dispersion effects becomes apparent. If the amplitude increases, there will be a state where the first wave breaks, but there is still an undular wave in the tailwater (Fig. 11.19c, d). If the wave amplitude is much higher than the final depth, a distinctly turbulent broken wave is generated (Fig. 11.19e, f) (Rouse 1961). The SWE are able to simulate broken surges, whereas the SGN equations can simulate undular waves. A criterion for wave breaking is needed to switch from the SWE to the SGN equations and thus predict the complete wave evolution.

**Fig. 11.19** Generation of surges after gate closure in a flume; surge displacement is from right to left **a, b** undular surge, **c, d** undular surge with incipient wave breaking, **e**, **f** broken surge (taken from movie Fluid motion in a gravitational field, by Rouse (1961), IIHR-Hydroscience & Engineering, The University of Iowa)



### 11.4.3 Dam Break Wave

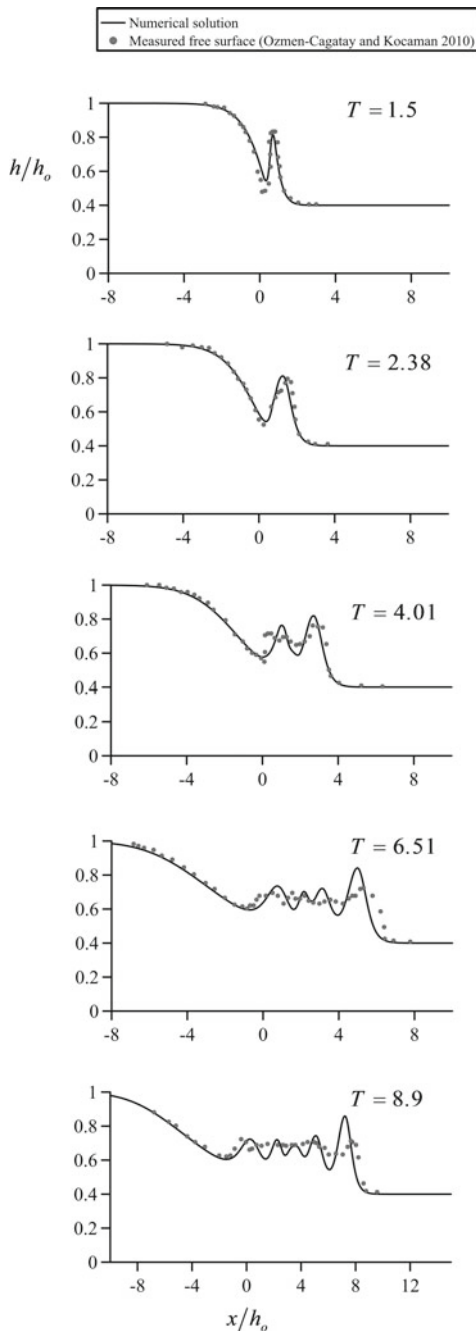
The experimental data of Ozmen-Cagatay and Kocaman (2010) at various normalized times  $T = t(g/h_o)^{1/2}$  starting at abrupt gate removal are considered in Fig. 11.20 for a subcritical dam break wave test ( $h_d/h_o > 0.138$ ) in a horizontal channel. Its upstream water depth was  $h_o = 0.25$  m, the flume width 0.3 m, and the downstream water depth for this series  $h_d = 0.10$  m. Simulations were conducted with the MUSCL-Hancock scheme for the SGN equations using  $CFL = 0.5$  and  $\Delta x = 0.01$  m. The wave profile is well predicted up to  $T = 4.01$ , but the detailed wave shape is affected by turbulence afterward, a feature not accounted for in the inviscid SGN model. The first solitary wave like undulations of the dispersive bore is in fact in excellent agreement with measurements. Experiments and numerical simulations using the MUSCL-Hancock scheme for a transcritical dam break wave test ( $h_d/h_o < 0.138$ ) are considered in Fig. 11.21, with  $h_d = 0.025$  m, using  $CFL = 0.5$  and  $\Delta x = 0.01$  m. For this test, the position of the surge is reasonably well predicted up to  $T = 2.38$ , yet the effects of turbulence are strong in the supercritical portion of the wave profile.

In this test, the predicted first solitary wave undulation is again in excellent agreement with measurements. The precise wave shape is not well predicted, given the irregularities produced by turbulence in the experiments. However, for the low tailwater depth  $h_d$  in this test, the amplitude of the undulations is small and the numerical solution is in general satisfactory.

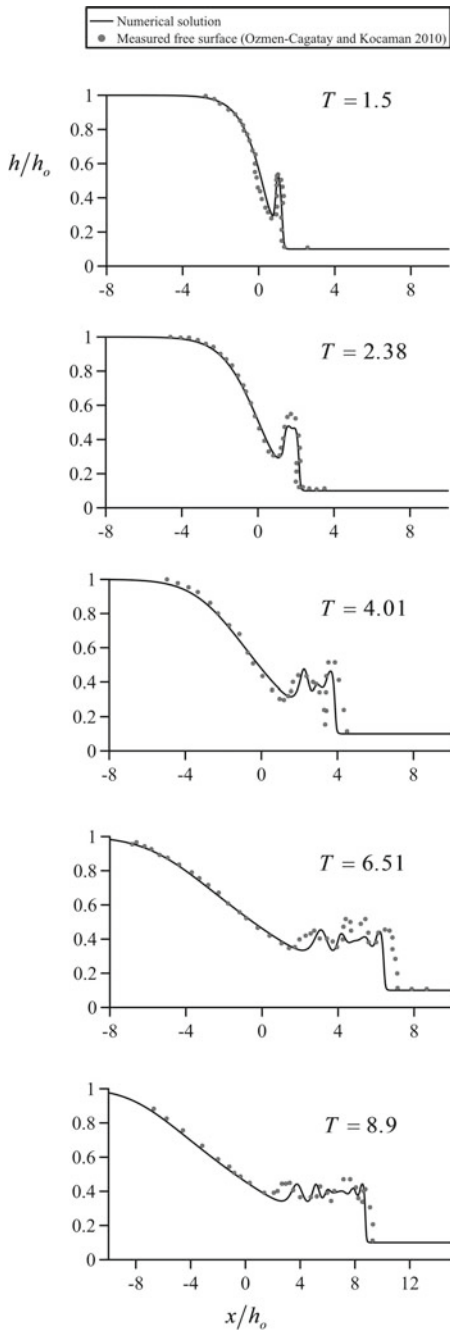
To verify the accuracy of the results obtained with the MUSCL-Hancock solver, the SGN equations were solved again for the test of Figs. 11.20 and 11.21 using the rk3MUSCL4 scheme. The output of both schemes is compared in Figs. 11.22 and 11.23, showing minor discrepancies in the secondary wave train.

In general, for  $h_d/h_o > 0.5$  an undular wave front is generated, e.g., see Fig. 11.24, where an undular wave front is clearly visible. Upon reflection (Fig. 11.24b) at the end of the flume, the undular front is again clearly visible (Fig. 11.24c).

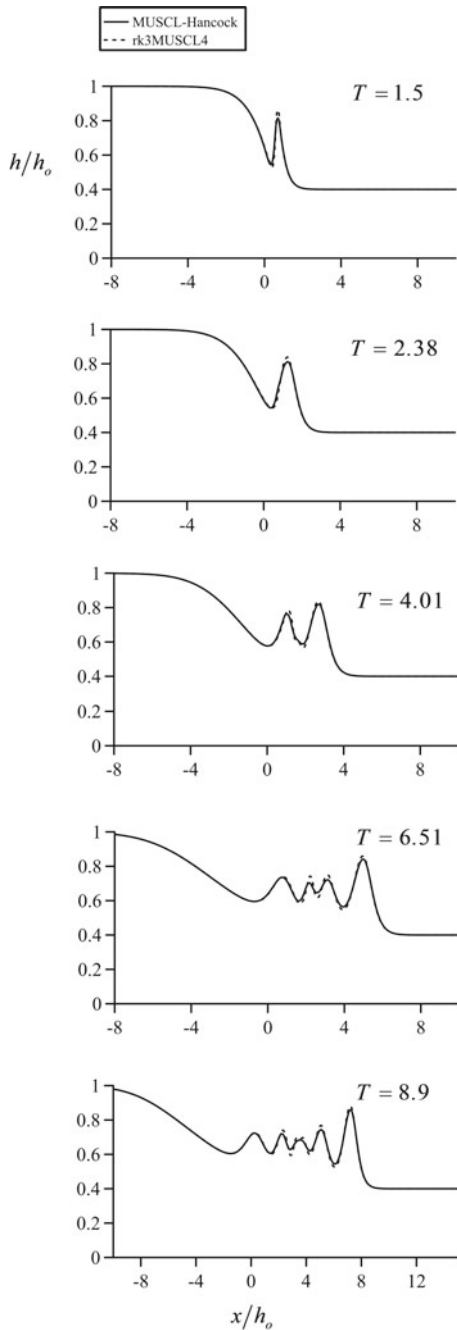
**Fig. 11.20** Comparison of numerical simulations using MUSCL-Hancock scheme for the SGN equations with experimental data (Ozmen-Cagatay and Kocaman 2010) for a subcritical dam break wave



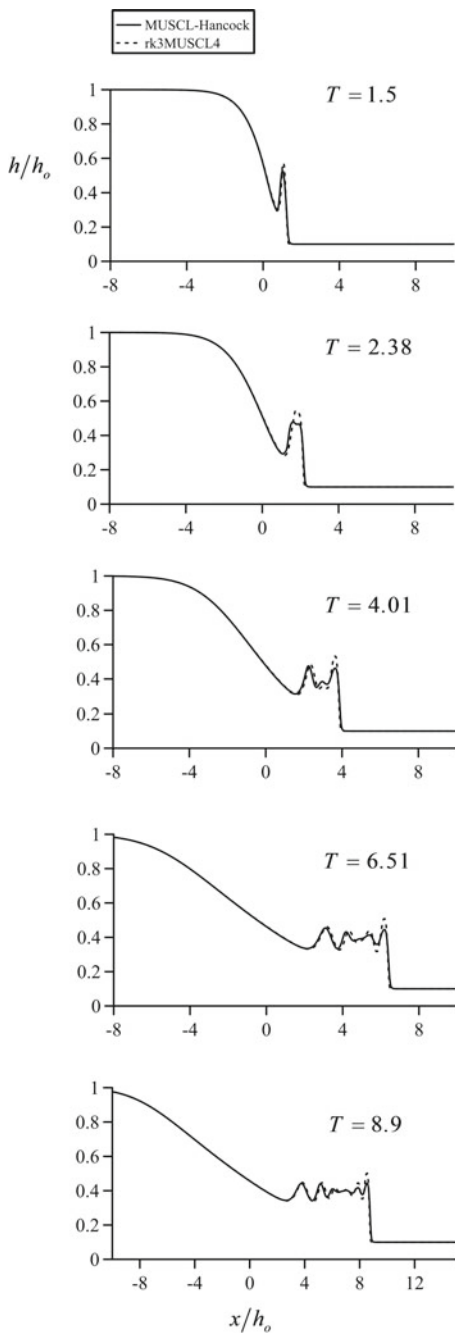
**Fig. 11.21** Comparison of numerical simulations using MUSCL-Hancock scheme for the SGN equations with experimental data (Ozmen-Cagatay and Kocaman 2010) for a transcritical dam break wave



**Fig. 11.22** Comparison of the MUSCL-Hancock scheme with rk3MUSCL4 scheme for the subcritical dam break wave of Fig. 11.19



**Fig. 11.23** Comparison of the MUSCL-Hancock scheme with rk3MUSCL4 scheme for the transcritical dam break wave of Fig. 11.20



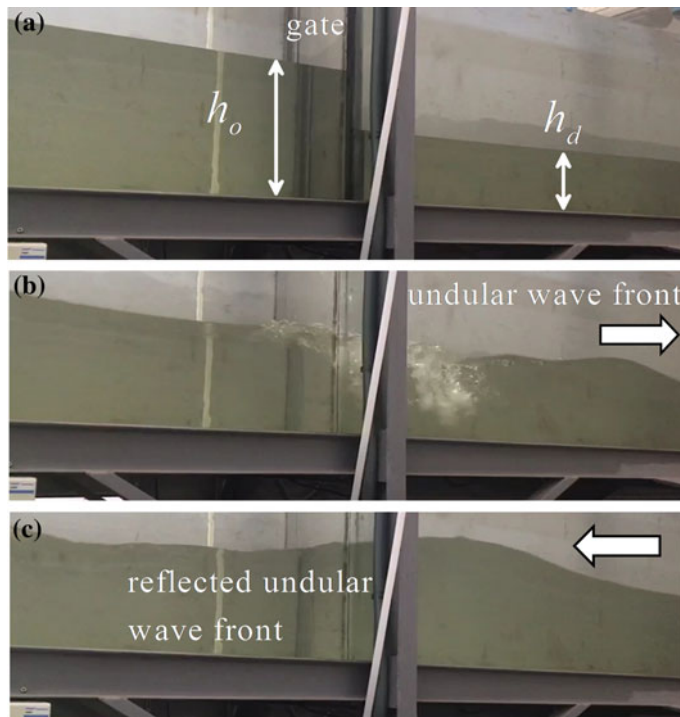


**Fig. 11.24** Non-hydrostatic dam break wave for  $h_d/h_o > 0.5$  (photos by O. Castro-Orgaz at hydraulic flume of University of Córdoba) **a** Initial condition **b** Undular wave front **c** Reflected undular wave front

## References

- Abramowitz, M., & Stegun, I. A. (1972). *Handbook of mathematical functions with formulas, graphs, and mathematical tables* (10th ed.). New York: Wiley.
- Barthelemy, E. (2004). Nonlinear shallow water theories for coastal waters. *Surveys In Geophysics*, 25(3), 315–337.
- Benjamin, T. B., & Lighthill, M. J. (1954). On cnoidal waves and bores. *Proceedings of the Royal Society London, A*, 224, 448–460.
- Blau, E. (1963). Der Abfluss und die hydraulische Energieverteilung über einer parabelförmigen Wehrschwelle [Distributions of discharge and energy over a parabolic-shaped weir]. *Mitteilungen der Forschungsanstalt für Schiffahrt, Wasser- und Grundbau, Berlin, Heft 7*, 5–72 (in German).
- Bonneton, P., Barthelemy, E., Chazel, F., Cienfuegos, R., Lannes, D., Marche, F., et al. (2011). Recent advances in Serre-Green-Naghdi modelling for wave transformation, breaking and runup processes. *European Journal of Mechanics B/Fluids*, 30(6), 589–597.
- Boussinesq, J. (1877). Essai sur la théorie des eaux courantes [Memoir on the theory of flowing water]. *Mémoires présentés par divers savants à l'Académie des Sciences, Paris* 23, 1–660; 24, 1–60 (in French).

- Cantero-Chinchilla, F. N., Castro-Orgaz, O., Dey, S., & Ayuso, J. L. (2016). Nonhydrostatic dam break flows I: Physical equations and numerical schemes. *Journal of Hydraulic Engineering*, 142(12), 04016068.
- Cantero-Chinchilla, F. N., Castro-Orgaz, O., & Khan, A. A. (2018). Depth-integrated nonhydrostatic free-surface flow modelling using weighted-averaged equations. *International Journal for Numerical Methods in Fluids*, 87(1), 27–50.
- Castro-Orgaz, O., & Cantero-Chinchilla, F. N. (2019). Non-linear shallow water flow over topography with depth-averaged potential equation. *Environmental Fluid Mechanics*, in Press.
- Castro-Orgaz, O., & Chanson, H. (2016). Closure to Minimum specific energy and transcritical flow in unsteady open channel flow. *Journal of Irrigation and Drainage Engineering*, 142(10), 07016015.
- Castro-Orgaz, O., & Hager, W. H. (2009). Curved streamline transitional flow from mild to steep slopes. *Journal of Hydraulic Research*, 47(5), 574–584.
- Castro-Orgaz, O., & Hager, W. H. (2013). Velocity profile approximations for two-dimensional potential channel flow. *Journal of Hydraulic Research*, 51(6), 645–655.
- Castro-Orgaz, O., & Hager, W. H. (2014). 1D modelling of curvilinear free surface flow: Generalized Matthew theory. *Journal of Hydraulic Research*, 52(1), 14–23.
- Castro-Orgaz, O., & Hager, W. H. (2017). *Non-hydrostatic free surface flows*. Advances in Geophysical and Environmental Mechanics and Mathematics. 696 p. Berlin: Springer. <https://doi.org/10.1007/978-3-319-47971-2>
- Castro-Orgaz, O., Hutter, K., Giraldez, J. V., & Hager, W. H. (2015). Non-hydrostatic granular flow over 3D terrain: New Boussinesq-type gravity waves? *Journal of Geophysical Research: Earth Surface*, 120(1), 1–28.
- Chanson, H. (2004). *The hydraulics of open channel flows: An introduction*. Oxford, UK: Butterworth-Heinemann.
- Cienfuegos, R., Barthélémy, E., & Bonneton, P. (2006). A fourth-order compact finite volume scheme for fully nonlinear and weakly dispersive Boussinesq-type equations. Part I: Model development and analysis. *International Journal for Numerical Methods in Fluids*, 51(11), 1217–1253.
- Dias, F., & Milewski, P. (2010). On the fully non-linear shallow-water generalized Serre equations. *Physics Letters A*, 374(8), 1049–1053.
- Erduran, K. S., Ilic, S., & Kutija, V. (2005). Hybrid finite-volume finite-difference scheme for the solution of Boussinesq equations. *International Journal for Numerical Methods in Fluids*, 49 (11), 1213–1232.
- Fenton, J. D. (1996). Channel flow over curved boundaries and a new hydraulic theory. *Proceeding of 10th IAHR APD Congress*, Langkawi (pp. 266–273). Malaysia.
- Fornberg, B. (1988). Generation of finite difference formulas on arbitrarily spaced grids. *Mathematics of Computation*, 51(184), 699–706.
- Gottlieb, S., Shu, C.-W., & Tadmor, E. (2001). Strong stability-preserving high-order time discretization methods. *SIAM Review*, 43(1), 89–112.
- Green, A. E., & Naghdi, P. M. (1976a). Directed fluid sheets. *Proceedings of the Royal Society. London, A*, 347, 447–473.
- Green, A. E., & Naghdi, P. M. (1976b). A derivation of equations for wave propagation in water of variable depth. *Journal of Fluid Mechanics*, 78, 237–246.
- Hager, W. H. (1985). Critical flow condition in open channel hydraulics. *Acta Mechanica*, 54(3–4), 157–179.
- Hager, W. H., & Hutter, K. (1984a). Approximate treatment of plane channel flow. *Acta Mechanica*, 51(3–4), 31–48.
- Hager, W. H., & Hutter, K. (1984b). On pseudo-uniform flow in open channel hydraulics. *Acta Mechanica*, 53(3–4), 183–200.
- Hasumi, M. (1931). Untersuchungen über die Verteilung der hydrostatischen Drücke an Wehrkronen und -Rücken von Überfallwehren infolge des abstürzenden Wassers [Studies on the distribution of hydrostatic pressure distributions at overflows due to water flow]. *Journal Department of Agriculture, Kyushu Imperial University* 3(4), 1–97 (in German).

- Henderson, F. M. (1966). *Open channel flow*. New York: MacMillan.
- Hoffman, J. D. (2001). *Numerical methods for engineers and scientists* (2nd ed.). New York: Marcel Dekker.
- Hosoda, T., & Tada, A. (1994). Free surface profile analysis on open channel flow by means of 1-D basic equations with effect of vertical acceleration. *JSCE Annual Journal of Hydraulic Engineering*, 38, 457–462.
- Hutter, K., & Castro-Orgaz, O. (2016). Non-hydrostatic free surface flows: Saint Venant versus Boussinesq depth integrated dynamic equations for river and granular flows. *Continuous Media with Microstructure* (Vol. 2, Chapter 17). Heidelberg: Springer, Berlin.
- Jaeger, C. (1956). *Engineering fluid mechanics*. Edinburgh: Blackie and Son.
- Khan, A. A., & Steffler, P. M. (1996a). Vertically averaged and moment equations model for flow over curved beds. *Journal of Hydraulic Engineering*, 122(1), 3–9.
- Khan, A. A., & Steffler, P. M. (1996b). Modelling overfalls using vertically averaged and moment equations. *Journal of Hydraulic Engineering*, 122(7), 397–402.
- Lesleighter, E., McPherson, B., Riddette, K., & Williams, J. (2008). Modelling procedures used for the spillway upgrade for Lake Manchester Dam. In *Proceeding of 2008 ANCOLD Conference*, Australian National Committee on Large Dams, Gold Coast.
- LeVeque, R. J. (2002). *Finite volume methods for hyperbolic problems*. New York: Cambridge Univ. Press.
- Marchi, E. (1992). The nappe profile of a free overfall. *Rendiconti Lincei, Matematica e Applicazioni*, Serie 9, 3(2), 131–140.
- Marchi, E. (1993). On the free overfall. *Journal of Hydraulic Research* 31(6), 777–790; 32(5), 794–796.
- Matthew, G. D. (1991). Higher order one-dimensional equations of potential flow in open channels. *Proc. ICE*, 91(3), 187–201.
- Mignot, E., & Cienfuegos, R. (2009). On the application of a Boussinesq model to river flows including shocks. *Coastal Engineering*, 56(1), 23–31.
- Mohapatra, P. K., & Chaudhry, M. H. (2004). Numerical solution of Boussinesq equations to simulate dam-break flows. *Journal of Hydraulic Engineering*, 130(2), 156–159.
- Montecinos, G. I., López-Ríos, J. C., Lecaros, R., Ortega, J. H., & Toro, E. F. (2016). An ADER-type scheme for a class of equations arising from the water-wave theory. *Computers and Fluids*, 132, 76–93.
- Montes, J. S. (1994). Potential flow solution to the 2D transition from mild to steep slope. *Journal of Hydraulic Engineering*, 120(5), 601–621.
- Montes, J. S. (1998). *Hydraulics of open channel flow*. Reston VA: ASCE Press.
- Nadiga, B. T., Margolin, L. G., & Smolarkiewicz, P. K. (1996). Different approximations of shallow fluid flow over an obstacle. *Physics of Fluids*, 8(8), 2066–2077.
- Naghdi, P. M. (1979). Fluid jets and fluid sheets: A direct formulation. In *Proceedings of 12th Symposium Naval Hydrodynamics* (pp. 505–515). Washington D.C.: National Academy of Sciences.
- Naghdi, P. M., & Vongsaripigoon, L. (1986). The downstream flow beyond an obstacle. *Journal of Fluid Mechanics*, 162, 223–236.
- Nwogu, O. (1993). Alternative form of Boussinesq equations for nearshore wave propagation. *Journal of Waterway Port Coastal and Ocean Engineering*, 119(6), 618–638.
- Onda, S., & Hosoda, T. (2004). Numerical simulation of the development process of dunes and flow resistance. In *Proceedings River Flow 2004* (pp. 245–252). London: T&F.
- Ozmen-Cagatay, H., & Kocaman, S. (2010). Dam-break flows during initial stage using SWE and RANS approaches. *Journal of Hydraulic Research*, 48(5), 603–611.
- Peregrine, D. H. (1966). Calculations of the development of an undular bore. *Journal of Fluid Mechanics*, 25(2), 321–330.
- Peregrine, D. H. (1967). Long waves on a beach. *Journal of Fluid Mechanics*, 27(5), 815–827.
- Peregrine, D. H. (1972). Equations for water waves and the approximations behind them. In R. E. Meyer, (ed.), *Waves on beaches and resulting sediment transport* (pp. 95–122). San Diego, CA: Academic Press

- Popinet, S. (2015). A quadtree-adaptative multigrid solver for the Serre-Green-Naghdi equations. *Journal of Computational Physics*, 302, 336–358.
- Rouse, H. (1938). *Fluid mechanics for hydraulic engineers*. New York: McGraw-Hill.
- Rouse, H. (1961). *Fluid motion in a gravitational field, IHHR movies*. Iowa: Univ.
- Seabra-Santos, F. J., Renouard, D. P., & Temperville, A. M. (1987). Numerical and experimental study of the transformation of a solitary wave over a shelf or isolated obstacle. *Journal of Fluid Mechanics*, 176, 117–134.
- Serre, F. (1953). Contribution à l'étude des écoulements permanents et variables dans les canaux [Contribution to the study of steady and unsteady channel flows]. *La Houille Blanche* 8(6–7), 374–388; 8(12), 830–887 (in French).
- Sivakumaran, N. S. (1981). *Shallow flow over curved beds (Ph.D. thesis)* Asian Institute of Technology, Bangkok, Thailand.
- Sivakumaran, N. S., Tingsanchali, T., & Hosking, R. J. (1983). Steady shallow flow over curved beds. *Journal of Fluid Mechanics*, 128, 469–487.
- Soares-Frazão, S., & Guinot, V. (2008). A second-order semi-implicit hybrid scheme for one-dimensional Boussinesq-type waves in rectangular channels. *International Journal for Numerical Methods in Fluids*, 58(3), 237–261.
- Soares-Frazão, S., & Zech, Y. (2002). Undular bores and secondary waves: Experiments and hybrid finite-volume modelling. *Journal of Hydraulic Research*, 40(1), 33–43.
- Steffler, P. M., & Jin, Y. C. (1993). Depth-averaged and moment equations for moderately shallow free surface flow. *Journal of Hydraulic Research*, 31(1), 5–17.
- Su, C. H., & Gardner, C. S. (1969). KDV equation and generalizations. Part III. Derivation of Korteweg-de Vries equation and Burgers equation. *Journal of Mathematical Physics*, 10(3), 536–539.
- Thom, A., & Apelt, C. (1961). *Field computations in engineering and physics*. London: Van Nostrand.
- Toro, E. F. (2001). *Shock-capturing methods for free-surface shallow flows*. Singapore: Wiley.
- Toro, E. F. (2009). *Riemann solvers and numerical methods for fluid dynamics: A practical introduction*. Berlin: Springer.
- Vallentine, H. R. (1969). *Applied hydrodynamics*. London: Butterworths.
- Van Dyke, M. (1975). *Perturbation methods in fluid mechanics*. Stanford, CA: The Parabolic Press.
- Wei, G., Kirby, J. T., Grilli, S. T., & Subramanya, R. (1995). A fully nonlinear Boussinesq model for surface waves 1: Highly nonlinear unsteady waves. *Journal of Fluid Mechanics*, 294, 71–92.
- Zerihun, Y. T. (2004). *A one-dimensional Boussinesq-type momentum model for steady rapidly varied open channel flows (Ph.D. thesis)*. Melbourne University, Australia.
- Zerihun, Y. T., & Fenton, J. D. (2006). One-dimensional simulation model for steady transcritical free surface flows at short length transitions. *Advances in Water Resources*, 29(11), 1598–1607.
- Zhou, J. G., Causon, D. M., Mingham, C. G., & Ingram, D. M. (2001). The surface gradient method for the treatment of source terms in the shallow-water equations. *Journal of Computational Physics*, 168(1), 1–25.
- Zhu, D. Z., & Lawrence, G. A. (1998). Non-hydrostatic effects in layered shallow water flows. *Journal of Fluid Mechanics*, 355, 1–16.
- Zhu, D. Z. (1996). *Exchange flow through a channel with an underwater sill (Ph.D thesis)*. The University of British Columbia, Vancouver, Canada.

# Chapter 12

## Numerical Library of Shallow Water Equations



### 12.1 The Library

#### 12.1.1 Introduction: Aims and Scope

Supporting material to the chapters of this book is a collection of source codes explaining the theory and used to produce the solutions presented. The material was originally prepared for students attending the course *Operation of Rivers and Reservoirs* of the *Environmental Hydraulics* master program held at the University of Córdoba, Spain. Most of the codes were used interactively during the lectures, and others are the homework assignment requested to students. Its purpose is to teach students how to make the important step from translating the theoretical material received during the lectures to a code where all the logic sequence is automatically implemented.

Originally, most of the codes were written in Fortran, but the average student taking the lectures lacked from previous knowledge of this language. Thus, MATLAB was tried as an alternative, and programs were therefore adapted, but the problem of having licenses to let any student use the material on any computer make this method unpractical. Finally, the approach suggested by Fenton (2010) was found to be practical and useful; it consists in presenting the codes in Visual Basic (VBA), which is a high-level programming language, such as Fortran, C++, or Pascal. Codes can be entered easily via the use of Excel Macros, which is the approach pursued in the material presented here. Excel is on most personal computers of students; thus, VBA is available to them, whereas separate compilers are necessary for other high-level languages (Fenton 2010).

---

**Electronic supplementary material** The online version of this chapter ([https://doi.org/10.1007/978-3-030-13073-2\\_12](https://doi.org/10.1007/978-3-030-13073-2_12)) contains supplementary material, which is available to authorized users.

The Visual Basic language is used to write scripts, and these scripts are run as “Macros” in Excel. Prior knowledge of VBA is necessary, however. Given that the language is fairly simple, this is not a real limitation. Excel itself is used as a means to organize the input data and receive the output from the code; graphics are immediately displayed with the computational results. Codes are written as clear as possible showing all steps. The use of subroutines is done to structure the computations into separate operations. Programs are by no means optimized; they are simply made to avoid losing any intermediate step. Further, most codes are tailored for a specific application, and, thus, are not to be used for general purposes. However, the reader may take pieces of the codes to develop his/her own general-purpose code. Despite the codes are written in VBA, their translation to FORTRAN is fairly simple, and the material can be used by readers as the base to develop codes for scientific purposes.

### **12.1.2 Summary of Available Codes**

The codes available as supporting material are listed in Table 12.1. Below, examples of the codes for steady and unsteady flows are given. The unsteady flow VBA codes are adapted from the FORTRAN code HW\_MUSH.F by Toro (2000, 2001).

## **12.2 Examples of Codes**

### **12.2.1 Gradually Varied Flow Computation Using Newton–Raphson Method**

```

Public b, Q, z, numero, sections, A, f, BSUP, error, direc
Public hsal, Froude, R, Sf, E, n, So, p
Public dEdh, dSfdh, dfdh, dx, h2, h1, ho, xo
Public h, Fo, hnew
Public i As Integer, j As Integer
Sub main()
    ' Program for the computation of steady gradually varied flow profiles in trapezoidal
    ' channels using
    ' the standard step method; implicit equation is solved applying Newton–Raphson
    ' iteration
    ' by Oscar Castro-Orgaz
    ' read data

```

**Table 12.1** Codes as supporting material of the book

File name	Book chapter	Features of the code
criticaldepth_NR	2	Computation of critical depth in trapezoidal section using Newton–Raphson method
criticaldepth_NR_pipe	2	Computation of critical depth in circular section using Newton–Raphson method
hump_NR	2	Computation of ideal flow profile over a hump using Newton–Raphson method
Analytical_hump_subsuper	2	Computation of analytical flow profile over a hump
conjugatedepth_trapezoidal	2	Computation of conjugate supercritical depth in trapezoidal section using Newton–Raphson method
EM_sluicegate	2	Computation of the discharge and supercritical depth at a sluice gate with a rejected jump using the Newton–Raphson method
normaldepth_NR_Manning	3	Computation of normal depth using Manning's equation in trapezoidal section applying Newton–Raphson method
Lake_discharge	3	Computation of the discharge released from a reservoir
Bresse_analytical	3	Analytical solution of GVF equation for wide rectangular channel
Bresse_RungeKutta4orden	3	Numerical integration of GVF equation for wide rectangular channel using the fourth-order Runge–Kutta method
watersurfaceprofiles_RungeKutta4orden	3	Numerical integration of GVF equation for trapezoidal channel using the fourth-order Runge–Kutta method
watersurfaceprofiles_Euler	3	Numerical integration of GVF equation for trapezoidal channel using the Euler method
watersurfaceprofiles_trapezoidalrule	3	Numerical integration of GVF equation for trapezoidal channel using the trapezoidal rule (iterative method)

(continued)

**Table 12.1** (continued)

File name	Book chapter	Features of the code
Flowprofiles_NR	3	Computation of water surface profiles using the standard step method with Newton–Raphson iteration
steepslope_RungeKutta4orden	3	Numerical integration of GVF equation for wide rectangular channel using the fourth-order Runge–Kutta method
Parabolicweir_transcritical	4	Application of GVF equation to transcritical flow over a parabolic weir using the fourth-order Runge–Kutta method
Gaussianhump_transcritical	4	Application of GVF equation to transcritical flow over a Gaussian hump using the fourth-order Runge–Kutta method
sluicegate_hydraulicjump	4	Computation of transcritical flow profile with a hydraulic jump beyond a sluice gate
rk4	5	Numerical integration of reservoir ODE using the fourth-order Runge–Kutta method
Euler	5	Numerical integration of reservoir ODE using the Euler method
Puls	5	Solution of reservoir routing by Puls modified method
DamBreakAnalytical	6	Analytical solution of ideal dam break waves over horizontal bottom for dry- and wet-bed conditions
DamBreak_Diffusive	7	Application of Lax diffusive scheme to ideal dam break waves
DamBreak_MacCormack_Jameson	7	Application of MacCormack scheme to ideal dam break waves with calibrated artificial viscosity
DamBreak_MacCormack_TVD	7	Application of MacCormack TVD scheme to ideal dam break waves

(continued)

**Table 12.1** (continued)

File name	Book chapter	Features of the code
DamBreak_Unstable	7	Application of unstable scheme to ideal dam break waves with calibrated artificial viscosity
DamBreak_Upwind	7	Application of upwind scheme to ideal dam break waves
Favre_FDM_TVD	7	Application of MacCormack TVD scheme to Favre waves
Favre_FDM_Jameson	7	Application of MacCormack scheme with calibrated artificial viscosity to Favre waves
Favre_FDM_TVD_BoundaryDiscont_Subcrit	7	Variant of MacCormack TVD scheme implementing boundary conditions for discontinuous flow in subcritical conditions
Favre_FDM_TVD_BoundaryDiscont_Supercrit	7	Variant of MacCormack TVD scheme implementing boundary conditions for discontinuous flow in supercritical conditions
Favre_FDM_TVD_BoundaryDiscont_Supercrit_Cont	7	Variant of MacCormack TVD scheme implementing boundary conditions for discontinuous flow in supercritical conditions with naive use of discretized continuity equation
SurgeAnalytical	7	Analytical solution to positive surge
ExactRiemannsolver_drybed	8	Solution of the Riemann problem for dry-bed conditions
ExactRiemannsolver_wetbed	8	Solution of the Riemann problem for wet-bed conditions
Partialgateopening	8	Solution of the partial gate opening of a sluice gate for ideal fluid flow and horizontal bed
DamBreakWave	9	Application of MUSCL-Hancock scheme to dam break waves over horizontal beds
FavreWave	9	Application of MUSCL-Hancock scheme to Favre waves over horizontal beds
Hydraulicjump_gate	9	Application of MUSCL-Hancock scheme to computation of the steady transcritical flow profile beyond a sluice gate

(continued)

**Table 12.1** (continued)

File name	Book chapter	Features of the code
Weir_DGM_parabolic	9	Application of MUSCL-Hancock scheme to computation of the steady transcritical flow profile over a parabolic weir
Weir_DGM_parabolic_MC	9	Same but with upstream water depth computed with backward characteristic
Weir_dry_terrain_SGM-DGM_MC	9	Same but allowing wetting and drying processes
Weir_upwind	9	Application of first-order upwind method to computation of the steady transcritical flow profile over a parabolic weir
Weir_DGM_Sivakumaran	9	Application of MUSCL-Hancock scheme to computation of the steady transcritical flow profile over a Gaussian hump
Dambreak_sill	9	Computation of the dam break wave propagation over a trapezoidal bottom sill using the first-order upwind method
solitarywaverunup	9	Application of MUSCL-Hancock scheme to computation of solitary wave run-up on a slope
Movablebed_DamBreak	10	Computation of dam break waves over erodible beds with first-order upwind method
Movablebed_Dikebreaching	10	Computation of dike overtopping erosion with first-order upwind method
Matthew_SVK_implicit	11	Application of implicit FDM to solve Matthew's equation for flow over a round-crested weir
Matthew_slopebreak	11	Application of implicit FDM to solve Matthew's equation for flow over a slope break
Matthew_embankmentweir	11	Application of implicit FDM to solve Matthew's equation for flow over a trapezoidal profile weir
MUSCLHancock_weir	11	Application of MUSCL-Hancock scheme to solve the SGN equations for round-crested weir flow

(continued)

**Table 12.1** (continued)

File name	Book chapter	Features of the code
MUSCLHancock_solitarywave	11	Application of MUSCL-Hancock scheme to compute the propagation of a solitary wave
rk3MUSCL4_weir	11	Application of a high resolution scheme (3 <sup>rd</sup> -order Runge-Kutta time stepping, 4 <sup>th</sup> -order MUSCL reconstruction) to solve the SGN equations for round-crested weir flow
rk3MUSCL4_solitarywave	11	Application of a high resolution scheme (3 <sup>rd</sup> -order Runge-Kutta time stepping, 4 <sup>th</sup> -order MUSCL reconstruction) to compute the propagation of a solitary wave
backwater_MUSCLHancock	12	Computations of steady gradually-varied flow profiles with MUSCL-Hancock scheme
weir_dry_terrain_complex	12	Wetting and drying over complex topography
steady rk4	12	rk4 solver for wide channel conditions
frictioncomparison	12	Comparison of explicit, implicit and semi-implicit discretizations of friction source term.

```

Q = Worksheets("hoja1").Cells(3, 4).Value
b = Worksheets("hoja1").Cells(4, 4).Value
z = Worksheets("hoja1").Cells(5, 4).Value
numero = Worksheets("hoja1").Cells(6, 4).Value
sections = Worksheets("hoja1").Cells(7, 4).Value
So = Worksheets("hoja1").Cells(8, 4).Value
n = Worksheets("hoja1").Cells(9, 4).Value
dx = Worksheets("hoja1").Cells(10, 4).Value
ho = Worksheets("hoja1").Cells(11, 4).Value
xo = Worksheets("hoja1").Cells(12, 4).Value
direc = Worksheets("hoja1").Cells(13, 4).Value

' boundary point
Worksheets("hoja1").Cells(7, 7).Value = xo

```

```
Worksheets("hoja1").Cells(7, 8).Value = ho
' select direction of computation
If direc = 0 Then dx = -dx
h2 = ho
x = xo
' loop to go across all the channel sections
For j = 1 To sections
Newton
x = x - dx
h = h1
h2 = h1
Worksheets("hoja1").Cells(7 + j, 7).Value = x
Worksheets("hoja1").Cells(7 + j, 8).Value = h
Next j
End Sub
Sub Newton()
'Program to compute the unknown depth using Newton–Rapshon method
' Initiate variables
hsal = h2
section
Fo = So * dx - E - 0.5 * dx * Sf
h1 = h2
' Iterative computation of depth
For i = 1 To numero
hsal = h1
section
functions
hnew = h1 - f/dfdh
If Abs((hnew - h1) /h1) < 10 ^ -8 Then GoTo 10
h1 = hnew
Next i
```

```

10
End Sub

Sub section()
    ' variables of trapezoidal cross section
    A = b * hsal + z * hsal ^ 2
    BSUP = b + 2 * z * hsal
    Froude = (Q ^ 2 /9.81 /A ^ 3 * BSUP) ^ 0.5
    p = b + 2 * hsal * (1 + z ^ 2) ^ 0.5
    R = A /p
    E = hsal + Q ^ 2 /2 /9.81 /A ^ 2
    Sf = n ^ 2 * Q ^ 2 /A ^ 2 /R ^ (4 /3)

    End Sub

    Sub functions()
        ' functions to apply the NR iteration method
        f = E - 0.5 * dx * Sf + Fo
        dEdh = 1 - Froude ^ 2
        dSfdh = Sf * (-10 /3 * BSUP /A + 4 /3 /p * 2 * (1 + z ^ 2) ^ 0.5)
        dfdh = dEdh - 0.5 * dx * dSfdh

        End Sub

```

### **12.2.2 Dam Break Wave Code**

```

' Define variables
Public x(5000), L, deltax
Public U(2, 5000), PIL(2), PIR(2), V
Public delta, t, dt
Public a, b, sig, d1, d2, factor
Public beta, Sf, nM, a1, a2, a3, Rh, width
Public dtdx, DU, DD, BEXT(2, 2, 5000), CDL(2), CDR(2), DL, VL, CL, DR, VR,
CR
Public FDL(2), FDR(2), Flux(2, 5000), DS, SL, SR, FHLL, U1, U2, c(5000),
Smax, SPELOC, CFL, Dup, Ddown
Public FIL(2), FIR(2), deltaflux, lambda, fric

```

Public TOLDEP

Public i As Integer, k As Integer, count As Integer

Public N As Integer, Tmax, xdam

Sub Main()

' Program for the computation of Dam Break waves using the Finite Volume method with: MUSCL linear reconstruction,

' minmod/superbee slope limiter, HLL approximate Riemann solver, and Euler time stepping

' Second order accuracy is achieved with Hancock's method

' Simplified test conditions are:

' \* Horizontal channel

' \* Rectangular cross section

' \* Dry and wet fronts allowed

' \* Friction computed using Manning's equation

' \* Higher water level is on the left, so flow is from left to right

' \* Waves can not reach the boundary sections of the domain

' by Oscar Castro-Orgaz,

' This code is based on the FORTRAN code HW\_MUSH.F by Prof. E. Toro (Numerica library, 2000)

TOLDEP =  $10^{-15}$

lambda = Worksheets("Input").Cells(11, 4).Value

fric = Worksheets("Input").Cells(13, 4).Value

' Read data for simulation

data

' Read initial conditions U(k,i) for conserved variables

initial

' Loop for transient computations

t = 0

count = 0

10

' Compute new dt to satisfy the CFL condition

CFLcon

' Reconstruction of the solution within the cells U(x) using the cell-averaged values U(k,i) obtained in previous time step

MUSCL

```
' Solve Riemann problem using the boundary extrapolated values of conserved  
variables, after application  
' of a limiter to avoid spurious oscillations
```

Riemann

```
' Compute cell-averaged conserved variables at new time level  
evolution
```

```
' Check dry bed conditions  
dry
```

```
' Include friction effects from source terms
```

```
' Implicit computation
```

If fric = 1 Then

friction

End If

```
' Explicit computation
```

If fric = 2 Then

friction2

End If

t = t + dt

count = count + 1

```
' Check final of transient computations
```

If t < Tmax Then GoTo 10

```
' Print water depth and discharge data
```

For i = 1 To N

Worksheets("Input").Cells(4 + i, 10).Value = x(i) - 0.5 \* deltax

For k = 1 To 2

Worksheets("Input").Cells(4 + i, 10 + k).Value = U(k, i)

Next k

If U(1, i) > 0 Then

Worksheets("Input").Cells(4 + i, 13).Value = U(2, i) / U(1, i)

Else

Worksheets("Input").Cells(4 + i, 13).Value = 0

End If

Next i

End Sub

Sub evolution()

' Program to compute the cell-averaged vector U(k,i) at the new time level using the computed vector F at interfaces

' Flux(k,i) is the vector of fluxes at interface  $i + 1/2$  of cell  $i$ ; k make reference to conservation laws (1 = mass, 2 = momentum)

' The domain is composed of  $N+2$  cells; only  $N-2$  cells are computational

' The conserved variables at cells  $i = 1$  and  $N$  are given by the boundary conditions

dtdx = dt /deltax

For k = 1 To 2

For i = 2 To N - 1

U(k, i) = U(k, i) - dtdx \* (Flux(k, i) - Flux(k, i - 1))

Next i

Next k

End Sub

Sub data()

' Program to generate the longitudinal mesh of cells

' Cell  $i$  is defined in terms of a right (index  $i$ ) and left hand side nodes (index  $i - 1$ )

L = Worksheets("Input").Cells(4, 4).Value

deltax = Worksheets("Input").Cells(5, 4).Value

' number of cells

N = L /deltax

x(1) = -L /2

' coordinates of right side of each cell

For i = 2 To N

x(i) = x(i - 1) + deltax

Next i

End Sub

Sub initial()

```
' Program to read simulation data and set initial values of the dam break problem
given the upstream (Dup) and downstream (Ddown) water depths

xdam = Worksheets("Input").Cells(6, 4).Value
Dup = Worksheets("Input").Cells(7, 4).Value
Ddown = Worksheets("Input").Cells(8, 4).Value
CFL = Worksheets("Input").Cells(9, 4).Value
Tmax = Worksheets("Input").Cells(10, 4).Value
nM = Worksheets("Input").Cells(12, 4).Value
width = Worksheets("Input").Cells(14, 4).Value

' Computational cells are from i = 2 to N - 1; ghost cells are i = 0, 1, N and
N + 1. Cells i = 0 and N + 1 are only
' used for a fictitious reconstruction of cells i = 1 and N

For i = 0 To N + 1
    U(2, i) = 0
    If x(i) <= xdam Then
        U(1, i) = Dup
    Else: U(1, i) = Ddown
    End If
    Next i
End Sub

Sub MUSCL()
    ' Linear reconstruction of the solution U(x) within each based on the cell-averaged
values,
    ' with slope limiters minmod or superbee
    ' U(k,i) at cells i = 1 and N is required to compute Fi + 1/2 at cells i = 1 and N - 1
    in the program Riemann

    For i = 1 To N
        For k = 1 To 2
            ' Computation of jumps of conserved variables upstream (U) and downstream (D)
            DU = U(k, i) - U(k, i - 1)
            DD = U(k, i + 1) - U(k, i)
            ' Limitation of the jumps in conserved variables
            limiters
            ' MUSCL linear reconstruction of conserved variables within a cell
```

PIL(k) = U(k, i) - 0.5 \* delta

PIR(k) = U(k, i) + 0.5 \* delta

Next k

For k = 1 To 2

' Temporal evolution of PIL and PIR (for second order time accuracy)

evolve

deltaflux = 0.5 \* dtedx \* (FIL(k) - FIR(k))

' Assignation of boundary-extrapolated (BEXT) values to temporal arrays

' BEXT(j,k,i) is the vector of boundary extrapolated values at cell i, with k as the conservation

' law index (1 = mass, 2 = momentum) and j as the face side index (1 = left face, 2 = right face)

BEXT(1, k, i) = PIL(k) + deltaflux

BEXT(2, k, i) = PIR(k) + deltaflux

Next k

'preserve positivity in water depths

If BEXT(1, 1, i) < 0 Then

BEXT(1, 1, i) = 0

BEXT(1, 2, i) = 0

End If

If BEXT(2, 1, i) < 0 Then

BEXT(2, 1, i) = 0

BEXT(2, 2, i) = 0

End If

' avoid high velocity in data

If BEXT(1, 1, i) < TOLDEP Then

BEXT(1, 2, i) = 0

End If

If BEXT(2, 1, i) < TOLDEP Then

BEXT(2, 2, i) = 0

End If

Next i

End Sub

**Sub Riemann()**

' Computation of Flux vector  $\mathbf{F}_i + 1/2$  at each interface using the approximate Riemann solver HLL

' The flux  $\mathbf{F}_i + 1/2$  at cells  $i = 1$  and  $N - 1$  is required in the program evolution to compute  $\mathbf{U}(k,i)$  at cells  $i = 2$  and  $N - 1$

For  $i = 1$  To  $N - 1$

' Assignment of values for Riemann problem at interface  $i + 1/2$  of cell  $i$ . CDR and CDL are the vectors of variables  $\mathbf{U}$  at the right (R)

' and left (L) side of the interface  $i + 1/2$  of cell  $i$

For  $k = 1$  To 2

CDL(k) = BEXT(2, k, i)

CDR(k) = BEXT(1, k, i + 1)

Next k

' Transformation to physical variables flow depth (D), velocity (V), and celerity (C). Check dry bed conditions

DL = CDL(1)

If DL = 0 Then

VL = 0

Else

VL = CDL(2) /DL

End If

CL = (9.81 \* DL) ^ 0.5

DR = CDR(1)

If DR = 0 Then

VR = 0

Else

VR = CDR(2) /DR

End If

CR = (9.81 \* DR) ^ 0.5

' Computation of vector fluxes FDL and FDR at interface  $i + 1/2$  of cell  $i$

FDL(1) = Flux1(CDL(2))

FDL(2) = Flux2(CDL(1), CDL(2))

FDR(1) = Flux1(CDR(2))

FDR(2) = Flux2(CDR(1), CDR(2))

' Compute wave estimates SL and SR for dry bed case

If DR < TOLDEP And DL > TOLDEP Then

SL = VL - CL

```
SR = VL + 2 * CL
GoTo 200
End If
If DL < TOLDEP And DR > TOLDEP Then
  SL = VR - 2 * CR
  SR = VR + CR
  GoTo 200
End If
If DR < TOLDEP And DL < TOLDEP Then
  SL = -TOLDEP
  SR = TOLDEP
  GoTo 200
End If
DS = (0.5 * (CL + CR) + 0.25 * (VL - VR)) ^ 2 /9.81
' Compute wave estimates SL and SR for wet bed case
If DS <= DL Then
  SL = VL - CL
Else
  SL = VL - CL * (0.5 * DS * (DS + DL)) ^ 0.5 /DL
End If
If DS <= DR Then
  SR = VR + CR
Else
  SR = VR + CR * (0.5 * DS * (DS + DL)) ^ 0.5 /DR
End If
200 ' Compute the Godunov intercell flux with HLL Riemann solver
' case 1
If SL > = 0 Then
  For k = 1 To 2
    Flux(k, i) = FDL(k)
  Next k
End If
' case 2
If SL <= 0 And SR > = 0 Then
```

For k = 1 To 2

$$\text{FHLL} = \text{SR} * \text{FDL}(k) - \text{SL} * \text{FDR}(k) + \text{SL} * \text{SR} * (\text{CDR}(k) - \text{CDL}(k))$$

$$\text{Flux}(k, i) = \text{FHLL} / (\text{SR} - \text{SL})$$

Next k

End If

' case 3

If SR <= 0 Then

For k = 1 To 2

$$\text{Flux}(k, i) = \text{FDR}(k)$$

Next k

End If

Next i

End Sub

Sub CFLcon()

' Computation of dt to satisfy the Courant-Friedrichs-Lowy (CFL) condition and get a stable time stepping

' Computation of the wave celerity c at each cell i using the cell-averaged values U(1,i) = flow depth(i)

Smax = 0

For i = 1 To N

' shallow water wave celerity

$$c(i) = (9.81 * U(1, i))^{0.5}$$

' Local speed; where U(2,i)/U(1,i) = water velocity (i). Check zero water depths

If U(1, i) = 0 Then

SPELOC = 0

Else

$$\text{SPELOC} = \text{Abs}(U(2, i) / U(1, i)) + c(i)$$

End If

If SPELOC >= Smax Then

Smax = SPELOC

End If

Next i

' New value of dt using the fixed value of the CFL number; i.e. 0.5 to 1

dt = CFL \* deltax /Smax

' Reduce dt for early times given the approximate Smax computation

If count <= 5 Then

dt = 0.2 \* dt

End If

' Check that dt+t is not greater than Tmax and recompute dt if required

If t + dt > Tmax Then

dt = Tmax - t

End If

dtdx = dt /deltax

End Sub

Public Function Flux2(U1, U2) As Double

' Computation of the flux vector component of momentum equation given vector U

If U1 = 0 Then

Flux2 = 0

Else

Flux2 = U2 ^ 2 /U1 + 0.5 \* 9.81 \* U1 ^ 2

End If

End Function

Public Function Flux1(U2) As Double

' Computation of the flux vector component of continuity equation given vector U

Flux1 = U2

End Function

Sub evolve()

' Computation of vector fluxes associated with PIL and PIR

FIL(1) = Flux1(PIL(2))

FIL(2) = Flux2(PIL(1), PIL(2))

FIR(1) = Flux1(PIR(2))

FIR(2) = Flux2(PIR(1), PIR(2))

```
End Sub

Sub limiters()
    ' Limitation of jumps in conserved variables
    ' If lambda = (1, Minmod limiter; 2, Superbee)

    If DU * DD < 0 Then
        delta = 0
    Else
        sig = Sgn(DU)
        a = Abs(DU)
        b = Abs(DD)

        If a < b Then
            d1 = a
        Else
            d1 = b
        End If

        d1 = lambda * d1

        If a > b Then
            d2 = a
        Else
            d2 = b
        End If

        If d1 < d2 Then
            factor = d1
        Else
            factor = d2
        End If

        factor = factor * sig

        delta = factor

    End If

    End Sub

    Sub friction()
        ' Implicit computation of the friction effects

        If nM = 0 Then
            GoTo 250
        End If
```

```
For i = 2 To N - 1
If U(1, i) > TOLDEP Then
    Rh = U(1, i) * width /(2 * U(1, i) + width)
    a1 = -9.81 * dt * nM ^ 2 /Rh ^ (4 /3)
    a2 = -1
    a3 = U(2, i) /U(1, i)
    V = (-a2 - (a2 ^ 2 - 4 * a1 * a3) ^ 0.5) /(2 * a1)
    U(2, i) = V * U(1, i)
Else
    U(2, i) = 0
End If
Next i
250
End Sub
Sub friction2()
    ' Explicit computation of the friction effects
    If nM = 0 Then
        GoTo 300
    End If
    For i = 2 To N - 1
        If U(1, i) > TOLDEP Then
            Rh = U(1, i) * width /(2 * U(1, i) + width)
            Sf = nM ^ 2 * (U(2, i) /U(1, i)) ^ 2 /Rh ^ (4 /3)
            U(2, i) = U(2, i) - 9.81 * U(1, i) * dt * Sf
        Else
            U(2, i) = 0
        End If
    Next i
    300
End Sub
Sub dry()
```

```
' check dry bed conditions  
' preserve positivity in water depths  
For i = 2 To N - 1  
If U(1, i) < 0 Then  
    U(1, i) = 0  
    U(2, i) = 0  
End If  
Next i  
' avoid high velocity in data  
For i = 2 To N - 1  
If U(1, i) < TOLDEP Then  
    U(2, i) = 0  
End If  
Next i  
End Sub
```

### 12.2.3 Flooding over an obstacle code

```
' Define variables  
Public x(5000), L, z(5000), S(2, 5000), deltax  
Public U(3, 5000), PIL(3), PIR(3), V  
Public delta, t, dt  
Public a, b, sig, d1, d2, factor  
Public beta, Sf, nM, a1, a2, a3  
Public dtdx, DU, DD, BEXT(2, 2, 5000), CDL(2), CDR(2), DL, VL, CL, DR, VR,  
CR  
Public FDL(2), FDR(2), Flux(2, 5000), DS, SL, SR, FHLL, U1, U2, c(5000),  
Smax, SPELOC, CFL, qo  
Public FIL(2), FIR(2), deltaflux, lambda, fric, deltasource(2), Flim
```

```

Public xR(5000), xL(5000), zL(5000), zR(5000), zjump(5000), Froude(5000),
depth(5000), Uold(2, 5000), xu, xd, c1, c2, Qtarget

Public qadv(5000), hd, sn, aa1, bb1, cc1, Tmax

Public out As Integer, inlet As Integer, count As Integer

Public TOLDEP

Public i As Integer, k As Integer, N As Integer

Sub Main()

' Program for the computation of flow over a hump using the Finite Volume method
with: MUSCL linear reconstruction, minmod/superbee slope limiter, HLL
approximate Riemann solver, and Euler time stepping

' Second order accuracy is achieved with Hancock's method

' Simplified test conditions are:

'   * Parabolic bed profile
'   * Rectangular cross section
'   * Dry and wet fronts allowed
'   * Hybrid reconstructed solution with SGM and DGM to grant
'     the C-property and increase stability of wet-dry front propagation
'   * Friction computed using Manning's equation
'   * Inlet discharge is constant

' by Oscar Castro-Orgaz
' This code is based on the FORTRAN code HW_MUSH.F by Prof. E. Toro
(Numerica library, 2000)

TOLDEP = 10-6

lambda = Worksheets("Input").Cells(11, 4).Value
fric = Worksheets("Input").Cells(13, 4).Value
out = Worksheets("Input").Cells(7, 4).Value
inlet = Worksheets("Input").Cells(5, 4).Value
Flim = Worksheets("Input").Cells(14, 4).Value

' Read data for simulation

data

' Define bed profile

bed

' Read initial conditions U(k,i) for conserved variables
' U(1,i)=flow depth; U(2,i)=discharge

initial

' Loop for transient computations

```

```
t = 0
count = 0
10
' Store previous solution
For k = 1 To 2
For i = 1 To N
Uold(k, i) = U(k, i)
Next i
Next k
' Compute new dt to satisfy the CFL condition
CFLcon
' Reconstruction of the solution within the cells U(x) using the cell-averaged values
U(k,i) obtained in previous time step
MUSCL
' Solve Riemann problem using the boundary extrapolated values of conserved
variables, after application of a limiter to avoid spurious oscillations
Riemann
' Evaluate bed slope source term
bedslope
' Compute cell-averaged conserved variables at new time level
evolution
' Check dry bed conditions
dry
' Include friction effects from source terms
' Implicit computation
If fric = 1 Then
friction
End If
' Explicit computation
If fric = 2 Then
friction2
```

End If

' Set boundary conditions

boundary

t = t + dt

count = count + 1

' Check final of transient computations

If t < Tmax Then GoTo 10

' Print water and discharge data

For i = 1 To N

Worksheets("Input").Cells(4 + i, 10).Value = x(i) - 0.5 \* deltax

Worksheets("Input").Cells(4 + i, 14).Value = z(i)

Worksheets("Input").Cells(4 + i, 15).Value = z(i) + U(1, i)

For k = 1 To 2

Worksheets("Input").Cells(4 + i, 10 + k).Value = U(k, i)

Next k

If U(1, i) > 0 Then

Worksheets("Input").Cells(4 + i, 13).Value = U(2, i) / U(1, i)

Else

Worksheets("Input").Cells(4 + i, 13).Value = 0

End If

Next i

End Sub

Sub bed()

' Definition of the bed profile

' A parabolic weir profile  $z=a1+a2x^2$  is defined

a1 = 0.2

a2 = -0.05

' weir edges

xu =  $-(a1 / a2)^{0.5}$

xd =  $(-a1 / a2)^{0.5}$

' weir profile

For i = 0 To N + 1

  xL(i) = x(i) - 0.5 \* deltax  
  xR(i) = x(i) + 0.5 \* deltax

Next i

For i = 0 To N + 1

  If xL(i) <xu Or xL(i) >xd Then

    zL(i) = 0

  Else

    zL(i) = a1 + a2 \* (xL(i)) ^ 2

  End If

  If xR(i) <xu Or xR(i) >xd Then

    zR(i) = 0

  Else

    zR(i) = a1 + a2 \* (xR(i)) ^ 2

  End If

  z(i) = 0.5 \* (zL(i) + zR(i))

Next i

End Sub

Sub initial()

' Program to read simulation data

Qtarget = Worksheets("Input").Cells(6, 4).Value

hd = Worksheets("Input").Cells(8, 4).Value

CFL = Worksheets("Input").Cells(9, 4).Value

Tmax = Worksheets("Input").Cells(10, 4).Value

nM = Worksheets("Input").Cells(12, 4).Value

' Computational cells are from i=2 to N-1; gosh cells are i=0,1,N and N+1. Cells i=0 and N+1 are only used for a fictitious reconstruction of cells i=1 and N

'Initial condition is static water at elevation hd; dry portions of terrain allowed

For i = 0 To N + 1

  If hd >= z(i) And x(i) <= 0 Then

    U(1, i) = hd - z(i)

  Else

U(1, i) = 0

End If

U(2, i) = 0

Next i

End Sub

Sub boundary()

' Use ghost cells to set boundary conditions

'INLET CONDITIONS

'\_\_\_\_\_

' Subcritical flow at the inlet section with constant discharge

If inlet = 1 Then

'Inlet discharge

U(2, 1) = Qtarget

U(2, 0) = Qtarget

'Water depth is determined solving the C- backward characteristic

aa1 = 9.81 / (9.81 \* Uold(1, 2)) ^ 0.5

bb1 = (Uold(2, 2) / Uold(1, 2)) - (9.81 / (9.81 \* Uold(1, 2))) ^ 0.5 \* Uold(1, 2))

cc1 = -Qtarget

U(1, 1) = (-bb1 + (bb1 ^ 2 - 4 \* aa1 \* cc1) ^ 0.5) / (2 \* aa1)

U(1, 0) = U(1, 1)

'\_\_\_\_\_

' Transmissive condition upstream

ElseIf inlet = 2 Then

For k = 1 To 2

U(k, 1) = U(k, 2)

U(k, 0) = U(k, 3)

Next k

'\_\_\_\_\_

'Reflective condition upstream

Else If inlet = 3 Then

$U(1, 1) = U(1, 2)$

$U(2, 1) = -U(2, 2)$

$U(1, 0) = U(1, 3)$

$U(2, 0) = -U(2, 3)$

End If

' OUTLET CONDITIONS

' \_\_\_\_\_

' Tailwater gate is fully open; transmissive condition

If out = 1 Then

For k = 1 To 2

$U(k, N) = U(k, N - 1)$

$U(k, N + 1) = U(k, N - 2)$

Next k

' \_\_\_\_\_

' Tailwater gate is closed; reflective condition

Else If out = 2 Then

$U(1, N) = U(1, N - 1)$

$U(2, N) = -U(2, N - 1)$

$U(1, N + 1) = U(1, N - 2)$

$U(2, N + 1) = -U(2, N - 2)$

End If

End Sub

Sub evolution()

' Program to compute the cell-averaged vector  $U(k,i)$  at the new time level using the computed vector F at interfaces

' Flux(k,i) is the vector of fluxes at interface  $i+1/2$  of cell i; k make reference to conservation laws (1=mass, 2=momentum)

' The domain is composed of  $N+2$  cells; only  $N-2$  cells are computational

' The conserved variables at cells  $i=1$  and  $N$  are given by the boundary conditions

dtdx = dt / deltax

For k = 1 To 2

For i = 2 To N - 1

```
U(k, i) = U(k, i) - dtdx * (Flux(k, i) - Flux(k, i - 1)) + dt * (S(k, i))
```

Next i

Next k

End Sub

Sub data()

' Program to generate the longitudinal mesh of cells

' Cell i is defined in terms of a right (index i) and left hand side nodes (index i-1)

L = Worksheets("Input").Cells(3, 4).Value

deltax = Worksheets("Input").Cells(4, 4).Value

' number of cells

N = L / deltax

x(1) = -0.5 \* L

' coordinates of right side of each cell

For i = 2 To N

x(i) = x(i - 1) + deltax

Next i

End Sub

Sub MUSCL()

' Linear reconstruction of the solution U(x) within each based on the cell-averaged values, with slope limiters minmod or superbee

' U(k,i) at cells i=1 and N is required to compute Fi+1/2 at cells i=1 and N-1 in the program Riemann

' SGM is needed to grant the C-property (at Froude=0), but the DGM is more robust during propagation of wet-dry interfaces. Here a limit Froude number Flim is defined to reconstruct using the SGM subcritical flows and with the DGM the remaining cases, including the supercritical flow in the tip portion of a wet-dry front

' Surface Gradient method (SGM) is used for reconstruction of water surface elevation for Froude <=Flim

' Depth Gradient method (DGM) is used for reconstruction of flow depths for Froude >Flim

' Store water depths, surface elevations and Froude number

For i = 1 To N

depth(i) = U(1, i)

'Solution at cell i is vector U(k,i), with k=1 for the water depth, k=2 for the discharge, and k=3 for the free surface elevation

U(3, i) = U(1, i) + z(i)

If U(1, i) = 0 Then

Froude(i) = 0

Else

Froude(i) = (U(2, i) ^ 2 / 9.81 / U(1, i) ^ 3) ^ 0.5

End If

Next i

For i = 1 To N

For k = 1 To 3

' Computation of jumps of conserved variables upstream (U) and downstream (D)

DU = U(k, i) - U(k, i - 1)

DD = U(k, i + 1) - U(k, i)

' Limitation of the jumps in conserved variables

limiters

' MUSCL linear reconstruction of conserved variables within a cell

PIL(k) = U(k, i) - 0.5 \* delta

PIR(k) = U(k, i) + 0.5 \* delta

Next k

' Values of the water depth at the interfaces of a cell for Froude<=Flim are computed from SGM

If Froude(i) <= Flim Then

PIL(1) = PIL(3) - zL(i)

PIR(1) = PIR(3) - zR(i)

End If

' In a dry cell the reconstruction is not allowed; thus, water depths at interfaces are set to zero. All the depths are zero in a cell marked computationally as dry. This is true in a full dry cell, but incorrect in a partially-filled cell

If depth(i) <= TOLDEP Then

PIL(1) = 0

PIR(1) = 0

End If

```
' Ensure positivity in water depths at interfaces
If PIL(1) < 0 Then
PIL(1) = 0
End If
If PIR(1) < 0 Then
PIR(1) = 0
End If
If PIL(1) < TOLDEP Then
PIL(2) = 0
End If
If PIR(1) < TOLDEP Then
PIR(2) = 0
End If
For k = 1 To 2
' Temporal evolution of PIL and PIR (for second order time accuracy)
evolve
deltaflux = 0.5 * dtdx * (FIL(k) - FIR(k))
deltasource(k) = 0.5 * dtdx * deltax * deltasource(k)
' Assigmentation of boundary-extrapolated (BEXT) values to temporal arrays
' BEXT(j,k,i) is the vector of boundary extrapolated values at cell i, with k as the
conservation law index (1=mass, 2=momentum)and j as the face side index (1=left
face, 2=right face)
BEXT(1, k, i) = PIL(k) + deltaflux + deltasource(k)
BEXT(2, k, i) = PIR(k) + deltaflux + deltasource(k)
Next k
'preserve positivity in water depths
If BEXT(1, 1, i) < 0 Then
BEXT(1, 1, i) = 0
BEXT(1, 2, i) = 0
End If
If BEXT(2, 1, i) < 0 Then
BEXT(2, 1, i) = 0
```

```
BEXT(2, 2, i) = 0  
End If  
' avoid high velocity in data  
If BEXT(1, 1, i) < TOLDEP Then  
BEXT(1, 2, i) = 0  
End If  
If BEXT(2, 1, i) < TOLDEP Then  
BEXT(2, 2, i) = 0  
End If  
Next i
```

' At the interface of a full wet cell and a dry cell a jump in water depths may be formed. However, the dry cell is in reality partially filled with water. That is, the dry front is contained inside the computationally dry cell. Therefore, an unrealistic dry-bed dam break wave problem at the interface of a full-wet and full-dry cells is formed. Remember that a cell is marked computationally as dry with zero water depth (cell-averaged value), but physically there is a portion of water inside this cell if it is in contact with a full-wet cell

```
For i = 1 To N  
'A reflective condition is imposed in the dry front if the water depth elevation in the wet cell is below the average bed elevation in the (full) dry cell  
If Froude(i) <= Flim Then  
' dry front is on the right  
If depth(i) < z(i + 1) - z(i) And depth(i + 1) <= TOLDEP Then  
BEXT(1, 1, i + 1) = BEXT(2, 1, i)  
BEXT(1, 2, i + 1) = -BEXT(2, 2, i)  
End If  
' dry front is on the left  
If depth(i + 1) < z(i) - z(i + 1) And depth(i) <= TOLDEP Then  
BEXT(2, 1, i) = BEXT(1, 1, i + 1)  
BEXT(2, 2, i) = -BEXT(1, 2, i + 1)  
End If  
End If  
Next i
```

End Sub

Sub Riemann()

' Computation of Flux vector  $\mathbf{F}_{i+1/2}$  at each interface using the approximate Riemann solver HLL

' The flux  $\mathbf{F}_{i+1/2}$  at cells  $i = 1$  and  $N - 1$  is required in the program evolution to compute  $\mathbf{U}(k,i)$  at cells  $i = 2$  and  $N - 1$

For  $i = 1$  To  $N - 1$

' Assigmentation of values for Riemann problem at interface  $i+1/2$  of cell  $i$ . CDR and CDL are the vectors of variables  $\mathbf{U}$  at the right (R) and left (L) side of the interface  $i+1/2$  of cell  $i$

For  $k = 1$  To 2

CDL(k) = BEXT(2, k, i)

CDR(k) = BEXT(1, k, i + 1)

Next k

' Transformation to physical variables flow depth (D), velocity (V), and celerity (C). Check dry bed conditions

DL = CDL(1)

If DL = 0 Then

VL = 0

Else

VL = CDL(2) / DL

End If

CL = (9.81 \* DL) ^ 0.5

DR = CDR(1)

If DR = 0 Then

VR = 0

Else

VR = CDR(2) / DR

End If

CR = (9.81 \* DR) ^ 0.5

' Computation of vector fluxes FDL and FDR at interface  $i+1/2$  of cell  $i$

FDL(1) = Flux1(CDL(2))

FDL(2) = Flux2(CDL(1), CDL(2))

FDR(1) = Flux1(CDR(2))

FDR(2) = Flux2(CDR(1), CDR(2))

' Compute wave estimates SL and SR for dry bed case

If DR < TOLDEP And DL > TOLDEP Then

SL = VL - CL

SR = VL + 2 \* CL

GoTo 200

End If

If DL < TOLDEP And DR > TOLDEP Then

SL = VR - 2 \* CR

SR = VR + CR

GoTo 200

End If

If DR < TOLDEP And DL < TOLDEP Then

SL = -TOLDEP

SR = TOLDEP

GoTo 200

End If

DS = (0.5 \* (CL + CR) + 0.25 \* (VL - VR)) ^ 2 / 9.81

' Compute wave estimates SL and SR for wet bed case

If DS <= DL Then

SL = VL - CL

Else

SL = VL - CL \* (0.5 \* DS \* (DS + DL)) ^ 0.5 / DL

End If

If DS <= DR Then

SR = VR + CR

Else

SR = VR + CR \* (0.5 \* DS \* (DS + DL)) ^ 0.5 / DR

End If

200 ' Compute the Godunov intercell flux with HLL Riemann solver

' case 1

If SL >= 0 Then

For k = 1 To 2

Flux(k, i) = FDL(k)

Next k

End If

' case 2

If SL <= 0 And SR >= 0 Then

For k = 1 To 2

FHLL = SR \* FDL(k) - SL \* FDR(k) + SL \* SR \* (CDR(k) - CDL(k))

Flux(k, i) = FHLL / (SR - SL)

Next k

End If

' case 3

If SR <= 0 Then

For k = 1 To 2

Flux(k, i) = FDR(k)

Next k

End If

Next i

End Sub

Sub CFLcon()

' Computation of dt to satisfy the Courant-Friedrichs-Lowy(CFL) condition and get a stable time stepping

' Computation of the wave celerity c at each cell i using the cell-averaged values U(1,i)=flow depth(i)

Smax = 0

For i = 1 To N

' shallow water wave celerity

c(i) = (9.81 \* U(1, i)) ^ 0.5

' Local speed; where U(2,i)/U(1,i)=water velocity (i). Check zero water depths

If U(1, i) = 0 Then

SPELOC = 0

Else

SPELOC = Abs(U(2, i) / U(1, i)) + c(i)

End If

If SPELOC >= Smax Then

```
Smax = SPELOC
End If
Next i
' New value of dt using the fixed value of the CFL number; i.e. 0.5 to 1
dt = CFL * deltax / Smax
' Reduce dt for early times given the approximate Smax computation
If count <= 5 Then
dt = 0.2 * dt
End If
' Check that dt+t is not greater than Tmax and recompute dt if required
If t + dt>Tmax Then
dt = Tmax - t
End If
dtdx = dt / deltax
End Sub
Public Function Flux2(U1, U2) As Double
' Computation of the flux vector component of momentum equation given vector U
If U1 = 0 Then
Flux2 = 0
Else
Flux2 = U2 ^ 2 / U1 + 0.5 * 9.81 * U1 ^ 2
End If
End Function
Public Function Flux1(U2) As Double
' Computation of the flux vector component of continuity equation given vector U
Flux1 = U2
End Function
Sub evolve()
' Computation of vector fluxes associated with PIL and PIR
FIL(1) = Flux1(PIL(2))
FIL(2) = Flux2(PIL(1), PIL(2))
```

```
FIR(1) = Flux1(PIR(2))
FIR(2) = Flux2(PIR(1), PIR(2))

' bed source term effect

' z-jump in the bed profile within a cell

' cell full filled with water

zjump(i) = zR(i) - zL(i)

' cell partially-filled with water, with zero water depth on its right side

If PIR(1) <= TOLDEP Then

zjump(i) = PIL(1)

End If

' cell partially-filled with water, with zero water depth on its left side

If PIL(1) <= TOLDEP Then

zjump(i) = -PIR(1)

End If

deltasource(1) = 0

deltasource(2) = -9.81 * (PIL(1) + PIR(1)) * 0.5 * zjump(i) / deltax

End Sub

Sub limiters()

' Limitation of jumps in conserved variables

' If lambda=(1, Minmod limiter; 2, Superbee)

If DU * DD < 0 Then

delta = 0

Else

sig = Sgn(DU)
a = Abs(DU)
b = Abs(DD)

If a < b Then
d1 = a
Else
d1 = b
End If

d1 = lambda * d1

If a > b Then
```

```
d2 = a
Else
d2 = b
End If

If d1 < d2 Then
factor = d1
Else
factor = d2
End If

factor = factor * sig

delta = factor

End If

End Sub

Sub friction()

' Implicit computation of the friction effects

If nM = 0 Then
GoTo 250
End If

For i = 2 To N - 1
If U(1, i) > TOLDEP Then
If U(2, i) > 0 Then
sn = 1
Else
sn = -1
End If

a1 = -9.81 * dt * nM ^ 2 / U(1, i) ^ (4 / 3) * sn
a2 = -1
a3 = U(2, i) / U(1, i)
V = (-a2 - (a2 ^ 2 - 4 * a1 * a3) ^ 0.5) / (2 * a1)
U(2, i) = V * U(1, i)

Else
U(2, i) = 0
End If
```

```
Next i
250
End Sub
Sub friction2()
' Explicit computation of the friction effects
If nM = 0 Then
GoTo 300
End If
For i = 2 To N - 1
' wet bed
If U(1, i) > TOLDEP Then
qadv(i) = U(2, i)
Sf = nM ^ 2 * (U(2, i) / U(1, i)) * Abs((U(2, i) / U(1, i))) / U(1, i) ^ (4 / 3)
U(2, i) = U(2, i) - 9.81 * U(1, i) * dt * Sf
' Friction can stop the flow, but a flow reversal is not physically feasible
If qadv(i) * U(2, i) < 0 Then U(2, i) = 0
Else
U(2, i) = 0
End If
Next i
300
End Sub
Sub dry()
' check dry bed conditions
' preserve positivity in water depths
For i = 2 To N - 1
' if the water depth is negative, both depth and discharge are set to zero
If U(1, i) < 0 Then
U(1, i) = 0
U(2, i) = 0
```

End If

' Notethat possible mass errors due to wet-dry updating are not corrected  
Next i

' avoid high velocity in data

' if the water depth is below the tolerance (and positive) only the continuity equation  
is solved, that is, discharge is set to zero

For i = 2 To N - 1

If U(1, i) < TOLDEP Then

U(2, i) = 0

End If

Next i

End Sub

Sub bedslope()

' Evaluation of source term from bed profile

For i = 1 To N

S(1, i) = 0

' Computation of the bed z-jump within a cell

' cell full-filled with water

zjump(i) = zR(i) - zL(i)

' cell partially-filled with water, with zero water depth on its right side

If BEXT(2, 1, i) <= TOLDEP Then

zjump(i) = BEXT(1, 1, i)

End If

' cell partially-filled with water, with zero water depth on its left side

If BEXT(1, 1, i) <= TOLDEP Then

zjump(i) = -BEXT(2, 1, i)

End If

S(2, i) = -9.81 \* (BEXT(1, 1, i) + BEXT(2, 1, i)) \* 0.5 \* zjump(i) / deltax

Next i

End Sub

## 12.3 Using the Library

### 12.3.1 Short Tutorial: Flooding of an Obstacle

The methods selected for the library are neither the only possible choices, nor universally valid. However, they are considered illustrative to introduce students to the computation of *Open Channel Flows*. In this section we will describe the use of the Library taking as example a code for flooding of an obstacle, printed in the former section, and inserted in the file “*weir\_dry\_terrain\_SGM-DGM\_MC.xls*”. This solver uses the MUSCL-Hancock scheme with a well-balanced discretization of the bed-slope source term, along with an approximate wetting-drying procedure. The code permits to simulate the flooding of a parabolic weir of bed profile  $z_b = 0.2 - 0.05x^2$ . The upstream weir side is initially wet with a water surface elevation  $h_o$ , whereas the tailwater portion is dry. We will use this code as example to show how to use the codes available as supporting material of the textbook. Observe in Fig. 12.1 the sheet used to insert the input data, print and plot the computational results. Note the input data selected for the current simulation.

The following input data must be supplied to the sheet for the computational simulation:

$L$  = length of computational domain

$\Delta x$  = cell width

Upstream section:

1 = discharge pulse at inlet section fixed ( $q_o$ ), water depth computed by using a backward  $C^-$  characteristic

2 = discharge and water depth computed using a transmissive condition (open boundary)

3 = discharge and water depth computed using a reflective condition (solid wall)

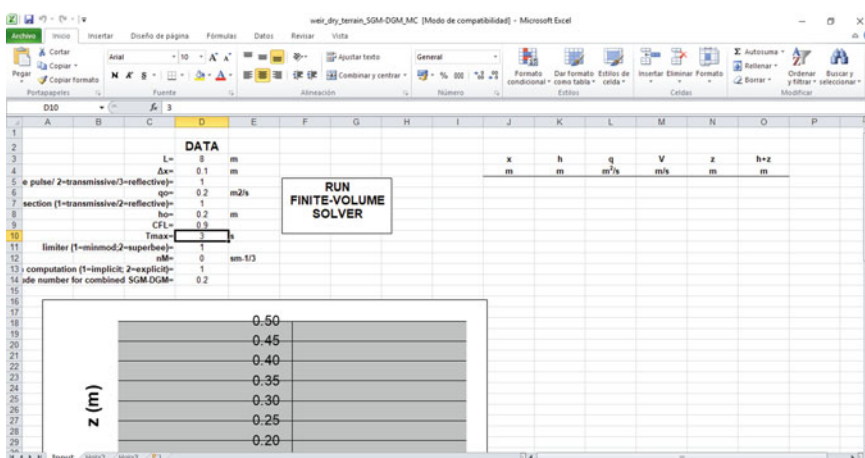


Fig. 12.1 Sheet for introducing input data, printing and plotting computational results

Downstream section:

1 = discharge and water depth computed using a transmissive condition (open boundary)

2 = discharge and water depth computed using a reflective condition (solid wall)

$h_o$  = initial water depth at the upstream weir face. It can be lower than the maximum weir height (0.2 m), but also higher (to simulate dam-break like flows)  
 $CFL$  = Courant-Friedrichs-Lowy number

$T_{\max}$  = simulation time

Limiter:

1 = minmod

2 = superbee

$n_M$  = Manning's roughness coefficient

Friction computation:

1 = implicit

2 = explicit

Froude number for the combined Surface Gradient Method (SGM)-Depth Gradient Method (DGM). The reconstruction of the solution is done with SGM below this limiting Froude number, and using the DGM in other cases.

To run the model press "RUN FINITE-VOLUME SOLVER", and the macros are called to conduct the simulation. Once finished, numerical results are automatically printed and plotted. Running the model for  $T_{\max} = 0$ , we observe the initial conditions (Fig. 12.2).

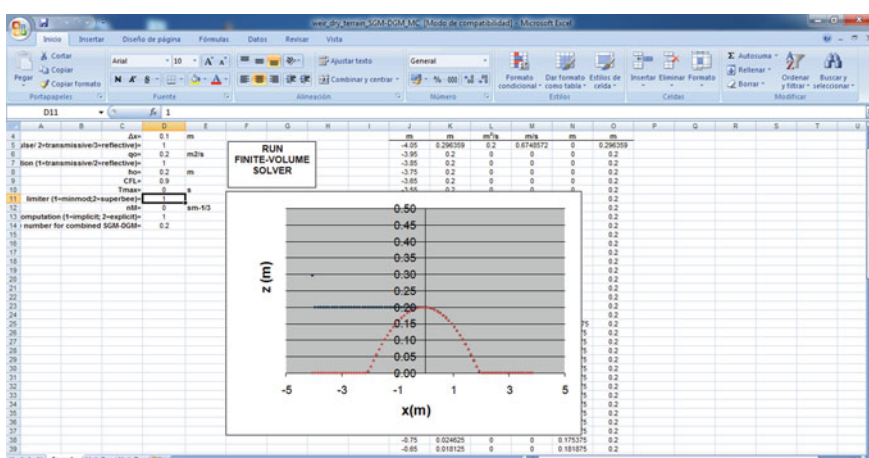


Fig. 12.2 Initial conditions running the solver for  $T_{\max} = 0$  s

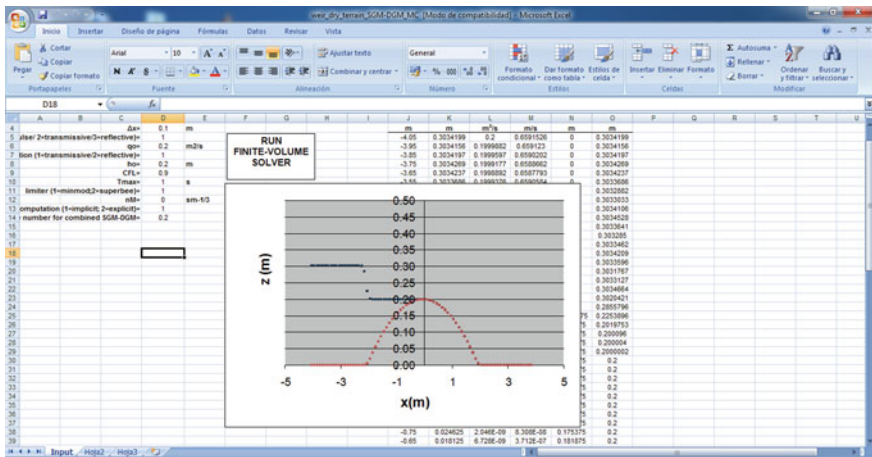


Fig. 12.3 Surge approaching the weir for  $T_{\max} = 1$  s

In this case we fix a constant discharge pulse at the inlet section and consider the tailwater section as an open boundary. Running the model for  $T_{\max} = 1$  s, we observe a surge approaching the weir crest (Fig. 12.3).

For  $T_{\max} = 2$  s, the bore is not yet at the weir crest (Fig. 12.4); note the deformation of the flow profile due to topography effects.

For  $T_{\max} = 2.5$  s, a dry front is propagated on the lee side of the weir (Fig. 12.5).

For  $T_{\max} = 3$  s, the dry front is propagated along the tailwater channel (Fig. 12.6).

For  $T_{\max} = 5$  s, the tailwater channel is wet (Fig. 12.7).

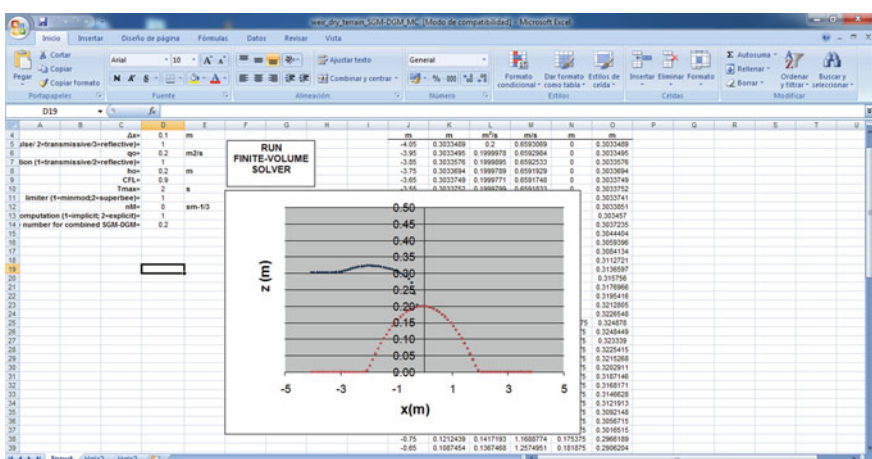


Fig. 12.4 Wave profile for  $T_{\max} = 2$  s

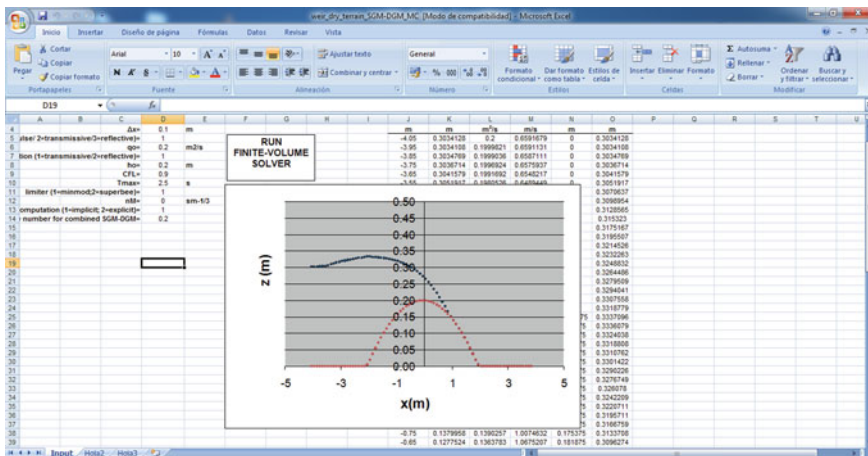


Fig. 12.5 Dry front propagation of the lee side of the weir for  $T_{\max} = 2.5$  s

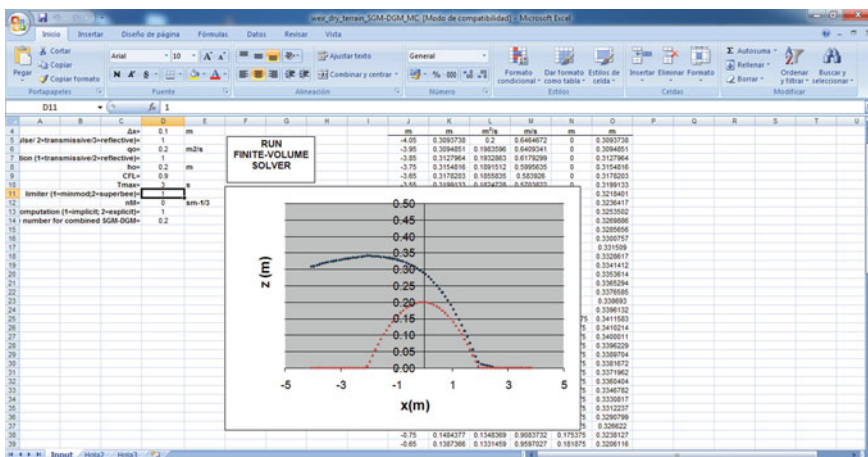


Fig. 12.6 Wetting of tailwater channel at  $T_{\max} = 3$  s

Now, let us change the boundary condition at the downstream section. If we model a solid wall, we must set option “2”. In this case, the dry front is reflected by the wall and a hydraulic jump propagates in the upstream direction, as seen below for  $T_{\max} = 6$  s (Fig. 12.8).

The user can also verify that the scheme is well-balanced; we set  $q_o = 0 \text{ m}^2/\text{s}$  and  $h_o = 0.15 \text{ m}$ , and run the model for  $T_{\max} = 50$  s. Note the horizontal free surface (Fig. 12.9).

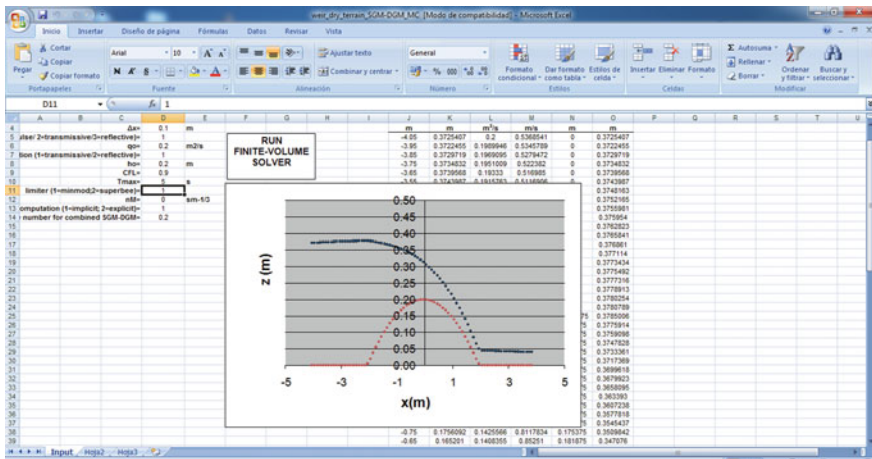


Fig. 12.7 Wet conditions along the entire computational domain for  $T_{\max} = 5$  s

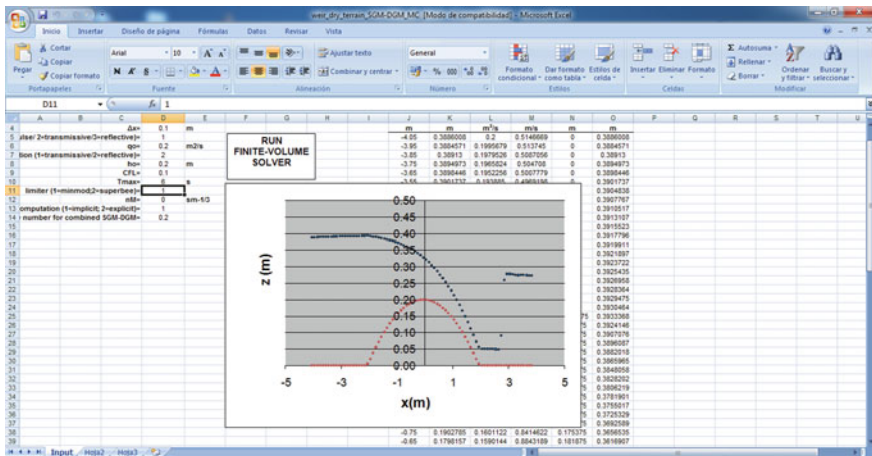
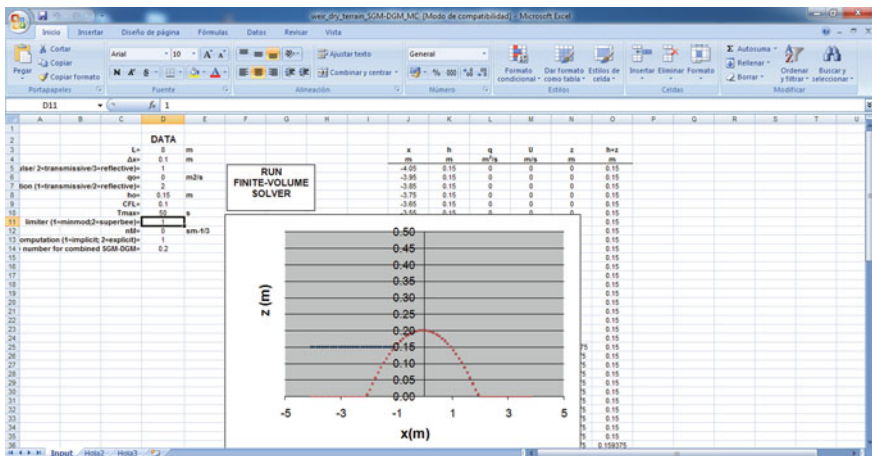


Fig. 12.8 Reflection of the wave for  $T_{\max} = 6$  s

Consider now the flooding if the upstream weir side is partially submerged, e.g.  $h_o = 0.1$  m; see simulation below for  $T_{\max} = 1$  s with a surge approaching the weir (Fig. 12.10).

During the run-up, a dry front is formed propagating in the downstream direction, while a surge propagates in the upstream direction; see simulation below for  $T_{\max} = 2$  s (Fig. 12.11).



**Fig. 12.9** Testing the C-property for  $T_{\max} = 50$  s

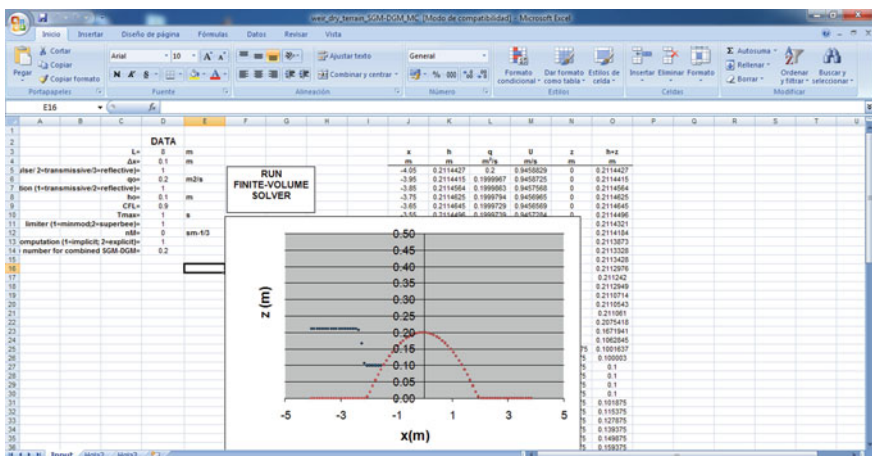


**Fig. 12.10** Surge approaching partially submerged weir for  $T_{\max} = 1$  s

For  $T_{\max} = 3$  s, the upstream surge is still propagating, while the dry front reaches the tailwater channel (Fig. 12.12).

The reader can access and edit the codes at the Vbasic editor (Fig. 12.13).

In the following sections examples on how to use the Library for homework assignment to students are presented.

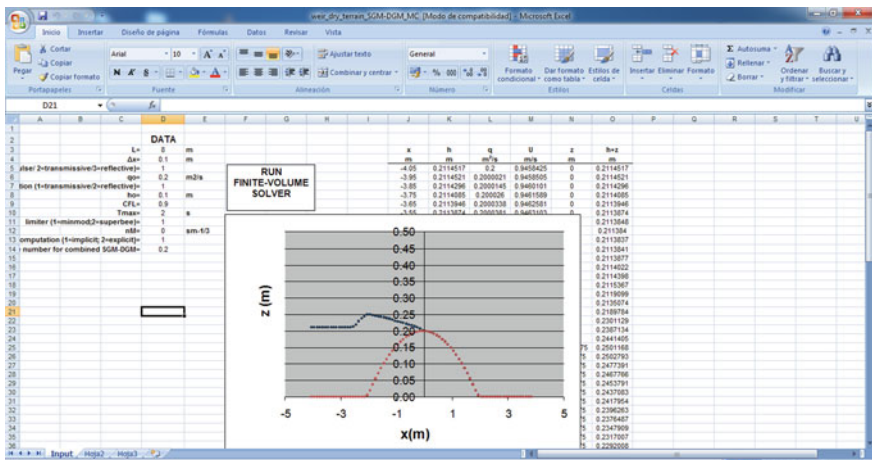


Fig. 12.11 Dry front and upstream surge for  $T_{\max} = 2$  s

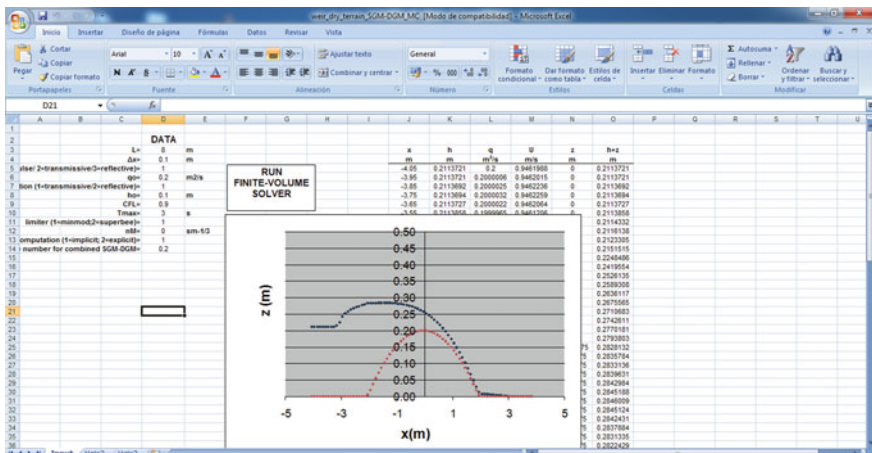
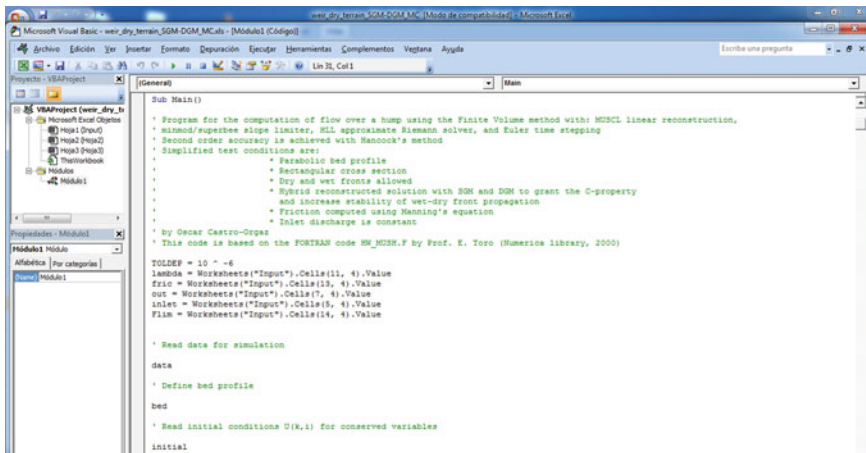


Fig. 12.12 Wave profile for  $T_{\max} = 3$  s

### 12.3.2 Example of Homework 1: Computation of Gradually-Varied Steady Flow Profiles

In this example students are requested to modify the former code “*weir\_dry\_terrain\_SGM-DGM\_MC.xls*” to compute the steady gradually-varied flow profiles presented in Chap. 3. In a first step, upon editing the code, the bed profile is modified to a constant slope prismatic channel (Fig. 12.14).

Step 2 is to modify boundary conditions to allow for sub- and supercritical flow profiles. Following the theory of Chap. 5, for the unsteady computation of a



```

Microsoft Visual Basic - weir_dry_terrain_SGM-DGM-MC.xls [Modo de compatibilidad] - Microsoft Excel
[General] Sub Main()
    ' Program for the computation of flow over a hump using the Finite Volume method with MUSCL linear reconstruction,
    ' minmod/extrapolate slope limiter, HLL approximate Riemann solver, and Euler time stepping
    ' Second order accuracy is achieved with Hancock's method
    ' Simplified test conditions are:
    ' * Uniform initial bed profile
    ' * Rectangular cross section
    ' * Dry and wet fronts allowed
    ' * Hybrid reconstructed solution with SGM and DGM to grant the C-property
    ' * advection term is treated by dry-front propagation
    ' * Friction computed using Manning's equation
    ' * Inlet discharge is constant
    ' by Oscar Castro-Orgaz
    ' This code is based on the FORTRAN code HM_MOSH.F by Prof. E. Toro (Numerics library, 2000)

TOLDEF = 1e-06
Input = Worksheets("Input").Cells(11, 4).Value
fric = Worksheets("Input").Cells(13, 4).Value
out = Worksheets("Input").Cells(7, 4).Value
inlet = Worksheets("Input").Cells(5, 4).Value
flim = Worksheets("Input").Cells(14, 4).Value

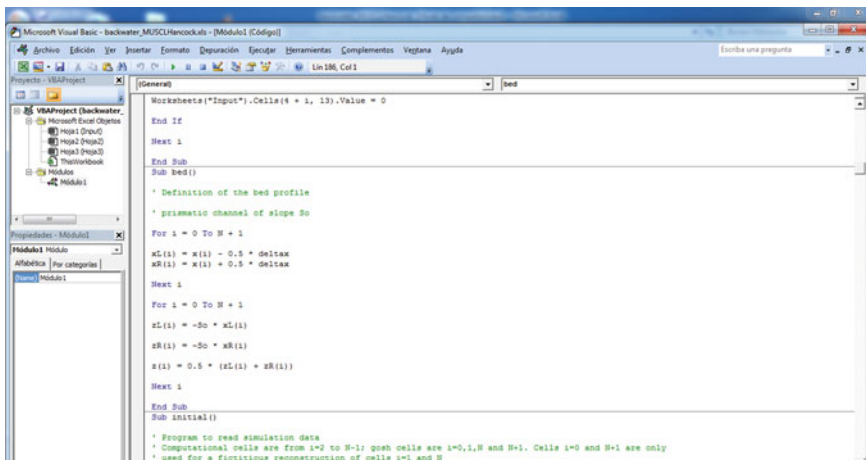
    ' Read data for simulation
    data
    ' Define bed profile
    bed
    ' Read initial conditions U(k,i) for conserved variables
    initial
End Sub

```

**Fig. 12.13** Access to the code inserted into the sheet

subcritical flow profile, one boundary condition is prescribed at the upstream section (typically the discharge), and another at the downstream section (typically the flow depth). For a supercritical profile, both boundary conditions are prescribed at the upstream section. The modification to the corresponding routine is seen in (Fig. 12.15).

Starting with the mesh at  $x = 0$ , Fig. 12.16 contains a computation of an S2 steady gradually-varied flow profile (see input data in the figure). The corresponding code is available at “*backwater\_MUSCLHancock.xls*”.



```

Microsoft Visual Basic - backwater_MUSCLHancock.xls [Modulo1 (Código)] - Microsoft Excel
[General] Sub bed()
    Worksheets("Input").Cells(4 + i, 13).Value = 0
    End If
    Next i
    End Sub
    Sub bed()
        ' Definition of the bed profile
        ' prismatic channel of slope 50
    For i = 0 To N + 1
    xL(i) = x(i) - 0.5 * deltax
    xR(i) = x(i) + 0.5 * deltax
    Next i
    For i = 0 To N + 1
    zL(i) = -50 * xL(i)
    zR(i) = -50 * xR(i)
    z(i) = 0.5 * (zL(i) + zR(i))
    Next i
    End Sub
    Sub initial()
        ' Program to read simulation data
        ' Computational cells are from i=2 to N-1; ghost cells are i=0,1,N and N+1. Cells i=0 and N+1 are only
        ' used for a fictitious reconstruction of cells i=1 and N
    End Sub
End Sub

```

**Fig. 12.14** Modification of bed profile for computation of gradually-varied flow profiles

The figure consists of three vertically stacked screenshots of the Microsoft Visual Basic Editor (VBE) interface. Each screenshot shows a different part of the VBA code for a 'boundary' module.

```

Sub boundary()
    ' Use ghost cells to set boundary conditions
    ' In subcritical flow the boundary conditions are the discharge at the upstream section, and the water depth
    ' at the downstream section
    ' In supercritical flow both water depth and discharge are prescribed at the upstream section
    ' INLET CONDITIONS
    '-----
    If flowtype = 1 Then
        'Subcritical flow at the inlet section
        'Inlet discharge fixed
        U(2, 1) = Qtarget
        U(2, 0) = Qtarget
        'Inlet flow depth computed
        U(1, 1) = U(1, 2)
        U(1, 0) = U(1, 2)
    End If

```

```

If flowtype = 2 Then
    'Supercritical flow at the inlet section
    'Inlet discharge fixed
    U(2, 1) = Qtarget
    U(2, 0) = Qtarget
    'Inlet flow depth fixed
    U(1, 1) = ho
    U(1, 0) = ho
End If
    ' OUTLET CONDITIONS
    '-----
    If flowtype = 1 Then
        'Subcritical flow at the outlet section
        'Outlet discharge computed
        U(2, N) = U(2, N - 1)
        U(2, N + 1) = U(2, N - 1)
        'Outlet flow depth fixed
        U(1, N) = ho
        U(1, N + 1) = ho
    End If

```

```

    U(1, N + 1) = ho
End If
If flowtype = 2 Then
    ' Transmissive condition at supercritical outlet section
    ' Depth and discharge computed
    For k = 1 To 2
        U(k, N) = U(k, N - 1)
        U(k, N + 1) = U(k, N - 2)
    Next k
End If
End Sub

```

**Fig. 12.15** Modification of boundary conditions for computation of gradually-varied flow profiles

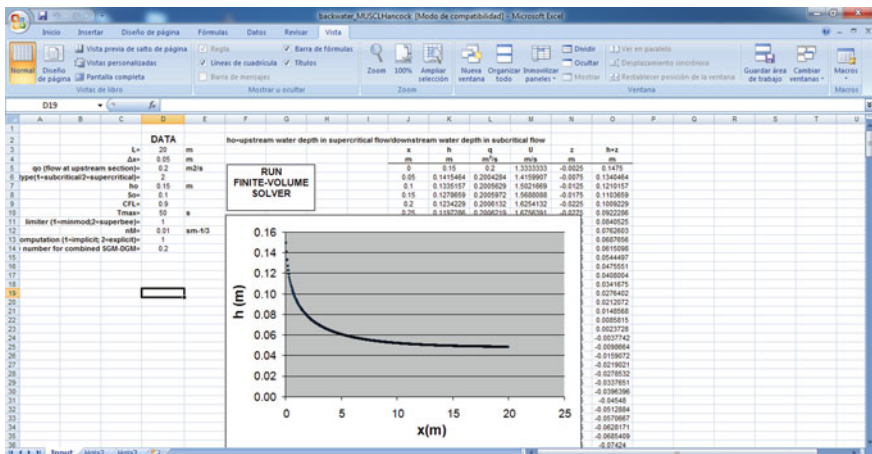


Fig. 12.16 Computation of S2 steady gradually-varied flow profile

In Step 3, students are asked to critically look at the correctness of the steady flow results produced by the unsteady flow solver. They are invited to compare with a steady flow solver based on the 4th-order Runge-Kutta method, presented in Chap. 3. The steady flow solver is available at “*steadyrk4.xls*”, and the results of both solvers are compared in Fig. 12.17, showing excellent agreement. This demonstrates the ability of the MUSCL-Hancock solver to converge to steady flow. Note that the unsteady program correctly approaches steady uniform flow, thus the discretization used for the friction source term is adequate.

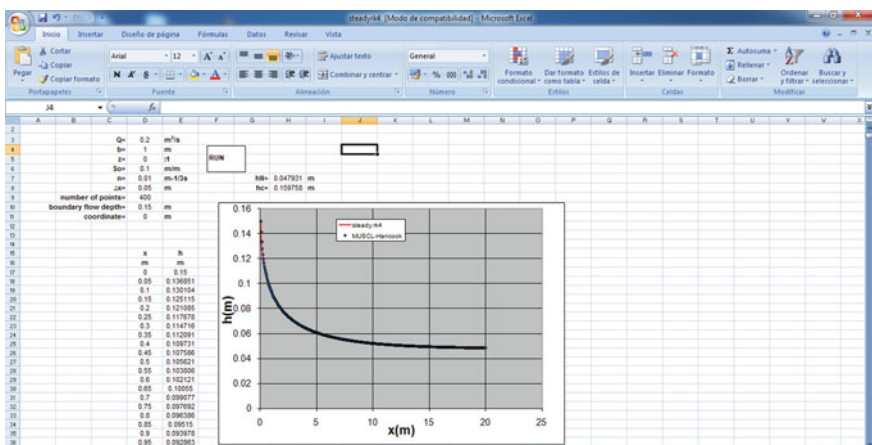


Fig. 12.17 Comparison of steady and unsteady flow solvers for S2 steady gradually-varied flow profile

### 12.3.3 Example of Homework 2: Wetting and Drying over Uneven Topography

Wetting and drying processes over uneven topography count among the most important problems in *Environmental Hydraulics*, including dam-break flows, run-up and overland flows produced by tsunamis, flooding in rivers, and flooding-draining of wetlands. Students are here requested to modify the code “*weir\_dry\_terrain\_SGM-DGM\_MC.xls*” to simulate wetting and drying processes over a bed profile of shape (units in m):

$$z_b = 0.7 \exp(-0.1x^2) + 0.3 \exp[-(x - 5)^2], \quad -7.9 \leq x \leq 7.9. \quad (12.1)$$

The topography is basically a smooth hump 0.7 m high, with an undulation on its lee side. For  $x > 0$ , the bed profile is a variable topography allowing to produce interesting flow transitions during wave run-up. Editing the code, the bed profile is defined as (Fig. 12.18).

The code is available at “*weir\_dry\_terrain\_complex.xls*”. Now, students are requested to generate a wave at  $x = 0$ , that will produce a wetting of the tailwater portion of the bed profile ( $x > 0$ ) while it travels downstream, and then force a run-up upon reflection on a wall. The purpose is to investigate the flow transitions during the motion of the wave across this highly variable terrain. For this task, reflective boundary conditions are prescribed at both ends of the computational model, and the initial condition to generate a wave is selected as dam-break type problem with  $h_o = 1$  m. Computations are conducted assuming frictionless flow. At  $T_{\max} = 1$  s, a dry front is observed travelling down the topography, thereby producing wetting of the terrain (Fig. 12.19).

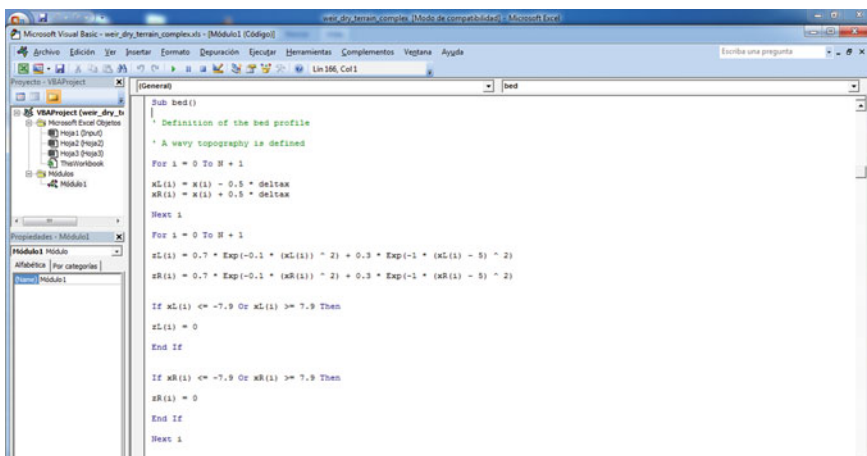


**Fig. 12.18** Modification of bed topography for simulation of wetting and drying processes

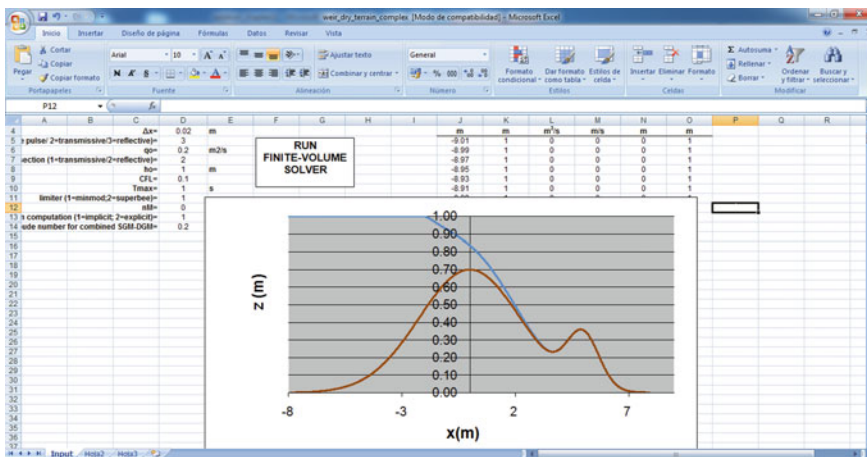


**Fig. 12.19** Wetting of terrain at  $T_{\max} = 1$  s

At  $T_{\max} = 6$  s the reflected flow at the wall produces a moving hydraulic jump travelling in the upstream direction (Fig. 12.20).

At  $T_{\max} = 12$  s the moving hydraulic jump is in its run-up over the lee-side undulation, which is covered with a shallow supercritical flow (Fig. 12.21).

At  $T_{\max} = 18$  s the moving hydraulic jump passes the lee-side undulation crest, and the resulting wave suffers a modification due to topographic effects (Fig. 12.22).

At  $T_{\max} = 21$  s, the front of the moving hydraulic jump is conducting a run-up over the sloping weir side, but at its tailwater portion a second shock front is formed past the lee-side undulation crest. The flow pattern is complex but extremely

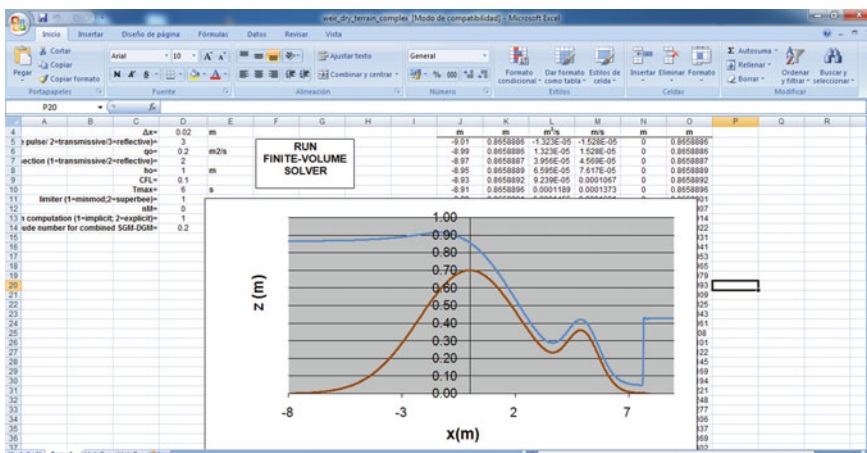


**Fig. 12.20** Moving hydraulic jump at  $T_{\max} = 6$  s

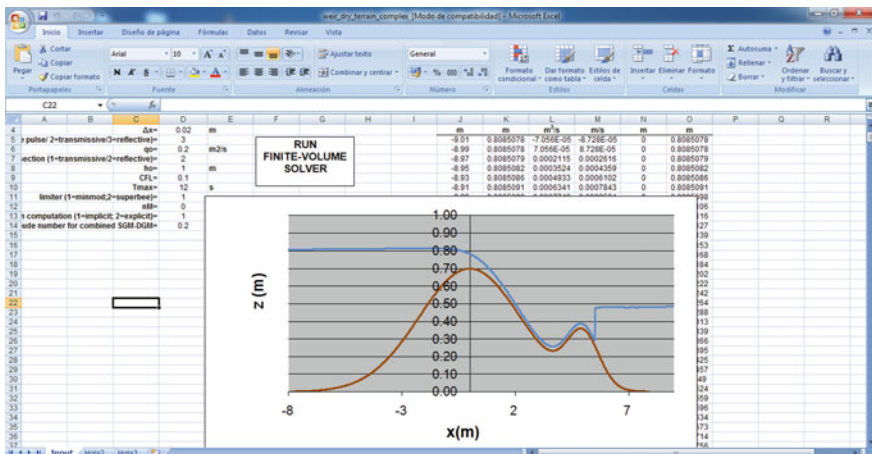


**Fig. 12.21** Moving hydraulic jump at  $T_{\max} = 12$  s

beautiful: an unsteady transcritical flow profile is formed at the lee-side hump, thereby forcing the formation of a second shock front at the tailwater portion of the water body that is in a run-up process over the sloping terrain (Fig. 12.23).

At  $T_{\max} = 23$  s the back-shock moves in the downstream direction towards the wall (Fig. 12.24).

Note the free surface depression at the lee-side hump crest, typical of a fully subcritical flow, and surge approaching the downstream wall, at  $T_{\max} = 25$  s (Fig. 12.25).

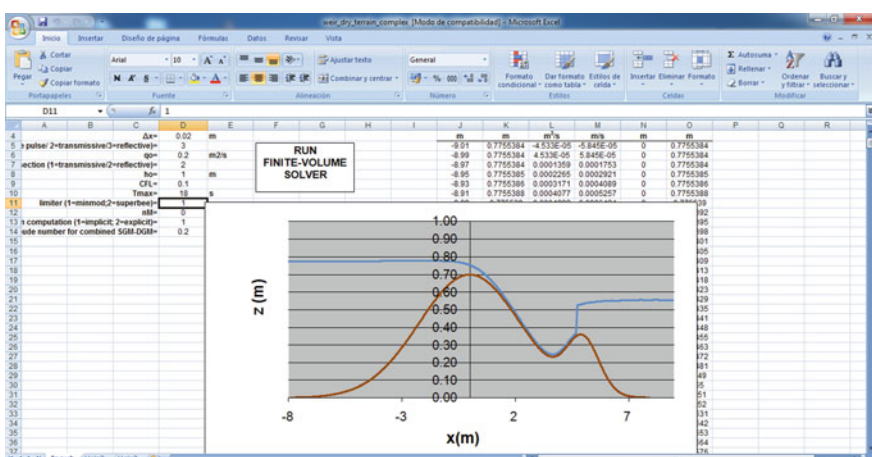


**Fig. 12.22** Moving hydraulic jump at  $T_{\max} = 18$  s

## 12.3 Using the Library

545

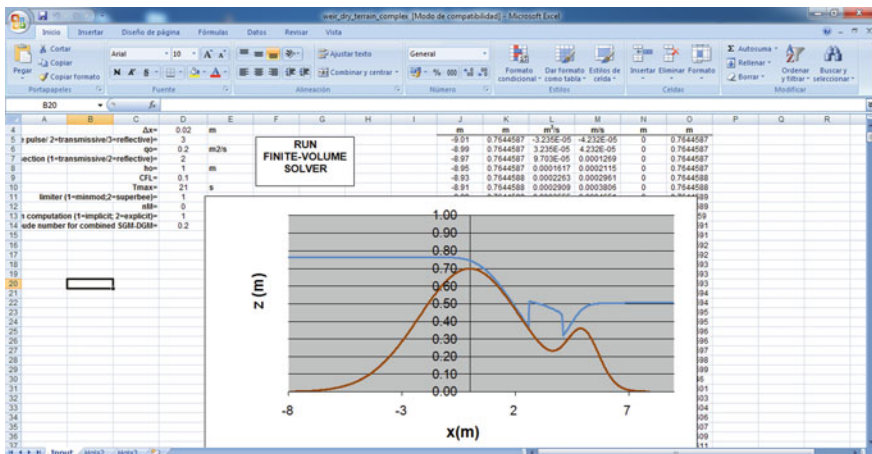


**Fig. 12.23** Continuous flow profile over the lee-side hump and two-shock wave pattern with run-up over the sloping terrain at  $T_{max} = 21$  s

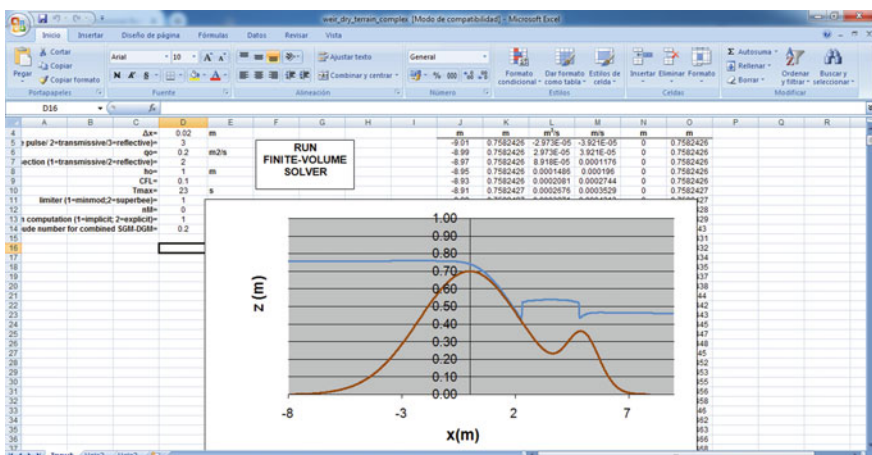


**Fig. 12.24** Flow profile at  $T_{max} = 23$  s

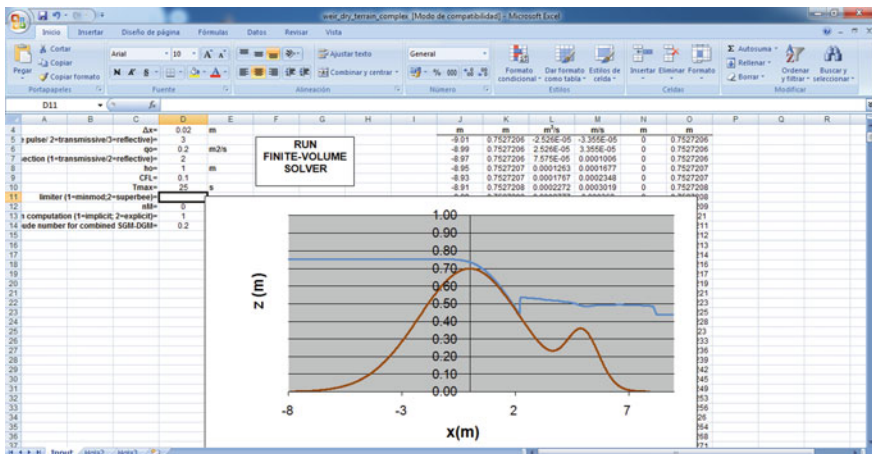


**Fig. 12.25** Flow profile at  $T_{\max} = 25$  s

### 12.3.4 Example of Homework 3: Study of Different Discretizations of the Friction Source Term

In this task, students are asked to go a step further and not only modify the bed profile, as also the initial and boundary conditions in the code, but actively contribute to add any new numerical component. To produce these skills, it is requested to investigate different discretizations of the friction source term. In Chap. 9 is presented the explicit discretization of the friction term as [see Eq. (9.107)]

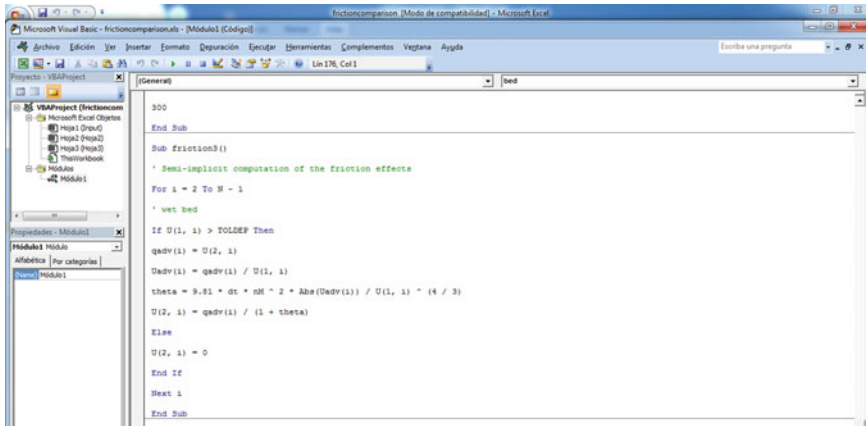
$$q_i^{k+1} = q_i^{\text{adv}} - (ghS_f)_i^{\text{adv}} \Delta t = q_i^{\text{adv}} - gn^2 \Delta t \frac{U_i^{\text{adv}} |U_i^{\text{adv}}|}{(h_i^{k+1})^{1/3}}, \quad (12.2)$$

where all the variables have the meaning as explained in Chap. 9. As previously stated, this solver works reasonably well for wet-bed conditions, but it may produce instabilities in propagation over dry terrain if friction is not limited [see Eq. (9.110)], given that its effect, at the limit, is to stop the flow. Thus, a flow reversal shall not be numerically permitted.

The implicit version of the model presented in Chap. 9 is [see Eq. (9.109)]

$$q_i^{k+1} = q_i^{\text{adv}} - (ghS_f)_i^{k+1} \Delta t = q_i^{\text{adv}} - \text{sg}(q_i^{\text{adv}}) gn^2 \Delta t \frac{(U_i^{k+1})^2}{(h_i^{k+1})^{1/3}}, \quad (12.3)$$

resulting in the quadratic equation



```

Sub friction3()
    ' Semi-implicit computation of the friction effects
    For i = 2 To N - 1
        ' wet bed
        If U(i, i) > TOLDEF Then
            qadv(i) = U(2, i)
            Uadv(i) = qadv(i) / U(i, i)
            theta = 9.81 * dt * m * 2 * Abs(Uadv(i)) / U(i, i)^(4 / 3)
            U(2, i) = qadv(i) / (1 + theta)
        Else
            U(2, i) = 0
        End If
        Next i
    End Sub

```

**Fig. 12.26** Implementation of semi-implicit friction computation

$$\frac{sg(q_i^{adv})gn^2\Delta t}{(h_i^{k+1})^{4/3}}(U_i^{k+1})^2 + U_i^{k+1} - \frac{q_i^{adv}}{h_i^{k+1}} = 0, \quad (12.4)$$

where the sign of the advection estimation of the flow is used to get a physically correct solution. Implicit and explicit solvers are available in the programs used by students during the practical sessions. Now, the task is to produce and implement a new option for the code allowing for a semi-implicit treatment of friction. A possible semi-implicit treatment is given by the statement

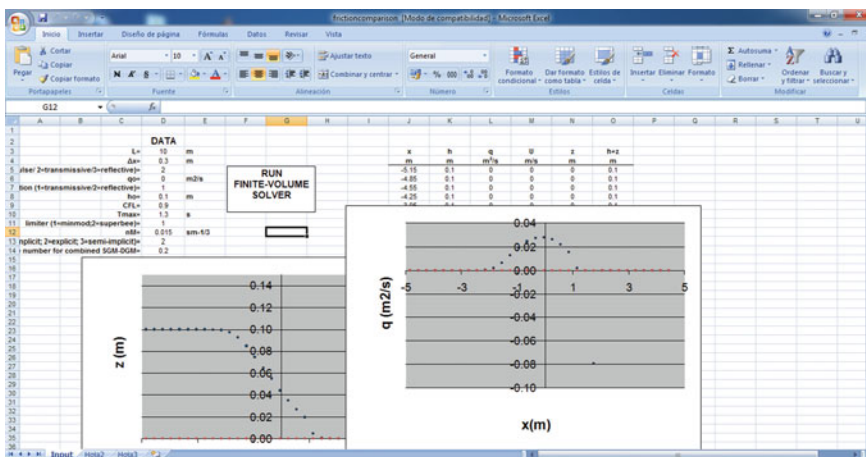


**Fig. 12.27** Computational results for explicit estimation of friction effects

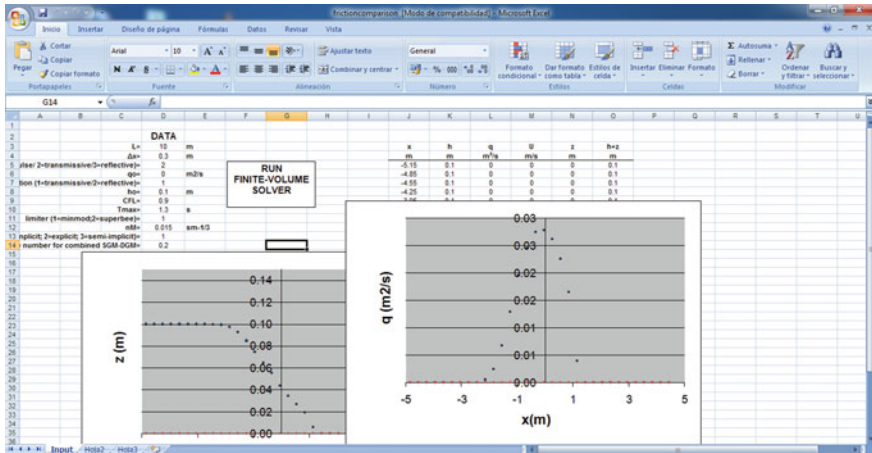


Fig. 12.28 Computational results for implicit estimation of friction effects

$$q_i^{k+1} = q_i^{\text{adv}} - gn^2 \Delta t \frac{U_i^{k+1} |U_i^{\text{adv}}|}{(h_i^{k+1})^{1/3}}, \quad (12.5)$$

from which follows the updating formula

$$U_i^{k+1} = \frac{U_i^{\text{adv}}}{1 + gn^2 \Delta t \frac{|U_i^{\text{adv}}|}{(h_i^{k+1})^{4/3}}}. \quad (12.6)$$

Therefore, the new routine requested to the students based on their analytical development is as follows (Fig. 12.26).

The resulting code is available in "frictioncomparison.xls", which was tailored to simulate dam break waves over horizontal beds. A first run was conducted using Eq. (12.2) without limiting the maximum value of the friction force (Fig. 12.27), thereby resulting in instabilities of the wet-dry front due to flow reversal ( $q < 0$ ). Therefore, computations are aborted shortly after this numerical artifact. This test reveals the importance of limiting the friction force in explicit computations. Implicit (Fig. 12.28) and semi-implicit (Fig. 12.29) simulations were both stable and similar to each other.

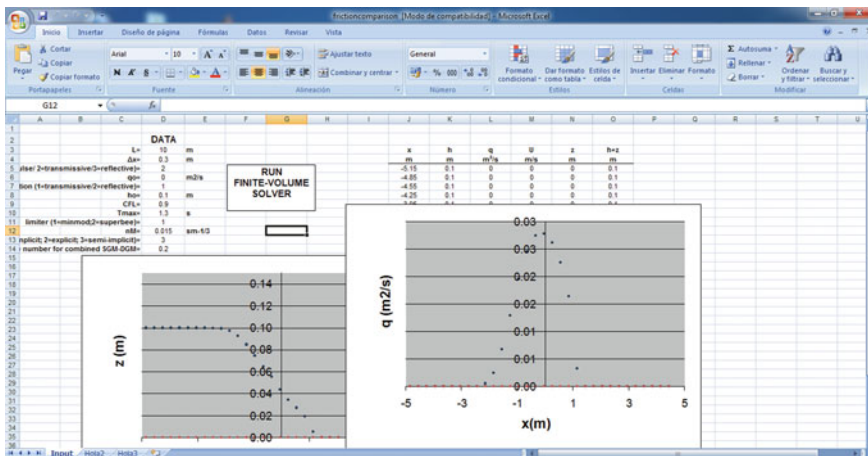


**Fig. 12.29** Computational results for semi-implicit estimation of friction effects

### 12.3.5 Example of Homework 4: Surge Reflection at a Wall

The purpose of this homework is to make the students critically assess the behavior of a code, without assuming that it works simply because computations are not crashed. Specifically, they are asked to demonstrate that the implementation of the reflective boundary condition is producing good physical results. At a solid wall,  $\mathbf{U}$  and  $\mathbf{F}$  are given by

$$\mathbf{U} = \begin{pmatrix} h \\ Uh \end{pmatrix} = \begin{pmatrix} h \\ 0 \end{pmatrix}, \quad \mathbf{F} = \begin{pmatrix} Uh \\ U^2 h + \frac{1}{2} gh^2 \end{pmatrix} = \begin{pmatrix} 0 \\ \frac{1}{2} gh^2 \end{pmatrix}. \quad (12.7)$$

A solid wall is modelled in the MUSCL-Hancock (second-order in space and time) solver as [see Eq. (9.168)]

$$\begin{aligned} q_N^{k+1} &= -q_{N-1}^{k+1}, \\ q_{N+1}^{k+1} &= -q_{N-2}^{k+1}, \\ h_N^{k+1} &= h_{N-1}^{k+1}, \\ h_{N+1}^{k+1} &= h_{N-2}^{k+1}, \end{aligned} \quad (12.8)$$

which produces at the last computational cell a numerical flux of

$$\mathbf{F}_{N-1/2} = \begin{pmatrix} 0 \\ \frac{1}{2} gh_{N-1}^2 \end{pmatrix}. \quad (12.9)$$

The method to check the accuracy of the implementation compares a numerically-reflected surge with its analytical counterpart. To check the implementation, we consider a surge travelling in the positive  $x$ -direction to be reflected upon arriving at a solid wall. Its analytical solution is with  $V_w$  as the absolute surge velocity, and subscripts 1 and 2 denoting conditions behind and in front of the surge [see Eq. (7.102)]

$$\mathbf{U}(x, t) = \begin{cases} \mathbf{U}_1 & \text{if } x < x_o + V_w(t - t_o) \\ \mathbf{U}_2 & \text{if } x > x_o + V_w(t - t_o) \end{cases}. \quad (12.10)$$

The discontinuity is located at  $x = x_o$  at start  $t = t_o$ . If a surge is reflected at a wall, the downstream values consist in a static water layer of depth  $h_2$  forced by the solid barrier, to be determined by using the conservation laws across the surge. The vector  $\mathbf{U}$  is thus

$$\mathbf{U}(x, t) = \begin{cases} \mathbf{U}_1 = \begin{pmatrix} h_1 \\ q_1 \end{pmatrix} & x < x_o + V_w(t - t_o) \\ \mathbf{U}_2 = \begin{pmatrix} h_2 \\ 0 \end{pmatrix} & x > x_o + V_w(t - t_o) \end{cases}. \quad (12.11)$$

The surge mass conservation states [Eq. (7.103)]

$$V_w = \frac{U_1 h_1 - U_2 h_2}{h_1 - h_2}, \quad (12.12)$$

whereas the momentum equation is [Eq. (7.104)]

$$V_w = U_2 + \text{sg} \left[ \frac{g h_1}{2 h_2} (h_1 + h_2) \right]^{1/2}, \quad (12.13)$$

where  $\text{sg} = \pm 1$ , depending on the direction selected for surge propagation. Combining Eqs. (12.12) and (12.13) results in

$$q_1 = U_2 h_1 + (h_1 - h_2) \text{sg} \left[ \frac{g h_1}{2 h_2} (h_1 + h_2) \right]^{1/2}. \quad (12.14)$$

A horizontal and frictionless channel 8 m long is considered in this test; see Fig. 12.30 for detailed test conditions. For the positive surge stage approaching the wall ( $\text{sg} = +1$ ), we select the test data  $q_1 = 0.2 \text{ m}^2/\text{s}$ ,  $h_2 = 0.1 \text{ m}$  and  $U_2 = 0 \text{ m/s}$  ( $x_o = 0 \text{ m}$ ,  $t_o = 0 \text{ s}$ ), resulting in  $V_w = +1.796 \text{ m/s}$  and  $h_1 = 0.2113 \text{ m}$  by solving Eqs. (12.13)–(12.14). The positive surge arrives at the end of the channel at  $t = 4.4532 \text{ s}$ , thus  $x_o = 8 \text{ m}$  and  $t_o = 4.4532 \text{ s}$  for the reflected surge. For the reflection at a wall ( $\text{sg} = -1$ ),  $q_1 = 0.2 \text{ m}^2/\text{s}$ ,  $h_1 = 0.2113 \text{ m}$ ,  $q_2 = 0 \text{ m}^2/\text{s}$ , resulting

in  $V_w = -1.277$  m/s and  $h_2 = 0.3679$  m. The analytical solution was easily constructed with the solver previously presented in Chap. 7 (*Surgeanalytical.xls*). The solution of the MUSCL-Hancock solver is compared with the analytical solution at the approaching stage to the wall ( $T_{\max} = 3.5$  s, Fig. 12.30), and after reflection, at  $T_{\max} = 7.453$  s (Fig. 12.31). The agreement of the numerical and analytical results is excellent before and after reflection, thereby confirming that the solid walls are correctly modeled in the numerical solver.

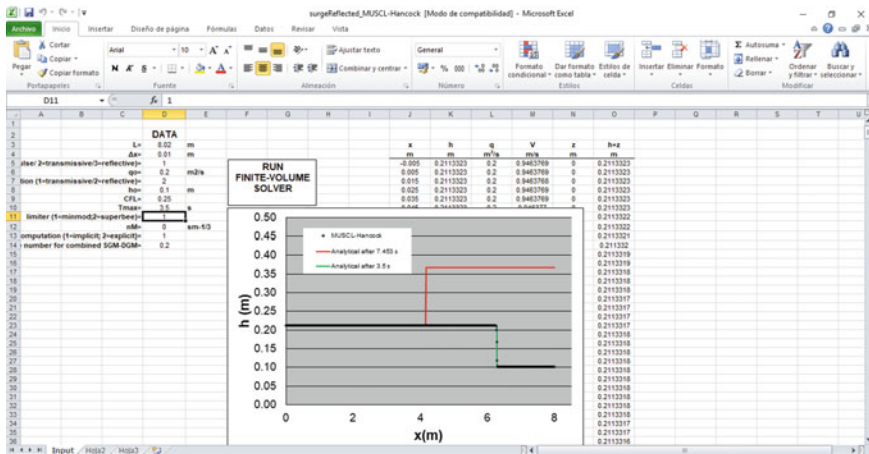


**Fig. 12.30** Numerical prediction of surge approaching the wall at  $T_{\max} = 3.5$  s

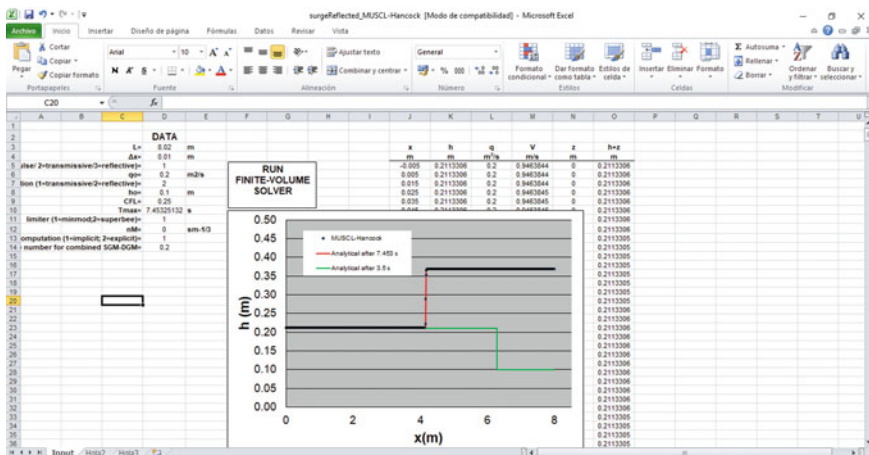


**Fig. 12.31** Numerical prediction of reflected surge at  $T_{\max} = 7.453$  s

### 12.3.6 Example of Homework 5: Analytical Solution for Transcritical Weir Flow

The purpose of this task is to construct an analytical solution of transcritical weir flow for an exponential variation of the primitive variables ( $h$ ,  $U$ ). The practical utility of this development is its use to check the convergence to steady transcritical flow of the unsteady flow computations. The process consists in setting the desired analytical solution to the primitive variables, and then resort to the steady momentum equation to find a bed profile compatible with this solution. Let the desired exponential variation of the primitive variables be

$$\begin{aligned} h(x) &= h_o \exp(-\alpha x), \\ U(x) &= U_o \exp(+\alpha x). \end{aligned} \quad (12.15)$$

Here  $\alpha$  is a coefficient controlling the shape of the profile and “ $o$ ” refers to the approach flow conditions. The parameter can be determined by selecting a target flow depth  $h_d$  at distance  $L$  from the inlet section, thus resulting in

$$\alpha = -\frac{1}{L} \ln\left(\frac{h_d}{h_o}\right). \quad (12.16)$$

Note that the discharge produced by the solution given by Eqs. (12.15) is

$$q(x) = U(x)h(x) = U_o h_o = \text{const.}, \quad (12.17)$$

as required in steady flow without sources or sinks of mass. The Froude number is for Eq. (12.15)

$$F = \frac{U}{(gh)^{1/2}} = \frac{U_o}{(gh_o)^{1/2}} \exp\left(\frac{3}{2}\alpha x\right), \quad (12.18)$$

which easily reveals the position of the critical point of the free surface profile from

$$F = 1 \Rightarrow x_c = \frac{2}{3\alpha} \ln(F_o^{-1}). \quad (12.19)$$

The steady momentum equation reads

$$\frac{d}{dx}(U^2 h + \frac{1}{2} g h^2) = -g h \frac{dz_b}{dx}. \quad (12.20)$$

The momentum function  $M$  is thus, using Eq. (12.15),

$$M = U^2 h + \frac{1}{2} g h^2 = U_o^2 h_o [\exp(\alpha x)] + \frac{1}{2} g h_o^2 [\exp(-2\alpha x)]. \quad (12.21)$$

Inserting this result into Eq. (12.20), the ODE describing the weir bed profile is

$$\frac{dz_b}{dx} = -\frac{U_o^2}{g} \alpha \exp(2\alpha x) + \alpha h_o \exp(-\alpha x). \quad (12.22)$$

Integration of this equation is simple, resulting in

$$z_b(x) = \left( h_o + \frac{U_o^2}{2g} \right) - h_o \exp(-\alpha x) - \frac{U_o^2}{2g} \exp(2\alpha x). \quad (12.23)$$

This is the bed profile compatible with the analytical solution given by Eq. (12.15) for weir flow. Finally, the free surface position is

$$z_s(x) = h(x) + z_b(x) = \left( h_o + \frac{U_o^2}{2g} \right) - \frac{U_o^2}{2g} \exp(2\alpha x). \quad (12.24)$$

It is simple to check analytically an important concept explained in Chap. 4, namely the critical point of weir flow. At the location where the Froude number is unity, there must be an extreme in the bottom topography, e.g., the crest of a weir for the transition from sub- to supercritical flow. Manipulation of Eq. (12.22) produces

$$\frac{dz_b}{dx} = \alpha h_o \exp(-\alpha x) \left[ 1 - \frac{U_o^2}{gh_o} \exp(3\alpha x) \right] = \alpha h (1 - F^2), \quad (12.25)$$

from which follows analytically the important result

$$F = 1 \Rightarrow \frac{dz_b}{dx} = 0. \quad (12.26)$$

The purpose of this task is first to motivate students to do analytical developments and manipulate the equations of motion. The result, aside from being an interesting mathematical exercise, is especially illustrative to clarify concepts relating to steady weir flow, namely the critical point. The analytical solution enables to check all the aspects with little effort. Second, the final solution is of utility to check the convergence of unsteady solvers to steady flow. Modification of the previous unsteady flow solver only entail an update of the bed profile, as previously explained. The MUSCL-Hancock solver is checked against the analytical solution in Fig. 12.32, where both the velocity and free surface position are excellently reproduced. In this test,  $q = 0.1 \text{ m}^2/\text{s}$ , so roughly  $h_c = 0.1 \text{ m}$ . We have fixed the critical depth about 1 m downstream from the inlet, resulting in  $\alpha \approx 1.386$ . The approach flow depth is 0.4 m.

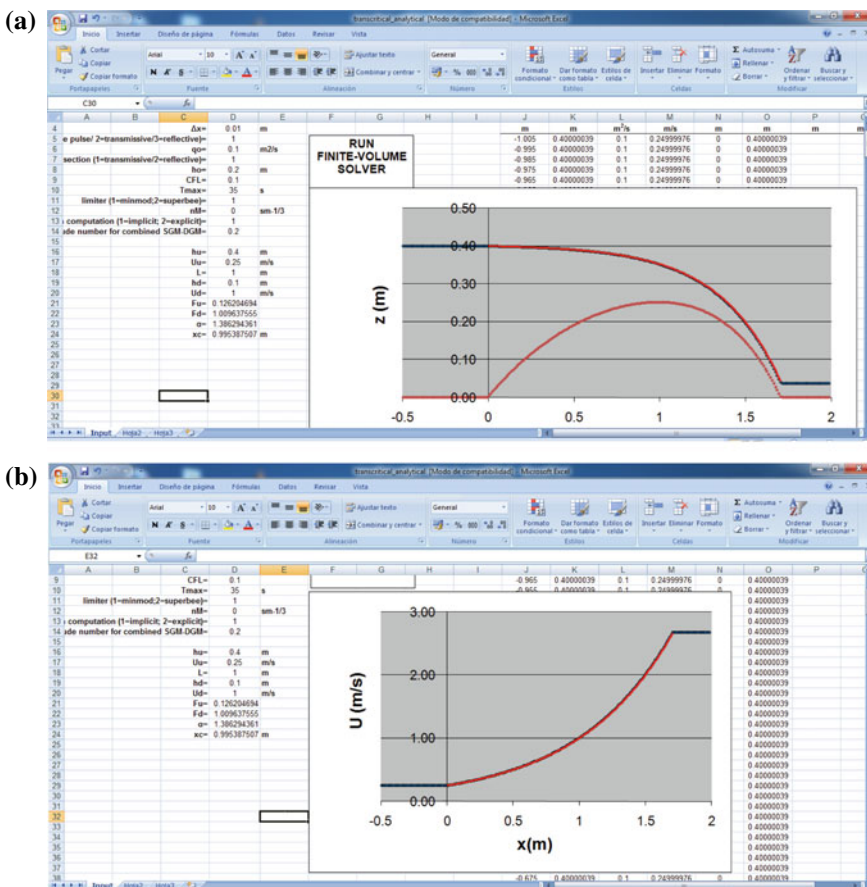


**Fig. 12.32** Analytical (red line) and numerical (blue points) solutions for weir flow: **a** free surface position **b** fluid velocity

In the above presentation, it is shown how a numerical solver can be easily implemented and run as a Vbasic script in Excel, to teach students during their first contact with the computation of open channel flows. Instructors can easily modify the material to suit their specific needs while teaching. It is fairly simple to translate the same logic to Fortran, where the programs would run faster, which is in fact a desirable exercise to those students interested in taking more advanced courses after the introduction presented in this book. In turn, the solvers presented in the Library are slow if a dense mesh is considered, e.g., during the check of mesh-independence results. However, this is a sacrifice to be accepted, given that debugging is simple in the Vbasic scripts, which is considered a desirable feature for beginners while taking the lessons and “getting their hands dirty” with a computational code for the first time.

## References

- Fenton, J.D. (2010). *Numerical methods*. Lecture notes, Vienna, Austria: Vienna University of Technology.
- Toro, E. F. (2000). *HYPER\_WAT: Library of 13 source codes for solving the non-linear time-dependent shallow water equations in one and two space dimensions*. Cheadle: NUMERITEK Ltd.
- Toro, E. F. (2001). *Shock-capturing methods for free-surface shallow flows*. New York: Wiley.

# Author Index

## A

- Abbott, M. B., 235  
Abramowitz, M., 470  
Ackers, P., 59, 119, 121  
Alcrudo, F., 294, 309  
Anderson, J. D., 274, 277, 281, 282, 283  
Apelt, C., 436, 437  
Apelt, C. J., 161, 171, 172  
Aureli, F., 385, 386, 388  
Ayuso, J. L., 41, 63, 66, 245, 246, 430, 461

## B

- Babbitt, H. E., 175  
Bakhmeteff, B. A., 54, 56, 97, 98, 147  
Barthelemy, E., 441, 462  
Baumann, E. R., 175  
Bélanger, J. B., 99, 138, 169, 191  
Benjamin, T. B., 465  
Bermudez, A., 297, 371, 375  
Bhallamudi, S. M., 279, 280  
Biot, M. A., 187  
Blau, E., 76, 196, 197, 444  
Bonneton, P., 441, 462  
Bos, M. G., 59, 117  
Boussinesq, J., 5, 438  
Bradford, S. F., 370, 382  
Bresse, J., 163, 165, 166  
Bretz, N. V., 100  
Brocchini, M., 369  
Brufau, P., 375  
Brunner, G. W., 166, 168

## C

- Canale, R. P., 171

- Cantero-Chinchilla, F. N., 41, 430, 433, 435, 446, 452, 459, 461, 464, 476, 478, 479  
Cao, Z., 420, 424, 427  
Capart, H., 423, 427–429  
Carling, P., 420, 424, 427  
Castro-Orgaz, O., 41, 60, 63, 66, 98, 118, 119, 121, 122, 124, 125, 130, 132, 184, 186, 187, 189, 196, 241, 268, 402–404, 430, 433, 435, 438–443, 445–448, 452, 454, 455, 458–461, 464, 465, 476, 478, 479  
Causon, D. M., 386, 468  
Chanson, H., 20, 55, 81, 119, 138, 139, 187, 196, 205, 232, 241, 253, 268, 396, 402–404, 445, 449, 450  
Chapra, S. C., 171  
Chaudhry, M. H., 5, 6, 20, 31, 37, 67, 141–143, 151, 156, 170–172, 189, 198, 199, 201–205, 207, 214, 216, 217, 275, 279, 281, 283, 286, 287, 292, 293, 300, 365, 399–402, 461, 470, 471  
Chazel, F., 441, 462  
Chen, C. L., 6, 25  
Chen, J., 187, 188  
Chow, V. T., 5, 6, 20, 25, 29, 38, 63, 67, 70, 118, 141, 147, 152, 154, 156, 165, 166, 179, 187, 205, 207, 234, 236, 237, 243, 245, 248, 253  
Chu, C. R., 295  
Cienfuegos, R., 441, 462, 471  
Cimorelli, L., 332  
Colella, P., 378  
Courant, R., 277, 283  
Covelli, C., 332  
Cozzolino, L., 332

Cunge, J. A., 29, 30, 201–203, 205, 210, 214–216, 238–240, 278, 288, 365, 376

**D**

Dawson, J. H., 116

Della Morte, R., 332

Denlinger, R. P., 8, 35, 39

De Saint-Venant, A. B., 5, 202, 211

Dey, S., 41, 130, 132, 430, 433, 461

Dias, F., 462

Dodd, N., 369

Dracos, T., 187, 188

Dressler, R., 268, 396

Dressler, R. F., 7, 257, 260

**E**

Erduran, K. S., 473

Escoffier, F. F., 187

Evers, F. M., 410

**F**

Favre, H., 205, 305, 308, 396, 400

Fennema, R. J., 293

Fenton, J. D., 141, 142, 244–247, 447, 493

Flannery, B. P., 134

Fornberg, B., 470

Fraccarollo, L., 423, 427, 429

Fread, D. L., 161, 166, 167

Friedrichs, K., 277, 283

**G**

Garcia-Navarro, P., 286, 288, 294, 307–309

Gardner, C. S., 461

Gersten, K., 7

Gharangik, A. M., 198, 199, 287, 293, 399–401

Giraldez, J. V., 37, 63, 66, 458, 459

Glaister, P., 368

Godunov, S. K., 313, 355, 358, 378

Gottlieb, S., 373, 473

Greco, M., 427

Greco, V., 334, 336, 340–345

Green, A. E., 439, 461

Grilli, S. T., 467

Guinot, V., 313, 461

**H**

Hafsteinsson, H. J., 410

Hager, W. H., 3–5, 10, 21, 23, 34, 37, 38, 60–64, 76, 93, 109, 116, 118, 119, 121, 122, 124, 126, 137, 184, 186, 187, 189, 241, 247, 268, 410, 427, 433, 435, 438–443, 445–448, 454, 455, 458, 459, 464, 465

Hancock, S. L., 383

Harbaugh, T. E., 161, 166, 167

Harleman, D. R. F., 111

Harrison, A. J. M., 59, 119, 121

Harten, A., 355, 361

Hasumi, M., 176, 455

Henderson, F. M., 5, 20, 38, 55, 59, 60, 67, 75, 77, 94, 105, 117, 118, 130, 140, 147, 184, 186, 187, 205, 235, 237–239, 253, 254, 260, 285, 313, 472

Henry, H. R., 132

Hicks, F. E., 216

Hirsch, C., 290, 292, 293, 296, 367

Hoffman, J. D., 73, 74, 134, 144, 264, 273–276, 290, 292, 305, 319, 367, 372, 449, 471

Holly, F. M., 29, 30, 201–203, 205, 216, 278, 288, 376

Hosking, R. J., 196, 198, 403, 404, 446, 447, 451–453, 475

Hosoda, T., 447, 448

Hseng, M., 295

Hutter, K., 7, 37, 438, 458–460

**I**

Iervolino, M., 427

Ilic, S., 473

Ingram, D. M., 385, 386, 388, 402, 468

Ippen, A. T., 109–111, 113, 114, 116

Isaacson, E., 277, 283

Iverson, R. M., 8–10, 17, 35, 39

Iwasa, Y., 187

**J**

Jaeger, C., 6, 30, 51, 52, 54, 59, 66, 94, 142, 165, 438

Jain, S. C., 5–7, 25, 30, 51, 53–55, 65, 77, 108, 110, 117, 141, 147, 151, 156, 161, 179, 180, 192, 202, 205, 209, 215, 217, 218, 231, 232, 237, 253–255, 257, 263, 285, 286, 313, 317, 332, 335, 337, 341, 344, 390

Jameson, A., 293, 300

Jan, C.-D., 165

Jeppson, R., 55, 73, 81, 97, 102, 105, 132, 144, 313, 344

Jia, Y., 421, 423

Jin, Y. C., 8, 19, 33, 34, 39, 435

**K**

Karni, S., 347

Katopodes, N. D., 19, 32, 171, 216, 240, 313, 344

Keulegan, G. H., 6, 28

- Khafagi, A., 91  
Khan, A. A., 4, 8, 21, 33, 35, 36, 39, 217, 368–370, 373, 376, 400, 425, 464, 478  
Kirby, J. T., 467  
Kirschmer, O., 253, 266  
Kocaman, S., 268, 394–398, 405–407, 484–486  
Kutija, V., 473
- L**  
Lai, C., 6, 216  
Lai, W., 217, 368–370, 373, 376, 400  
Lannes, D., 441, 462  
Lauber, G., 268, 396  
Lauffer, H., 38  
Lawrence, G. A., 439, 447  
Lax, P., 279, 284, 365  
Lax, P. D., 279, 365  
Lecaros, R., 469  
Lee, M. T., 175  
Le Méhauté, B., 32  
Leopardi, A., 427  
Lesleighter, E., 456  
LeVeque, R. J., 205, 313, 344, 351, 367, 390, 391, 402, 471, 472  
Lewy, H., 277, 283  
Liggett, J. A., 5, 6, 19, 28, 52, 67, 93, 106, 112, 114, 115, 123, 189, 207, 231, 278, 288  
Lighthill, M. J., 237, 238, 465  
López-Ríos, J. C., 469
- M**  
MacCormack, R. W., 291  
Macdonald, I., 215, 223, 225  
Maidment, D. R., 29, 207, 234, 236, 237, 243, 245, 248  
Maranzoni, A., 385, 386, 388  
Marche, F., 441, 462  
Marchi, E., 438, 439  
Margolin, L. G., 456, 461  
Massé, P., 183, 186, 187  
Mateos, L., 130, 132  
Matthew, G. D., 124, 438–440, 442, 446, 451  
Mays, L. W., 29, 207, 234, 236, 237, 243, 245, 248  
McPherson, B., 456  
Mignosa, P., 385, 386, 388  
Mignot, E., 471  
Milewski, P., 462  
Mingham, C. G., 386, 468  
Mohapatra, P. K., 461, 470, 471  
Montecinos, G. I., 469  
Montes, J. S., 5, 6, 20, 28, 30, 33, 51, 52, 54, 55, 59, 61, 66, 76, 93, 94, 99, 105, 112, 114, 117–119, 121–127, 137, 138, 150, 167, 187, 210, 216, 232, 241, 261, 278, 438, 443, 454  
Montuori, C., 334–336, 340–345
- N**  
Nadiga, B. T., 456, 461  
Naghdi, P. M., 439, 447, 461  
Nujic, M., 388  
Nwogu, O., 464
- O**  
O’Connell, D. R. H., 8, 39  
Onda, S., 447, 448  
Ortega, J. H., 469  
Ouyang, C., 8, 10  
Ozmen-Cagatay, H., 268, 394–398, 405–407, 484–486
- P**  
Patterson, G. W., 6, 28  
Pender, G., 420, 424, 427  
Percy, A., 121  
Peregrine, D. H., 205, 462  
Perkins, J. A., 59, 119, 121  
Pianese, D., 332  
Poincaré, H., 187  
Pontillo, M., 427  
Popinet, S., 480  
Posey, C. J., 147, 165  
Press, W. H., 134  
Pudasaini, S. P., 7  
Puertas, J., 71–73, 141, 148, 150, 151, 186, 192, 193
- R**  
Ré, R., 253  
Rees, M., 277, 283  
Regamey, J.-M., 247  
Renouard, D. P., 462  
Richtmyer, R. D., 284  
Riddette, K., 456  
Riemann, B., 313  
Ritter, A., 253, 259, 393  
Roache, P. J., 215, 276, 277, 351  
Roberts, S., 280, 281, 293, 297, 303, 321–324, 393  
Roberts, W. W., 383  
Rodi, W., 17  
Roe, P. L., 368  
Roth, A., 126  
Rouse, H., 7, 52, 55, 79, 80, 85, 87, 88, 117, 118, 122, 124–126, 139, 156, 161, 165, 408, 436, 441, 482, 483

**S**

Sánchez, M., 71–73, 141, 148, 150, 151, 186, 192, 193

Sanders, B. F., 369, 370, 382

Sargison, J. E., 121

Savage, S. B., 7

Saviron, J. M., 286, 288, 294, 307, 308

Schlichting, H., 7

Schmidt, W., 293, 300

Schmocke, L., 427, 433

Schoklitsch, A., 260, 396, 399

Seabra-Santos, F. J., 462

Selby, S. M., 81, 97

Serre, F., 23, 458, 460, 461, 465

Shu, C.-W., 373, 473

Simmons, A. N., 77

Sinniger, R., 215

Sivakumaran, N. S., 196, 198, 403, 404, 446, 447, 451–453, 475

Skaugset, A. E., 77

Smolarkiewicz, P. K., 456, 461

Soares-Frazão, S., 461

Stansby, P. K., 23

Steffler, P. M., 4, 8, 19, 21, 33–36, 39, 216, 435, 464

Steger, J. L., 296

Stegun, I. A., 470

Stoker, J. J., 223, 225, 232, 239, 253, 255, 257, 260, 300, 313, 393

Strelkoff, T., 6, 7, 288, 308, 396

Sturm, T. W., 5, 30, 66, 67, 77, 98, 141, 147, 179, 180, 189, 201, 202, 237, 275, 278, 281

Su, C. H., 461

Subramanya, K., 85, 147, 156, 157, 467

Sweby, P. K., 355, 383

Synolakis, C. E., 408, 410

**T**

Tada, A., 447

Tadmor, E., 473

Temerville, A. M., 462

Terzidis, G., 288, 308, 396

Teukolsky, S. A., 134

Thom, A., 436, 437

Tingsanchali, T., 196, 198, 403, 404, 446, 447, 451–453, 475

Toman, E. M., 77

Toro, E. F., 1, 23, 203, 205, 213–216, 232, 238–240, 253, 274, 279, 283, 296, 313, 316, 317, 319, 320, 323, 327, 329–331, 347–349, 351, 354, 358, 361, 363–365,

367–369, 371, 372, 378, 424, 426, 427, 432, 435, 468, 469, 471, 494

Turkel, E., 293, 300

**V**

Vacca, A., 427

Vallentine, H. R., 436, 437

van Albada, G. D., 383

Van Dyke, M., 438

van Leer, B., 378, 383

Vazquez-Cendón, M. E., 297, 347, 351, 371, 375

Verwey, A., 29, 30, 201–203, 205, 216, 278, 365

Vetterling, W. T., 134

Vieira, D. A., 421

Vischer, D. L., 63, 64, 109, 116

Vongsaripigoon, L., 439, 447

von Kármán, T., 187

Vreugdenhil, C. B., 1, 23

**W**

Wallis, S., 420, 424, 427

Wang, S., 351

Wang, S. S. Y., 417, 419, 420, 424, 427, 430

Warming, R. F., 296

Wei, G., 467

Wendroff, B., 279, 365

White, F. M., 17, 20, 106, 119, 120, 124, 140, 203, 375

White, W. R., 59, 119, 121

Whitham, G. B., 237, 238, 260

Wilkinson, D. L., 196, 197

Williams, J., 456

Wilson, E. H., 187

Woodward, P., 378

Woodward, S. M., 147

Wu, W., 8, 29, 41, 42, 46, 47, 242, 417, 419–421, 423, 424, 427, 430

**Y**

Yen, B. C., 6–8, 17, 53, 138–141, 143

Ying, X., 351, 375–377, 402, 405–407, 425

Young, D. L., 427, 428

**Z**

Zech, Y., 461

Zerihun, Y. T., 447, 456

Zhou, J. G., 23, 385, 386, 388, 402, 468

Zhu, D. Z., 439, 440, 447, 450, 451

Ziveri, C., 385, 386, 388

Zoppou, C., 280, 281, 293, 297, 303, 321

# Subject Index

## A

Analytical solution, 163  
Approximate Riemann solver, 361

## B

Basic numerical concept, 273  
Bed deformation, 419  
Boundary condition, 161, 286, 388

## C

Channel transitions by change of bed elevation, 78  
Channel transitions by change of channel width, 89  
Comparative of numerical methods, 173  
Complete gate closure, 337  
Complete gate opening, 332  
Compound channels, 178  
Computation of steady flow profiles, 159  
Conservative property, 350  
Continuity equation, 12  
Control sections, 117  
Control volume equation for hydraulic jump, 189  
Critical flow, 67, 118  
Critical flow in arbitrary sections, 73

## D

1D cross-sectional averaged continuity equation, 41  
1D cross-sectional averaged equations, 24  
1D cross-sectional averaged  $x$ -momentum equation, 43

1D shallow water non-hydrostatic equations, 33

2D flows in horizontal plane, 19  
3D flow equations, 8  
Dam break wave, 484  
Dam break wave evolution, 405  
Dam break wave over movable bed, 426  
Dam break waves with friction, 393  
Depth-integrated equations, 5  
Dike erosion due to overtopping, 430  
Discontinuous solutions, 203  
Dry-bed treatment, 369  
Dry tailwater condition, 254

## E

Energy principle, 51  
Euler's method, 169  
Explicit and implicit scheme, 280  
Explicit integral method, 169  
Explicit scheme, 288

## F

Finite-difference approximation, 274  
Finite difference method, 273  
Finite volume method, 213, 347  
First-order upwind finite volume method, 424  
First-order upwind scheme, 376  
Flooding of an obstacle, 532  
Flow on mild slope, 175  
Flow on steep slope, 37, 175  
Flow over round-crested weir, 196, 401, 446, 475  
Flow over trapezoidal profiled weir, 456

- Flow profile for unknown discharge, 157  
 Flow profiles in prismatic channels, 147  
 Flow resistance, 139  
 Fourth-order Runge–Kutta method, 170  
 Free surface flow  
     fundamental equations, 1  
 FTCS scheme, 288  
 Fundamental equations of  
     free surface flows, 1
- G**  
 Gate flow, 132, 125  
 Gate maneuver, 332  
 Godunov first-order scheme, 358  
 Godunov-type scheme, 348  
 Godunov upwind numerical flux, 351  
 Governing equation for  
     non-uniform flow, 137  
 Gradually varied flow computation, 494
- H**  
 Hancock step, 383  
 High-order scheme, 473  
 HLL Riemann solver, 361  
 Horizontal plane, 19  
 Hydraulic jump, 98, 399  
 Hydraulic jump beyond a sluice gate, 198  
 Hydraulic jump position, 193  
 Hydrologic routing, 242  
 Hydrostatic flow, 3
- I**  
 Ideal dam break wave, 253, 392  
 Implicit integral method, 166  
 Initial and boundary conditions, 221  
 Initial condition, 285, 392
- K**  
 Kinematic boundary condition, 10  
 Kinematic wave, 234
- L**  
 Lax diffusive scheme, 290  
 Lax numerical flux, 365  
 Limitations of SWE, 241  
 Location of critical flow, 59
- M**  
 MacCormack predictor–corrector scheme, 291  
 MacCormack scheme with calibrated artificial  
     viscosity, 292  
 Method of characteristics, 217  
 Momentum equation, 13, 132
- Momentum principle, 51  
 Movable bed, 41, 417  
 MUSCL-Hancock scheme, 467  
 MUSCL-Hancock second-order TVD scheme,  
     378  
 MUSCL reconstruction, 378  
 Muskingum channel routing, 248
- N**  
 Negative surge, 232  
 Non-conservative form of SWE, 238  
 Non-hydrostatic free surface flow, 435  
 Non-hydrostatic theory, 33  
 Non-uniform flow  
     governing equation, 137  
 Numerical library, 493  
 Numerical scheme, 424  
 Numerical solution of energy-momentum  
     equations, 132
- O**  
 ODE solver, 372  
 One-dimensional Serre equations, 461  
 Open channel flow, 5  
 Open channel flow classification, 1
- P**  
 Partial gate closure, 338  
 Partial gate opening, 333  
 Picard iteration, 438  
 Positive surge, 203  
 Positive surge moving upstream, 210  
 Positive surge with friction, 308, 396  
 Possible wave patterns, 321  
 Predictor–corrector method, 172
- R**  
 Rarefaction wave, 230  
 Reservoir routing, 242  
 Reynolds’ transport theorem, 205  
 Riemann problem, 313  
 Riemann solver, 315  
 Roe Riemann solver, 368
- S**  
 Saint-Venant theory, 19  
 Sediment transport, 41, 417  
 Sediment transport closure, 421  
 Sediment transport layer, 419  
 Sequent depths for general cross sections, 101  
 Shallow water equations, 201, 417  
 Shock-capturing method, 214  
 Shock-capturing scheme, 278

- Simple wave, 230  
Singular point in free surface flows, 183  
Sketching of flow profiles, 156  
Slope limiting, 380  
Solitary wave, 464  
Solitary wave propagation, 480  
Solitary wave run-up, 408  
Source term, 425  
Specific energy head, 54  
Specific energy head for general sections, 66  
Specific momentum, 93  
Spillway crest, 441  
Stability, 280  
Stability condition, 355, 426  
Steady transcritical open channel flow, 183  
Steep slope, 445  
Subcritical dam break wave, 300  
Surge reflection at a wall, 549  
Supercritical surge, 307  
Surface gradient method, 386  
SWE in characteristic form, 217
- T**  
Total-load equation, 420  
Transcritical dam break wave, 303  
Transition from mild to steep slope, 454
- Transition from sub- to supercritical flows, 183  
Transition from super- to subcritical flows, 189  
Transitions in supercritical flow, 106  
Treatment of friction, 375  
TVD MacCormack scheme, 293  
Two-dimensional Serre equations, 456  
Two-dimensional steady potential flow, 436
- U**  
Uniform flow, 117, 138  
Uniform flow depth, 143  
Unsteady flow, 475  
Unsteady ideal fluid flow, 456  
Unsteady open channel flow, 201  
Upwind scheme, 295
- W**  
Water surface slope at critical point, 187  
Wave celerity, 228  
Wave motion, 67  
Weir flow, 119  
Well-balanced scheme, 373  
Wet tailwater condition, 260  
Wetting and drying over uneven topography, 542